International Journal of $\backslash A_{ko}\ 39164.1-EGCF$

IMPACT ENGINEERING

Editor-in-Chief
Norman JONES

HYPERVELOCITY IMPACT

PROCEEDINGS OF THE 1998 SYMPOSIUM
PART I: PAGES 1–518

Huntsville, Alabama, USA

17–19 November 1998

Guest Editor
CHARLES E. ANDERSON, JR

20000627 120

PERGAMON

REPORT DOCUMENTATION PAGE

Form Approved
OMB NO. 0704-0188

1. AGENCY USE ONLY (Leave Blank)	2. REPORT DATE - Jan 2000	3. REPORT TYPE AND DATES COVERED Final Report

4. TITLE AND SUBTITLE
HVIS98 Conference Grant

5. FUNDING NUMBERS

DAAG55-98-1-0492

6. AUTHOR(S)
William P. Schonberg, principal investigator

7. PERFORMING ORGANIZATION NAME(S) AND ADDRESS(ES)

University of Alabama in Huntsville
Huntsville, AL 35899

8. PERFORMING ORGANIZATION REPORT NUMBER

9. SPONSORING / MONITORING AGENCY NAME(S) AND ADDRESS(ES)

U. S. Army Research Office
P.O. Box 12211
Research Triangle Park, NC 27709-2211

10. SPONSORING / MONITORING AGENCY REPORT NUMBER

ARO 39164.1-EG-CF

11. SUPPLEMENTARY NOTES
The views, opinions and/or findings contained in this report are those of the author(s) and should not be construed as an official Department of the Army position, policy or decision, unless so designated by other documentation.

12 a. DISTRIBUTION / AVAILABILITY STATEMENT

Approved for public release; distribution unlimited.

12 b. DISTRIBUTION CODE

13. ABSTRACT (Maximum 200 words)

NO ABSTRACT FURNISHED

14. SUBJECT TERMS

15. NUMBER OF PAGES

16. PRICE CODE

17. SECURITY CLASSIFICATION OR REPORT **UNCLASSIFIED**	18. SECURITY CLASSIFICATION ON THIS PAGE **UNCLASSIFIED**	19. SECURITY CLASSIFICATION OF ABSTRACT **UNCLASSIFIED**	20. LIMITATION OF ABSTRACT **UL**

NSN 7540-01-280-5500

Standard Form 298 (Rev.2-89)
Prescribed by ANSI Std. 239-18
298-102

HYPERVELOCITY IMPACT

PROCEEDINGS OF THE 1998 SYMPOSIUM

Huntsville, Alabama, USA

17–19 November 1998

Guest Editor
CHARLES E. ANDERSON, JR

Published in two parts:
Part I comprises pages 1–518
Part II comprises pages 519–1024

PERGAMON

AIMS AND SCOPE

The *International Journal of Impact Engineering* exists for the publication of original research work concerned with the response of structures and bodies to dynamic loads arising from exposure to blast, collision or other impact events. The topics encompassed by the journal include the elastic and plastic response of structures and bodies to impact and blast loading, terminal ballistics, vehicle crashworthiness, containment and other processes and phenomena in which effects due to impact predominate, such as explosive welding. In addition, related matters such as research into fire hazards in association with impact loads will be included. Every paper accepted for publication is strictly refereed and assessed for its contribution to the understanding of impact phenomena or the insight gained for engineering design in areas of high rate loading.

Papers whose concerns are only in the fields of mathematics, materials science or computation are not requested. Similarly, papers whose contents are purely descriptive will not be accepted.

This journal should be of interest to engineers, designers and research workers in the fields of structural crashworthiness, energy-absorbing systems, structural failure, hazard assessments and safety calculations which involve impact loadings. Thus, papers in this journal will be of interest to aeronautical engineers, civil engineers, mechanical engineers, naval architects, nuclear engineers, ocean engineers, offshore engineers, transportation engineers and workers in other branches of engineering and science who are involved in impact loading of various kinds.

PROCEEDINGS OF THE 1998 HYPERVELOCITY IMPACT SYMPOSIUM

Contents

Contents v

EDITORIAL

This special issue of the International Journal of Impact Engineering contains the proceedings of the 1998 Hypervelocity Impact Symposium, which was held in Huntsville, Alabama, 17 - 19 October 1998.

I wish to take this opportunity to thank Charles E Anderson Jr for his considerable assistance in preparing this special issue of the International Journal of Impact Engineering. Many thanks are also due to the Organising Coimmittee of the Hypervelocity Impact Symposium

The proceedings of the 1986, 1989, 1992, 1994 and 1996 Hypervelocity Impact Symposia were also published as special issues of the International Journal of Impact Engineeering (Volume 5, Nos 1 - 4, Volume 10, Nos 1 - 4, Volume 14, Nos 1 - 4,Volume 17, Nos 1 - 6 and Volume 20, Nos 1 - 10). The next Hypervelocity Impact Symposium will be held in Galveston, Texas, USA, during 6 - 9 November 2000. Further announcements will be published in this journal as they become available.

Norman Jones

Editor-in-Chief

PREFACE

This volume contains the papers presented at the *1998 Hypervelocity Impact Symposium (HVIS 98)* held in Huntsville, Alabama, on November 17-19, 1998. This was the sixth symposium since the re-initiation of the symposia in 1986, and the proceedings for the 1986, 1989, 1992, 1994, and 1996 *HVIS* are published as Volumes 5, 10, 14, 17, and 20, respectively, of the *International Journal of Impact Engineering*. The 85 papers in this volume address advancements in the basic understanding of hypervelocity impact physics, related phenomenology, and engineering applications.

Each paper in this volume has undergone peer review by experts in their respective fields of research. The authors are to be commended for keeping to the schedule for providing their draft manuscripts for review, making appropriate modifications and corrections, and preparing the final manuscript.

A listing of the various chairmen for *HVIS 98* is given on the following page; their time and dedication greatly assisted in making the symposium a technical success. A special note of thanks to Dr. William Schonberg, the Symposium Chair, and his Technical Co-Chairs, Drs. James Wilbeck and Joel Williamsen. These gentlemen worked tirelessly to ensure a technical and social program of distinction.

There were four special plenary presentations of distinction at this symposium. These were the Distinguished Scientist Award Keynote Presentation by the 1998 award recipient, Mr. Hallock (Hal) Swift, President of Physics Applications, Inc. Hal received the Distinguished Scientist Award for his sustained leadership, innovation, and technical excellence in hypervelocity research. Mr. Swift's paper should appear in the proceedings of the next *Hypervelocity Impact Symposium*. Mr. Dennis Orphal, President of International Research Associates, gave a plenary talk entitled "Effects of Strength on the Hydrodynamic Approximation," based on a paper by C. E. Anderson, Jr., D. L. Orphal, R. R. Franzen, and J. D. Walker, *Int. J. Impact Engng.*, **22**(1), 23-43, 1999. Robert C. Cauble, at the Lawrence Livermore National Laboratory, presented "Laboratory Measurements of Materials in Extreme Conditions: The Use of High Energy Lasers for High Pressure Studies." This presentation reviewed some of the work conducted at the NOVA facility, and provided a preview of the planned capabilities of the National Ignition Facility (NIF). Dr. Cauble's presentation starts on page 87 of this volume. Professor J. A. M. (Tony) McDonnell, from the University of Kent at Canterbury, gave the plenary presentation "Building a Bridge Between Microscale and Macroscale Hypervelocity Impact Phenomena with Applications to Space Design." Dr. McDonnell's presentation is contained in this volume, starting on page 597.

We are indebted to Ms. Janet Banda who worked diligently with us to assemble this volume. She has carefully reviewed formatting of the manuscripts, contacted authors where required to ensure consistency of the format, made minor corrections, and cleaned up smudges, etc.

On a sad note, several individuals who have played a major role in hypervelocity impact research and related areas passed away between the 1996 and 1998 symposia. Andrew (Andy) E. Williams (Naval Research Laboratory), who made substantial contributions in hypervelocity research using the two-stage light-gas guns at the Naval Research Laboratory, died suddenly of a heart attack in September 1997. Andy was 57. Some of Andy's work is documented in six articles in the 1986,

1992, and 1994 symposia proceedings. Daniel (Dan) J. Steinberg (retired from Lawrence Livermore National Laboratory) died in March 1997, at age 62, approximately a year and a half after diagnosed with pancreatic cancer. Although active in many areas, Dan was internationally known for his contributions to high-pressure, high-rate numerical constitutive modeling. A summary of the Steinberg-Guinan model is in *IJIE*, **5**, 603-611, 1997. Mr. Neil Blaylock (Southwest Research Institute) died in a freak automobile accident in October 1998, at age 52. Neil played a key role in the planning and organization of the *1986* and *1989 Hypervelocity Impact Symposia*. Neil helped in establishing the Constitution and By-Laws for the *Hypervelocity Impact Society*, and in the incorporation of the *Society* in October 1988. As these proceedings were being assembled, Dr. Alexander (Alex) C. Charters, the recipient of the first Distinguished Scientist Award from the *Hypervelocity Impact Society*, died after a short illness, May 1999. Up to his death at age 82, Alex remained vigorous and active, playing tennis almost daily. Alex's Distinguished Scientist keynote presentation is published in *IJIE*, **17**, 151-182, 1995. Alex also had articles in Volumes 5 and 10 of *Impact Engineering*. Andy, Dan, Neil, and Alex—we will all miss you, but are extremely grateful for your friendship and accomplishments.

We are deeply appreciative of Professor Norman Jones, the Editor-in-Chief of the *International Journal of Impact Engineering*, and his assistance in bringing these proceedings to publication. We also thank Mr. Ian Salusbury, Publishing Editor of Engineering and Technology for Elsevier Science, for his support and attention to details. Plans are to continue the Hypervelocity Impact Symposia, and we hope that the proceedings of future symposia can also become part of the archival literature.

HVIS 98 was supported by the generous contributions of the following organizations: Alabama Space Grant Consortium, Army Research Laboratory, Army Research Office, Ernst-Mach-Institut, European Research Office, Lawrence Livermore National Laboratory, NASA/Marshall Space Flight Center, Sandia National Laboratories, University of Alabama at Huntsville, and US Army Aviation and Missile Command. The views, opinions, and/or finds contained in this volume are those of the authors and should not be construed as an official Department of the Army or Department of Energy position, policy, or decision, unless so designated by other documentation.

Charles E. Anderson, Jr.
William P. Schonberg
July 1999

HVIS 98 SYMPOSIUM CHAIRMEN

ORGANIZING COMMITTEE

Lalit C. Chhabildas
Sandia National Laboratories

Andrew J. Piekutowski
University of Dayton Research Institute

William P. Schonberg
University of Alabama in Huntsville

Charles E. Anderson, Jr.
Southwest Research Institute

Jeanne L. Crews
NASA/Johnson Space Center

Dennis Grady
Applied Research Associates

Alois J. Stilp
Ernst-Mach-Institute

SYMPOSIUM CHAIRMAN

William P. Schonberg
University of Alabama in Huntsville

TECHNICAL CHAIRMEN

James S. Wilbeck
ITT Systems Corporation

Joel E. Williamsen
University of Denver Research Institute

Publications Editor
Charles E. Anderson, Jr.
Southwest Research Institute

Awards Committee Chairman
Jeanne L. Crews
NASA/Johnson Space Center

Educational Outreach
Gordon R. Johnson

Exhibition Co-Chairmen

Lanny P. Bell
AEDC/Sverdrup Technology, Inc.

Justin H. Kerr
NASA/Johnson Space Center

SESSION CHAIRMEN

Hypervelocity Impact Phenomenology
Hallock A. Swift
Physics Applications, Inc.

Alois J. Stilp
Ernst-Mach-Institute (ret.)

Penetration Mechanics
Scott A. Mullin
Southwest Research Institute

Bert Peskes
TNO-Prins Maurits Laboratory

Analytical Techniques
William A. Gooch
U.S. Army Research Laboratory

James D. Walker
Southwest Research Institute

Pulsed Power
James R. Asay
Sandia National Laboratories

Peter Thompson
Atomic Weapons Establishment

Experimental Techniques
Michelle Rucker
NASA/White Sands Test Facility

Don Berry
Institute for Advanced Technology

Shielding
Roberto Destefanis
Alenia Aerospazio

Eric P. Fahrenthold
University of Texas at Austin

SESSION CHAIRMEN (Cont'd)

Material Response
Leonard T. Wilson
Naval Surface Warfare Center

Tim Holmquist
Network Computing Services, Inc.

Planetary Impacts
David A. Crawford
Sandia National Laboratories

Olivier Barnouin-Jha
Johns Hopkins University

Fracture and Fragmentation
Dennis E. Grady
Applied Research Associates, Inc.

Donald R. Curran
SRI International

Numerical Modelling
Klaus Thoma
Ernst-Mach-Institut

Eugene S. Hertel, Jr.
Sandia National Laboratories

Spacecraft Studies
Jennifer Robinson
NASA/Marshall Space Flight Center

Kim Luu
U.S. Air Force Research Laboratory

Special Applications
Randolph S. Coates
U.S. Army Research Laboratory

James Pearson
U.S. Army ARDEC

Glenn W. Pomykal
Lawrence Livermore National Laboratory

TRIBUTE TO BURTON G. COUR-PALAIS

DENNIS L. ORPHAL

International Research Associates, Inc., 4450 Black Ave, Suite E., Pleasanton, CA 94566

Editor's Note: The following was used to introduce Burton (Burt) Cour-Palais at the 1996 Hypervelocity Impact Symposium, held in Freiburg, Germany, 8-10 October 1996.

The Hypervelocity Impact Society is honored to present its Distinguished Scientist Award to Burton G. Cour-Palais.

All those familiar with the progressive development of spacecraft shielding against meteor and debris impact are well aware of Burt's work. For more than 30 years, beginning with Apollo, Burt has been at the forefront of designing meteor and debris protection systems. He was responsible for meteoroid environment definition and shielding design for the Apollo Command and Service Module as well as the Lunar module during the conceptual design phase. As part of this effort he laid the initial groundwork for meteoroid protection reliability calculations. He was ultimately responsible for specifying the meteor shielding requirements for the Apollo spacecraft and the astronaut's space suit.

Following Apollo, Burt continued to lead research to better define the meteor and debris threat environment, and to improve the effectiveness of shielding. As part of this effort, he analyzed data on impacts against the Apollo Command Module window as well as conducted a long series of fundamental hypervelocity impact experiments using two-stage light-gas guns.

A result of all this effort is a continually evolving set of engineering design equations for spacecraft meteor and debris shields. Burt developed the methodology, including the general form of the equations, over 30 years ago, and they are still in use today. He and others have continued to update the equations for new materials and alternative designs, based on that pioneering work. These equations are used worldwide for shield design.

Burt has played a leading role in the development of advanced concepts for spacecraft protection. Most recently he has been instrumental in conceiving and developing advanced, multi-material shields based on the concept of multi-shock effects on impacting meteors and debris. Tests and analyses of these concepts have led to engineering design equations and more effective shielding for Space Station Freedom. Burt and Jeanne Crews received a patent in 1992 for the multi-shock shield concept.

Burt was born a British citizen in India in 1925. He received his B. S. in mathematics, physics, and chemistry at St. Xavier College in Calcutta in 1945. He pursued post-graduate studies at both the College of Aeronautical Engineering in London and at the University of Houston at Clear Lake. He worked in England at Vickers-Armstrong and Bristol Aircraft from 1947 to 1957. He then went to Avro Aircraft in Canada until joining NASA in 1960. Burt became a U. S. citizen in 1966.

Over the years Burt has published a very large number of papers and NASA reports. It is probably fair to say that if one wanted to get up to speed on meteor and debris shielding, both it's history and the current state of the art, one should start by going to "Burt's literature". Burt has received many awards for his work at NASA. These include the Superior Achievement Award in 1969 and Superior Performance Awards in 1976, 1980. Burt received NASA's Sustained Superior Performance Award in 1988. In addition, Burt's research group received 13 Group Achievement Awards, beginning in 1966.

For a lifetime of superior achievement, innovation, and contribution to the discipline of meteor and debris shielding of spacecraft, and his continuing contributions to the science of hypervelocity impact in general, the *Hypervelocity Impact Society* is pleased to present the 1996 HVIS Distinguished Scientist Award to Burton G. Cour-Palais.

Editor's Note: Mr. Cour-Palais' Distinguished Scientist keynote presentation begins on page 137 of this volume.

LONG-ROD PENETRATION INTO HIGHLY OBLIQUE, WATER-FILLED TARGETS

CHARLES E. ANDERSON, JR.[*], JAMES S. WILBECK[**], and JEFFREY S. ELDER[**]

[*]Southwest Research Institute, Engineering Dynamics Department, P. O. Drawer 28510, San Antonio, TX 78228-0510; [**]ITT Industries Systems Division, 600 Boulevard South, Suite 208, Huntsville, AL 35802

Summary— Two and three-dimensional numerical simulations have been conducted to help better understand the penetration and perforation of chemical submunition targets by tungsten-alloy long-rod projectiles. In particular, the computational results are analyzed to assess modeling assumptions in the application of the modified Bernoulli model of Tate to this class of problems. For the study, the chemical submunitions were treated as long steel cylinders filled with water. Impacts near the submunition ends were neglected. Many of the simulations conducted looked at rod penetration through two successive submunitions. For purposes of the computational study, the cylinders were idealized as flat plates. The study considered three impact obliquities (60°, 70°, and 80°) and two impact velocities (2.0 and 4.0 km/s). Penetration velocities, erosion rates, and the effects of a finite projectile diameter were investigated as a function of obliquity and impact velocity. © 1999 Elsevier Science Ltd. All rights reserved.

INTRODUCTION

Analytical models are used to conduct weapon systems assessments. Such assessments typically require many thousands of cycles of the program to assess variations in engagement scenarios such as impact point, impact speed, angle of attack, and orientation of projectile and target at impact. Because the total number of cycles is large, the analytical models have to be very efficient and fast running. This last requirement generally requires that the models be relatively simple. The validity of the models are established by comparing model results to experimental data; and in many cases, experimental data are used to calibrate parameters in the model to insure that the experimental data can be reproduced. Therefore, when the models are applied to situations outside the calibration database, further work must be conducted to establish the validity of the model. A penetration model that is typical of the type of models used for such analysis is the one developed by Tate [1-3]. In addition to the models being relatively simple so as to have fast execution speeds, additional simplifying assumptions must be invoked to apply the model to geometries such as layered targets and oblique impacts. The present study examines several issues related to the applicability of this model to the penetration of complex, layered targets such as chemical submunitions.

For the cases studied, impact velocities are sufficiently high that the projectile will erode as it penetrates water. The disparate densities and strengths of the projectile and water make this problem atypical of traditional penetration problems. Therefore, the first issue of importance is: How well does the Tate model predict the penetration velocity and projectile erosion rate as a function of impact velocity?

The second issue deals with the penetration of a layered target. Real target materials bulge as the projectile nears the rear surface of the target, i.e., target resistance does not go to zero when

the projectile nose reaches the original geometric location of the rear surface of a target element [4]. Penetration resistance continues, albeit at a reduced rate. Therefore, the second issue addressed in this paper is: What should be the effective thickness of the target element to take into account perforation dynamics in some approximate manner?

The third issue deals with how to model obliquity effects with a one-dimensional model. Historically, for oblique impacts, the target line-of-sight thickness has been used to represent the target element thickness. This has certainly provided a reasonable estimate of the effective thickness for lower impact obliquities. But the interaction time between the projectile and target increases as the obliquity angle increases due to the geometric effect of a finite projectile diameter. Thus, for higher impact obliquities, how should the target element thickness be modeled to account for projectile diameter effects?

DESCRIPTION OF THE PROBLEM

The canonical problem selected for the simulations is illustrated in Fig. 1. A tungsten-alloy, long-rod projectile (diameter D of 4 mm) impacts a water-filled target at an impact velocity v. The angle of obliquity is θ, where θ is the angle between the normal to the target and the velocity vector of the projectile. The steel walls of the submunition have a thickness of 6.0 mm, which represents a thickness-to-projectile-diameter ratio of 1.5. A second water-filled submunition, identical to the first, lies behind the first submunition; the two submunitions are separated by 4.0 mm.
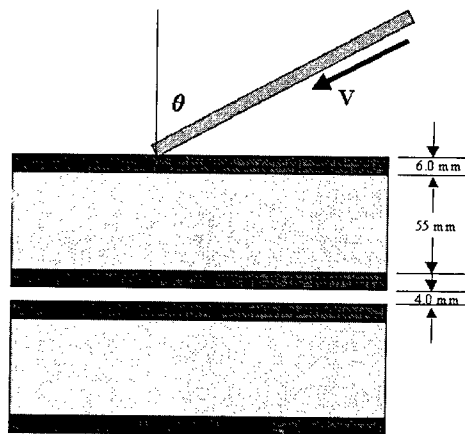
Fig. 1. Schematic of canonical impact problem.

Two impact velocities were selected for the study, 4.0 and 2.0 km/s. The obliquity angle was parametrically varied; θ's of 60°, 70°, and 80° were considered. The penetration velocity and erosion rate were response parameters of interest as a function of impact velocity v and obliquity angle θ. Effect of a finite rod diameter and any tendency of the projectile to rotate were also of interest.

NUMERICAL SIMULATIONS

The nonlinear, large deformation, multi-material Eulerian wavecode CTH [5] was used for the simulations. CTH uses a van Leer algorithm for a second-order accurate advection [6] that has been generalized to account for a non-uniform and finite grid, and multiple materials [5]. CTH also has an advanced material interface algorithm for the treatment of mixed cells [5,7]. A Mie-Grüneisen equation of state (EOS) was used to compute the thermodynamic material response. CTH allows the flow stress to be a function of strain, strain rate, and temperature [8-9]. Constitutive behavior for the materials was modeled as elastic-viscoplastic using the Johnson-Cook [10] model to determine the flow stress. The EOS for water was recently re-evaluated [11], and this revised EOS was used for these calculations.

AXISYMMETRIC SIMULATIONS

The first series of simulations idealized the problem as an axisymmetric impact problem; the 2-D cylindrical symmetry option of CTH was used. The line-of-sight thickness of the target elements was used to describe the target geometry. These simulations were used to provide the

baseline for the line-of-sight approximation, and they also permitted an evaluation of mesh convergence for the 3-D calculations.

Square zoning, with 10 zones across the projectile radius, was used to define the computational grid. The radius of the projectile used in the simulations was 4 mm, thus giving a zone dimension of 0.4 mm on a side. Square zoning was used in the direction of projectile travel, and radially for 20 mm (10 projectile radii). Beyond this radial dimension, the zoning was allowed to increase at a rate of approximately 5% to the dimensions of the target. The projectile used in the computations had a length-to-diameter (L/D) ratio of 20.

The penetration and tail velocities for the 70° case are shown as a function of time in Fig. 2; the results for both impact velocities are given. It is somewhat easier to interpret the penetration velocities if the velocity data of Fig. 2 are plotted versus penetration (eroding nose) position instead of time. Now the initial material boundaries of the target can also be plotted, as shown in Fig. 3. Referring to Fig. 3, the penetration velocities are seen to be considerably slower in the steel than in the water. The line-of-sight thickness of the metal wall is sufficiently thick for the 70° case that the projectile establishes a quasi-steady penetration rate (2.25 km/s for the 4.0-km/s impact, and 1.2 km/s for the 2.0-km/s impact). But as the projectile nose approaches the rear surface of the wall, the resistance to penetration decreases and the nose velocity increases. After perforation, the projectile nose achieves a quasi-steady-state velocity in the water of 3.27 km/s and 1.82 km/s, for the 4.0- and 2.0-km/s impact velocities, respectively. Note that the penetration velocity does not instantaneously jump from one representing penetration of metal to one of penetration of water. Instead, because of bulging of the plate, the perforation process occurs over several projectile diameters. (The 2-D axisymmetric results shown here overpredict the "duration effects" of perforation because the steel was modeled with "infinite ductility" in these simulations. Real materials will fail at some finite strain. Experiments with a variety of metal targets show that bulge heights are typically on the order of 0.5 – 1.5 projectile diameters.) After perforation of the aft steel wall of the first submunition, the nose and tail velocities begin to equilibrate; but there is not a sufficient gap between the two submunitions for velocity equilibration before the projectile strikes the steel wall of the second submunition.
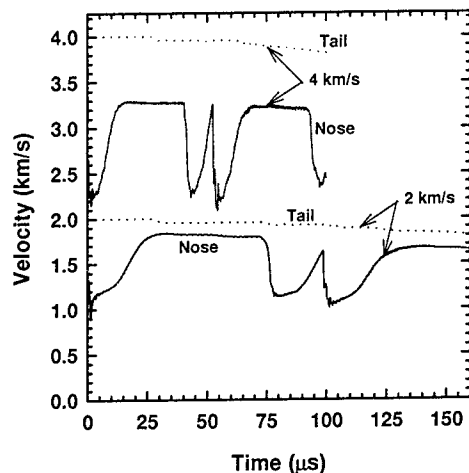
Fig. 2. Penetration and tail velocities versus time for the 70°-axisymmetric target.
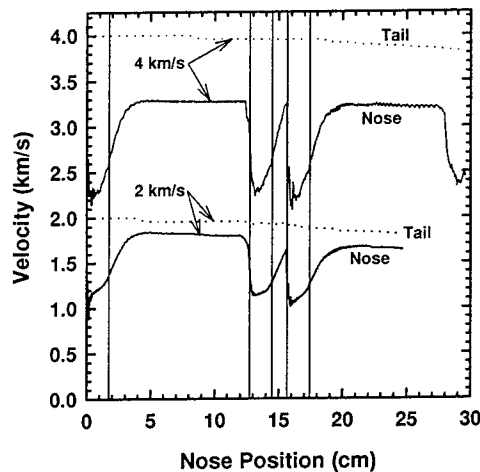
Fig. 3. Penetration and tail velocities versus position for the 70°-axisymmetric target.

The erosion rate is given by the difference of the penetration (nose) and tail velocities, that is, $(v - u)$. (Technically, this should be a negative quantity as the length of the projectile is getting shorter with time, but for the purposes here, the magnitude of the erosion rate will be plotted.) The erosion rates and the normalized lengths of the projectiles are shown in Figs. 4 and 5 for 60° and 80° obliquities. The results for the two impact velocities at each obliquity are plotted in the

same graphs since the line of sight thicknesses are the same. It should be noted that for computational efficiency, the thickness of the water was not changed as the obliquity angle increased (the line-of-sight thickness was kept constant at 110 mm); however, the line-of-sight thicknesses of the steel were scaled correctly.   In both figures the projectile is seen to have a very low erosion rate in water at an impact velocity of 2 km/s. (This corresponds to the fact that the penetration velocity in water was almost equal to the tail velocity in Figs. 2 and 3). Therefore, the projectile length decays very slowly with distance for the 2-km/s-impact case.

Penetration velocities and erosion rates were calculated for penetration into steel and water. It has been demonstrated that numerical simulations reproduce experimental results for tungsten-alloy projectiles into steel targets [12].   However, numerical simulations of a high-density projectile into a low-density target have historically been a very difficult problem computationally because of the disparate densities and strengths [13]. Therefore, before proceeding with a discussion of the 3-D results, the computational results for penetration velocities and erosion rates in the water are compared to experimental data and with hydrodynamic theory. In the remainder of the paper, because of space limitations, only the results of the 60° and 80° obliquity cases will be given. The 70° results fall between those of the 60° and 80°-obliquity cases.
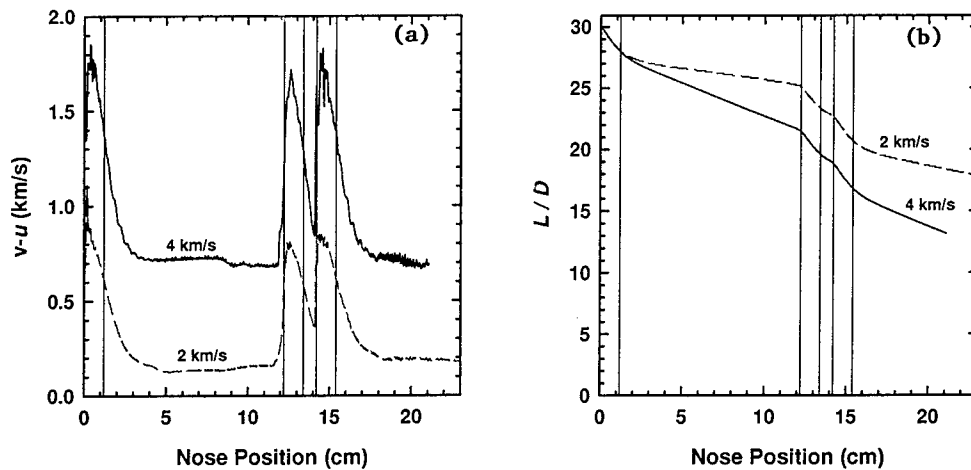
Fig. 4 (a) Erosion rate versus position for 60°-axisymmetric target;
(b) *L/D* versus position for 60°-axisymmetric target.
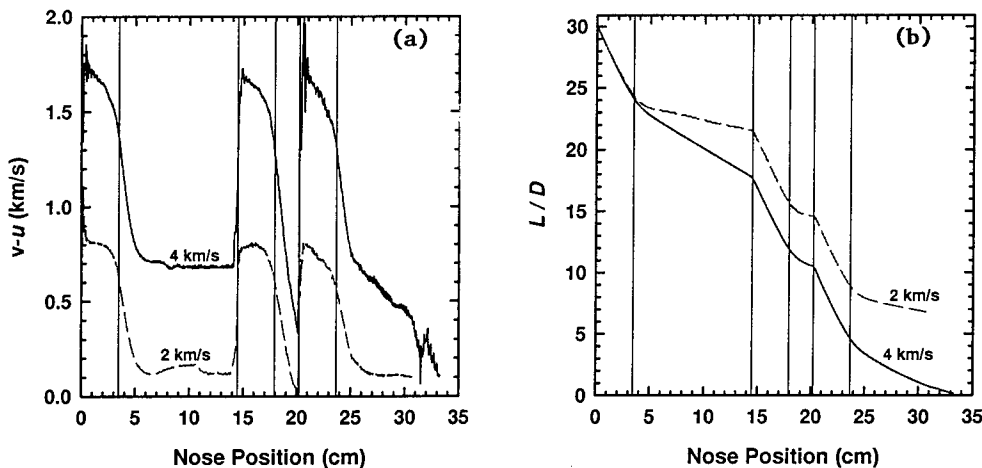
Fig. 5 (a) Erosion rate versus position for 80°-axisymmetric target;
(b) L/D versus position for 80°-axisymmetric target.

COMPARISON TO HYDRODYNAMIC THEORY

The simulation results can be compared to hydrodynamic and modified hydrodynamic theory. Steady-state hydrodynamic theory provides a relationship between the impact velocity v, penetration velocity u, and projectile and target densities, ρ_p and ρ_t, respectively:

$$\frac{1}{2}\rho_p(v-u)^2 = \frac{1}{2}\rho_t u^2 \tag{1}$$

$$u = \frac{v}{1+\beta} \qquad \beta = \left(\rho_t/\rho_p\right)^{1/2} \tag{2}$$

Because the projectile has strength and the target (water) does not, hydrodynamic theory will underestimate the penetration velocity. Equation (1) can be modified to include the strength of the projectile, Y_p:

$$\frac{1}{2}\rho_p(v-u)^2 + Y_p = \frac{1}{2}\rho_t u^2 \tag{3}$$

$$u = \frac{\left[v^2 - \left(1-\beta^2\right)\left(v^2 + 2Y_p/\rho_t\right)\right]^{1/2}}{\left(1-\beta^2\right)} \tag{4}$$

The rate of rod erosion normalized by the penetration velocity, $(v-u)/u$, also represents the length of rod eroded per unit penetration, i.e.,

$$\frac{(v-u)}{u} = -\frac{dL}{dP} = \frac{-\Delta L}{P} \tag{5}$$

where L is the projectile length, P is the depth of penetration, and the minus sign is introduced because the projectile length decreases as it erodes.

Using Eqns. (3-4), $(v-u)/u$ is calculated and then plotted versus impact velocity for various values of Y_p, Fig. 6. The dynamic flow stress for a typical tungsten-alloy projectile material is on the order of 1.0 to 2.0 GPa, depending upon the alloy. The hydrodynamic limit, i.e., $Y_p = 0$, is also shown in the figure. When the projectile has strength, there is a threshold velocity below which the projectile will not erode as it penetrates water. As shown in the figure, this threshold velocity depends upon projectile strength; the greater the strength of the projectile, the higher the threshold velocity. The theory also shows that $(v-u)/u$ becomes very steep near the threshold velocity, which suggests that experimental data near the threshold velocity will have considerable variability (similar to the residual projectile velocity near the ballistic limit velocity, e.g., see Zukas, et al. [14]).

$(v-u)/u$ is calculated from the numerical simulations by using the impact velocity and quasi-steady penetration velocity. The computational results—shown as circles—are also plotted in Fig. 6. As already stated, simple hydrodynamic theory underestimates the penetration velocity and erosion rate. Depending upon the selection of Y_p, the modified hydrodynamic theory is in good agreement with the CTH results. Assuming that the computational results are reasonably accurate, these results imply that the projectile strength in the modified hydrodynamic theory would have to be varied slightly with velocity to properly match the data. The projectile strength should be a material property, however, so such "tweaking" is not warranted. Instead, since the values of $(v-u)/u$ from the simulation and modified hydrodynamic theory are within approximately 8% of each other (using $Y_p = 1.5$ GPa), it is more appropriate to state that the modified hydrodynamic model is a "90%-accurate" model; to expect it to be more accurate is unreasonable.
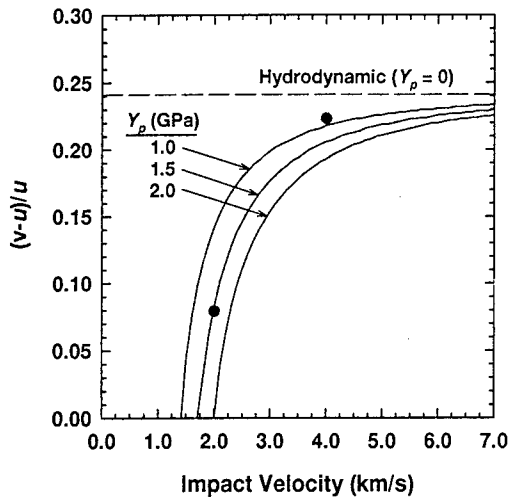
Fig. 6. Rod length loss per unit penetration into water versus impact velocity for different projectile strengths.

COMPARISON TO EXPERIMENTS

Comparing the simulation results with experiments assesses the validity of the numerically calculated penetration velocities and erosion rates in water. Williams and Dickinson [15] conducted experiments where a tungsten-alloy rod impacted a water target. They used $L/D = 3$ and 15 projectiles, and the impact velocities were varied between 2.26 km/s and 3.86 km/s. Flash X-rays were used to measure the depth of penetration into the water target and the length of the projectile as a function of time. Rod erosion was measured in all tests. The authors report that the $L/D = 15$ rods broke while penetrating the water, making measurements more difficult and questionable. The tests are summarized in Table 1.

Table 1. Summary of experiments

Test No.	Impact Velocity (km/s)	Rod Diameter (cm)	Rod Length (cm)	L/D
589	2.32	7.62	23.9	3.14
695	2.66	4.78	71.5	15.0
688	2.84	7.62	22.9	3.00
687	3.60	7.62	22.9	3.00
690	3.86	7.62	23.9	3.14

The simulations were not performed at the same impact velocities as the experiments. However, comparisons can be made between the simulations and experiments to determine whether the simulation results are in nominal qualitative agreement with those of the experiments. Penetration velocities and rod erosion (length of rod loss) obtained from the simulations are compared in Fig. 7 with those measured in the experiments.

The projectile has penetrated further and there is more rod erosion for the 4-km/s-impact-velocity simulation, compared to the 3.60-km/s and 3.86-km/s impact experiments, Figs. 7(a) and 7(b). Similarly, the penetration depth and rod erosion for the 2.0-km/s-impact simulation are less than those of the 2.32-km/s, 2.66-km/s, and 2.84-km/s impact experiments, Figs. 7(c) and 7(d). Examining eroded length more closely, it might be argued that the differences between the 3.86-km/s-impact experiment and the 4.0-km/s-impact simulation are greater than those between the 3.86-km/s and the 3.60-km/s impact experiments; thus suggesting that the simulations may be overpredicting rod erosion. On the other hand, the 2.66-km/s-impact experiment has a higher erosion rate than the 2.84-km/s-impact experiment, Fig. 7(d). Given the uncertainties observed in the experimental data and the two different rod lengths involved, it can be concluded that the simulation results for penetration into water show the correct trends and are quantitatively consistent with the existing experimental data. We note, though, that Wilson, et al. [16], have conducted a study where they specifically simulated the experiments using CTH. They find that CTH generally reproduces the experimental results but that the erosion rate is overpredicted by approximately 8%. Therefore, there may be some inaccuracies in the numerical results. Nevertheless, it has been demonstrated that the numerically calculated erosion rates are reasonably ac-

curate, and that the modified hydrodynamic (Tate) model also provides reasonably accurate estimates of the erosion rates for the impact velocities studied.
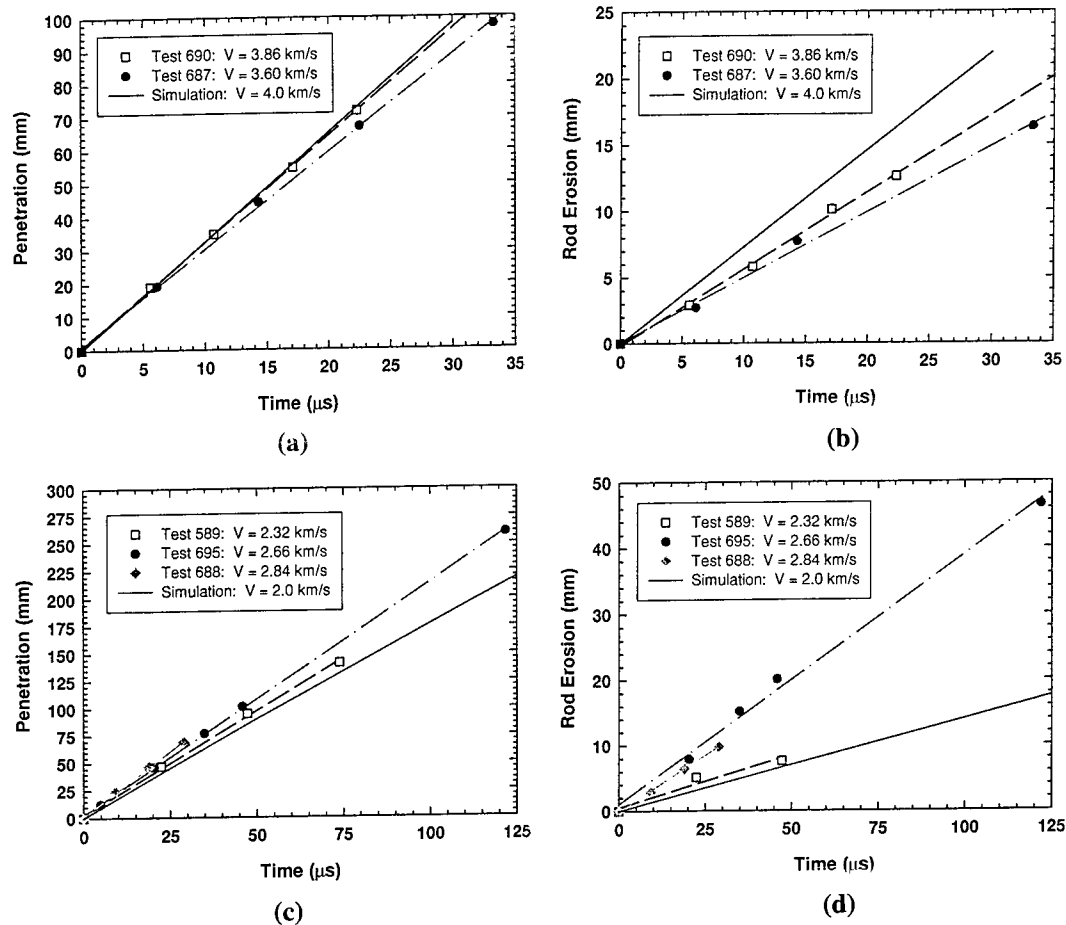
Fig. 7. Comparison of simulation results to experiments by Williams and Dickinson [15]. (a) Penetration depth versus time for v > 3.5 km/s; (b) Projectile erosion versus time for v > 3.5 km/s; (c) Penetration velocity versus time for v < 3.0 km/s; (d) Projectile erosion versus time for v < 3.0 km/s.

3-D SIMULATIONS

Zone Resolution Study

The first parametric study examined numerical convergence. The 60°-obliquity case for an impact velocity of 4.0 km/s was selected for the computational investigation. Two zonal resolutions were examined for the 3-D simulations: 4 zones across the projectile diameter, and 6 zones across the diameter. The 2-D cylindrically symmetric problem was used as the baseline; the 2-D simulation has an equivalent zonal resolution of 20 zones across the projectile diameter. Although the difference in the number of zones between the 2-D and 3-D simulations is large, Littlefield and Anderson [17] found that numerical convergence, as a function of zonal resolution, requires fewer zones in 3-D than in 2-D calculations. For the 3-D calculations, square zoning was used in the axial (z) direction; square zoning was maintained for 20 mm in the x-direction

(plane of symmetry); and square zoning was 40 mm centered on the projectile centerline in the y-direction. Outside of these regions, the zoning was allowed to grow at a rate of 5%.

The computational results are compared in Fig. 8. The 4-zone simulation underpredicts the penetration velocity in the water, and it does not resolve very well the air gap between the two submunitions. In comparison, it is seen that the 3-D results with the 6-zone mesh compare extremely well with the 2-D axisymmetric results. The primary difference between the results of these two simulations is breakout (perforation) of the metal plates. The penetration velocities are reliably reproduced, providing confidence that the 6-zone simulation is numerically resolved. Thus, the differences in breakout can be attributed to 3-D effects not captured in the 2-D simulation. The remainder of the 3-D simulations used 6 zones across the projectile diameter.

Line-of-Sight Thickness Approximation: Finite-Diameter Effects

Oblique impacts of a rod, by definition, necessitate a three-dimensional geometrical description. The application of analytical models to oblique impacts must, therefore, invoke an approximation to account for geometric effects. Typically, the thickness of material that must be penetrated is defined by the line-of-sight thickness t_{LOS}, given by the simple geometric equation:

$$t_{LOS} = \frac{t_{plate}}{\cos\theta} = t_{plate} \sec\theta$$

(6)

where t_{plate} is the plate thickness, and θ is the obliquity angle. The focus of this investigation is to determine if the line-of-sight approximation is suitable for the very large obliquities being examined here. The 2-D cylindrical symmetry option of CTH was used to calculate the penetration histories of the oblique targets where the equivalent line-of-sight thickness described the target geometry. These results are compared to full 3-D calculations of the oblique impacts.

The penetration velocities for the 60°-obliquity case are shown in Fig. 9. The penetration velocities compare reasonably well at both impact velocities. There are some small differences in the initial entry phase of the steel plate, but this is expected. The tracer point, at which the velocities are monitored, is on the projectile centerline. The edge of the projectile encounters the target before the centerline in oblique impacts (see Fig. 1). Therefore, there are some differences in the 2-D and 3-D results due to finite-diameter effects of the projectile. Slight differences in the penetration velocities are also seen in the perforation of the plates, with the 2-D results taking slightly longer in penetration depth to reach the steady-state penetration velocity into the water. These finite-diameter effects are amplified in the erosion rates, shown in Fig. 10. However, the integrated response of the erosion rate, which is loss in projectile length, is essentially the same for the 3-D result and the 2-D line-of-sight approximation, as shown in Fig. 11. Therefore, it is concluded that the line-of-sight thickness approximation as given by Eqn. (6) is accurate up to impact obliquities of 60°. However, the conclusions reached for the 60°-obliquity case were not found to be true at larger impact obliquities.

The penetration velocity for the 3-D, 80°-obliquity calculation is given in Fig. 12. Because of the very large line-of-sight thicknesses—the effect of the secant term in Eqn. (6) is to multiply the actual thicknesses by a factor of 5.76—only penetration through the first steel plate and subsequent penetration into the water are shown. The little plateau in the penetration velocity that occurs at a penetration depth of approximately 4.5 cm is a consequence of the very high impact obliquity. The penetration velocity accelerates as the projectile senses the rear surface of the steel. Due to the large obliquity, the erosion products from the projectile continue to interact—albeit quite asymmetrically—with the steel wall during the exit of the projectile from the wall.

The 3-D predictions are compared with the 2-D predictions in Figs. 12-14 for a line-of-sight thickness at 80° obliquity. The vertical dashed line represents the line-of-sight thickness at 80°. Examining Fig.12, there are again slight differences due to entrance effects. More noticeable are the remarkably different velocities during perforation of the steel plate prior to reaching a steady-state penetration velocity of 3.3 km/s in the water. These differences are amplified in the erosion
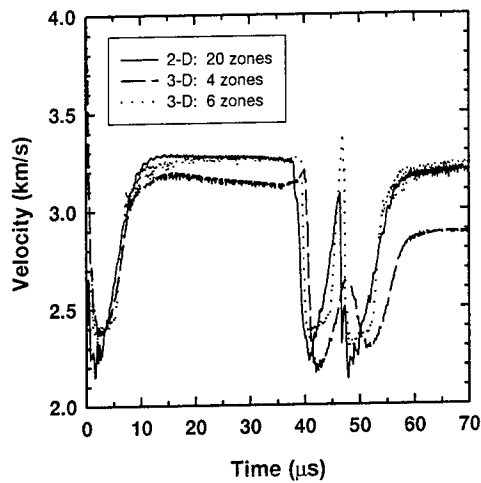
Fig. 8. Results of zoning study; the zonal resolution refers to the number of zones across the projectile diameter.
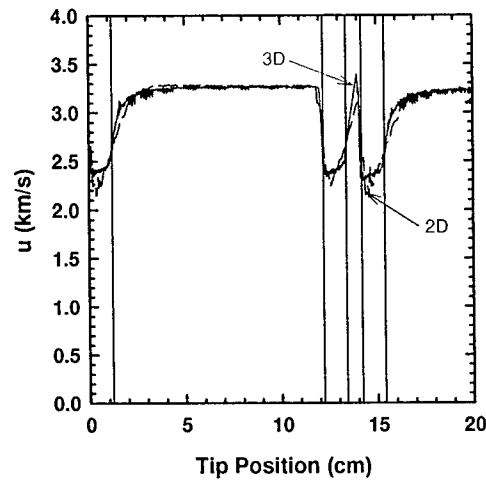
Fig. 9. Comparison of penetration velocities for 60°-obliquity impact study (4 km/s).
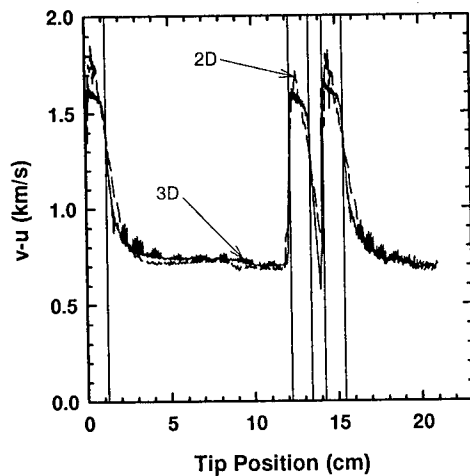
Fig. 10. Comparison of erosion rates for 60°-obliquity impact study (4 km/s).
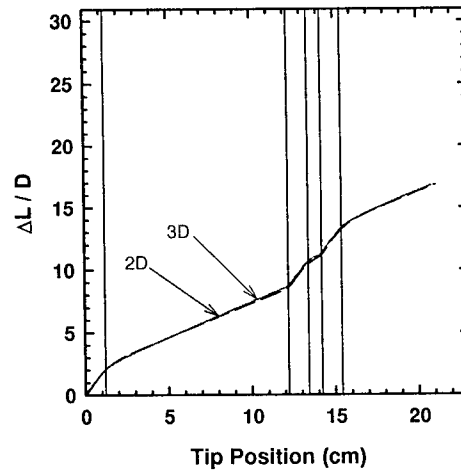
Fig. 11. Comparison of normalized projectile erosion for 60°-obliquity study (4 km/s).

rates, Fig. 13, since the erosion rate is the difference of two numbers. The normalized eroded lengths are compared in Fig. 14, and significant differences are observed between the results of the 3-D simulation and the 2-D simulation using the line-of-sight thickness approximation of Eqn. (6).[1]

The problem with the usual line-of-sight thickness approximation, as given by Eqn. (6), is that it does not take into account the finite diameter of the projectile. The projectile interacts with the

---

[1] Because of the very large obliquity angle, the centerline of the projectile is almost one-half diameter from the impact surface when the corner of the projectile first strikes the target. The zero position in Fig. 14 is taken at the impact surface. Because of the large deformation stresses resulting from the impact, the centerline length of the projectile has decreased by the time the centerline point has reached the "zero-point" surface. This results in an offset of the 3-D results, not shown in Fig. 14, compared to the 2-D results. The eroded length for the 3-D case was adjusted so that erosion began at "zero" to facilitate direct comparisons with the 2-D results.
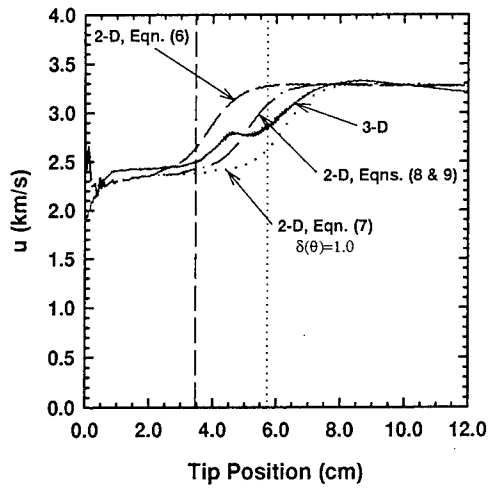
Fig. 12. Comparison of penetration velocities for 80°-obliquity study (4 km/s).
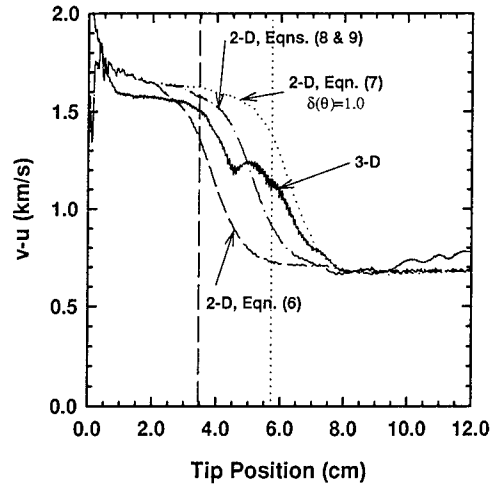
Fig. 13. Comparison of erosion rates for 80°-obliquity impact study (4 km/s).
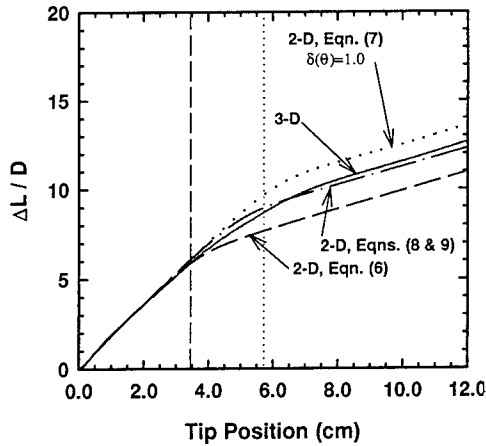
Fig. 14. Comparison of normalized projectile erosion for 80°-obliquity study (4 km/s).
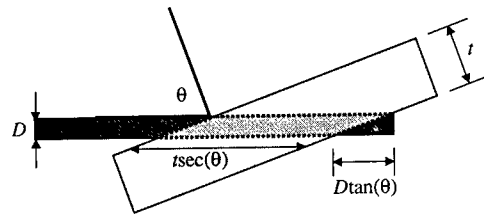
Fig. 15. Schematic of geometric model for oblique impacts.

target element over a distance $D\tan\theta$ more than the simple line-of-sight thickness, as depicted in Fig. 15, because of the finite projectile diameter. An interaction thickness $t_{interact}$ is given by:

$$t_{interact} = t_{plate}\sec\theta + \delta(\theta)D\tan\theta = t_{LOS} + \delta(\theta)D\tan\theta \tag{7}$$

where the factor $\delta(\theta)$, $0 \le \delta(\theta) \le 1$, is introduced as an adjustment factor that can depend on the obliquity angle θ. Note that the prediction using Eqn (6) is equivalent to Eqn. (7) with $\delta(\theta) = 0.0$. The 2-D results using the interaction thickness given by Eqn. (7), with $\delta(\theta) = 1.0$, are shown as the dotted lines in Figs. 12-14. The vertical dotted lines in the figures depict this effective thickness. It is seen that the adding the $D\tan\theta$ term to the line-of-sight thickness overestimates the *effective* thickness of the steel.

Equation (7) can be rewritten as:

$$t_{\text{interact}} = \frac{t_{\text{plate}}}{D} D \sec\theta + \delta(\theta) D \tan\theta = D\sec\theta \left[\frac{t_{\text{plate}}}{D} + \delta(\theta)\sin\theta \right] \qquad (8)$$

The term t_{plate}/D dominates the $\delta(\theta)\sin\theta$ term as the plate thickness becomes thick relative to the projectile diameter. Thus, whether a projectile diameter effect needs to be considered depends upon the magnitude of the first term relative to the second term.

An engineering approach was adopted to estimate the functional form of the term $\delta(\theta)\sin\theta$ in Eqn. (8). It has already been observed that the line-of-sight plate thickness is a very good approximation for three-dimensional obliquity effects for $\theta = 60°$. Evidently, the mechanics of perforation "compensate" for the increased geometric interaction of a finite-diameter projectile up to an angle of 60° (alternatively, there are compensating effects during entry and exit of the plate for $\theta \le 60°$). Thus, $\delta(\theta)\sin\theta$ should be zero for $\theta \le 60°$. After several simulations where the effective line-of-sight thickness was varied, it was determined that $D\delta(\theta)\tan\theta \approx D[\tan(80°)]/2$ provided a reasonable approximation for the increase in effective plate thickness at an obliquity angle of 80°. A continuous function with the appropriate limits at 60° and 80° is given by:

$$\delta(\theta)\sin\theta = \begin{cases} 0 & \theta < 60° \\ 1.5\sin(\theta - 60) & \theta \ge 60° \end{cases} \qquad (9)$$

The 2-D results using an interaction thickness defined by Eqns. (8-9) are shown as the dot-dashed lines in Figs. 12-14. It is observed that the prediction based upon an *effective* line-of-sight thickness given by Eqns. (8-9) captures the overall trend of penetration velocity and erosion rate of the 3-D solution better than the other two approximations. The differences in the 2-D and 3-D results for the eroded rod lengths, Fig. 14, are less than half a rod diameter.

Thus, Eqns. (8-9) provide a reasonably accurate adjustment to the effective interaction thickness of a target element impacted at very large obliquities. This is clearly a complex problem and the approximation of Eqn. (9) should be re-examined for impact conditions that are significantly different than studied here.

Projectile Rotation and/or Translation

For the studies here, the initial velocity vector of the projectile was aligned with the axis of the rod, i.e., zero angle of inclination (yaw). Tracer particles were position along the centerline of the projectile. Associated with these tracer particles are the local material (Lagrangian) velocities. These tracer particles were monitored to determine if the projectile underwent any translation or rotation due to perforation of the steel plate at the very high impact obliquities studied. Prior to impact, the lateral motion (velocity) of the projectile was zero. At the exit surface of the plate, local stresses on the projectile material cause local bending (hooking) of the rod. (Local stresses result in asymmetric deformation of the projectile as it enters the plate, but this material is eroded at the impact velocities of interest.) However, there was no translational velocity imparted to the center of mass of the projectile, nor was rotation induced about the center of mass. These results are specifically for the case where the length of the residual projectile is a number of rod diameters, and for a yaw of zero degrees. Anderson, *et al.* [18], show that a lateral translational velocity is given to a projectile for a yawed impact (but no rotation is induced), and that the translational velocity can be estimated from the encountered conditions.

SUMMARY AND CONCLUSIONS

A numerical study was conducted to examine penetration and perforation of chemical submunition targets by tungsten-alloy, long-rod projectiles. Penetration velocities, erosion rates, and

eroded lengths of the projectile at two impact velocities (2 and 4 km/s) and three obliquities (60°, 70°, and 80°) were calculated using the equivalent line-of-sight thicknesses for target elements. It was demonstrated that the simulation results were consistent with experimental data for tungsten-alloy rods into water. The computational results were compared to estimates using the modified Bernoulli model; agreement was reasonably good, and given the assumptions of the modified Bernoulli model, probably sufficiently accurate for analytical parametric studies.

Next, 3-D simulations were conducted to evaluate the accuracy of the line-of-sight approximation for oblique targets. The results demonstrated that the line-of-sight approximation provided a very good estimate of penetration response up to 60° obliquity. However, at 80° obliquity, the line-of-sight approximation was in considerable error. The disagreement between simulations and the analytical approximation was attributed to increased projectile interaction time with the target. This increased interaction time is a consequence of the finite diameter of the projectile. A revised analytical approximation that accounts for these geometric effects was proposed and compared against numerical simulations. The modified 2-D line-of-sight results were shown to be in reasonable agreement with the 3-D results.

REFERENCES

1. A. Tate, "A theory for the deceleration of long rods after impact," *J. Mech. Phys. Solids*, **15**, 287-399 (1967).
2. A. Tate, "Further results in the theory of long rod penetration," *J. Mech. Phys. Solids*, **17**, 141-150 (1969).
3. A. Tate, "Long rod penetration models—Part II. Extensions to the hydrodynamic theory of penetration," *Int. J. Engng. Sci.*, **28**(9), 599-612 (1986).
4. C. E. Anderson, Jr., S. A. Mullin, and C. J. Kuhlman, "Computer simulations of strain-rate effects in replica scale model penetration experiments," *Int. J. Impact Engng.*, **13**(1), pp. 35-52 (1993).
5. J. M. McGlaun, S. L. Thompson, and M. G. Elrick, "CTH: A three-dimensional shock wave physics code, *Int. J. Impact Engng.*, **10**, 351-360 (1990).
6. B. van Leer, "Towards the ultimate conservative difference scheme IV. "A new approach to numerical convection," *J. Comp. Phys.*, **23**, 276-299 (1977).
7. D. L. Youngs, "Time-dependent multi-material flow with large fluid distortion," *Numerical Methods for Fluid Dynamics*, pp. 273-285, Orlando (1982).
8. W. W. Predebon, C. E. Anderson, Jr., and J. D. Walker, "Inclusion of evolutionary damage measures in Eulerian wavecodes," *Comput. Mech.*, **7**(4), 221-236 (1991).
9. S. A. Silling, "Stability and accuracy of differencing methods for viscoplastic models in wavecodes," *J. Comp. Phys.*, **104**, 30-40 (1993).
10. G. R. Johnson and W. H. Cook, "A constitutive model and data for metals subjected to large strains, high strain rates and high temperatures," *Proc. 7th Int. Symp. on Ballistics*, pp. 541-547, The Hague, The Netherlands (1983).
11. C. E. Anderson, Jr., T. R. Sharron, J. D. Walker, and C. J. Freitas, "Numerical simulations of a hydrodynamic ram experiment," *Proc. Transient Loading and Response of Structures Symp.*, pp. 333-352 (M Langseth and T. Krauthammer, Eds.), Trondheim, Norway, May 25-27 (1998).
12. C. E. Anderson, Jr., D. L. Orphal, R. R. Franzen, and J. D. Walker, "On the hydrodynamic approximation for long-rod penetration," *Int. J. Impact Engng.*, **22**(1), 23-42 (1999).
13. D. L. Orphal, International Research Association, Inc., private communication (1998).
14. J. A. Zukas, T. Nicholas, H. G. Swift, L. B. Greszczuk, and D. R. Curran, *Impact Dynamics*, Chapter 5, John Wiley & Sons, NY (1982).
15. A. Williams, Naval Research Laboratory, private communication (1996): A. E. Williams and D. L. Dickinson, "Hypervelocity impact of water by a tungsten rod," presented at *47th Aeroballistic Range Assoc. Meeting*, Saint-Louis, France, Oct. 13-18 (1996).
16. L. T. Wilson, D. L. Dickinson, and E. S. Hertel, Jr., "The impact of tungsten long rod penetrators into water filled targets," *17th Int. Symp. on Ballistics*, Vol. 3, pp. 191-198, Midrand, South Africa, March 23-27 (1998).
17. D. L. Littlefield and C. E. Anderson, Jr., "A study of zoning requirements for 2-D and 3-D long-rod penetration," **Shock Compression in Condensed Matter—1995**, (S. C. Schmidt and W. C. Tao, Eds.), pp. 1131-1134, AIP Press, Woodbury, NY (1996).
18. C. E. Anderson, Jr., S. J. Bless, T. R. Sharron, S. Satapathy, and M. Normandia, "Investigation of yawed impact into a finite target," **Shock Compression of Condensed Matter—1997**, (S. C. Schmidt, D. P. Dandekar, and J. W. Forbes, Eds.), pp. 925-928, AIP Press, Woodbury, NY (1998).

BEHIND ARMOR BLAST (BAB) CAUSED BY SHAPED CHARGES

WERNER ARNOLD* and FRANK K. SCHÄFER†

*TDW Gesellschaft für verteidigungstechnische Wirksysteme mbH, Hagenauer Forst,
D - 86529 Schrobenhausen, Germany, and

†Ernst-Mach-Institut - Fraunhofer Institut für Kurzzeitdynamik, Eckerstr. 4, D - 79104 Freiburg i. Br., Germany

Summary—Steel targets were shot by shaped charges. Instead of using conventional copper liners, in this test series liners made of aluminium and magnesium were used. The jet velocities ranged from 5 to 7 mm/μs. Behind the steel target a large Behind Armor Blast (BAB) - effect occurred. The measurement of this BAB was carried out by pressure and temperature probes located at different positions. Another measured parameter was the hole size in a thin aluminium witness plate mounted 1 meter behind the steel target. For a better understanding of the physical phenomena responsible for this strong BAB effect, hypervelocity impact tests with conventional spherical projectiles were carried out. These tests were conducted on a two-stage light gas gun using Al and Mg projectiles at the same impact velocity as in the shaped charge tests. The target consisted of a thin steel plate, followed by a thin aluminium witness plate. The first tests showed comparable BAB effects. The experimental test set-up, results and interpretation of the results are reported. © 1999 Elsevier Science Ltd. All rights reserved.

INTRODUCTION

When the jet of a shaped charge from a conventional Cu liner penetrates and perforates an armor steel target, a secondary fragmentation phenomenon occurs behind the target (BAD - Behind Armor Debris). For constant target plate thickness, the intensity of this effect increases with increasing shaped charge performance (increasing overmatch) [1]. At velocities above 3000 m/s the generation of secondary fragments by a shaped charge impact is comparable to the formation of a fragment cloud induced by hypervelocity impact (HVI) on a target with a thickness comparable to the dimension of the projectiles. An essential difference to the shaped charge impact, however, lies within the fact that the target is thick compared to the jet diameter and has to be penetrated deeply until it is perforated. During shaped charge penetration into steel targets, shock waves are produced inside the target which detach from the crater ground, propagate and are reflected from the opposite surface in the form of release waves. The last thin target material layer is thus already strongly pre-shocked.

Conventional Cu liner shaped charges do not produce considerable blast pressures, they only generate BAD. This changes when aluminium or magnesium alloys are used as liner materials. Besides the secondary fragments (BAD), a considerable blast pressure represents another secondary effect. In this context we therefore refer more precisely to a Behind Armor Blast (BAB) effect.

In the frame of a test campaign the BAB from shaped charge impact on Rolled Homogeneous Armor (RHA) steel targets was studied with the liner materials copper, aluminium and a

magnesium alloy. The question was to clarify the physical origins and thus, the significant parameters of this effect. Further, the question arised if this effect is typical for shaped charges or if such blast pressures can be produced also in a conventional hypervelocity impact. For this purpose HVI tests were performed on a two-stage light gas gun, using spherical projectiles made of aluminium and magnesium alloy.

EXPERIMENTAL SET-UP OF THE SHAPED CHARGE TESTS

The set-up for the shaped charge tests is presented in Figure 1. The test chamber consists of a steel container with the dimensions 1.5 m x 1.6 m x 1.8 m (height x width x depth). The chamber can be walked in and is closed with a plywood plate from the side. This plate is decomposed by the blast overpressure created inside the chamber. Four pressure probes are attached inside the chamber. The measurement locations were chosen in order to avoid destruction of the probes by the impact of secondary fragments. Two pressure probes were attached in the upper section (head-on, side-on), another one on the sidewall behind the X-ray cassettes and the fourth on the rear wall, behind a stack of stopping and witness armor steel plates. Two temperature probes are mounted in the upper front and center chamber section, a third one in the lower center section. The shaped charge is placed outside the test chamber in a 510 mm stand-off to the 80 mm thick armor steel target. The 2.5 mm thick, 1 x 1 m² aluminium witness plate is placed 1 m behind the armor steel target plate.
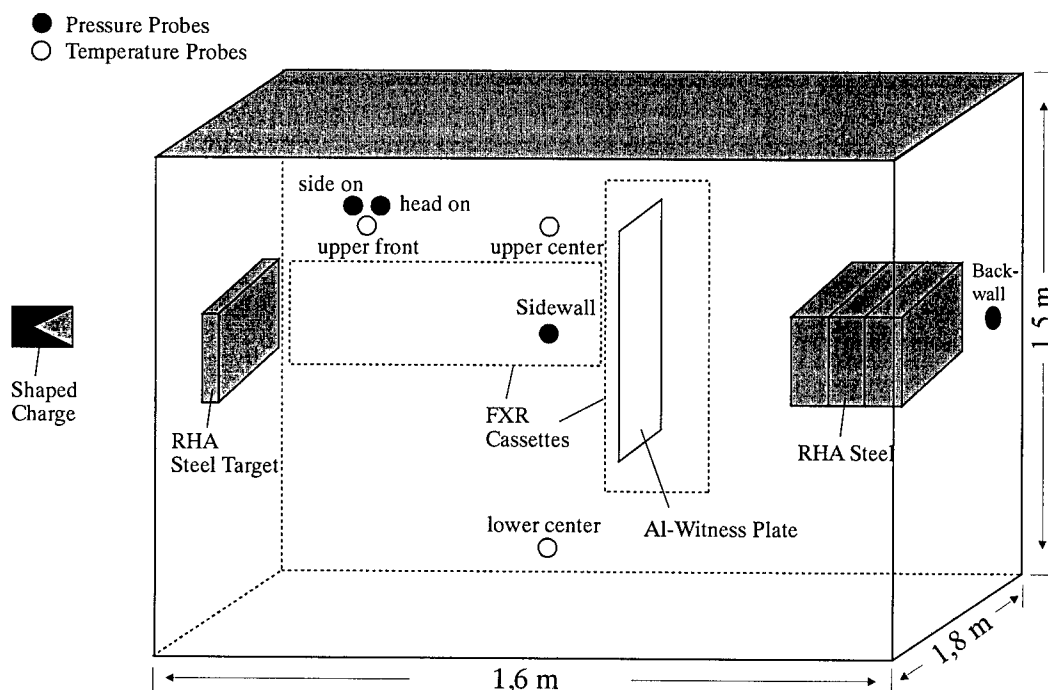
Fig. 1. Set-up for shaped charge tests

A RHA steel plate stack is located 1.8 m behind the target plate and serves to determine the residual performance of the shaped charge. Inside the chamber, X-ray film cassettes are placed to allow for X-ray flash radiography of the jet.

SHAPED CHARGE TEST PROGRAM

The caliber of the employed shaped charge was 106 mm with a charge length of 170 mm. The High Explosive (H.E.) used was cast TNT/RDX 25/75. The liner materials and basic designs were varied as follows:

Cu	liner,	angle: 60°,	wall thickness:	2.25 mm,	mass: 330 gr.
Al	liner,	angle: 90°,	wall thickness:	7.0 mm,	mass: 230 gr.
Mg alloy	liner,	angle: 95°,	wall thickness:	9.5 mm,	mass: 200 gr.

The Mg liners turned out to produce the strongest blast effects which was witnessed by a big hole produced in the aluminium plate. As a consequence, the Mg liner design was subjected to further variation with respect to the basic design:

Mg alloy	liner,	angle: 85° and 105°,	wall thickness: 9.5 mm,	mass: 227 gr. and 193 gr.
Mg alloy	liner,	angle: 95°,	wall thickness: 8.5 mm, and 10.5 mm,	mass: 185 gr. and mass: 230 gr.

In this way, jet velocity and jet shape were changed empirically. Earlier measurements had shown that the luminosity of the debris cloud increases in the material order Cu - Al - Mg. The measurement chamber was therefore filled with argon gas at atmospheric pressure during one Mg liner test to prevent reaction of the debris cloud with the oxygen comprised in the surrounding air and to allow the study of its influence on the blast effect.

SHAPED CHARGE TEST RESULTS

Figure 2 shows the increase in hole size in the aluminium witness plates obtained by the basic shaped charge designs with the liner materials Cu - Al - Mg. As the plates were illuminated from the backside, the impact holes from the secondary fragments are also visible.

Cu liner   Al liner   Mg alloy liner
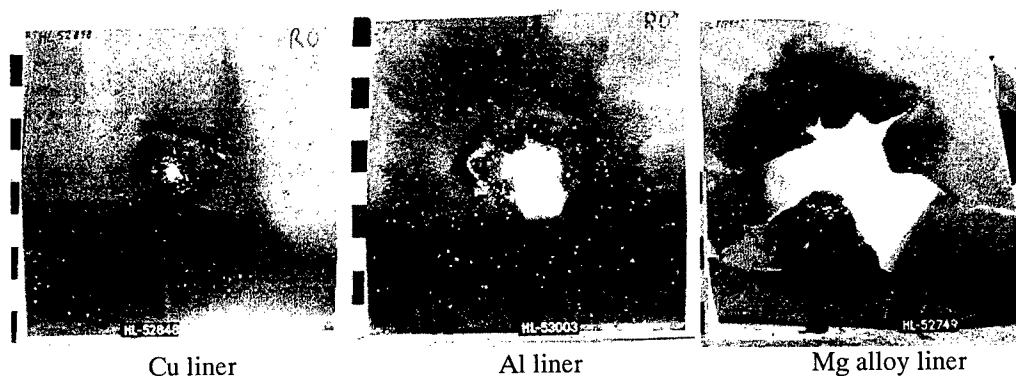
Fig. 2. Aluminium witness plate damages

The hole area in the aluminium witness plates was evaluated from its projection as shown in Figure 3. The results of all shaped charge tests are listed in table 1 and are plotted in the diagram in Figure 4. The hole from the Cu liner is essentially caused by the perforation of its jet and slug portion. The blast effect observed is insignificant. The holes created with the Al liner are

considerably bigger. Shaped charges with Mg liners however, showed the strongest blast effect relative to the other materials. The blast produced a strong petalling effect in the aluminium witness plate, i. e. cracks in the plate and lips which were bent outwards. Thus, the holes from Al and Mg shaped charges referred to in this article were not created by punching.
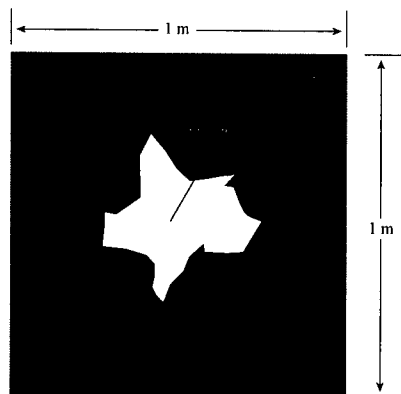
Fig. 3. Measurement of projected
hole area in Al witness plate
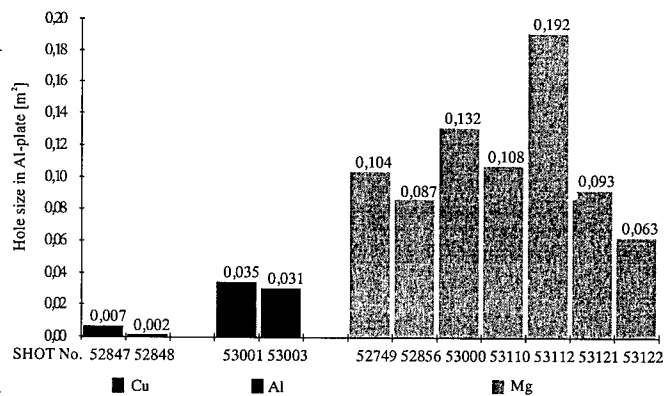
Fig. 4. Projected hole area in Al-witness plates

Table 1   Performance in RHA Steel and hole area in Al-witness plate

Test No.		Liner	Performance in RHA Steel		Hole Area in Witness Plate	
			depth [mm]	avg. depth [mm]	A [m^2]	A(avg.) [m^2]
52847	Cu	dia. 106	218		0.007	
52848	60°	2.25 mm	215	217 ± 2	0.002	0.005 ± 0.004
53001	Al	dia. 106	164		0.035	
53003	90°	7.0 mm	163	164 ± 1	0.031	0.033 ± 0.003
52749	Mg	dia. 106	99		0.104	
52856	95°	9.5 mm	89		0.087	
53000	Mg	dia. 106	96		0.132	
	95°	9.5 mm				
	Ar atmosphere			88 ± 7		0.111 ± 0.041
	Mg	dia. 106				
53110	85°	9.5 mm	85		0.108	
53112	105°	9.5 mm	81		0.192	
53121	95°	8.5 mm	85		0.093	
53122	95°	10.5 mm	83		0.063	

A comparison of the various Mg liner tests showed that the suppression of the additional energy released by the oxidation of the debris cloud (# 53000) obviously influences the blast effect in a negligible way. By variation of the liner design, different blast performances were achieved. The largest hole in the witness plate (0.192 m²) was achieved with the 105° angle and a wall thickness of 9,5 mm (# 53112). This shows that the variation of jet velocity and jet shape has a remarkable influence on the BAB performance.

In Table 1 the cumulated penetration depths of the RHA steel target plate and the RHA steel residual stack are also listed. The mean values of penetration depth and hole area in the Al witness plates for each of the liner materials are graphically presented in Figure 5. Shaped charges with Cu liners have an excellent penetration performance, but produce the smallest holes in the aluminium witness plates. Mg liners produce the largest hole sizes in the witness plates, but show poor penetration performance. Thus, blast and penetration performances are countercurrent.
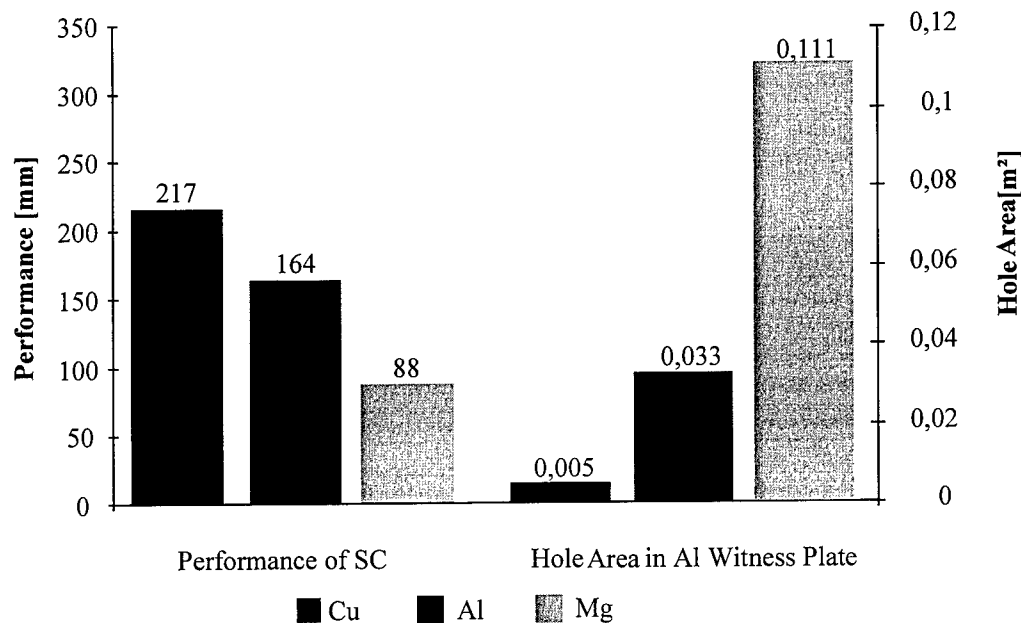
Fig. 5. Cumulated penetration depths and hole areas in the Al witness plate for various liner materials

From the measured pressure-time-histories the blast impulse was determined by time integration. In order to avoid influence of pressure reflexions, the integration was restricted to 1.3 ms. In Table 2, only mean blast pressures are provided because the pressure measurements exhibited a somewhat higher scatter than the mechanical performance, and furthermore several measurements failed due to fragment impact on gauges.

Table 2   Mean blast impulses and temperatures measured for all liner materials at different locations in the test chambers

Liner	Mean Blast Impulses [bar ms]				Mean Temperature [°C]		
	head-on	side-on	sidewall	backwall	upper front	upper center	lower center
Cu	-	0.2	-	0.1	73	70	50
Al	0.1	0.2	0.7	0.7	140	166	65
Mg	0.7 ± 0.5	0.4 ± 0.2	1.3 ± 0.3	1.5 ± 0.9	101 ± 15	115 ± 23	82 ± 3

The mean blast pressures and impulses increased considerably in the liner material sequence Cu-Al-Mg. For reasons of comparison the mean hole areas in the aluminium witness plate and the mean blast impulses measured at the rear wall position are represented graphically in Figure 6. This representation shows clearly that the big holes in the aluminium plate can be related directly to the blast pressures. Particle impact on the witness plate obviously is not the important parameter.
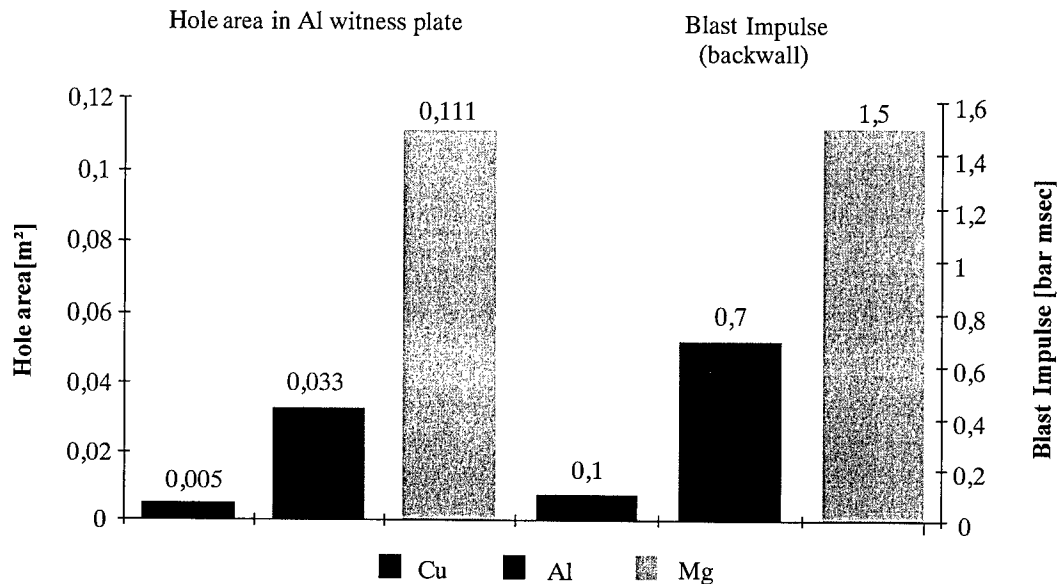
Fig. 6. Comparison between hole area in witness plate and blast impulse

The maximum temperatures were determined from the temperature versus time histories at the three different locations and are listed in Table 2. On the average, shaped charges with Al liners generate the highest temperatures, followed by shaped charges with Mg liners. This sequence is in contrast to the BAB strength. This means that oxidation rather seems to heat the gas than, to contribute to the blast pressure generation. The reason for this reverse behaviour might be the higher combustion enthalpy of Al (31.0 kJ/g) compared to Mg (24.7 kJ/g).

HYPERVELOCITY IMPACT TESTS WITH A LIGHT GAS GUN

To a reasonable approximation, hypervelocity impact (HVI) tests on thin target plates can simulate shaped charge impacts on steel targets in the last stage of penetration, just before the shaped charge jet perforates the target and enters the space behind the target. In this situation, the shaped charge has already penetrated deeply into the target and created a crater for the remaining shaped charge jet particles. In the final stage of shaped charge jet penetration into a solid target, the jet particles basically encounter just a residual thin layer of the steel target, comparable to the situation in a hypervelocity impact experiment on a thin target plate when neglecting the physical state of the shaped charge material. Figure 7 compares schematically shaped charge tests and hypervelocity impact tests.

The tests were performed in order to investigate if a blast can be produced by hypervelocity impact tests on thin target plates in a pressurized environment.

Fragments and Blast

Shaped Charge

Armor steel   Al witness plate

Fragments and Blast

Light Gas Gun

Armor steel   Al witness plate
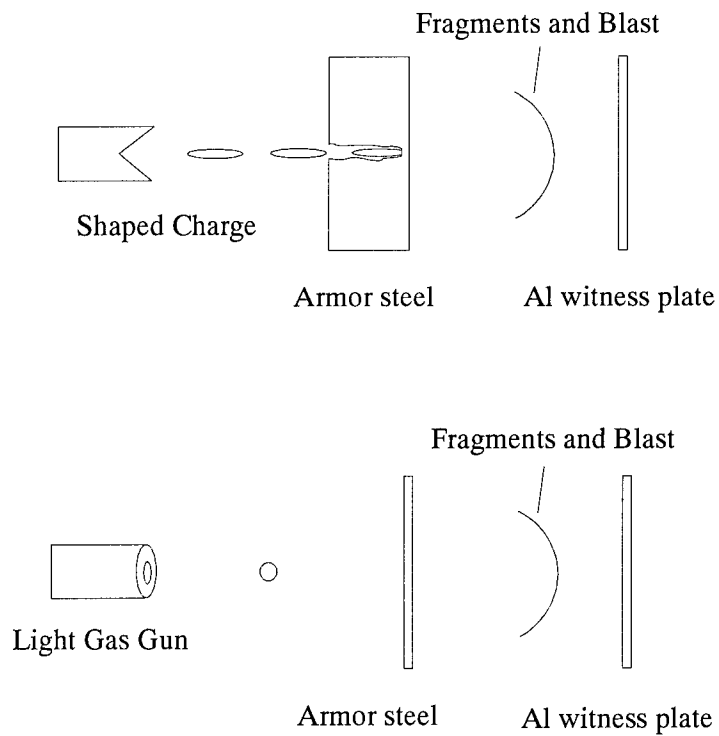
Fig. 7. Experimental simulation of shaped charge impact on RHA steel by Light Gas Gun impact tests
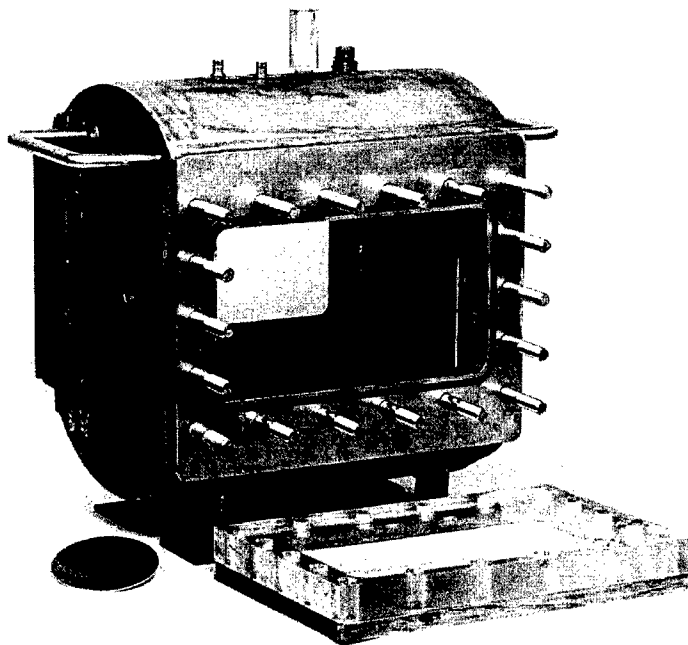
Fig. 8. Pressure container used for shaped charge jet impact simulation by Light Gas Gun impact tests

HYPERVELOCITY IMPACT TEST SET-UP

In the hypervelocity impact tests, spherical Al and Mg alloy projectiles were accelerated to jetlike velocities by means of a two-stage light gas gun [2, 3]. The target was a thin RHA steel plate, mounted in a pressure container (Figure 8). Inside the pressure container an aluminium witness plate was placed 100 mm behind the target plate. The pressure inside the container can be varied arbitrarily between fore-vacuum conditions and 25 bar. The propagation of the debris cloud was photographed in a shadowgraph technique by means of an image converter camera through side windows made of plexiglas. Details of the pressure container can be found in [4].

HYPERVELOCITY IMPACT TEST RESULTS

The test parameters and results are listed in Table 3. The test program was started with 5 mm diameter Mg alloy spheres and a 1.1 mm thick steel plate, which was followed by a 1 mm Al-witness plate at a stand-off of 200 mm. At fore-vacuum pressure, no blast effect was observed on the Al witness plate, just fragments hit the Al witness plate. The high-speed photographs of the cloud behind the steel plate are shown in Figure 9. In order to produce a blast performance, the pressure was increased to about 4 bar in the following tests, the steel plate and aluminium witness plate thicknesses were reduced to 0.30 mm and 0.50 mm respectively, and the spacing between target plate and witness plate was reduced to 100 mm. As a result, the blast was capable to deform the thin Al witness plate strongly. Furthermore, a black dust deposit was observed on the witness plate, which was indentified as Magnesium Oxide. It was thus proven that a strong blast effect can be achieved by tuning plate thicknesses, spacing and gas pressure. Furthermore it was shown that the ratio of impactor diameter to the thickness of the armor steel bumper plate is the governing parameter for the blast performance.

Table 3   Test parameters of LGG tests and rough results

Exp. No.	Air pressure [bar]	Projectile			Target thickness [mm]			performance/ blast intensity
		material	mass [g]	v [km/s]	Steel	Spacing	Al	
3492	0.15	Mg alloy	0.117	6.2	1.10	200	1.0	no blast, just fragments
3493	2.8	Mg alloy	0.117	5.7	0.85	200	0.5	no blast, just fragments and deposit of black dust
3495	3.5	Mg alloy	0.117	5.8	0.30	100	0.5	blast effect, bulging of Al-plate, black dust
3498	4.3	Al	0.176	5.8	0.25	100	0.5	strong blast effect (comparable to shaped charge), big hole in Al-plate
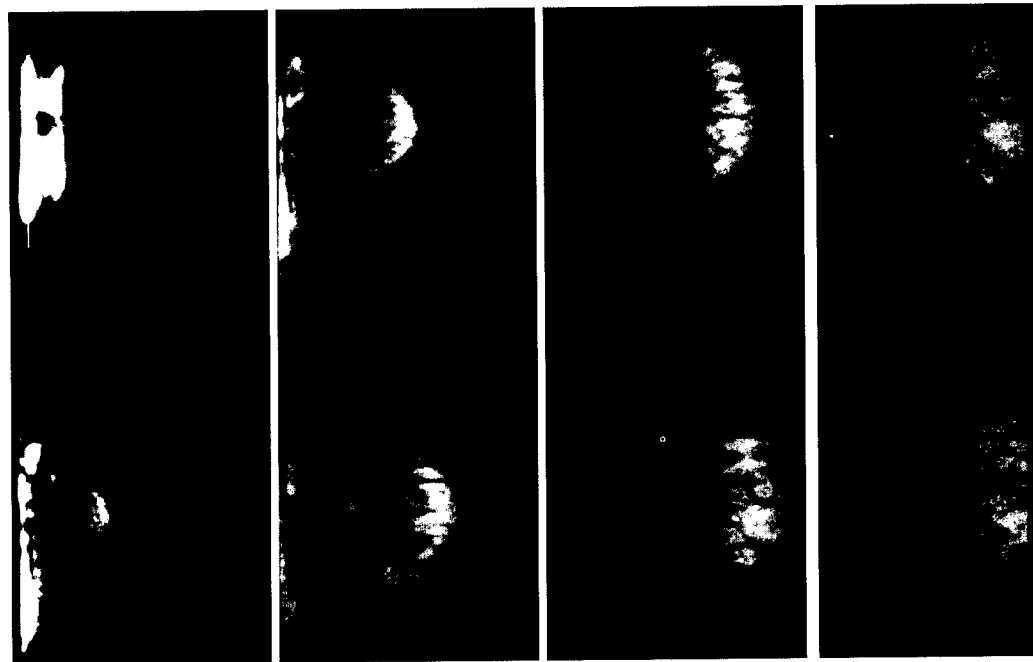
Fig. 9. Image converter photographs for HVI on steel plate in fore-vacuum conditions
using an Mg sphere (Exp. No. 3492)

A considerable BAB effect was observed with an Al sphere as projectile. A big hole was
produced in the Al witness plate by petalling. High speed image converter photographs of this
test are displayed in Figure 10, showing also the strong light flash that is generated, which
indicates oxidation reactions. The damage in the Al witness plate is shown in Figure 11.
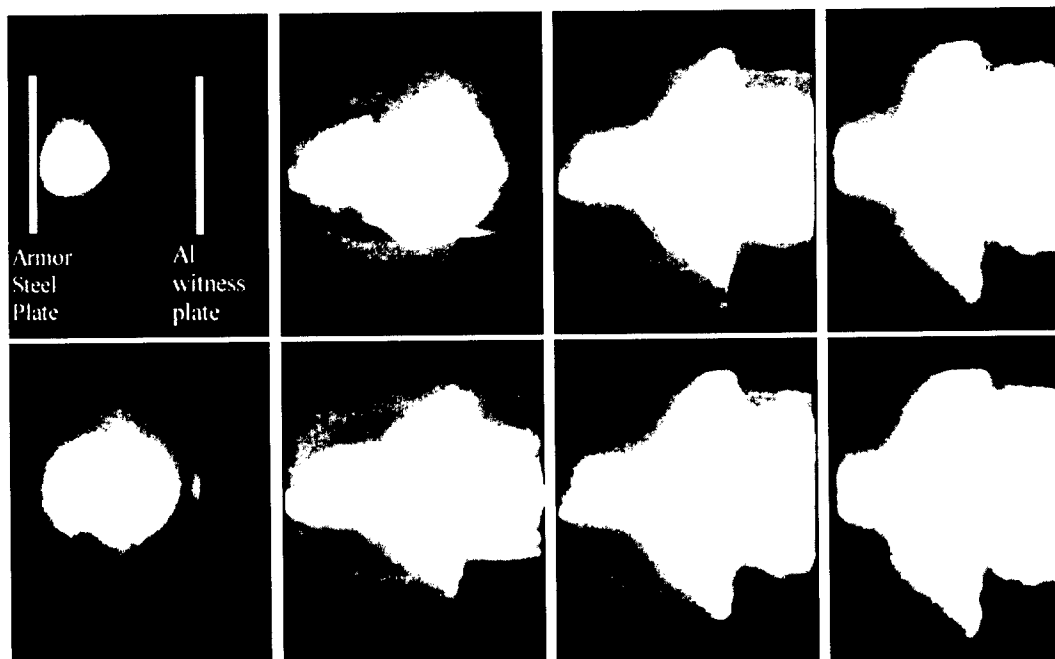
Fig. 10. Image converter photographs for HVI on steel plate in compressed air
using an Al sphere (Exp. No. 3498)

Although some differences prevent direct comparison of shaped charge tests to the hypervelocity impact tests (i. e. physical state of the jet versus "cold" hypervelocity projectile, increased pressure in the HVI tests, etc.), it can be noted that the effects of the BAB are similar in both light gas gun and shaped charge arrangements.
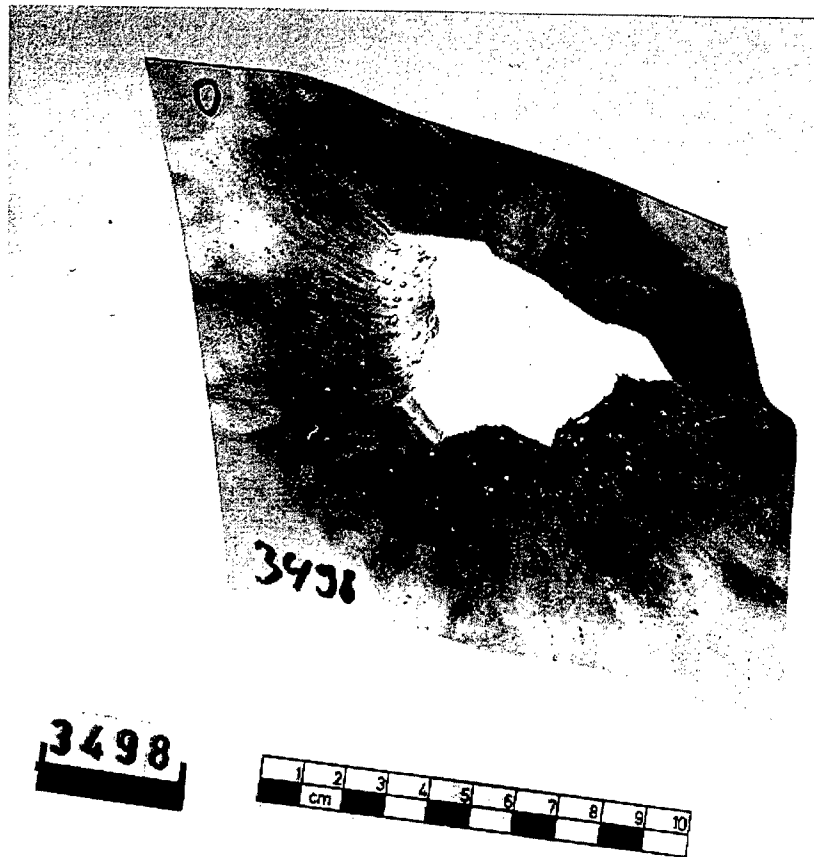
Fig. 11. Blast and impact damage in Al witness plate from Figure 10

DISCUSSION AND CONCLUSIONS

The individual phases of the penetration of a shaped charge into a steel target and the processes behind the target are illustrated schematically in Figure 12. During penetration into the armor steel target, strong shock waves are generated and propagate in the virgin material. When the shock waves reach the rear side of the armor steel plate, the shock compression wave is reflected as a rarefaction wave, thus producing tensile forces. The shaped charge jet thus penetrates into shocked and partially unloaded material. Finally the shaped charge jet reaches the rear side of the target and perforates it and produces a debris cloud analogous to hypervelocity impact on a thin plate. The remaining shaped charge jet particles penetrate undisturbed the space behind the armor steel plate and interact with the air. Particularly the first particle is strongly ablated and decelerated. This phenomenon, in turn, is referred to here as "ablation cloud". Both debris cloud and ablation cloud contribute to the integral BAB effect and thus deserve to be analyzed in more detail.
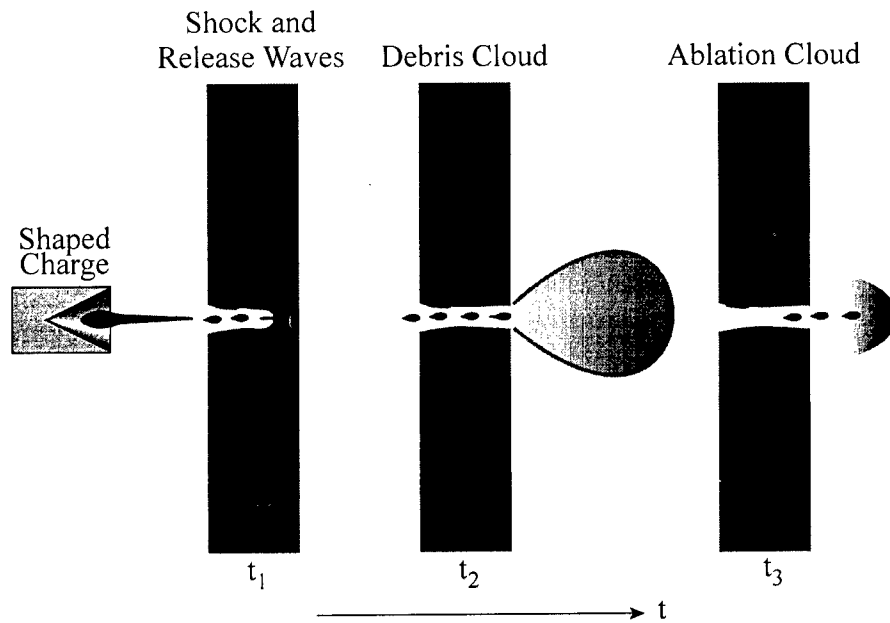
Fig. 12. Generation of blast by Mg shaped charge impact on armor steel plate

Debris cloud

The one-dimensional Hugoniot theory analogous to [5] was applied to the problem as a first order approximation. Hugoniot parameters were taken from [6]. In the pressure versus particle velocity diagram of Figure 13, the situation right before break-through of the shaped charge jet at the steel target is shown. The shock pressures in the interface between jet and target can be derived from the intersections of the corresponding Hugoniot curves. Shaped charges with copper liner have the highest shock pressures, shaped charges with Mg liner the lowest, thus the shock pressures are countercurrent to the strength of the BAB effect.
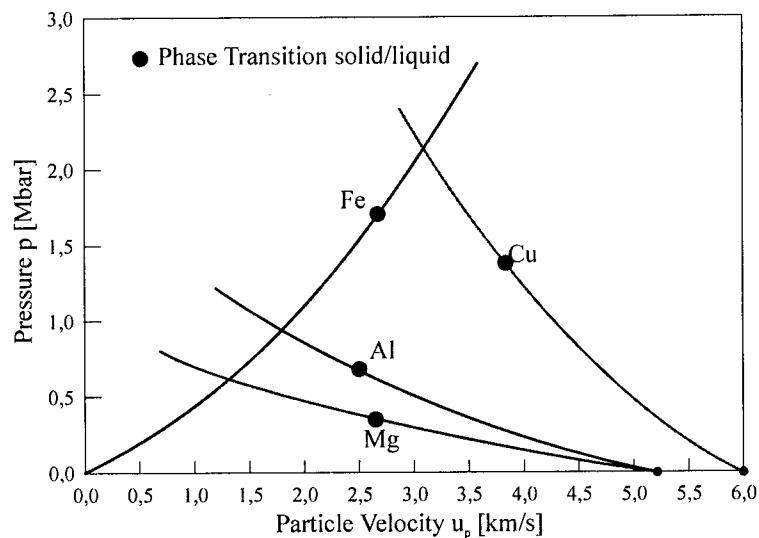
Fig. 13. Hugoniot impact pressures

Furthermore, analogous to [5] the thermal energy after release of the shock was estimated. Geometrically the thermal energy that remains in the target and in the impactor correspond to the area between the isentrope and the Rayleigh line. In a first approximation the isentrope was replaced by the Hugoniot curve. A numerical integration of the area yielded the desired thermal energy e_{th}. This energy was compared to the total enthalpy of the corresponding liner material that is needed to heat the material to the melting temperature and to melt it (e_m). The heating up of the jet during the collaps process was neglected. The results of these energy relations are listed in Table 4. From this we can conclude that the shaped charge jet energy is sufficient to melt the whole liner material during impact, thus the debris cloud consists mainly of molten droplets. This finding was supported by examination of the deposits on the aluminium witness plates. Considering the Cu liner material, part of the steel target material is likely to be molten, too. A comparison between total thermal energy and necessary melting enthalpy yields for Cu, Al, and Mg: 2.9, 2.2, and 2.9. Thus it is not possible to explain the relative intensity of the BAB effect by such energy considerations.

A more phenomenological approach to the problem consists in the structure of the shaped charge jets for the different materials. The difference between Cu and Al jets on the one hand, and Mg jets on the other hand is considerable. The jet of the former materials is composed of macroscopic particles as is well known in literature, the jet of the latter material consists of finely fragmented particles. X-ray pictures of shaped charge tests do not resolve any details of the debris- and ablation cloud. However, such pictures can be used to determine the lateral extension of the jet. The lateral extension of the Mg jet was 30 mm, the lateral extensions of the Al and Cu jets 7 mm and 4 mm, respectively. The corresponding crater diameters in the steel targets amounted to 24 mm, 31 mm, and 36 mm, each. Thus for the shaped charge with Mg liner, the jet diameter was bigger than the crater diameter in the steel target. It is reasonable to assume that in this case, the permanent interaction of the Mg jet with the crater walls leads to a strong debris cloud, increasing thus the BAB effect when Mg is the liner material. However, the difference in BAB performance between Al and Cu cannot be explained this way.

Table 4   Material properties and results from Hugoniot calculation

Parameter	Material			
	Cu	Al	Mg	Fe
Density [g/cm^3]	8.93	2.70	1.74	7.85
Melting Temperature T_m [°C]	1085	660	650	1536
Vaporization Temperature T_v [°C]	2563	2520	1090	2862
Specific Heat [J/(g°C)]	0.385	0.897	1.023	0.449
Melting Enthalpy [kJ/g]	0.207	0.397	0.345	0.247
Vaporization Enthalpy [kJ/g]	4.8	10.9	5.5	6.3
Total Melting Enthalpy e_m [kJ/g]	0.62	0.97	0.99	0.93
Jet velocity at impact v_{j0} [km/s]	6.8	6.6	6.5	
Jet velocity prior to complete perforation of steel target v_{j1} [km/s]	6.0	5.2	5.2	
Jet diameter [mm]	4	7	30	
Themal Energy after impact e_{th} [kJ/g]	1.8	2.1	2.9	
e_{th}/e_m	2.9	2.2	2.9	

Ablation cloud

The interaction of the tip shaped charge particle with air leads to ablation and deceleration. Through this interaction, the jet looses kinetic energy which can be transformed into airblast energy and thus increases the BAB performance. In [7, 8] these contributions and the lateral extension of the ablation cloud were analyzed theoretically. Using the measured jet parameters, these formulas have been applied. The calculated BAB performance as well as the lateral extension of the BAB effect increased in the order of the applied liner materials Cu, Al, and Mg, and thus correlated well with the experimental observations.

The conclusion is that although evidence of the origin of the BAB was recognized, more analysis is needed to be able to explain the dominant BAB effect when Mg is used as a liner material. To do so, both experiments and theoretical analysis have to be continued. Numerical simulations could be very helpful in this context.

ACKNOWLEDGEMENT

REFERENCES

1. W. Arnold, "F&T - Hohlladungstechnologie-Studie, Splittersekundärwirkung", Final Report, TDW-TN-TD-96-0045, 1996
2. W. D. Crozier and W. Hume, "High Velocity Light Gas Gun", J. of Appl. Phys., Vol. 28, 1957
3. A. Stilp, "Review of Modern Hypervelocity Impact Facilities", Int. J. of Impact Engng., Vol. 5, 613-621, 1987
4. F. Schäfer, E. Schneider, M. Lambert, and M. Mayseless, "Propagation of Hypervelocity Impact Fragment Clouds in Pressure Gas", Int. J. Impact Engng. Vol. 20, pp. 697-710, Pergamon 1997
5. Ch. E. Anderson, T. G. Trucano, S. A. Mullin, "Debris Cloud Dynamics", Int. J. Impact Engng. Vol. 9, No. 1, pp. 89-113, Pergamon 1990
6. R. Kinslow, "High Velocity Impact Phenomena", p. 531, Academic Press, 1970
7. T. D. Costello, J. E. Backofen, "Penetration Rate of a Shaped Charge Jet through Air under the Effects of both Erosion and Aerodynamic Drag on a Finite Tip Particle", Proc. Intern. Symp. on Ball., Vol. 7, No. 1, 1983
8. J. E. Backofen, "Shaped Charge Jet Aerodynamics, Particulation and Blast Field Modeling", Proc. Intern. Symp. on Ball., Vol. 2, 1987

USE OF Z-PINCH SOURCES FOR HIGH-PRESSURE EQUATION-OF-STATE STUDIES

J.R. ASAY*, C.A. HALL*, C.H. KONRAD* W.M. TROTT*, G.A. CHANDLER*, K.J. FLEMING*, K.G. HOLLAND*, L.C. CHHABILDAS*, T.A. MEHLHORN*, R. VESEY*, T.G. TRUCANO*, A. HAUER**, R. CAUBLE*** and M. FOORD***

Sandia National Laboratories, Albuquerque, 87185, NM; **Los Alamos National Laboratory, Los Alamos, NM,87545; ***Lawrence Livermore National Laboratory, Livermore, CA 94551

Summary — In this paper, we describe a new technique for using a pulsed power source (Z pinch) to produce planar shock waves for high-pressure equation of state (EOS) studies. Initial EOS experiments indicate that these sources are effective for shock wave studies in samples with diameters of a few millimeters and thicknesses of a fraction of one millimeter, and thus provide the possibility for achieving accuracy in shock and particle velocity measurements of a few percent. We have used the Z pinch source to produce the first in-situ time-resolve particle velocity profiles obtained with pulsed radiation sources in the Mbar regime. Particle velocity profiles obtained with a VISAR interferometer are compared with 1-D numerical simulations performed with a radiation-hydrodynamics code, ALEGRA. Good agreement with experimental results was achieved in the simulations and suggests that the Z pinch source should be a valuable tool for high-pressure EOS studies in thermodynamic regimes important to hypervelocity impact. © 1999 Elsevier Science Ltd. All rights reserved.

INTRODUCTION

There is a continuing need to determine the equation of state (EOS) and constitutive properties of materials at multi-megabar pressures in support of both weapons and non-weapons applications. Shock wave techniques have been a principal tool for determining the high-pressure equation of state (EOS) of materials in regimes inaccessible by other methods [1]. A variety of loading techniques have been developed for producing well-controlled planar shock waves for material response studies. For ultra-high EOS measurements, underground nuclear tests [2] have also been used to produce shock compression to 3000 Mbar.

High-velocity launchers remain the standard tool for these measurements. However, conventional gun technology is limited to launch velocities of about 8 km/s, which will produce shock pressures ranging from about 1 Mbar in low-Z materials to approximately 7 Mbar in high-

Z materials. Recent developments by Chhabildas et al. [3] extend gun launch capability to about 10 km/s for planar impact studies; this unique development extends the pressure range achievable with gun launchers to over 10 Mbar. However, existing scientific and programmatic applications require EOS studies to even higher shock pressures and create a need to develop other sources of shock loading.

A variety of radiation sources are being explored for accessing the extremely high-pressure states of matter. The leading candidates include high intensity lasers and pulsed power methods. Recent EOS data obtained with laser-driven shock waves have produced promising results for high-pressure EOS studies in deuterium [4]. In addition, Evans et al. [5] have used laser techniques to produce shock waves in copper to pressures of about 20 Mbar. More recently, Cauble et al. have developed a laser back-lighting technique for making absolute shock wave measurements of low atomic-number materials at extremely high pressure [6]. A limitation of laser deposition techniques is that the maximum sample sizes are typically on the order of a few hundred μm in diameter and a few μm in thickness. This restriction limits the accuracy with which these measurements can be made and also the possibilities for studying a broader range of material properties other than EOS.

Pulsed power sources are potentially attractive for planar shock wave studies because of the larger sample sizes that are possible. As an example, Baumung et al. [7] and Kanel et al. [8] are developing proton beam techniques to launch thin flyer plates of several mm diameter to velocities of about 20 km/s. Another approach is to use the intense radiation generated by imploding plasmas to produce a short burst of x-rays for ablatively driving shock waves. Fortov and coworkers [9] have previously explored this approach for EOS applications; Olson et al. [10] also used this technique for making shock velocity measurements at high pressure.

Recent advances in Z pinch technology at Sandia National Laboratories provide an opportunity to extend x-ray ablation capabilities to very high shock pressures [11]. In this approach, magnetically imploded cylindrical plasmas (referred to as the Z pinch technique) are used to produce radiation temperatures of over 150 eV in primary containment chambers [12]. The Planckian x-ray temperature produced in this way can be used to create planar shock pressures up to several tens of Mbar.

We are developing experimental techniques for making precise time-resolved measurements of planar shock waves produced by Z pinch sources. Results presented in this paper represent the first time-resolved particle velocity records obtained using a Z pinch source to ablatively shock aluminum samples to pressures exceeding 1 Mbar. These time-resolved wave profiles have been compared with 1-D computer simulations using a radiation-hydrodynamics code, ALEGRA. The good agreement achieved with the early-time shock response indicates that much of the ablation physics are properly modeled in the code and that the code can be used to both design and analyze shock wave experiments on the Sandia Z accelerator.

EXPERIMENTAL TECHNIQUE

The Z accelerator is a 4.5 MV current generator that uses 36 Marx generators in a cylindrical array to capacitively store electrical energies up to 11 MJ [11]. Parallel transmission lines conduct the electrical charge to a central target chamber, which is about 3 m in diameter. Fast switching techniques are used to produce currents up to 20 million amperes (20 MA). The resulting current flows through a cylindrical array of fine wires connecting the anode and cathode over a time interval of approximately 100 ns. The wires are thus quickly heated and form a

plasma which is magnetically imploded onto a central (Z) axis. The Z pinch thus acts as a power amplifier in converting stored electrical energy into x-ray energy over a short time interval.

An overall picture of the cathode-anode arrangement for producing high currents in a cylindrical wire array is shown in Figure 1a. Figure 1b shows a photograph of the wire array that conducts current in the center of the machine.

(a)   (b)
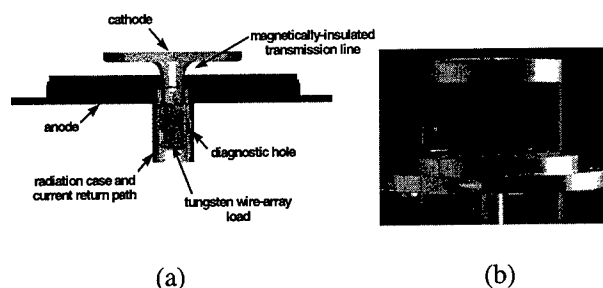
Fig. 1.   (a) Vacuum hohlraum configuration for shock wave experiments.
          (b) photograph of a typical wire array.

The sequence of events for accomplishing the plasma implosion is as follows. Typically, about 300 individual wires of tungsten with diameters of about 10 μm are arranged in a cylindrical array of 2-5 cm diameter and 1 cm long. As the wires begin to conduct current, they vaporize and form individual plasmas that coalesce into a cylindrical sheath. The azimuthal magnetic field produced by the current results in a JxB force, which implodes the wire plasmas at velocities approaching 1000 km/s [11]. Stagnation of the plasma on axis converts the plasma kinetic energy into internal energy, resulting in the production of intense x-rays.

(a)   (b)
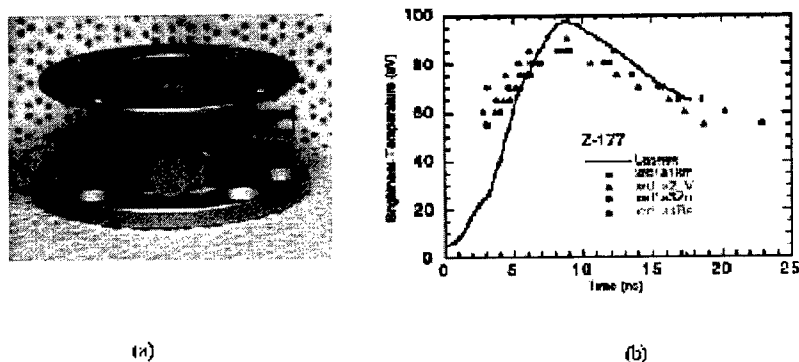
Fig. 2. (a) Photograph of hohlraum used for EOS experiments. The hohlraum is 2.5 cm diameter and 1 cm in height. (b) typical temperature history produced in the hohlraum.

The resulting x-ray energy is contained in an enclosure referred to as a hohlraum [10]. A photograph of a typical hohlraum is illustrated in Figure 2a. The surface of the hohlraum is gold coated to re-radiate the incident radiation from the pinch. Although line radiation is produced from the ionization of valence electrons during stagnation of the wire plasma, re-radiation from the walls of the holhraum produces a near-Planckian or blackbody source of radiation, which can

be used to ablatively drive shock waves. Figure 2b shows a typical temperature history with peak temperature of 100 eV measured with an XRD array on one of the experiments.

The configuration originally developed for VISAR measurements of time-resolved wave profiles on Z is illustrated in Figure 3. The typical sample is a concentric cylindrical specimen with diameters ranging from 6-9 mm and thickness of a few hundred μm. This is placed directly on the end of the secondary hohlraum and perpendicular to its axis. The objective of this configuration is to uniformly irradiate the full ablation surface of the specimen, causing a planar shock wave. The finite time duration of the radiation pulse illustrated in Figure 3b produces a ramping pressure history at the input surface x_1, followed by an attenuating pressure pulse in the sample. The objective of shock wave experiments is to choose the first step height, x_2, so that a fully developed shock is formed by that time. The second step, x_3, is chosen so that the shock wave is not significantly attenuated at that propagation distance. A series of fiber optic breakout detectors is used to measure shock arrival at the first step; a VISAR interferometer [13] is used to measure shock arrival at the second step and to simultaneously measure the particle velocity profile at that point. The combined measurements can be used to determine shock pressure and density through the shock jump conditions (1):

$$P = \rho_0\, U_s\, u_p \tag{1}$$

$$\rho_0\, U_s = \rho\, (U_s - u_p), \tag{2}$$

where P is shock pressure, ρ_0 and ρ are the initial and final densities respectively, U_s is shock velocity and u_p is particle velocity.
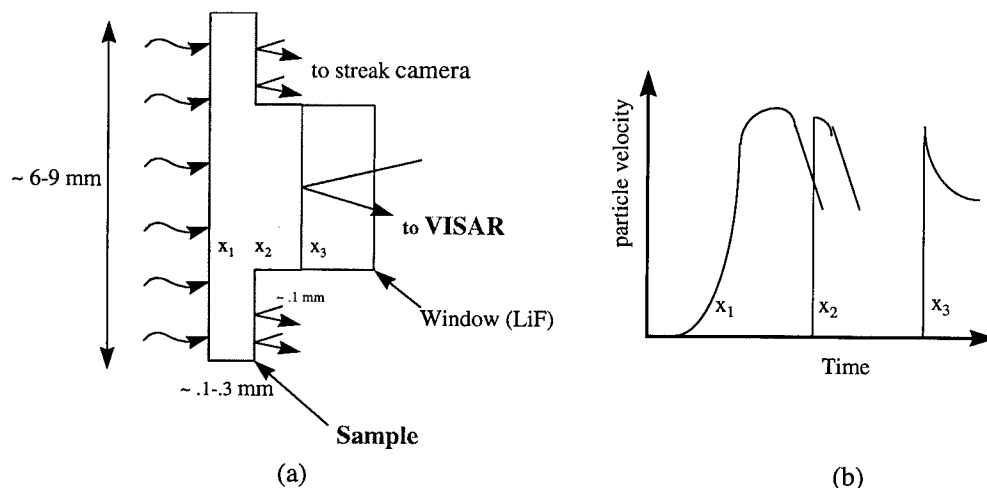
Fig. 3.   Sample configuration for EOS experiments.

Two VISAR interferometers were used to determine the extent of shock attenuation in preparation for EOS experiments planned in the near future and to also validate a radiation hydrodynamics code, ALEGRA [14] being used to help design and interpret the experiments. The configuration used to determine shock propagation is illustrated in Figure 4. In this case, a stepped aluminum sample was inverted so that radiation was incident on the stepped surface as shown. A LiF laser window [15] was bonded to the aluminum specimen with a thin layer of epoxy adhesive and used to measure the particle velocity profiles at the two sample thicknesses.

A cross-sectional view of the hohlraum configuration being used in the present shock physics experiments is illustrated in Figure 5. The primary hohlraum is about 2.5 cm in diameter and 1

cm in height. Two secondary hohlraums were used for shock experiments. The secondary hohlraums were 6 mm in diameter and either 6 mm or 8 mm in length.

A thin layer of plastic, Parylene-N[1], was placed at the entrance to each of the secondary
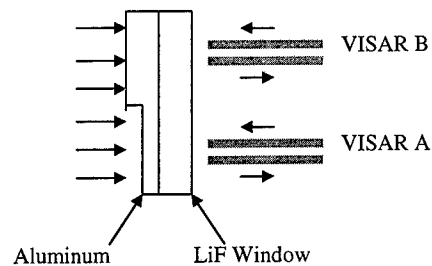
Fig. 4.   Specific sample configuration used for the present VISAR
          experiments.

hohlraums. The purpose of this layer, referred to as a burn–through foil, was to protect the sample from run-in radiation produced as the plasma shell implodes, causing the sample to change from its initial state. The plastic layers were 1.8 and 6.3 μm in thickness in the present experiments; both were effective for removing run-in radiation. In addition to the plastic films, the body of the primary hohlraum was extended a slight amount, as shown in Figure 5, to prevent direct viewing of the stagnated pinch by the ablation surface of the sample, which was mounted directly on the end of the secondary hohlraum.   XRD   diagnostics   [10]   were   used   to characterize the radiation temperature history in the primary and secondary hohlraums. These diagnostics measure the spectral intensity of the emitted radiation and are calibrated to produce a measurement of radiation temperature versus time, as illustrated in Figure 3b. The measurement was made by viewing the secondary hohlraum walls opposite the diagnostic holes, as shown in Figure 5.

In the present experiments, a specimen with two steps, as illustrated in Figure 4, allowed two separate VISAR experiments at different propagation distances in one of the secondary hohlraums, S1.   A second hohlraum, S2, contained an array of fiber optics to measure the uniformity of the drive temperature and the shock velocity through a stepped aluminum sample. The VISAR signals were transmitted from a solid state laser at a wavelength of 532 nm to the target and then to a recording station through 200–μm diameter radiation-hard optical fibers. Optical fibers, 100 μm in diameter, were used to transmit laser light from a dye laser operating at 514.5 nm to the target and then to a recording station.   Both sets of fibers were moderately shielded using a thin, flexible metallic tubing.

One of the major issues to be considered when making EOS measurements on Z is uniformity of the drive temperature. This issue refers to how equally radiation is deposited onto the area of interest.   The ablatively induced pressure is strongly dependent upon the temperature of the source and is given approximately by the equation [16],

$$P = CT^{3.5} \text{ Mbar,} \tag{3}$$

where P is the pressure behind the ablative shock, C is a constant (Mbar units), about 3 for this material and pressure regime, and T is the radiation source temperature (in 100 eV units). As inferred by Equation (3), small temperature variations cause large differences in shock pressure.

---

[1] Parylene-N is a trademark for a plastic produced by Union Carbide. Its density is 1.18 g/cm^3.

Non-uniform temperature sources therefore lead to non-planar shock fronts that cannot be accurately described by the Rankine-Hugoniot jump conditions.

We are developing the computational and experimental tools to make these hohlraum designs more uniform for EOS experiments. The experiments conducted to date have been performed in the secondary hohlraum configurations shown in Figure 5, which were designed to keep the experimental sample from directly viewing the Z pinch and thus eliminate sample preheating due
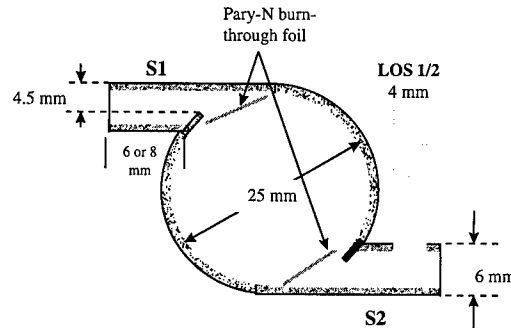
Fig. 5   Hohlraum design used for VISAR and shock breakout
         experiments.

to non-Planckian radiation. The Planckian or blackbody radiation absorbed by the sample was thus confined to re-radiation from the hohlraum walls, a condition that was originally thought to produce the most uniform drive source.

To verify these assumptions, an effort to understand and ultimately modify the source uniformity is currently underway. The purpose of the computational effort is to simulate the radiation flux in order to determine geometries that produce the most uniform radiation drive. Presently, calculations using viewfactor codes, [17], were performed to determine the effect of hohlraum geometry on drive uniformity. The radiosity simulations model the hohlraum assuming a static wall and pinch geometry, which includes the inner-reflection of radiation among surfaces in the problem. Reflecting surfaces were discretized into elements and assigned constant albedo (reflectivity) values so that the problem becomes a linear system of equations relating the energy leaving each element to the energy arriving from all other elements. The code incorporated progressive radiosity in conjunction with adaptive mesh refinement, which improves the spatial resolution on surfaces with the highest radiation flux gradients. Results of several simulations for correlating secondary geometries in the present experiments indicate that the drive conditions used in the present experiment are not optimal for producing uniform shock pressures in a tangent secondary hohlraum [17]. Thus, it is important to note that radiation-loading condition must be improved for accurate EOS measurements. In this regard, we are exploring several options for producing more uniform drives on Z. The various hohlraum options for producing better uniformity will be experimentally explored in the near future.

EXPERIMENTAL RESULTS

The experimental parameters for the VISAR shots are reported in Table I. The measured secondary temperatures in each case are presented, which show some variation due to the different lengths, volumes and Parylene thicknesses employed in the experiments. The aluminum step heights for each of the VISAR samples are also given.

The four VISAR records obtained from these experiments are illustrated in Figure 6. These results were recorded on photomultiplier tubes with time resolution of 1-2 ns. Figure 6a and 6b show the wave profiles obtained at two different propagation distances in Z189. Figures 6c and 6d represent the wave profiles obtained at two propagation distances in Z190. The initial time for each

Table 1. Experimental Parameters for VISAR Data

Exp. No.	Primary Hohlraum dia.	Secondary Temp.	Secondary Hohlraum dia.	Secondary Length	VISAR A Al step height	VISAR B Al step height
Z189[2]	25 mm	82 eV	6 mm	6 mm	154μ	308μ
Z190[1]	25 mm	77 eV	6 mm	8 mm	154μ	308μ

1. Parylene-N burn-through foil thicknesses of 6.28 microns were used at the entrance to the secondary hohlraum. The VPF was 2.095 km/s for VISAR A and 7.345 km/s for VISAR B in both experiments.
2. Parylene-N burn-through foil thickness of 1.83 microns were used at the entrance to the secondary hohlraum.
3. A 4-mm diameter diagnostic hole was mounted on the short side to allow access of XRDs for temperature measurement in shots Z189 and Z190.

record is referenced to peak pinch time, which is indicated by the vertical dashed lines. Note that the wave profile features obtained from the radiation drive are similar to those typically measured in gun experiments with the exception of the compressed time base. A distinctive feature is the small noise structure just before the main shock arrives. This is barely apparent in Figures 6a and 6c, which represent velocity sensitivities (VPF) of 2.095 km/s/fringe, but is more apparent in Figures 6b and 6d, which used VPFs of 7.345 km/s/fringe. It is thought that this electrical noise results from high-energy photons interacting with the fiber optic transmission lines occurring through a Bremsstrahlung process during formation of the pinch radiation.

We performed several experiments to characterize and minimize the radiation effect on the fibers. Use of radiation-hard pure silica fibers[1] in conjunction with moderate shielding eliminated most of the problem. Studies are in progress to further reduce the problem through additional shielding and by optimal location of the transmission fibers in the radiation environment. Some of the background noise near the peak of the shock wave is also thought to occur from this mechanism.

Figure 6a shows a sharp shock to within the noise background whereas Figure 6c shows that a slight lead-in particle velocity before main shock is observed. Lead-in pressure loading can result from the radiation produced during the implosion phase of the wire plasma, which is about 100 ns. Previous experiments demonstrated that during this interval, the plasma is radiating at a temperature of about 30 eV, which would produce initial ablation pressures up to about 45 kbar in the aluminum sample. Use of sufficiently thick plastic foils between the source and sample prevents radiation deposition on the sample until the main pinch forms at temperatures of about 140 eV. This technique therefore allows sharp shocks to form more quickly, which minimizes the required target thicknesses and reduces the amount of shock attenuation.

The inherent accuracy of the VISAR data is 0.02 fringes, or a particle velocity uncertainty of about ±0.04 km/s for VISAR A (Figures 6a and 6c) and ±0.14 km/s for VISAR B (Figures 6b and 6d). This represents about 6 kbar in aluminum. However, the accuracy of the velocity records is determined mainly by the background electro-magnetic noise in the present experiments. The background noise, which is evident in the trace just before the main shock arrives, overrides these limits, at least for the region near the shock wave front and affects the uncertainty in peak particle velocity. Work is in progress to improve the shielding of both the

---

[1] Rad hard fibers, high OH content purchased from Polymicro Inc.

photomultiplier tubes and the transmission fibers, which may also improve the VISAR records and allow the more sensitive VPF to be used. To obtain better time resolution, future VISAR experiments will include streak camera recording, which should reduce timing uncertainties to about 100 ps.

It is important to note that the peak particle velocities from Z189 VISAR A and B are nearly equal, whereas the peak velocity on VISAR B from shot Z190 is significantly less than that for VISAR A. As discussed in the next section, the shock wave is expected to attenuate over the 150 μm propagation distances used in these experiments. Thus, the similarity in amplitude for the two VISARs in Z189 is inconsistent with expected response. This discrepancy could result from the expected non-uniformity of the drive temperature or from the nominal EM-induced noise signal on the B VISARs.

Another point to note from the measured shock waves at the small and large steps is the apparent risetime for the thicker samples. For the photomultiplier system used in the present experiments, the expected risetime of step changes in pressure should be 1-2 ns. Thus, it is not clear at this time whether the apparent risetime is real or an artifact of the electronic resolution.
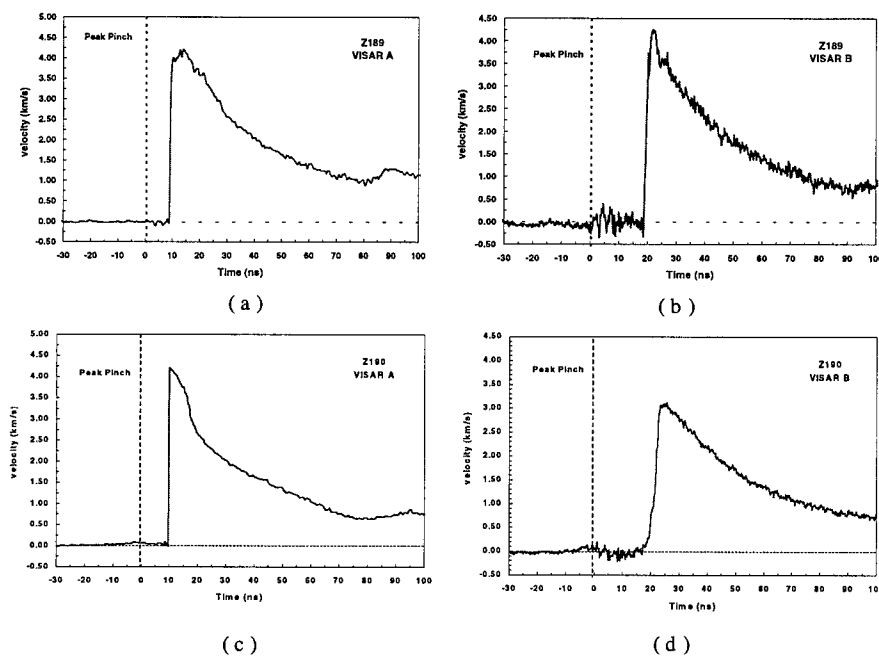
Fig. 6.   Particle velocity profiles measured at two propagation
          distances on an aluminum stepped sample. (a) 154 μm, (b)
          308 μm, (c) 154 μm, (d) 308 μm.

The unloading profiles from the peak particle velocity reflect both the input ablation temperature history and the non-linear response of the sample. The VISAR records on the small step (Figures 7a and 7c) clearly illustrate this effect, since the velocity records are concave near the peak. The velocity records on the thicker steps (Figures 7b and 7d) show the conventional convex nature, which is representative of nonlinear material response.

NUMERICAL SIMULATIONS

The ALEGRA radiation-hydrodynamics code [14] was used for numerical simulations of the experiments. ALEGRA is a multi-material, arbitrary-Lagrangian-Eulerian (ALE) strong shock wave physics code being developed at Sandia National Laboratories. It combines the features of modern Eulerian shock codes with modern finite element Lagrangian codes. In ALEGRA, ALE shock hydrodynamics is finite-element-based. In addition to the physically based shock wave hydrodynamics algorithms, a variety of coupled physics capabilities have been implemented, including coupled electro-mechanical response, magnetohydrodynamics, and radiation transport. A variety of accurate material models are being implemented, including modern EOS, constitutive and fracture models, thermal conduction behavior, radiative opacity, electrical resistivity, plasma transport coefficient, piezoelectric and ferroelectric material descriptions.

The present calculations are performed for one-dimensional motion with Lagrangian radiation-hydrodynamics. A full-range tabular SESAME EOS, #3715, was used to model aluminum [[18]. LiF was approximated as aluminum for these calculations and material strength was neglected.

The SPARTAN radiation transport method [14] was used in the simulations. SPARTAN is an implementation of a simplified PN radiation transport algorithm, SPN, which is an asymptotic treatment of PN radiation transport. Planckian radiation without multigroup effects was assumed in the calculations.

(a)   (b)
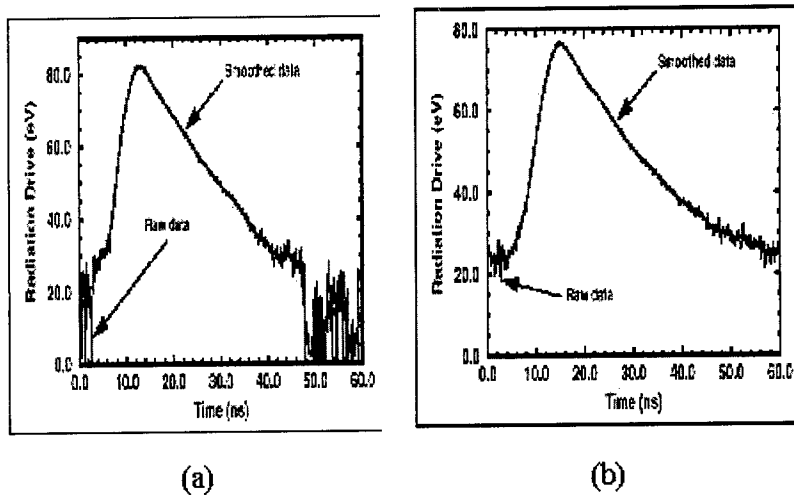
Fig. 7.   Drive temperatures used in numerical simulations (a)
           Z189; (b) Z190.

Figure 7a shows the measured Planckian drive data for Shot Z189, along with a smoothing of the raw data. Figure 7b shows the corresponding data for Shot Z190. A 1-D capability of the basic hydrodynamic computational algorithms is not presently available in ALEGRA. Hence, the "1-D" response for the Z189 and Z190 experiments was simulated using a two-dimensional configuration with a single line of finite elements having boundary conditions appropriate to 1-D

uniaxial strain. For this case, the mesh was divided into two regions. In the first, which contained 40 elements, a variable mesh was used that starts with a very fine element of approximately 0.4 mm width at the boundary where the Planckian radiation boundary condition is applied. The mesh was configured to grow uniformly in the second region to obtain good numerical matching. Symmetry boundary conditions were applied to the top and bottom of the mesh for both radiation and hydrodynamic motion. The hydrodynamic constraint effectively enforced 1-D uniaxial motion.

Figure 8 shows the calculated and experimental records for Z189. The time bases of both VISAR records have been adjusted to pinch time, but there has been no shifting of either record to obtain the appropriate shock arrival. For the thin step, the calculated shock arrival is in good agreement with experiment; for the second step, there is a discrepancy of 3 ns which is within experimental error.

<div align="center">(a)   (b)</div>
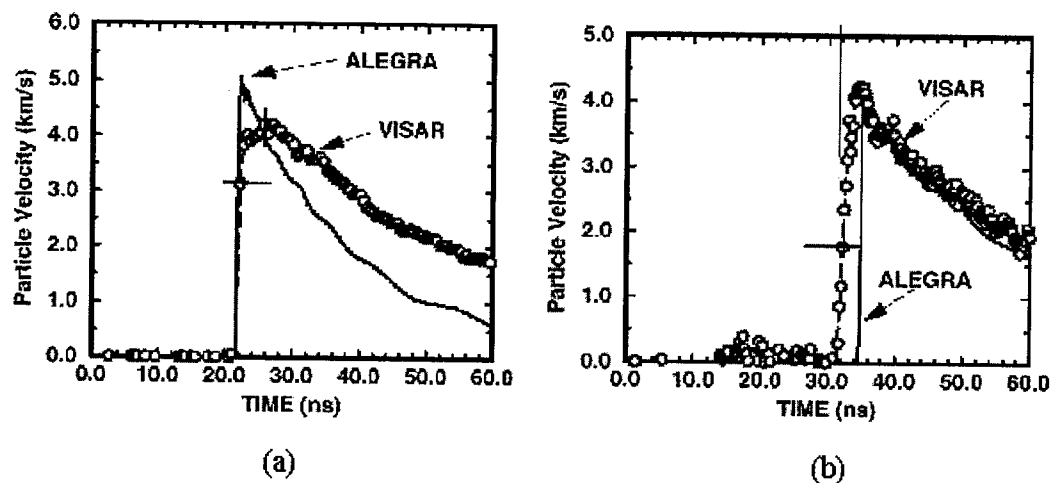
Fig. 8. Comparison of computed and measured particle velocity histories for Z189. The non-peak error bars are smaller than the size of the data symbols. (a) 154-μm sample. (b) 308-μm sample.

Shot Z190 is nearly a repeat of Z189 with the exception of small variations in drive temperature (77 eV in Z190 versus 82 eV in Z189). Since the measured peak drive temperature is smaller for Z190, the calculated shock amplitudes are also smaller (roughly in the ratio of the scaling relation reported in Equation 1). However, the calculations showed that a finite risetime to peak drive temperature in Z190 was still present in the pressure at 100 μm thickness, unlike the case for Z189 where a sharp shock was observed at 100 μm. The risetime essentially vanished by the time the shock propagates to the experimental observation thickness of 154 μm. The experimental VISAR data for Z190 are compared with numerical simulations in Figure 9.

The finite gradient observed can not be explained in terms of the computational results. As discussed earlier, this effect could result from electromagnetic noise problems or from a finite glue bond thicknesses. In addition, a diagnostic hole was located on the secondary hohlraum that the VISAR measurements were made in shot Z190, which may also have created a highly non-uniform illumination of the temperature drive side. We are planning additional calculations to study potential temperature heterogeneities associated with the drive conditions and to understand the effects of the diagnostic hole closure on the accuracy of the temperature drive.

SUMMARY

The ability to make measurements relevant to EOS and constitutive material properties using Z pinch technology has now been demonstrated. This paper presents the first time-resolved particle velocity measurements of 1.2 Mbar-shock waves produced in aluminum with a Z pinch source. These results have been compared with numerical simulations from a radiation-hydrodynamics code, ALEGRA, to evaluate the experimental design and to validate ALEGRA for radiation deposition calculations. Good agreement was obtained for one-dimensional
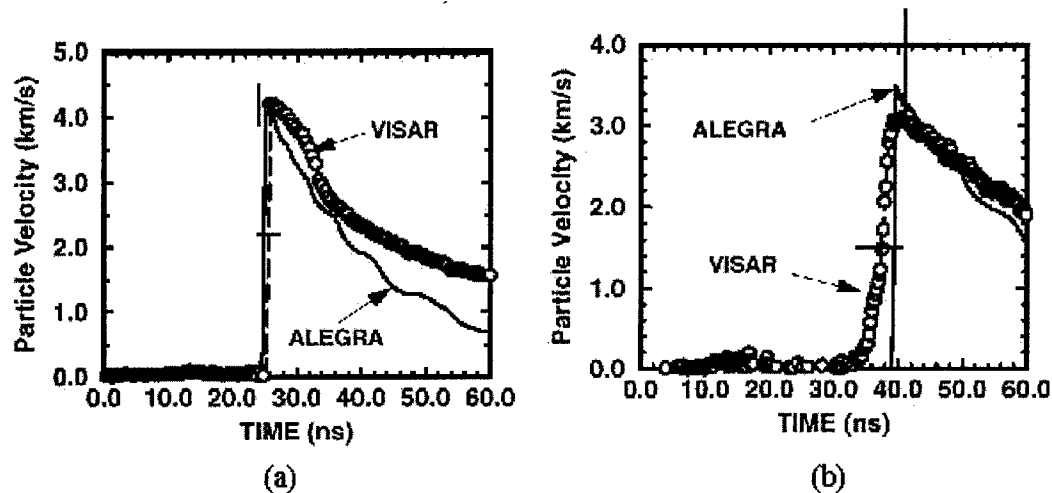
Fig. 9. Comparison of computed and measured particle velocities for
Z190. The non-peak error bars are smaller than the data
symbols. (a) 154.μm sample. (b) 308 μm sample.

simulations of the experiments, except for the late-time divergence which may be due to hohlraum dynamic effects such as closure of the diagnostics hole used for viewing the wall temperatures. These results show that (1) the ablation physics of aluminum are properly modeled in this temperature regime, (2) the Hugoniot and unloading response of aluminum is adequate at shock pressures of about 1.2 Mbar, and (3) with further improvements, the experimental configuration should be useful for EOS work in support of hypervelocity impact phenomenology.

These experiments also indicate that, with further development, it should be possible to tailor the input profile to allow a variety of EOS and material property data, such as isentropic EOS, shock-induced compressive strength, dynamic tensile strength, kinetics of phase transitions, and surface stability studies. Achieving this goal will require major improvements in the precision and control of the loading technique and the recording diagnostics. First, the effects of Bremsstrahlung-induced radiation effects on optical components should continue to be assessed and minimized. Second, the time-resolution of the recording diagnostics must be improved to 100 ps or better. Third, the temperature drive must be improved to provide uniformity to within ½% or better over a 2-mm diameter sample. Fourth, the ability to control the pressure loading history must be developed, including the ability to maintain constant pressure for times of about 10 ns.

REFERENCES

1. J.R. Asay and G.I. Kerley, G.I., "Response of Materials to Dynamic Loading", *J Impact Engng.* **5**, 69 (1986).
2. C.E. Ragan III, *Phys. Rev.* **A25**, 3360 (1982).
3. L.C. Chhabildas, L.M. Barker, J.R. Asay, T.G. Trucano, G.I. Kerley and J.E. Dunn, "Launch capabilities to over 10 km/s", Proceedings of the 1991 APS Topical Conference on Shock Waves in Condensed Matter, Williamsberg, VS, June 17-20, (1991).
4. G.W. Collins et al. *Science* **281**, 1178 (1998).
5. A.M. Evans et al., *Laser and Particle Beams* **14**, 113 (1996).
6. R.Cauble, et all, "Absolute Equation-of-state data in the 10-40 Mbar regime", *Phys Rev. Lett.*, **6**, 1248 (1998).
7. K. Baumung et al., *Laser and Particle Beams* **14**, 181 (1996).
8. G.I. Kanel, "Applications of the Ion Beam Technique for Investigations of Hypervelocity Impacts", Proceedings of the 1998 HVIS, Huntsville, AL, Nov., (1998).
9. V. Fortov et al., *Shock Compression of Condensed Matter 1995* Proceedings, Seattle, WA 370,Part 2,1255-1258,(1995).
10. R.E. Olson et al., *Phys. Plasmas*, Volume 4, May (1997).
11. M.K. Matzen, *Phys. Plasmas* **4** (5), 1519 (1997).
12. J.L. Porter, private communication (1998).
13. L.M. Barker and R.E. Hollenbach, *J. Appl. Phys.* **45**, 4872-4887, (1974).
14. K.G. Budge and Peery, J.S. *J. Impact Engng.* **14**, 107-120 (1993).
15. J.L. Wise and L.C. Chhabildas, "Laser interferometer measurements of refractive index in shock compressed materials", from Shock Waves in Condensed Matter, Ed. By Y.M. Gupta, Plenum Publishing, (1986).
16. J. Lindl, "Development of the indirect-drive approach to inertial confinement fusion and the target physics basis for ignition and gain", *Physics of Plasmas*, Nov. (1995).
17. R. Vesey, to be published (1998).
18. Los Alamos National Laboratory Equation of State library.

A WIEN DISPLACEMENT LAW FOR IMPACT RADIATION

JAMES K. BAIRD* and THOMAS R. KING**

*Department of Chemistry, University of Alabama in Huntsville, Huntsville, AL 35899, USA; **Air Force Research Laboratory, Kirtland AFB, NM 87117, USA

Summary —A flash of radiation is produced when a hypervelocity projectile strikes a target. By the term hypervelocity, we mean a collision in which the sound speeds characterizing the materials in the target and the projectile are less than the impact velocity. When the temperature and pressure ahead of the shock are low, it can be shown that the temperature, T_o, behind the shock varies quadratically with impact velocity, v. If the shocked material and the radiation it emits are in thermodynamic equilibrium, the initial intensity of the radiation varies according to T_o^4, so that we obtain, finally, $I \sim v^8$. Because I is the total radiated power per unit area of the source, integrated over all wavelengths, it can be accurately measured only by a detector with a very wide spectral response. If a detector having a limited spectral response is used instead, one observes $I \sim v^z$, where the value of z depends on the detector. Although such a detector will not, in general, be able to confirm the v^8 rule, it may be able to confirm that the wavelength of maximum emission satisfies $\lambda_{max} \sim 1/v^2$, a result which can be derived from the Wien displacement law under the same assumptions used to obtain the velocity dependence of the source intensity. To confirm the Wien law, the response time of the detector must be less than 1 ns for a shock release temperature of 100 kK and less than 1 μs for shock release temperature of 10 kK. Between these limits, the required response time decreases as the release temperature increases.
© 1999 Elsevier Science Ltd. All rights reserved.

NOTATION

A	area
$a(\lambda)$	spectral absorptivity at wavelength, λ
b	$\left(= 9\sigma T_o^3 / r\rho C_v\right)$
C_v	heat capacity at constant volume
E_o	$\left(= 3\sigma A T_o / b\right)$
$E(T_o,t)$	radiated energy as a function of temperature T_o and time t.
I	total radiated power per unit area of the source
$I(\lambda, T)$	blackbody radiant exitance as a function of wavelength λ and temperature T
m	impactor mass
P	pressure
$P(T_o,t)$	radiated power as a function of T_o and t
Q	heat per unit mass
$R(\lambda)$	detector responsivity as a function of λ
r	impactor radius
S(T)	detector response source exitance as a function of T
s_o	sound speed

s_n	(n=1,2,...) coefficients in shock Hugoniot equation
s_{oAu}	sound speed in gold
s_{1Au}	value of s_1 for gold
s_{oFe}	sound speed in iron
s_{1Fe}	value of s_1 for iron
T	absolute temperature
T_o	absolute temperature just after passage of the shock
$T(T_o,t)$	absolute temperature as a function of T_o and t
t	time
U	shock speed
u	particle speed
v	impact velocity
V	specific volume
V_o	specific volume of material behind of the shock
x	$\left(= 1 - V_o / V\right)$
$Y(\lambda',\lambda)$	fluorescence yield at λ due to excitation at λ'
z	exponent of v
λ	wavelength of emitted electromagnetic radiation
λ'	wavelength of absorbed electromagnetic radiation
ρ	mass density
ρ_{Au}	mass density of gold
ρ_{Fe}	mass density of iron
σ	Stefan-Boltzmann constant
Ω	solid angle

INTRODUCTION

When a hypervelocity impact occurs, shock waves are generated that compress both target and impactor materials, heating them to high temperatures. We have recently shown that when the temperature and pressure in the undisturbed materials ahead of a shock can be assumed to be zero, the initial absolute temperature, T_o, behind the shock varies approximately as v^2, where v is the velocity of impact [1]. If the shocked material and the radiation which it emits are in thermodynamic equilibrium, then the initial radiation has an intensity, $I\left(W / m^2\right)$, proportional to T_o^4. Eliminating T_o, we find $I \sim v^8$, which is a power law of the kind often observed [2-5].

The shocks produced in an impact decay during a time that is proportional to the shock-wave transit time to the nearest free surface (usually the impactor side or rear surface). Since in the experiments [2-8], the impactor particle sizes were of the order of a few microns while the shock velocities were of the order of tens of km/s, the release times were of the order of 100 ps. When the shocks are released, the temperature of the shocked material drops due to the reversible part of the shock compression process, and continues to decrease as the debris cloud expands [9]. Thus the photodetectors used in the typical experiment are exposed to a dense, very hot object, whose density and temperature both begin to decrease after about 100 ps.

These photodetectors have response times that are longer than 1 ns and wavelength response bands corresponding to source temperatures lower than our estimates of the shock release temperature. Such effects must be taken into account when comparing the experiments with theory. The effect of the limited response band, we believe, may be behind the fact that although the power law, $I \sim v^z$, is universally observed, the exponent z = 8 does not always provide the best fit to the data.

We note also that the non-focussing property of these of detectors can play a role in determining the intensity of the radiation which they record. Consider, for example, that the radiating area of an impact debris cloud increases as it expands, so that the source area from which the detector is receiving radiation is also expanding. For a non-imaging detector, such as a photomultiplier, this should lead to an increase in signal, if it weren't for the fact that the effective source temperature is also decreasing. The net effect ordinarily causes the total radiated power (integrated over wavelength) to decrease with time. Contributing also to this decrease is the fact that, although the debris cloud is initially optically thick and behaves like a black body radiator, its subsequent expansion causes it to become optically thin, and hence a less effective radiator. Nevertheless, a decreasing signal is not universal. Even in the face of decreasing total radiated power, the signal from a photomultiplier can actually increase as the debris cloud expands and cools, because the peak of the radiated spectrum can move into the wavelength band to which the photomultiplier responds.

In the second section of this paper, we discuss the effects of the limited detector spectral response. In the third section, we take into account the time decay of the shock heating, and consider the finite detector response time. In the fourth section, we conclude that the determination of the wavelength of the maximum of the Planck spectrum of the emitted radiation is less affected by these factors than is the total radiated power. This leads us to consider a Wien displacement law for estimating the impact velocity. In the last section, we summarize our results.

DETECTOR WAVELENGTH RESPONSE ANALYSIS

All data at present extant have been taken using photomultipliers to detect the light from impacts. The spectral responsivity of a photomultiplier is nonzero over a limited range of wavelengths, usually in the visible; in particular, the commonly-used S-5 photocathode/UV-glass-window combination has a maximum responsivity (measured in mA/W) at 330-360 nm, falling to 10% of maximum at 220 nm and 700 nm on the short wavelength and long wavelength sides, respectively. Other photocathode/window combinations may be used, or course, but all will have a limited wavelength response band. Note that the transmittance of even a fused quartz window falls rapidly for wavelengths below about 200 nm, limiting the ability of a photomultiplier to detect short-wavelength photons. MgF_2 or LiF windows may be used down to about 100 nm, but only windowless detectors are effective below 100 nm, and these have not been used in impact-flash measurements to date. Moreover, although the window may not transmit short-wavelength photons, such photons may cause fluorescence in the window material, which may in turn be transmitted to the photocathode, resulting in a signal; this further complicates interpretation of the data.

Narrow band filters are sometimes used to provide information about the spectral distribution of the radiated energy. Short-wavelength photons can cause fluorescence also in these filters, effectively shifting the wavelength into the response band of the photomultiplier.

Absolute wavelength calibration of a multiband radiometer as an optical pyrometer, using available commercial blackbody sources, is nontrivial. This is particularly true in the case of the non-imaging, time-resolved systems that are typically used [10]. This leads us to take up issues associated with source temperature. At impact velocities of 10 km/s and above, the initial temperature in the shocked material generally exceeds 10,000 K (10 kK). By contrast the wavelength of maximum responsivity of a typical (S-20) photomultiplier corresponds to the peak in the spectral radiance of a 7 kK blackbody, which renders it fully adequate to study only the temperature of shocked material after the shocks are released, and the temperature has fallen below 10 kK. Electric arcs can produce continuum radiation in this general temperature range for calibrating detectors, but they are sources also of characteristic line radiation, which complicates their use. By comparison, both 7 kK and 10 kK far exceed temperatures available from standard pure continuum radiation calibration sources, which are limited to 3 kK and below.

Because of the T^4 dependence of the power radiated from a blackbody, by the time the expanding impact debris cloud has cooled sufficiently to be radiating in the response band of a phototube, much of the thermal energy from the impact event has already been radiated away. Figure 1 shows the power, as measured by a phototube, from a uniform blackbody at temperature T. The exitance response curves in Figure 1 are defined as follows: Let $I(\lambda,T)$ be the source

spectral radiant exitance of a black body of area A.   Let $R(\lambda)$ be the detector responsivity, and Ω the solid angle it subtends at the source, then the curves, S(T) in Figure 1 are given by

$S(T) = A\Omega \int I(\lambda,T)R(\lambda)d\lambda$, where the integral extends over all wavelengths for which the detector has nonzero response. In order to account for fluorescence, one should add a term describing the yield of fluorescence photons that fall within the detector response band, and perform the appropriate integral over the exitance, $I(\lambda,T)$. This leads to

$$S(T) = A\Omega \left[\int I(\lambda,T)[1 - a(\lambda)]R(\lambda)d\lambda + \int R(\lambda)d\lambda \int I(\lambda',T)a(\lambda')Y(\lambda',\lambda)d\lambda' \right] \qquad (1)$$

where $a(\lambda)$ is the spectral absorptivity at λ, and $Y(\lambda',\lambda)$ is the fluorescence yield, at wavelength λ, caused by exitation photons whose wavelength is λ'. Equation (1) really only describes fluorescence in the photomultiplier window; transport process in the source are ignored and the results in Figure 1 represent application of Eqn (1) with $a(\lambda) = 0$. Curves for S(T) for a tube with unit response between 300 nm and 800 nm, for an S-20 response, and for an S-5 response are given. The S-5 tube responds down to about 230 nm. Note that the S(T) curves for the S-20 response and the unit flat-response are very similar.

Fig. 1. Effective source exitance, S(T) (W/m^2), seen by detectors with various spectral responsivities, for a blackbody source at various temperatures. The exitance observed by a detector having unit response at all wavelengths is represented by the blackbody curve (straight line in the figure). This is to be compared with S(T) for a detector having a unit response between 300 nm and 800 nm and zero response elsewhere. Values of S(T) observed using S-5 and S-20 detectors are also shown.
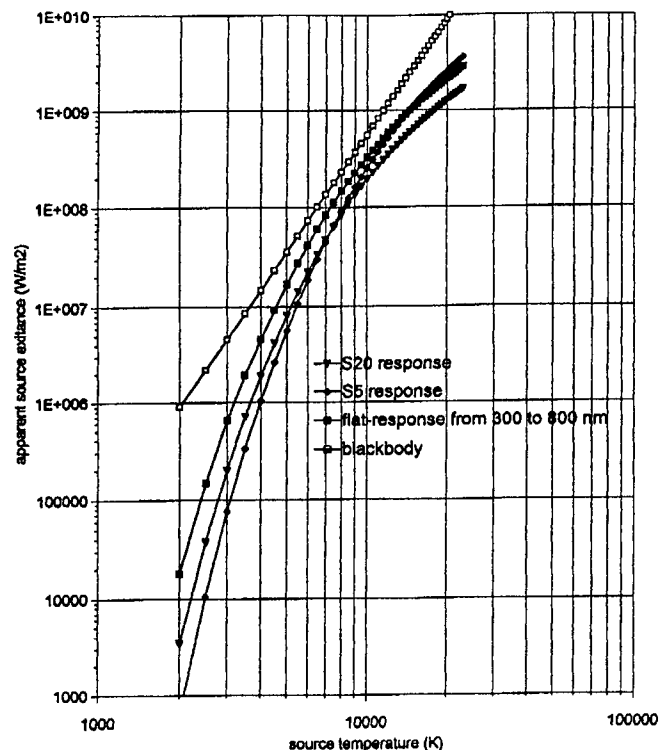
According to Figure 1, if we measure the power radiated by a blackbody, using a detector with limited spectral responsivity, we find that in general it does not vary as T^4. From local values of the slope of irradiance versus temperature in Figure 1, we see that a detector with an S-20 response detects the source strength apparently varying as $T^{10.2}$ for a blackbody at 2000 K, as T^4

at about 8000 K, and as $T^{1.6}$ at 20,000 K. Suppose we know that the effective blackbody temperature of the source varies as the square of the impact velocity. In this case, if we were viewing the impact with an S-20 detector, we would see the source strength varying as $v^{20.4}$ at low impact velocities and $v^{3.2}$ at high impact velocities, with all values in between being represented at intermediate impact velocities. This, we believe, is one of the reasons that the experiments [2-5] have reported v^z power laws with exponents other than $z = 8$.

In the next section, we take up (one dimensional) shock heating calculations that are applicable to planar collisions in which the dimensions in the transverse directions are large compared with the dimension in the direction of the impact. This simplification to one dimension is appropriate in the case of non-imaging detectors [2-8] which are largely insensitive to the shapes of the projectile and the target.

SHOCK HEATING AND DETECTOR RESPONSE TIME

The shock Hugoniot is usually written in the shock-velocity/particle-velocity plane

$$U = s_o + s_1 u + \dots = \sum_{n=0} s_n u^n \tag{2}$$

where U is the shock velocity and u is the particle velocity behind the shock, and where one ordinarily considers only terms up to first order in u. The Rankine-Hugoniot equations, which express conservation of mass, momentum, and energy across the shock front, can be solved, for a linear Hugoniot, to obtain the pressure, P_o, behind the shock as a function of specific volume, V_o

$$P_o(V_o) = \left(\frac{s_o}{s_1}\right)^2 \frac{V - V_o}{\left(V_o - V + \frac{V}{s_1}\right)^2} \tag{3}$$

where the initial (unshocked) state is assumed to have specific volume V and negligible pressure. Setting $x = 1 - V_o / V$ and integrating $P_o dV_o$ along the Hugoniot gives

$$\int_V^{V_o} P_o dV_o = -PVx - \left(\frac{s_o}{s_1}\right)^2 \left[\ln\left(1 - s_1 x\right) + \frac{s_1 x}{1 - s_1 x}\right] \tag{4}$$

Since the change in internal energy across the shock is $(P_o + P)(V - V_o) / 2$ (the Rankine-Hugoniot energy jump equation), we can use Eqn (4) to integrate the first law of thermodynamics to calculate the heat. We find

$$Q = (P_o + P)(V - V_o) / 2 + \int_V^{V_o} P_o dV_o = \left(\frac{s_o}{s_1}\right)^2 \left[\ln\left(1 + \frac{s_1 u}{s_o}\right) - \frac{s_1 u}{s_o} + \frac{1}{2}\left(\frac{s_1 u}{s_o}\right)^2\right] \tag{5}$$

In the limit $s_1 u / s_o \ll 1$, the right hand side of Eqn (5) becomes

$$Q \simeq \left(\frac{s_o}{s_1}\right)^2 \left[\frac{1}{3}\left(\frac{s_1 u}{s_o}\right)^3 - \frac{1}{4}\left(\frac{s_1 u}{s_o}\right)^4 + \dots\right] \tag{6}$$

Since all materials have values of s_1 near unity, the limit represented by Eqn (6) demonstrates that the shock heating is rather small until the particle velocity nears the sound speed in the unshocked material. For the assumed linear Hugoniot, the exact logarithmic integral form shown on the right of Eqn (5) indicates that the shock heating varies as u^2 in the case that $s_1 u / s_o \gg 1$. For hypervelocity impacts at velocities above 10 km/s, the particle velocity generally is greater than the initial sound speed. For example, in the case of iron impacts onto gold, the particle velocity exceeds the initial sound speed in gold when the impact velocity exceeds about 8 km/s.

If we define a normalized (dimensionless) particle velocity, $y = s_1 u / s_o$, then it is evident that the quantity in square brackets in Eqn (5) is dimensionless, and we may define it to be the normalized heating. A plot of normalized heating versus normalized particle velocity is given in Figure 2. For a typical material, having a sound speed of about 3 km/s and an Hugoniot slope parameter, s_1, of about 1.3, we get to $y = 1$ when u is about 2.3 km/s, which requires, in a symmetric impact, an impact velocity of about 4.6 km/s. By the time the impact velocity reaches 20 km/s, we are in a regime where the shock heating varies essentially as the square of the impact velocity.
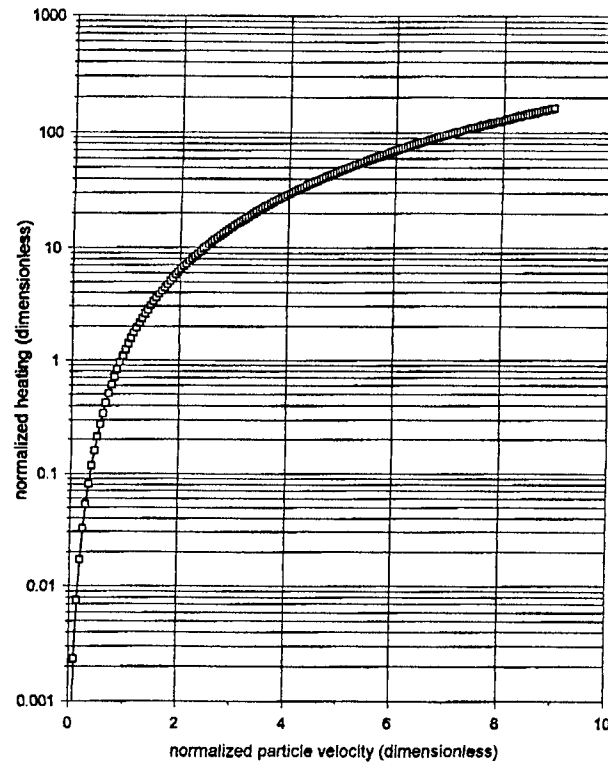
Fig. 2. Normalized shock heating as a function of normalized particle velocity. The normalized shock heating is the quantity inside the square bracket in Eqn. (5).

Eichhorn, [2-5], has studied the impact flash from iron microparticles colliding with a variety of materials, at velocities up to about 30 km/s. Values of s_o and s_1 are shown in Table 1 for some of these materials obtained by least-squares fits of data [11] to Eqn (2) cut off at $n = 2$ with s_o, s_1, and s_2 as free parameters.

Table 1. Shock parameters for Al, Fe, Cu, and Au

	aluminum	iron	copper	gold
$\rho\left(g / cm^3\right)$	2.7	7.8	8.9	19.2
$s_o\left(km / s\right)$	5.23	3.70	3.93	2.95
s_1	2.01	1.76	1.41	2.03

Using the parameters for gold and for iron (above the α - γ polymorphic phase transition at 12.5 GPa), we can calculate the particle velocity produced by impacts of iron onto gold, as a function of impact velocity. By equating the pressure and particle velocities in target and impactor and substituting the (linear) Hugoniot relations we arrive at a quadratic expression,

$$u^2\left[\rho_{Au}s_{1Au} - \rho_{Fe}s_{1Fe}\right] + u\left[\rho_{Au}s_{oAu} - \rho_{Fe}\left(s_{oFe} - 2s_{1Fe}v\right)\right] + \rho_{Fe}v\left(s_{oFe} - s_{1Fe}v\right) = 0 \qquad (7)$$

for the particle velocity, u. Equation (7) can be used to solve for u in terms of the impact velocity, v, and the Hugoniot constants for the two materials. The value of u can be substituted into Eqn (5) to calculate the shock heating from iron impacting onto gold. Results for impact velocities from below 1 km/s to 30 km/s are given in Figure 3.
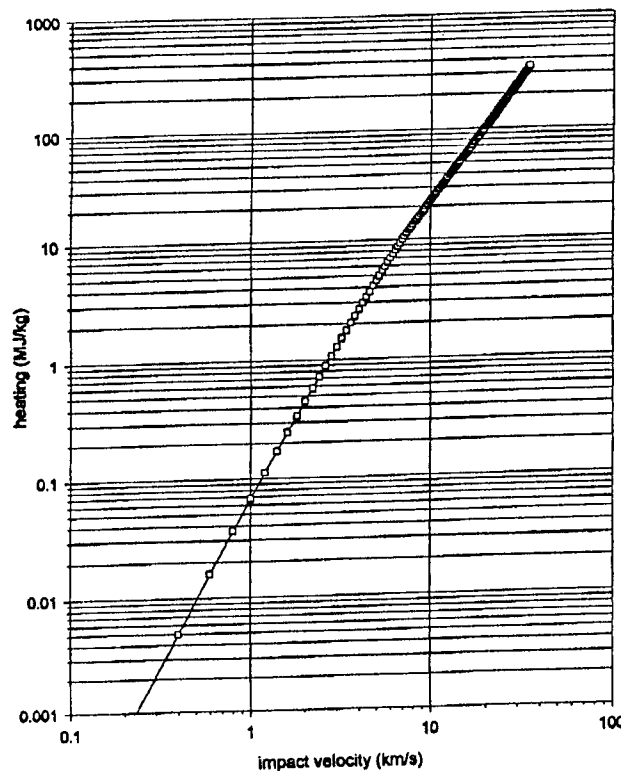
Fig. 3. Shock heating in gold versus impact velocity for iron impacting gold.

In order to calculate a temperature history, we need an equation of state; in order to calculate what a detector sees, we need to know the opacity of the ejecta cloud, as a function of time. Both of these are difficult to obtain, and lead us to look for another way to estimate the temperature of the cloud as a function of time. For the present, we assume that the opacity of the cloud is very large, so that it radiates like a blackbody, and that the specific heat can be approximated by handbook values [12]. In the case of gold, the specific heat varies from about 124 J/kgK at 500 K to about 150 J/kgK at 1500 K, and we assume the higher value in what follows; this results in a calculated temperature behind the shock of about 30,000 K for a 5 km/s impact. This is high enough that electronic excitation and ionization will be important, so that our handbook specific heat estimate errs on the low side; the actual specific heat will be higher, and the temperature will be lower than we have estimated above.

Although shocks in micron-sized projectiles [2-5] release in a few hundred picoseconds, which is too fast to be observed by ordinary detectors, they leave behind a residual (release) temperature that may be observable. We now estimate this subsequent temperature history. If we assume that the release temperature of the source is T_o, and ignore the fact that the source is an

expanding cloud of vapor and debris (assume the source is just a sphere of density, ρ, and radius r), then

$$mC_V\frac{dT}{dt} = -\sigma AT^4 \tag{8}$$

where m is the mass and C_V the specific heat of the projectile, T is the temperature (K), A is the radiating area, and σ is the Stefan-Boltzmann constant (5.67×10^{-8} Wm^{-2}K^{-4}). Equation (8) may be integrated to obtain the temperature,

$$T(T_o,t) = T_o\left(1 + \frac{9\sigma T_o^3 t}{r\rho C_V}\right)^{-1/3} = T_o\left(1 + bT_o^3 t\right)^{-1/3} \tag{9}$$

Using Eq. (9), the radiated power is

$$P(T_o,t) = \sigma AT^4 = \sigma AT_o^4\left(1 + bT_o^3 t\right)^{-4/3} \tag{10}$$

The temperature is plotted as a function of time in Figure 4, for a 1 μm-radius iron sphere, for three values of T_o. The temperature profiles in Figure 4 can be sensed by a photomultiplier having a response time less than 1 ns.

By integrating Eq. (10) over time, we can compute the cumulative radiated energy. The result is

$$E(T_o,t) = \int_o^t P(T_o,t')dt' = \frac{3\sigma AT_o}{b}\left[1 - \frac{1}{\sqrt[3]{1 + bT_o^3 t}}\right] = E_o\left(1 - \frac{T(T_o,t)}{T_o}\right) \tag{11}$$

The fraction of the total radiated energy, E/E_o, that has been radiated after a time t, is plotted in Figure 5, for the same conditions assumed in Figure 4. Recall that the shocks are released after about 10^{-10}s or so; note that even a body at 100 kK does not radiate a significant fraction of its heat energy in this amount of time. However, note also that most of the heat (see Figure 4) has been radiated away after a few hundred microseconds.
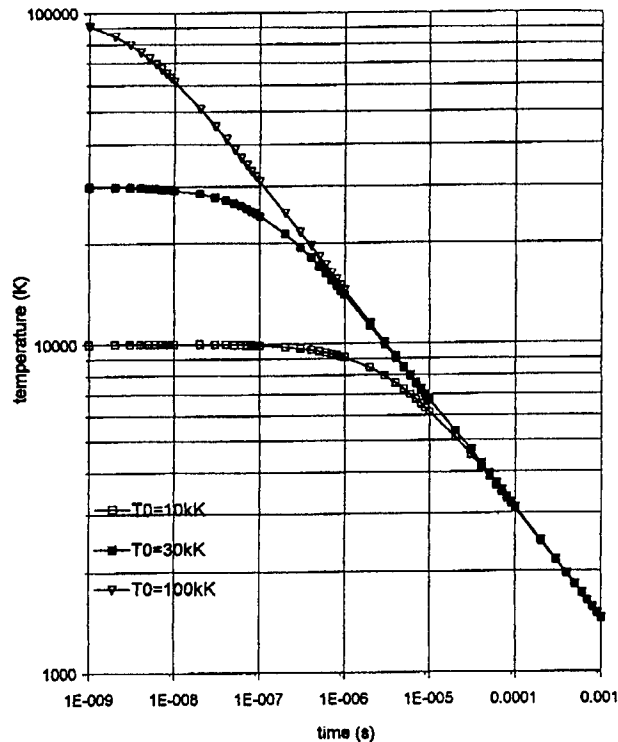
Fig.4.Temperature versus time, for
1 μm radius iron sphere

$\left(C_V = 0.2\ J / gK, \rho = 7.8\ g / cm^3\right)$

for initial temperatures of 100 kK,
30 kK and 10 kK. Note the
convergence of all curves as t
approaches 100 μs.

Fig. 5. Cumulative radiated energy for a 1 μm radius iron sphere as a function of time after impact. The top curve is for a release temperature of 100 kK; the bottom for 10 kK. Note that, even for an initial temperature of 100 kK, less than 10% of the total radiated energy has been emitted after a nanosecond has elapsed.
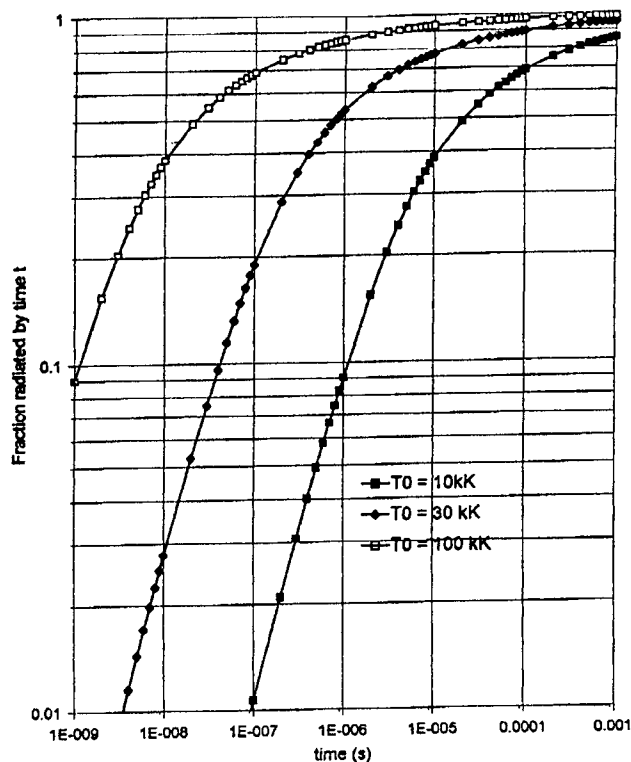
WIEN DISPLACEMENT LAW

The Wien displacement law, which can be derived from the Planck distribution, states that the wavelength of maximum radiated power varies inversely as the temperature

$$\lambda_{max} = \frac{2898 \ \mu m \cdot K}{T(K)} \tag{12}$$

Since the initial temperature after the impact is proportional to v^2 [1], the Wien displacement law for impact radiation is $\lambda_{max} \sim v^{-2}$. This applies under the same simplifying assumptions that lead to $I \sim v^8$ [1]. The rule for λ_{max} is obtained from the derivative of the Planck function, as opposed to the rule for I, which is obtained from its integral. Hence, given a detector with sufficient speed and wavelength response, the λ_{max} rule may be more suited to estimating the temperature history resulting from the impact.

Assuming the temperature history in Figure. 4, it is interesting to see how λ_{max} varies with time. Figure 6 shows the wavelength of the blackbody peak as a function of time, as calculated from Eqns. (9) and (12), for initial temperatures of 100 kK, 30 kK, and 10 kK. For iron impacts onto gold, as studied by Eichhorn [2-5], impact velocities above 10 km/s are needed in order to have release temperatures above 10 kK. Beginning about 1 μs after impact, the blackbody peak locations all begin to converge; after about 10 μs, most of the information about the initial temperature is lost, and the radiation from all impacts peaks at the blue end of the visible. By 100 μs after impact, all information about the initial temperature is lost, and the radiation from any impact peaks at about 900 nm. Given sufficient wavelength sensitivity, it is clear from Figure 6

that a detector with a response time of 1 ns should be fast enough to record the time dependence of λ_{max} and determine the release temperature, T_o, when it falls in the range 10 kK to 100 kK. Even slower detectors become adequate as the value of T_o approaches 10 kK.
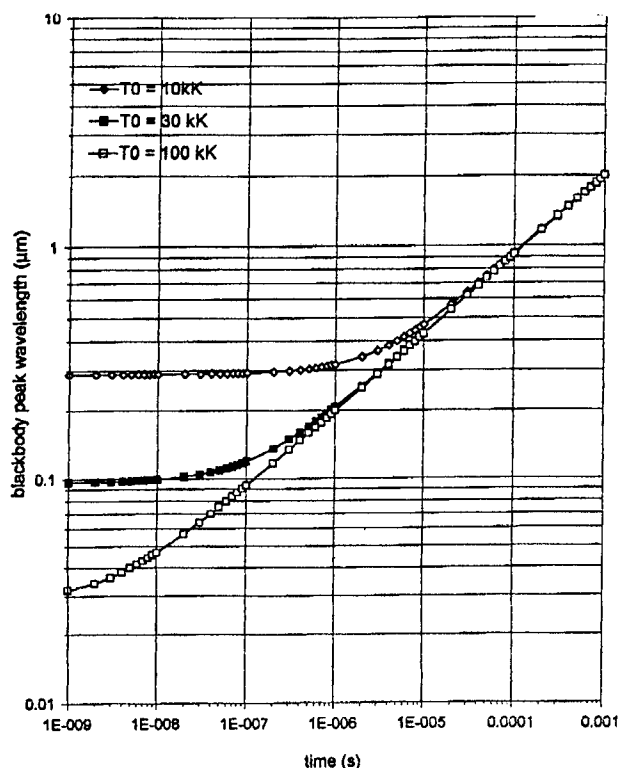
Fig. 6. Wavelength of the black body peak radiated by a 1 µm radius iron sphere, as a function of time, for initial temperatures of 10 kK, 30 kK, and 100 kK.

DISCUSSION AND CONCLUSIONS

What actually can we determine using a photomultiplier with S-20 response, as has been used in the experiments [2-5] done to date? The signal risetime for small signals using a well-designed tube base, can be slightly shorter than a nanosecond; the region of good responsivity extends from about 300 nm to 750 nm. Hence, most of the radiation from blackbodies whose temperature is between about 9.6 kK and 3.8 kK will be detected. A detector that has a response time much greater than 1 ns is too slow to observe the shocking-up and release processes from impacts of micron-sized projectiles: it only sees the expanding hot debris cloud, and residual heat left in the target. Nevertheless, according to Figure 4, it is still possible to make measurements that allow T_o, the source temperature immediately after release, to be determined, since $T\left(T_o, t\right)$ remains constant for at least several ns when $T_o < 100 \text{ kK}$.

Examination of Eqns. (9), (10), and (11) suggests that T_o may also be inferred from measurements of total radiated energy at long times, because the risetime in Eqn (11) depends on T_o. Nonetheless, one must bear in mind that Eqn (11) was derived under the simplifying assumption that the debris cloud had large opacity. A more careful analysis is required to obtain an accurate T_o dependence. Use of carefully-calibrated fluors (which shift short-wavelength photons into the visible) in conjunction with photomultipliers allows one to measure the energy radiated in parts of the spectrum that cannot directly be measured, thus enabling a more precise accurate determination of the total radiated energy as predicted by Eqn (11).

By contrast, to make use of Eqn (12) (Wien displacement law), an absolute calibration of the detector is not necessary. Rather, the calibration need determine only the sensitivity of one

wavelength relative to the others with an accuracy sufficient to locate the peak of the spectrum. For best results, bandpass filters should be placed in front of the detectors, with fluorescence shields in front of the filters in order to prevent fluorescence in the filters from confusing the results. The signals from the detectors are synchronously recorded, and the (relative) intensity in each (narrow) wavelength band at a given time is used to locate the peak of the spectral radiance, and thereby determine the temperature at that time. Proper choice of the narrowband filters should allow measurement of temperatures as high as 20,000 K, using S-5 photomultipliers, for example.

Modern microchannel plate detectors constitute the next improvement in experimental detector technique over the photomultipliers that have been used so far [2-8]. When read with a streak camera, these multichannel plates can have a response time as short as 25 ps. Other than this, the optical considerations associated with multichannel plates are similar to those associated with photomultipliers in the sense that account must still be taken of image size, fluorescence in exposed materials and wavelength transmission along the optical path.

REFERENCES

1. "Velocity Dependence of Impact Fluorescence", J. K. Baird, G. R. Hough, and T. R. King, Int. J. Impact Engng., 1997, **19**, 273-276.
2. Eichhorn, G., "Measurements of the light flash produced by high velocity particle impact", *Planet. and Space Sci.*, 1975, **23**, 1519-1525.
3. Eichhorn, G., "Analysis of the hypervelocity impact process from impact flash measurements" *Planet. and Space Sci.*, 1976, **24**, 771-781.
4. Eichhorn, G., "Heating and vaporization during hypervelocity particle impact", *Planet and Space Sci.*, 1978, **26**, 463-467.
5. Eichhorn, G., "Primary velocity dependence of impact ejecta parameters", *Planet. and Space Sci.*, 1978, **26**, 469-471.
6. Burchell, M. J., Kay, L., and Ratcliff, P. R., "Use of combined light flash and plasma measurements to study hypervelocity impact processes", Adv. Space Res. 1996, **12**, 141.
7. Kissel, J., and Dreuger, F.R., "Ion impact of fast dust particles and comparison with related techniques", Appl. Phys. A. (Solids and Surfaces) 1987, **42**, 69-85.
8. Ratcliff, P. R., and Allahdadi, F., "Characteristics of the plasma from a 94 kms^{-1} micro-particle impact", Adv. Space Res. 1996, **17**, 87-91.
9. Ang, J. A., "Impact flash jet initiation phenomena", Int. J. Impact Engng. 1990, **10**, 23-28.
10. Schooley, James F., ed., *Temperature, Its Measurement and Control in Science and Industry*, vol. 5, American Institute of Physics, New York, NY, 1982, p. 395-505.
11. Marsh, Stanley P., *LASL Shock Hugoniot Data*, University of California Press, Berkeley, CA, 1980.
12. Gray, D. E., ed., *American Institute of Physics Handbook, third ed.*, McGraw-Hill, New York, NY, 1972, p. 4-108.

INTERACTIONS BETWEEN AN IMPACT GENERATED EJECTA CURTAIN AND AN ATMOSPHERE

OLIVIER S. BARNOUIN-JHA[*] and PETER H. SCHULTZ[**]

[*]The Johns University Applied Physics Laboratory, Johns Hopkins Road, Laurel, MD 20723-6099, USA; [**]Dept. of Geological Sciences, Box 1846, Brown University, Providence, RI 02912

Summary—A theoretical model investigates the interaction between an ejecta curtain and a variety of differing atmospheric conditions in order to determine the ejecta entrainment capacity of winds generated by an advancing curtain. The model assesses the curtain shape, the position along the curtain where flow separation occurs, the velocity of winds winnowing ejecta out of the effectively impermeable portions of the curtain and the velocity of winds flow separating at its top. Wind velocities allow estimating the size range of ejecta entrained. Tested against laboratory impacts into coarse sand, the model results duplicate observation of curtain shape and size of ejecta entrained. The position where flow separation occurs is duplicated when the curtain porosity is assumed to increase with time. © 1999 Elsevier Science Ltd. All rights reserved.

NOTATION

Γ	curtain circulation (m^2/s)
L	effectively impermeable length of the ejecta curtain(m)
U	velocity of an advancing ejecta curtain(m/s)
t	time since initial impact (s)
θ	angle of ejecta curtain with respect to the target surface (rad)
R	pre-collapsed transient crater radius cutting pre-impact surface (m)
g	acceleration due to gravity
t_p	time when the ejecta curtain becomes impermeable (s)
$M = U / a$	curtain Mach number
a	ambient speed of sound (m/s)
ζ	hydraulic resistance
μ	ambient atmospheric viscosity (kg/(m.s))
ρ	ambient atmospheric density (kg/m^3)
$v = \mu / \rho$	ambient atmospheric kinematic viscosity (m^2/s)
d	nominal or dominate ejecta diameter in the ejecta curtain (m)
C_{Ds}	drag coefficient of particles (assumed to be spheres) in the ejecta curtain
S	surface area of each ejecta zone (m^2)
w	curtain width at each ejecta zone (m)
u	velocity of each ejecta zone (m/s)
u_1	horizontal velocity component of u (m/s)
u_2	vertical velocity component of u (m/s)
α	angle of ejecta zone velocity relative to the horizontal (rad)
ϕ	curtain porosity
ϕ_t	target porosity
Δp	pressure difference across each ejecta zone (Pa)
v_i	interstitial flow speed through each curtain ejecta zone (m/s)
v_d	local average downstream velocity behind each curtain ejecta zone (m/s)
x	distance from crater center to base of curtain

T	time when transient (pre-collapsed) crater cavity ceases to grow (s)
Z	exponent describing rate of crater growth in Z-model
k_t	constant of proportionality for time when transient crater cavity ceases to grow
D	drag acting on a curtain zone (N)
v_e	ejecta excavation velocity (m/s)
C_D	drag coefficient of each ejecta zone providing measure of Δp
δ	angle subtended by the velocity of each ejecta zones relative to its surface (rad)
x_1	horizontal coordinate of each ejecta zone (m)
x_2	vertical component of each ejecta zone (m)
m	mass of each ejecta zone (kg)
U_{up}	ejecta entrainment velocity at point of flow separation (m/s)
V_L	projectile launch velocity (km/s)

INTRODUCTION

Several studies have investigated the mechanics by which an atmosphere may modify ejecta emplacement processes during impact cratering [1, 2, 3, 4, 5]. Such studies conclude that the bottom thick and dense portions of the ejecta curtain act like an outward-moving solid plate that displaces the surrounding atmosphere to generate a distinctive vortex ring (Fig. 1). In the laboratory, this vortex ring winnows fine-grained ejecta out of the curtain, while larger ejecta continue along ballistic paths. The vortex ring moves downwards to the target surface and outwards behind the ballistic ejecta, sometimes scouring both target and newly deposited ejecta. As the vortex flow decays, coarser ejecta are deposited in a sinuous contiguous rampart while finer ejecta contribute to lobate fluidized flows. Eventually the vortex ring evolves into a turbidity-like flow. The resulting morphologies strongly resemble non-ballistic ejecta observed at craters on Mars [1,2,3,6,7], Venus [4,8] and Earth [9] (Fig. 2).
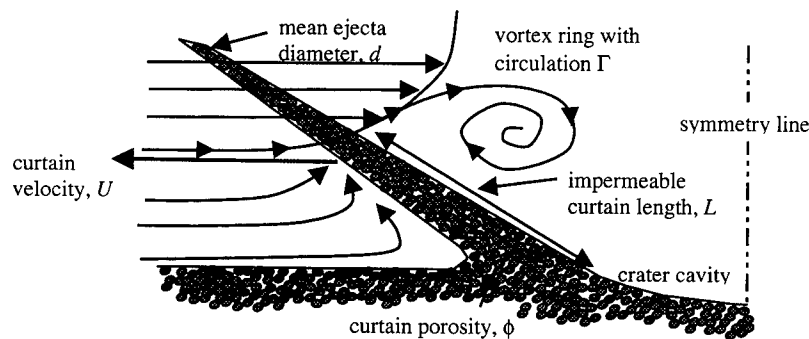
Fig. 1. Schematic of flow separation at the top of the impermeable portion of an advancing ejecta curtain that generates a vortex ring which entrains and deposits fine grained ejecta.

First-order analytical models of the curtain-driven vortex ring illustrate the possible importance of an atmosphere in modifying ejecta morphology. Such models show that curtain-driven winds should entrain up to millimeter-sized ejecta on Mars, centimeter-sized ejecta on Earth and meter-sized ejecta on Venus [1, 3, 5] and that instabilities in the curtain-driven vortex ring could be responsible for the sinuosity or lobateness of distal ejecta (less than 5 crater radii) on Mars and Venus [10].

Previous estimates of entrained ejecta size, however, possess several simplifying assumptions. For example, in one set of studies, the entrainment winds were assumed to correspond to the velocity of the advancing curtain defined by the trajectories of constituent ejecta [1, 3]. The diameter of particles entrained was then calculated using ambient atmospheric conditions.

More realistic estimates of the amount of ejecta entrained at large scales require improved es-

timates of the flow strength achieved in the curtain-derived vortex. This flow strength controls the amount of ejecta entrained and transported by the vortex. The entrainment of ejecta in the vortex significantly affects the flow in the vortex and the manner in which it deposits ejecta. Estimating this entrainment capacity, therefore, becomes critical if observations of either ejecta runout or sinuosity are to be used to assess either target properties (including volatile content) or atmospheric conditions present during crater formation.
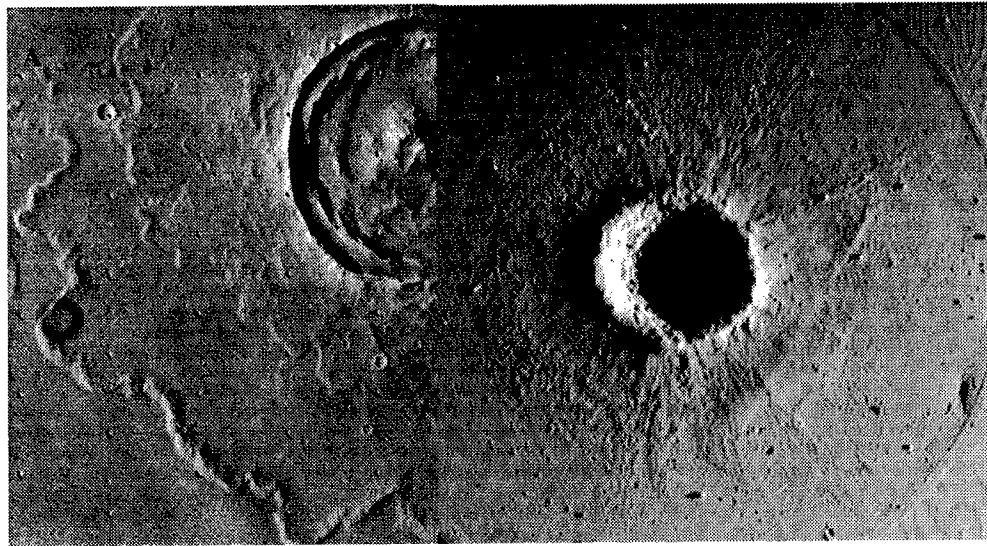
Fig. 2. (A) A 17.7 km diameter on Lunae Planum, Mars (17.5N48, Viking image 65A68) and (B) a 15 cm diameter laboratory crater formed in pumice by 0.635 cm Al projectile launched at 5.17 km/s in 0.94 atms of N_2.

Consequently, two studies investigated the interactions between an atmosphere and an ejecta curtain [11,12]. Using wind tunnel and numerical results, these studies show how the flow strength generated by an advancing curtain could be estimated using the curtain porosity, width and velocity, the prevalent diameter of ejecta comprising a curtain, the velocity of individual ejecta parallel to the surface of the curtain and ambient atmospheric viscosity, density and compressibility. These studies also showed how drag acting on the impermeable portions of the curtain generates a pressure difference across the curtain that drives atmosphere slowly through it. Although, inconsequential to the macroscopic flow field generated by the curtain, this flow winnows ejecta out of the curtain.

The objective of the present study is to take the next logical step wherein the derived results above are used to estimate the size range of ejecta carried by winds created by the curtain-derived flow and winnowing winds. The following discussion describes (1) implementation of theoretical models that contribute to estimating the entrainment capacity of both the flow separating and winnowing winds, and (2) comparison of model results with laboratory scale experiments. The comparison with the laboratory data will focus on impacts into coarse sand where ejecta is not significantly entrained out of the curtain by the impinging winds. Such an approach test the various assumptions that contribute to the overall curtain model developed in this study, without adding the complication of significant ejecta removal. A later contribution will investigate how significant ejecta erosion affects the overall curtain behavior before applying the model to broad scales.

THEORETICAL MODELS

The strength of winds generated by an advancing curtain and capable of entraining ejecta depends upon the flow strength or circulation Γ in the curtain-generated vortex ring and is given by [5, 12]

$$\Gamma = \frac{2\pi}{\sqrt{1-M^2}}\left(\frac{1}{0.13+\theta}\right)^{4/9}\left(\frac{1}{\theta}\right)^{1/3}UL\left(\frac{Ut}{L}\right)^{1/3} \tag{1}$$

(see Fig. 1 and NOTATION for definitions of variables). This solution for the curtain circulation includes energy losses in the flow passing through the upper semi-permeable portions of the curtain, increases in flow velocity due to the motion of ejecta parallel to the surface of the curtain, and effects of atmospheric compressibility [12].

Various cratering models and results from *Barnouin-Jha et al.* [11, 12] can be combined to estimate U, L, θ and a needed to compute Γ. First, we describe the approach used to compute these variables of Γ. Second, we present the individual models and assumptions made that allow achieving our goal of realistically describing the interactions between an ejecta curtain and an atmosphere.

The velocity U can be obtained from an impact-cratering model that describes the rate of crater growth. Such a model also can provide the velocity and volume of ejecta excavated during crater growth from which L and θ can be determined. The steps leading to L and θ requires first splitting the volume of ejecta excavated between 0.2 and 1 crater radii into a series of particulate-filled zones each assigned with three initial excavation velocities. Assuming each zone takes the shape of fustrum, its fastest velocity designates its top and its slowest designates its bottom. The middle velocity of the fustrum/zone is representative of the velocity u of the entire zone. A drag model determines the horizontal and vertical position of the fustrum's center as it travels through an atmosphere and requires values for the surface area S and the width w of each zone at each time step (Fig. 3).
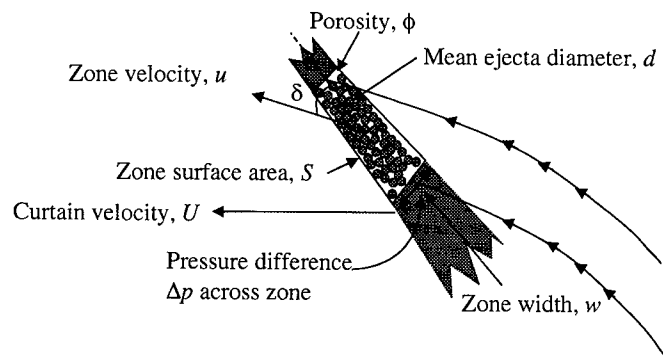
Fig. 3. Schematic of one ejecta zone making up the ejecta curtain model.

The second step towards obtaining L and θ requires, therefore, determining S and w. The surface area S can be determined by assuming that the paths taken by the top and bottom of each zone/fustrum remain ballistic even though the impinging atmosphere decelerates each zone (Fig. 3). With S, w can be calculated assuming the volume of ejecta in each zone does not change in time.

The third step in computing L and θ requires computing the hydraulic resistance ζ for each particulate zone from w. This ζ acts as a proxy for the curtain's permeability [11], providing an estimate of the energy loss associated with porous flow [e.g. 13] through the curtain. The value of ζ can be computed for each zone from a particle-packing model, which in addition to w re-

quires conditions of the surrounding atmosphere (viscosity μ and density ρ), the dominant (nominal) diameter d of ejecta in the curtain and the curtain porosity ϕ. Also important is the curtain velocity U. The value of ϕ is assumed, whereas d, ρ, μ and a are provided by the laboratory conditions.

The fourth step leading to values for L and θ requires using the magnitude of ζ to determine several important variables. The first important variable is the average flow speed v_d downstream of each zone, which indicates where significant flow gets through the curtain top [11] and, thus, defines L. Second, ζ controls the magnitude of the drag coefficient that should be assigned to each zone (i.e. whether or not the zone acts as a barrier or not), thereby determining the position of each ejecta zone as it travels through the atmosphere. This controls both the curtain shape and θ. The third bonus variable ζ provides is the interstitial velocity $v_i (= v_d/\phi)$ of the fluid that creeps through the impermeable zones due to the pressure difference Δp that exists across the curtain by drag. From this v_i, the size range of ejecta winnowed out of the curtain can be determined. Thus, ζ provides L and θ necessary for determining the circulation Γ, which controls the speed and size range of ejecta carried by the winds shed at the curtain top. Also, ζ establishes the speed and size range of ejecta that can be winnowed out of the effectively impermeable sections of the ejecta curtain.

Another important variable, the time t_p, determines the initial velocity profile and hence, the dusty flow conditions in the vortex before it begins to decay. This t_p is reached when ζ for each zone is small enough to allow significant flow through the entire curtain. Modeling should provide this time as well.

The above discussion reveals that three models are needed in order to estimate the variables controlling Γ and the winnowing flow speeds: (1) an impact cratering model to determine the rate of crater growth, the initial velocity and the volume of ejecta excavated; (2) a packing of particles model to compute ζ; and (3) a drag model to estimate the velocity and shape of the curtain as it is re-shaped by the surrounding atmosphere. Laboratory conditions prescribe the local density, viscosity and speed of sound through which the curtain travels. The three models are discribed below.

Impact cratering model

The relatively simple analytical Z-model [14] provides an estimate of the rate of crater growth. Since the ejecta curtain is coupled to and expands with the growing transient cavity, the Z-model, thus, provides the velocity U of the ejecta curtain. Moreover, it supplies the velocity of ejecta excavation at a given distance from the crater center. The variables computed by the Z-model are easily normalized to scale appropriately with gravity and crater radius [e.g. 1].

The derivative of

$$\left(\frac{x}{R}\right)^{Z+1} = \frac{t}{T} \tag{2}$$

where T is given by

$$T = k_1 \sqrt{\frac{R}{g}} \tag{3}$$

leads to the curtain velocity U

$$U = \frac{\sqrt{Rg}}{k_1(Z+1)}\left(\frac{x}{R}\right)^{-Z} \tag{4}$$

In this simplification, the value of Z is assumed to be constant. By using this U to calculate Γ, we

assume that atmospheric interference does not significantly alter the advancing velocity of an ejecta curtain during crater growth. Although such an assumption is not strictly correct [15,16], it provides an excellent estimate of the actual curtain velocity for impacts into coarse targets [5, 15].

The velocity v_e of ejecta excavated at the target surface is calculated using

$$v_e = \frac{\sqrt{Rg}}{k_1(Z+1)\cos\theta}\left(\frac{x}{R}\right)^{-Z} \tag{5}$$

where the similarity factor $\sqrt{gR}$ non-dimensionalizes the ballistic equations for gravity-controlled crater growth [17,18,19]. We consider typical excavation angles θ of 45° [20,21].

The volume of ejecta excavated during crater growth is provided from numerical calculations of crater excavation and growth. While many numerical calculations of the cratering process exists [22, 23, 24,25], we have chosen to use the calculations generated by *Orphal et al.* [25] because they treat the late-stages of crater formation. These calculations generate estimates of the volume of ejecta excavated during crater formation normalized to total ejecta excavated and predict near-rim ejecta thicknesses ($1.5 < x/R < 3$) that are consistent with laboratory and planetary observations [26]. This study uses *Orphal et al's* [25] NASA-2 calculations for a 3.12 m-diameter projectile impacting at 15.8 km/s into a solid half-space [see 26].

Packing of particles model

The average local flow speed v_d downstream of each zone in our simulated ejecta curtain determines its permeability [11]. From air-flow experiments, the zones behave impermeably when v_d is less than 40% and permeably when v_d is greater than 40% of the flow speed impinging upon curtain [11]. This impinging flow speed in the curtain frame of reference is equal to the curtain velocity U in the stationary frame of reference.

The magnitude of v_d can be computed from [11]

$$v_d = \sqrt{\frac{2\Delta p}{\rho\zeta}} \tag{6}$$

where Δp is the pressure difference across each zone. This equation illustrates the importance of ζ in controlling the permeability of the zones. By strict analogy to the ejecta-like plate investigated in wind tunnel experiments [11], this pressure difference can be computed using the drag coefficient C_D of each ejecta zone defined in terms of U, the velocity of the entire ejecta curtain

$$C_D = \frac{D}{\frac{1}{2}\rho U^2 S} = \frac{S\Delta p}{\frac{1}{2}\rho U^2 S} = \frac{\Delta p}{\frac{1}{2}\rho U^2} \tag{7}$$

where D is the drag acting on the entire ejecta zone. Using Eqn. (7) to replace Δp in Eqn. (6) gives

$$v_d = U\sqrt{\frac{C_D}{\zeta}} \tag{8}$$

where $C_D = 2.0$ [11].

The results we present include the position along an ejecta curtain where significant flow through occurs; the interstitial or winnowing flow velocity v_i ($= v_d/\phi$) passing through the effectively impermeable portions of the curtain; and the ejecta size this winnowing flow can entrain.

An ejecta curtain is actually comprised of individual ejecta; consequently, this study uses existing formulations of ζ for packing of particles. Because these formulations of ζ apply strictly to particle packing in 1-dimensional channel flow, they do not account for dispersive forces that may displace or disperse individual ejecta as flow impinges upon the curtain over a long period of time. Applying ζ to an ejecta curtain, therefore, should provide good results early during ejecta

excavation. We use the formulation for ζ derived by combining the experimental results of *Richardson and Zaki* [27] with the analyses of *Soo* [28] to give

$$\zeta = \frac{3(1-\phi)}{2\phi^{3.7}}\frac{w}{d}C_{Ds} \tag{11}$$

where C_{Ds} is the drag coefficient of the particles (assumed to be spheres) comprising the packing.

Drag model

The drag model computes the velocity and position of the curtain zones as they advance through an atmosphere. The approach is analogous to the particle-by-particle drag deceleration in *Schultz and Gault* [1] but here we consider the ensemble of particles that comprise each zone. Solving for gravity and drag forces acting on each zone allows determining their horizontal and vertical velocity u_1 and u_2 (Fig. 3) from the following ordinary differential equations

$$\frac{du_1}{dt} = \frac{S\Delta p}{m} = -\frac{\rho C_D S U^2}{m}\cos\alpha$$

$$\frac{du_2}{dt} = -g - \frac{S\Delta p}{m} = -g - \frac{\rho C_D S U^2}{m}\sin\alpha \tag{13}$$

where the square of the velocity of the zone $u^2 = u_1^2 + u_2^2$ and the direction of the velocity $\alpha = \tan^{-1}(u_1/u_2)$ relative to the horizontal. The mass m of the zone is maintained constant for each zone through time, thereby maximizing the advance of each zone. The drag coefficient C_D varies with the angle δ subtended by the velocity of each ejecta zone relative to its front surface (Fig. 3) to allow ejecta to escape craters under high atmospheric pressures [1].

The equations

$$\frac{dx_1}{dt} = u_1$$

$$\frac{dx_2}{dt} = u_2 \tag{14}$$

give the horizontal coordinate x_1 and the vertical coordinate x_2 of the center of the zone. The initial conditions of the drag model are provided by the Z-model results. Equations (10) and (11) are solved simultaneously using a fourth-order Runge-Kutta method.

The surface area S is computed by assuming that the top and bottom of each ejecta zone travel along purely ballistic (no drag) paths. Such an approach requires estimating the theoretical time for the center of the zone to reach its present decelerated position assuming no atmosphere is present. This theoretical time then allows calculating the position of the top and bottom of the zone, thereby providing an estimate of S.

Such calculations also provide the width w of the fustrum-zone assuming that its volume does not change in time. From w, ζ and v_d can be estimated. The value of v_d then determines the magnitude of C_D assigned to each ejecta zone. If v_d is less than 40% of the curtain speed U, then C_D equals 2.0; otherwise, C_D remains equal to 2.0 for ζ greater than 2.0, but equals ζ for ζ less than 2.0, thereby providing reasonable estimates (within a factor of 2) of the actual C_D for the semipermeable portions of the curtain [11].

Ejecta entrainment

The wind velocity generated by flow separation at the top of the impermeable curtain [given in 5] determines the size range of ejecta entrained out of the curtain. In fact, this velocity must be combined with the velocity of the ejecta zone at this height (as given by the drag model) in order

to compute the net wind velocity acting on the particles in the zone. A positive vertical component of this net velocity (U_{up} in Fig. 4) should entrain ejecta from the zone.

Path of
V_1 separating flow

Zone
velocity, u

Net flow velocity V
acting on particles in the
ejecta zone

V_1

V_2

V_2

q

$U_{up} = |V| \sin q$

Path of the
ejecta zone
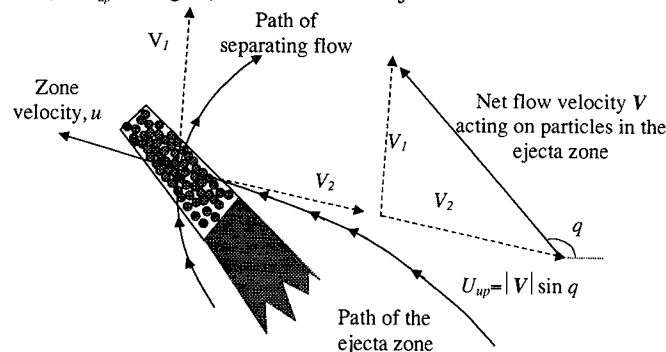
Fig. 4. Schematic of the top of an ejecta curtain where flow separation occurs.

The drag due to U_{up} determines the size range of particles entrained in the curtain-derived winds by balancing gravity acting on a particle. In the discussions below, entrainment flow speeds include both the winnowing or interstitial flow speed v_i and the upwards velocity component, U_{up}.

LABORATORY TESTS

The theoretical models need to be tested at laboratory scales in order to establish their validity and limitations before they can be applied at large scales. The observational tests used are derived from the theoretical results that allow computing Γ. The theoretical results tested, therefore, include the curtain shape, the impermeable curtain length and the size range of ejecta entrained by the curtain generated winds.

Quarter-space (half-craters) experiments at the NASA Ames vertical gun range allow to test the theory. During such experiments, a high speed video camera (500-1000 f/s) and high speed film (500 f/s) record curtain distortion, the impermeable curtain length and whether or not target material is being entrained by the curtain-derived winds. Such imaging techniques also provide input for the theory essential to compare theory and experiments accurately. Indeed, such data provide the position of the ejecta curtain as a function of time, thereby providing the Z exponent and the k_1 constant of the impact cratering model.

The high-speed video and film were used to observe both 1/4" and 3/16" Al projectiles launched at both 2 km/s and 4 km/s impact into a coarse sand target (bulk density = 1700 kg/m^3; d~457-μm). Sprinkled on top of the target were small low-density micro-spheres (bulk density = 500 kg/m^3; d~100-μm). The theoretical computations of curtain shape and motion did not include the effects of the atmospheric blast. Such effects dissipate nearly instantaneously when compared to the time of ejecta excavation [3].

Results

The comparison between experiments and theory indicate a good match. Experiments indicate that impacts in coarse sand generate ejecta curtains that do not distort while advancing in a wide range of atmospheres [3, 5, 15]. Fig. 5 shows two examples of the computed curtain profile. In each example, the curtain travels in an atmosphere (drag) and a vacuum (no-drag). For the atmospheric case, no significant distortion of the curtain occurs along its entire length. The theory, therefore, matches the impact experiments.
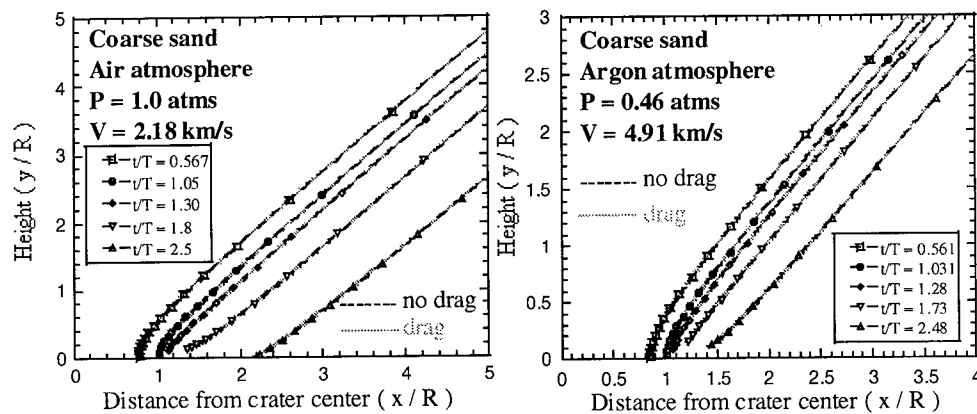
Fig. 5. The theoretical profile of an advancing curtain generated by a 3.175 mm Al projectile launched at 2.18 km/s in 1 atms of Air and 4.19 km/s in 0.46 atms of Argon.

The entrainment capacity for wind speeds determined by the theoretical models are also consistent with laboratory data. For a projectile launched at 2.18 km/s in 1 atms of Air, for example, little or no coarse sand ejecta are entrained by the curtain-driven winds. The micro-spheres sprinkled over the surface, on the other hand, do get entrained and allow visualizing the flow field generated by the moving curtain. For identical impact conditions, Fig. 6a shows the computed range of flow speeds as atmosphere seeps through the effectively impermeable portions of the curtain and undergoes flow separation at the top of the curtain when crater growth ceases. Fig. 6b presents the evolution of the maximum flow speed (peak velocity shown in Fig. 6a) generated at the top of the sand curtain as it advances in time. The combined theoretical result show these flow speeds range from 0.1 to 3.5 m/s. Fig. 7 indicates that such speeds easily entrain most of the micro-spheres, but should not entrain any of the coarse target sand.
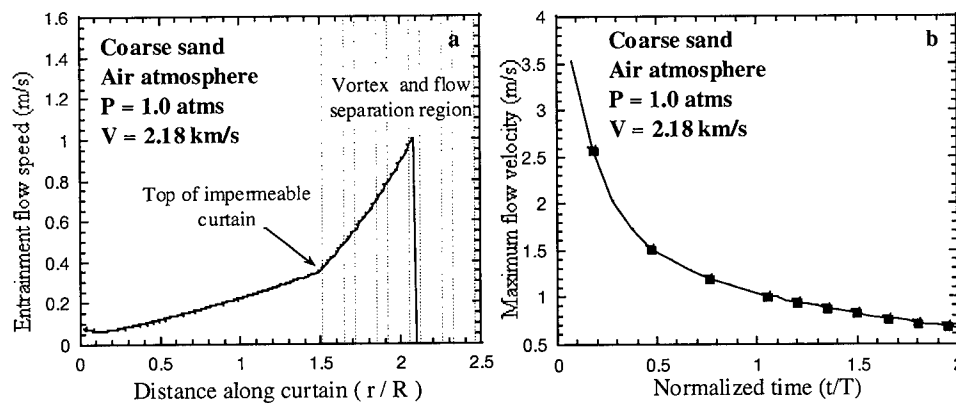
Fig. 6. (a) The theoretical entrainment flow speed achieved by an advancing curtain when crater growth ceases for a ¼" Al projectile launched at 2.18 km/s in 1.0 atms of Air into course sand. (b) The evolution of the maximum entrainment velocity achieved at the point of flow separation by an advancing ejecta curtain generated for the same impact conditions as in (a).

In the experiments, a curtain length can be equated to the distance from the curtain base to the position where significant flow can pass through. This position is easily observed because the micro-spheres are so easily entrained. The theory also provides such a length L by using the

wind tunnel based result that when v_d equals 40% of the curtain velocity significant flow through occurs. We present theoretical results for three different curtain porosities: a constant porosity equal to the target porosity; a constant porosity equal to four times the target porosity, and a porosity that changes exponentially with time (Fig. 8).
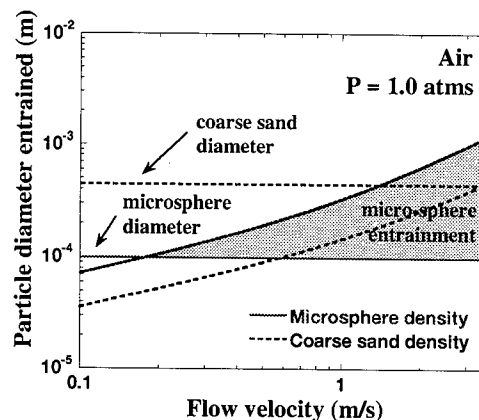
Fig. 7. The particle diameter of sand and micro-spheres that can be entrained by winds in 1.0 atms of Air. Consistent with laboratory observations, the coarse sand cannot be lifted by the winds generated during the impact, while the micro-spheres are easily entrained

The comparison between observation and theory of this curtain length shows the theoretical curtain length L agrees well at early time when the assumed curtain porosity is small, but over estimates observations at late times (Fig. 8). When a greater curtain porosity is assumed, the estimated curtain length is too short at early times, but begins to approach observed lengths at late times. Qualitatively, both the theory and observation indicate that at lower atmospheric pressures (i.e. greater kinematic viscosity $v = \mu / \rho$) the vortex length increases. This is because the Reynolds numbers of ejecta in the curtain decreases, thereby increasing their boundary layer thickness, their drag and hence ζ (note that the ejecta undergo Stokes flow-like conditions). Observations of impacts into Helium [15] indicate very long curtain lengths consistent with such a theoretical assessment.

Carefully examination of the ejecta curtain in vacuum conditions indicates that initially the curtain porosity is low, but that after sometime it increases rapidly [20]. Such an increase is due to small differences in excavation velocity between individual ejecta, and the collision and dispersion of ejecta within the curtain. In a third set of calculations, we assume, therefore, a curtain porosity that increases exponentially with time. The curtain porosity starts with that of the target but increases by a factor of 10 by $t=2T$. For such a curtain porosity, theory matches observation remarkably well (Fig. 8).

CONCLUDING REMARKS

Comparison between theory and laboratory experiments indicates that the theory accounts for the observed curtain shape and the size range of ejecta that should and should not be entrained. A constant porosity model reproduces the ejecta curtain length at early time, while a realistic increase in curtain porosity consistent with observations of ejecta in a vacuum reproduces the entire evolution of the observed curtain length. Furthermore, theory and observations indicate that an increase in curtain length occurs when the ambient kinematic viscosity $v (= \mu / \rho)$ increases.

Future research will assess how the theory describes the flow speeds and curtain length generated when significant amounts of ejecta can be entrained by the impinging winds. Such ejecta

entrainment conditions are expected to prevail during cratering on Mars, Venus and Earth. Testing and modifying our theory to describe such impact conditions is necessary to accurately estimate the initial dusty flow conditions (ejecta entrainment capacity and flow speed) in the curtain-derived vortex. Such dusty flow conditions ultimately control the distal ejecta deposition process, including ejecta run-out and sinuosity. Accurate models of this flow strength, the ejecta entrainment process and the ejecta deposition process should permit interpreting the relationship between different styles of ejecta morphology, target properties (including volatile content) and atmospheric conditions.
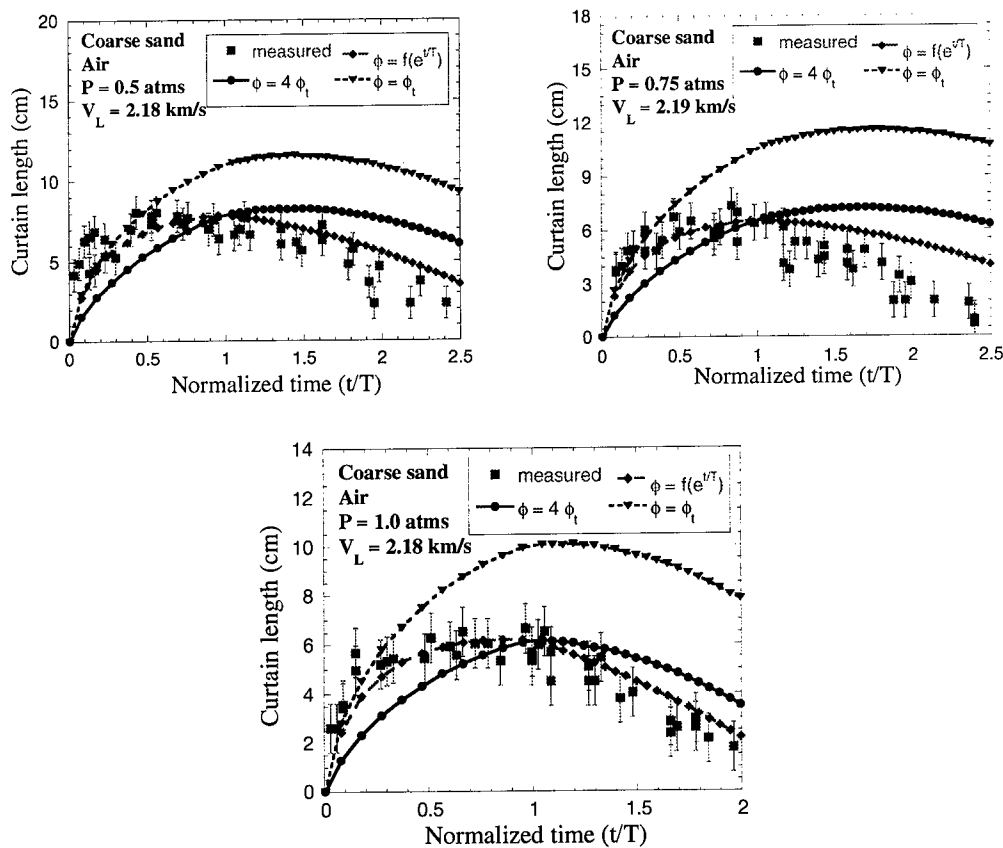
Fig. 8. Measured (squares) and estimated curtain length assuming a constant curtain porosity equal to (down triangles) and four (circles) times that of the target, and a time varying porosity that increases exponentially with time (diamonds). Three atmospheric conditions are presented: 0.5 atms, 0.75 atms and 1 atms of air. Projectiles are ¼" Al launched with velocity V_L into coarse sand.

The particle-by-particle approach used in previous studies [e.g. 1, 3, 4] provided both a first-order assessment of entrained ejecta sizes due to air drag and a basic understanding of curtain-generated winds. Results presented here build on this technique to establish a working kinematic model for the underlying mechanism for entrainment resulting from the response of an atmosphere to ejecta.

REFERENCES

1. Schultz, P.H. and D.E. Gault, Atmospheric effects on Martian ejecta emplacement, *J. Geophys. Res.*, **84**, 7669-7687, (1979).
2. Schultz, P.H. and D.E. Gault, Impact ejecta dynamics in an atmosphere: Experimental results and extrapolations, in Geological implications of impacts of large asteroids and comets on the Earth, edited by L. T. Silver and P.H.Schultz, *Geol. Soc. Am. Spec. Pap.*, **190**, 153-174, (1982).
3. Schultz, P.H., Atmospheric effects on ejecta emplacement, *J. Geophys. Res.*, **97**, 11623-11662, (1992a).
4. Schultz, P.H., Ejecta emplacement and crater formation on Venus, *J. Geophys. Res.*, **97**, 16183-16248, (1992b).
5. Barnouin-Jha, O.S. and P.H. Schultz, Ejecta entrainment by impact-generated ring vortices: Theory and experiments, *J. Geophys. Res.*, **101**, 21099-21115, (1996).
6. Carr, M., L.S. Crumpler, J.A. Cutts, R. Greeley, J.E. Guest, and H. Masursky, Martian Impact Craters and Emplacement of Ejecta by Surface Flow, *J. Geophys. Res.* **82**, 4055-4065, (1977).
7. Schultz, P.H. and J. Singer, A comparison of secondary craters on the Moon, Mercury and Mars, *Proc.Lunar and Planet. Sci. Conf.*, **XI**, 2243-2259, (1980).
8. Phillips, R.J., R.E. Arvidson. J.M Boyce, D.B. Campbell, J.E. Guest, G.G. Schaber and L.A. Soderblom, Impact Craters on Venus: Initial Analysis from Magellan, Science **252**, 288-297, (1991).
9. Schultz, P.H., and J. Grant, Styles of ejecta emplacement, Meteor Crater (abstract), *Lunar Planet. Sci.*, **XX**, 972-973, (1989).
10. Barnouin-Jha, O.S. and P.H. Schultz, Lobateness of impact ejecta deposits from atmospheric interactions, *J. Geophys. Res.*, **103**, 25723-25756, (1998).
11. Barnouin-Jha, O.S., Schultz, P.H. and J. Lever, Investigating interactions between an atmosphere and an ejecta curtain: I. Wind Tunnel Tests, submitted to *J. Geophys. Res.*, (1999).
12. Barnouin-Jha, O.S., Schultz, P.H. and J. Lever, Investigating interactions between an atmosphere and an ejecta curtain: II. Numerical experiments, submitted to *J. Geophys. Res.*, (1999).
13. Idelchik, I. E., *Handbook of hydraulic resistance*, CRC Press, Boca Raton, FL, 790pp, (1994).
14. Maxwell, D.E. Simple Z model of cratering, ejection and the overturned flap, In *Impact and Explosion Cratering*, edited by D.J. Roddy, R.O. Pepin and R.B. Merrill, Pergamon Press, New York, 1003-1008, (1977).
15. Schultz, P.H. Atmospheric effects on cratering efficiency, *J. Geophys. Res.*, **97**, 975-1005, (1992c).
16. Schultz, P.H. and Barnouin, O.S., Atmospheric containment of crater growth, *Lunar Planet. Sci. Conf.* **XXV**, 1213-1214, (1994).
17. Cooper, H.F, and F.M. Sauer, Crater-related ground motions and implication for crater scaling, In *Impact and Explosion Cratering*, edited by D.J. Roddy, R.O. Pepin and R.B. Merrill, Pergamon Press, New York, 1133-1163, (1977).
18. Schultz, P.H. and W. Mendell, Orbital infrared observations of lunar craters and possible implication for impact cratering emplacement, *Proc. Lunar Planet. Sci. Conf.*, **IX**, 2857-2883, (1978).
19. Housen, K.R.,Schmidt, R.M. and K.A. Holsapple, Crater Scaling Laws: Fundamental Forms Based on Dimensional Analysis, *J. Geophys. Res.*, **88**, 2485-2499, (1983).
20. Gault, D.E., W.L. Quaide and V. R. Oberbeck, Impact cratering mechanics and strictures. In *Shock Metamorphism of Natural Materials*, edited by B.M. French and N.M. Short, pp. 87-100, Mono, Baltimore, MD, (1968).
21. Oberbeck, V.R., The role of ballistic erosion and sedimentation in lunar stratigraphy, *Rev. Geophys.*, **13**, 337-362, (1975).
22. O'Keefe, J.D. and T.J. Ahrens, Impact-induced energy partitioning, melting and vaporization on terrestrial planets, *Proc. Lunar Planet. Sci. Conf.*, **VIII**, 3357-3374, (1977).
23. Ahrens, T.J. and J.D. O'Keefe, Energy and mass distributions of impact ejecta blankets on the moon and Mercury, *Proc. Lunar Planet. Sci. Conf.*, **IX**, 3787-3802, (1978).
24. Bryan, J.B. Burton, D.E., Cunningham, M.E. and L.A. Lettis Jr., A two-dimensional computer simulation of hypervelocity impact cratering: Some preliminary results for Meteor Crater, Arizona, *Proc. Lunar Planet. Sci. Conf.*, **IX**, 3931-3964, (1978).
25. Orphal, D.L., Borden W.F., Larson,S.A. and P.H. Schultz, Impact melt generation and transport, *Proc. Lunar Planet. Sci. Conf.*, **XI**, 2309-2323, (1980).
26. Schultz, P.H., D. Orphal, B. Miller, W.F. Borden and S.A. Larson, Multi-ring basin formation: Possible clues from impact cratering calculations, In *Multi-ring basins, Proc. Lunar Planet Sci*, **12A**, edited by P.H. Schultz and R.B. Merrill, 181-195, (1980).
27. Richardson, J.F. and W.N. Zaki, Sedimetation and fluidization, *Trans. Inst. Chem. Engrs.* **39**, 35-52, (1954).
28. Soo, S.L., *Fluid dynamics of multiphase systems*, Blaisdell Publishing Company, Waltham, 524pp., (1967).

PENETRATION OF COMPACT STEEL PROJECTILES IN TO HETEROGENEOUS METAL TARGET OF TIED - WIRE FABRIC (TWF) TYPE

GENNADY V. BELOV, EVGENY P. DYAKIN, SERGEI A. PROTASOV, ANDREI V. PETRUSHIN, and GEORGY S.SMIRNOV

Russian Federal Nuclear Center-All-Russian Scientific Research Institute of Experimental Physics, Mir Avenue 37, 607190, Sarov, Nizhni Novgorod Region, RUSSIA

Summary — Behaviour of heterogeneous targets made of tied-wire fabric is considered in comparison with behaviour of homogeneous steel targets under effect of compact projectiles. We determined ranges of impact velocities related to different penetration mechanisms. © 1999 Elsevier Science Ltd. All rights reserved.

Application of various materials in power-intensive and power elements of up-to-date engineered systems makes it necessary to investigate their propeties comprehensively, and resistance to effect of different loads in particular. One of these loads is an impact caused by a fragment.

In this work behaviour of heterogeneous targets made of steel tied-wire fabric is considered in comparison with behaviour of homogeneous steel targets under effect of compact steel projectiles having masses 10-12 g and impact velocity range 300 - 4700 m/s.

For manufacturing TWF samples we used set of plates with side sizes 250 x 250 mm. Standard sizes of TWF with cell side equal to 2 and 5 mm and wire diameter equal to 0.5 (small) and 1.2 (large) mm correspondingly were employed. Formation of package (target) from TWF was carried out with use of frames and fastening tools. Plates were placed in packages having wires directed parallel to each other. Change of average density ($\bar{\rho}$) of a package in the range 1.24-1.66 g/cm^3 was achieved by change of its thickness, if the number of plates was constant. Design of TWF targets is shown in Fig.1. Homogeneous steel targets were manufactured from soft steel.
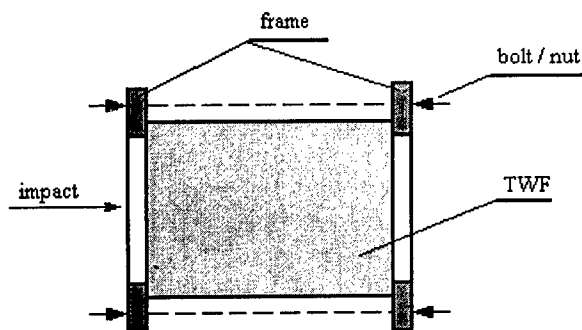
Fig.1. Design of TWF targets

Loading of samples was carried out by compact steel projectiles having masses 10-12g. The projectiles were accelerated by different launchers in dependence on needed velocity of projectile. To accelerate projectiles up to 1600 m/s, we employed balls of a bearing with diameter 14.3 mm (m=12g) as projectiles, which were accelerated by gun-type launcher. Explosive launchers forming compact steel elements from shaped shell accelerated projectiles up to higher velocities (1600 - 4700 m/s). These projectiles masses were 10-12 g. Relation between the maximum and minimum sizes of projectiles did not exceed 1.5.

Experiments to investigate penetration of compact steel projectiles having masses 10-12g and velocities 300-4700m/s in TWF packages show that dependence of projectile penetration on velocity, depicted in Fig. 2, is characterized by existence of three zones corresponding to different penetration mechanisms, which are typical for the interaction of strong projectile with less strong target [1],[2],[3]:

1. Low-velocity zone related to impact velocities up to ~1130m/s. This zone is characterized by quick growth of penetrating ability practically in accordance with linear dependence $\bar{\rho}*l = 0.27*V$ (for packages with wire diameter 0.5mm, l - penetration depth, V-velocity of impact), and a projectile keeps "intact" (a crater has cylindrical shape, Fig.3).

2. Zone of critical velocities, which begins from velocity ~1200m/s. It is characterized by destruction of the projectile, drop of its penetrating ability as impact velocity grows, and significant instability of the results due to dispersion of the strength properties and other factors. The crater becomes "cigar-shaped" (Fig.3).

3. Zone, where penetration has "hydrodynamic" mechanism (V≥2000m/s). In this zone penetrating ability of the projectile begins to grow again as velocity increases in accordance with the law $\sum \bar{\rho}*l \approx V^{⅔}$ (it is the dependence from paper [4] in Fig.2) established for homogeneous metal targets. The projectile fails completely at such velocities, and the crater becomes "barrel-shaped" (Fig.3).
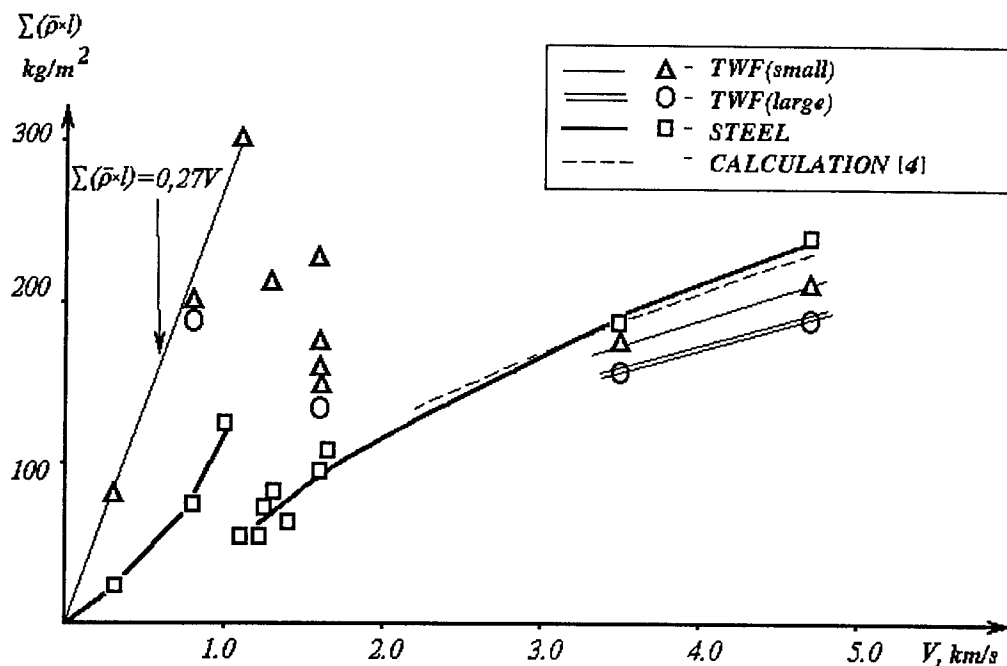
Fig 2. Dependence of projectile penetration on velocity

It should be noted that in the all zones of dependence $\sum \overline{\rho} * l - V$ a net of thick wire with large cells is more effective than a net of thin wire and small cells.

A comparison between projectile penetration in TWF packages and projectile penetration in homogeneous thick targets made of soft steel (data are also presented in Fig.2) gives an idea of efficiency of the protection provided by TWF package. Change of TWF efficiency is depicted in Fig.4, where relation between projectile penetration in TWF package and projectile penetration in homogeneous steel target is presented in dependence on impact velocity ($K_{ef} = \sum \overline{\rho} * l_{TWF} / \rho * l_{st}$).
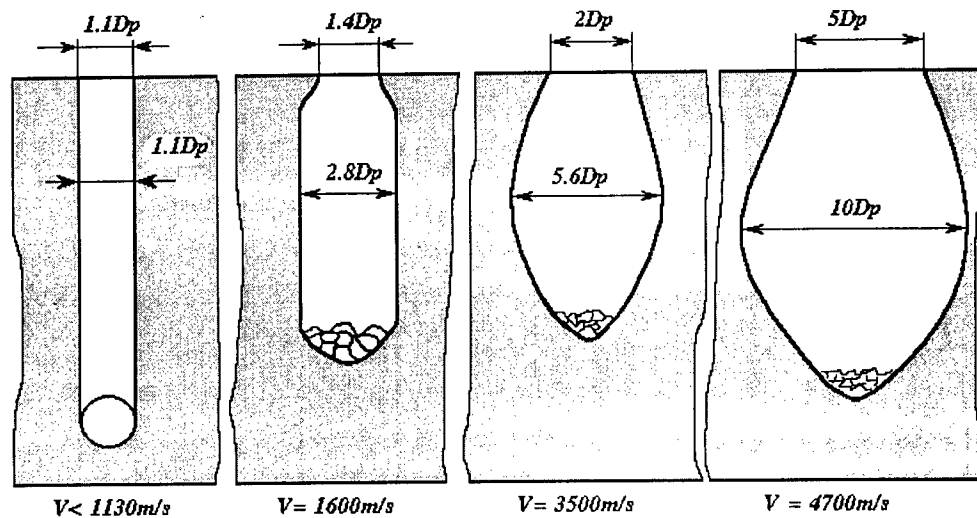
Fig. 3. Shapes of craters in TWF packages in dependence on impact velocity.
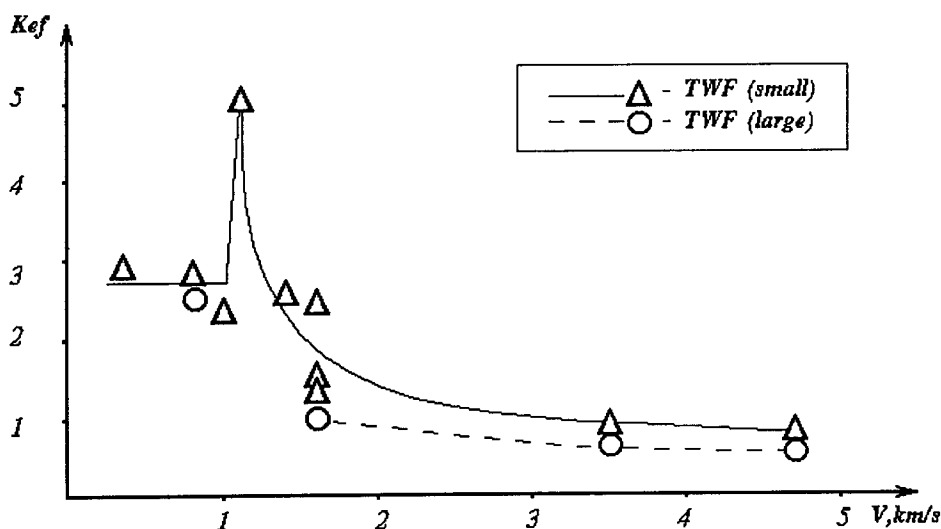
Fig 4. Dependence of K_{ef} on projectile velocity

In accordance with Fig.4 maximum value of K_{ef} is achieved in the area of transfer from low-velocity zone to the zone of critical velocities due to discrepancy between the

critical velocities for steel and TWF (dependence $\sum \bar{\rho}*l(V)$ keeps growing for TWF as velocity increases, but it begins to drop for steel).

Change of average density of TWF package in the range $1.24\text{-}1.66 \text{g/cm}^3$ causes no noticeable changes of specific mass of package part, which is punched ($\sum \bar{\rho}*l \approx const$).

Results of tests for determination of the maximum thickness of package from TWF , wich is punched through by projectile, showed that the maximum thickness of the punched package less 1.1 times exceeds depth of penetration into "thick" packages for the all considered range of impact velocities ("thick" or "heminfinite" packages - packages, where depth of projectiles penetration does not depend on the package thickness). These values are lower noticeably than corresponding values for homogeneous steel plates (1.3-1.5 at V=2-5 km/s [5],[6]). It can be explained by significant attenuation of the amplitude and blurring of the front of a compression wave generated by a projectile in heterogeneous structure of TWF.

So, protection provided by TWF packages against penetration of compact projectiles at high impact velocities (in the zone with "hydrodynamic" mechanism of penetration) is better than protection provided by homogeneous steel screen (up to 30-45%, what masses are concerned). At the same time packages made of TWF rank below homogeneous steel screens noticeably (up to 2-5 times) in the zones of low and critical impact velocities.

Investigated peculiarities of TWF protection characteristics should be taken into consideration while designing specific engineered systems.

REFERENCES

1. G.V.Pryakhin, V.M.Titov, *Prikladnaya Matematika i Technicheskaya Fisika*, N5,(1969).
2. L.V.Belyakov, F.F.Vitman, N.A.Zlatin, *Zhurnal Technicheskoi Fisiki*, N8, t.33,(1963).
3. V.M.Zakharov, I.E.Khorev, *sb. materialov 2 Vsesoyuznogo soveshchaniya po detonatsii. Chernogolovka*, s.153-158, (1981).
4. D.R.Christman, J.W.Gehring, *Journal of Applied Physics*, v.37, N4, p.p.1579-1587, (1966).
5. E.I.Andriankin, Iu.S.Stepanov, *Kosmicheskie issledovaniya*, t.6, v.5, s.752-758, (1968).
6. V.M.Titov, Iu.I.Fadeenko, *Kosmicheskie issledovaniya*, t.10, v.4, s.589-595, (1972).

A PLASMA DRAG HYPERVELOCITY PARTICLE ACCELERATOR (HYPER)

STEVE R. BEST* and M. FRANK ROSE**

*Space Power Institute, Auburn University, 231 Leach Science Center, Auburn University, Auburn, AL 36849, U.S.A.; **Space Sciences Laboratory, Room 4481, Mail Code ES01, NASA Marshall Space Flight Center, AL, 35812, U.S.A.

Summary—Current debris models are able to predict the growth of the space debris problem and suggest that spacecraft must employ armor or bumper shields for some orbital altitudes now and that the problem will become worse as a function of time. The practical upper limit to the velocity distribution is on the order of 40 km/s and is associated with the natural environment. The velocity distribution of the man-made component peaks at 9-10 km/s with maximum velocity in the 14-16 km/s range. Experience in space has verified that the "high probability of impact" particles are in the microgram to milligram range. These particles can have very significant effects on coatings, insulators, and thin metallic layers. The surface of thick materials becomes pitted and the local debris component is enhanced by ejecta from the impact events. In this paper, the HYPER facility is described which produces a reasonable simulation of the man-made space debris spectrum in a controlled environment. The facility capability is discussed in terms of drive geometry, energetics, velocity distribution, diagnostics, and projectile/debris loading. The facility has been used to study impact phenomena on Space Station Freedom's solar array structure, the calibration of space debris collectors, other solar array materials, potential structural materials for use in the space, electrical breakdown in the space environment, and as a means of clarifying or duplicating the impact phenomena on surfaces which have been exposed in space. © 1999 Elsevier Science Ltd. All rights reserved.

INTRODUCTION

In addition to the natural space micrometeoroid environment, constant space activity by man has led to a non-natural debris component that has led to additional concern. This "space pollution" is accelerating due to the frequency of launches by the industrialized countries even though there is a growing awareness that the debris problem must be addressed. The debris environment will be especially of concern when the International Space Station is in orbit. As more countries become active in space, it is inevitable that future spacecraft will have to devote some mass fraction of the total spacecraft mass to the armoring of critical components. The debris and plasma produced by hypervelocity impact can trigger electrical breakdown reducing the effectiveness of insulators for space use. For the most favored low-to-medium earth orbits it is projected from some models [1] that significant design changes will be necessary in the near future. At geosynchronous orbits the problem could be a design driver not too many years thereafter. The LDEF experiment showed that over its limited time in space there were no impacts that could cause severe structural damage [2]. There were, however, large numbers of impacts, which could effect solar arrays, transmission lines, optical and thermal coatings, and protective coatings. The analysis to date has shown that the damage produced is synergistic with other space environmental factors such as atomic oxygen and ultraviolet radiation [2]. By far the largest number of impacts is particles with masses in the microgram to milligram range over the entire velocity spectrum.

Several options exist [3] for studying space impact phenomena. The most expensive technique

is to place suitable materials in space for an adequate period of time to allow a statistically significant sampling of the local debris spectrum. This was done with the LDEF experiment and has also been a standard technique on the Russian MIR space station. Light gas gun technology can also be used to accelerate macro-projectiles in the gram range for impact studies. Due to the hydrodynamics of staged, light gas guns, the velocity limit which can be achieved is on the order of 10 km/s and is unsuited to accelerating particles which are less than 100 microns in diameter. Further, for light gas guns, massive unwanted debris from the seals and sabots, and the "large gas slug" must be eliminated or the resulting damage on impact will mask any controlled particle impact. As a result, it is difficult to do experiments on active systems or "mock ups" designed to simulate active spacecraft components with light gas guns. The best technique for small particle sizes is to employ an electromagnetic device [4] to drive suitable projectiles in a vacuum chamber. Using this technique, it is possible to more closely duplicate the space environment as well as inflict minimum additional damage to a sample.

HYPERVELOCITY FACILITY (HYPER)

Accelerator Hardware

Figure 1 shows the gun and target vacuum chambers, and the flight tube geometry for HYPER. The first chamber houses the armature/gun assembly, variable drive section, and an experimental impact station. This chamber has four viewing ports and several diagnostic feedthrough flanges for use as needed. Conical skimmers are placed in the exiting port to allow gun effluent exhaust gas diversion away from the flight drift tube. An aperture in the skimmers also allows only particles traveling within a narrow solid angle to continue into the drift tube to the target. This eliminates particle collisions with the drift tube walls and the resultant particle debris cloud diameter at the target is approximately 13 cm. The chamber has its own vacuum pump system and diagnostic station. The maximum chamber diameter is 36 cm and allows about 1 m of linear experimental space within the beam line along the flight axis.

Capacitor Bank

Gate Valve

PMT Diagnostics

Gun Chamber   Flight Drift Tube   Target Chamber
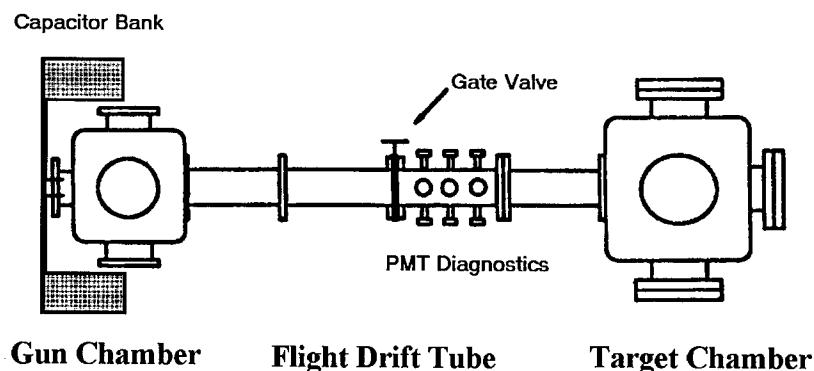
Fig. 1. Vacuum chambers for hypervelocity facility.

The target chamber made out of stainless steel is 1.45 m in diameter and 2 m long. It has numerous diagnostic ports, instrument feedthrough stations, and specimen assembly racks. Both chambers operate at approximately 10^{-6} Torr. Connecting the chambers is a 7-m (variable) flight drift tube. The length of this tube allows all electrical and optical events due to gun firing to

subside before impact occurs in the main chamber. This time-of-flight isolation also allows the hot expanding gases to be cooled and trapped, thereby allowing almost the entire "unwanted" armature residue to be captured before striking the specimen in the main chamber. To facilitate the diversion of unwanted gas and gun debris, additional skimmers are placed in the flight tube and an electronically activated shutter is placed in the beam line near the specimen assembly. This shutter eliminates all debris traveling less than 2 km/s. An in-line gate valve, allowing the gun to be reworked without disturbing the experiment in the target chamber isolates the chambers. In this mode, operational systems or semi-operational subsystems can be exposed repeatedly without returning to atmospheric pressure. The target chamber feedthroughs and the Institute's power capability allow for as much as 100-kW DC power to be supplied to the target chamber as needed. Further, electrical power sources for bias potential, plasma and light sources are available to closely simulate solar illumination and the local space plasma conditions at the experiment/target location.

Particle Acceleration

Figure 2 shows a block and schematic diagram of the electrical drives for the HYPER accelerator, which is capable of driving small projectiles to velocities greater than 10 km/s. The energy storage system for HYPER consists of a capacitor bank made up of four segments with total capacitance of 53.6 μF and storing 67 kJ at a charging potential of 50 kV. For a given experiment, the capacitor voltage determines the energy and velocity spectrum of the accelerated particles. In the event of a misfire, an array of protective circuits is provided to discharge the stored energy into a suitable 'dump' load. Once the desired voltage has been reached, a closing switch is triggered, resulting in a current pulse of 1 to 1.25 MA flowing through an exploding foil driver. The current rise time is governed by circuit inductance and is on the order of 300 ns for the facility as currently configured. The foil driver assembly rapidly explodes producing extremely hot metallic plasma, which dissociates a buffer plastic film. The gases from the film and the metallic plasma are accelerated due to $\vec{J} \times \vec{B}$-forces and internal pressure from the gases produced by the explosion. The contacts to the assembly are constructed of stainless steel and, due to the enormous dynamic forces, are constrained by an insulating structure composed of G-10 composite. The entire assembly is fastened to a high current feedthrough plate.
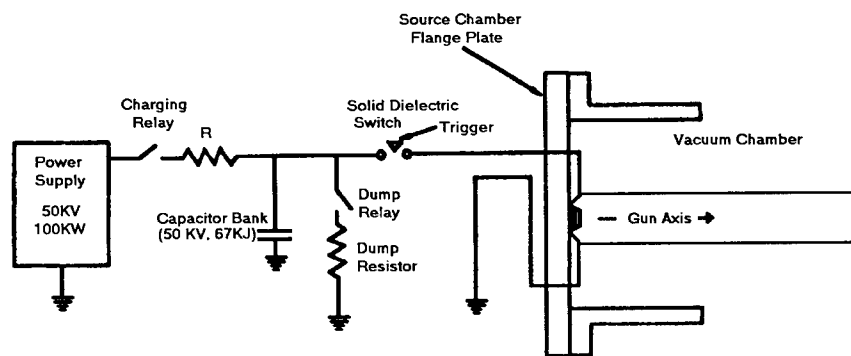
Fig. 2. Block and schematic diagram of the facility and the gun drive circuits.

In order to do controlled impacts, an ablator film, suitably loaded with small particles, is used to provide impacting particles. When the aluminum foil explodes, the hot metallic plasma totally decomposes the plastic ablator film into constituent gases such as hydrogen and carbon at a

temperature of several thousand °K. This plasma/gas-slug/debris package is accelerated through a contained dielectric gun barrel due to both $\bar{J} \times \bar{B}$-forces and pressure generated by hot gases. As a result the microprojectiles are 'dragged along' at a substantial fraction of the plasma velocity. The gas/plasma velocity has been measured by high-speed photography to be greater than 40 km/s at the exit of the drive section. Obviously, loading of the armature assembly with a selected particle size and mass determine the velocity distribution of the particles and there will be a distribution of velocities for the particles dragged along with the gas slug.

Diagnostics of Hypervelocity Impact

It can be extremely difficult to measure the velocities of many particles in the particulate stream moving at hypervelocities. The primary diagnostic technique most often used is a high-speed image converter camera operated in the streak mode. The experimental set-up and an example of an 'impact event' are shown in Figures 3a and 3b. Referring to Figures 3a and 3b, a Hadland Imacon 790 high-speed framing/streak camera is used to monitor impact events by imaging the optical flash occurring on impact. Using a system of lenses and mirrors, both the x- and y- coordinates of any individual impact event is measured directly from the streak photo record and the crater located precisely after applying an appropriate scaling factor. Each pair of dots in Fig. 3b represents one impact. Since the image is "streaked" across the film plane at a known rate, the position of the impact event on the film uniquely determines the velocity of the particle impacting the specimen. Modulated light emitting diodes are placed at the edges of the specimen to allow easy determination of the x-, y-coordinates and to facilitate measuring the time of arrival. The camera is started after a suitable delay in order to improve resolution. This method is particularly suited to the measurement of particles, which are moving at high velocities and produce highly luminous plasma clouds on impact. Within the limits of sensitivity of the film, plasma lifetime can be measured within the field of view and correlated with particle size, species, and velocity. One single streak image now contains information on:

- x-, y-coordinates of each impact,
- number of impacting particles,
- velocity of each particle,
- duration of optical flash.

There are two other diagnostic techniques that have been used in this facility to characterize particle impact. First, for those particles sufficiently large, high bandwidth piezo sensors can be mounted on the back of the specimen to record time of arrival, and hence velocity, over a wide range of particle velocities. As with the optical curtain technique described below, this method does not allow unambiguous localization of a specific impact event with a specific velocity without the use of special two-dimensional time-domain reflectometry equipment. This technique also makes it difficult to resolve two particles arriving simultaneously. Also, sensitivity is very limited. The other technique detects scattered light from particles passing through a section of the drift tube containing a multiple diagnostic ports. One set of the ports is used to provide three "optical curtains" produced by high intensity lights or lasers. The "other set of ports" are fitted with sensitive photomultiplier tubes to look for scattered light from the passing particulate beam. The flight tube is segmented in three equal sections, allowing the six-port to be placed at a location, which minimizes electromagnetic interference and residual illumination from the expanding gun effluents. The ability of this technique to resolve particulate matter is a function of the particle size, its velocity, the width of the optical curtains, particle scattering cross-section, optical intensity, and the sensitivity of the detector system. It is mostly used to generate data on

the total size of the particle packet and the range of velocities rather than individual particle velocities, since it is impossible to resolve particles entering the light curtain simultaneously.
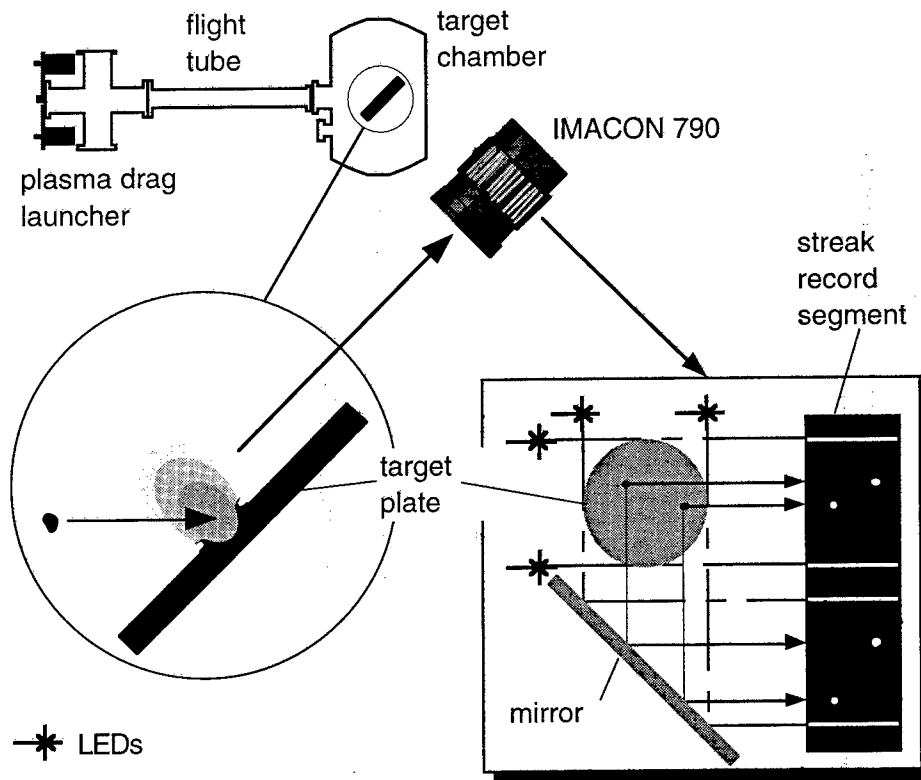
Fig. 3a. Experimental assembly and streak camera diagnostic system schematic.
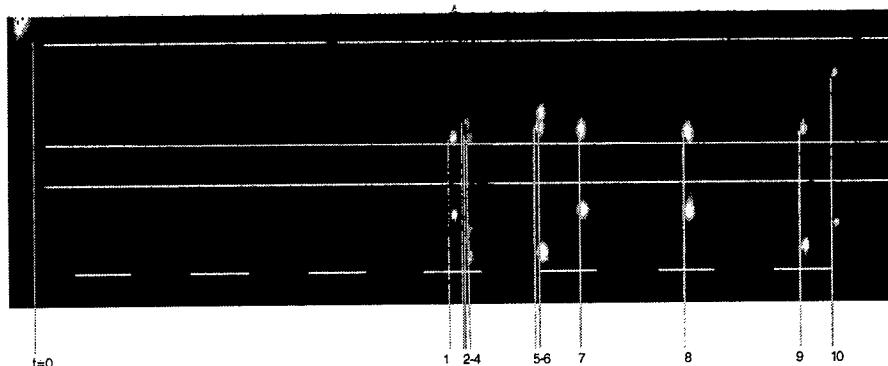
Fig. 3b. Typical optical record obtained from an actual hypervelocity event.

The only remaining piece of information necessary to uniquely characterize the impact event is to have a measure of the particle size. For particles moving at sufficiently high velocities impacting very thin films where the particle size diameter-to-film thickness ratio is approximately 75, the particle will penetrate, suffering almost no damage and leave a "footprint"

characteristic of its dimensions [5,6]. In general, the characteristic particle dimension should be many times the thickness of the film and the velocity greater than 5 km/s. In this facility, ballistic films made of plastics, 0.4 microns in thickness, are supported on a frame and placed on a holder about 3 cm above the specimen. The film and specimen share a common reference mark, allowing an impact crater to be uniquely identified with a 'footprint' on the ballistic film.

In order to test the hypothesis that the ballistic film technique could be used to measure gun-induced breakup and particle size, the length (L) to width (W) ratio for nominal 100-micron aluminum oxide particles was measured. The average and deviation of this ratio was 1.6±0.5 for 500 particles. Twenty-nine impact events were used to determine the L/W-ratio for penetrations of the ballistic film resulting in 1.98±0.7. A correction factor for random orientation at penetration was also used. The lower limit in velocity for this experiment was on the order of 3 km/s, which would leave a bigger footprint in the film. The absolute values in both L and W were comparable for the particles and the penetration "footprint". Our assessment is that there is little particle breakup during acceleration and that the ballistic film technique is valid to determine the approximate size for an impacting particle.

Since the primary acceleration process is "plasma drag", there is always a gradient in the velocity of the particle stream. The maximum velocity obtainable and the velocity distribution are a complex function of the particle shape, particle density, absolute particle dimensions, and the gun parameters. Just as in space, there is always a wide range of particle velocities in a given experiment. From the point of view of simulation, this is desirable since it probably is a more accurate representation of the actual conditions in space. Figure 4 illustrates one of the many derived particle velocity distributions from the facility and is somewhat typical of the debris flux in space.
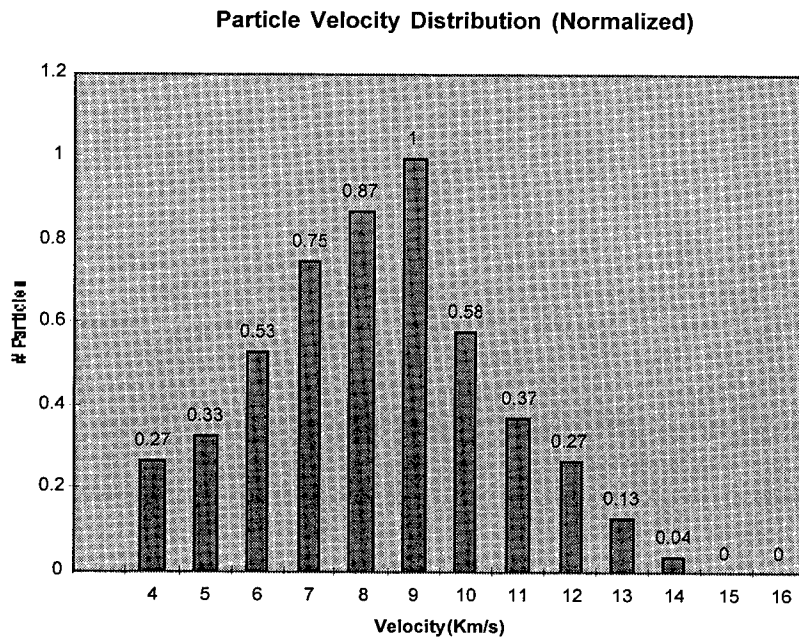
Fig. 5. Typical particle-velocity distribution for HYPER using olivine particles.

This distribution is based upon several experiments and while it does not duplicate the 'Erickson distribution', it does overlap in the region of the distribution peak. Further, the particulate used in this experiment was one to two orders of magnitude larger than that typically

seen in space as determined by the LDEF experiments. We have collected experimental data on the velocity distribution for 100-micron aluminum oxide, 100-micron silicon carbide, and 100-micron olivine particles. At this facility, the upper limit on the velocity distribution for 100-micron aluminum oxide particles is 11.5 km/s as compared to 14.5 km/s for the same size silicon carbide and olivine particles.

TYPICAL APPLICATIONS

The HYPER facility has been used to study impact phenomena for a variety of space applications. Hill [6] used the HYPER facility to study impact angles and their effect on crater dynamics. Figure 6 shows an impact crater in high purity copper produced by an olivine particle moving at 7 km/s. The angle of impact was 30° with respect to the surface normal, while the arrow indicates the impact direction. An EDX/SEM (Energy Dispersive X-Ray/Scanning Electron Microscope) analysis of the residue indicated that the particles seen at the bottom of the crater are olivine fragments.
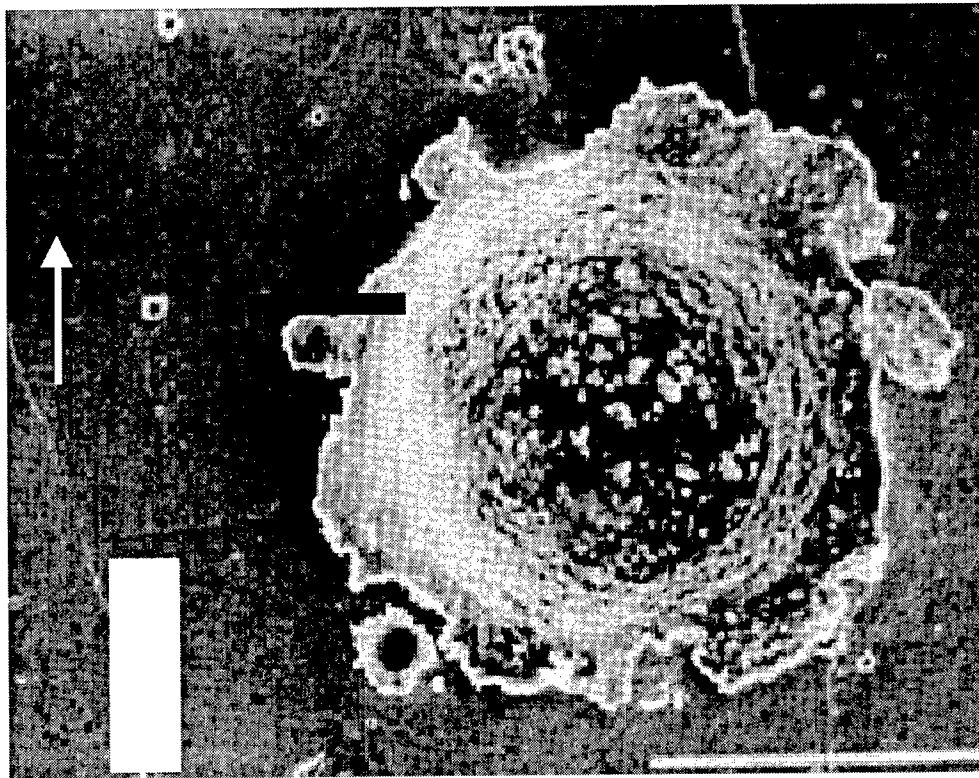
Fig. 6. Impact site formed by a 7-km/s olivine particle at impact angle of 30°.

Figure 7 shows a similar impact event with an impact angle of 45°. With an impact velocity of 10.5 km/s, there was little debris found in the bottom of the crater. At this velocity, the shock heating effect was sufficient to vaporize most of the material in the impact crater. Compared with the spherical craters of impact sites produced at impact angles of 0°, there is little or no difference to the crater shape. Hill's study showed that significant deviations did occur at impact angles greater than 45° and could be used as a rough discriminator of the angle of impact.
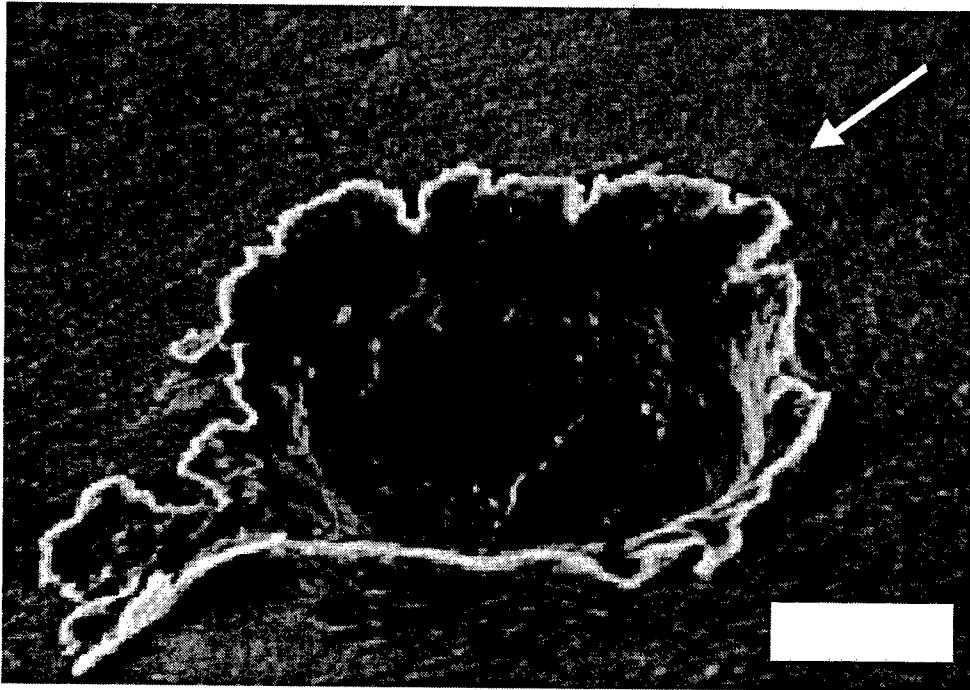
Fig. 7. Oblique view of impact site formed by a 10.5-km/s olivine particle at impact angle of 45°.

There has been considerable interest in the development of techniques to capture high velocity space debris and return it to earth for analysis. The primary method used is to capture the debris in an Aerogel foam. Figure 8 shows two tracks of olivine particles moving at approximately 8 km/s. Both particles were stopped within the Aerogel without breakup. The particles can be removed from the Aerogel for laboratory analysis and examination. HYPER has been used to calibrate several such Aerogels for both NASA and the Japanese Space Agency NASDA. Based on the data from HYPER, particles moving at velocities greater than about 11 km/s cannot be captured intact due to breakup within the Aerogels.
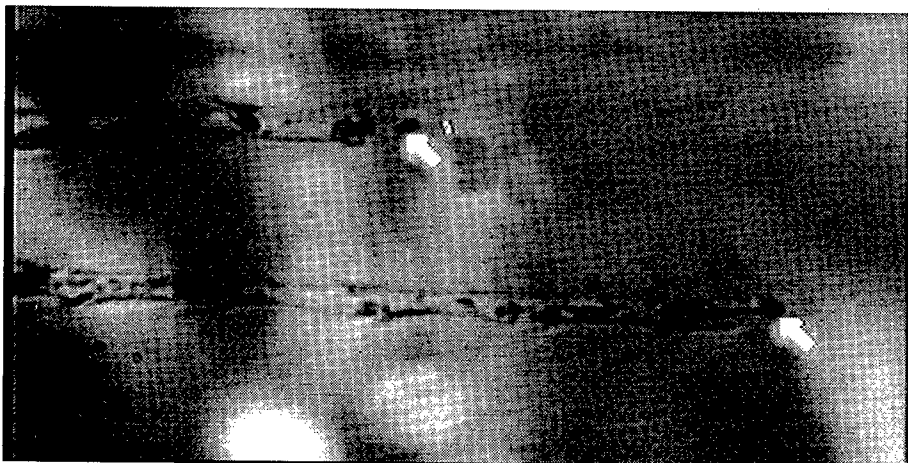
Fig. 8. Olivine particle tracks within carbon Aerojel.

A final typical application for HYPER is the testing of solar cells, cell covers, optical coatings, and thermal blankets to determine damage as a function of exposure to the debris flux. Many particles can be accelerated simultaneously, with a velocity distribution roughly typical of that of the man-made debris spectrum. One exposure in the HYPER facility corresponds to the number of impacts received in a 7-year exposure in space for the same particle size distribution. Figure 9 illustrates impact damage on solar cells typical of those intended to be used in an early version of the Space Station. The impacting particles were aluminum oxide, which is a fuel residue, with particle sizes in the range of 10 to 50 microns. Numerous damage sites are readily visible and mainly show up as damage in the glass cover plates. The damage in the cover plates can be the site for synergistic effects with atomic oxygen or provide a "short circuit" path to the local plasma.
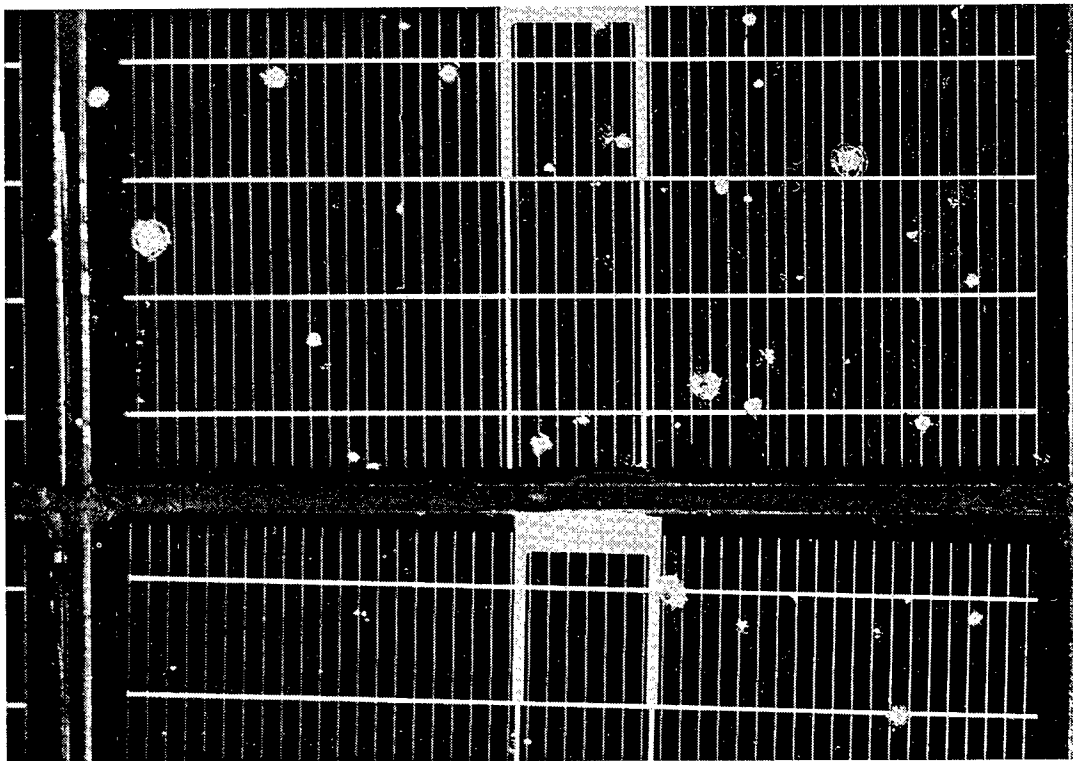
Fig. 9. Typical damage to cover plates on solar cells exposed within the HYPER facility.

SUMMARY

The HYPER facility has evolved into a sophisticated method of analyzing the effects of space debris on any material contemplated for use in space. The debris spectrum and the choice of particles, which can be used, allow the experimenter to more closely duplicate the natural conditions, which will be encountered in space. The optical diagnostics are unique and allow adequate characterization of both the impacting particle stream and the damage inflicted at impact. Inherent in the facility is the ability to look at long term effects. Typically, 20-50 particles are accelerated in any given event. By choosing the particle size in correlation with the expected number of impacts based on known space flux, it is possible to estimate end-of-life

characteristics due to debris in addition to local damage. HYPER has had some 25-user groups, representing industry, academia and the government, utilize the facility and is currently used in hypervelocity research within the Space Power Institute.

REFERENCES

1. D.J. Kessler and Shin-Yi Su, Editors, Orbital Debris, Proceedings of a Workshop sponsored by the NASA Lyndon B. Johnson Space Center, NASA Conf. Publication 2360, 1985.

2. Meteroid and Debris Impact Features Documented on the Long Duration Exposure Facility, a preliminary report compiled by Members of the LDEF Meteroid and Debris Special Investigation Group. JSC #24608, Aug. 1990.

3. J. A. Zucas, T. Nicholas, H. A. Swift, L. B. Greszczuk and D. R. Curran, Impact Dynamics, John Wiley & Sons, 1981.

4. Proceedings, 3rd Symposium on Electromagnetic Launch Technology, Austin, TX, 1986.

5. W. P. Schonberg and R. A. Taylor, Oblique Hypervelocity Impact Response of Dual-Sheet Structures, NASA TM 100358, Jan. 1989.

6. D. A. Hill, Duplication and Analysis of Meteoroid Damage on LDEF and Advanced Spacecraft Materials, Final Report for NASA Research Grant NAG-11329, NASA Langley Research Center, December 1994

TRANSVERSE LOADS ON A YAWED PROJECTILE

STEPHAN J. BLESS, SIKHANDA SATAPATHY, and MICHAEL J. NORMANDIA

Institute for Advanced Technology, The University of Texas at Austin
4030-2 W. Braker Lane, Austin TX 78759

Summary—Yaw has been known to greatly influence the penetration performance of long-rod projectiles. Experiments have shown that even small angles of yaw can significantly degrade performance. We show that a critical feature of a yawed impact is the transverse load on the penetrator. Transverse loads tend to decrease the misalignment of rod axis and velocity vector. We use classical cavity expansion theory to quantify the impact transients and determine the magnitude of the transverse load. Then, a steady-state slot-cutting model is used to calculate the shape and orientation of a projectile that exits a finite plate. We find that this is contrary to the findings of some previous studies considered. The strength of the projectile may be ignored compared to the inertial loads even at the relatively high impact velocities. The theory agrees well with reverse impact experimental data on finite plates. © 1999 Elsevier Science Ltd. All rights reserved.

INTRODUCTION

The mechanics of yawed long-rod projectiles at hypervelocity has been receiving a lot of attention recently due to their importance for several contemporary terminal ballistic systems [1]. Solutions exist for cases where the penetrator stays rigid [2] or elastic [3]. There have been a number of experimental studies [4, 5] and numerical evaluations [6, 7, 8] of yaw effects for problems where erosion is present. Due to the complexity of these problems there have been only a few attempts at analytical modeling of this important phenomena [9, 10]. Discussions of yaw mechanics have attributed penetration degradation variously to rigid-body rotation of the projectile [11], strike of the tail on the crater lip [5, 10], collapse of the projectile into a trough [12], reduction in effective length [13], and altered penetration direction [5, 14]. While all of these effects may play a role, for very high velocity impact of tungsten rods onto steel targets, the paramount importance of lateral loads that redirect the projectile velocity vector has been recently identified [9]. In this study, we have attempted to quantify the lateral load, and combine it with models for steady-state slot cutting and initial transients to describe yawed penetration of finite-plate targets.

Fig. 1 defines the geometrical quantities associated with the yaw problem. Yaw angle, γ is defined as follows:

$$\gamma = \sin^{-1}\left[\text{sgn}(\mathbf{V}x\mathbf{L})\frac{|\mathbf{V}x\mathbf{L}|}{|\mathbf{V}||\mathbf{L}|} \right], \tag{1}$$

where $\mathbf{V}$ is the velocity vector and $\mathbf{L}$ is the length vector pointing from tail to tip of the projectile. The angle of obliquity is defined by,

$$\beta = \sin^{-1}\left[\text{sgn}(\hat{n}x\mathbf{V})\frac{|\mathbf{V}x\hat{n}|}{|\mathbf{V}|} \right], \tag{2}$$

where $\hat{n}$ is unit normal into the target surface on the impact side. As we shall discuss later, it is essential to differentiate between the path of a point on the rod and the instantaneous shape of the rod itself. Thus, θ defines the angle that the instantaneous velocity vector at a point makes with the X-axis. This angle defines the tangent to the particle path. The angle ϕ at a point is the angle between the tangent to the rod and X-axis, and hence defines the shape of the rod. R is the radius of curvature of the particle path. All the calculations are made in stationary plate coordinates, where the relative velocity between the projectile and the target is assigned to the projectile. We also break up the penetrator velocity V into components parallel (V_p) and transverse (V_n) to the local rod axis.
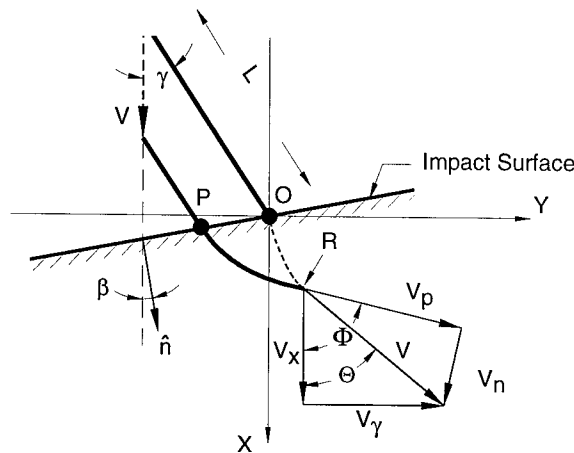
Fig. 1. Geometry preimpact and during penetration.

The surface interaction point is defined as the point on the rod (target face) which is in contact with the target (rod) for the first time (points O and P in Fig. 1).

Velocity of the interaction point along the rod axis: $V_{ir} = V\dfrac{\cos\beta}{\cos(\beta-\gamma)}$ (3)

Velocity of the interaction point normal to the rod axis: $V_{in} = V\sin\gamma$ (4)

Velocity of the interaction point along the plate surface: $V_{ip} = V\dfrac{\sin\gamma}{\cos(\beta-\gamma)}$ (5)

STAGES OF INTERACTION

Impact of a yawed and eroding rod projectile is a complex event that may consist of three distinct phases. The phases may overlap in time. Figure 2 illustrates the phases. They are:

primary penetration. In this stage a penetration cavity is induced in the target by the penetrator's parallel (axial) velocity component. The penetrator elements that strike the crater floor are unaffected by lateral penetration.

lateral penetration. In this stage, the projectile comes in contact with the side of the cavity. This usually happens first on the target surface. At the velocities considered here the projectile cuts a slot in the cavity wall. The lateral penetration is due to the transverse component of the penetrator velocity. If there is no or negligible open cavity from primary penetration, the rod also penetrates into the target from its leading face, which penetration is driven by the local parallel velocity component.

terminal penetration. In the final stage, the rod that has exited the slot strikes the bottom or sides of the cavity where it may cause additional penetration. The exiting rod has an altered velocity vector and may be broken. This phase is important for thick targets and is most likely absent for relatively thin plates.
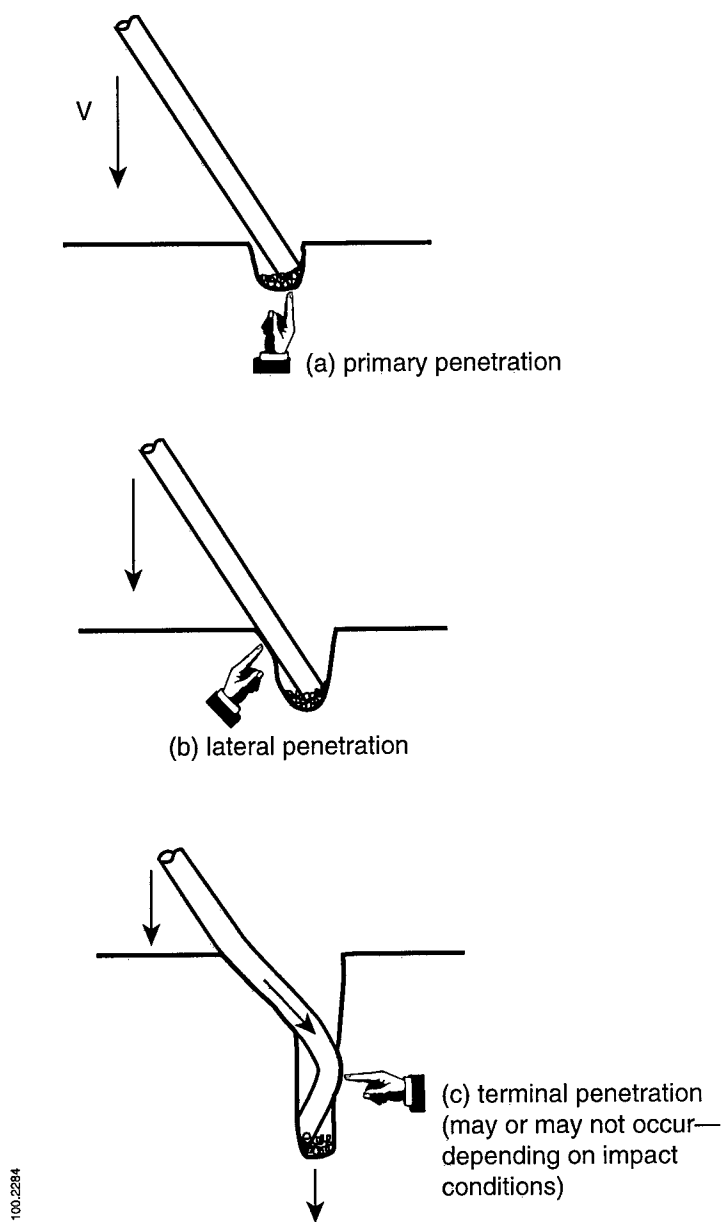
Fig. 2. **Stages in yawed rod penetration: (a) primary penetration. (b) lateral penetration. (c) terminal penetration**

INITIAL TRANSIENTS

Lateral penetration begins after a delay associated with the time required for the rod to contact the crater wall. This "cavitation delay" is over when:

$$V_{ip}t > a(t) \qquad (6)$$

where a is the cavity radius (at the surface).

If the crater size is large enough, the entire rod can pass through without interacting with the side-wall, and the effect of initial yaw is minimal. Bjerke et al. [5] presented a formula to calculate the maximum yaw (critical yaw) for this condition. Bjerke et al. assumed that the crater grows

rapidly enough that the final size is attained almost instantaneously. Recently, the time-dependence of crater growth was reconsidered by Lee and Bless [15] but their treatment does not include the initial impact crater.

The growth rate of the initial cavity can be estimated by assuming spherical cavitation. The differential equation that describes the dynamics of a spherical cavity in an incompressible elastic-plastic medium is [16]:

$$a\ddot{a} + \frac{3}{2}\dot{a}^2 + \frac{2Y}{3\rho}\left\{1 + \ln\left(\frac{2E}{3Y}\right)\right\} = \frac{P}{\rho} \tag{7}$$

where a denotes the cavity radius, P is the initial pressure, ρ is the density, Y and E are the flow stress and Young's modulus respectively. The initial conditions for this problem have to be chosen carefully. The first is that the initial cavity radius is equal to the rod radius. The initial condition on the velocity is intriguing. As in any initial-boundary value problems in solid mechanics, both the velocity and the pressure cannot be specified simultaneously at the cavity wall. We examined the condition that $\dot{a} = V$ at $t = 0$. We found, as shown in Fig. 3, that agreement with Bjerke et al.'s empirical relations for final cavity diameter for normal impacts was rather good. Figure 4 shows the crater diameter as a function of time that is implied by this solution, compared to the interaction point motion (Eqn. 5) for some cases of interest that are discussed in the next section. We note that for oblique targets, the crater is not centered on the rod axis, and this will affect the time for onset of lateral penetration predicted by Fig. 4.
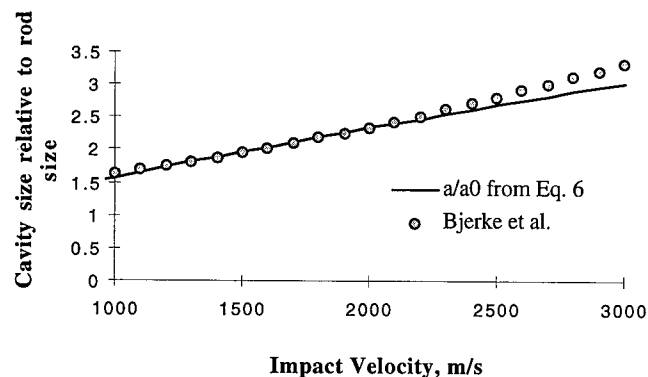
Fig. 3. Final impact crater size at different velocities.
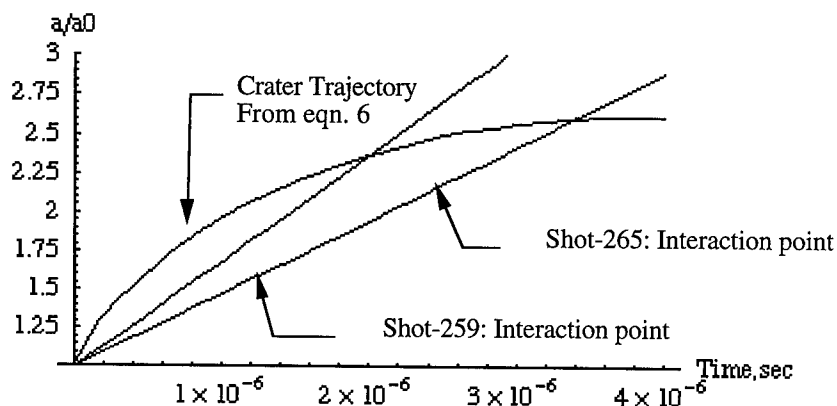
Fig. 4. Trajectories of interaction point and impact crater on target surface. Embedment starts where the trajectories cross.

There is an additional transient associated with lateral penetration: radial embedment. At the velocities considered here, embedment is analogous to indentation [17]. It is driven by the geometrical interference of the rod and target. In such a situation, penetration due to the frontal portion of the rod, which is already inside the crater at the instant of initial lateral contact, is not affected. The rod starts to embed at a speed V_{in} given by Eqn. (4). The lateral load is the transverse component of the load due to the cavity expansion pressure acting on the partially embedded cross-section [9]. The embedment factor, f, which is the ratio of current load, F, to the maximum load F_{max} is given by:

$$f = \frac{F}{F_{max}} = \min\left\{1, \frac{2}{\pi}\cos^{-1}\left[1 - \frac{2V}{d}\sin\gamma\right]\right\}. \tag{8}$$

The minimum function is used to denote the fact that after full embedment the embedment factor is unity.

SLOT-CUTTING DYNAMICS

From this point, we restrict our analysis to consider finite plates that are perforated. For this problem, once embedment is complete, the slot cutting becomes steady state, and the process is self similar (unless the penetrator fractures). The terminal phase (c) of yawed rod penetration is considered to be absent.

To calculate the slot evolution in the target, it is necessary to distinguish between the instantaneous rod shape and the path followed by a point on the rod (particle path, as shown in Fig. 1).

The target-penetrator interaction is assumed to be due to: i) frontal resistance to penetration along the rod axis, and ii) lateral resistance to slot-cutting. We assume that Alekseevski-Tate theory [18] applies in the axial direction, by virtue of which erosion and deceleration in the axial direction can be calculated. The lateral resistance is given by cavity expansion pressure, which acts in the normal direction to the rod.

No erosion is envisioned in the lateral direction. We have experimentally verified this assumption for yaw angles $\leq 10°$ and speeds to 2.6 km/s for tungsten penetrating armor steel [8]. Erosion can occur during this process, however.

From Alekseevski-Tate theory, we obtain the following equations for motion in the rod's axial direction:

$$\left.\begin{array}{l} \dfrac{1}{2}\rho_p\left(V_p - u\right)^2 + Y = \dfrac{1}{2}\rho_t u^2 + R_t \\[2mm] \dot{L} = -\left(V_p - u\right) \\[2mm] \dot{V}_p = -\dfrac{Y}{\rho_p L} \end{array}\right\} \tag{9}$$

where ρ_p is the projectile density, ρ_t is the target density, u is the penetration velocity of the rod (assumed to be in the parallel direction), Y is the projectile strength, and R_t is the target resistance.

Equations (9) provide very useful insight regarding the penetration direction during the primary penetration stage. These equations imply that the velocity of the projectile/target interface is the vector sum of u and V_n.

In the transverse direction, the cavity expansion speed is V_n. Using self-similarity transformations, Forrestal [19] has solved the field equations for dynamic cylindrical cavity expansion problem with an elastic-plastic constitutive law. His solution is in the form of a set of non-linear equations, evaluation of which yields the pressure required to open a cylindrical cavity at a speed V_n. We have numerically solved these equations for RHA and have plotted the same in Fig. 5. A quadratic curve fit formula of the following form represents the solution reasonably well:

$$\sigma_c = \sigma_0 + b\rho_t V_n^{\,2} \tag{10}$$

where σ_0 is the quasi-static cylindrical cavity expansion pressure. For RHA steel, with a flow stress of 1.2 GPa, σ_0 is 3.3 GPa and b is equal 2.2.
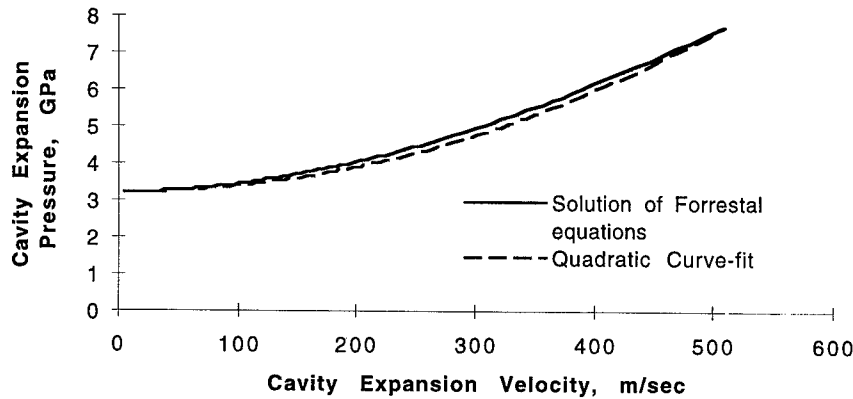
Fig. 5. Dynamic cylindrical cavity expansion solution.

We use this cavity expansion pressure as an approximation to the lateral stress present at the projectile-target interface. Considering an element of penetrator length ΔL, we express Newton's 2nd law for the element as follows:

$$d\Delta L\left[-\left(\sigma_0 + b\rho_t V_n^2\right)f\right] = \frac{\pi d^2 \rho_p}{4}\,\Delta L\left[\dot{V_n} - \frac{V^2}{R}\cos(\phi - \theta)\right]. \tag{11}$$

The first term in the square bracket of the RHS represents the acceleration of the point in the target in contact with the rod element. The second term in the square bracket of the RHS is the normal component of the acceleration of the rod element with respect to the target point that is required to maintain the rod in a curvilinear motion.

The angle, θ, is given by,

$$\tan(\theta) = V_y/V_x. \tag{12}$$

Differentiating Eqn. (12) with respect to time we obtain:

$$\dot{\theta} = \frac{V_x\dot{V_y} - V_y\dot{V_x}}{V^2}. \tag{13}$$

From geometry, V_x and V_y are related to V_n and V_p through:

$$\left.\begin{aligned} V_x &= V_p\cos\phi + V_n\sin\phi \\ V_y &= V_p\sin\phi - V_n\cos\phi \end{aligned}\right\}. \tag{14}$$

Inserting Eqn. (14) into Eqn. (13) we obtain:

$$\dot{\theta} = \dot{\phi} - \cos(\phi - \theta)\frac{\dot{V_n}}{V} + \sin(\phi - \theta)\frac{\dot{V_p}}{V} \tag{15}$$

where we have used $V_p = V\cos(\phi-\theta)$ and $V_n = V\sin(\phi-\theta)$.

Solving Eqns. (11) and (15) along with the relation $R = V/\dot{\theta}$, we obtain:

$$\dot{V}_n = \frac{V\dot{\phi}\cos(\phi - \theta) + \left(\frac{4}{\pi\rho_p d}\right)\left(\frac{\sigma_0 + b\rho_t V_n^2}{V}\right) - \frac{Y}{2\rho_p L}\sin 2(\phi - \theta)}{1 + \cos^2(\phi - \theta)} \tag{16}$$

and

$$\dot{\theta}_n = \frac{\dot{\phi} + \left(\frac{4}{\pi\rho_p d}\right)\left(\frac{\sigma_0 + b\rho_t V_n^2}{V}\right)\cos(\phi - \theta) - \frac{Y}{V\rho_p L}\sin(\phi - \theta)}{1 + \cos^2(\phi - \theta)}. \tag{17}$$

At any given time step, the angle, ϕ and its derivative are given by,

$$\tan\phi = \frac{dy}{dx} \quad and \quad \dot{\phi} = cos^2\phi\frac{dV_y}{dx}. \tag{18}$$

Finally, to conserve mass, incompressibility in the rod material dictates that axial derivative of V_p be zero. Thus V_p is taken to be a constant for the whole rod at any given instance.

The solutions to equations (9), (16), and (17) comprise our transverse load model, which is called SLOTPEN. These equations form a set of ODEs which can be time integrated along with Eqn. (18) and the initial conditions to obtain a time-dependent evolution of the rod shape. It should be noted that when the normal component of the particle velocity, V_n becomes zero, θ becomes equal to ϕ. When V_n is zero the cavity stress should be zero since the rod is not interacting with the target in the lateral direction. Thus from Eqn. 16, $\dot{V}_n$ is also zero.

In our formulation of the lateral interaction, we have assumed that any penetrator deformation occurs only at the load location. This is consistent with observations [20] and can be theoretically justified as follows: The rod strength is clearly negligible and a plastic hinge develops when the moment at any section is enough to yield the entire penetrator cross-section. From elementary beam theory, for a cantilever beam of circular cross section, this should happen at a distance,

$$\frac{x}{D} = \sqrt{\frac{\pi}{12}\frac{Y}{\sigma_c}}. \tag{19}$$

For the tungsten-steel interaction this value is about 0.6. Thus the cavity stress causes local plastic flow and there is no effective elastic resistance of the rod to bending within the cavity. A similar argument applies to shear loads. The section yields completely under shear at,

$$\frac{x}{D} = \frac{\pi}{2}\frac{\tau}{\sigma_c} \tag{20}$$

when τ is the shear strength of the penetrator. This ratio is about 0.3 for our materials. These arguments imply that only axial stress can be transmitted along the axis of the rod; the off-axis components should cause local plastic deformation.

To further verify the locality of rod deformation, we utilized DYNA-3D [21]. A lateral triangular pressure pulse of a width of 3.3 μs was set to travel at 2.37 km/s along the axis of a tungsten long rod. The length and diameter of the rod were 88 mm and 2.6 mm, respectively. The height of the pressure pulse was 4.6 GPa. The constitutive response of tungsten was assumed to be elastic-perfectly plastic with a flow stress of 2 GPa. Figure 6 shows the total velocity of a node in the middle of the rod with time. The bar wave speed for tungsten is about 4.5 km/s. Thus the elastic wave should arrive at this location at 9.8 μs, and the load pulse should arrive at 18.5 μs.
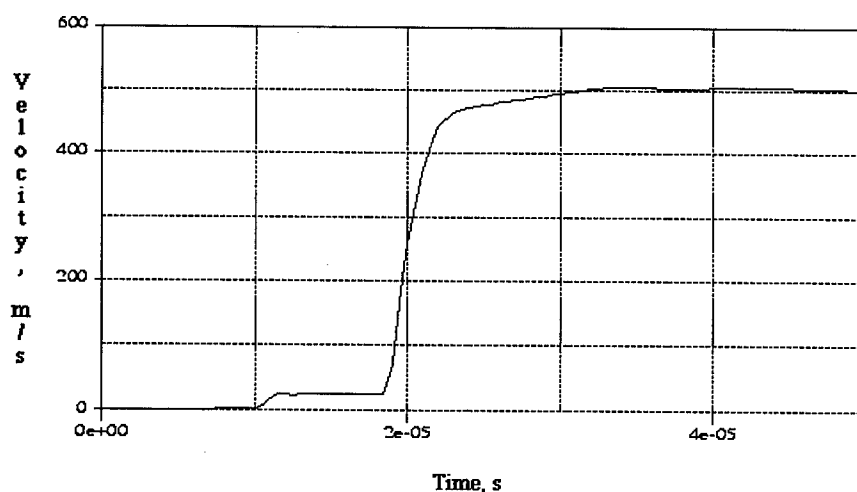
Fig. 6. DYNA-3D simulation of total velocity at the center of the projectile subjected to a traversing load pulse.

From Fig. 6 it appears that a small amplitude deformation arrives at this point corresponding to the axial elastic wave speed. The bulk of the deformation however accompanies the traveling pulse. There is no appreciable deformation ahead of this pulse.

COMPARISON WITH EXPERIMENTS

Bless et al. [4] have reported reverse ballistic testing with yawed penetrators. We have chosen two cases, one each with a positive and a negative yaw angle. Table 1 summarizes the experimental data.

Table 1. Experimental Data (Bless et al.)

Shot No.	Plate Thickness (mm)	Obliquity	Yaw	Impact Velocity (km/s)	Rod Diameter (mm)	Rod Length (mm)	Erosion (Exp.) (mm)	Erosion (computed) (mm)
259	3.13	70.4	-9.67	2.39	2.19	78.96	11	9.4
265	4.5	53	6.9	2.37	2.58	88.3	6	5.52

In Figs. 7 through Fig. 10 we have plotted the shape of the rod predicted by our SLOTPEN model along with the radiographs taken during the experiments at different time. The model includes erosion, cavitation delay, embedment transient, and steady-state slot cutting. The data show the rod emerging from the plate with a bent nose and a rotated or deflected shank. The nose bend is due to the embedment transients; it experiences less deflection than the shank.

The embedment speeds calculated from Eqn. (4) are 285 m/s for shot 265 and 400 m/s for shot 259. The velocity of the interaction point along the target surface are 567 m/s and 821 m/s for shot 265 and shot 259 respectively. This entails a cavitation delay of about 2 ms to 3 ms on the target surface (see Fig. 4).

The agreement for shot 265 is excellent. Both the steady-state slope and the transient parts are matched reasonably well. For shot 259 we are able to obtain good agreement with data as far as the steady-state slope is concerned. But the transient part is not matched well with the calculated embedment speed. However, we obtained much better agreement when we set the embedment speed to 100 m/s. We believe that this discrepancy may be due to a more complex form of the embedment transient when the yaw and obliquity have opposite signs. In this case, the initial cavity profile is shaped so that first contact with the crater wall occurs on the exit side of the crater,

rather than on the entrance side as was assumed in Fig. 4. It is possible then that the cavity has a component of growth due to the penetration and that the appropriate embedment speed is a relative velocity between the embedment and the cavity growth.
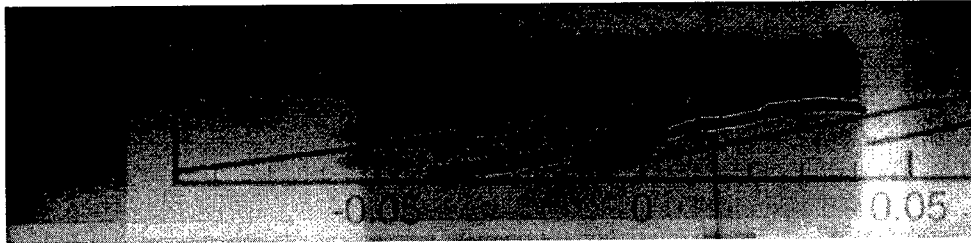
Fig. 7. Shot 265: t = 20 μs. The solid lines are the model prediction for rod axial position. The white lines are enhanced outlines of the image visible on the radiograph. The dark lines show the rod axis and plate position. (In stationary plate coordinates, the rod travels from left to right.)
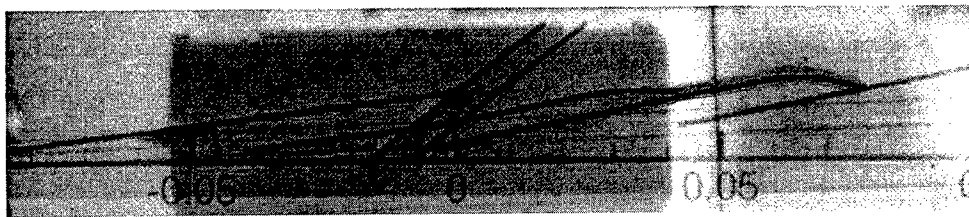
Fig. 8. Shot 265: t = 35 μs.
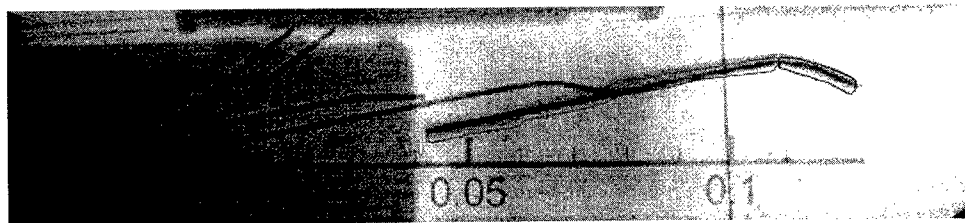
Fig. 9. Shot 265: t = 55 μs.
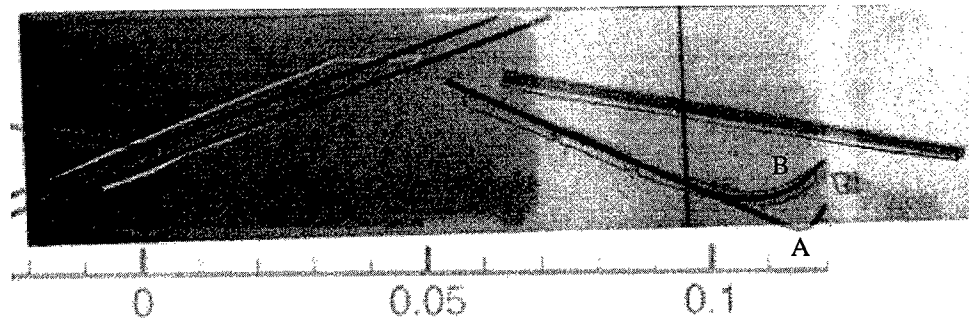
Fig. 10. Shot 259: time = 55 μs. Dark lines are model predictions: A) embedment speed, V_{in} calculated from Eqn. 4 = 400 m/s; B) adjusted embedment speed, V_{in} = 100 m/s. Outlined images are from radiographs, including, in the last image, the initial undisturbed image of the rod.

CONCLUSIONS AND DISCUSSION

We presented a theory for yawed penetration into oblique plate targets. The theory includes models for the cavitation delay, embedment transient phase, and the steady-state slot-cutting phase. The theory has been incorporated in a mathematical model called SLOTPEN. The agreement between the theory and data for the rod exit shapes indicates that the lateral load calculated from cylindrical cavity expansion theory is accurate. This is an important conclusion since it can lead to more efficient design procedures for yaw-tolerant projectiles. This agreement also confirms the assumption that the material strength is much less important than inertia in affecting the lateral response for the cases considered. Both the data and the theory show that the lateral deformation is, to first order, a local phenomena and does not propagate or affect the upstream portions of the rod significantly. The good agreement for the erosion for both cases indicates that the travel path in the target plate which determines the erosion amount is correctly approximated from the theory. The qualitative success of predicting nose deflection shows that it is the embedment transient which causes the rotation of the projectile components after perforation.

REFERENCES

1. W. Goldsmith, "Non ideal projectile impacts on targets," *Int. J. Impact Engng.*, **22** (2-3), 95-395 (1999).
2. A. J. Piekutowski, M. J. Forrestal and K. L. Poorman, T. L. Warren, "Perforation of aluminum plates with ogivenose steel rod at normal and oblique impacts," *Int. J. Impact Engng.*, **18** (8), 877 (1996).
3. S. Satapathy, A. Bedford and S. Bless, "Behavior of a yawed projectile penetrating a thin plate," to appear in *Int. J. Impact Engng.*
4. S. Bless, M. Normandia, J. Campos and V. Chan, "Experimental study of yawed impacts on thin plates using a reverse impact technique," in preparation (1998).
5. T. W. Bjerke, G. F. Silsby, D. R. Scheffler and R. M. Mudd, "Yawed long-rod armor penetration," *Int. J. Impact Engng.*, **12**, 281-292 (1992).
6. G. R. Johnson and W. H. Cook, "Lagrangian EPIC code computations for oblique, yawed-rod impacts onto thin-plate and spaced-plate targets at various velocities," *Int. J. Impact Engng.*, **14**, 373-383 (1993).
7. G. C. Bessette and D. L. Littlefield, "Analysis of transverse loading in long-rod penetrators by oblique plates," Proc. 1997 Conf. Shock Compression of Condensed Matter, Amherst, MA (1997).
8. C. E. Anderson Jr., S. J. Bless, T. R. Sharon, S. Satapathy and M. J. Normandia, "Investigation of yawed impact into a finite target," Proc. 1997 Conf. Shock Compression of Condensed Matter, Amherst, MA (1997).
9. S. Bless and S. Satapathy, "Penetration of thick targets by yawed long rods," Proc. 1997 Conference Shock Compression of Condensed Matter, Amherst, MA (1997).
10. M. Lee and S. J. Bless, "A discreet impact model for effect of yaw angle on penetration by rod projectiles," 1997 Conf. Shock Compression of Condensed Matter, Amherst, MA (1997).
11. Y. I. Bukharev and V. I. Zhukov, "Model of the penetration of a metal barrier by a rod projectile with an angle of attack," *Fizika Goreniya Ivzryva*, **31**, 104-109 (1995).
12. S. Bless, J. Barber, R. Bertke and H. Swift, "Penetration mechanics of yawed rods," *Int. J. Engng. Sci.*, **16**, 829 (1978).
13. D. Yaziv, Z. Rosenberg and J. P. Riegel, "Penetration of yawed long rod penetrators," Proc. 12th International Ballistics Symposium, San Antonio, TX (1990).
14. M. Normandia, "Model for yawed penetrator impacting stationary, finite oblique targets," 1998 Hypervelocity Impact Symp., Classified Session, Huntsville, AL (1998).
15. M. Lee and S. Bless, "Cavity models for solid and hollow projectiles," to appear *Int. J. Impact Engng.*
16. H. G. Hopkins, "Dynamic expansion of spherical cavities in metal," *Progress in Solid Mechanics*, **1**, chapter III (edited by I. N. Sneddon and R. Hill), North-Holland Publishing Co., Amsterdam, NY (1960).
17. S. Bless, S. Satapathy and M. Normandia, "Projectile damage in yawed impacts," Proc. ICES98, Atlanta, GA, (1998).
18. A. Tate, "Further results in the theory of long rod penetration," *J. Mech. Phys. Solids*, **17**, 141 (1969).
19. M. J. Forrestal, "Penetration into dry porous rock," *Int. J. Solids Structures*, **22** (12) 1485-1500 (1986).
20. S. Bless and J. Barber, "Bending waves in yawed rod impacts," *J. of Ballistics*, **2**, 281-298 (1978).
21. S. Satapathy and S. Bless, "Response of long rods to moving lateral pressure pulse: numerical evaluation in DYNA-3D and Autodyn," in preparation (1998).

LABORATORY MEASUREMENTS OF MATERIALS IN EXTREME CONDITIONS: THE USE OF HIGH ENERGY RADIATION SOURCES FOR HIGH PRESSURE STUDIES

R. CAUBLE, B. A. REMINGTON, and E. M. CAMPBELL

Lawrence Livermore National Laboratory, Livermore, CA 94550

Summary—High energy lasers and pulsed power radiation sources are now being used to study material conditions that have never been explored in the laboratory. Future facilities, like the National Ignition Facility (NIF), designed as a high energy multi-beam laser to achieve thermonuclear ignition of a mm-scale DT-filled target, will offer even more extreme and interesting opportunities. NIF will provide the physics community with a unique tool for the study of high energy density matter at states unreachable by any other laboratory technique. Here we describe how existing lasers and pulsed power devices contribute to investigations of high energy density matter in the areas of material properties and equations of state, augment laboratory shock techniques such as high-speed jets to new regimes, and allow study of extreme conditions found in astrophysical phenomena. We will also describe how such studies are extensible to NIF. © 1999 Elsevier Science Ltd. All rights reserved.

INTRODUCTION

The purpose of this article is to introduce and describe several kinds of high energy density experiments that are now being done with high energy radiation sources – lasers and pulsed power devices – on present-day facilities and to indicate where these investigations might proceed with larger facilities either on the drawing board or under construction. Large pulsed power and laser facilities have been funded predominantly for research in inertial confinement fusion (ICF) or, additionally in the case of pulsed power, as high flux, short-wavelength x-ray sources. The idea that they could be used to investigate specific areas of high energy density physics took some time to germinate. The recent growth of such physics-specific experiments on lasers and pulsed power has been driven largely by the need for high energy density information in the absence of nuclear testing.

Although the use of high energy lasers for studies of, *e.g.*, material properties at extremely high pressure or high-Mach-number hydrodynamic flow, is recent – less than 10 years – the use of pulsed power machines for such experiments is even newer. Since there is a base of high-endrgy-density laser experiments at Lawrence Livermore National Laboratory (LLNL), the bulk of this article will discuss those experiments. Extensions of these experiments to next generation lasers, like the National Ignition Facility (NIF, to be built at LLNL) will be made. Pulsed power facilities like the Z machine at Sandia National Laboratories can and will perform measurements similar to those described below. The accompanying article by Asay *et al.*[1] describes Z and its use in high pressure measurements. The next generation pulsed power machine, designated *X-1*, may be built early in the next century.

Lasers and pulsed power devices can produce high energy radiation sources but can be seen as somewhat complementary. The most energetic laser for the past 15 years has been Nova[2], although the OMEGA laser[3] at the University of Rochester is now equivalent. Nova is a ten-beam laser that can produce about 100 kJ of 1-μm-wavelength laser light. This long wavelength, characteristic of a Nd:YaG-doped glass system, turns out to be experimentally more difficult than shorter wavelengths (absorption of shorter wavelength light is more efficient and tends to generate less instability at the absorption surface), so the light is most often frequency-doubled or -tripled using inline optics. The useable energy of 0.35 μm light is about 30 kJ. By contrast, NIF will generate about 1.8 MJ of 0.35 μm light[4]. Pulsed power machines are more energetic: Z already produces 1.8 MJ with the energy in broadband x-rays[5]. The timescale for high energy lasers like Nova is a few ns, while the timescale for Z is generally 10's of ns. Lasers are extraordinarily flexible with respect to the temporal shape of the pulse – the laser pulseshape can be changed at the oscillator that feeds the amplification system – while pulse power facilities must incorporate pulseshaping into the target design. The spatial scales for laser targets is generally about 1 mm while targets on Z will be several mm. Lasers can focus to very small spots to produce very high temperatures or pressures but often the accuracy of an experiment relies on having larger targets. In general, Nova can produce more extreme target conditions with better control over how the energy is delivered than Z. Z has the advantage of more energy: Z can deliver its energy over a longer period of time than Nova and do so on multiple, larger targets. The differing drive characteristics of the two facilities means that high energy density experiments, e.g., high pressure equation of state research, will tend to complement each other, but that there will also be a regime where the two will overlap.

INERTIAL CONFINEMENT FUSION, LARGE LASERS, AND EXPERIMENTS

Inertial confinement fusion (ICF) has driven the development of large lasers. The goal of ICF is to implode and heat a small capsule containing deuterium and tritium, compressing it with progressively staged shocks to densities and temperatures capable of sustaining thermonuclear ignition. The primary purpose of ICF is the support of two major national activities: maintaining relevant scientific expertise in the absence of nuclear testing and the development of electrical energy production from fusion[6]. The driving mechanism will be multi-beam, megajoule-class lasers built with advanced but available technology. The precise timing of the shocks that will implode a DT microsphere requires that the driver be able to deliver the necessary high power on target in a carefully staged manner, thereby controlling the adiabat of the fuel. The National Ignition Facility (NIF)[4] is expected to accomplish this feat in the US; France is planning to build a similar facility called *Le Laser Megajoule* (LMJ)[7]. These are billion-dollar facilities. NIF (see Fig. 1) is scheduled to come partially on-line in 2001 and be fully operational in 2003-2004. The LMJ is scheduled to follow NIF by 6-7 years.

A typical ignition target will be a thin spherical low-atomic-number (low-Z) shell surrounding a solid DT shell; DT gas will fill the interior. The conditions necessary for ignition of the target require that the fuel be compressed to very high density (10^3-10^4 times liquid) and that a central spark region with a temperature of ~ 10 keV be formed[8]. In order to efficiently compress the fuel, multiple strong shocks (pressures of 1-100 Mbar; 1 Mbar = 100 GPa) are used so that at ignition the fuel is at enormous pressures but not at high temperature; it will be kept on a low adiabat. Thus the necessary conditions for ignition are an incongruity: a cold, dense fuel shell enclosing a 10 keV hot spot at pressures near 100 Gbar. This is an extremely difficult shock physics problem that requires large facilities to accomplish. The lasers that will used to create these conditions will be unique facilities for producing and diagnosing matter in a range of

extreme conditions in the laboratory, high energy-density regimes that have never before been experimentally explored.

These lasers will use either direct or indirect drive to compress the ignition capsule. Both of these methods are used in the high energy-density experiments described in detail in the following sections. Irradiating a target directly with one or more laser beams is commonly referred to as direct drive. High intensity produces high pressures. At an intensity I the pressure produced in a low-atomic-number material is given by P(Mbar) $\approx$ few times $[I(10^{14}$ W/cm$^2)/\lambda(\mu m)]^{2/3}$ [9]. A laser intensity of 10^{14} W/cm^2 is typical of even moderate energy lasers, so shocks of 10's of Mbar are easily achievable. However, if such an intensity can only be produced by focusing to a very small area and then for only a very short time duration, the laser may not be useful for precision experiments. Lasers with high *energy* are needed for most high energy-density experiments. The indirect drive technique uses a high-atomic-number hohlraum into which usually several laser beams are focused. The laser light is absorbed and re-emitted from the interior hohlraum wall and then scatters many times within the cavity. The resulting x-rays, contained in the hohlraum and characterized by a radiation temperature T_r, are then used as the driving source. The risetime of T_r in the hohlraum follows the risetime of the laser beam itself and can be less than 150 ps. The pressure generated in the hohlraum is $\approx 10^4 \, T_r(\text{keV})^{3.5}$ Mbar[10]. Typical hohlraum temperatures are 150 - 250 eV producing radiation pressures of ~100 Mbar over periods of 1-2 ns. NIF hohlraum pressures will be higher, near 500 Mbar, and on larger spatial scales.
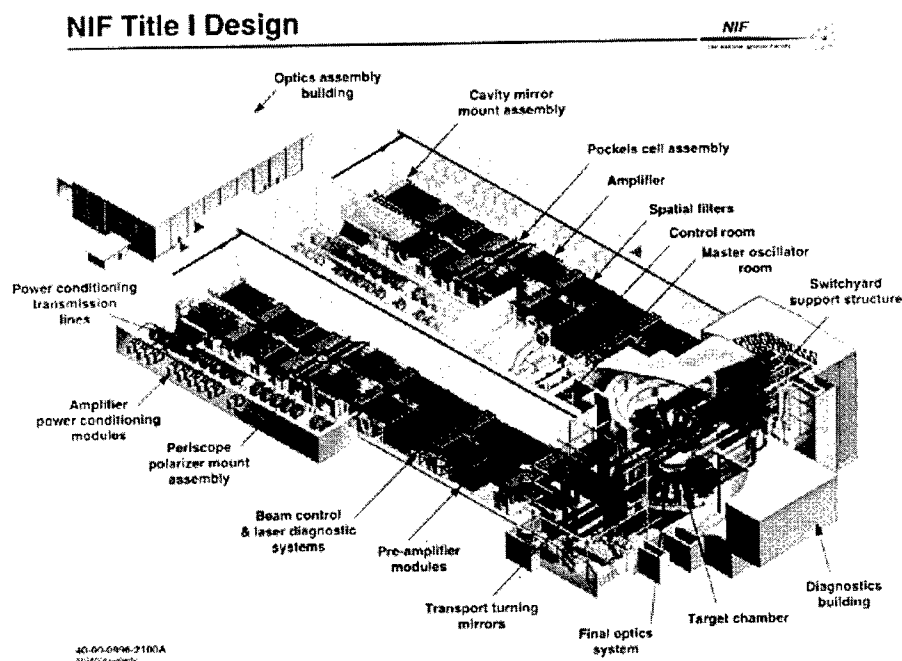
Fig. 1. Scaled drawing of the National Ignition Facility being constructed at Lawrence Livermore National Laboratory.

Pulsed power will be utilized in a manner similar to indirect drive described above[1]. Z, *e.g.*, also uses a hohlraum but whereas the Nova-scale hohlraum is one-to-a-few mm, the Z-scale hohlraum is several cm in diameter. The source of the radiation is a number of thin metal wires in a cylindrical arrangement through which a large current (20 MA) is passed. The wires

vaporize and $J \times B$ forces cause the wires to accelerate toward the axis of the hohlraum. Upon stagnating, the wire plasmas release stored kinetic energy in x-rays. (See figures in Ref. [1].) The characteristic radiation temperature achieved in the large hohlraum is 80-150 eV. If a cylindrical material is placed on axis so that the wires stagnate on the cylinder, T_r in the smaller cylinder can be higher (~ 180 eV). T_r in the hohlraum is approximately gaussian with a 5-10 ns rise and a long precursor that can be removed by target design. The arrangement on Z is to construct two or three smaller chambers on the larger hohlraum wall with experimental packages mounted in or to the smaller hohlraums.

In addition to producing radiation-driven shock waves, both direct and indirect drive can be used to accelerate a small foil and collide the foil with a target, creating a shock in the target that is reminiscent of the more mature high-explosive-driven and gas-gun-accelerated flyer plate experiments. There is a considerable advantage in utilizing this technique: the drive energy is efficiently stored in the flyer and released suddenly as kinetic energy in collision. Indeed, the highest pressure recorded in any planar shock in the laboratory – 750 Mbar (75 TPa) – was created by an gold flyer foil accelerated by x-rays produced in a Nova hohlraum[11]. However, the flyer foil in that experiment was not expected to be "cold," i.e., at a known density, so that no useful EOS data were obtained. In spite of this, it was determined that the spatial dimensions of the target were large enough to use the technique. Early experience with thin directly-driven flyers showed that small spatial nonuniformities in the laser beam would break up the foil rather than accelerating it[12]. However, new research on directly-driven flyers using layered foils shows promise[13]. The radiation-driven flyer foil technique is now being tested on Z and the early results appear promising[14].

Kilojoule-class lasers like Nova are being used to investigate fundamentals of high energy-density science. The following sections discuss a few areas of high energy-density physics that are being explored with Nova. These range from Mbar-pressure equation of state measurements to studies of hydrodynamic processes in supernovae. In each case the advantages of performing similar experiments on megajoule-class lasers are described. One very important point: not all high energy-density experiments on NIF will be designed and performed by staff members of the national laboratories who will propose experiments to be performed on the facility. A fraction of the shots will be set aside for use by "outside" users, i.e., university researchers.

EQUATION OF STATE EXPERIMENTS AT EXTREME CONDITIONS

The experimental and theoretical investigation of equations of state (EOS) of materials at high energy density are of interest not only in ICF, but also in aspects of nuclear explosive design, astrophysics and other related fields. Matter shocked to Mbar pressures is highly compressed and hot enough to become ionized. The usual theories of condensed matter become difficult to apply as interparticle potentials become more complex. Interparticle interactions exhibit density effects; they are affected by the presence of a large number of near-neighbors. The presence of delocalized electrons and strongly interacting ion cores adds a dynamically screened coulomb component to the mixture of molecular and atomic species. Nevertheless, EOS tables that include this regime must be constructed not only to design and interpret ICF target data, but also to study objects such as large planets and stars. In regimes where the difficulty of the theory is exhibited by the profusion of very different model predictions, EOS data are needed. To date, most multi-Mbar data have been driven by nuclear explosions in underground tests[15,16].

Lasers have been known to be capable of producing Mbar shocks for more than a quarter-century[17] and there have been a number of published articles describing strong laser-driven shocks with both direct[18] and indirect[19] drive. But it was not until recently that the first

laser-produced multi-Mbar EOS data were published[20]. Laser-driven shock waves have proved difficult to use for Mbar EOS measurements. Several challenges must be overcome when using lasers in such experiments. First, in order to reduce uncertainties in the data it is necessary to have a large, spatially uniform, steady-state shock front driven for as long as possible. This requires considerable *energy* , not just a high intensity; the energy required to maintain a given uncertainty in shock speed at pressure P varies as $P^{5/2}$ [21]. Second, preventing preheat of the sample is a stringent requirement since heating of the sample prior to it being shocked changes the initial sample density in an unknown way. Since laser deposition can produce very high temperatures ($\sim$ keV), sample preheat by x-rays or hot electrons is a major concern for laser-driven experiments. Third, diagnostics are needed that have few-μm spatial and few-ps temporal resolutions. These are formidable challenges to laser-driven EOS measurements but are not insurmountable[22]. Because of the surfeit of energy, larger sample sizes, and lower power (slower) radiation drives, these challenges may be slightly less worrisome for pulse-power-driven experiments. There is, however, the necessity of working in an electromagnetically rich environment so shielding is a major concern. One final consideration is the acceptance that radiation-driven measurements will not soon be able to match the experimental precision to which researchers have grown accustomed in sub-Mbar EOS measurements with more mature techniques. What intense radiation-driven sources offer is the opportunity to explore more extreme regimes than those techniques cannot access.

The laser experiments described below are all Hugoniot measurements (the Hugoniot is the locus of density, pressure, and energy states in a material following passage of a single shock and is a well-defined curve on the EOS surface). Because of the ability of the laser to produce a very fast risetime pulse, a shock can be developed in a target in $\sim$ 100 ps, a time that is 1-10% of the laser drive time. In contrast, pulsed power machines, with a many-ns risetime and a more gaussian temporal shape, take longer to generate the appropriate shock profile. These characteristics can be readily applied to "shockless" (near-isentropic) high pressure experiments.

Indirectly-Driven Hugoniots of Polystyrene and Beryllium

Hugoniot measurements of two low-atomic-number materials have be made on Nova using indirect drive. Indirect drive has some advantages over direct drive. Because x-rays in the hohlraum undergo multiple reflections, the shock generated in a package attached to the hohlraum is spatially uniform; there are no hot spots characteristic of direct irradiation by an unsmoothed laser beam. There is the additional advantage of having a much lower effective drive temperature, reducing the potential for preheating of a sample. The primary disadvantage of using a hohlraum is that the hohlraum fills with plasma and the laser entrance holes close within a few ns; thus shock measurements must be made within this time duration or corrections made for slowing of the shock in the sample.

Polystyrene (CH) and beryllium, ICF capsule candidates, were examined. Eight beams of the Nova laser were focused into a 3-mm-long by 1.6-mm-diameter gold hohlraum; the EOS package was attached to the side of the hohlraum. (See Fig. 2.) Two additional beams irradiated a scandium foil; x-rays from this backlighter were used to radiograph the shock moving through the package. The package consisted of two sections, a "pusher" of bromine-doped CH, CH(Br), close to the hohlraum and the EOS sample attached to the CH(Br). Because CH(Br) is opaque to the backlighter x-rays, the interface between the two sections is visible on film. Following this interface in time after the shock passes through the CH(Br) revealed the particle speed behind the shock U_p. The shock front was visible as the boundary between the highly transmissive unshocked sample and the less transmissive (higher density) shocked sample[23]. The shock speed U_s was obtained by following this boundary. Putting U_s and U_p into the Hugoniot relations[24], $\rho = \rho_o U_s/(U_s\text{-}U_p)$ and $P = P_o + \rho_o U_s U_p$, gave the shocked pressure and density. Since both U_s and U_p were measured, the Hugoniot data were absolute, in contrast to relative

(impedance match) experiments where the results are dependent on a knowledge of the EOS of a co-shocked "standard." Data on CH were obtained from 10 Mbar to 40 Mbar and Be to 14 Mbar (Fig. 2) [25]. Be data are in the same pressure regime as relative nuclear-explosion-driven experiments[15,16].
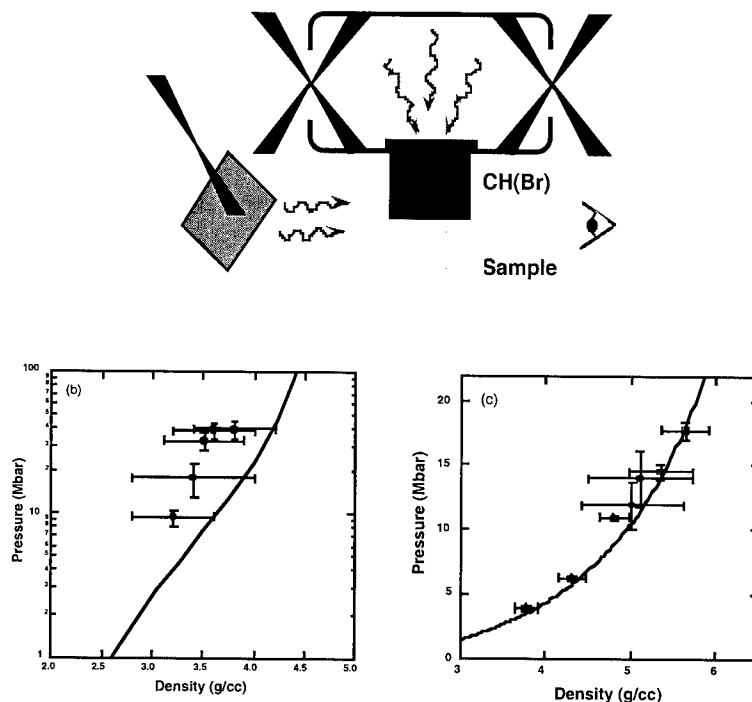
Fig. 2. Target schmatic for the Nova measurement of the Hugoniot of low-atomic-number solids by indirect laser drive employir.g a gold hohlraum. The experimental package is mounted to the side of the hohlraum. The measurements were made with streak radiography using x-rays from a laser-heated backlighter. Absolute CH data are shown in (b) and Be Hugoniot data compared with SESAME EOS table Hugoniot[26] and nuclear impedance match data[15,16] are in (c) [25].

Directly-Driven Hugoniot of Deuterium at the Metal-Insulator Transition

The first shock in the proposed design for a NIF ignition target will be 900 kbar[8], which lies in a regime where a transition from a diatomic to a monatomic fluid is expected in the DT fuel. The transition is complicated by the likelihood that pressure ionization is commensurate with high-density-driven molecular dissociation. Many theoretical predictions about how the EOS might be affected by the phase transition[26-34], and even whether the transition is of first order[30,31,34], have been made with widely varying results. This regime is particularly important for the description of Jovian planets and low-mass stars, which are 90% hydrogen, and where the metal-insulator transition is expected within the atmosphere at a pressure near 1 Mbar. (The EOS of all of the hydrogen isotopes are similar; there is only a scale factor in density between them.) Gas gun experiments had been done[35] but the highest Hugoniot pressure datum was about 200 kbar, not high enough to exhibit the predicted effects.

A Nova experiment was designed that utilized a spatially-smoothed laser beam with a 9-ns pulse to drive a strong shock into a metal pusher. After transiting the pusher the shock propagated into a cryogenic D_2 sample. Employing side-on radiography, the pusher/D_2 interface and the shock front were imaged in time on a calibrated streak camera. Similar to the CH and Be

experiments described above, the motion of the interface provided the particle speed U_p, and the motion of the shock front revealed the shock speed U_s. (See Fig. 3.) Hugoniot data[36] were obtained up to 3.4 Mbar that showed a significantly more compressible EOS (up to 50%) than had been previously believed. The data, shown in Fig. 3, include points at 250 kbar that agree well with the earlier gas gun data. The Nova data closely follow a model that incorporates molecular dissociation in a new way[37].

In these experiments, a considerable effort was made to minimize preheat. Preheat was monitored by reflecting a probe laser off the rear surface of the pusher in a Michelson interferometry arrangement[38]. Results showed no detectable preheat. Using a different kind of interferometer, a velocity interferometer, or VISAR, it was shown that the shocked deuterium was highly reflecting, indicating that it had been driven into a metallic state[39]. An optical pyrometer was able to determine the temperature of the shocked deuterium[40].
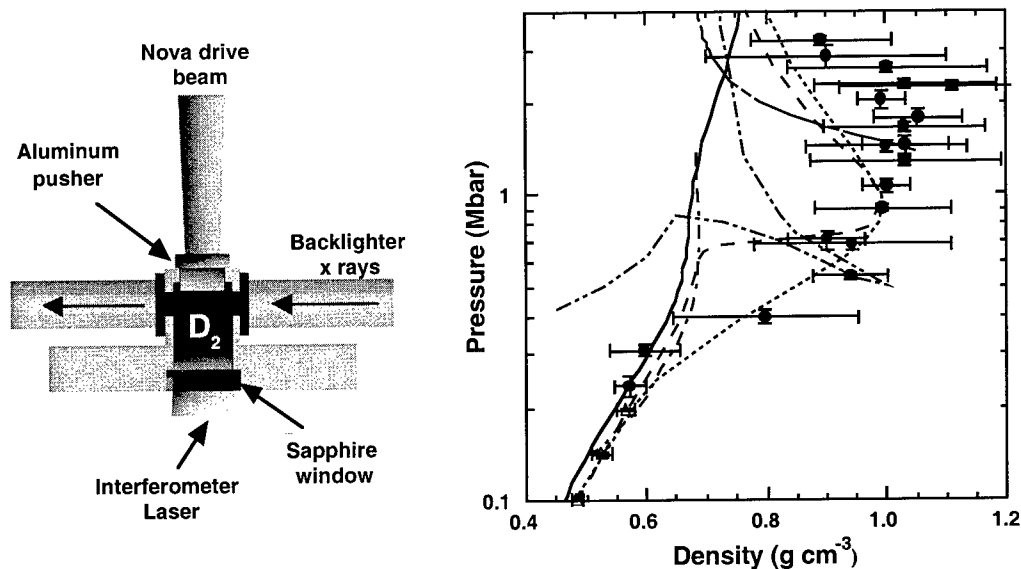
Fig 3. Cryogenic cell for the Nova measurement of the Hugoniot of deuterium by direct laser drive, including interferometry to verify preheat. Absolute D_2 Hugoniot data[36] are shown along with gas gun data (triangles)[35] compared with theoretical results: SESAME (solid)[27]; molecular dynamics (dot-dash)[32]; Monte Carlo (dash-double-dot)[30]; ACTEX (chain-dash)[33]; Saumon and Chabrier (dashes)[29]; and linear mixing model (dots)[37].

The Future of Laser-driven EOS Shock Experiments

These results were produced using a kilojoule-class laser. A megajoule-class laser will allow directly driven shock experiments up to 50 Mbar over longer drive times (> 20 ns) and larger shock diameters. It will be possible to perform absolute EOS measurements with improved accuracy. Scaling of optimized hohlraums from Nova to NIF are expected to allow ~ 2% precision EOS measurements at pressures greater than 1 Gbar in an impedance match arrangement[41].

HYDRODYNAMIC MIX AT HIGH ENERGY DENSITY

Matter in motion at high energy density can be susceptible to hydrodynamic instabilities. In an extreme example, Nova has been used to create high-Mach-number jets (M=15 to 30) by using a laser-driven "shaped charge."[42]. Instabilities are especially problematic in ICF: mixing of cold fuel into the central hot region can reduce the capsule burn performance or entirely quench the burn[8]. The three most common hydrodynamic instabilities are the acceleration-driven Rayleigh-Taylor (RT) instability, its shock-analog the Richtmyer-Meshkov (RM) instability, and the shear-induced Kelvin-Helmholtz (KH) instability. Mitigating high-energy-density-driven hydrodynamic instabilities is critical in ICF, but they are also observable in astrophysical objects. The RT instability can occur at an interface between a low density fluid and a high density fluid where the lighter fluid is accelerated into the heavier. In the linear regime, initial perturbations in the interface will grow exponentially in time with a growth rate γ $\sim (Ag/\lambda)^{1/2}$, with A being the density-dependent Atwood number, g the acceleration, and λ the perturbation wave length. In the nonlinear asymptotic limit, the interface evolves into bubbles of the lighter fluid rising at their terminal velocity and spikes of the heavier fluid falling through the lighter fluid.

High explosives can generate pressures up to 200-300 kbar[43] and gas guns can generate pressures up to a few Mbar in solids, but with modest compression[44]. Large lasers like Nova and NIF can produce extreme accelerations (up to 10^{14} earth gravities) and higher pressures. Such lasers can achieve high growth factors, large compressions, and high levels of radiation flow and ionization in arbitrary geometry.

There have been a number of experiments to investigate high energy-density hydrodynamic instabilities using a laser drive[10,45-47]. One important example is the experimental verification of the differences between two-dimensional (2D) and three-dimensional (3D) RT-induced perturbation growth[48] (this result will be important in the following section). A perturbation was pre-imposed on one side of a CH(Br) foil. This foil was mounted across an opening on a laser hohlraum that then ablatively accelerated the foil. The experimental arrangement is similar to that in Fig. 2, except that the backlighter and detector are positioned so that radiographic images obtained are face-on (through the foil) rather than side-on. Perturbations at the ablation front grow due to the RT instability. The three perturbations studied all had the same magnitude wavevector, $k=(k_x^2+k_y^2)^{1/2}$, where $k=2\pi/\lambda$, and amplitude, differing only in their shape. The labels are: square $k_x=k_y$, stretched $k_x=3k_y$, and ripple $k=k_x=k_{2D}$. Time-resolved, face-on radiographs are shown in Fig. 4, where dark regions correspond to spikes, bright regions to bubbles. The growth versus time of the fundamental mode Fourier amplitudes of the perturbations are also shown. In the linear regime, all three modes grow at the same rate. This is expected from linear theory since they all have the same magnitude wavevector. However, in the nonlinear regime, the square mode grows the largest, the ripple grows the least, and the stretched perturbation falls in between. This result is easily explained. At the bubble tip, the ratio of drag over buoyancy is smallest for the square mode; basically, the square mode bubble is more streamlined and this shape grows the fastest[49]. The energy of Nova is sufficient to just begin to see these effects. The energy available on NIF will allow 3D, fully multimode experiments to be pushed well into the nonlinear regime. It is important to drive instability experiments longer in order to observe the growth with better accuracy. The longer drives available on *Z* make *Z* favorable for hydrodynamic instability experiments.

Three-dimensional effects in RT development can also be seen in convergent geometry. This is evident in preliminary Nova experiments in which square mode perturbations were inscribed on the outer surface of a doped-plastic hemisphere and, similar to the planar RT experiments described above, the hemisphere was mounted on the wall of a hohlraum, facing inwards[50]. As

in the planar case, the perturbations grew as the plastic target was accelerated. But since the hemisphere converges as it is driven, the perturbation wavelength λ decreases as the shell accelerates. Since the RT growth rate $\sim \lambda^{-1/2}$, RT growth was expected to be larger in the linear regime in the convergent case and to saturate sooner. This was indeed observed. Had the foil been planar, the growth would still be in the linear regime at the times observed. Megajoule-class lasers will be required to drive these 3D experiments well into the nonlinear regime especially, as in the case of planar RT, with multimode targets. The ability to perform fully 3D experiments to study high energy-density hydrodynamics finds application not only in ICF but also in astrophysics, as shown in the following section.

Hydrodynamics at high pressure can also be studied in the solid state. Careful tailoring of the drive pulse in a hohlraum can result in Mbar-pressure shock waves in a metallic targets without melting the target. See the article by Kalantar et al. In this volume[51].
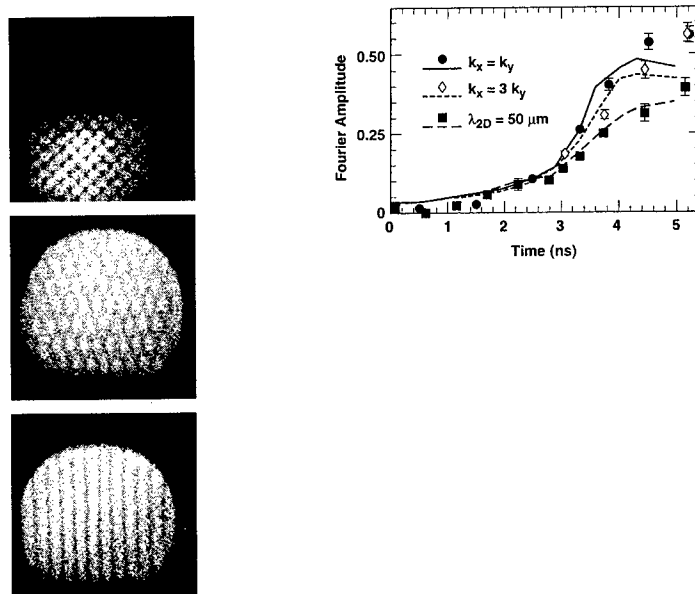
Fig. 4. Face-on radiographs of three different planar Rayleigh-Taylor targets driven indirectly by Nova lasers. The experiment used a hohlraum as in Fig. 2, except that the backlighter was positioned above the hohlraum and the recording device, an x-ray framing camera, was positioned below. The three shapes are square $k_x=k_y$ (top), stretched $k_x=3k_y$ (middle), and ripple $k=k_x=k_{2D}$ (bottom). Plot of perturbation Fourier amplitude vs. time for the three shapes showing that the 3D square mode grows fastest and the 2D mode grows slowest[48].

LABORATORY EXPERIMENTS AND SUPERNOVAE

The application of high energy density experiments to astrophysics was discussed in the preceding section, where Nova-driven equation of state measurements were found to be important for some low-mass stars. It turns out that laboratory experiments can be directed toward the understanding of far more energetic astrophysical objects. Because of enormous gravitational and nuclear forces, many astrophysical objects are indeed high energy-density phenomena. Exploding stars can create high speed hydrodynamical jets, not dissimilar to those already described[52]. Supernovae in particular exhibit a range of high energy-density hydrodynamical features that can be scaled to experiments on megajoule-class lasers. Here we

describe two experiments developed to investigate supernova phenomena: (1) hydrodynamic-instability-driven core mixing during the SN1987A explosion and (2) strong shock formation in the SN1987A remnant evolution. These experiments are described in detail in Ref. [53].

SN1987A Mix Experiments

A model of a supernova (SN) progenitor star is a series of concentric shells with hydrogen, forming the outer envelope, helium just below the H layer, and so on to an iron core. A SN explosion occurs when the core undergoes catastrophic gravitational collapse; a strong radial shock is driven outward through the star. At the H/He boundary, the post-shock density, temperature, and pressure are about 2.3 g/cm^3, 6 keV, and 75 Gbar. Much effort has been invested in developing models to understand the underlying processes of SNs. These efforts have focused on one-dimensional (1D) stellar evolution models. Observations of SN1987A highlighted two distinct defects with these models[54].

Each SN model predicts a light curve, the total luminosity of the SN versus time. The SN luminosity decreases sharply immediately after the explosion as ejected gas hydrodynamically cools due to expansion. Subsequently the luminosity exhibits a broad peak as the heat wave due to radioactive decay of the core then diffuses out of the star. In SN1987A, however, the core became visible much earlier than 1D diffusion models predicted[55]. The reason was traced to unexpected mixing of the core with the outer stellar atmosphere. The boundaries between the atmospheric layers are Richtmyer-Meshkov (RM) unstable. RM-induced perturbations then grow because the decelerating layer interfaces are unstable to Rayleigh-Taylor (RT) growth. Two-dimensional SN models were required to explain this.[56,57].

However, even after 2D SN models were developed, the models predicted peak core velocities of < 2000 km/s for SN1987A while observed velocities were much higher, > 3000 km/s[58]. The solution to this puzzle can be deduced by recalling the results of 3D laser mix experiments described in the preceding section. There it was found that strongly driven RT growth was observed to be larger in target foils where the perturbations resembled squares (3D), compared to (2D) ripple-like perturbations[48]. Here was an indication that even 2D modeling was insufficient and 3D SN codes must be developed. How can they be benchmarked?

Noting, somewhat remarkably, that we can scale supernova hydrodynamics to the millimeter scales of laser-driven experiments, attempts to simulate SN hydrodynamics have been performed on the Nova laser using a hohlraum x-ray drive with Cu and CH_2 as surrogates for He and H respectively[53]. The indirectly driven shock tube arrangement (as in Fig. 2) was utilized. A scaled representation of the correct shock-plus-deceleration drive was created. Radiographs of the interface showed how far and how fast bubbles and spikes form due to RM followed by RT instability. These images were compared to code predictions. Employing a single mode 2D surface, gross features of the experiment were reproduced by the simulations[59]. However there is insufficient drive energy available with Nova to allow these experiments to be done in a multimode 3D configuration or experiments in (the correct) exploding geometry. NIF will have sufficient energy to drive more realistic experiments.

SN1987A Remnant Collision Experiments

SN1987A is now evolving into the early remnant stage; a 1994 optical image is shown in Fig. 5. The expanding SN ejecta is the central bright spot, surrounded by an assembly of nebular rings, the origin of which is a mystery. Gaseous SN ejecta, moving at $\sim 10^3$-10^4 km/s, will collide with the inner circumstellar ring in a few years; observations of the collision may shed light on the nature of the rings[56]. However, using this collision to probe the nature of the rings depends

on correctly interpreting observations of a complex, energetic, hydrodynamically unstable collision between two interstellar plasmas. Simulations are being performed now to predict the outcome of the collision.

When the two plasmas collide, shocks will be launched forward into the ring and backward into the SN ejecta. Cooling of the strongly shocked plasma by radiation causes the compressed ejecta to collapse to an even higher density leading to strong RT growth at the contact discontinuity. [60]. Qualitatively different mixing evolves depending on the density profile of the ejecta and the initial evolution of the contact discontinuity. Large differences also result from inclusion of radiation transfer in the simulations.

An experiment has been designed as a proxy to the stellar collision. In the experiment, CH(Br) was used to provide a surrogate for the SN ejecta; SiO_2 aerogel foam represented ambient plasma and a solid CH foil corresponded to the ring plasma. Attached to a Nova hohlraum, x-rays drive a 50 Mbar shock into the CH(Br), ejecting plasma into a gap between the CH(Br) and the foam. The ejecta stagnated in the foam driving shocks forward into the foam and backward into the ejecta. Imaging revealed the positions of the shocks and the relative shock densities. Experiments on Nova have successfully produced and imaged both shocks[61]. However, the shocks are not strong enough so that cooling radiation is a factor in the Nova experiment. Further, longer x-ray drives are needed to evince the expected RT development in the plasma. NIF will provide the drive energy to overcome both of these difficulties.
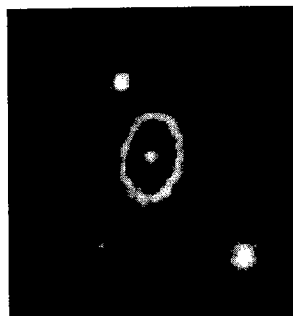
Fig. 5. An image of SN1987A obtained by the Hubble Telescope in Feb. 1994. The expanding supernova ejecta is the central dot. The rings are planetary nebulae of uncertain origin and will be impacted by ejecta from the supernova in a few years.

CONCLUSIONS

A primary mission of megajoule-class lasers such as NIF will be to compress, inertially confine, and initiate nuclear fusion in DT capsules. This approach to ICF ignition requires a flexible, high-energy facility capable of producing conditions of matter unattainable by other laboratory methods while simultaneously allowing experimental investigation of shocked, high energy-density matter. Several examples of high energy-density experimental investigations have been described that have already been initiated on present-day kilojoule-class lasers and how those studies will be extended on NIF. The examples described included material properties at Mbar pressures, production of high-Mach-number jets, and the growth and development of hydrodynamic instabilities in planar and convergent geometries that reveal the limitations of two-dimensional models. High energy lasers can even make contributions to the study of shocks in astrophysical phenomena, in particular supernovas. Further details on these experiments, and on many others, can be found in Ref. [62], which is an explorable website. It is expected that pulsed power devices, such as *Z* and *X-1*, if it is built, will enhance the repertoire of high energy density experiments. A final note: experiments at NIF will be performed not only by the staff at

US national laboratories, but also in collaboration with and by members of the physics academic community. At this time the fraction of all NIF shots dedicated to outside user is expected to be about 15%[63].

REFERENCES

1.   J. R. Asay et al., "Use of Z-Pinch Sources for High-Pressure Equation-of-State Studies," this volume.
2.   E.M. Campbell, Laser Part. Beams **9**, 209 (1991).
3.   J. M. Soures *et al., Phys. Plasmas* **3**, 2108 (1996).
4.   J. A. Paisner, E.M. Campbell, and W.J. Hogan, *Fusion Technology* **26**, 755 (1994).
5.   M. K. Matzen, *Phys. Plasmas* **4**, 1519 (1997).
6.   E. M. Campbell, N. C. Holmes, S. B. Libby, R. A. Remington, and E. Teller, *Laser Part. Beams* **15**, 607 (1997).
7.   M. André, "Conceptual Design of the French LMJ Laser," First SPIE International Conference on Solid State Lasers for Application to ICF, Monterey, (1995).
8.   John Lindl, *Phys. Plasmas* **2**, 3933 (1995).
9.   See, e.g., Th. Löwer and R. Sigel, *Contrib. Plasma. Phys.* **33**, 355 (1993).
10.   B. A. Remington *et al., Phys. Plasmas* **2**, 241 (1995).
11.   R. Cauble *et al.*, Phys. Rev. Lett. **70**, 2102 (1993).
12.   R. Cauble *et al., Phys. Rev. Lett.* **74**, 3816 (1995).
13.   K. A. Tanaka, proceedings of the Worskhop on Equation of State of Hydrogen at High Energy Density, Livermore (1998).
14.   J. R. Asay, private communication (1998).
15.   C. E. Ragan III, *Phys. Rev. A* **29**, 1391 (1984).
16.   W. J. Nellis, J. A. Moriarity, A. C. Mitchell, and N. C. Holmes, *J. Appl. Physics* **82**, 2225 (1997).
17.   C. G. M. van Kessel and R. Sigel, *Phys. Rev. Lett.* **33**, 1020 (1974); L. R. Veeser and S. C. Solem, *Phys. Rev. Lett.* **40**, 1391 (1978); R. J. Trainor, J. W. Shaner, J. M. Auerbach, and N. C. Holmes, *Phys. Rev. Lett.* **42**, 1154 (1979).
18.   S. P. Obenschain *et al., Phys. Rev. Lett.* **50**, 44 (1983); F. Cottet, J. P. Romain, R. Fabbro, and B. Faral, *Phys. Rev. Lett.* **52**, 1884 (1984); R. Fabbro *et al., Laser Part. Beams* **4**, 413 (1986); K. A. Tanaka *et al.*, in *Shock Waves*, ed. K. Takayama (Springer-Verlag, Berlin, 1992), p. 863.
19.   Th. Löwer *et al., Phys. Rev. Lett.* **72**, 3186 (1994).
20.   M. Koenig *et al., Phys. Rev. Lett.*, **74**, 2260 (1995); S. Fu, Y. Gu, J. Wu, and S. Wang, *Phys. Plasmas* **2**, 3461 (1995); A. Benuzzi *et al., Phys. Rev. E* **54**, 2162 (1996); A. M. Evans *et al., Lasers Part. Beams* **14**, 113 (1996).
21.   N. C. Holmes, private communication.
22.   Y. M. Gupta and S. M. Sharma, *Science* **277**, 909 (1997).
23.   R. Cauble *et al.*, Phys. Plasmas **4**, 1857 (1997).
24.   Y. B. Zel'dovich and Y. P. Raizer, *Physics of Shock Waves and High-Temperature Hydrodynamic Phenomena* (Academic Press, New York, 1966).
25.   R. Cauble *et al., Phys. Rev. Lett.* **80**, 1248 (1998).
26.   S. P. Lyon and J. D. Johnson, "SESAME: The Los Alamos National Laboratory Equation of State Database," Los Alamos National Laboratory report LA-UR-92-3407 (1992).
27.   G. I. Kerley, "A Theoretical Equation of State for Deuterium," Los Alamos Laboratory Report LA-4776 (1972); G. Kerley, *J. Chem. Phys.* **73**, 460 (1980).
28.   M. Ross, F. H. Ree, and D. A. Young, *J. Chem. Phys.* **79**, 1487 (1983).
29.   D. Saumon and G. Chabrier, *Phys. Rev A* **44**, 5122 (1991); **46**, 2084 (1992).
30.   W. R. Magro, D. M. Ceperley, C. Pierleoni, and B. Bernu, *Phys. Rev. Lett.* **76**, 1240 (1996); B. Militzer, W. Magro, and D. Ceperley, Proceedings of the International Conference on Strongly Coupled Coulomb Systems, Boston (1997).
31.   H. Reinholz, R. Redmer, and S. Nagel, *Phys. Rev. E* **52**, 5368 (1995).
32.   T. J. Lenosky, J. D. Kress, and L. A. Collins, *Phys. Rev. B* **56**, 5164 (1997).
33.   F. J. Rogers, *Astrophys. J.* **310**, 723 (1986); F. J. Rogers, F. J. Swenson, and C. A. Iglesias, *Astrophys. J.* **456**, 902 (1996).
34.   D. Saumon and G. Chabrier, *Phys. Rev. Lett.* **62**, 2397 (1989).

35. W. J. Nellis *et al.*, J. Chem. Phys. **79**, 1480 (1983); N. C. Holmes, M. Ross, and W. J. Nellis, *Phys. Rev. B* **52**, 15835 (1995).
36. L. B. Da Silva et al., *Phys. Rev. Lett.* **78**, 483 (1997); G. W. Collins *et al.*, *Science* **281**, 1178 (1998).
37. M. Ross, *Phys. Rev. B* **58**, 669 (1998).
38. K. S. Budil *et al.*, "Characterization of Laser-Driven Shock Waves using Interferometry," to appear in *Inertial Confinement Fusion Quarterly Report*, LLNL report (1997).
39. P. M. Celliers *et al*, submitted to *Phys. Rev. Lett.* (1998).
40. G. W. Collins *et al.*, submitted to *Phys. Rev. Lett.* (1998).
41. N. Landen, private communication (1997).
42. P. L. Miller et al., "Shock-hydrodynamic Experiments on Nova," Proceedings of the 20th International Symposium on Shock Waves," Pasadena (1995).
43. R.F. Benjamin and J.N. Fritz, *Phys. Fluids* **30**, 331 (1987).
44. N.C. Holmes *et al.*, *Appl. Phys. Lett* **45**, 626(1984).
45. K. Budil *et al.*, *Phys. Rev. Lett.* **76**, 4536 (1996); G. Dimonte *et al.*, *Phys. Rev. Lett.* **74**, 4855 (1995); T.A. Peyser *et al.*, *Phys. Rev. Lett.* **75**, 2332 (1995).
46. W. Hsing *et al.*, *Phys. Rev. Lett.* **78**, 3876 1997); *Phys. Plasmas* **4**, 1832 (1997).
47. K. Nishihara and H. Sakagama, *Phys. Rev. Lett.* **65**, 432 (1990).
48. M. Marinak *et al.*, *Phys. Rev. Lett.* **75**, 3677 (1995);M. Marinak *et al.*, *Phys. Plasmas* **5**, 1125 (1998); M. Marinak *et al.*, *Phys. Rev. Lett.* **80**, 4426 (1998).
49 J. Hecht *et al.*, Laser and Part. Beams **13**, 423 (1995).
50. S.G. Glendinning *et al.*, in *Proceedings of the 6th International Workshop on the Physics of Compressible Turbulent Mixing*, Marseille, in press (1997).
51. D.H. Kalantar *et al.*, "High Pressure Solid State Experiments on the Nova Laser," in this volume.
52. S. Heathcote *et al.*, *Astron. J.* **112**, 1141 (1996).
53. B. A. Remington *et al.*, *Phys. Plasmas* **4**, 1994 (1997).
54. I. Hachisu, T. Matsuda, K. Nomoto, T. Shigeyama, *Astron. Astrophys. Suppl.* **104**, 341 (1994); M. Herant and S.E. Woosley, *Astrophys. J.* **425**, 814 (1994).
55. T. Shigeyama and K. Nomoto, *Astrophys. J.* **360**, 242 (1990).
56. R. McCray, Ann. Rev. Astron. Astrophys. **31**, 175 (1993).
57. D. Arnett, Astrophys. J. **427**, 932 (1994).
58. B. Fryxell, W. M?ller, and D. Arnett, Astrophys. J. **367**, 619 (1991).
59. J. Kane *et al.*, *Astrophys. J.* **478**, L75 (1997).
60. R.A. Chevalier and J.M. Blondin, *Astrophys. J.* **444**, 312 (1995).
61. R. P. Drake *et al.*, *Phys. Rev. Lett.* **81**, 2068 (1998).
62. R. W. Lee, "Science on High Energy Lasers from Today to the NIF," at http://www.llnl.gov/science_on_lasers/ucrl119170.html. Copies of the report can be obtained by contacting R. W. Lee (dicklee@llnl.gov) at LLNL.
63. See the report "Facility Use Plan for the National Ignition Facility," eds. A. Hauer, R. Kauffman, A. Satsangi, T. Haill, R. Cauble, and T. Saito, available from US Department of Energy, Office of the NIF, 1000 Independence Avenue, S.W. Washington, DC 20585.

A METHODOLOGY TO VALIDATE 3D ARBITRARY LAGRANGIAN EULERIAN CODES WITH APPLICATIONS TO ALEGRA

L. C. CHHABILDAS, C. H. KONRAD, D. A. MOSHER, W. D. REINHART, B. D. DUGGINS, T. G. TRUCANO, R. M. SUMMERS, and J. S. PEERY

Sandia National Laboratories, Shock Physics Applications Department,
Albuquerque, New Mexico 87185-1181

Summary—In this study we provided an experimental test bed for validating features of the Arbitrary Lagrangian Eulerian Grid for Research Applications (ALEGRA) code over a broad range of strain rates with overlapping diagnostics that encompass the multiple responses. A unique feature of the ALEGRA code is that it allows simultaneous computational treatment, within one code, of a wide range of strain-rates varying from hydrodynamic to structural conditions. This range encompasses strain rates characteristic of shock-wave propagation (10^7/s) and those characteristics of structural response (10^2/s). Most previous code validation experimental studies, however, have been restricted to simulating or investigating a single strain-rate regime. What is new and different in this investigation is that we have performed well-controlled and well-instrumented experiments, which capture features relevant to both hydrodynamic and structural response in a single experiment. Aluminum was chosen for use in this study because it is a well-characterized material. The current experiments span strain rate regimes of over 10^7/s to less than 10^2/s in a single experiment. The input conditions were extremely well defined. Velocity interferometers were used to record the high strain-rate response, while low strain rate data were collected using strain gauges. Although the current tests were conducted at a nominal velocity of ~ 1.5 km/s, it is the test methodology that is being emphasized herein. Results of a three-dimensional experiment are also presented.
© 1999 Elsevier Science Ltd. All rights reserved.

INTRODUCTION

Sandia National Laboratories is developing a code referred to as ALEGRA which is a multi-material arbitrary Lagrangian Eulerian code [1] for use in many programs related to research applications. A unique feature of ALEGRA is that it allows simultaneous computational treatment, within one code, of a wide range of strain-rates varying from encompasses strain rates characteristic of shock-wave propagation (10^7/s) and those characteristics of structural response (10^2/s) [2]. It combines the features of modern Eulerian codes such as CTH [3] with modern Lagrangian shock wave physics codes and transient structural analysis codes. Some examples of applications with varying strain rates include (but are not limited to) high velocity impact and penetration processes [4], explosively formed projectiles, and shaped charge jet formation.

Validating a code requires both postdating and predicting pertinent experimental data. The most useful validation experiments are reproducible and highly instrumented [5], with well-understood experimental errors. There are many parts of a calculation that we must validate: geometry, initial conditions, boundary conditions, material flow algorithms (remeshing and remapping algorithms), and material models, including EOS, constitutive relations and fracture models. There are also issues associated with meshing resolution and geometric fidelity. In many cases pertinent experimental data are available for a single strain rate regime and are used when appropriate to this regime. However, within certain applications that ALEGRA is

addressing, there is a need to perform well-controlled experiments that capture material response at both high and intermediate strain rate regimes.

In this study, we provided an experimental test bed and a methodology for validating features of the ALEGRA code [1], including material models, over a broad range of responses with overlapping diagnostics that encompass multiple strain rates. Aluminum was used in these experiments because it is a well-characterized material - its equation of state (EOS) and constitutive properties are well established over a wide range of loading rates. Pretest calculations were performed to *design and optimize* the experiment and to assist in instrumenting the experiment. Velocity interferometers were used to record the high strain-rate response and to determine the input conditions extremely accurately, while low strain rate data were collected using strain gauges. In particular, the current experiments span strain rate regimes of over 10^7/s to less than 10^2/s in a single experiment. Even though the experiments are conducted at impact velocities of ~ 1.5 km/s, what is significant in this investigation is the methodology that is being established to validate modern 3-D Arbitrary Lagrangian Eulerian (ALE) codes, and can be easily extended to high impact velocities. The test methodology developed for use in this investigation is described in the next section. Results of these experiments including a well-controlled three-dimensional experiment are discussed and compared with ALEGRA simulations in subsequent sections.

EXPERIMENTS

Methodology

A series of experiments were conducted on the Sandia terminal ballistics facility [6]. This is a two-stage light-gas gun that can launch a sabot package carrying spherical projectiles to velocities over 6 km/s. A 9.52 mm, 6061-T6 aluminum sphere was launched to ~ 1.5 km/s. The exact impact velocity for each experiment is given in Table 1. The impact velocity in each experiment was determined to an accuracy of 0.2% using a magnetic pick-up coil method [7]. The spherical projectile impacted one end of a hollow cylindrical can (also made of 6061-T6 aluminum) whose outer diameter was ~ 63.5 mm, inner diameter was ~ 57.2 mm, axial length was ~ 90 mm, with a front plate thickness of ~ 14 mm. The thicknesses of the front plate and the cylinder wall for each experiment is shown in Table 1. In this study, the impact velocity and the front plate thickness was controlled to prevent rupture of the plate, while causing sufficient deformation/bulging as a result of impact.

Table 1. Summary of experimental conditions

Experiment Nos.	Impact Velocity (km/s)	Front Plate Thickness (mm)	Wall Thickness (mm)	Impact Location (X,Y mm)	Radius (mm)	x-t Slope
L1	1.48	13.614	3.18	+ 0.12 , + 2.5	2.502	5.82
L2	1.52	13.919	3.18	+ 2.5 , + 2.5	3.535	5.59
L3	1.47	13.919	3.20	+ 11.4 , - 3.8	12.016	5.73
L4	1.55	14.021	3.23	- 3.8 , + 4.3	5.738	5.57
L5	1.52	13.665	3.19	- 2.0 , + 5.2	5.571	5.66
L6	1.52	13.614	3.23	- 2.0 , + 3.0	3.606	5.66

The experimental configuration is indicated in Figure 1(a). A velocity interferometer, VISAR, [8] is used to monitor the back surface motion of the free surface both along the central axis and at off-axis locations. A total of twelve strain gauges, six to determine the axial strain (stress) and six to determine the hoop strain (stress), were used. The measurements were determined to an accuracy of better than 2% for velocity histories and 3% for strain gauge records. In experiments L1 and L2, two polyvinyldifluoride (PVDF) gauges were also used on the circumferential surface but orthogonal to the strain gauge records. Because the output signals from the PVDF gauges perturbed the strain gauge records they were no longer used in subsequent experiments. In subsequent experiments they were replaced with strain gauges. Figure 1(a) illustrates the location of the velocity interferometer, and the strain gauges used in this study. An instrument can assembly is shown in Figure 1(b). Strain gauges 1 to 3 are positioned on one side of the can while gauges 4 to 6 are installed diametrically to strain gauges 1 to 3. The strain gauges are positioned nominally at 19 mm (gauges 1 & 4), 48 mm (gauges 2 & 5) and 78 mm (gauges 3 & 6) from the impact plane, and along the circumferential surface of the cylinder.
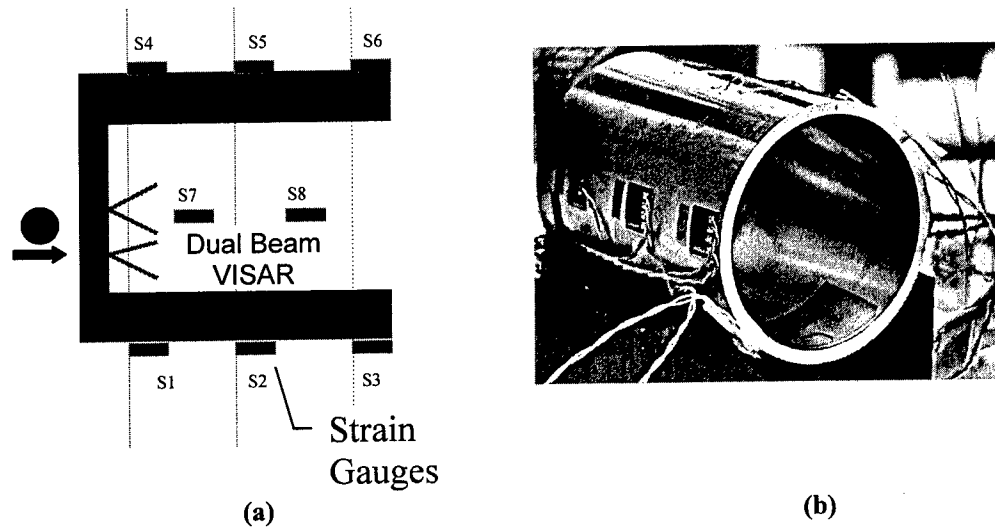
Fig. 1. Experimental configuration is shown in (a), while the instrumented can is shown in (b).

The measured free-surface particle velocity history is shown in Figure 2 for all the experiments. The strain gauge records, which represent the axial strain measurements of strain gauges 1 to 3, and 4 to 6 along the circumference are indicated in Figures 3 and 4, respectively, for experiment L5. The arrival time of the stress front as indicated by the strain gauge records is plotted versus its location in Figure 5. (In this graph, the times are arbitrarily shifted to allow a display of all experiments.) This yields the rate at which the stress front sweeps up in the cylindrical tube. As indicated in Table 1, multiple experiments were performed to determine the accuracy, and the repeatability of the experiments. The impact velocity was reproducible to within 1.3 % of the mean impact velocity of 1.5 km/s. All impact locations (except L3) are within 2.5 mm and 5.7 mm from the geometric center of the instrumented can, and are well within half the projectile sphere diameter.
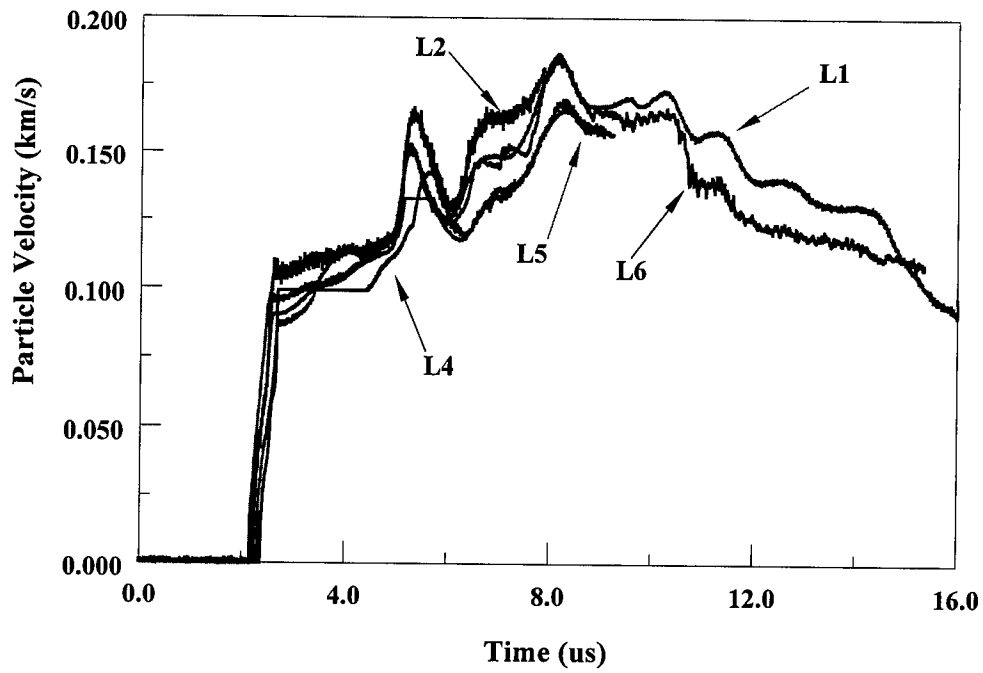
Fig. 2. Free-surface velocity time history of back surface motion along the central axis of the can.
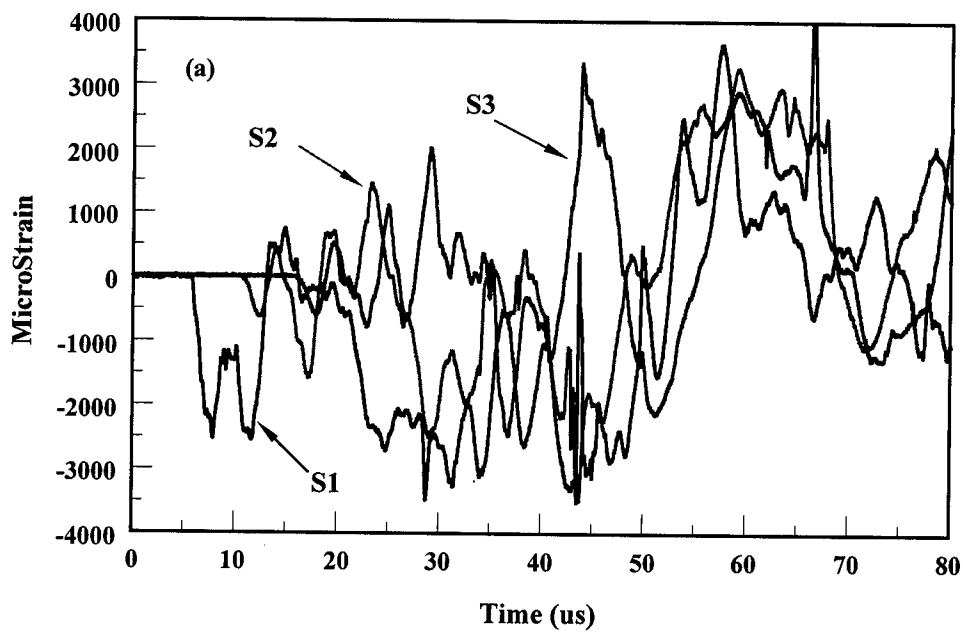
Fig. 3. Axial strain gauge records 1, 2, and 3 for experiment L5.
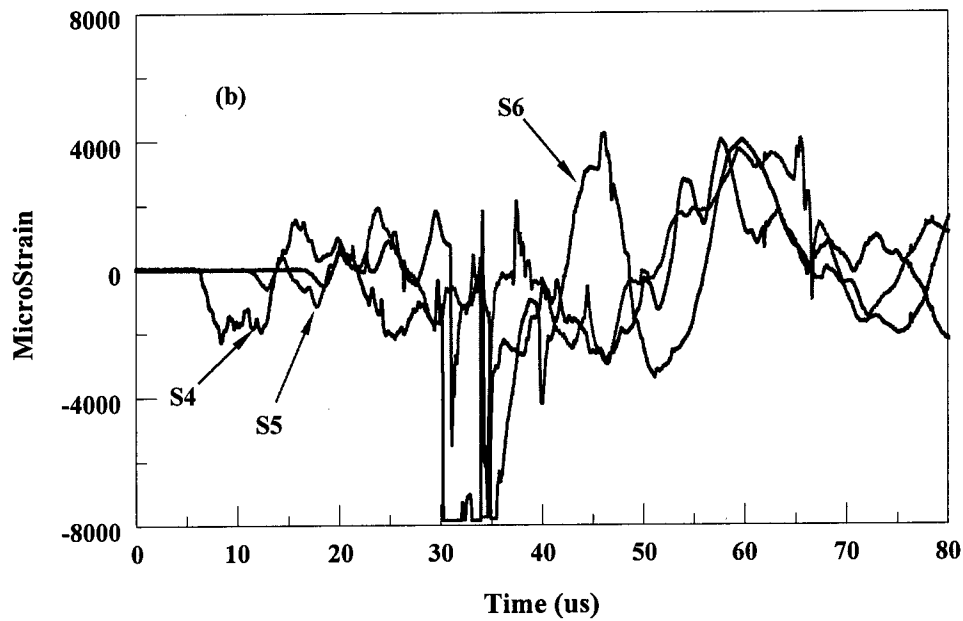
Fig. 4. Axial strain gauge records 4, 5, and 6 for experiment L5.
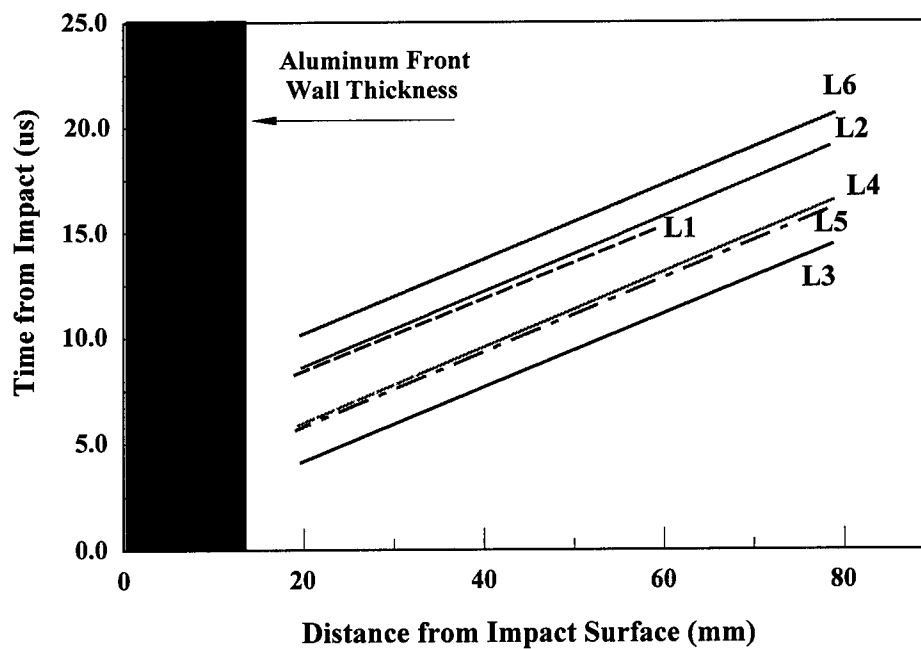
Fig. 5. x,t diagram of axial gauge records for all experiments. The slope of the
lines represents the speed of the wave propagation front (see Table 1).

For the purposes of discussion in this paper these experiments are characterized as two-dimensional. This potentially allows a detailed analysis to capture the effects of slight variations in experiments while assuming a two-dimensional axis symmetric configuration for computational analysis. (Note the deviation is small considering that the sphere is launched over a distance of 6 meters from the muzzle of the gun to the impact location.) In experiment L3, the sphere impacted the front face of the aluminum can at a radius of ~ 12 mm from the center, i.e., the axis of symmetry. This is clearly over one ball diameter; the results of this experiment will address three –dimensional impact effects both experimentally and computationally.

Results

Two-Dimensional (2D) Experiments – VISAR Records. Impact locations are within 2.5 mm and 5.7 mm from the geometric center of the instrumented can, and are well within half the projectile sphere diameter. Upon impact, peak stresses approaching 13 GPa are generated at the contact point. The loading strain rates at that point are in excess of 10^7/s. A spherical diverging wave, in combination with edge relief, attenuates the resulting stress wave. The peak velocity measurement of approximately 0.2 km/s at the rear free surface for all the experiments indicates substantial wave attenuation. The velocity interferometer was set up to monitor the particle-velocity at the exact geometric center of the can. The variation in free-surface particle velocities in Figure 2 results from variation in impact velocity and the impact location. These results, therefore, would allow an estimate of the dispersion/attenuation of the wave propagation process occurring radially over the impact locations of 2 mm to 5 mm from the center axis. The leading edge of the wave in the front plate is determined to travel at 6.4 km/s, which is representative of the elastic wave velocity in 6061-T6 aluminum. Although not shown in this paper, the off-axis velocity interferometer measurements also suggest that the initial arrival time of the diverging stress wave is indicative of an elastic wave front. The leading precursor wave velocity is determined to an accuracy of 1 %.

Two-Dimensional (2D) Experiments – Strain Gauge Records. In these experiments, the relative time of arrival of all strain gauge records are known to within the sampling rate of the recording equipment, which is 20 ns for the current strain gauge records. The strain gauge records for experiment L5 are indicated for gauges 1 to 3 in Figure 3 and for gauges 4 to 6 in Figure 4. Not all experiments are indicated in this paper but they have been documented elsewhere (9). Gauge records indicate peak strain of ~2500 x 10^{-6} at a strain rate of 1.2 x 10^3/s at approximately 20 mm from the impact interface. This reduces to a strain of 500 x 10^{-6} at a strain rate of 2 x 10^2/s at about 80 mm from the impact interface.

X-t Diagram. Figure 5 shows the least squares fit lines to the first arrival time of the strain gauge record versus its location for all the strain gauges used in the experiment. All experiments are shown in Figure 5. The initial arrival time is intentionally shifted arbitrarily to display the slopes of the lines for all experiments. The gauge pairs {1,4},{2,5}, and {3,6} are located at the same location but diametrically opposite from the impact interface on the circumferential surface. Experimentally, however, the arrival time of the leading edge of the wave is different for the complementary gauge (See Figure 3 and Figure 4). The time difference between the two gauges at the same location but diametrically opposite to each other is due to the non-centered nature of the impact. The data indicates that the stress front sweeps by at an average velocity of 5.66 km/s in the cylindrical tube. Thus, results of the strain-gauge records versus location in each experiment yield a velocity that is independent of the minor variations in both impact velocity and impact location for the series of experiments reported herein. This suggests that an inclined wave front is propagating in the cylindrical tube and it travels at the same wave speed.

Three-Dimensional (3D) Experiment – VISAR Records. In experiment L3 the impact occurs at a radius of 12 mm from the geometric center. Peak stresses approaching 13 GPa are generated at the contact point at impact. The loading strain rates as in other experiments is in excess of 10^7/s. A spherical diverging wave, in combination with edge relief, attenuates the resulting

stress wave. The peak velocity measurement of ~ 0.035 km/s monitored at the exact geometric center of the can, shown in Figure 6, indicates significant wave attenuation for non-centered impact. The attenuation is an order of magnitude more than what is indicated for the 2D experiments in Figure 2. The leading edge of the wave in the front plate is determined to travel at 6.4 km/s as determined by the distance from impact point to the center of the can. This is representative of the elastic wave velocity in 6061-T6 aluminum. This leading precursor wave velocity is also determined to an accuracy of 1 % in this experiment.
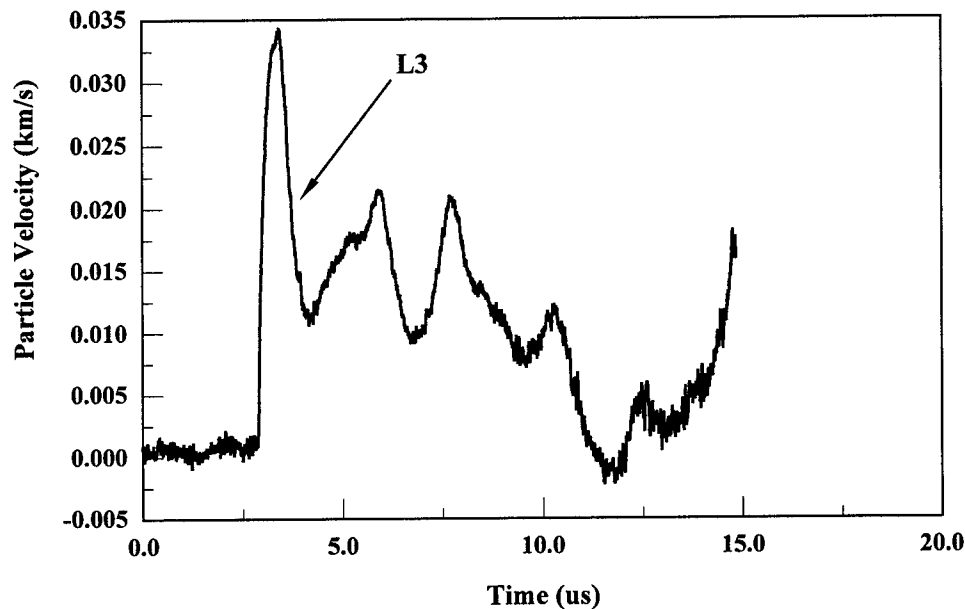
Fig. 6. Free-surface velocity time history of back surface motion along the central axis of can L3. Impact occurred at a radius of 12 mm from center.

Three-Dimensional (3D) Experiment – Strain Gauge Records. The strain gauge records for experiment L3 are shown for gauges 1 and 2 in Figure 7 and for gauges 4 to 6 in Figure 8. The records indicate peak strain of over 8000×10^{-6} at a strain rate of 1.2×10^{3}/s at approximately 20 mm from the impact interface. The oscillatory behavior appears to be considerably asymmetric when compared to the strain gauge records of the two-dimensional L5 experiment in Figures 3 and 4.

X-t Diagram. Figure 5 shows the least squares fit line to the first arrival time of the strain gauge record versus gauge location for gauges 4 to 6 in experiment L3 (Only 4, 5, and 6 were used because we did not get a gauge record 3 for the companion gauge 6). All other experiments are also shown in Figure 5. As shown in Figures 7 and 8, the arrival time of the leading edge of the wave is approximately 3.5 μs different for the complementary gauges 1 and 4. This large time difference between the two gauges at the same location but diametrically opposite to each other is evidently due to the 3D aspect of the experiment. The data nevertheless indicates that the stress front sweeps by at a velocity of 5.73 km/s in the cylindrical tube, and is quite comparable to the mean velocity of 5.66 km/s observed in the 2D experiments. The large time differences between the complementary gauge records suggest considerable obliquity in the 3D experiment. Incidentally, this wave speed is very close to the estimates of theoretical plate velocity in 6061-T6 aluminum, which is about 5.60 km/s.
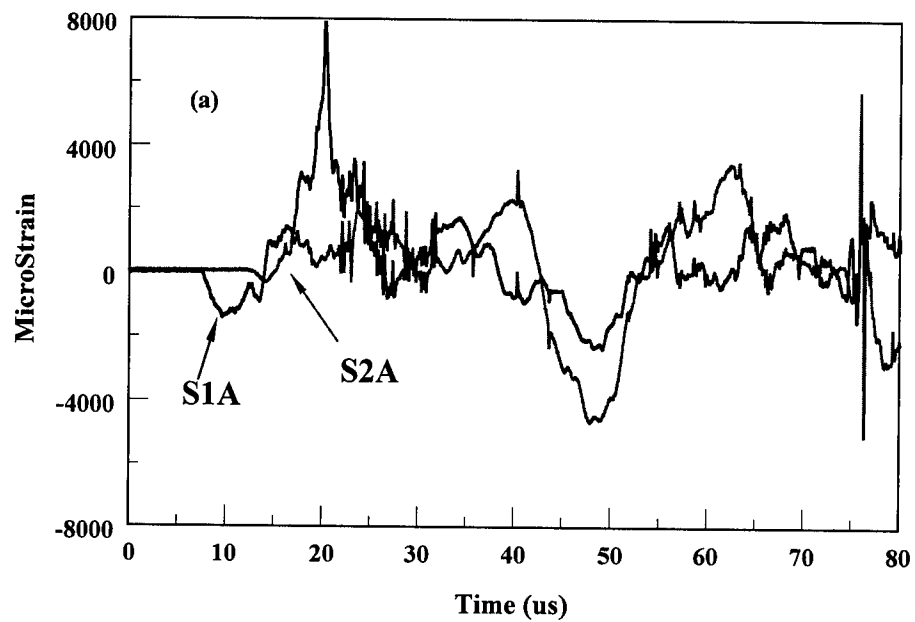
Fig. 7. Axial strain gauge records 1 and 2 for experiment L3.
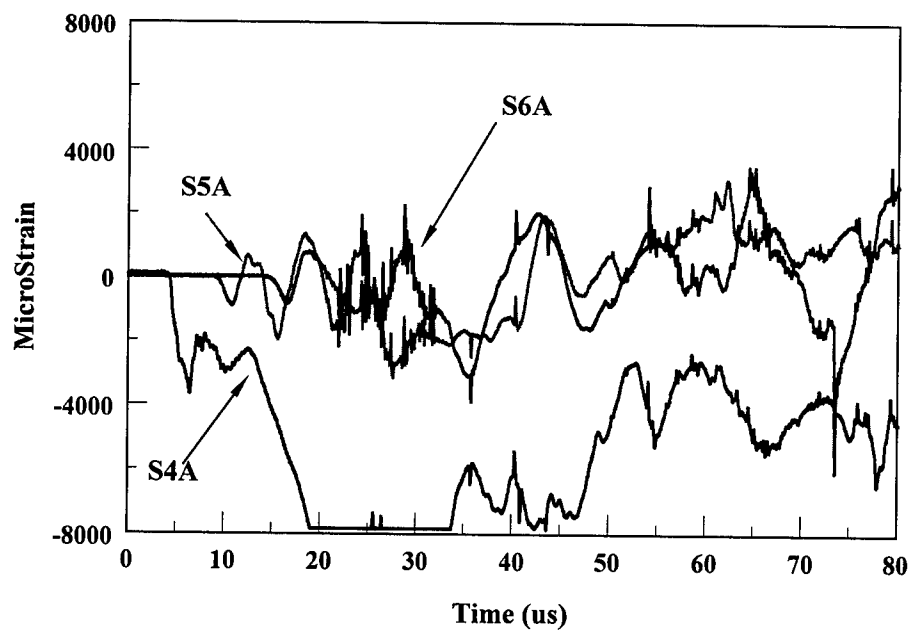
Fig. 8. Axial strain gauge records 4, 5, and 6 for experiment L3.

Degree of Asymmetry. Table 1 summarizes the location of impact both as an x, y coordinate and also as the radius measured from the center of the can, which is regarded as the origin. The degree of asymmetry is defined as the difference between the lines (RR_1) and (RR_4). R is the location of the impact (see Table 1), and the coordinates for R_1 and R_4 are (-31.6, 0) and (31.6, 0), respectively, the edges of the front surface where gauges 1, 2, 3 and 4, 5, 6 are installed. These lines are shown schematically in Figure 9. Note, if impact occurs along the y-axis then the impact location is symmetric with respect to the gauges located diametrically opposite to each other. There will not be any asymmetry with respect to the arrival times of the stress front at the gauge locations – even though the experiment may be a 3-D experiment. The time difference between the two gauges at the same location but diametrical to each other is primarily due to the asymmetry, and not merely due to the non-centered nature of the impact. The experiment L3 is, therefore, not only a 3D experiment, but from the viewpoint of strain-gauge locations, an asymmetric experiment. The degree of asymmetry is plotted versus the time difference between the two strain gauges at the same location in Figure 9. There appears to be a systematic correlation as indicated in the figure. Also shown in the figure are photos of recovered cans displaying the impact location in each experiment. From the stand point of code validation and computational analysis experiment L1 is the best experiment to investigate axis symmetric 2D effects, while experiment L3 is the best asymmetric 3D-experiment. The results of experiment L2 are not indicated in Figure 9. This is because good strain gauge records were not recorded in experiment L2.
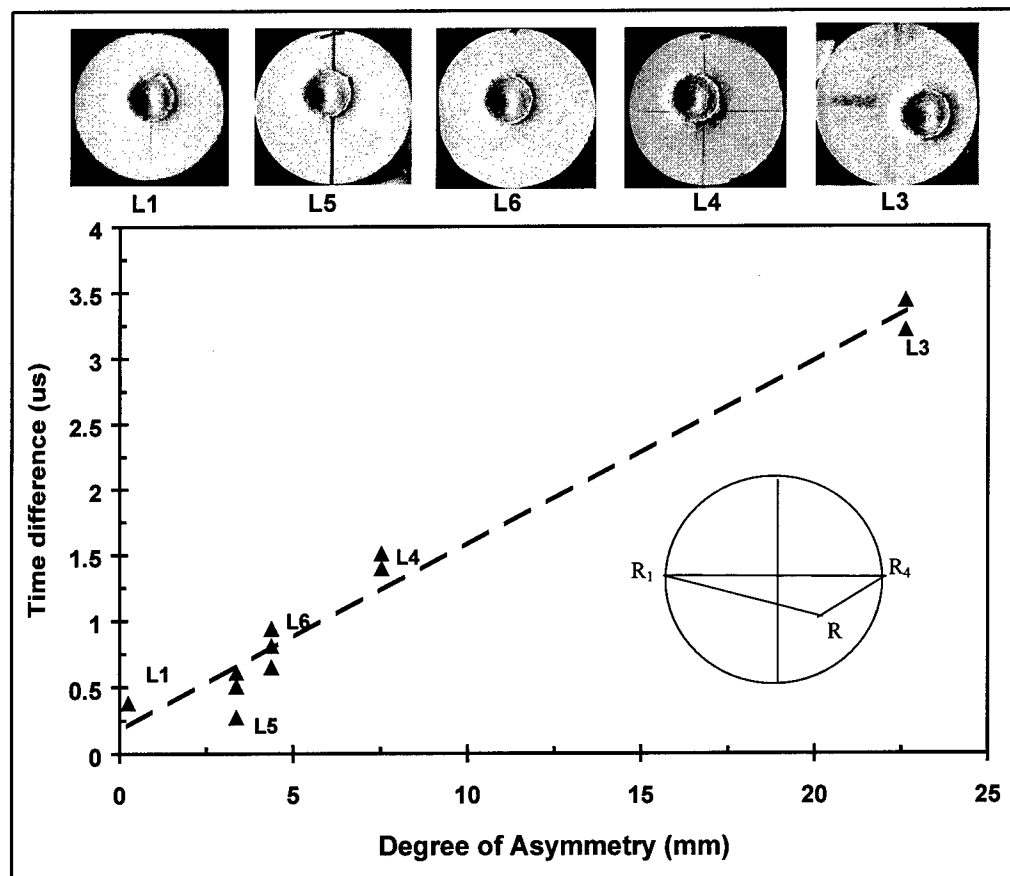
Fig. 9. Degree of asymmetry versus time difference between opposing
strain gauges. Degree of asymmetry is defined as the difference in lines
RR_1 and RR_4.

COMPUTATIONAL SIMULATIONS

The reasons for conducting the ALEGRA simulations are three-fold: 1) to assist in the design of the validation experiments; 2) to produce results for comparison with the experimental data; and 3) to utilize the code and discover errors and inadequacies from a user's perspective. The combined goal is ultimately to contribute to the validation of the ALEGRA code for a certain class of problems or determine the net uncertainty from various possible sources of error. Since there is always the desire to improve the accuracy of a code, an additional goal is also to discriminate between the dominant individual sources of error.

Axi-symmetric two-dimensional simulations with Eulerian meshes were run in the baseline studies. A Mie-Gruneisen EOS and an elastic perfectly plastic constitutive relation were used for simplicity. In the experiments, velocities at the centerline were measured for the off-center impacts, whereas in the two dimensional simulations this was approximated by off-center velocity measurements of centered impacts. This approximation will be most appropriate for early times (less than 20 μs) and for lower frequencies at the longer times.

Both the VISAR and strain gauge measurements were made on the material surface. Time-resolved data for Eulerian calculations in ALEGRA are acquired by the use of massless Lagrangian tracers. These tracers move with the Lagrangian motion of the materials during the course of calculations. Because of tracking problems these tracers must be placed at least one zone away from material boundaries in order to move most accurately. Otherwise, numerical diffusion associated with multi-material Eulerian interface tracking will partially corrupt the data recorded by the tracers. In our simulations, results were recorded at locations, which were 1.5 and 2.5 zones from the free surface to examine the effect of tracer location. Meshes with 0.5, 0.25 and 0.125 mm cell dimensions were used to examine mesh convergence effects. For the velocity type data as shown in Figure 2, a mesh size of 0.25 mm produced adequate convergence to ~ 2% error for the early time response. There was very little change in the calculated velocity history when the mesh size was further reduced to 0.125 mm, indicating mesh convergence for these mesh dimensions.

The agreement in Figure 10 between experiment and simulation is good, particularly at early times and for lower frequencies at later times. The higher frequency details at longer times are not captured well due in part to the off center effects mentioned above. Three dimensional analyses are currently being set up to more accurately model the experiment. Based on a limited set of materials testing data, the yield strength of the aluminum was initially taken to be 300 MPa, and the early time velocity comparison had significant disagreement, as shown in Figure 11.
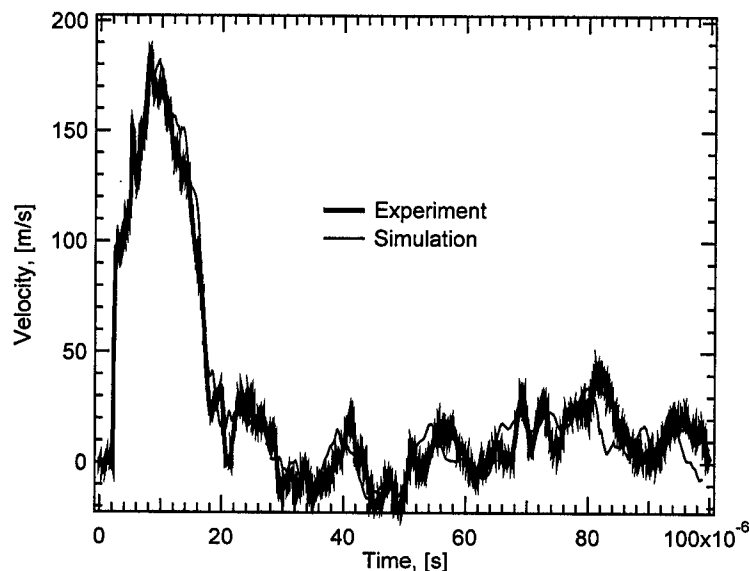
Fig. 10. Comparison of calculational simulations (indicated as faint line) of the velocity history in experiment L1 with the measured velocity history (dark line).

Subsequent examination of split Hopkinson bar results indicated that a choice of 400 MPa would be more appropriate. As indicated in Figure 11, the use of this value in the calculation resulted in much better agreement.

Total strain currently is not output from the code, but the stress components are. Since yielding was not observed at the strain gauge locations in the simulations, the elastic strains were calculated from the stresses and used in comparisons with experiment. Figure 12 shows the simulation and experiment for the strain gauge location S2. Initially, the results agree reasonably well, but at later times disagreement becomes more significant. Possible causes are the accumulation of error from advection, three-dimensional effects, or the effect of artificial viscosity on elastic wave propagation. The mesh size convergence of the strain gauge records did not appear to be as good as for the velocity data because long time response is desired from the former, so that there is more time for errors to accumulate. Likewise, studies with ALE meshes, in which the strain gauged side wall was Lagrangian, did exhibit slightly better agreement with experiment than pure Eulerian ones, and it is anticipated that the improvement would be greater at longer times. Further study, including three dimensional simulations, and further study of ALE approaches, is required to draw firm conclusions about the uncertainty of the code for this type of problem.
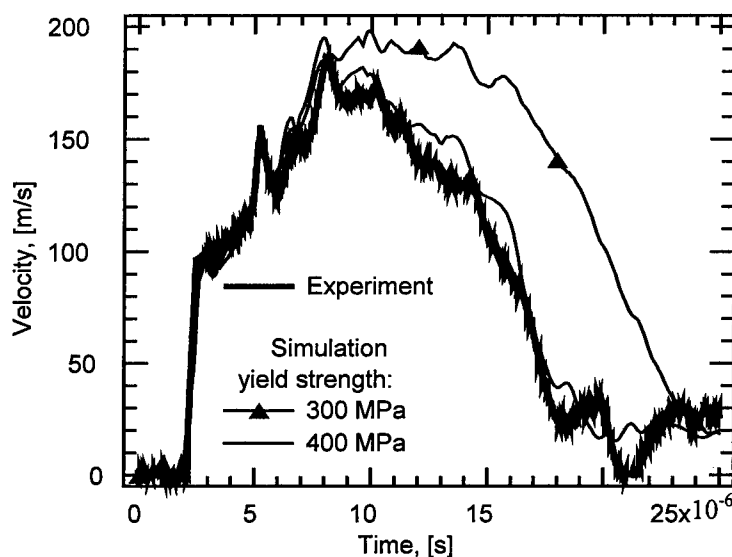
Fig. 11. Computational simulation of the velocity history in experiment L1 indicating the effect of yield strength on the simulations.
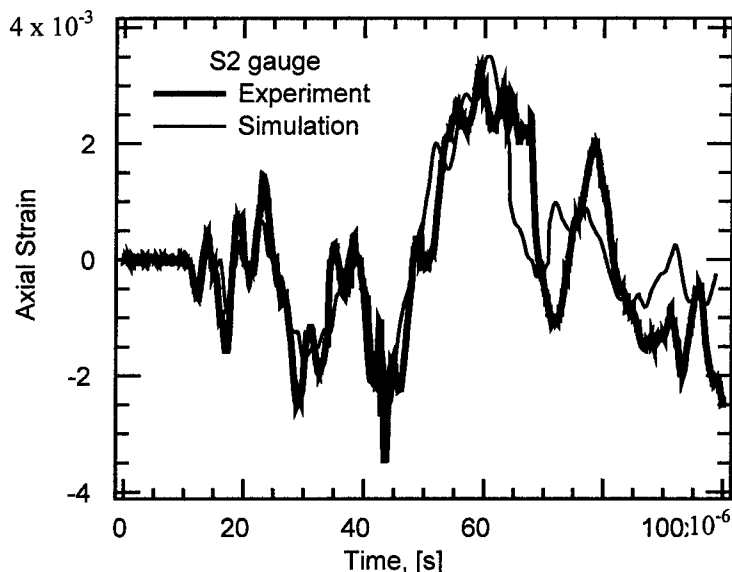
Fig. 12. Comparison of calculations with experiments for strain gauge S2 for experiment L6.

CONCLUSIONS

In this study, we provide an experimental test bed and a test methodology for validating features of the ALEGRA code over a broad range of responses with overlapping diagnostics that encompass the multiple strain rates. Specifically, the current experiments span the strain rate regimes from 10^7/s to less than 10^2/s. Input conditions are well characterized; the input conditions are known to better than 0.2%, while the measurement precision is approximately 2% for the interferometer records and about 3% for the strain gauge records. The current experiments are well controlled two-dimensional and three-dimensional loading experiments.

Results of the experiments indicate that in the front thick plate the diverging wave propagates at an elastic wave-velocity of 6.4 km/s. The wave transitions into the thin cylindrical tube at an average plate wave velocity of 5.66 km/s. The strain gauges located on the tube wall suggest an asymmetry in wave propagation and can be correlated to the degree of asymmetry as defined in this paper. The data is collected over long time scales. Even though it is not displayed in this study strain gauge records have been gathered for up to a millisecond.

Future experiments will consist of well-controlled three-dimensional loading conditions. Future experiments will also include a test bed at higher impact velocities, and an increased complexity of the test bed. The cylindrical can will be filled with structural materials of interest such as foam and steel to simulate many research and structural applications. This is ongoing work and it is anticipated that the current data set will be continuously used to evaluate many aspects and issues related to ALEGRA code validation.

REFERENCES

1. R. M. Summers, J. S. Peery, M. W. Wong, E. S. Hertel, T. G. Trucano, L. C. Chhabildas, Recent progress in ALEGRA development and applications to ballistic impact. *Int. J. Impact Engng.*, **20**, 779-788 (1997).
2. K. G. Budge, J. S. Peery, RHALE: a MMALE shock physics code written in C++. *Int. J. Impact Engng.*, **14**, 107-120 (1993).
3. J. M. McGlaun, S. L. Thompson, M. G. Elrick, A brief description of the three-dimensional shock wave physics code CTH. *Sandia National Laboratories Report SAND89-0607*, (1989).
4. D. E. Carroll, E. S. Hertel, T. G. Trucano, Simulation of armor penetration by tungsten rods: ALEGRA validation report. *Sandia National Laboratories Report SAND97-2765*, (1997).
5. L. C. Chhabildas, Survey of diagnostic tools used in hypervelocity impact studies. *Int. J. Impact Engng.*, **5**, 734-743 (1987).
6. J. R. Asay, L. C. Chhabildas, L. M. Barker, Projectile and impactor designs for plate-impact experiments. *Sandia National Laboratories Report SAND85-2009*, (1989).
7. R. L. Moody, C. H. Konrad, Magnetic induction system for two-stage gun projectile velocity measurements. *Sandia National Laboratories Report SAND84-0638*, (1984).
8. L. M. Barker and R. E. Hollenbach, Laser interferometer for measuring high velocities for any reflecting surface. *J. Appl. Phys.*, **43**, 4669-4675.
9. L. C. Chhabildas, C. H. Konrad, D. A. Mosher, W. D. Reinhart, B. D. Duggins, T. G. Trucano, R. M. Summers, J. S. Peery, ALEGRA code validation: experiments and simulations. *Sandia National Laboratories Report* in preparation.

EXTRAVEHICULAR ACTIVITY SUIT PENETRATION RESISTANCE

E. L. CHRISTIANSEN[1], B. G. COUR-PALAIS[2], and L. J. FRIESEN[3]

[1]NASA Johnson Space Center, Mail Code SN3, Houston TX 77058; [2]Consultant, Southwest Research Institute, San Antonio, TX 78228; [3]Lockheed-Martin, Houston TX 77058

Summary—The penetration resistance to hypervelocity impact (HVI) has been determined based on test and analysis for the extravehicular mobility unit (EMU) space suit used by astronauts to perform extravehicular activities (EVA). The suit is broadly divided into two categories: soft goods and hard goods depending on their flexibility. In the soft good category, HVI tests were conducted on samples representative of the arms, legs, briefs, gloves, glove gauntlet, and overlap regions. Hard goods examined include the hard upper torso (HUT), portable life support system (PLSS), and helmet. Ballistic limit equations have been developed that define the particle size on the perforation threshold of the suit bladder as a function of impact conditions (velocity, angle, and density). Penetration equations have also been developed for predicting particle sizes causing uncontrollable leaks (i.e., with bladder hole sizes exceeding 4 mm diameter). These equations are necessary to perform orbital debris and meteoroid risk assessments for EVAs. © 1999 Elsevier Science Ltd. All rights reserved.

NOTATION

C	coefficients
d_c	critical diameter of particle causing threshold perforation of bladder (cm)
E_c	critical kinetic energy at the failure ballistic limit (J)
ρ	projectile density (g/cm^3)
psi	lb-force per square inch (1 psi = 6895 Pa)
TMG	thermal meteoroid garment
θ	impact angle measured from surface normal (deg)
$\cos \theta$	cosine of impact angle
V	projectile velocity (km/s)
	subscripts:
H	high velocity
hi	intermediate high velocity
li	intermediate low velocity
L	low velocity

INTRODUCTION

Crews wearing Extravehicular Mobility Units (EMUs) or space suits as shown in Fig. 1 perform extravehicular activities (EVAs). Crews conducting EVAs are exposed to meteoroid and orbital debris (M/OD) impact. There is a remote possibility that these impacts could penetrate through the outer layers of the suit to perforate the bladder causing an oxygen leak, and an even more remote possibility of suit decompression. Oxygen pressure is regulated to maintain suit pressure at safe levels for a minimum of 30 minutes with holes up to 4mm in diameter. This paper provides penetration equations for the various regions of the suit using two failure criteria: (1) a perforation ballistic limit resulting in a hole of any size in the bladder, and (2) the uncontrolled leak criteria, caused by holes exceeding 4mm diameter in the bladder. The penetration equations are then used in a probability analysis code, i.e., BUMPER [6] to assess the risks of receiving an impact from meteoroid and orbital debris during an EVA that would cause a leak of any size, or a subset of these, a critical leak.
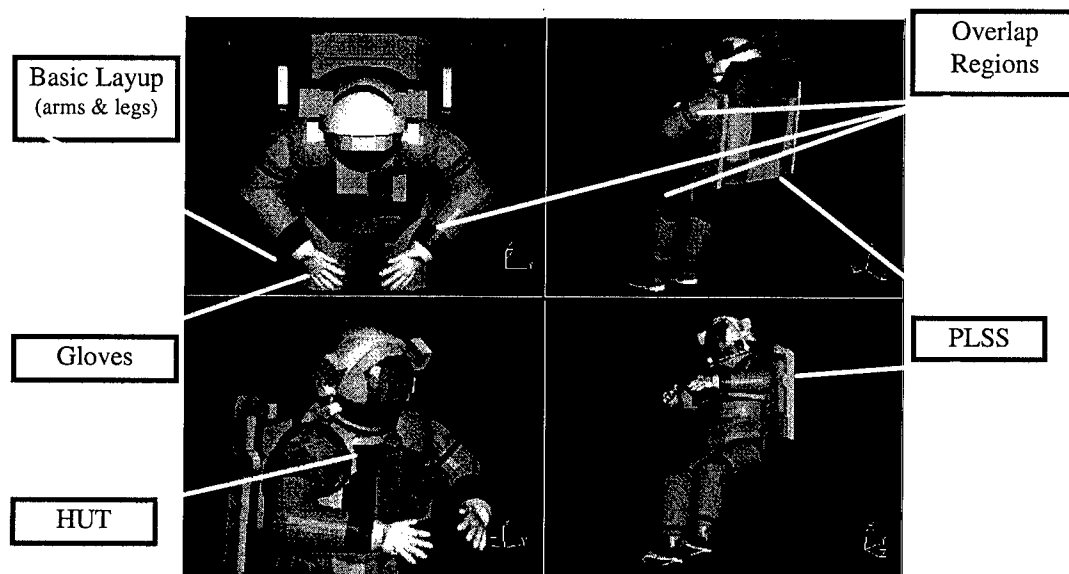
Fig. 1. EMU and locations of materials tested.

To assess M/OD risks, samples of the EMU have been tested by hypervelocity impacts (HVI) in the past using mainly aluminum particles at normal impact angle [1, 2]. From these tests, ballistic limits were established for the various parts of the EMU based on kinetic energy values that were on the threshold of perforating the bladder of the suit. Due to the need to accurately predict risks from the orbital debris threat, an extensive hypervelocity impact test program has recently been conducted using aluminum and non-aluminum particles at oblique impact angles over a range of velocities. As part of this effort, 65 hypervelocity impact tests were completed at the JSC Hypervelocity Impact Technology Facility [6] on 3 different sample types (Fig. 1) representing major areas of the EMU: (1) a "basic" layup corresponding to the EMU configuration in the arms and legs, (2) an "overlap" layup corresponding to regions in the arm and leg where sections of the suit overlap, and (3) a "glove" layup representative of the finger region.

TARGET SPECIMENS

Cross-sections of the targets are given in Fig. 2-4. The basic suit layup has an areal density of 0.145 g/cm². It consists of an outer ortho fabric layer which is a combination of Nomex, Kevlar and Teflon, followed by 5 layers of aluminized Mylar separated by dacron mesh, a neoprene coated nylon ripstop layer, a dacron fabric restraint layer, and a urethane coated nylon bladder. The overlap target has an areal density of 0.27 g/cm² and includes an additional ortho fabric layer, two Teflon layers and 5 layers of aluminized Mylar over the basic layup. The glove layup has an areal density of 0.098 g/cm² and consists of Teflon fabric followed by 3 layers of aluminized Mylar, 2 layers of Dacron fabric and a rucothane 5225 bladder. The targets were typically 10cm x 10cm squares to avoid edge effects and sewn together along an edge. Targets were securely taped to a frame with an 8cm x 8cm square opening in the center. A 1mm thick aluminum witness plate was mounted 5cm behind the targets to record damage from perforating projectiles. Targets were tested unpressurized and pressurized with nitrogen to 4.3 psi (30 KPa).

θ

Ortho Fabric (0.048 g/cm²)
(5) Al-Mylar/Dacron scrim (0.017 g/cm²)
Nylon ripstop (0.029 g/cm²)
Dacron restraint (0.020 g/cm²)
Urethane/Nylon bladder (0.028 g/cm²)

Inside
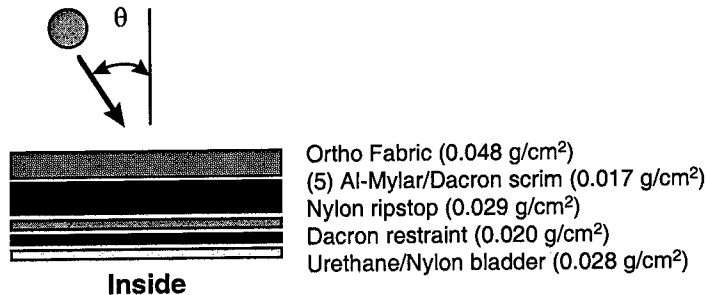
Fig. 2. EMU "Basic Suit" Target Specimen.

Teflon Fabric (0.030 g/cm²)
(5) Al-Mylar/Dacron scrim (0.017 g/cm²)
Teflon Fabric (0.030 g/cm²)
Ortho Fabric (0.048 g/cm²)
Ortho Fabric (0.048 g/cm²)
(5) Al-Mylar/Dacron scrim (0.017 g/cm²)
Nylon ripstop (0.029 g/cm²)
Dacron restraint (0.020 g/cm²)
Urethane/Nylon bladder (0.028 g/cm²)

Inside
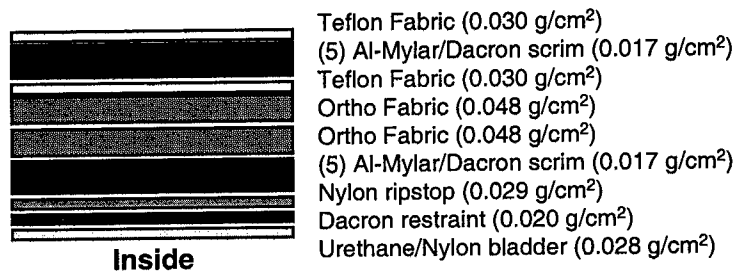
Fig. 3. EMU Overlap (Arm/Leg/Glove-Gauntlet) Target Configuration.

Teflon Fabric (0.030 g/cm²)
(3) Al-Mylar/Dacron scrim (0.010 g/cm²)
(2) Dacron Fabric (0.006 g/cm²)
Rucothane 5225 bladder (0.052 g/cm²)

Inside
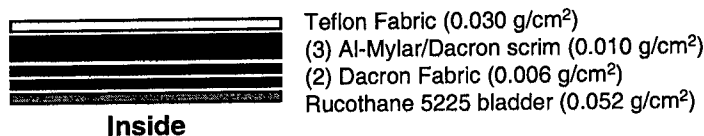
Fig. 4. Glove Finger Target Cross-Section.

TEST RESULTS AND DISCUSSION

Tables 1 and 2 provide results of representative HVI tests on the EMU soft goods. All tests in Table 1 were conducted with targets having a 4.3psi pressure differential across the bladder

(inside of bladder was pressurized with nitrogen to 4.3psi). Table 2 provides results on unpressurized targets. The results of tests to determine the perforation threshold of the bladder when the target was pressurized did not differ significantly from the results of tests when the target was unpressurized for the same impact conditions [5]. Additional test results can be found elsewhere [3-5]. Fig. 5 illustrates the results of a 0.5mm aluminum sphere impacting a basic suit layup at 6.84 km/s and 30° to normal. A 1.6mm hole is created in the ortho fabric, while the hole is ~2X larger in the aluminized Mylar layers under the ortho fabric. Several holes occur in the Dacron restraint layer, one with a maximum diameter of 0.9mm (Fig. 6). The bladder was not perforated, although the bladder darkened on both the front and back surfaces (Fig. 7).
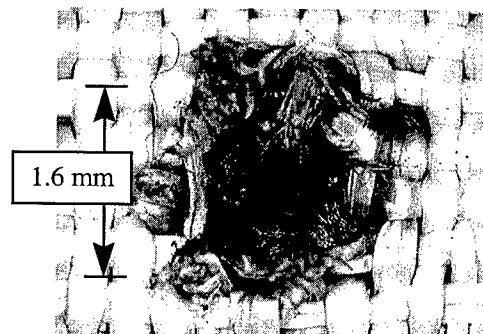
Fig. 5. JSC HITF Test A2930, ortho fabric outer layer, 0.5mm Al2017T4 sphere impacted at 6.84 km/s, 30° obliquity.
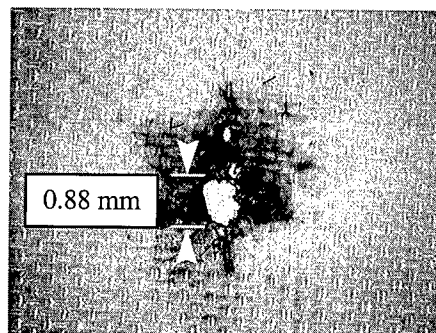
Fig. 6. JSC HITF Test A2930, Dacron restraint layer (rear side).
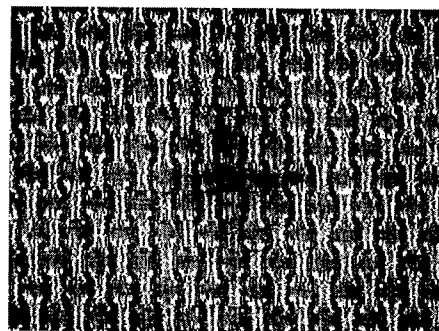
Fig. 7. JSC HITF Test A2930, urethane coated nylon bladder (front), darkened but no perforation.

The test results indicate that EMU materials resemble small-scale spaced bumper shields. At higher velocities (~7 km/s), the impact hole on the ortho fabric on the sample exterior is relatively small (a few multiples of the projectile diameter) with the ortho fabric outer layer providing a bumper which breaks up small particles. The cloud of debris particles resulting from the collision expands behind the ortho fabric bumper as is observed in impact experiments on spaced bumper shields. As the debris cloud expands, it interacts with the thin aluminized Mylar, liner and Dacron restraint layers in the interior of the target (holes are typically larger in these layers than in the outer ortho fabric layer). The susceptibility of the bladder to puncture failure depends on how effectively the small particles in the debris cloud are stopped, slowed or ablated by the subsequent collisions with the inner layers. The debris cloud leaves a dark smudge on the inner bladder that is many times larger than the projectile diameter when close to the perforation ballistic limit of the bladder at high velocities (~7 km/s). Above the perforation ballistic limit of the bladder, perforation failure occurs from small particle point loads; i.e., failure does not appear to be from impulsive loads. Oblique impact failures can cause relatively long but narrow "gashes" in the bladder. As with a spaced bumper shield, the EMU suit layups are more susceptible to failure from lower velocity impacts at near normal impact angles. At low velocity (4-5 km/s), impacting particles do not break up as well on the ortho fabric "bumper". This behavior can result in reduced ballistic limits (i.e., smaller particles perforate at 4-5 km/s than at 7 km/s for normal impacts). Similar velocity effects are observed for the gloves [3].

Table 1. Test Results on Pressurized Basic Suit Samples

BASIC SUIT TARGETS *(4.3 psi pressure differential)*					
Shot Number	Projectile Material	Projectile Diameter (mm)	Impact Speed (km/s)	Impact Angle (deg)	Bladder Perforated?
HITF A2184	Al 2017T4	0.40	7.65	0	No
HITF A2181	Al 2017T4	0.40	7.47	0	No
HITF A2174	Al 2017T4	0.40	7.40	0	No
HITF A2200	Al oxide	0.40	7.56	0	No, BL
HITF A2204	Al oxide	0.40	7.84	0	Yes

Table 2. HVI Test Results on EMU Samples

		BASIC SUIT TARGETS			
Shot Number	Projectile Material	Projectile Diameter (mm)	Impact Speed (km/s)	Impact Angle (deg)	Bladder Perforated?
HITF A2896	Al 2017T4	0.39	6.90	0	No
HITF A2900	Al 2017T4	0.50	7.03	0	No
HITF A2907	Al 2017T4	0.60	6.95	0	No
HITF A2910	Al 2017T4	0.60	5.79	0	Yes
HITF A2911	Al 2017T4	0.52	4.35	0	No
HITF A2959	Al 2017T4	0.51	5.64	0	No
HITF A3071	Al 2017T4	0.50	7.48	0	No
HITF A3049	Al 2017T4	0.81	7.25	0	Yes
HITF A3043	Al 2017T4	0.60	3.73	0	Yes
HITF A3044	Al oxide	0.57	7.39	0	Yes
HITF A2967	Al 2017T4	0.52	6.95	30	No
HITF A2968	Al 2017T4	0.61	7.11	30	Yes
HITF A2932	Al 2017T4	0.52	5.66	30	Yes
HITF A3038	Nylon	1.24	7.38	30	Yes
HITF A3048	Al oxide	0.40	7.29	30	No
HITF A2969	Al 2017T4	0.53	6.89	45	No
HITF A2935	Al 2017T4	0.60	7.29	45	No
HITF A2971	Al 2017T4	0.61	7.15	45	Yes
HITF A2936	Al 2017T4	0.72	7.02	45	Yes
HITF A3039	Nylon	1.22	7.34	45	Yes
HITF A3047	Al oxide	0.40	7.28	45	No
HITF A3081	Steel	0.39	7.13	45	Yes
HITF A2940	Al 2017T4	0.41	5.76	45	No
HITF A2939	Al 2017T4	0.51	5.56	45	Yes
HITF A3019	Nylon	1.26	5.56	45	Yes
HITF A3070	Nylon	0.99	7.45	50	Yes
HITF A3082	Steel	0.39	6.99	50	Yes
HITF A3083	Steel	0.39	7.18	55	No
HITF A2941	Al 2017T4	0.52	6.87	60	No
HITF A2978	Al 2017T4	0.60	6.95	60	No
HITF A3023	Nylon	1.27	6.94	60	No
HITF A3069	Steel	0.39	7.34	60	No
HITF A2956	Al 2017T4	0.72	5.73	60	No
HITF A2958	Al 2017T4	0.81	5.56	60	Yes
HITF A3009	Nylon	1.40	5.44	60	No
		GLOVE FINGER TARGETS			
HITF A3006	Al 2017T4	0.22	7.00	0	No
HITF A2895	Al 2017T4	0.32	7.00	0	Yes
HITF A2917	Al 2017T4	0.40	5.55	0	No
HITF A2918	Al 2017T4	0.52	5.45	0	Yes
HITF A3041	Al 2017T4	0.40	4.22	0	Yes
		OVERLAP/GLOVE GAUNTLET TARGETS			
HITF A2966	Al 2017T4	0.80	7.00	0	No
HITF A2915	Al 2017T4	1.00	6.15	0	Yes
HITF A2945	Al 2017T4	1.03	6.74	60	No

BALLISTIC LIMIT EQUATIONS

Ballistic limit equations were developed for the EMU soft good components as given below.

High-Velocity: when $V \geq 6.95/(\cos \theta)^{0.45}$,

$$d_c = C_H \, \rho^{-0.5} V^{-2/3} (\cos \theta)^{-0.45} \tag{1}$$

Intermediate-Velocity: when $5.1/(\cos \theta)^{0.132} < V < 6.95/(\cos \theta)^{0.45}$,

$$d_c = C_{hi} \, \rho^{-0.5} (\cos \theta)^{-0.15} (V - 5.1/(\cos \theta)^{0.132})/(6.95/(\cos \theta)^{0.45} - 5.1/(\cos \theta)^{0.132}) +$$
$$C_{li} \, \rho^{-0.5} (\cos \theta)^{(0.088-X)} (6.95/(\cos \theta)^{0.45} - V)/(6.95/(\cos \theta)^{0.45} - 5.1/(\cos \theta)^{0.132}) \tag{2}$$

Low-Velocity: when $V \leq 5.1/(\cos \theta)^{0.132}$,

$$d_c = C_L \, \rho^{-0.5} (\cos \theta)^{-X} V^{-2/3} \tag{3}$$

Coefficients

	C_H	C_{hi}	C_{li}	C_L	X	X@θ>50
Basic Suit	0.38	0.104	0.078	0.232	0.2	0.8
Finger	0.19	0.052	0.071	0.21	0.2	0.8
Overlap	0.51	0.140	0.172	0.51	0.2	0.8

The results of the tests with aluminum projectiles are shown in Fig. 8-11. The dotted line in Fig. 8-10 shows the previous constant kinetic energy to fail ballistic limit while the solid line is the new ballistic limit based on the current work.
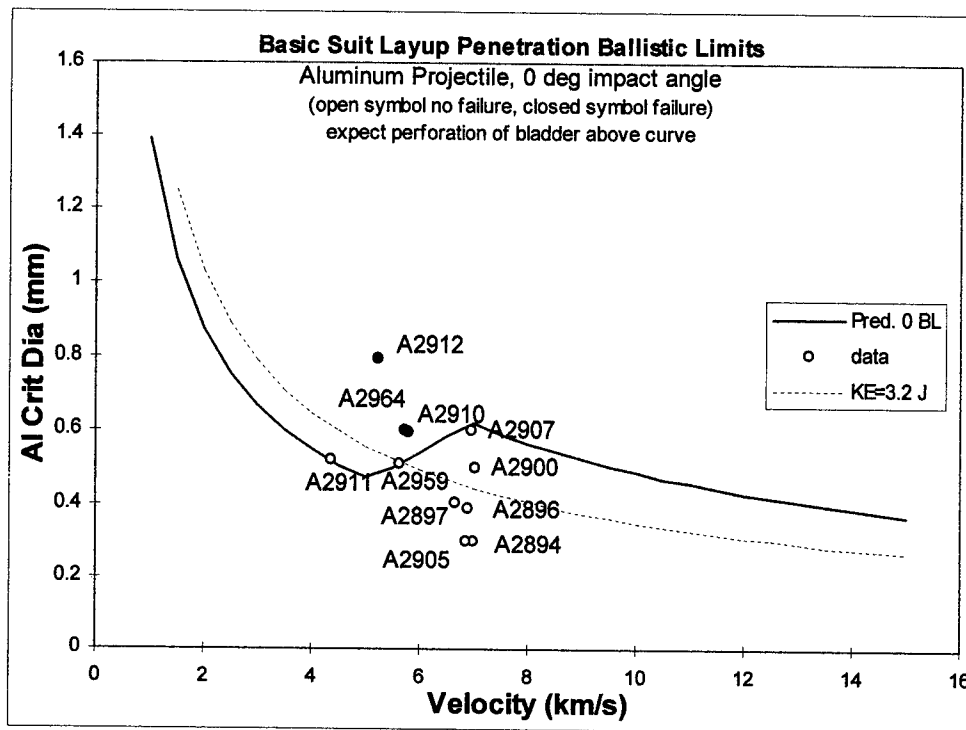
Fig. 8. Basic Suit, 0° impacts.
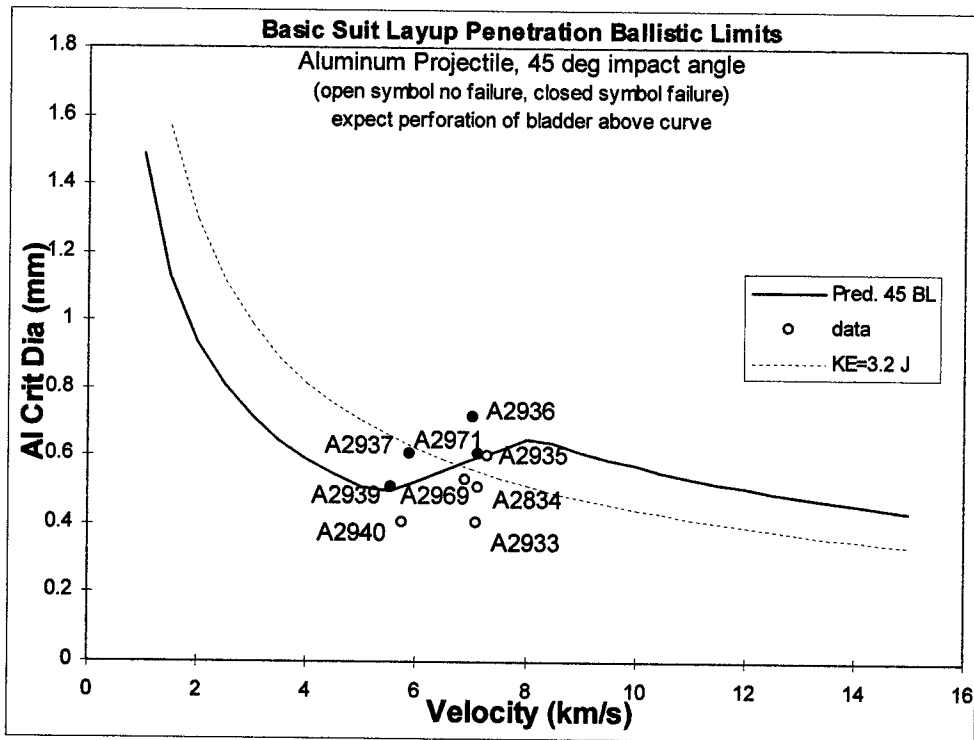
Fig. 9. Basic suit, 45° impacts.
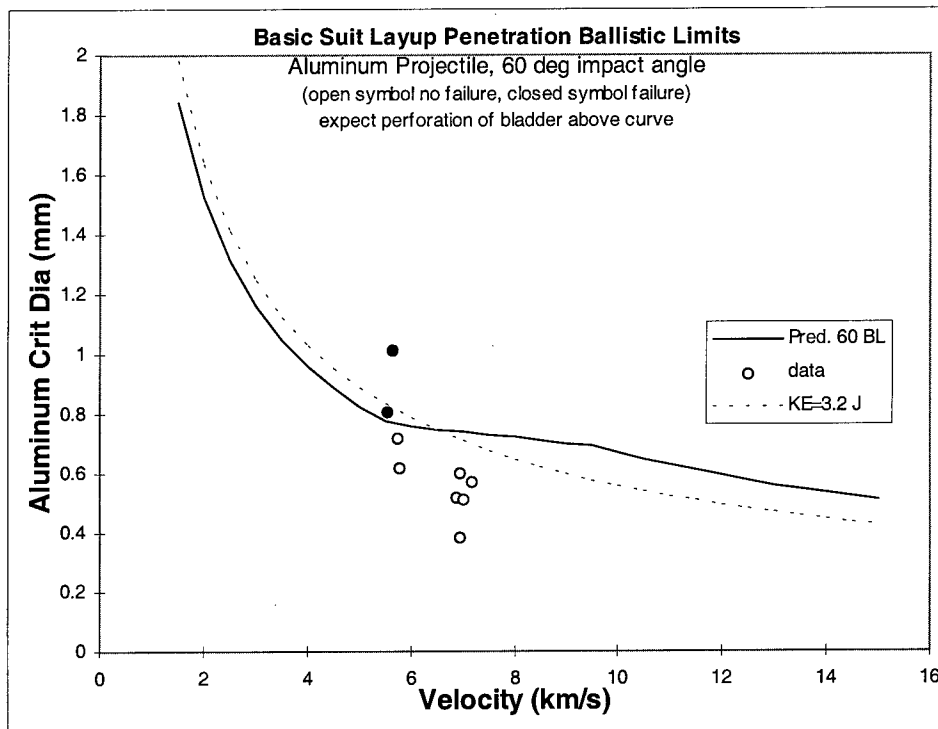
Fig. 10. Basic Suit, 60° impacts.
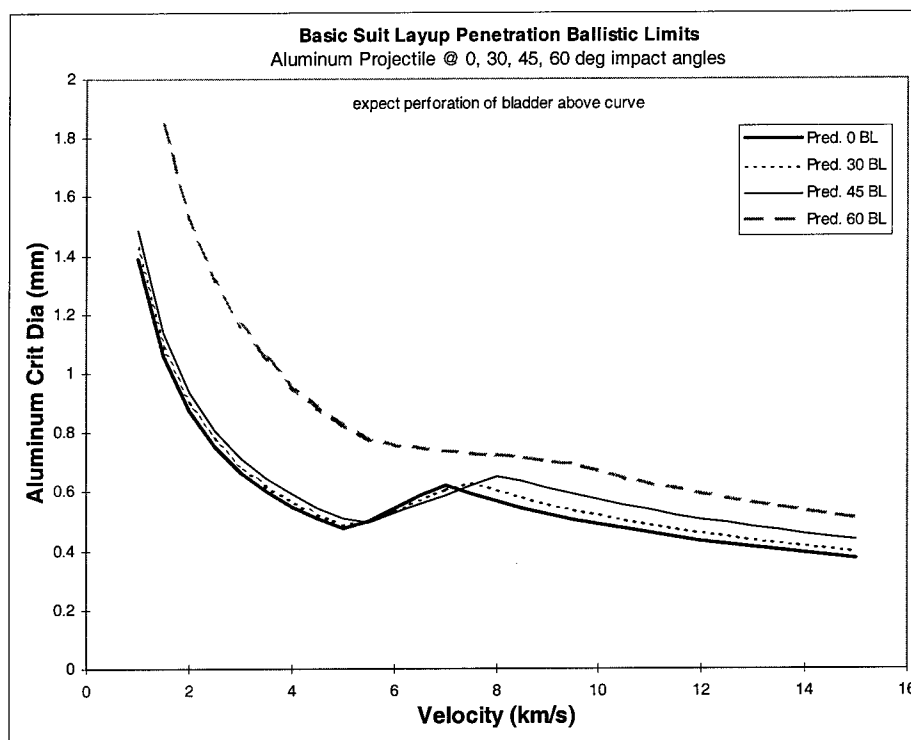
Fig. 11. Basic Suit Ballistic Limit Curves: 0°, 30°, 45°, and 60° impact angles.

BALLISTIC LIMITS FOR HARD GOODS

The following ballistic limit equation for "hard" portions of the EMU has been developed based on HVI test results [2, 5].

$$d_c = 0.156 \, E_c^{1/3} \, \rho^{-1/3} \, (V \cos\theta)^{-2/3} \tag{4}$$

Table 3 provides the ballistic limit parameters in Eqn. (4) for the EMU hard goods. The failure criterion for these items is no leak or no spall from the rear side of the material. For some items such as the oxygen tanks, this is a very conservative criterion because spall from the PLSS shell is considered a critical "failure" although if it does happen, it will damage the tank but might not necessarily cause a leak or catastrophic rupture. However, the meteoroid/debris penetration risk assessments are not significantly affected by this assumption, because the risks are driven by the ballistic limits for the soft goods, particularly the arms, legs, briefs, and gloves.

Table 3. EMU Hard Components and Ballistic Limit Parameters

Item**	Materials/Thicknesses*	E_c Critical Energy (J)
HUT	TMG & Fiberglass	44
Bearings/Sizing Rings	TMG & 3.2mm Al 6061T6	39
Helmet & Visors	Lexan & 1.7mm Polysulfone	71
Face plate	2.4mm Lexan	39
Eyeshades	Lexan & Polysulfone	71
PLSS: Primary O2	TMG & 3.6mm Al 2219T851	60
PLSS: Metox Contamination Control Cartridge	TMG & 2.3mm Al 2219T851	21
PLSS: battery cover	TMG & 0.46mm Al 6061T6	3.5
PLSS: Secondary O2	TMG & 1.8 mm Al 2219T851	13
SAFER GN2 Tank	TMG & Gr-Ep overwound Al	20
DCM Critical Components	TMG & 1.6mm Al 4027-T6	10
*where TMG = thermal meteoroid garment composed of ortho fabric, 5 layers aluminized mylar/dacron scrim, 1 neoprene coated nylon ripstop layer		
**Other Notes: DCM = Display & control module, HUT = hard upper torso, PLSS = portable life support system		

CRITICAL HOLE SIZE

HVI tests were also conducted to assess impact conditions that will result in uncontrollable leaks, i.e., when holes exceed the allowable 0.4cm diameter hole in the bladder. It was found that Eqn. (4) with $E_c = 56J$ provides a reasonable fit to the data, and can be used to predict particles that cause a 0.4cm or larger hole in the bladder for areas of the suit covered by the basic suit layup (arms, legs, briefs).

CONCLUSIONS

HVI tests have been performed on EMU components at a variety of impact angles, velocities and impactor densities, and bladder perforation ballistic limit equations have been developed. These equations have been used in meteoroid/debris risk assessments for Shuttle and Space Station EVAs. Although the risks of penetration of the EMU are small because of the small exposed area and relatively short duration of the EVAs, the HVI test and analysis results indicate ways to reduce the risks further. The EMU soft goods (arms, legs, briefs, and gloves) control the penetration risks of the EMU because relatively small particles can penetrate the suit in these areas.

Because the soft goods of the EMU perform like miniature standoff shields, methods employed to increase the penetration resistance for standoff shields are relevant to the EMU as well. The following are suggested ways to enhance the performance of any shield, specifically tailored for the EMU:

- Increase the shield "standoff" by using more lightweight Dacron scrim between each layer of the thermal insulation layers. This will improve high velocity ballistic protection (>4 km/s).
- Improve the shock properties of the shield bumper by adding ceramic or glass fabric or fibers to the outer ortho fabric layer. A separate fabric layer could be added over or under the ortho fabric, or weave ceramic or glass fibers into the ortho fabric.
- Improve penetration resistance by adding high-strength cloth materials (e.g., Kevlar, Spectra, etc) near the bladder. High-strength materials work best lower in shields.
- Thicken the shield rear wall (i.e., bladder) or add a redundant bladder.

Additional testing of the EMU soft goods is currently under way to evaluate additional impact conditions, determine the repeatability of the test results, assess new materials and evaluate self-sealing bladder materials [7]. Based on these tests, the EMU ballistic limit equations will be updated.

REFERENCES

1. W.E. McAllum, Development of Meteoroid Protection for Extravehicular Activity Space Suits, AIAA Hypervelocity Impact Conference Proceedings, Paper No. 69-366, 1969.
2. B.G. Cour-Palais, Spacecraft Outer Thermal Blankets as Hypervelocity Impact Bumpers, Proceedings of the American Physical Society Topical Group on Shock Compression of Condensed Matter, 1995, American Institute of Physics (AIP) Press Conference Proceedings 370, pp.1175-1178.
3. L.J. Friesen and E.L. Christiansen, Hypervelocity Impact Tests of Extravehicular Mobility Unit (EMU) Material Samples, Part 1, JSC 27856, May 1997.

4. L.J. Friesen and E.L. Christiansen, Hypervelocity Impact Tests of Extravehicular Mobility Unit (EMU) Material Samples, Part 2, JSC 27995, June 1998.
5. B.G. Cour-Palais, A Review of the EMU Ballistic Limit Tests and Analyses Performed in Conjunction with Space Suit Meteoroid and Orbital Debris Protection Capability, SwRI Report No. 6684/002, June 1996.
6. NASA Johnson Space Center (JSC) Hypervelocity Impact Technology Facility (HITF) Web Page, http://hitf.jsc.nasa.gov/ or http://hitf.jsc.nasa.gov/hitfpub/main/index.
7. F. Lyons, Hypervelocity Impact Testing of EMU Alternative Materials, JSC 28445, September 1998.

FLEXIBLE AND DEPLOYABLE METEOROID/DEBRIS SHIELDING FOR SPACECRAFT

E. L. CHRISTIANSEN[1], J. H. KERR[1], H. M. DE LA FUENTE[2], and W. C. SCHNEIDER[2]

[1]NASA Johnson Space Center, Mail Code SN, Houston TX 77058; [2]NASA Johnson Space Center, Mail Code EA, Houston TX 77058

Summary—The penetration resistance of various flexible multi-layer shielding concepts has been assessed in hypervelocity impact (HVI) tests at NASA Johnson Space Center (JSC) and at Southwest Research Institute (SwRI). The shields tested consist of 3 to 4 spaced bumpers made of ceramic cloth (Nextel™) and a rear wall composed of high-strength cloth (Kevlar™). Low-density polyurethane foam is used between bumper layers and rear wall to deploy the bumpers after the shield is delivered to orbit and maintain bumper standoff while on-orbit. Ballistic limit equations have been derived from the HVI test results. These equations are being used to size shielding for an inflatable module, which is planned for potential use on Space Station. © 1999 Elsevier Science Ltd. All rights reserved.

NOTATION

C_H	high-velocity coefficient in high-velocity BL equation
C_{hi}	high-velocity coefficient in intermediate velocity BL equation
d_{crit}	critical diameter (cm) on threshold failure of shield
ρ	projectile density (g/cm^3)
m_B	effective areal density of all bumpers, RTV/adhesive, MLI, & foam encountered by the projectile (g/cm^2)
m_K	areal density of Kevlar in solid rear wall & any additional solid Kevlar added to shield (g/cm^2)
m_w	areal density of Kevlar in solid rear wall (g/cm^2)
m_2	areal density of Kevlar fabric layers added to shield (above the restraint layer) (g/cm^2)
θ	impact angle (deg) measured from the surface normal (i.e., 0 deg is perpendicular to surface)
V	impact velocity (km/s)
S	total thickness of target (cm)

™ Nextel is a trademark of 3M Corporation, Kevlar is a trademark of DuPont Corporation

INTRODUCTION

Lightweight, fully flexible shields are required to provide protection from meteoroid and orbital debris impact for inflatable spacecraft under consideration for missions in Earth orbit and beyond [1-2]. These shields, originally conceived as add-on protection to cryogenic tanks on the Shuttle [3], are constructed entirely of fabrics and foams to allow them to be packaged in a low-volume thus providing an easily manifested shield for adding protection to any spacecraft in general. The foam is compressed during launch to minimize volume and released on-orbit to deploy the bumpers of the shield. Figure 1 illustrates an inflatable module concept called "TransHab" attached to Space Station. Multi-layer, multi-shock ceramic bumpers and a high-strength rear wall protect the bladder of the inflatable from puncture by meteoroids and debris.

"TransHab" Inflatable Module
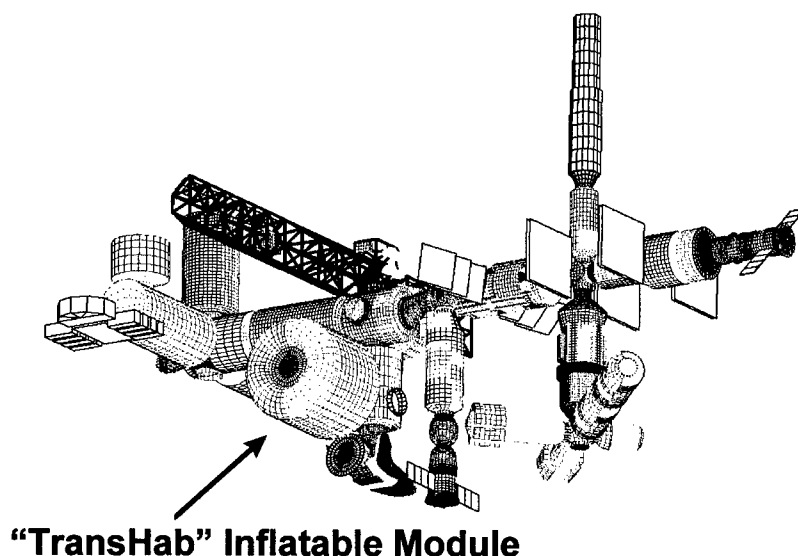
Fig. 1. TransHab inflatable module attached to Space Station.

TEST ARTICLES

Figure 2 illustrates a typical flexible shield, which have several Nextel™ ceramic fabric bumpers and a Kevlar™ fabric rear wall. The bumper concept is derived from the Multi-Shock shield [4]. Distances are equal between the bumper layers and between the last bumper and the rearwall. Rearwall materials have been used successfully in the Mesh Double-Bumper [5] and the "Stuffed" Whipple shield [6]. The multi-shock Nextel ceramic bumpers provide an excellent bumper system to disrupt an impacting particle while the Kevlar rear wall provides high strength to weight to stop the debris cloud of particles resulting from the disruption of the particle on the bumpers. A low-density, open cell foam provides the support structure separating the bumper layers. The foam is bonded to the bumpers by RTV adhesives. To reduce weight, the foam is typically cored with 7.6cm diameter holes such that 50% to 70% of the foam is removed. Several thin aluminized mylar sheets attached behind the Kevlar were used to represent an impermeable bladder for applications where the interior volume is pressurized (i.e., crew modules). Multi-layer insulation (MLI) is added to the outside of the first bumper to provide thermal insulation.

Various shielding options have been evaluated to assess the effect of number of bumper layers, bumper spacing, bumper fabric weight, foam properties (targets with no foam and lighter

foams have been tested), adhesive quantity, rear wall weight and distribution. The shields tested can be grouped into 4 types depending on number of bumpers (3 or 4) and on whether there is a single rear wall or a "split" rear wall where another Kevlar layer is positioned a short distance (5cm) from the rear wall (Fig. 3). Shielding performance is improved by adding a fourth bumper and by including a Kevlar layer in front of the rear wall [4-6].

Table 1 provides target parameters for hypervelocity impact tests on flexible shield concepts. Light-gas gun tests up to 7 km/s with aluminum particles from 0.3cm to 1.0cm diameter have been completed at JSC Hypervelocity Impact Technology Facility (HITF), and up to 1.7cm diameter at White Sands Test Facility (WSTF). The inhibited shaped charge launcher at Southwest Research Institute (SwRI) has been used to assess performance with aluminum fragments impacting at ~11 km/s. The test results have been used in conjunction with previous tests and analyses to develop preliminary ballistic limit equations for design purposes.

Additional testing of the concept is planned in the near term to determine the effect of weaving the rear wall from Kevlar webbing instead of using layers of Kevlar cloth. This is more realistic than continuous cloth layers for flight articles.

Nextel (AF10) Ceramic Cloth
low-density, open cell foam

Nextel (AF10) Ceramic Cloth
low-density, open cell foam

Nextel (AF10) Ceramic Cloth
low-density, open cell foam

Kevlar (5 layers)

12" (30cm) standoff
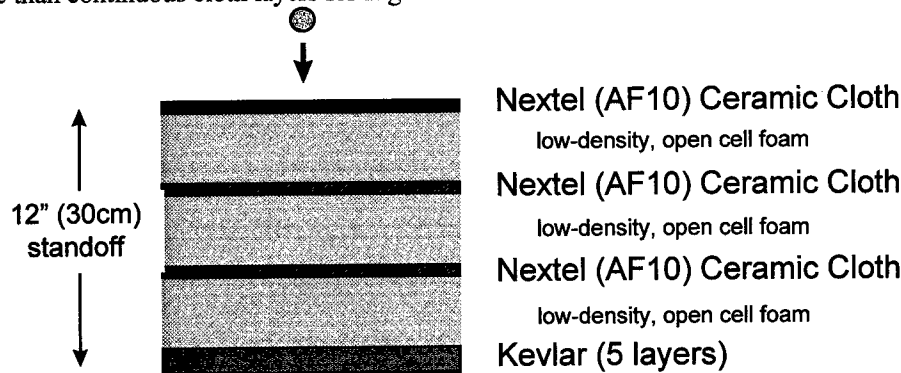
Fig. 2. State-of-the-art shield concept features multi-shock Nextel bumpers and Kevlar (high-strength) rear wall with large standoff using low-weight, deployable support structure

Type 1
3 Bumpers
1 Rear Wall

Type 2
4 Bumpers
1 Rear Wall

Type 3
3 Bumpers
2 Rear Walls

Type 4
4 Bumpers
2 Rear Walls

Exterior

Interior
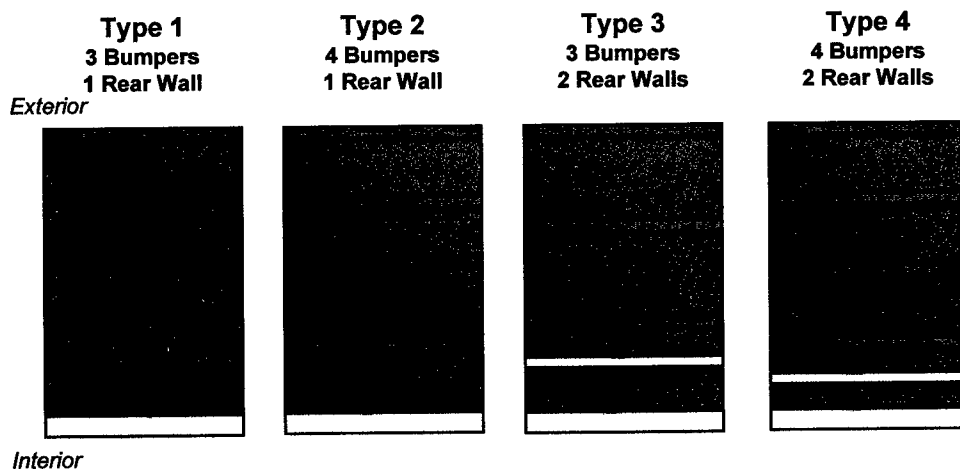
Fig. 3. Four Types of Test Articles. Bumpers are equally spaced Nextel fabric. Rear wall(s) are Kevlar cloth. Gaps generally filled with low-density foam, although targets without foam also tested.

Table 1. Target Parameters

Test Number	Shield Type	Number Bumpers	Nextel Areal Density (g/cm^2)	Nextel Fabric Style	RTV Areal Density (g/cm^2)	Foam Areal Density (g/cm^2)	Overall Standoff (cm)	Kevlar Areal Density (g/cm^2)	Total Areal Density (g/cm^2)
TransHab M/D HVI Test Program									
Target Parameters									
Light Gas Gun Tests									
HITF A3000	1	3	0.08	AF10	0.19	0.51	30	0.16	0.94
HITF A3004	1	3	0.08	AF10	0.19	0.51	30	0.16	0.94
HITF B1132	1	3	0.08	AF10	0.19	0.51	30	0.16	0.94
HITF B1133	1	3	0.08	AF10	0.19	0.51	30	0.16	0.94
HITF B1135	1	3	0.08	AF10	0	0	30	0.16	0.24
HITF B1143	1	3	0.08	AF10	0	0.51	30	0.16	0.75
HITF B1147	1	3	0.08	AF10	0.19	0	30	0.16	0.43
HITF B1173	1	3	0.08	AF10	0	0	30	0.16	0.24
HITF B1211	1	3	0.26	AF40	0	0	30	0.16	0.42
HITF B1213	4	4	0.40	AF62	1.20	0.68	41	0.22*	2.50
HITF B1224	1	3	0.30	AF62	0.90	0.51	30	0.16	1.87
HITF B1225	3	3	0.30	AF62	0.90	0.51	30	0.22*	1.93
HITF B1239	4	4	0.40	AF62	1.20	0.68	41	0.22*	2.50
HITF B1240	1	3	0.30	AF62	0.90	0.51	30	0.16	1.87
HITF B1251	4	4	0.40	AF62	1.20	0.51	30	0.22*	2.33
WSTF 31845	2	4	0.40	AF62	1.20	0.85	30	0.16	2.61
WSTF 31890	4	4	0.80	AF62	1.60	0.44	61	0.38*	3.22
Shaped Charge Tests									
SwRI 7139-42	1	3	0.08	AF10	0.19	0.51	30	0.16	0.94
* split rear wall									

LIGHT-GAS GUN (LGG) TEST RESULTS

Table 2 provides impact data and results for the HVI tests performed to-date for the TransHab program. All LGG tests in Table 2 were performed with spherical aluminum (2017-T4 alloy) projectiles at an impact angle normal to the target. Many oblique impact tests have been performed on similar shields [5-8], and this larger database along with test results in Table 2 form the basis of the ballistic limit equation development.

The LGG tests established the following results:

- There is little added contribution to ballistic protection from the low-density foam when cored with >50% by volume holes. This is demonstrated by similar test results obtained from tests B1147 (without foam) and B1132 (with foam) with a target including RTV, and from tests B1143 (with foam) and B1135 (without foam) for a target without RTV. However, the foam may make a positive difference if the lightening holes in the foam were smaller diameter or less dense.

- The adhesive adds to ballistic protection as indicated by test results from B1143 without RTV and B1132 with RTV. However, in these targets, the RTV was ~2.5 times heavier than the Nextel bumpers.

- Nextel ceramic cloth bumpers will provide improved protection over equivalent weight bumpers of RTV/Nextel combination. Under similar impact conditions, less damage occurred to the rear wall using lower weight all-Nextel bumpers (Test No. B1211) compared to one with heavier bumpers of RTV and Nextel (Test No. B1147).

- All-flexible shielding was successfully scaled up to defeat a 1.7cm diameter aluminum spherical projectile at ~7 km/s. Additional testing is pending to show scaled-up TransHab type shields are capable of defeating up to 2cm diameter aluminum projectiles.

A result of one of the 1.7cm diameter aluminum tests is shown in Fig. 4. The Kevlar rear wall was intact in its mounting frame after the shot, although the bumpers were completely knocked off the target due to the relatively small target dimensions of 30cm wide by 30cm high. A larger target size (60cm wide by 60cm high) was tested with a 1.7cm diameter aluminum projectile and some of the bumpers remained on the target after the test although the outer layers were blown off due to delamination of the Foam/RTV adhesive bond layer (Fig. 5). However, this would not be as likely to occur in the actual case of a full size module because the shield segments are large and the ends are encased, not free as in the test. The entry hole on the outer bumper is small (only a 2-3 diameters larger than the projectile) and the foam cannot easily escape out the entry hole. Foam is lost in the tests because the sides are open and the layers fall off after the RTV adhesive debonds. But in the actual flight article the shield layers are contained within an outer cover which will be securely fastened onto the lower restraint layer (by snaps, sewn or combination).

Table 2. HVI Test Data

Test Number	Projectile Diameter (cm)	Projectile Mass (g)	Velocity (km/s)	Result
	TransHab M/D HVI Test Program			
	Projectile Parameters			
Light Gas Gun Tests				
HITF A3000	0.24	0.020	6.58	No perforation
HITF A3004	0.32	0.047	6.58	No perforation
HITF B1132	0.48	0.158	6.82	No perforation
HITF B1133	0.64	0.375	6.74	No perforation
HITF B1135	0.48	0.158	6.77	Perforation
HITF B1143	0.48	0.158	6.78	Perforation
HITF B1147	0.48	0.158	6.77	No perforation
HITF B1173	0.40	0.094	6.80	No perforation
HITF B1211	0.48	0.158	6.93	No perforation
HITF B1213	1.0	1.47	6.85	No perforation
HITF B1224	1.0	1.47	6.70	No perforation
HITF B1225	1.0	1.47	6.52	No perforation
HITF B1239	1.0	1.47	4.94	No perforation
HITF B1240	1.0	1.47	2.79	Perforation
HITF B1251	1.0	1.47	6.70	No perforation
WSTF 31845	1.7	7.20	6.5	No perforation
WSTF 31890	1.7	7.20	6.5	No perforation
Shaped Charge Tests				
SwRI 7139-42	0.5 OD x 1.4 Long	0.47	11.1	Perforation threshold
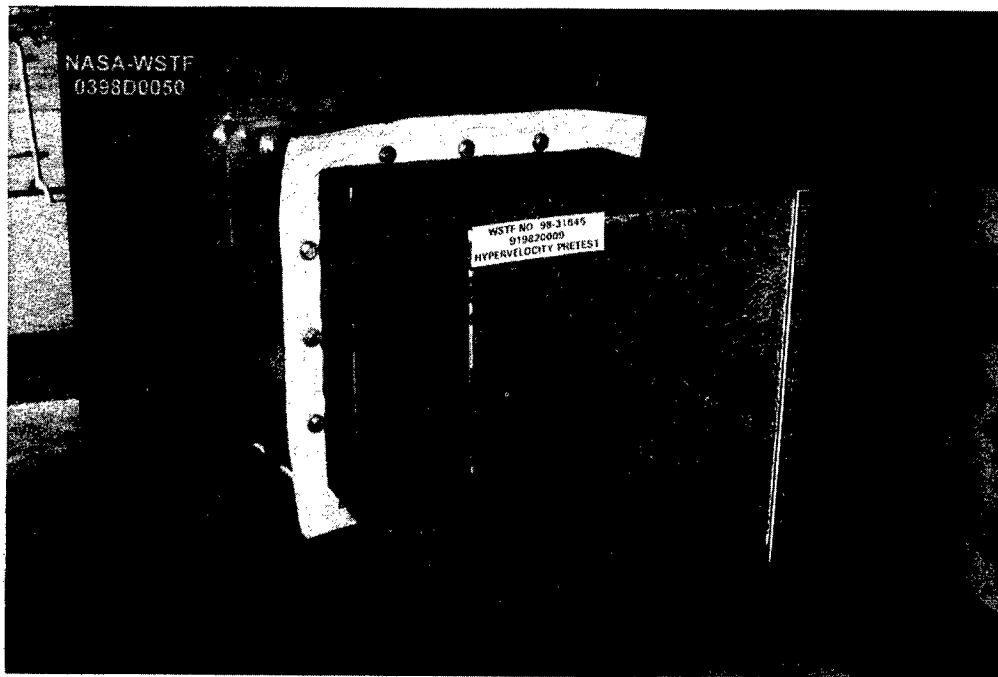
PRE-TEST

POST-TEST

Fig. 5. WSTF Shot 31845, 1.7cm diameter Al spherical projectile at 6.8 km/s, 0 deg on a TransHab shield type (30cm x 30cm x 30cm) resulted in no penetration of bladder. Small target sample size resulted in some impact load absorbed by test support structure.

PRE-TEST
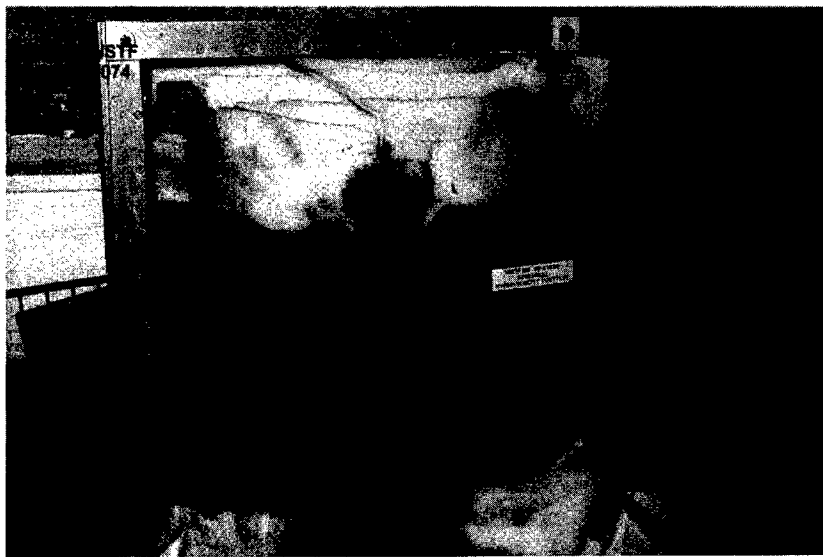
POST-TEST

Fig. 6. WSTF Shot 31890, 1.7cm diameter Al spherical projectile at 6.8 km/s, 0 deg on a TransHab shield type (60cm x 60cm x 60cm) resulted in no penetration of bladder and no deformation of support structure. In the pre-test photo, a small square piece of MLI is attached to the Nextel bumper at the aim point. Post-test the outer 3 bumper layers have fallen off the target after impact, but the rear wall is intact (no damage to rear wall).

SHAPED CHARGE TEST RESULTS

The Inhibited Shaped Charge Launcher (ISCL) is capable of launching aluminum projectiles from 0.25g to ~2g mass in excess of 11 km/s [9]. The projectiles are "hollow" cylinder shaped projectiles. Radiographs of the projectile in flight allow measurement of the outside and inside diameters, and length of the projectile.

These projectiles are generally more damaging than equal mass spheres. A factor called the "ballistic limit mass ratio" or BLMR was previously defined as the ratio of the mass of a solid spherical projectile over the mass of a non-spherical projectile that is on the perforation ballistic limit of a shield [10]. The BLMR varies with projectile geometry, impact velocity, and shield type. For a double bumper shield (3-walls), a BLMR of ~1.9 is estimated for the shaped-charge tests with projectile length to diameter ratio of 2 [4,10]. Additional effort is required to assess the BLMR for the TransHab type of multi-shock shields.

A ISCL test (SwRI Test No. 7139-42) on a light-weight TransHab shield design launched a 0.47g aluminum ISC projectile at 11.1 km/s. The aluminum projectile measured 4.72mm outside diameter by 13.56mm long, with an inside (hollow) diameter of 2.44mm. Its length to diameter ratio is 2.9. The total yaw/pitch angle at impact was 15° off the longitudinal axis. Without correcting for shape effects, a 0.68cm aluminum sphere has the same mass as the shaped charge projectile. Using a 1.9 BLMR factor to correct for shape effects, the "equivalent" spherical projectile diameter on the ballistic limit of the shield is 0.86cm.

The particle trajectory was normal to the TransHab shield surface and a small pinhole perforation occurred in the Kevlar rearwall. This test is therefore considered to be at the threshold perforation ballistic limit for this particular shield.
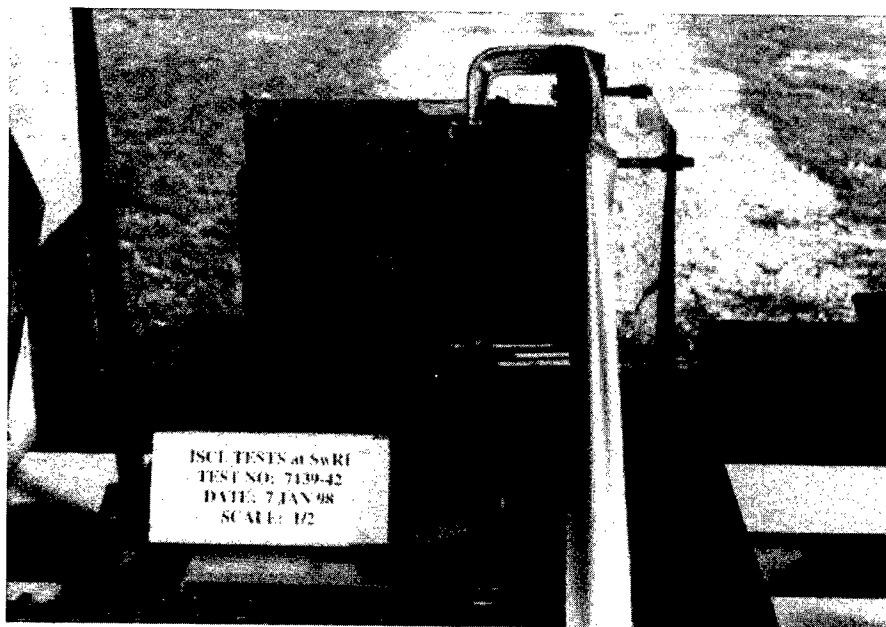
Shaped Charge PRE-TEST Photo

Fig. 7. SwRI Test No. 7139-42, 0.47g aluminum cylindrical projectile impact at 11.1 km/s (Length/Diameter ratio of 2.9) resulted in a pinhole perforation of Kevlar rear wall.

BALLISTIC LIMIT EQUATIONS

The following equations have been developed based on the test results given in Table 2 as well as the tests performed on similar multi-shock shielding [4-8]. The equations will define the particle size that is on the threshold perforation ballistic limit of a Nextel/Kevlar multi-shock shield (Fig. 8). The equations were developed to size shielding for configurations somewhat different than that tested in that a Kevlar restraint layer is included composed of woven straps of

2.5cm wide Kevlar (nominally 3.2 mm thick in total) while less RTV adhesive is used between layers.
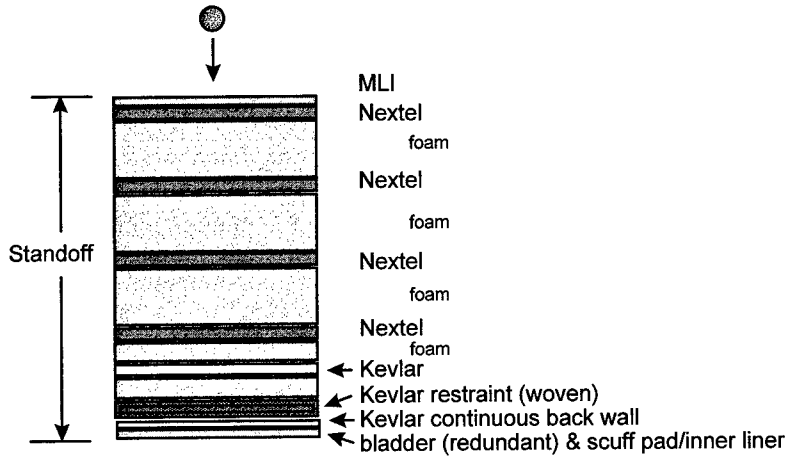
Fig. 8. General Shield Configuration for iterative design process.

User Supplied Inputs

$N_{bumpers}$ = number of bumpers (usually 3 or 4)
N_{nextel} = total Number of Nextel AF62 fabric layers in shield (3 to 8 or more)
$N_{kevlar @ 2}$ = Number of Kevlar 710 fabric layers added to shield in front of restraint layer

High velocity BL equation:

when $V \geq 6.5/(\cos\theta)^{1/3}$,

$$d_{crit} = C_H \, m_K{}^{1/3} \, \rho^{-1/3} \, V^{-1/3} \, (\cos\theta)^{-0.5} \, S^{2/3} \tag{1}$$

where:

$$C_H = 0.43(m_{nextel}/0.3)^{1/3} \tag{2}$$
$$m_K = m_w + m_2 \tag{3}$$
$$m_w = 0.032 \, N_{kevlar \, @wall} \tag{3a}$$
$$m_2 = 0.032 \, N_{kevlar \, @2} \tag{3b}$$

Intermediate velocity BL equation:

for $2.7/(\cos\theta)^{0.5} < V < 6.5/(\cos\theta)^{(1/3)}$,

$$d_{crit} = 3.61 \, \rho^{-0.5} \, (m_K + m_{restraint} + 0.37 \, m_B) \, (\cos\theta)^{-1} \, (6.5/(\cos\theta)^{1/3} - V) \, / \, (6.5/(\cos\theta)^{1/3} - 2.7/(\cos\theta)^{0.5})$$
$$+ C_{hi} \, m_K{}^{1/3} \, \rho^{-1/3} \, (\cos\theta)^{-0.38889} \, S^{2/3} \, (V - 2.7/(\cos\theta)^{0.5}) \, / \, (6.5/(\cos\theta)^{1/3} - 2.7/(\cos\theta)^{0.5}) \tag{4}$$

where:

$$m_B = m_{Nextel} + 0.75 \, m_{MLI} + 0.75 \, m_{RTV\text{-}adhesive} + 0.5 \, m_{foam} \tag{5}$$

$$m_{Nextel} = 0.1 * N_{nextel} \qquad \text{(for Nextel AF62)} \tag{5.1}$$

$$m_{Nextel} = 0.025 * N_{nextel} \qquad \text{(for Nextel AF10)} \qquad (5.2)$$

$$m_{RTV\text{-}adhesive} = ((1 + 2\ N_{bumpers}) * 0.0127) \qquad (5.3)$$

$$m_{MLI} = 0.06 \qquad (5.4)$$

$$m_{foam} = S * 0.016 * 0.3 \qquad (5.5)$$

$m_{restraint} = 0.1345$ (only when restraint is included composed of woven webbing of
2.5cm wide Kevlar straps, nominally 3.2mm thick total) $\qquad (5.6)$

$$C_{hi} = 0.5358\ C_H \qquad (6)$$

Low-Velocity BL Equation

for $V \le 2.7/(\cos\theta)^{0.5}$,

$$d_{crit} = 7\ (m_K + m_{restraint} + 0.37\ m_B)/((\cos\theta)^{4/3}\ \rho^{0.5}\ V^{2/3}) \qquad (7)$$

Figure 9 illustrates the ballistic limit curve for normal impact angle from application of the above equations to the Type 1 shield represented in Fig. 2. The effect of the foam was neglected for the BL curve in Fig.9 because the original Mars TransHab targets had large foam "lightening" holes (7.6cm diameter) that were aligned along the center of the target (Fig.10). The shaped charge data point (threshold failure) is placed with the actual projectile mass plotted (which is conservative) with an error bar indicating the same point with a 1.9X correction factor applied to the projectile mass to account for L/D effects. The ISCL data indicates the high velocity equation is probably conservative and might be raised given additional confirmation data and analysis of shape effect.
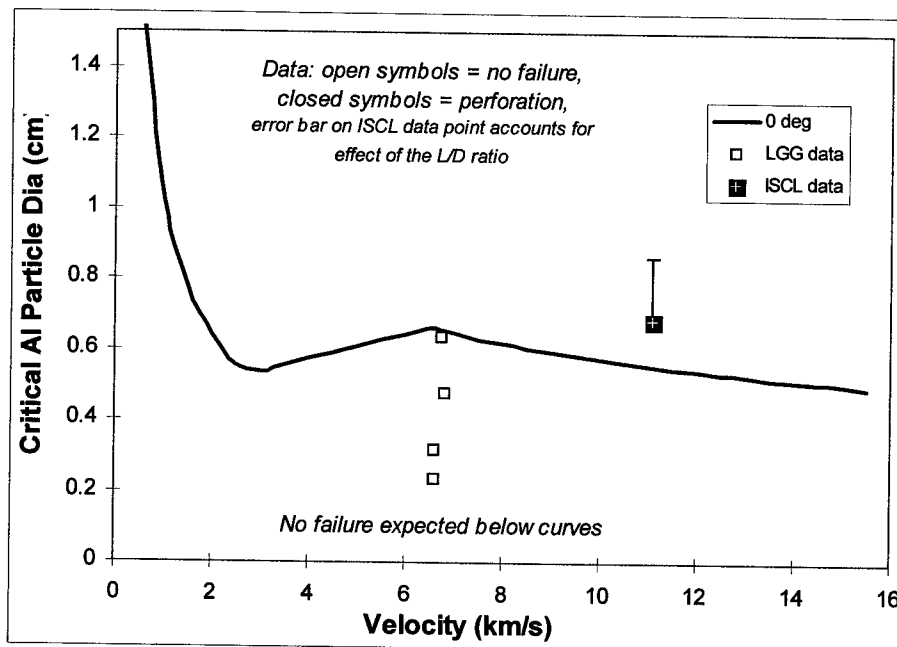
Fig. 9. Predicted perforation ballistic limits for shield shown in Figure 2 for aluminum particles impacting at normal impact angle (3 Nextel AF10 bumpers with RTV, 5 layers of Kevlar 120 in rearwall, 30cm total standoff, 10cm between bumpers, foam neglected, see Fig.10).
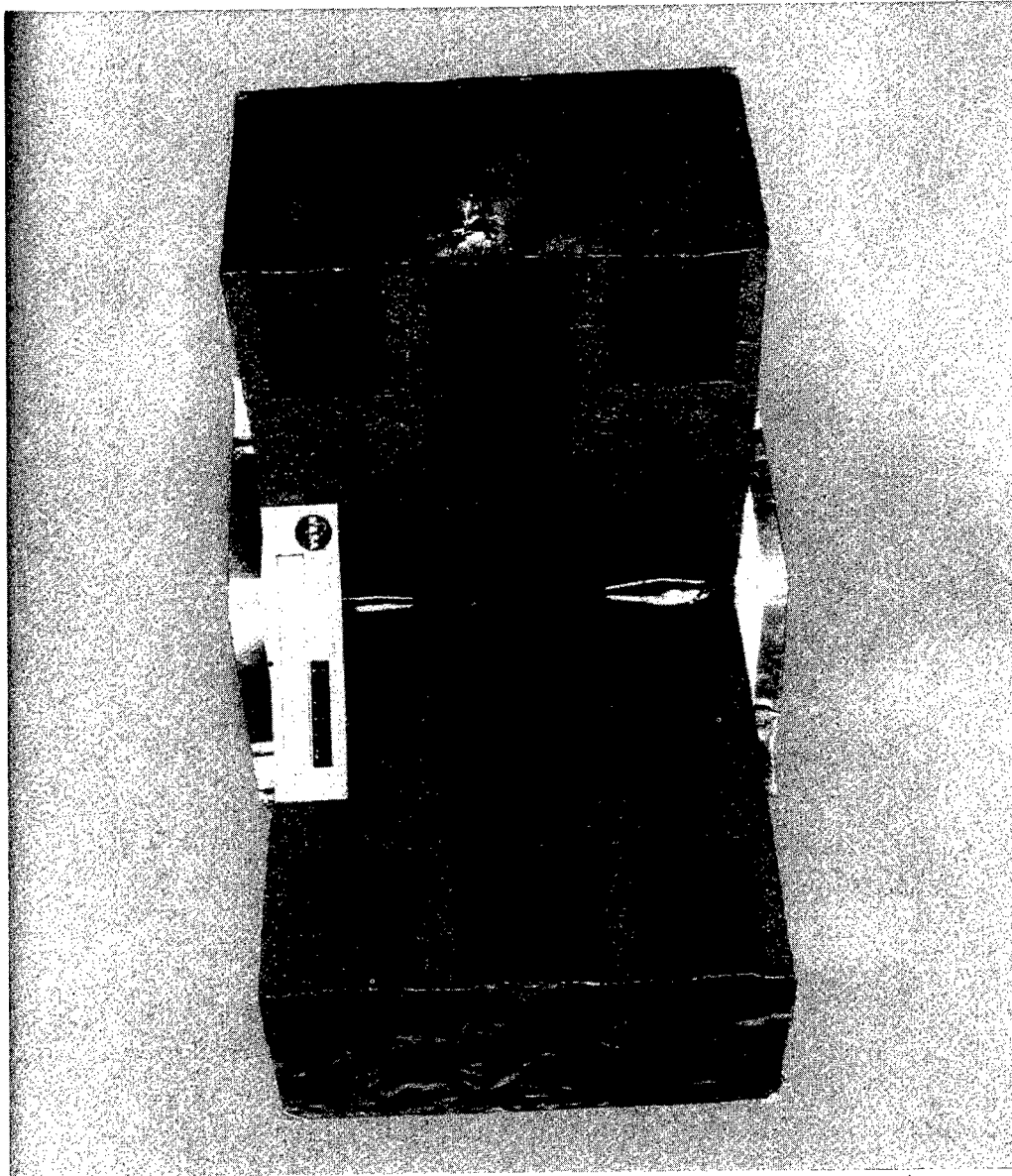
Fig. 10. Sectioned view of target after test number B1132. Progressively larger holes occurred to the 3 bumpers, but the Kevlar rear wall had very little damage (no perforation).

CONCLUDING REMARKS

The TransHab shields represent the state-of-the-art in hypervelocity impact protection. They combine many positive attributes including multiple ceramic bumpers, flexible and deployable (reduce stowed volume), large standoffs, high-strength rear wall, and integral support structure. Hypervelocity impact tests up to 11 km/s have been performed on a variety of TransHab multi-shock shielding types, although additional testing is required to fully characterize each shield's protection capability. Ballistic limit equations have been developed for use in sizing and optimizing the shielding for spacecraft protected by this type of shielding. A version of the TransHab shield has demonstrated that it can stop a 1.7cm diameter aluminum particle. Further

tests are planned and these equations will be updated as warranted by the results of further tests and analysis.

REFERENCES

1. G. Shortliffe and E. Christiansen, Mars TransHab Meteoroid and Orbital Debris Shield Performance Assessment, NASA JSC 27892, June 1997.
2. W.C. Schneider *et al.*, Mars TransHab Design Study Team (executive summary), Presented to the NASA Johnson Space Director, May 1997 and the NASA Administrator, July 1997.
3. W.C. Schneider *et al.*, Space Shuttle Meteoroid and Orbital Debris Damage Assessment Team report, presented to the Space Shuttle Program Manager, November 1996.
4. B.G. Cour-Palais and J.L. Crews, A Multi-Shock Concept for Spacecraft Shielding, *Int. J. Impact Engng*, Vol. 10, pp. 135-146 (1990).
5. E.L. Christiansen, Advanced Meteoroid and Debris Shielding Concepts, AIAA Paper No. 90-1336 (1990).
6. E.L. Christiansen, J.L. Crews, J.E. Williamsen, J.H. Robinson, and A.M. Nolen, Enhanced Meteoroid and Orbital Debris Shielding, *Int. J. Impact Engng*, Vol. 17, pp. 217-228, (1995).
7. E.L. Christiansen, Design and Performance Equations for Advanced Meteoroid and Debris Shields, *Int. J. Impact Engng*, Vol.14, pp.145-156 (1993).
8. NASA Johnson Space Center (JSC) Hypervelocity Impact Technology Facility (HITF), Web Page, http://hitf.jsc.nasa.gov/
9. J.D. Walker, D.J. Grosch, and S.A. Mullin, Experimental Impacts Above 10 km/s, *Int. J. Impact Engng*, Vol.17, pp.903-914 (1995).
10. E.L. Christiansen, J.L. Crews, J.H. Kerr and L.C. Chhabildas, Hypervelocity Impact Testing above 10 km/s of Advanced Orbital Debris Shields, Proceedings of the APS Shock Compression of Condensed Matter Conference, August 1995, pp.1183-1186, 1996 American Institute of Physics.

A CAREER IN APPLIED PHYSICS:
APOLLO THROUGH SPACE STATION

BURTON G. COUR-PALAIS

Consultant, Southwest Research Institute, San Antonio, TX 78228-0510

Summary—This paper is an expansion of the Distinguished Scientist Award presentation made at the 1996 Hypervelocity Impact Symposium at Freiburg, Germany. It details the author's contributions to the research and development of practical meteoroid shielding for the Apollo Project. The work described ranges from the early Apollo design studies, through the Lunar landings to the Skylab project. Later work, pertaining to the protection of the Space Station against the larger sized and more prolific orbital debris environment, is also included. Equations used to determine the penetration resistance of metallic, glass and low-density ablative components are given, along with the rationales for their derivation. A history of the development of the Nextel* ceramic fabric multi-shock shield that is the subject of a joint patent with Ms. Jeanne Crews, is also given. Brief references are made to the use of the Apollo windows as a micrometeoroid detector for environment definition, and also tests and analyses of space suit materials and components. © 1999 Elsevier Science Ltd. All rights reserved.

INTRODUCTION

Mister Chairman, members of the Hypervelocity Impact Society, ladies and gentlemen: I am greatly honored to have received the Distinguished Scientist Award for 1996. It is a humbling experience to have been elected to join the prestigious previous recipients of this award, Drs. Alex Charters, Alois Stilp, Volker Hohler, and Jim Asay. Little did I think that my life's work, which has been a sheer pleasure for me, would lead to me standing before you today in this capacity. I have called my talk "A Career in Applied Physics: Apollo through Space Station", which spans a period of 35 years, which is just about half my life at this time. Actually, I joined the U.S. space program in January 1960, when I went to work for the NASA Space Task Group at the Langley Research Center before the first sub-orbital flight of the Mercury space capsule. Anyway, I consider myself to be an applied physicist in the engineering world, because I have tried to ensure that practical spacecraft shielding against meteoroid and orbital debris impacts is based on sound physical principles. But more about this later. At this point let me fill you in on a little of my prior history.

I arrived in England in 1946 after spending the first 21 years of my life in India, with a Bachelors degree in Physics, Mathematics and Chemistry from a Jesuit college, St. Xavier's, in Calcutta. I had had an exciting life in India, my father being involved in the construction and operating phases of one of the railroad systems there, but I never looked back after I left. In England I attended the College of Aeronautical Engineering in London, from which I graduated with an Associate

---

*Trademark of 3M Company.

Fellowship degree of the Royal Aeronautical Society. I will always remember that in my entry psychological screening I was told that I had what it took to be an aeronautical engineer, but that "you won't set the Thames on fire!" To those of you who have never heard this expression, it means that one would do alright but not be exceptional. I think that in presenting me this award you have lifted this "curse" from me!

I spent 10 years in English aircraft design offices working as a stress analyst before I moved to Canada to do the same in one of their aircraft plants, Avro Aircraft near Toronto. I spent three years there, and would probably have still been there, or perhaps back in England, except for the sudden cancellation of the project I was working on. This was caused by an election and a change of controlling party. Anyway, I was out of a job until NASA came recruiting for their fledgeling space program, early in 1960. I was hired by them, along with a bunch of others, and we were known ever after as the "Canadians", although some of us were not citizens of that country. This was when the career that is the focus of this talk began.

My entry into the world of meteoroid environment definition, impact physics and shielding design was due to a colleague (Jack Hall) at NASA in Langley, Virginia. It was sometime in 1961 and we were working on the preliminary design of the Apollo capsule. I was looking at a traditional frame and stringer design, borrowed from usual aircraft fuselage practice, and another friend was considering a design based on honeycomb panels. Jack was given the task of looking into the meteoroid problem and its effect on both designs. He didn't want it and "gave" it to me and I accepted! Looking back on it, that was a momentous decision for me as it opened the way into an exciting career,—understanding the meteoroid environment and how to shield against it. It was apparent that what I had to do was: (1) learn more about the meteoroid environment; (2) obtain a design mass flux and a velocity distribution; (3) find out what the mass density of typical meteoroids was expected to be; and (4) determine how to protect the Apollo spacecraft elements from catastrophic impacts. This is what fueled the different phases of my career!

METEOROID ENVIRONMENT DEFINITION

I don't intend to say much about my work in the definition of the meteoroid environment as it pertained to the Apollo mission. Fred Whipple and his staff at the Smithsonian Astrophysical Observatory, SAO, in Cambridge, Mass had been studying it since the early 1930's and had a very good idea of the influx rate of meteoroids and their atmospheric entry velocity distribution as a function of meteor brightness or peak magnitude. What we needed to know was the meteoroid influx rate and velocity distribution as a function of mass, their typical mass density and composition near Earth, in cislunar space and at the Moon. Added to this we needed to know the Lunar surface secondary or impact ejecta mass distribution.

Well, we made quite a nuisance of ourselves at the SAO trying to get the answers we needed for our design environment. They eventually agreed to a zero magnitude mass of 1 gm. This allowed us to use this reference point with other data from satellites and radar measurements to come up with a mass flux distribution to 10^{-12} gm. Following this, we had our velocity distribution and an agreed mass density of 1 g/cm^3, and put together the meteoroid environment definition for the Apollo missions.

One of the hypervelocity meteoroid-related projects that I was involved in was the experimental determination of the meteor luminosity coefficient. Like NASA Langley's Trailblazer artificial meteor project which fired an iron shaped-charge slug into the atmosphere at apogee, I wanted to use the High Altitude Research Project, HARP, on Barbados for a similar experiment. The dual 16 inch guns in tandem had been designed by Gerry Bull to place small payloads in orbit for the United States Navy. In my case, the projectile would have been a reentry rocket which would power a known mass into the atmosphere where the meteor trail would be measured by cameras on another

island. The payloads launched in this project were encased in wooden sabots. During the preliminary negotiations, I was present at a night-time firing of the HARP gun and remember, in addition to the mighty muzzle flash, having to remain in the concrete bunker while the broken up wooden sabot rained tooth-picks down on us for quite a long time afterwards! For some reason this project did not come about. Later on, I tried to do the same sort of thing in Canada using their Black Brant V rockets. This project was too late to affect the Apollo design and did not get the funding required.

INTRODUCTION TO HYPERVELOCITY IMPACT

My first venture into hypervelocity impact research was during a visit to the NASA Ames gun lab sometime in 1962 where I met Jim Summers and Bob Nysmith. This was after Alex Charters had moved to GMDRL. Jim showed me around the lab and some of their hypervelocity research, and told me about the big improvement in velocity that had resulted from going to the tapered-bore high pressure coupling. I was very impressed by the 8 km/s they were achieving with 3.2 mm pyrex glass projectiles. Some time after this, the NASA Space Task Group was moved to Houston, Texas, where we were temporarily housed in a converted warehouse building. During this phase, I was assigned to a Branch that was continuing the Apollo design work and a young engineer, Ken Baker, was assigned to assist me with the meteoroid investigations. I was still learning about spacecraft shielding, when we were visited by Sid Perry, a Technical Representative for GMDRL, who told us about the work that was going on there. Once again I went out to see for myself. During that and many subsequent visits, I became acquainted with Alex Charters, Colin Maiden, Bill Gehring, Alex Wenzel and Bill Isbell. They would become very much a part of shielding research for the Apollo at various times. They were willing to sell us a carbon copy of their 30 caliber two-stage, accelerated reservoir light gas gun along with the necessary diagnostic equipment, set it up and teach us how to use it. I was able to convince my bosses that we needed a hypervelocity gun of our own at JSC. Eventually, it was installed in an old barracks building at Ellington AFB, near Houston, which was our temporary home before the Space Center was built, Fig. 1. The only reinforcing we had for the walls were the railroad ties that are shown in the figure, but the building was in a remote part of the base.

We hired Tom Lee, an engineer who had worked with Dr. Emerson Cannon in hypervelocity impact research at the Utah Research and Development Corporation, to run our laboratory and to train a bunch of technicians. One of these technicians was "Big" Jim Moncrief, who was capable of lifting the high pressure coupling without assistance. We added a powder gun for the under 2 km/s impact work required for the Lunar Landing Module shield tests, and a shot-gun! The shot gun was used to test our first space suit layup in a ditch outside the building. After one successful test, an interested by-stander, who happened to be an elderly African-American, observed that he could have done with such a suit, when he used to liberate water-melons in his youth! Later on, when we had learned how to launch hypervelocity 0.4 mm glass projectiles, we abandoned the shot-gun! By the time the permanent facility was completed at Clear Lake, the gun lab was a fully functional entity of our hypervelocity research program. After the Center was built, the gun was moved to a specially constructed laboratory in Building 31, as is seen in Fig. 2. All the open space shown in the photograph was not wasted, but would later be occupied with the powder and experimental guns.

One of the laboratory practices we borrowed from Ames was table-tennis during the lunch break! We eventually got to be good enough to draw in outside challengers which eventually led to the end of our recreation because we were taking too long a lunch break!

NASA S 64 671

GUN RANGE ASSEMBLY
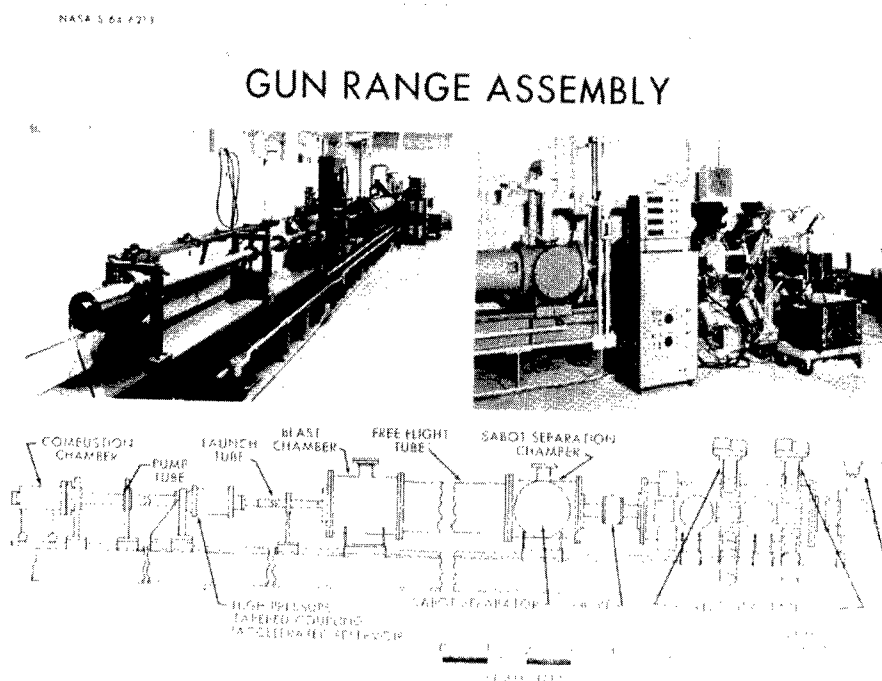
Fig. 1. GM 30 cal light-gas gun at Ellington Air Force Base.

In the continuing search for higher launch speeds, I sponsored many promising ideas that came along. One of these was the collapsible piston or "Chinese Hammer", invented by Bob Teng who ran the hypervelocity gun laboratory at McDonnell-Douglas, Huntington Beach. It was designed to maintain a constant base pressure in the launch tube for a longer time than the ordinary piston, thereby increasing the projectile velocity. We were about to use this piston in our GM gun at JSC when the lab was closed down by our Director after the initial Apollo landings. He felt that we had done our job too well and that the laboratory had become a "hobby shop". Actually, the space was needed for the growing effort in support of the lunar rock sample studies. Other promising ideas that I funded were a "traveling charge" hypervelocity gun that was proposed by Dr. Rodenberger at Texas A & M, an inhibited shaped charge launcher from B.F. Goodrich scaled down to launch 1 gm aluminum projectiles at 11 km/s, and the explosive lens driver of Physics International in Oakland. E.T. Moore and Dennis Baum had developed it to launch a 1 g magnesium-lithium projectile to 11 km/s also. These latter two were proceeding very well when they were canceled in the post-Apollo funding cut-back. I revived the inhibited shaped charge idea later with Jeanne Crews and we funded the Southwest Research Institute in San Antonio, SwRI, to look into it. Don Grosch, Scott Mullin and James Walker developed the concept into a viable impact facility at SwRI, as they have reported at previous symposia.
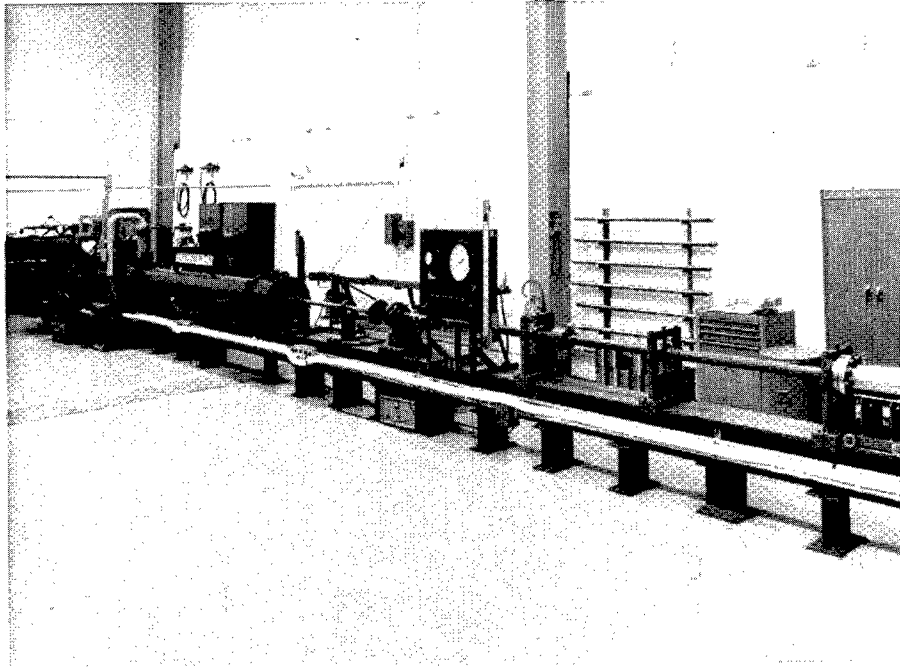
Fig. 2. GM 30 cal LGG in Building 31 at JSC, Clear Lake, Texas.

DIAMETER SCALING AND ITS EFFECT ON HVI RESEARCH

Now I would like to turn to some of the accomplishments of which I am most proud. Of course, they could not have been done without the help of others in running the tests and doing the initial data reduction. The first of these is the diameter scale effect in semi-infinite crater formation, which was very important as it meant that I could now use Norm Scully's 45.7 micron data to 15 km/s. He was achieving these speeds using an exploding wire, plasma gun at the North American-Rockwell facility at Downey, California. The projectiles were soda-lime glass spheres doped with iron oxide to give them a green color to prevent the thermal effect of the accelerating plasma cloud. This was to ensure that the initial projectile diameter would remain the same at impact. Scully's 45.7 micron cratering and hole diameter data were considered erroneous, because the p/d and D/d measurements were less than those obtained using larger projectiles and the reliable light-gas gun. These parameters were supposed to be constant with projectile diameter at hypervelocity, according to hydrodynamic theory. However, in Fig. 3, which is a plot of p/d for 45.7 micron, 1.59 mm and 6.36 mm glass projectiles impacting aluminum 2024-T4 semi-infinite targets at 7 km/s, we can see that this was not so. The points for the 45.7 micron and the 1.59 mm projectiles were actual test data; the point for the 6.36 mm projectile was calculated using the Summers-Charters equation. The equation to the straight line through the data is:

$$p/d = 2.072d^{1/17.75}, \text{ where d is in microns.}$$
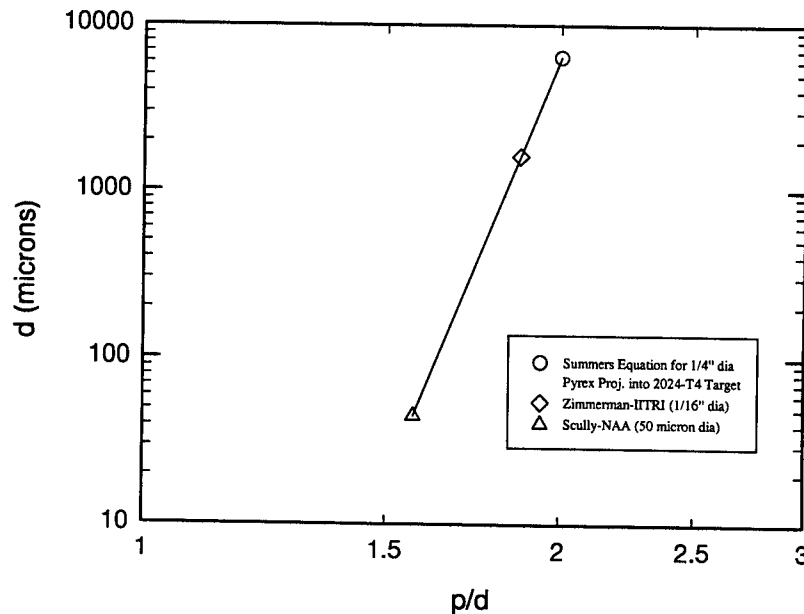
Fig. 3. Penetration parameter p/d as a function of particle diameter at 7 km/s.

Denardo at the Ames Research Center had reported that he had found that p/d was proportional to the 1/18 power of the diameter, therefore I felt that my result was valid. Just to be sure I felt that I should ask Colin Maiden's opinion, who was still with GMDRL at that time. He reminded me that scaling holds exactly during the hydrodynamic phase of cratering, but that Denardo's and my result indicated that this was not so in the strength-dependent phase of the process. He added that this did not surprise him. Armed with this confirmation, I now proceeded to examine some of the data that I had obtained in a new light.

Figure 4 is a plot of p/d as a function of velocity using the 45.7 micron Scully data compared with the Summers and Charters cratering equation with a $V^{2/3}$ dependency and Bjork's $V^{1/3}$ equation. It is clear from the plot that the data to near 15 km/s shows that p/d is proportional to the 2/3 power of the velocity. As some of you may remember this was the big controversy of the early Hypervelocity Impact Symposia. It was not conclusively settled until Walsh and Johnson concluded that the exponent of velocity was close to 0.6 by running their computer calculations longer than Bjork.

In Figs. 5 and 6, we can see that the diameter scale effect brings the 45.7 micron and the 1.59 mm data into agreement with the larger projectiles, which was further vindication that the form of the Summers-Charters equation was valid up to 15 km/s. This allowed us to formulate penetration equations that I felt should be applicable for the average meteoroid impact velocity of 20 km/s.

Shortly after this I was appointed Sub-System Manager for Meteoroid Protection by the Apollo Program Office. This meant that I had to ensure that the spacecraft components met the mission success probability requirements by working closely with my North American-Rockwell opposite number, Al Richardson. My Division Chief's comment was that "it and 10 cents would buy me a cup of coffee"! He was very wrong because it was the instrument by which I was able to do most of the work that is the subject of my talk.
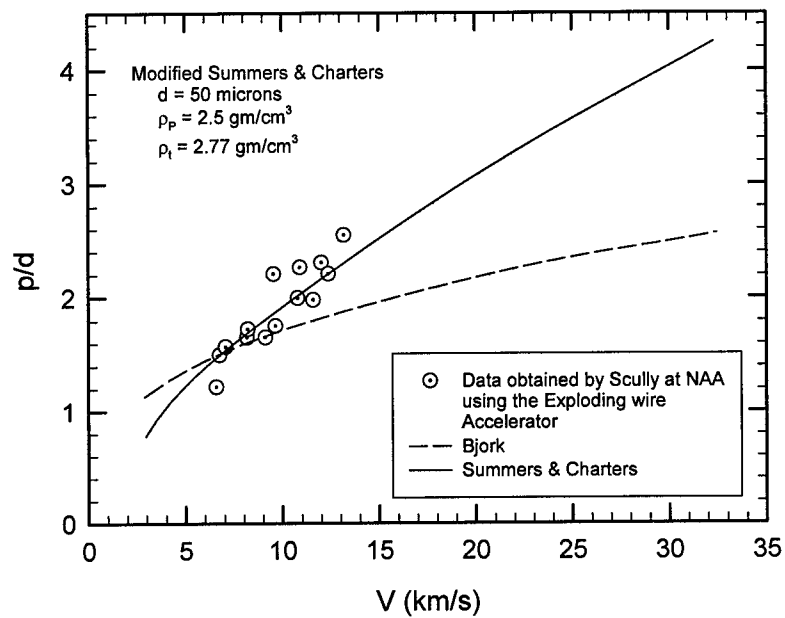
Fig. 4. Scully's 50 micron p/d vs V data compared with S&C and Bjork equations.
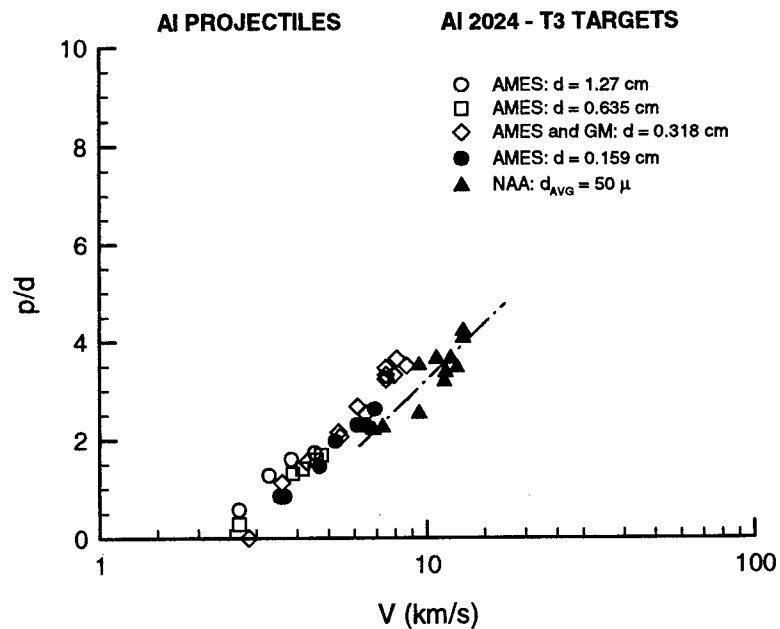
Fig. 5. p/d vs V data for 45.7 micron to 6.35 mm projectiles showing scatter.

Al PROJECTILES   **Al 2024 - T3 TARGETS**

- ○   AMES: d = 1.27 cm
- □   AMES: d = 0.635 cm
- ◇   AMES and GM: d = 0.318 cm
- ●   AMES: d = 0.159 cm
- ▲   NAA: d_{AVG} = 50 μ
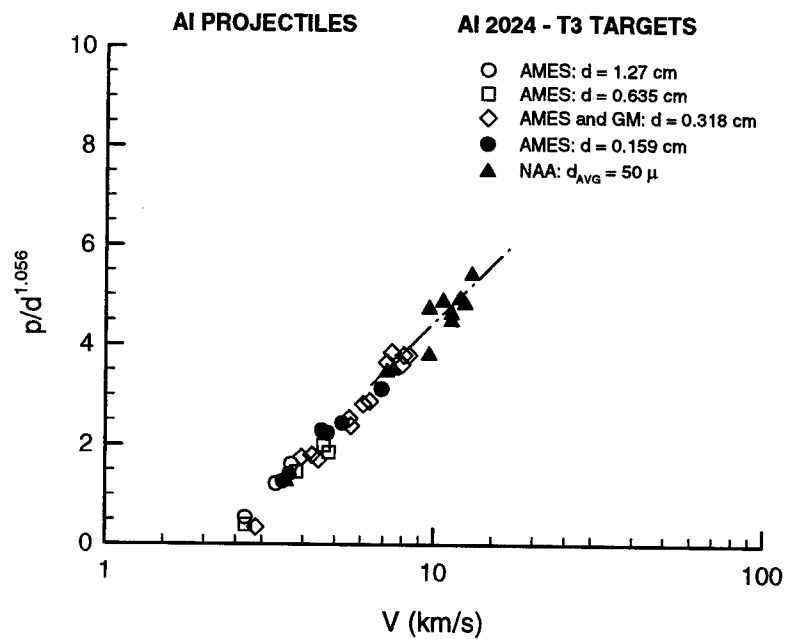
Fig. 6. $p/d^{19/18}$ vs V for same data shows closer agreement.
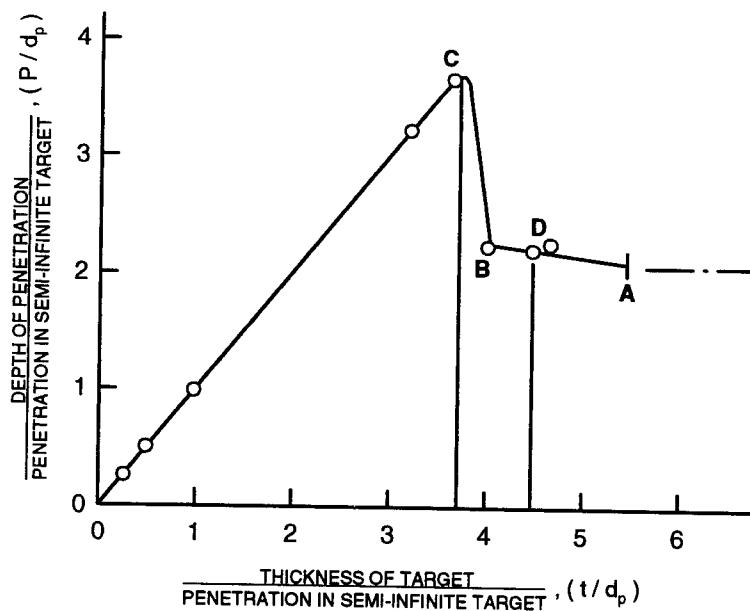
Fig. 7. Depth of penetration vs target thickness: GM work.

PENETRATION RELATIONSHIPS INVOLVING METALLIC TARGETS

The first thing we had to agree on was the predictive equations for metallic targets. Figure 7 is a spectrum of hypervelocity impact effects ranging from holes in thin sheets, through perforations of thicker targets by a combination of crater formation and spallation, to cratering in semi-infinite targets. The figure shows a plot of the ratio of penetration depth to semi-infinite crater depth, as a function of target thickness to semi-infinite crater depth. It was put together by GM for aluminum 2024-T4 targets impacted by 3.2 mm aluminum 2017 spheres at 7.4 km/s. All of the types of equations represented were necessary for various parts of the Apollo Service and Lunar Landing modules.

In the next figure, the semi-infinite crater depth predictive equations for metallic targets, derived by Rockwell and myself, are compared. They were both based on the diameter scale effect and preserved the 2/3 exponent of velocity derived by Summers and Charters. The only differences were the equation coefficients and in my use of the target Young's Modulus, E. With Brinell Hardness, H, both equations were applicable to different materials. These equations were derived after surveying test results of the effect of projectile and target physical and material properties on crater depth, reported by various researchers. One study, I sponsored, involved fitting existing test data with a polynomial equation that included most of the possible properties that could be considered to affect cratering. Although the correlation coefficient was very good, the equation was too cumbersome for engineering use. Remember, this was in the early 1960's and computers were still limited in memory and speed. The equations shown in Fig. 8 were user-friendly, while preserving the essential target and projectile properties for a reasonable correlation coefficient.

Rockwell equations

$$\text{Crater depth, } p_\infty = 1.38\, d_m^{1.1} \cdot H_t^{-0.25} \cdot \rho_m^{0.5} \cdot \rho_t^{-0.167} \cdot V_m^{0.67};\ cm$$

$$\text{Thickness to prevent perforation, } \bar{t} = 1.8\, p_\infty$$

NASA equations

$$\text{Crater depth, } p_\infty = 5.24\, d_m^{1.056} \cdot H_t^{-0.25} \cdot \rho_m^{0.5} \cdot \rho_t^{-0.167} \cdot E_t^{-0.33} \cdot V_m^{0.67};\ cm$$

$$\text{Thickness to prevent perforation, } \bar{t} = 2.0\, p$$

Minimum thickness for no spall effect, $\tau = 3\, p$

Fig. 8. Apollo penetration equations for single thickness metallic sheets.

The semi-infinite crater depth equations were the baseline for the finite, single sheet thickness equations for Apollo and later spacecraft applications. These equations are obtained by using "spallation" factors, which are the ratios of the thickness of the sheet that corresponds to a specific failure mode to the semi-infinite crater depth in the same material. Spallation factors were determined by test and examples are given in Fig. 8. The equations for minimum weight pressurized structures, where rear surface spallation is not a problem, are obtained by using the factors that prevent perforation, i.e., there is a very thin layer of material between the crater and the spall. This factor is different for soft and hard alloys, and for 2024-T4 aluminum Richardson favored 1.8 for the Rockwell equation and I used 2 for the equation used by NASA-JSC. The two equations give

identical perforation thicknesses. The minimum semi-infinite wall thickness was obtained by using a larger factor, such as the one given in the same figure.

The Apollo equations that corresponded to the regions shown previously in Fig. 7 are given in Fig. 9. The semi-infinite equations, applicable to the region to the right of A have already been discussed. When the rear surface is just beginning to spall, to the left of A, to B where the spall is well developed and nearly detached, "finite sheet" equations apply. Finite sheet equations were obtained by factoring crater depth equations. One of these equations derived by me is given in Fig. 9, using a factor of 2.2 from the range of about 2.5 to 1.8 from Fig. 7. The perforation limit has already been discussed and an equation is shown in Fig. 8. An alternative to using the spall factor approach was obtained by direct tests at NASA Ames, and their equation is shown in Fig. 9. This is applicable for the region B to C. After C the sheet begins to be perforated and a hole equation is required, and the applicable equation was obtained by GM and is given in Fig. 9.

Crater depth in a semi-infinite block: Two equations already discussed (Region A)

Finite sheet equation to prevent incipient spall detachment (Region A-D)

$$\bar{t} = 2.2\ p_\infty, \text{ where } p_\infty \text{ is the crater depth in the semi-infinite block}$$

$$= 11.5 \times (H_t)^{-1/4} \times (\rho_p/\rho_t)^{1/2} \times (V_p/C_t)^{2/3} \times d_p^{19/18}; \quad cm \ \left[for\ 0.5 \leq \rho_p < 2.78\ gm/cm^3 \right]$$

Perforation limit equation, i.e., rear spall is detached (Region B - C)

$$t_{perf} = 0.65 \times (1/\epsilon_t)^{1/18} \times (\rho_p/\rho_t)^{1/2} \times V_p^{7/8} \times d_p^{19/18}; cm$$

Hole diameter equation (Region C to origin).

$$D_H/d_p = 0.45 \times V_p \times (t/d_p)^{2/3} + 0.90$$

H_t =	Target Brinell hardness number	V_p =	Impact velocity; km/sec
ϵ_t =	Target elongation %	d_p =	Projectile diameter; cm
ρ =	Mass density: gm/cm³	C_t =	Target sound speed; km/s
		D_H =	Hole diameter; cm

Fig. 9. Equations that describe the thickness for the regions on the previous sheet.

HYPERVELOCITY IMPACT IN GLASS TARGETS

Before I get to the equations we used for glass targets, i.e., windows, let us look at some of the phenomenology involved. Most of the glass targets impacted at light gas gun velocities, for projectiles greater than 0.2 mm, resulted in a center-line section as shown in the lower portion of Fig. 10. There is extensive spallation of the impacted side with a central pit. Usually, the pit is not
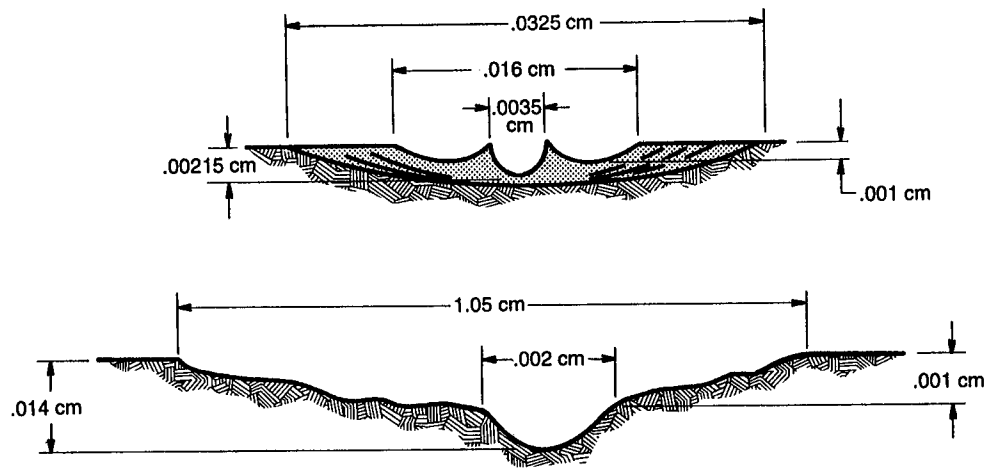
Fig. 10. Typical impact cross-sections in glass targets.

lipped and shows signs of melt and crushing. This cross-section happens to be one that was found on the window of Mercury 9, which had the longest time in orbit and was flown by astronaut Gordon Cooper. Scanning electron microscopy of the residue in the pit and on the surrounding surfaces showed evidence of an iron-rich impactor. It was tempting to think that this was caused by an iron meteoroid, but the low area-time product made that a rare possibility. The upper cross-section resulted from a 50 micron (0.05 mm), soda-lime glass projectile impacting at 11 or 12 km/s, obtained by Norm Scully with the plasma drag accelerator. This time, notice that the lips are still in place, and there is an inner spall area surrounded by an area of fragmented glass. The crater and lips show signs of having been molten, but the energy was not large enough to cause the crushed outer spall to be ejected, as in the other cross-section.

In Fig. 11 we see the onset of the inner spall zone and partial ejection, obtained by Friichtenicht at TRW, using the 1.5 Mev accelerator. The left hand view shows inner spall ejected and large outer spall plates still attached. In the right hand view, the inner spall is formed, but not ejected. In both views a pit is intact with evidence of heavy melting having taken place during the impact.

It was obvious from the previous figures that the crater was ejected at some impact shock pressure leaving the typical pit that is seen on most glass impacts. In Fig. 12, you see two complete ejected pits that were found in our impact chamber after a test. There is substantial melt around the crater and the evidence of the fused, crushed glass seen in the bottom of pits. This particular impact resulted from a 0.04 mm tungsten-carbide sphere at about 7 km/s.

The phenomenology of hypervelocity impacts into glass targets is illustrated in Fig. 13 which shows a 7 km/s impact into a semi-infinite block of aluminum formed by stacked, thin sheets tightly bolted together to maintain good surface contact. The target simulated glass in that it had good compressive strength but no lateral tensile strength, which is equivalent to brittleness. The cross-sectional view in (a) shows the onset of the outer and inner spall formation, and the ejection of the central crater. If this were a thick glass target it would end up looking like the lower one in
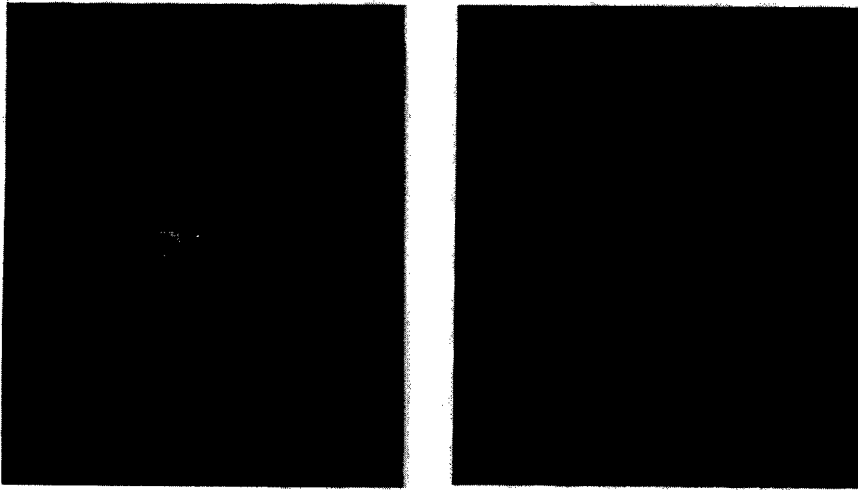
Fig. 11. The onset of front surface spallation.

Fig. 12. Ejected crater pits.
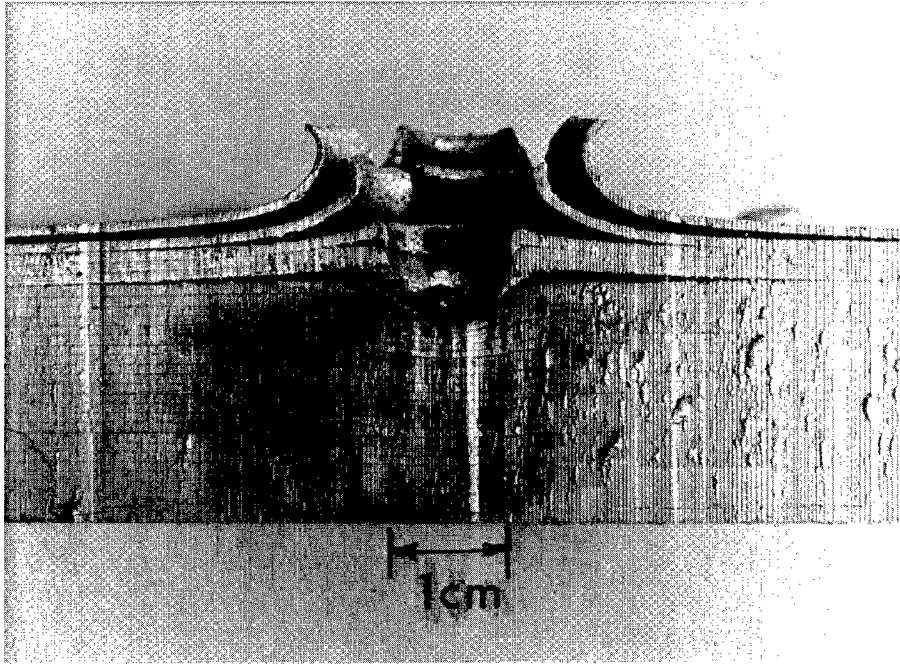
(a) cross-section
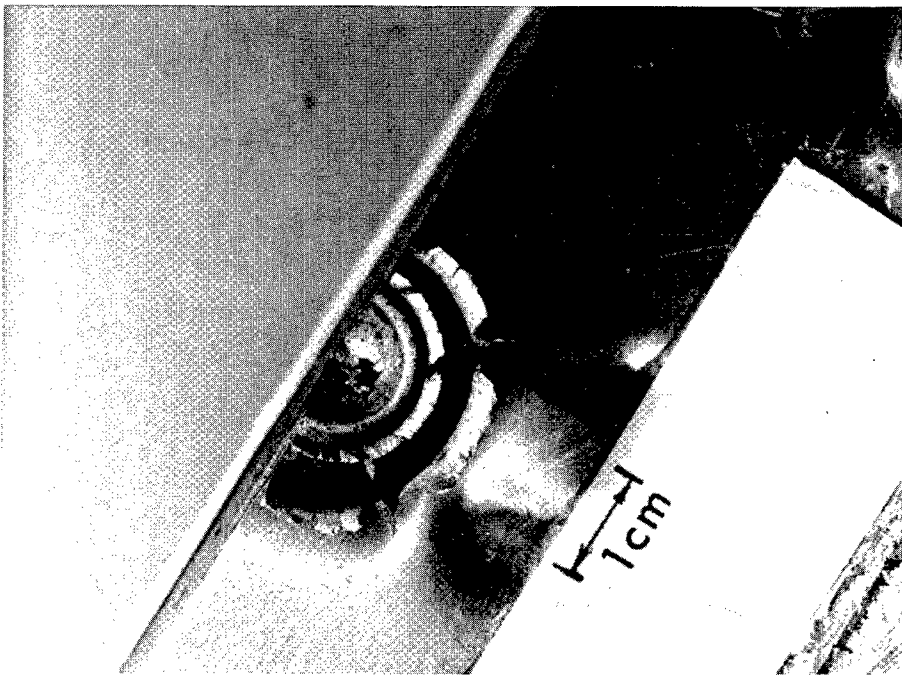
(b) top view

Fig. 13. Phenomenological model using thin aluminum sheets bolted together.

Fig. 10. However, the aluminum model is too thick to show evidence of the rear spall formation. Note the shock compression under the pit, analogous to the blocky, fracture zone seen in glass impacts. In the top view, (b), we can see the original lipped crater before ejection and the concentric rings with radial cracks so typical of impacts into glass. The top view of a typical hypervelocity impact into glass is shown in Fig. 14 for reference below.
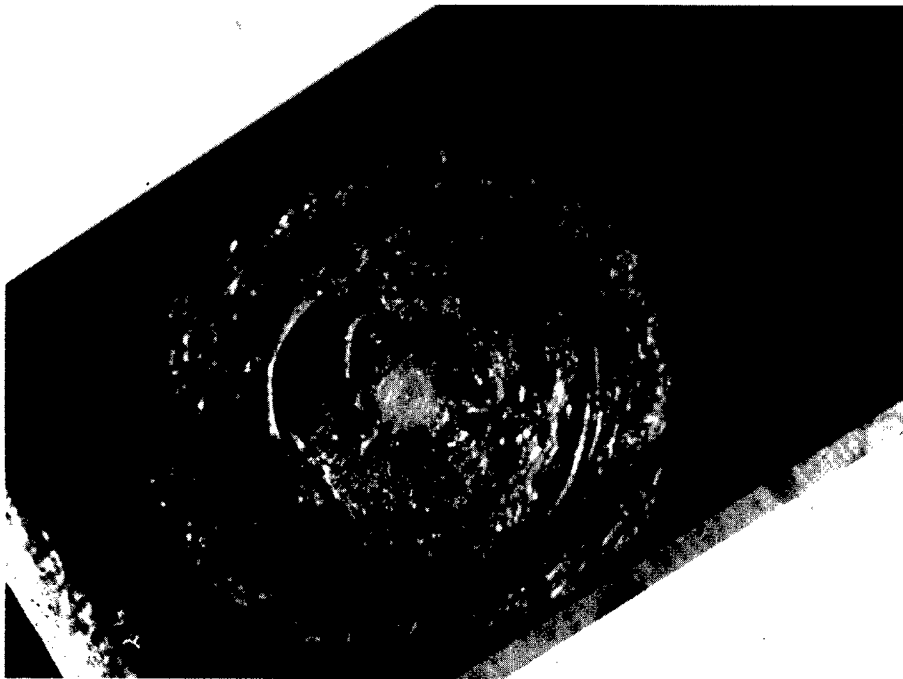
Fig. 14. Top view of hypervelocity impact into glass.

Hypervelocity impacts into glass targets are far more dramatic than those into metallic targets, as we have seen. Although the initial impact pressure generated by a hypervelocity impact into glass would not be much different than for aluminum, the damage is more extensive. The front surface outer spall diameter to projectile diameter ratio for a 1.59 mm, 7 km/s impact into fused silica glass, is 40 to 45. Under the same conditions, the diameter of the crater after the pit is ejected is 13 to 15 projectile diameters. In contrast, the spall diameter in a hard aluminum target is only slightly larger than the crater diameter which is about 4 projectile diameters.

The equations for crater depth for the Apollo windows, shown in Fig. 15, were derived in consultation with Richardson from tests done at JSC and at North American-Rockwell. Again, the depth is measured to the bottom of the crater in semi-infinite fused silica glass. The formula is similar to that for semi-infinite aluminum, but with the material properties for glass incorporated into the constant. I used the same diameter scale factor for "hard" aluminum, but Richardson preferred 1.2 and adjusted the constant appropriately. The factor to prevent rear surface spallation is shown to be much larger than for semi-infinite aluminum. This is because glass has a much lower tensile strength than aluminum and therefore, the shock compressive takes longer to decay. An additional relationship based on the semi-infinite penetration depth is for the prevention of crack development

Cratering: $p = 0.53 \cdot \rho_m^{0.5} \cdot d_m^{1.06} \cdot V_m^{0.67}$

No spall: $t_s \geq 7 \cdot p$

No cracking: $t_c \geq 0.14 \cdot V_p^{1.28} \cdot p$

Combined thermal-meteoroid criterion: $d_{flaw} = 2 \cdot p$

Fig. 15. Apollo window or glass equations.

due to an initial impact. This was an important criterion for the Apollo and Shuttle Orbiter outer or thermal windowpanes, because of the potential of a piece falling out and exposing the vulnerable inner structure to thermal effects. The last expression is a combined thermal-meteoroid equation for Apollo or Shuttle reentry. It gives the relationship between crater depth in a semi-infinite glass window and the critical flaw depth that could start running under a thermally induced tensile stress. Re-entry heating causes the majority of the outer surface to be in tension. The relation was obtained as the result of impact tests at low, medium and hypervelocity that were followed by thermal tests in an arc-jet facility. Flaherty using an optical technique obtained measurements of the crater cross-sections and visible flaws before and after exposure to thermal stresses. He did not find any significant changes. However, it is well known that there are invisible hairline flaws present in glass that can be removed by polishing with grits of decreasing size. For this reason, an invisible flaw depth criterion, fixed at twice the crater depth, was imposed to cover any possibility of window failure. If the flaw depth was equal to the window thickness it was replaced.

THE APOLLO/SKYLAB PASSIVE WINDOW EXPERIMENT

From the time we found the first impact crater on the Mercury 9 window, it became routine procedure to examine the windows of all spacecraft after a mission. As mentioned earlier, an impact in glass leaves a much larger front surface spall than metallic targets. It is more easily identified, so it was natural that the glass surfaces of the Apollo Command Module be used as a cheap, passive micrometeoroid and debris detector. The experience gained with earlier spacecraft led to the creation of an official experiment called the Apollo/Skylab Passive Window Experiment, S-176. Its purpose was to compare the relative micrometeoroid flux in near Earth orbit to that in deep space and on the Lunar surface. The Lunar missions offered the opportunity of sampling space away from the Earth's gravitational influence, and the Surveyor III lunar lander provided data on the Lunar surface environment. The experiment, for which I was named the Principal Investigator, examined the Command Module windows optically before and after flight, and recorded the number of impacts as a function of mission time. It began with Apollo 8, continued on through Apollo 17, and ended with the three Apollo/Skylab missions. Figure 16 shows the Command Module attached to the Skylab, and the positions of the windows relative to the shadow shielding of the other elements.

Several papers were written on the results obtained from this experiment and one in particular was ground breaking. My colleagues Herb Zook and Uel Clanton examined several of the craters from the Command Module Windows of the Apollo attached to Skylab 3, using a Scanning Electron Microscope and discovered aluminum lining the pits. This was the first direct evidence of the orbital
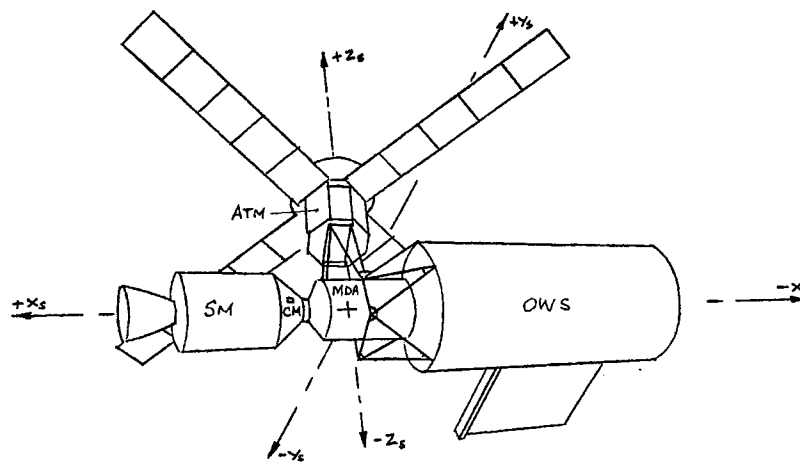
Fig. 16 Apollo/Skylab Window Experiment.

Crater - Right Side Window

Crater - Hatch Window

Crater - Left Side Window

Splash - Hatch Window
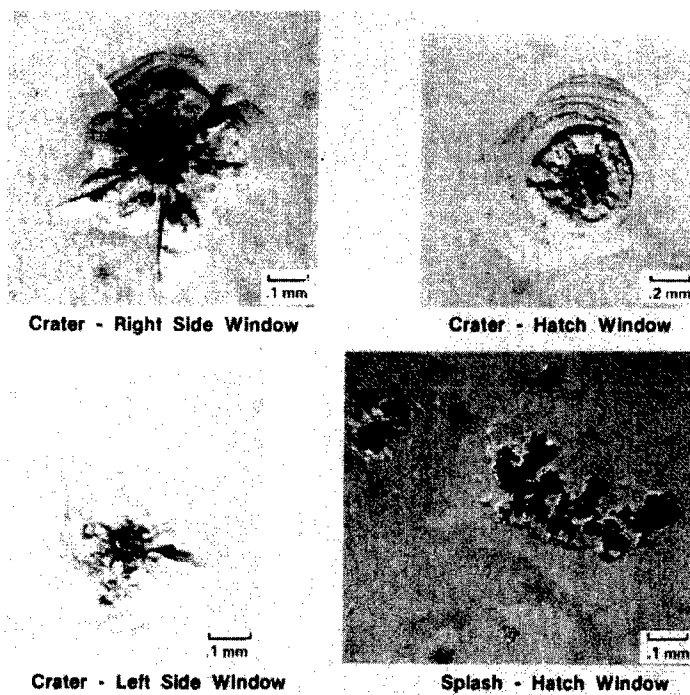
Fig. 17. Typical impacts and splashes found on Apollo-Skylab using 10X optical microscopy.

debris environment. Figure 17 shows two typical craters and dark, glassy residue seen on one of the windows from the same Apollo at 10X magnification. I believe the residue to be ejecta from an impact on a solar panel. The calibration for the craters was obtained at TRW and North-American (10 Mev Van de Graaf plasma drag accelerators.)

APOLLO HEAT SHIELD EQUATION

The Apollo Command Module heat shield was a critical component of the mission success and crew safety reliability calculations. The criterion for failure was a crater large enough to allow reentry heat to affect the bond-line between the ablative material and the honeycomb support structure. If the temperature at the bond-line exceeded 400°F the ablative material could be stripped off. Hypervelocity impact tests were conducted to create craters of various depth to diameter ratios that were subsequently exposed to re-entry heat in an arc-jet facility. A cross-section of an impact crater in the low density Apollo ablative material is shown in Fig. 18. None of the craters tested in the arc-jet resulted in failure of the bond.

Heat shield penetration data are given in Fig. 19 for two different glass projectiles and a nylon projectile for size and density variations. Equations based on least square fits to the data are shown in the figure for crater depth as a function of velocity. It is apparent that the diameter scale factor used for the metallic and glass crater depth equations, 1.06, is effective for the heat shield materials as well. Also, the projectile density and velocity exponents used for the other materials fitted the data. However, the equation constant for the low-density projectile was slightly higher than for the glass, but whether this was a real additional density effect or measurement error was not established. For the sake of safety the higher constant was used to determine the Command Module reliability at the expected meteoroid impact size and velocity.

METALLIC DOUBLE-WALL OR "WHIPPLE" SHIELDS

The double-wall meteoroid shield was the recognized form of spacecraft protection at the beginning of the Apollo program. It was based on a concept originally proposed by Dr. Fred Whipple, the noted meteor physicist, in 1958. He suggested that the way to protect the wall of a spacecraft was to put a "bumper" some distance away from it. The bumper would break up the incoming meteoroid and the wall could be thinner than it would have been without it. This concept became known as the Whipple shield and it worked very well in hypervelocity tests. The combined weight of the bumper and wall was less than a single wall under the same impact conditions. When I became responsible for protecting the Apollo, the total thickness of the bumper and wall required for a particular application was obtained as a fraction of the corresponding single wall thickness, using one of the equations mentioned previously. The fraction was called the "K" factor, and it was established by test for double-walls with and without fillers in the space between the walls. One of the most effective fillers considered at that time was low-density, open-cell polyurethane foam. However, the Service and Command Modules were constructed of aluminum honeycomb bonded to outer and inner sheets that were also aluminum. Consequently, most of the Apollo-related tests and analyses concerned the performance of double-walls with honeycomb fillers. This was the one type of filler that made the double-wall structure heavier than the single, due to the focusing effect of the cells. One thing I would like to say is that the weight of the meteoroid shield for the Apollo was nil because the structure was designed by other factors. This is still the case today. The additional weight required for orbital debris and meteoroid protection does not include the protected module wall, nor any added space radiation shielding. I will now discuss another approach to
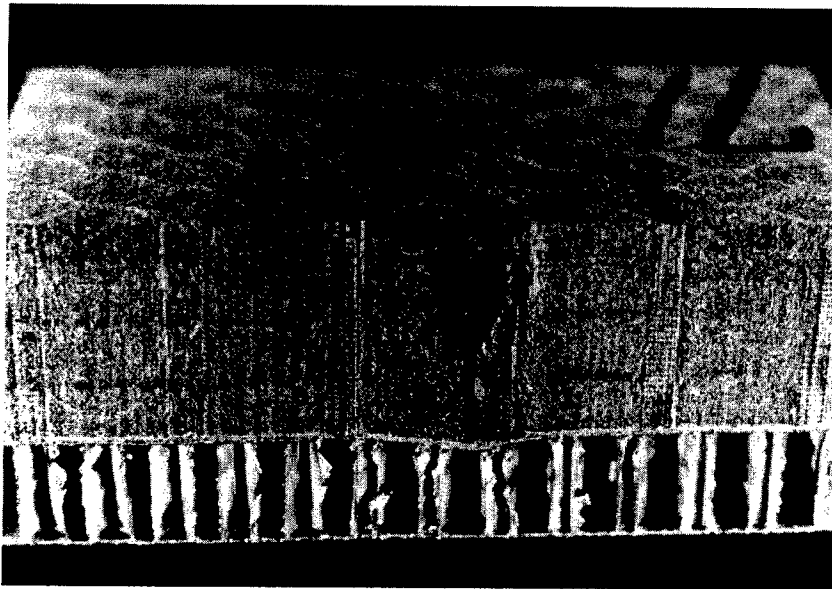
Fig. 18. Typical crater in heat shield ablative material.
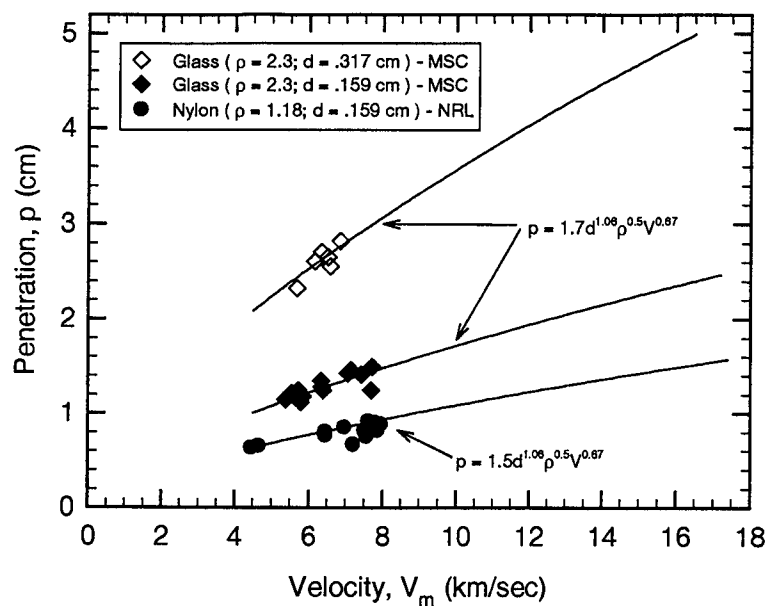
Fig. 19. Apollo heat shield equations: p vs V for nylon and glass projectiles.

determining the resistance to hypervelocity impact of a double-wall structure that I called the phenomenological approach. By this I mean that it is possible to deal with the various elements individually, thus optimizing the double-wall's performance. This method was a combination of work performed by GMDRL and us at JSC.

From this point, I shall refer to the bumper as the shield because that is what it does. In medieval times shields were used to protect against all forms of attack on the person! The shield is the most

important element in any multi-wall structure because it determines the physical state of both the impacting projectile and the material removed by the impact. The impact velocity and the area density ratio of the shield to the projectile determine the condition of the combined debris cloud. This amounts to the ratio t_s/d when their mass densities are the same. The debris cloud can contain solid particles when the shield thickness is either too thick or too thin in relation to the projectile diameter. There is an optimum range for the ratio when the debris cloud causes the least damage to the wall being protected. Figure 20 is a combined plot of the optimum t_s/d as a function of velocity for completely melting an aluminum shield and projectile.
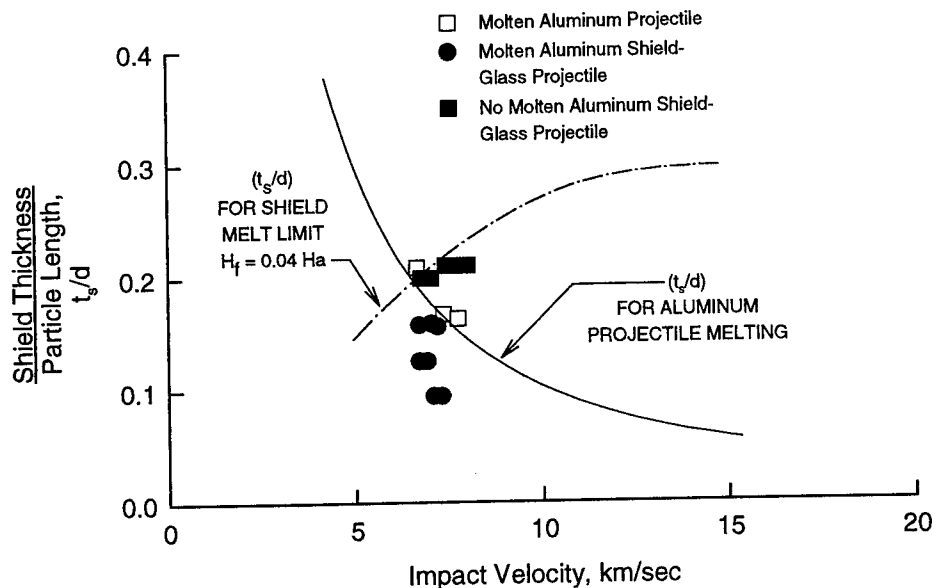
Fig. 20. Theoretical shield optimum t_s/d ranges for melt of projectile and bumper.

The projectile curve was obtained by GMDRL and it shows that the optimum ratio for complete melt decreases inversely with the velocity raised to a 1.5 power. The curve for the shield melt limit was based on a suggestion by Jim Chamberlin at JSC, best known as the designer of the Gemini spacecraft. It was obtained by calculating the amount of heat required to melt the shield plug as a proportion of the amount of heat available in the impact. The hole equation given in Fig. 9 was used to calculate the amount of material in the shield plug, together with a heat of fusion for aluminum of 235 cal/g. As can be seen, the test data shows that the heat required to melt the plug is a little less than 4% of the impact heat available at 7.5 km/s. The region between the curves defines the optimum t_s/d range to completely melt both the projectile and shield debris particles. Above the shield curve and to the right of the projectile curve the debris cloud would include solid shield particles. Below the shield curve and to the left of the projectile curve the debris cloud would also include solid particles from the projectile break up. Figure 20 was one way of ensuring a minimum total shield and wall weight.

The next element in the phenomenological double-wall protection concept is the rear sheet or spacecraft wall. Its reaction depends on the physical state of the debris cloud from the shield and any intervening material. In Fig. 21, the combined shield and wall thickness to projectile diameter ratio, $(t_s + t_b)/d$, is plotted as a function of t_s/d. It was derived by GMDRL for a 7.4 km/s aluminum projectile impact on a 7075-T6 aluminum shield, but is typical of dual-wall performance at hypervelocity. The data point at t_s/d equal to zero, where there is no shield, is the thickness of the wall itself. This was calculated using a finite sheet equation with a 2.3 no rear spall factor. As the

shield becomes thicker the projectile breaks into increasingly finer solid fragments and the total thickness decreases until it reaches a minimum. As the shield thickness continues to increase the total weight of the shield and rear wall also increases. Eventually, the shield is thick enough to act as a finite single sheet. The data point shown on Fig. 21 at t_s/d equal to 5.3 is the same as that at t_s/d equal to zero, as a rear wall is no longer required.
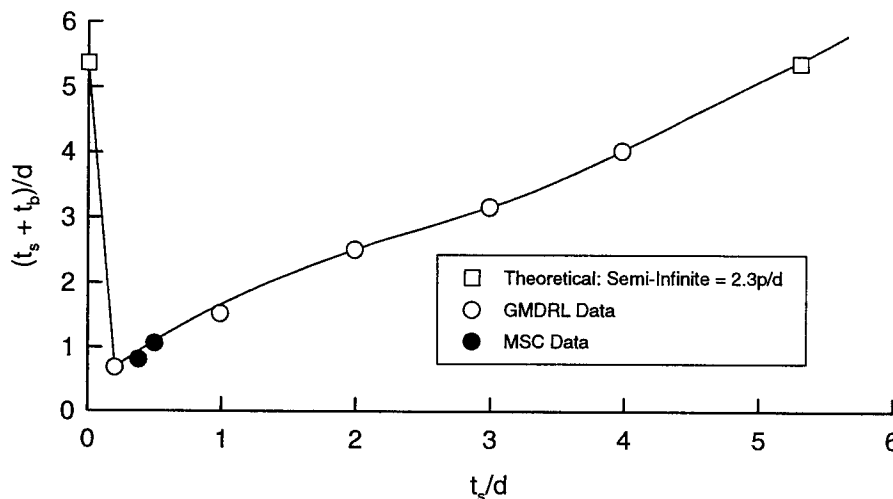
Fig. 21. GMDRL double-wall shielding spectrum for Al 7075-T6 at 7.4 km/s.

It was necessary to define the region of optimum performance in greater detail and Fig. 22 shows the form of the curve that I obtained between t_s/d equal to zero and 0.6. The data points are from dual-wall experiments conducted by Bob Miller at NASA-Ames and Bob Teng at Douglas Aircraft. Both test series were conducted with aluminum projectiles impacting 2024-T3 aluminum walls at 7 km/s. It can be seen that the lowest total sheet thickness to diameter ratio is for a t_s/d value between about 0.17 and 0.32. This differs from the calculated optimum range shown in Fig. 19 at 7.5 km/s, mainly because the shield debris particles did not completely melt in the tests at 7 km/s.

In Fig. 22 we saw that an optimized dual-wall protection system can be designed by fixing it so that the thickness of the shield resulted in the least damaging debris particles. The physical state of the debris could be very hot fine particles, completely molten, or heavy vapor depending on the impact velocity. In this section, I will describe two different equations for designing the rear wall and how it was possible to combine them for the meteoroid and orbital debris environments.

The first of these is what I have called the "non-optimum" equation shown in Fig. 23 in its generalized and specific forms. It was developed for the regions on either side of the optimum shield where the debris particles are still solid or nearly molten. The generalized equation is used when the projectile and shield material mass densities are significantly different. The value of the coefficient is 0.055; derived for 0.08 and 0.16 cm diameter glass projectiles at velocities between 6.5 and 8 km/s. When the mass densities of the projectile and shield are the same or very close, the equation can be simplified. The specific equation coefficients for glass and aluminum projectiles impacting aluminum shields, shown in Fig. 23, are almost identical. A material correction factor relative to aluminum alloys with a 0.2% yield stress of 70,000 psi is included in both forms of the equation. The 0.2% yield stress gives a rear wall that can deflect without rupturing, and is thick enough to prevent perforation or spallation. In its original form, the non-optimum equation is applicable to double-wall applications without any filler or internal support structure in the space between the walls.
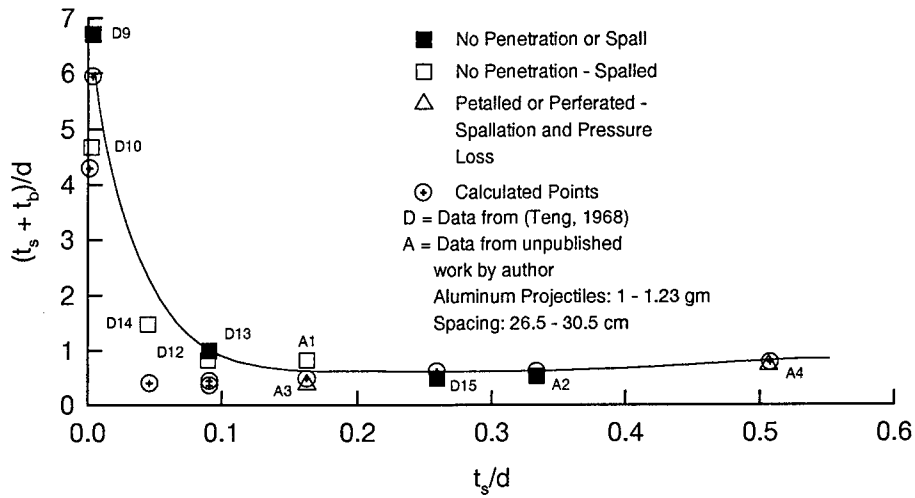
Fig. 22. Detailed double-wall spectrum for zero bumper effect to $t_s/d = 0.06$.

SOURCE: AIAA Hypervelocity Impact Conference, May 1969

GENERALIZED EQUATION: $t_b = K \bullet (\rho_p \bullet \rho_t)^{1/6} \bullet m_p^{1/3} \bullet V_p \bullet \left(\dfrac{70,000}{S \bullet \sigma_y}\right)^{1/2}$; cm

where K = 0.055

ρ = mass density; gm/cm^3

m = mass; gm

V = velocity; km/sec

S = spacing; cm

σ_y = 0.2% yield stress; lb/in^2

p = projectile

t = target

SPECIFIC EQUATION: $t_b = K' \bullet m_p^{1/3} \bullet V_p \bullet \left(\dfrac{70,000}{S \bullet \sigma_y}\right)^{1/2}$; cm.

where: K' = 0.075 for Glass →Aluminum

Fig. 23. Original Apollo equation for solid and nearly molten debris.

The spacing is the third element in the phenomenological approach to the design of double-wall structures. The inverse square root dependence of the spacing, S, shown in Fig. 23 was obtained by tests run at JSC. It applies to a mixture of small solid and molten particulates produced when the shield is not quite optimized. The exponent of S obviously varies between 0, as the debris is composed of large solid fragments and spacing would not matter in a vacuum, to -2.0 when it is completely vaporized. The latter exponent of S will be used in the optimum equation to be discussed later.

When the shielding studies for the Space Station started the combination of the longer duration and the orbital debris environment required protection against larger impactors than the 0.08 to 0.16 cm used for Apollo. Tests showed that the non-optimum equation did not scale with projectile diameter over an order of magnitude. As a result, a comprehensive test program to update the equation constants was undertaken during 1988 while I was still at NASA-JSC. This consisted of new hypervelocity tests at HIRL and NASA-Ames on aluminum Whipple shields using 0.32, 0.95 and 1.27 cm aluminum projectiles. These data were complemented with Whipple shield data obtained during an earlier project in the late 1960's using 0.88 and 1.91 cm aluminum projectiles. With the original 0.16 cm Apollo data, the effect of size scaling was analyzed over a wide range. The information obtained during this effort is discussed next.

The variation of the specific coefficient for the 0.08 and 0.16 cm diameter glass and aluminum projectiles with the normalized shield thickness and spacing parameters is shown in Fig. 24. It is obvious that the original coefficients mentioned previously, apply to a S/d value of approximately 50 and larger. When the spacing parameter is equal to 30 and less the specific coefficient is about 30% higher. Another fact obvious from Fig. 24 is that the coefficient is shown to rise sharply when t_s/d is less than 0.1, based on the total thickness spectrum shown in Fig. 21. The actual rise in the coefficient at low values of t_s/d is dramatically shown in Fig. 25 for projectiles ranging between 0.32 and 0.95 cm. In this size range the minimum value of the coefficient is obtained when t_s/d is between 0.2 and 0.3 and s/d is 30 or larger.

Finally, Fig. 26 gives the variation of the specific coefficient for a 1.91 cm projectile. The effect of spacing is apparent at a ts/d equal to about 0.18, but there was insufficient data to really obtain a minimum value of the specific coefficient. As a result of these tests, it was decided that the specific coefficient K' was .09, .15, and 0.3 for the three diameter ranges in Fig. 24, 25 and 26, respectively. From these the general coefficients, K, can be derived to be 0.064, 0.107, and 0.214. It was unfortunate that funding did not allow further refinement of the coefficient, however, a diameter dependent coefficient was derived by Eric Christiansen of NASA-JSC based on the above results. He replaces K in the generalized equation given on Fig. 23 with the product of a constant C and the square root of the projectile diameter, where C is 0.16.

The second equation that was considered for the Apollo design was the "optimum" equation derived by GMDRL from their cadmium projectile and shield tests in the 1960's. At light-gas gun speeds the cadmium projectile and shield plug are vaporized, as you all know, and therefore the rear wall thickness can be optimized. The form of the equation is given in Fig. 27. As one can see, the rear wall is directly proportional to the projectile impact momentum and inversely proportional to the square of the distance from the shield. Also, GMDRL determined two coefficients for the 7075-T6 aluminum rear walls. The 0.2% yield stress gives a wall that does not rupture or throw off spall from its rear surface. On the other hand, the fracture coefficient results in a rear wall that will fail in tension and leave a petalled hole, but absorb most of the impact energy. Obviously, the latter result is more or less academic and only the 0.2% equation is used.

A theoretical treatment of the region between $t_s/d = 0$ and 0.5 of Fig. 21 is shown in Fig. 28. It was originally constructed for a meteoroid impact on a 7075-T6 structure that had a 0.01 cm shield and a 5.08 cm spacing. The curve was constructed by using the non-optimum and optimum equations in the appropriate regions, and using arbitrary transition curves between the two. Note the extent of the considerable reduction in total thickness that is possible when the optimum equation
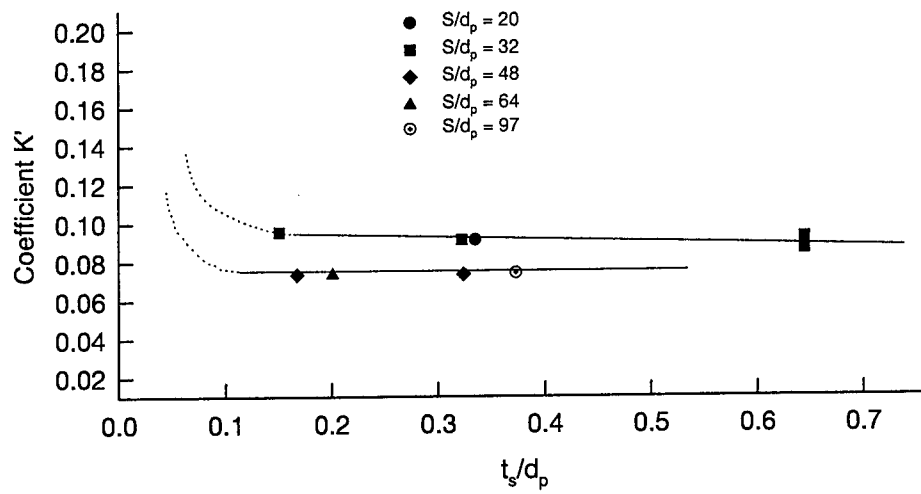
Fig. 24. Original equation: variation of constant with S/d and t_s/d.
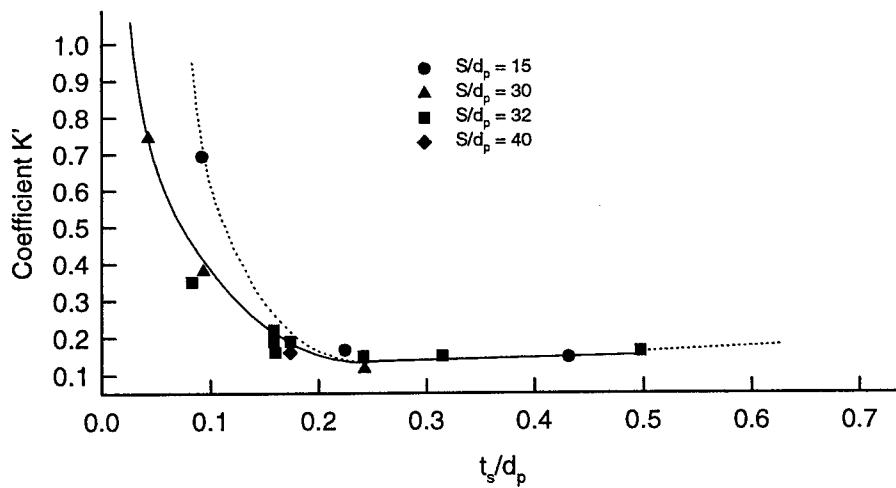
Fig. 25. Variation of constant for d = 3.2 mm to approximately 1 cm.
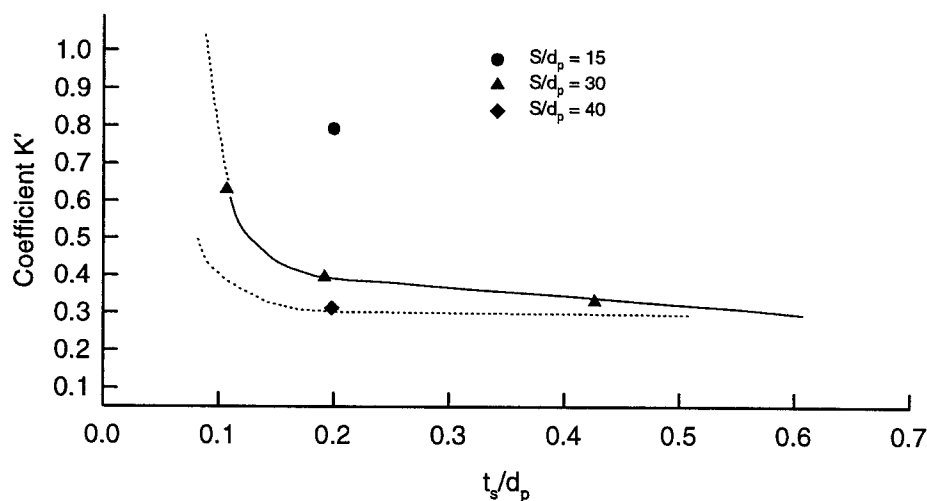
Fig. 26. Variation of constant for d = 1.9 cm.

Rear sheet, $t_b = \dfrac{C \bullet m_p \bullet V_p}{S^2}$; cm

where C = 41.5 ± 14 for the 0.2% yield condition

= 8.2 ± 1.4 for the fracture condition

m_p = particle mass; gm

Vp = impact velocity; km/sec

S = spacing; cm

Fig. 27. GMDRL rear-wall optimum bumper equation.

is instead of the non-optimum in the optimum shield range. Unfortunately, it was not possible to take advantage of the thinner rear wall by careful selection of an optimum shield. If the shield thickness was chosen to result in a minimum rear wall at t_s/d = 0.2, the meteoroid or orbital debris reliability, P_o, would not be the minimum possible. This is because there are more small particles in these distributions than the sizes corresponding to t_s/d = 0.2 and a t_s/d value of 0.3 is more probable. In practice, the rear-wall thickness should not be designed by the optimum equation when there is a cumulative size distribution involved.

After the Apollo landings on the Moon, my reward for being a part of these achievements was to have my Branch abolished in the general restructuring that followed. My first re-assignment was to the Environment Effects Office where I worked on the environmental impact of Space Shuttle launches on the area surrounding Cape Canaveral. My job was to manage the research effort in the Troposphere and it was a very interesting time. I was getting used to this new career when the office was downsized again. During this time in my life, I had become re-acquainted with Don Kessler who had just got interested in orbital debris. Don had been a member of my Branch and had spent time in other organizations in the interim. After the Environmental Effects Office closed down, we went our different ways and I ended up in the Technical Planning Office under Joe Loftus. In time

The figure shows a plot of $(t_s + t_b)/d$ versus t_s/d with the equation:

$$t_b/d = 0.624d^{.056} \text{ FOR NON-OPT AND } m^{.352}$$

labeled regions: NONOPTIMUM AND SINGLE SHEET, TRANSITION REGION, OPTIMUM RANGE, TRANSITION REGION, NON-OPTIMUM RANGE.
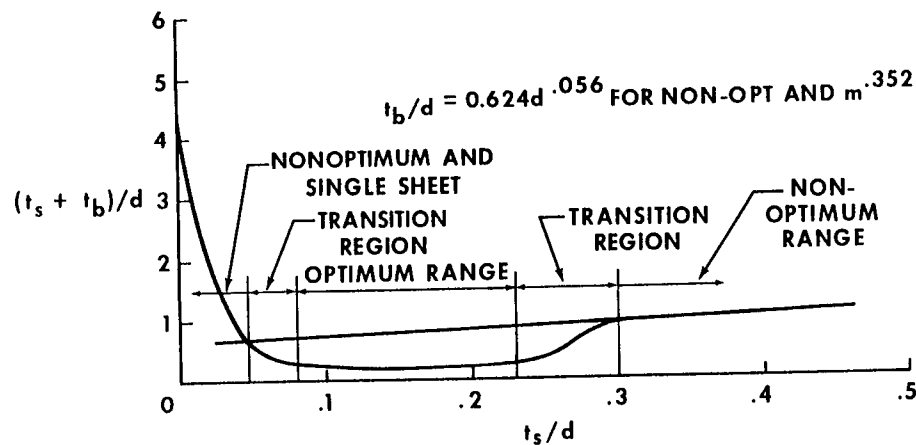
Fig. 28. Combined shield design curve showing limited optimum range.

this job also came to an end, but not before I was able to get Joe interested in the orbital debris issue. He took it to top management and the rest is history. NASA-JSC became the lead effort in defining the orbital debris environment with Don Kessler in the forefront. I linked up with him again in the Space Sciences Division where Jeanne Crews was just getting the hypervelocity impact work started. I joined her in this effort and we have been colleagues ever since. It was great to get back into impact physics again after nearly 10 years, and this time the asset to be protected was the Space Station. The major threat was orbital debris, which meant that the impacting objects were large, mainly aluminum objects and the average and maximum impact velocities were 10 and 15 km/s, respectively. This meant that we had to re-think the shielding practices that had been used for the Apollo program. I will discuss how we tackled the problem at JSC next. Before I do that, let me tell you that my return to the Space Sciences group made some people very anxious. They thought that I had come to close down yet another organization!

MULTI-SHOCK SHIELD DEVELOPMENT

The size dependent non-optimum equation was used in the early phases of the Space Station meteoroid and orbital debris protection definition studies because we were still thinking of using the single bumper approach. Thermal protection for the modules consisting of many layers of aluminized Mylar, mounted between the bumper and the rear wall, absorbed some of the bumper debris, but was torn in the process. Other designs had an intermediate wall spaced between the bumper and the insulation layer. The really new concept to come out of the need to protect the station against impacts was the Nextel multi-shock shield that was developed by Jeanne and myself. The concept is shown in Fig. 29.

As the illustration shows, a number of very thin bumpers are arranged in line in front of the wall to be protected. Each bumper is very thin, typically $t_s/d = 0.03$ and the spacing is critical. The principle is that the first bumper breaks up the projectile into a few large fragments. These fragments then hit the next bumper and are fragmented again and in the process are shock heated to a higher thermal state. Eventually, after interacting with a number of bumpers the debris is completely molten and could be partially vaporized. The distance between the bumpers must be long enough to ensure that the fragments arrive at the next surface before the blast destroys it, as illustrated in Fig. 29. This concept was checked out in hypervelocity impact tests and Fig. 30 shows a typical

aluminum splash on a rear wall placed behind five 0.102 mm aluminum bumpers. They were spaced 2.54 cm apart and the projectile was a 3.2 mm diameter aluminum sphere that impacted the first bumper at 7 km/s. Note that there is a vapor deposit on the witness sheet that probably was the result of the final impact by the very hot, highly molten aluminum residue.

In this and other related tests the number of bumpers, their thickness to projectile diameter ratio and the spacing required for a minimum weight shield were established. The validity of the concept at larger diameters was also investigated. Figure 31 shows the result of a 9.53 mm diameter aluminum sphere impact at 7 km/s on eight 0.406 mm bumpers spaced 7.62 cm apart. A molten aluminum splash that had started to rebound is shown on a 2.29 mm aluminum rear wall, surrounded by vapor deposit. In this particular test the rear wall was dented but not split or perforated. It is important to note that the impulsive load on the rear wall was produced at 7 km/s. The same impulsive load effect was obtained by GMDRL using low melting point cadmium projectiles and bumpers at the same velocity in their double-wall tests. An all aluminum double-wall affording the same protection as the five-element multi-shock shield shown in Fig. 30 would weigh 30% more.
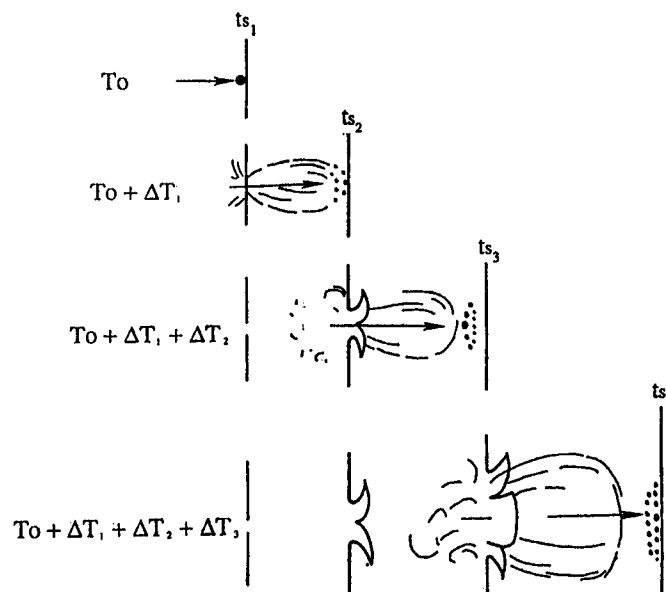
Fig. 29. Theoretical concept using multiple thin sheets to re-shock debris fragments.

About the same time a I was investigating the multi-shock aluminum shield, Jeanne Crews, my colleague became interested in using flexible Nextel ceramic material in place of aluminum for the double-wall bumper. Nextel is an aluminum oxide cloth obtainable in different weaves and area densities produced by the 3-M company. It worked better than the equivalent aluminum bumper because of the effect of the weave and higher mass density of the ceramic fiber. The next step was to go for a Nextel multi-shock shield and again this proved to be even more effective than the aluminum. Four Nextel surfaces were found to give the same result shown in Fig. 30 as the five aluminum sheets, i.e., a molten splash on the witness sheet.

The next step was to check out the multi-shock concept and to optimize the design for possible use on the Space Station. This was when we called on the expertise of Andy Piekutowski at UDRL. As you know, Andy was the first to develop the unique orthogonal X-ray diagnostic system coupled with a light-gas gun which has made his research on projectile breakup invaluable.

Figure 32 shows the result of the first three impacts of a 0.95 cm aluminum sphere on a five-element aluminum multi-shock shield at nearly 7 km/s. Each shield was made from 0.305 mm thick 1100-0 aluminum, spaced 7.62 cm apart and the t_s/d or area-density ratio of the first impact was 0.032. The successive breakup stages are easily seen in the orthogonal views and the solid remnants are in the forefront of a molten cloud after the third shield as desired. A 2.29 mm, 6061-T6 aluminum rear wall in this test was covered with a bright aluminum splash and dented under the impulsive load. The results of the first two impacts on a four-element Nextel ceramic fiber cloth shield for the same size original projectile diameter and velocity are seen in Fig. 33.

They are similar to the aluminum for the same space between the shields, however, the effect of the weave causes a wider dispersion of the projectile remnants. Also, there is no evidence of shield plug debris on the radiographs. The area density of each shield was 0.1 g/cm², hence the area-density ratio at the first impact surface is 0.038. A 2.29 mm aluminum rear wall was again dented under the impulsive loading, but the aluminum splash was covered with a black deposit. For the same ballistic limit, the ceramic and aluminum multi-shock shield total weights are approximately equal, 1.037 and 1.05 g/cm², respectively. However, from a practical standpoint, the ceramic multi-shock shield is better because the support structure would weigh less. The form of the multi-shock design equation is shown in Fig. 34 for the aluminum design. As can be seen, it is basically the same as the GMDRL optimum equation because the load on the rear wall is impulsive. The coefficients for both the total shield and wall thickness, and the wall thickness by itself, were obtained for 6061-T6 aluminum and therefore a material correction factor has been added. The Nextel ceramic fabric shield design equations have the same form, but are written for area-density instead of thickness.

Figure 35 is a print of a photograph that appeared in National Geographic in November 1991 of Jeanne and myself with a four-element Nextel multi-shock shield. Notice the increasingly large black area around the hole caused by the shield debris, and the blackened splash on the rear wall. Jeanne and I were awarded a joint patent for the Nextel multi-wall shield.

This shield was being seriously considered for the Space Station Freedom before it was superseded by the International Space Station. I hear that it has been proposed for a possible manned Martian mission.

Other work that I have been associated with is the testing and analysis of space suits, beginning with Gemini and booster upper stage breakup. I won't go into details in this paper, but my work in these areas is continuing to this day.

Fig. 30. Result of five 0.102 mm aluminum bumpers in front of a copper plate.
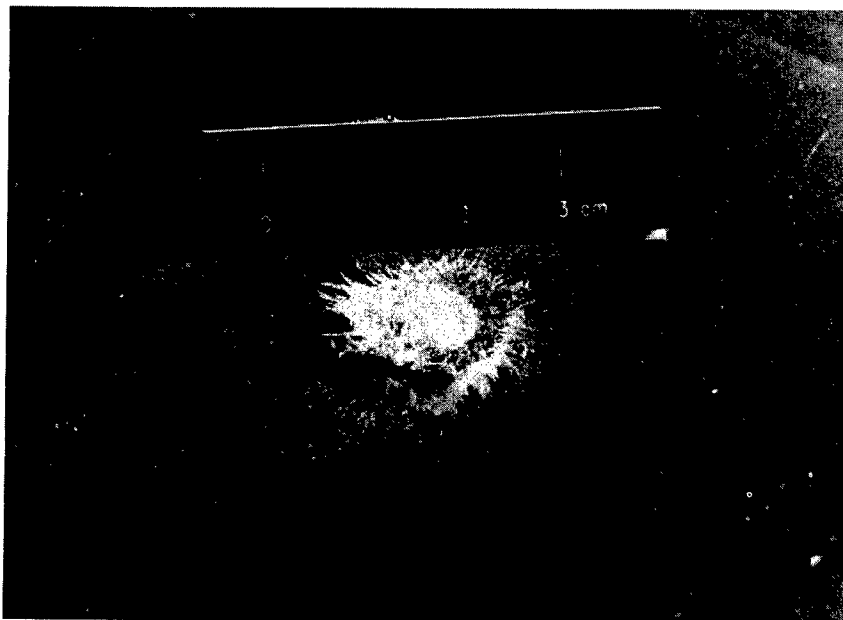
Fig. 31. Result of eight 0.406 mm aluminum bumpers
in front of a 2.29 mm aluminum rear-wall.
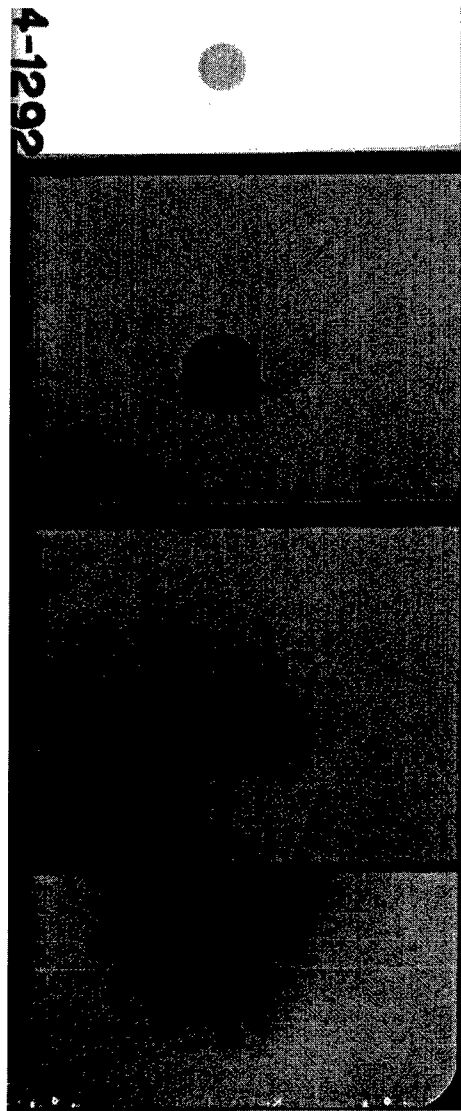
Fig. 32. X-ray photographs of aluminum multi-shock shield in action.
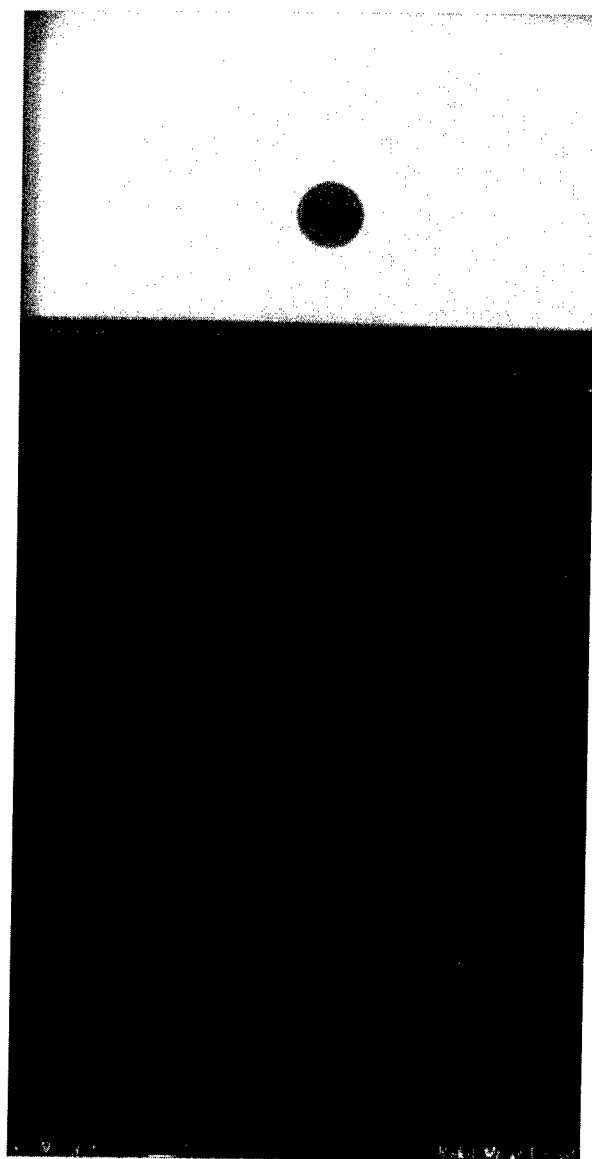
Fig. 33. X-ray photographs of Nextel multi-shock shield in action.

For the total thickness required to defeat a projectile mass M_p (gm) and velocity V_p (km/sec) we have

$$\left\{ \sum_{1}^{n} t_s + t_b \right\} = \frac{C_1 \bullet M_p \bullet V_p}{\left(\sum_{1}^{n} \Delta_s \right)^2} \times \left[\frac{40,000}{\sigma_y} \right]^{1/2} \; ; cm$$

where $c1$ =   61; $cm^3 \bullet sec \bullet km^{-1} \bullet gm^{-1}$

Δ_s =   spacing between individual surfaces; cm

σ_y =   0.2% yield stress; psi

For the wall thickness by itself, the equation becomes

$$t_b = \frac{C_2 \bullet M_p \bullet V_p}{\left(\sum_{1}^{n} \Delta_s \right)^2} \times \left[\frac{40,000}{\sigma_y} \right]^{1/2} \; ; cm$$

where $C_2 = 34.3$; $cm^3 \bullet sec \bullet km^{-1} \bullet gm^{-1}$

Note that n is the number of bumpers.

Fig. 34. Metallic multi-wall shield design equations.

Fig. 35. National Geographic photograph of Nextel multi-shock shield.

CONCLUDING REMARKS

I want to conclude this stroll down memory lane with a few observations. It has been a great "ride" starting with the Mercury program and continuing through all of the U.S. space programs including the Space Station. The Apollo Program was the most challenging and exciting time in my professional career. There was so much to learn and do for the exciting race to be first on the Moon. We were on the cutting edge of technology in every aspect of it. I have worked with many wonderful and intelligent experts in various fields and some of them became personal friends. Maybe I did not set the Thames on fire, but I believe that I poured some gasoline on it! I just could not light a match to set it ablaze during my NASA career. Somehow the winds of change kept blowing out the flame. Let me thank you again for the great honor that you bestowed on me with this award. It has been a great pleasure to be with you at the 1996 Hypervelocity Impact Symposium in such beautiful surroundings. What my wife and I have seen of Freiburg and the Black Forest will add to the memories we have of a truly extraordinary chapter in my life. I would like to close on a personal note. I thank God for my life and my wife for nursing me through my heart problem and for getting me here. I am also very grateful to my brother and sister-in-law for coming over from England to support me.

ACKNOWLEDGEMENTS

ELECTROMAGNETIC PROPERTIES OF IMPACT-GENERATED PLASMA, VAPOR AND DEBRIS

DAVID A. CRAWFORD* and PETER H. SCHULTZ**

*Computational Physics and Mechanics Dept. 9232, Sandia National Laboratories, Albuquerque, NM, 87185, USA;
**Department of Geological Sciences, Brown University, Providence, RI, 02912, USA.

Summary—Plasma, vapor and debris associated with an impact or explosive event have been demonstrated in the laboratory to produce radiofrequency and optical electromagnetic emissions that can be diagnostic of the event. Such effects could potentially interfere with communications or remote sensing equipment if an impact occurred, for example, on a satellite. More seriously, impact generated plasma could end the life of a satellite by mechanisms that are not well understood and not normally taken into account in satellite design. For example, arc/discharge phenomena resulting from highly conductive plasma acting as a current path across normally shielded circuits may have contributed to the loss of the Olympus experimental communications satellite on August 11, 1993. The possibility of significant storm activity during the Leonid meteor showers of November 1998, 1999 and 2000 (impact velocity, 72 km/s) has heightened awareness of potential vulnerabilities from hypervelocity electromagnetic effects to orbital assets. The concern is justified. The amount of plasma, electrostatic charge and the magnitude of the resulting currents and electric fields scale nearly as the cube of the impact velocity ($\propto v^{2.6}$). Even for microscopic Leonid impacts, the amount of plasma approaches levels that could be dangerous to spacecraft electronics. The degree of charge separation that occurs during hypervelocity impacts scales linearly with impactor mass. The resulting magnetic fields increase linearly with impactor radius and could play a significant role in our understanding of the paleomagnetism of planetary surfaces. © 1999 Elsevier Science Ltd. All rights reserved.

The electromagnetic properties of plasma produced by hypervelocity impact have been exploited by researchers as a diagnostic tool [1-3], invoked to potentially explain the magnetically jumbled state of the lunar surface [1-4] and blamed for the loss of the Olympus experimental communications satellite [5]. The production of plasma in and around an impact event can lead to several effects: (1) the plasma provides a significant perturbation to the ambient magnetic field via the electromagnetic pulse; (2) it supports the production of transient radiofrequency electromagnetic fields; (3) it charges ejected debris which, because of inertial separation, leads to significant electrostatic and magnetostatic field production; and (4) its high electrical conductivity provides a convenient path for discharge of the resulting high electrostatic fields. Effects (1) and (2) have been discussed by the authors elsewhere [1-3]. Effects (3) and (4) will be discussed here.

Typical studies of kinetic energy warheads focus on lethality as a function of impactor momentum or energy as they couple mechanically to the target. At high enough energies, however, additional physical processes come into play [6]. Vaporization plays an important role and a partially ionized plasma can form (Figure 1). Impact-generated plasma, charged debris and magnetic fields have been characterized by laboratory hypervelocity impact experiments and are shown to be more abundant when certain easily ionized materials (such as alkali metals) are used in either projectile or target [1-3,7].
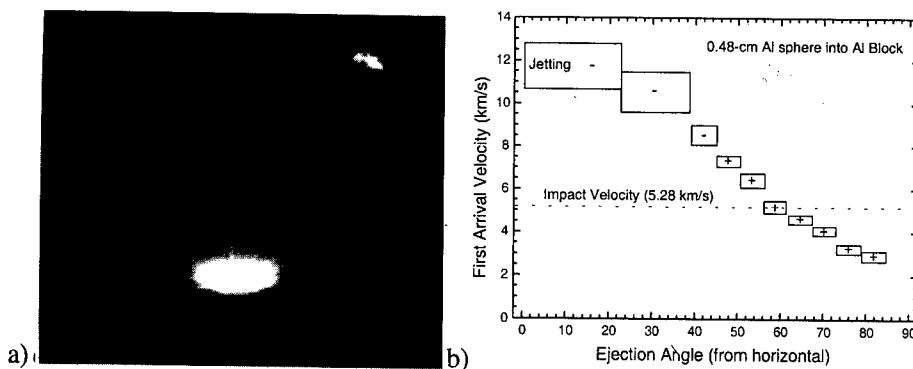
Fig. 1. a) Impact flash from 0.48 cm diameter aluminum sphere impacting vertically on an aluminum target block at 5.28 km/s (open shutter photograph). b) In this experiment, the target block was instrumented to measure departing charge and electric probes located in the arc seen at the top of the image (55 cm from the impact) measured the arrival of charged debris (traveling up to 12 km/s) jetting out from the point of impact. The +/- signs indicate the polarity of the initial arriving charge.

Dietzel *et al.* [7], studied the production of plasma from small particles in the hypervelocity impact regime. They used a parallel plate capacitor with 40 V/cm electric field to separate and measure the positive and negative constituents of the plasma for 10^{-15} to 5×10^{-10} g iron projectiles striking a tunsten target at 1-40 km/s. The net charge liberated from an impact is zero, but, over the range of experimental conditions, the magnitude of the positive or negative charge carriers (Q) was found to have an approximate linear dependence on mass (m) and to have a strong dependence on impact velocity (v):

$$Q = 9 \times 10^{-9} m^{0.9 \pm 0.15} v^{2.75 \pm 0.4} \text{ C (SI units)} \tag{1}$$

At modest impact velocities (5 km/s), the level of ionization is low (typically 10^{-6}) [2]. At 40 km/s, however, the ionization level can be as much as 0.1 [7]. It is reasonable to suppose that at very high velocities the level of ionization and the amount of neutral vapor asymptotically approach a linear dependence on energy (v^2) and the fractional ionization will approach a constant value (<1) which is only dependent on impact geometry, projectile and target materials. Little evidence of this asymptotic behavior, however, is seen in the Dietzal *et al.* [7] data. With a reasonably conservative extrapolation of Equation (1) to Leonid encounter velocities (72 km/s), 10-20% of the plasma produced by Leonid impacts on spacecraft will be ionized and highly conductive.

In addition to plasma, a typical hypervelocity impact will produce melt and fragmental debris. Because electrons are much more mobile than ions, any debris in contact with plasma will typically acquire a negative charge. Inertial separation of the materials could then lead to separation of charge over macroscopic distances. This process, similar to static electrification that occurs in thunderclouds, can lead to substantial electric fields that are surprisingly easy to measure in the laboratory.

In experiments performed at the NASA Ames Vertical Gun Range, macroscopic charge separation during hypervelocity impact has been characterized for a variety of impactor and target geometries. The experiment depicted in Figure 2 was designed to measure the electrostatic field produced during a hypervelocity impact into a granular carbonate (dolomite) target. Aluminum plates were placed on the target plane radial to the impact point (Figure 2a). The voltage of each plate was measured with two digitizer channels: one to record strong, early-time signals (Figure

2b) the other to measure weak, late-time signals (Figure 2c). Each plate was terminated to ground via a 1 MΩ resistor.

a)

b)

c)
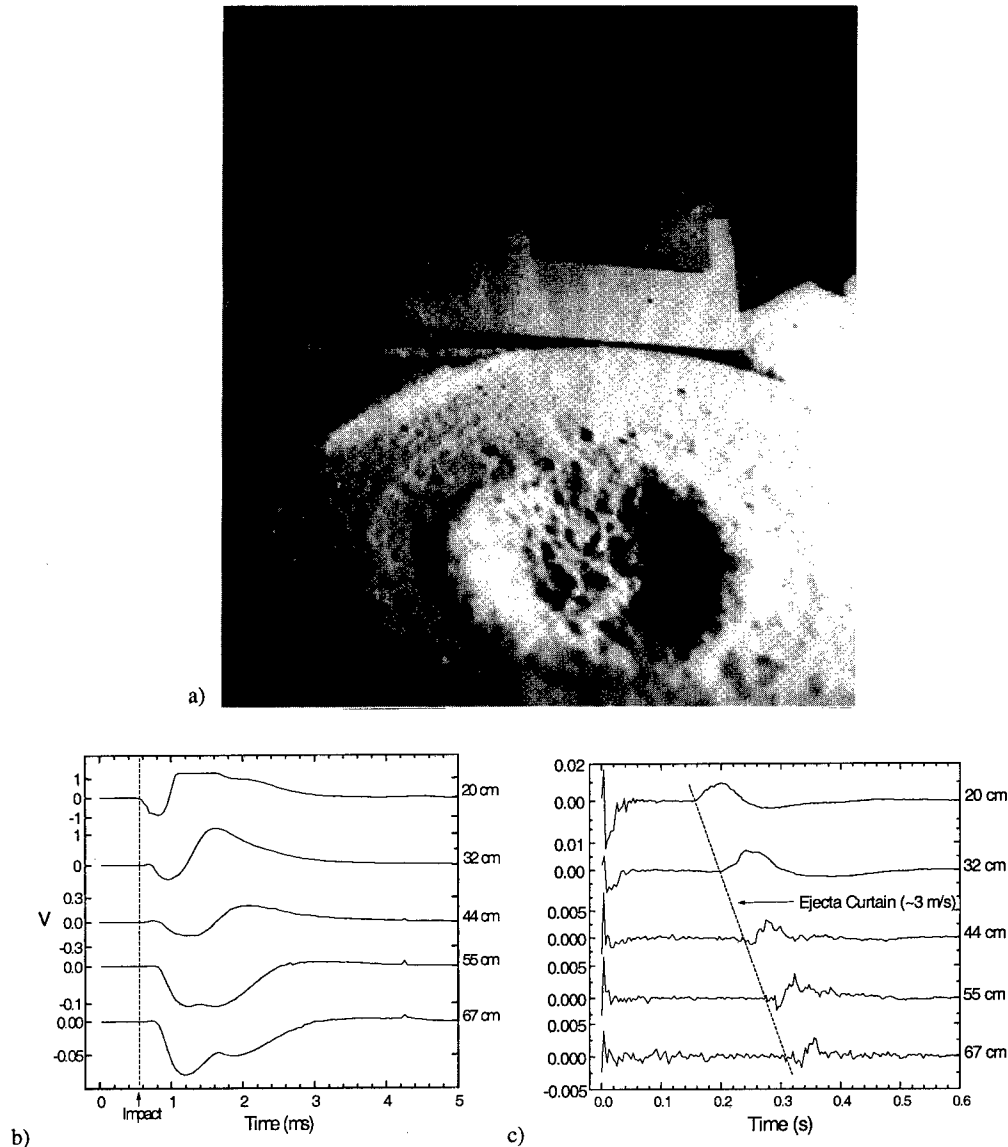
Fig. 2. Experiment to measure the electrostatic field produced by the impact of a ¼ inch Al projectile into a particulate carbonate target (impact velocity: 5 km/s, vertical). a) The impact crater (10 cm diameter) can be seen in the foreground and several of the plates located 20 and 32 cm from the impact are shown in the background. b) The electrostatic potential on a radial distribution of plates is shown with distance from the center of the impact crater indicated. c) At late time, charged ejecta land on the plates producing a discernable signal that allows ejecta curtain velocity to be measured.

The negative potential of the early time data in Figure (2b) and the positive charge of the ejecta landing on the plates at late time are consistent with early ejecta acquiring a negative charge and leaving behind a residual positive charge in the plasma, the transient cavity and material ejected at late time. The arrival time of the ejecta landing on the plates is consistent with an ejecta curtain velocity of 3 m/s (Figure 2c).
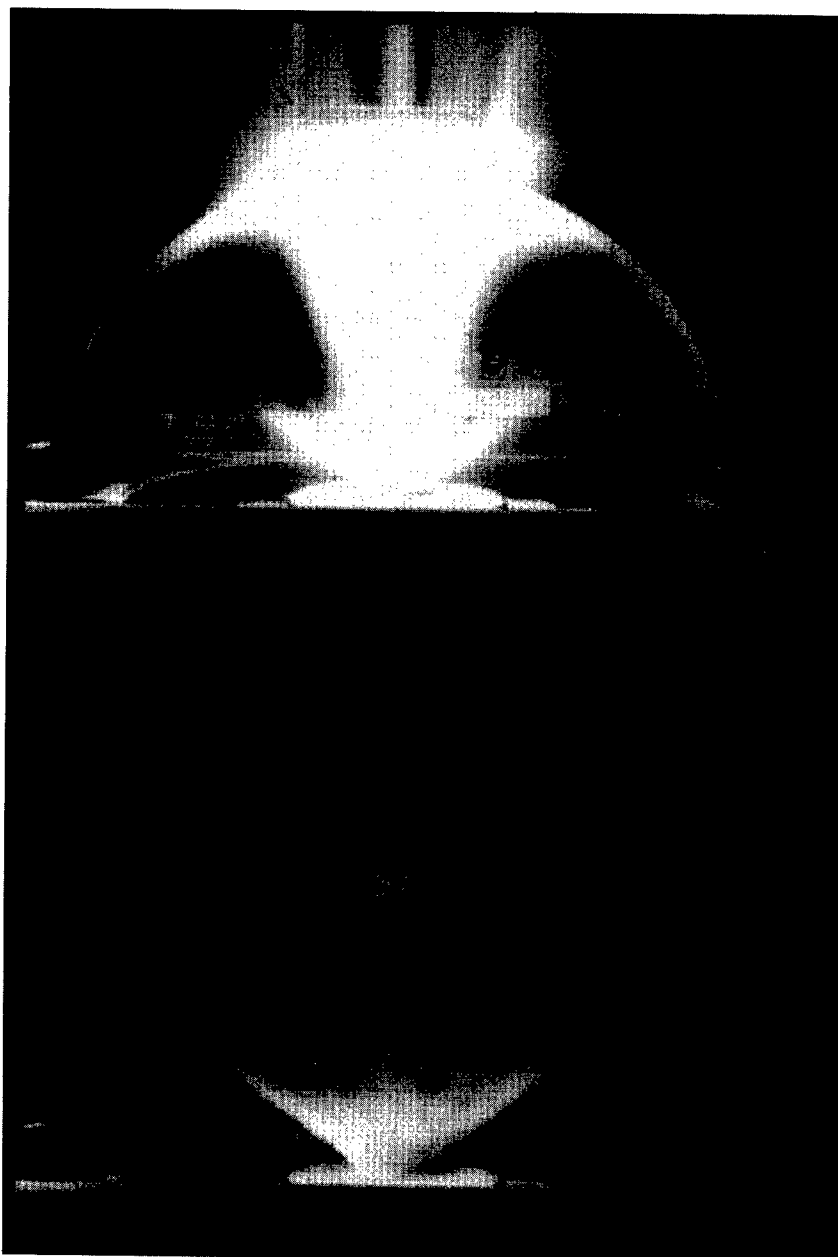
Fig. 3. Two movie frames from an experiment designed to measure the angular distribution of charge ejected from an impact in a particulate carbonate target. The projectile is a 0.48 cm aluminum sphere impacting at 5 km/s in an evacuated target chamber. The upper frame shows the luminescent impact-generated plasma impinging on the upper portion of an arc of 16 charge detection plates. The lower frame (2 ms later) shows ejecta hitting the arc at 35 degrees. The radius of the arc is 55 cm.

Unlike the experiment depicted in Figure 2, the experiment shown in Figure 3 was designed to directly measure the charge ejected at early time from impact craters formed by vertical hypervelocity impacts. The experiment contained an array of 16 aluminum plates used to detect the arrival of charge as a function of angle of ejection from the target surface. The arc of plates had a radius of 55 cm centered on the impact point. Each plate covered 5.5 degrees of arc and

was terminated with a 1 kΩ resistor. The resulting current traces are generally bimodal, showing negative or positive charge collection during certain times (Figure 4) A possible configuration of charge consistent with all the observations is illustrated in Figure 5.
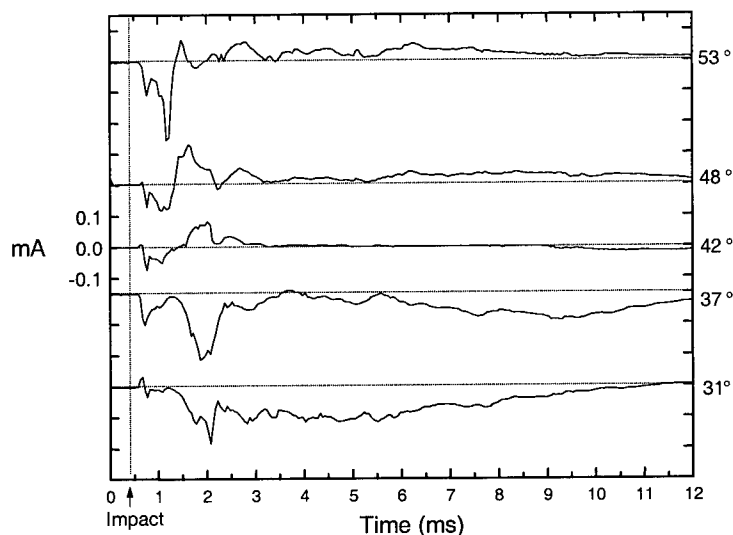
Fig. 4. Electric current collected by probes located 55 cm from the impact point of 0.48 cm Al sphere into granular carbonate target (impact velocity: 4.9 km/s). Each probe's ejection angle is indicated.
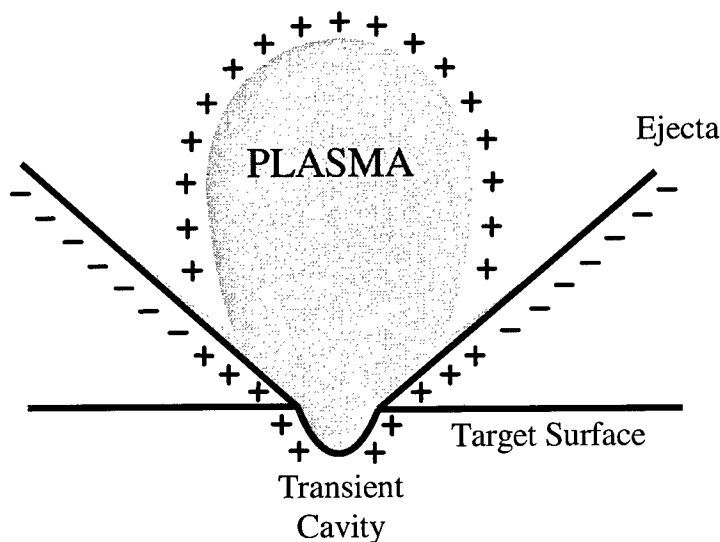
Fig. 5. Possible configuration of charge that explains the data.

Figure 6 shows the total, integrated charge collected at each range of solid angle for several impacts, demonstrating the consistency of the measurement and the dependence on impactor mass and velocity. Depending on ejection angle, the total charge is dominantly negative or positive. To demonstrate this, the positive and negative contributions to the total charge have been plotted separately in Fig. 6 (projecting above and below the horizontal lines respectively). A comparison with Fig. 3 suggests that early time ejecta is negatively charged and impact-generated plasma (moving to the top of Fig. 3) is positively charged.

Variable Mass, Constant Impact Velocity

a)

Constant Mass, Variable Impact Velocity
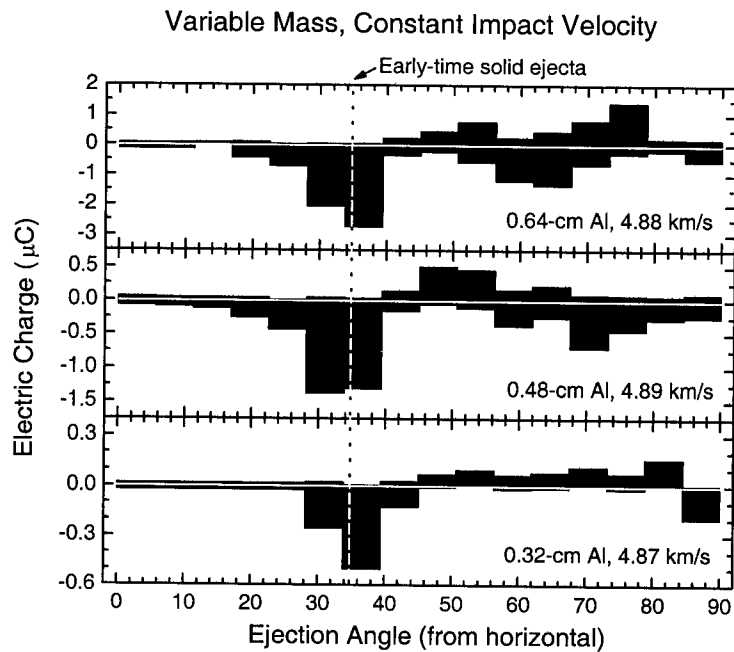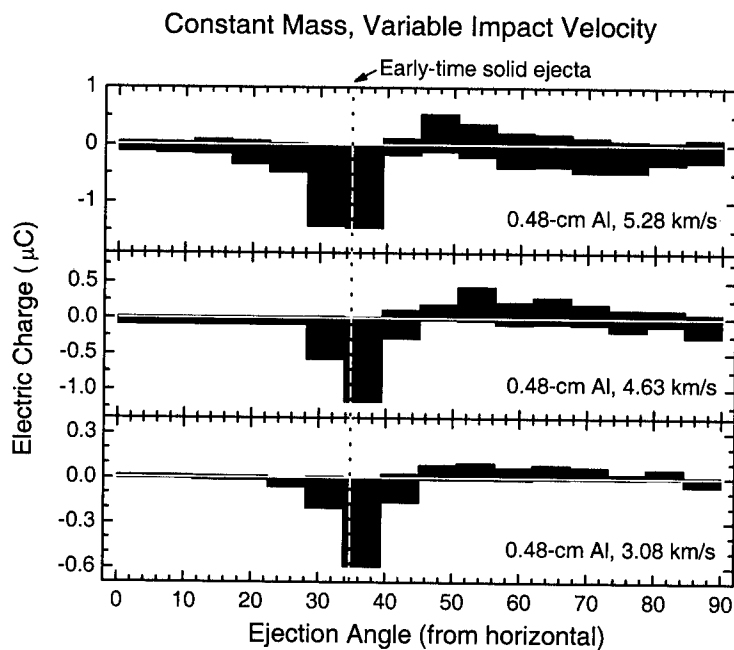
b)

Fig. 6. a) Total electric charge detected during impacts of 0.32, 0.48 and 0.64-cm Al projectiles into granular carbonate targets at 4.88 km/s. b) Total electric charged detected during 0.48-cm Al projectiles impacting at 3.08, 4.63 and 5.28 km/s. Location of early-time solid ejecta (measured from Fig. 3) is indicated.

In these experiments, dependence on impactor mass and velocity has been determined for a limited class of materials. Total charge separation is a function of impactor kinetic energy with a near linear dependence on mass and a velocity dependence of $v^{2.6}$ (Figure 7) comparable to the

dependence seen by Dietzel *et al.* [7]. This velocity dependence has strong implications for the degree of charge separation expected at Leonid encounter velocities (72 km/s) whereas the linear mass dependence has significant implications for the production of magnetostatic fields during planetary-scale impacts.
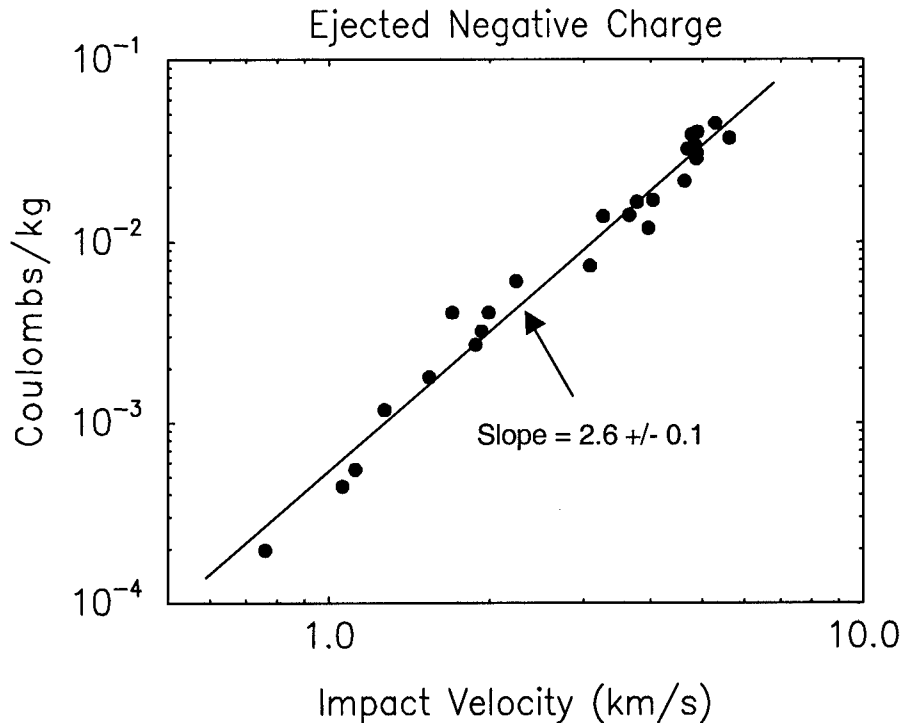
Fig. 7. Negative charge per unit mass ejected by impacts of spherical aluminum projectiles into granular carbonate (dolomite) targets vs. impact velocity.

Similar to Equation (1), the amount of charge separated by a macroscopic distance (ΔQ) can be expressed as functions of projectile mass (m) and impact velocity (v):

$$\Delta Q = 10^{-2} m \left(\frac{v}{3000}\right)^{2.6\pm0.1} \text{C (SI units)} \tag{2}$$

Table 1 compares the total charge (Q), the separated charge (ΔQ) and the degree of charge separation ($\Delta Q/Q$) for impact of 1 gram projectiles at different velocities:

Table 1. Electric charge as a function of impact velocity.

Velocity (km/s)	Total Charge (Q) (Coulombs)	Separated Charge (ΔQ) (Coulombs)	Degree of Separation (ΔQ/Q)
5	0.3	4×10^{-5}	1.4×10^{-4}
20	12	1.4×10^{-3}	1.2×10^{-4}
70	380	4×10^{-2}	9.5×10^{-5}

The extreme differences in projectile and target materials from which Equations (1) and (2) were determined make such comparisons problematic; nevertheless, they do provide some insight into the magnitude of charge separation that might occur. Even if only 10^{-4} of the total charge is

separated macroscopic distances, it is still significant for the production of electrostatic and magnetostatic fields.

The electric field produced by macroscopic charge separation during hypervelocity impacts is complicated by the contribution of electrostatic charge in the ejecta, the plasma and the transient cavity. To simplify the analysis and to provide a simple expression that exhibits the appropriate scaling behavior, we estimate the strength of the electric field by a spherical charge, $\pm \Delta Q$, centered at the impact point and expanding at a rate proportional to the impact velocity, v (as is approximately the case for expanding vapor or ejecta). If we make a measurement of the electric field at a distance x from the impact point, the magnitude of the electric field will last for a time, $\tau \propto x/v$. Using the data of Figure (2b) as a guide, we estimate $\tau \sim 20x/v$ in SI units. During this time, the electric field will have a magnitude:

$$E = \frac{3\Delta Q}{4\pi\varepsilon_0 x^2} = 2.7\times10^{10}\frac{\Delta Q}{x^2}\ \text{Volts/m} \tag{3}$$

Charge separation will drive currents of magnitude:

$$I = \frac{\Delta Q}{\tau} = \frac{\Delta Q v}{20x}\ \text{Amps,} \tag{4}$$

and magnetic fields with magnitude:

$$B = \mu_0\frac{I}{2\pi x} = 10^{-8}\frac{\Delta Q v}{x^2}\ \text{Tesla,} \tag{5}$$

will be produced. Substituting Equation (2) into Equations (3-5), we find:

$$E = 0.24\frac{mv^{2.6\pm0.1}}{x^2}\ \text{Volts/m,} \tag{6}$$

$$I = 5\times10^{-13}\frac{mv^{3.6\pm0.1}}{x}\ \text{Amps,} \tag{7}$$

$$B = 9\times10^{-20}\frac{mv^{3.6\pm0.1}}{x^2}\ \text{Tesla.} \tag{8}$$

For naturally occurring impacts on planetary surfaces, the distance at which the electric and magnetic fields are significant is often proportional to the size (r_c) of the resulting impact crater. Because $x \propto r_c \propto r$ and $m \propto r^3$, the electric and magnetic fields of interest would tend to scale linearly with impactor radius (r). In the laboratory and during impacts on spacecraft, however, the location of the measurement is governed by other things and it is useful to maintain an independent measurement location (x).

Table 2 shows estimates for the magnitude and duration of the electric field, electric current and magnetic field for several cases: 1) a laboratory experiment $(m=2\times10^{-4}$ kg, $x=0.5$ m, $v=5$ km/s), 2) a Leonid meteoroid $(m=10^{-7}$ kg, $x=1$ m) striking a spacecraft at 72 km/s, 3) a small meteoroid $(m=1$ kg, $x=3$ m) striking the Moon at 15 km/s and 4) a 1 km asteroid $(m=10^{12}$ kg, $x=100$ km) striking a planetary surface at 20 km/s.

Table 2. Electromagnetic properties of representative impacts.

	τ (sec.)	E (Volts/m)	I (Amps)	B (Tesla)
1) Laboratory	2×10^{-3}	8×10^{5}	4×10^{-3}	10^{-9}
2) Leonid Meteoroid	3×10^{-4}	10^{5}	0.02	10^{-8}
3) Small Meteoroid	4×10^{-3}	2×10^{9}	180	10^{-5}
4) 1 km Asteroid	100	4×10^{12}	2×10^{10}	0.03

Except for the electric field, which was not measured, the laboratory numbers here agree well with experiments performed as part of this study (Figure 4) once a solid angle correction is performed. The magnetic field value agrees well with previous studies of fields observed during hypervelocity impacts [3].

A microscopic Leonid meteoroid striking a spacecraft at 72 km/s has the potential of inducing stronger electrical currents than those seen during typical macroscopic impact experiments. Discharges will drive higher currents in inverse proportion to their duration. A three microsecond discharge during a Leonid impact, for example, can drive a brief two amp current before exhausting the available charge.

The electric fields shown here are significant. By way of comparison, air typically becomes conducting at about 3×10^{6} V/m although the small amount of air that could support a discharge would interfere substantially with charge separation at the laboratory scale (Figure 8). Even without the presence of air, the electric field of large asteroid impacts may still be self limiting. In the presence of 10^{10} V/m electric fields, sub-micron dust grains, with just a few excess electrons of charge, will acquire accelerations of several km/s^{2}. Perhaps electrostatically-driven dust transport may occur during impacts on airless bodies. The resulting 'dust discharges' would tend to limit the buildup of charge and the strength of the electric and magnetic fields to some saturation level.
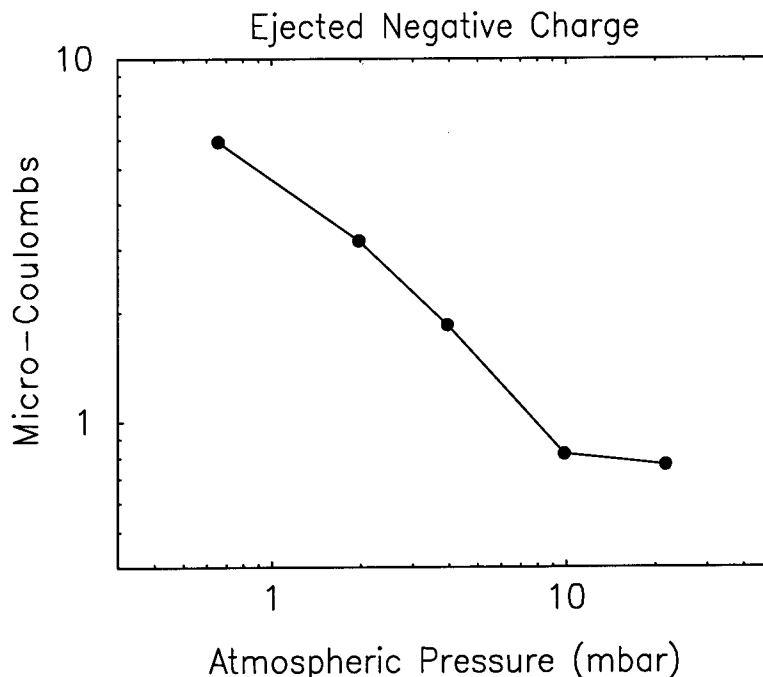
Fig. 8. Negative charge ejected by impacts of 0.48-cm spherical aluminum projectiles into granular carbonate (dolomite) targets at 4.8 km/s vs. atmospheric pressure.

The strength of the magnetic fields shown in Table 2 are only significant for the larger impact events. The 0.03 tesla magnetic field strength during a 1 km asteroid impact is about 1,000 times greater than Earth's natural surface field strength. Of course, due to the mechanism of 'dust discharge' suggested above, fields of this strength may not occur during actual events, but fields comparable to Earth's are perhaps possible. The magnetic field could last 100's of seconds, comparable to the crater formation time, and perhaps long enough for materials transported, shocked and heated by the impact to acquire a remnant magnetization.

Sample 70019   S-73-15333
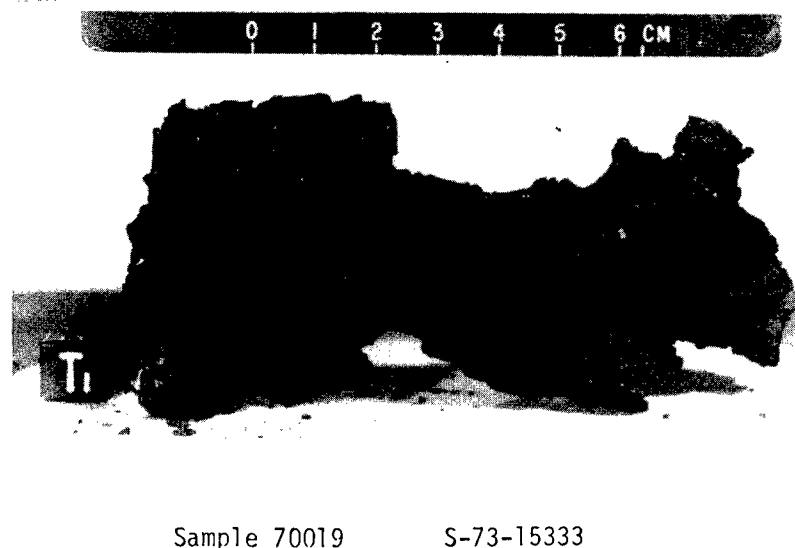
Fig. 9. Sample 70019 collected during Apollo 17 from the bottom of a 3-m glass-lined crater (Fig. 10). It was collected as a good candidate for obtaining a magnetic paleointensity estimate of the landing site.

It has been known since Apollo that the Moon possesses a patchy remnant magnetism associated predominantly with heavily cratered terrain [8]. There are two generally accepted possibilities for the origin of this magnetism: 1) that the Moon originally possessed an internal core dynamo field which is retained today in a heavily modified state by the older regions of the lunar surface or 2) that some, if not all, of the remnant magnetism may be due to spontaneous production by impacts. The recent arrival of Lunar Prospector, with magnetic mapping among its many tasks, may finally answer this question. We suggest that macroscopic charge separation and subsequent magnetic field production during hypervelocity impact may play an important role in understanding the lunar magnetic record.

Sample 70019 (Figure 9), was collected from the bottom of a 3-m glass pit crater (Figure 10) in the hope that it would provide a relatively recent magnetic paleointensity value for the Apollo 17 landing site [9]. It is a glass-bonded agglutinate of a dark, weakly coherent breccia, presumably formed by the impact that made the crater. A paleomagnetic experiment conducted by Sugiura et al. [10] demonstrated that sample 70019 (or more accurately, its glassy rind) was formed in a magnetic field of ~2500 nT, which is almost ten times stronger than the largest present-day field measured at the lunar surface. Because the young age of the sample (3 to 200 million years) precludes an ancient core dynamo origin for the magnetic field, this is a good candidate for a magnetic field formed by hypervelocity impact. We estimate that a 1-5 kg meteoroid impacting the lunar surface at 15 km/s would, in the process of making a 3-m crater, produce a several thousand nanotesla field for 4-8 milliseconds (Example 3 in Table 2), long enough for small beads of impact melt to acquire a permanent magnetic remanence.
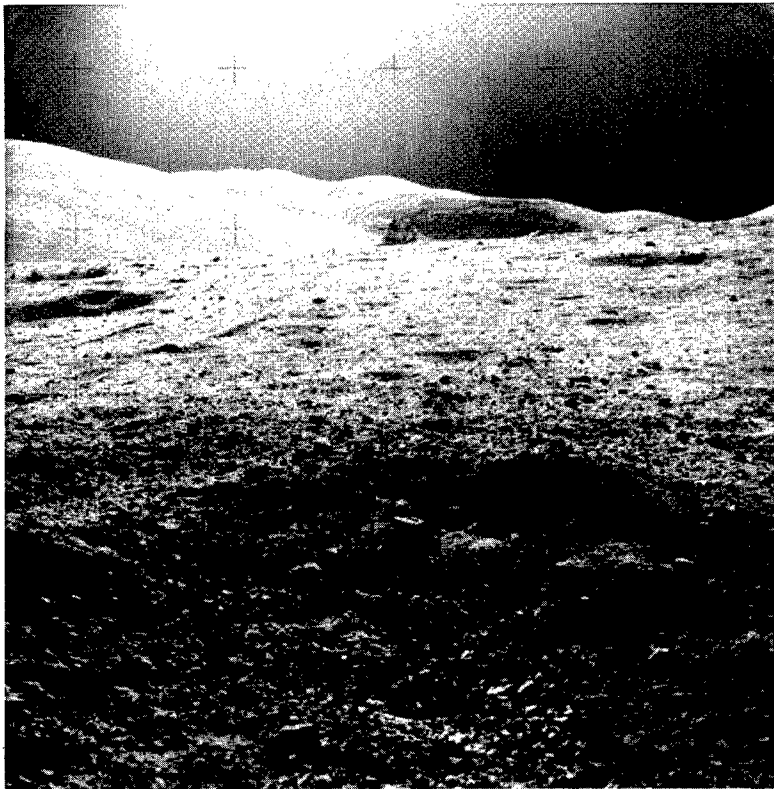
Fig. 10. A 3-m impact crater observed by the astronauts of Apollo 17. Sample 70019 was collected from the central glass-lined pit at the extreme foreground of the image (NASA photograph AS17-145-22185).

CONCLUSION

The production of a charged debris environment during hypervelocity impact is inevitable. A straightforward experimental technique, using conducting plates connected to digitizing electronics, can measure the degree of charge separation and map out the spatial extent and velocity distribution of the charged debris. In this study, we have demonstrated that the amount of plasma, electrostatic charge and the magnitude of the resulting currents and electric fields have near linear dependence on impactor mass and near cubic dependence on the impact velocity ($\propto v^{2.6}$). A straightforward extrapolation for microscopic Leonid meteoroids impacting spacecraft at 72 km/s, suggests that electric currents from potential discharges may approach several amps, levels that could be dangerous to spacecraft electronics. The resulting magnetic fields, while insignificant at microscopic and laboratory scales, increase linearly with impactor radius and can potentially explain the otherwise puzzling paleomanetic field determined for at least one young lunar sample and can help our more general understanding of the paleomagnetism of the Moon, Mars, asteroids and other planetary surfaces.

REFERENCES

1. D. A. Crawford and P. H. Schultz, Laboratory observations of impact-generated magnetic fields, *Nature*, **336**, 50-52 (1988).
2. D. A. Crawford and P. H. Schultz, Laboratory investigations of impact-generated plasma, *J. Geophys. Res.*, **96** (E3), 18,807-18,817 (1991).
3. D. A. Crawford and P. H. Schultz, The production and evolution of impact-generated magnetic fields, *Int. J. Impact Engng.*, **14**, 205-216 (1993).
4. L. L. Hood and A. Vickery, Magnetic field amplification and generation in hypervelocity meteoroid impacts with application to lunar paleomagnetism, *Proc. Lunar Planet. Sci. Conf. 15, J. Geophys. Res.*, **89** (suppl.), C211-C223 (1984).
5. R. D. Caswell, N. McBride and A. Taylor, Olympus end of life anomaly – a Perseid meteoroid impact event?, *Int. J. Impact Engng.*, **17**, 139 (1995).
6. M. M. Campbell and D. F. Medina, Kinetic Damage to External Satellite Materials due to the Impact of Leonid Micrometeoroids in the 10 Microgram Mass Range, presented at the Leonid Meteoroid Storm and Satellite Threat Conference, Manhattan Beach, CA, April, (1998).
7. H. Dietzel, G. Neukum and P. Rauser, Micrometeoroid Simulation Studies on Metal Targets, *J. Geophys. Res.*, **77**, 1375-1395 (1972).
8. M. Fuller, Lunar Magnetism, *Reviews of Geophys. And Space Phys.*, **12**, 23-70 (1974).
9. Apollo 17 Preliminary Examination Team, Apollo 17 Lunar Samples: Chemical and Petrographic Description, *Science*, **182**, 659-672 (1973).
10. N. Sugiura,. *et al.*, A new magnetic paleointensity value for a "young lunar glass", *Proc. Lunar Sci. Conf.*, **10**, 2189-2197 (1979).

COLUMBUS DEBRIS SHIELDING EXPERIMENTS AND BALLISTIC LIMIT CURVES

ROBERTO DESTEFANIS, MORENO FARAUD, and MARCO TRUCCHI

Alenia Aerospazio, Divisione Spazio, C.so Marche 41, 10146 Turin, Italy
Phone: 39-11-7180320, Fax: 39-11-7180028, Email: rdestefa@to.alespazio.it

Summary—An extensive Light Gas Gun test campaign has been performed to develop a high resistance shielding to protect the Columbus module - the European laboratory attached to the International Space Station - against the threat posed by orbital debris. In a 3-year period – from Summer '95 to Summer '98 – more than 100 hypervelocity impact tests have been made on a 3-wall shield system, based on an aluminium Whipple Shield plus an intermediate bumper made of Nextel fabric and a Kevlar™-Epoxy™ plate. Two shielding configurations have been selected, which both reported excellent ballistic performance against aluminium spherical projectiles impacting with velocities between 3 and 7 km/s and angles between 0 and 60 degrees. The results showed that the response of a 3-wall system to hypervelocity impacts is more complex than expected. For instance - in the test range - the shielding resistance does not increase linearly with the velocity but shows non-monotonic variations; the ballistic limit shows little oscillations with the increase of the impact angle in the 0 - 45 degrees range as well. The projectile fragmentation level is shown to play a key role in the target failure process. A thorough analysis of the impacted target is on going to gain insight into the complex damage mechanism with particular attention paid to the X-ray pictures taken of the debris cloud formation and evolution. The present paper summarizes the activities performed and the results obtained so far, focusing on the more recently performed experiments.© 1999 Elsevier Science Ltd. All rights reserved.

INTRODUCTION

The Columbus pressurized module is composed of a cylindrical section with a truncated cone at both ends. The aluminium pressure shell (4.8 and 3.8 mm thick in the Cylinder and Cone area, respectively) is protected by a high resistance debris shielding made of advanced materials and referred to as Advanced Shielding (AS). AS is similar to the Stuffed Whipple (SW) system developed by NASA [1] for the American modules attached to the International Space Station, and is composed of a Whipple Shield structure plus an intermediate wall made of a combination of blankets of advanced materials. The external shield, or 1st Bumper Shield (1st BS), is used to fragment the impacting projectile and is made of aluminium alloy. The intermediate bumper, or 2nd Bumper Shield (2nd BS), is made of 4 layers of Nextel™ fabric, and of Kevlar™ fabric composed with Epoxy resin. Figure 1 shows the
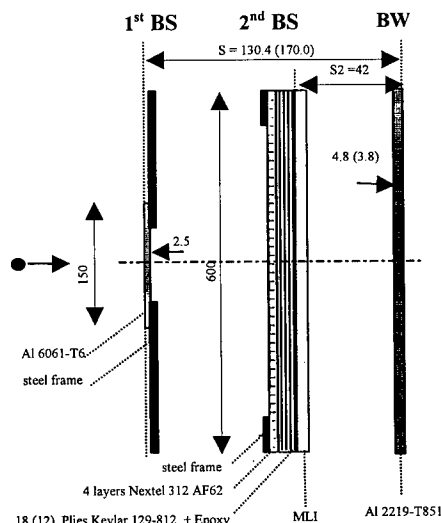
Fig. 1. Advanced Shielding, Cylinder configuration. Target layout for LGG testing. All dimensions are in mm. S is the overall spacing; S2 is the internal spacing.

layout of the AS configurations used for impact testing. In Table 1 the two AS configurations tested (one for the Cylinder and one for the Cones) are compared with the NASA Stuffed Whipple shielding.

Table 1. Columbus Cylinder and Cone AS configuration data compared with the NASA Stuffed Whipple shielding. N stands for Nextel™, KE stands for Kevlar™ composed with Epoxy resin, followed by a number giving the number of layers/thickness. The materials used are: Nextel™ 312 AF62, with an areal density of 0.1 g/cm² per layer, Kevlar™ 129, style 812, with an areal density of 0.028 g/cm² per layer, Epoxy resin Brochier 914 (40% by volume)

		Cylinder (AS2-N4KE6)	*Cone* (AS2-N4KE6)	*NASA* (SW MOD-2)
1ˢᵗ BS	Material	Al 6061-T6	Al 6061-T6	Al 6061-T6
	Thickness [mm]	2.5	2.5	2.0
	Areal density [g/cm²]	0.7	0.7	0.5
2ⁿᵈ BS	Material and Thickness [mm]	Nextel, 4 layers Kevlar-Epoxy, 6 mm	Nextel, 4 layers Kevlar-Epoxy, 4 mm	Nextel, 6 layers Kevlar Fabric, 6 layers
	Areal density [g/cm²]	1.1	0.9	0.8
BW	Material	Al 2219-T851	Al 2219-T851	Al 2219-T851
	Thickness [mm]	4.8	3.8	4.8
	Areal density [g/cm²]	1.4	1.1	1.4
Spacing	Overall (S) [cm]	13.04	17.00	11.40
	Internal (S2) [cm]	4.2	4.2	5.7 (TBC)
Total	Areal density [g/cm²]	3.2	2.7	2.7 (TBC)

TEST CAMPAIGN DESCRIPTION

An extensive hypervelocity impact test campaign has been performed at the Ernst Mach Institut, in Freiburg, Germany, using the 65/20 mm calibre Large Light Gas Gun (LGG) [2]. More than 100 shots have been performed in this 3-year program. The present paper deals with the experiments performed from Spring '97 to Spring '98, according to the test matrix reported in Table 2. The experiments performed from Summer '95 to Spring '96 have already been discussed elsewhere [3, 4].

To simulate debris impacts, aluminium spheres with a diameter from 0.9 to 1.75 cm have been fired at three velocities: Low Velocity (LV, about 3 km/s), Medium Velocity (MV, approximately 5 km/s) and High Velocity (HV, about 6.5 km/s). The upper limit of 6.5 - 7 km/s is related to the maximum velocity achievable by Light Gas Guns for a projectile with a mass in the range of interest. The impact angle has been varied from 0 to 60 degrees, with the major number of tests performed at 0 degrees and at 45 degrees. A few experiments have been performed

Table 2. Columbus LGG test matrix. LV stands for Low Velocity (3 km/s), MV for Medium Velocity (5 km/s) and HV for High Velocity (6.5 km/s)

Velocity / Angle	Number of Shots	Remarks	Projectile diameter [cm]
Cylinder			
LV-0	4	1 with MLI	1.35 – 1.50
LV-30	1		1.50
LV-45	3	1 with MLI	1.45 – 1.50
LV-60	1		1.75
MV-0	5	1 with MLI	1.45 – 1.50
MV-30	1		1.55
MV-45	4	1 with MLI	1.40 – 1.50
MV-60	1		1.75
HV-0	4	1 with MLI	1.45 – 1.55
HV-30	2		1.50 – 1.55
HV-45	4	1 with MLI	1.45 – 1.55
HV-60	2		1.65 – 1.75
Total	32	6	
Cone			
LV-0	3	1 with MLI	1.35 – 1.40
LV-30	2		1.35 – 1.45
LV-45	4	1 with MLI	1.25 – 1.40
LV-60	1		1.75
MV-0	3		1.50 – 1.60
MV-30	2		1.50 – 1.55
MV-45	3	1 with MLI	1.45 – 1.50
MV-60	1		1.75
HV-0	4		1.45 – 1.60
HV-30	2		1.55 – 1.65
HV-45	7	1 with MLI	1.35 – 1.60
HV-60	3		1.60 – 1.75
Total Cone	35	4	

introducing a multi-layer insulation blanket (MLI) between the 2nd BS and the BW. Excluding the 10 shots with MLI, 57 experiments have been devoted to assess 24 parameter combinations (2 configurations x 4 angles x 3 velocities), i.e., to determine 12 ballistic limit points for each configuration. Target dimensions are 400 x 600 mm to limit edge effects. Flat, unpressurized, unstressed plates have been used to represent the pressure shell. A target mounted in the LGG impact chamber is shown in Figure 2.

The main purpose of the LGG testing was to derive damage describing equations for the Advanced Shields, giving the projectile critical mass (or diameter) which is just able to penetrate the rear wall as a function of the other projectile characteristics (i.e., velocity and impact angle). Therefore the shots have been performed very close to the penetration/no penetration threshold of the structure (i.e., to the ballistic limit, BL). The ballistic limit formulas are usually based on simple physical laws, but the AS testing showed a very complex physical behavior. As the impact response did not show a clear regularity, additional investigations have been performed to gain insight into the impact phenomenon and to help the definition of the ballistic limit equations.

Fig. 2. Target set-up in the LGG impact chamber at EMI.

During the impact experiments on the Cone targets, double X-ray pictures were taken to monitor the formation and evolution of the debris cloud in the stand-off between the 1st BS and the 2nd BS. For the Cylinder target just one exposure of the debris cloud in this small stand-off could be taken. Another exposure was taken to detect the residual cloud in the small space (42 mm) between the 2nd BS and the BW. The X-ray pictures have been scanned and a software program has been developed to make measurements on the pictures assisted by the computer. Figure 3 shows two triple-exposed X-ray pictures, with the points used when making measurements of the basic features of the cloud (according to the description given by Piekutowsky [5]). The debris cloud fragmentation has been evaluated qualitatively, while a quantitative assessment (on partial data) has been made of the residual velocity, the spray angle between the 1st and the 2nd BS, and of the velocity of the cloud fragments reaching the BW. The computer-aided procedure improved the measure precision, but, unfortunately, the computer scansion caused a loss of definition, leading to insufficient accuracy in some measurements.

Fig. 3. Triple exposure X-ray picture of the expanding debris cloud with some points used when making measurements.
Left: Test No. 8657, Cone target, 1.55 cm projectile at 6.46 km/s, 0 degrees, ts/d ratio =0.16.
Right: Test No. 8622, Cone target, 1.40 cm projectile at 3.11 km/s, 0 degrees, ts/d ratio =0.18.

Particular attention has also been paid to the damage induced by the debris cloud on Nextel, which has been carefully measured. The typical damage features on the Nextel fabric are shown in Figure 4, together with the quantities measured. Data reduction has been performed considering the dimensions of the area with damaged fibers of the external Nextel layer (i.e., the trace left by the debris cloud in the top layer) and the dimensions of the hole punched in the Nextel 4-layer mattress.
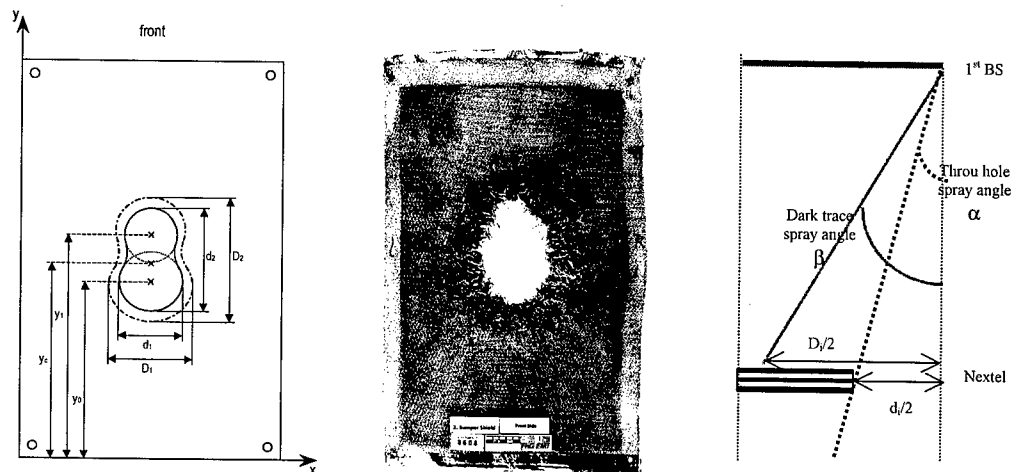
Fig. 4. Impact damage features on Nextel fabric and related spray angles. Experiment 8608: Cylinder target, 1.55 cm projectile at 6.44 km/s, 45 degrees, ts/d ratio =0.16. The measured quantities are:

d_1,d_2:   diameter of the through hole in the Nextel mattress along x and y axes (the through hole area is $\pi\, d_1 d_2$)
D_1,D_2:   diameter of the 1st Nextel layer zone with damaged fibers along x and y axes (the dark trace area is $\pi\, D_1 D_2$)
y_c,y_0,y_1: coordinates along the y-axis of hole center, normal and oblique component of the fragment cloud.

TEST RESULTS

Overall Results

The advanced targets reported very good ballistic performance. For the Cylinder configuration (AS-N4KE6), at high velocity (6.5 km/s) normal and 45-degree impacts, typical critical mass (diameter) is above 4.5 g (1.45 cm). The values obtained at low and medium velocity are in the same mass range. For 60-degree impacts, even very massive projectiles (above 8 g, 1.75 cm in diameter) could not penetrate the structure. The Cone configuration (AS-N4KE4) reported a similar behaviour, with resistance capabilities not as good as for the Cylinder when the projectile is not well fragmented (i.e., at 45 degrees and for low velocities), but with slightly better capabilities for normal and 30-degree impacts at high velocity. In almost all of the 10 experiments performed with the MLI, the ballistic resistance increased. The MLI effect was especially strong for 6.5 km/s, 45-degree impacts on Cylinder targets: the ballistic limit jumped from above 4.5 g to above 5.5 g. The experimental data for the Cylinder are shown in Figure 5, where the projectile mass is reported as a function of the impact velocity. In the figure on the left, 0, 45 and 60 degrees test data without MLI are plotted. The right graph shows 0 and 45 degrees experimental data with MLI. Note the strong influence of the MLI: the same projectile mass which was able to penetrate the structure without MLI could not penetrate the same target with MLI. Note also the excellent resistance against 60-degree impact, with a critical mass above 8.0 g in the complete velocity range. The experiments gave some evidence of data scattering, as shown in Figure 5 left: two projectiles with similar mass (around 4.5 g) and velocity (around 4.75 km/s) gave opposite results. The advanced targets seem to be quite intrinsically affected by a scattered response to hypervelocity impacts induced by the non-homogeneity of the Kevlar-Epoxy plates and by the many small local differences in the Nextel large fibers overlapping.

Moreover, small differences have been reported in the Nextel mattress position with respect to the KE from experiment to experiment. The data scattering makes the results analysis/interpretation more difficult (and uncertain). Unfortunately, a statistical assessment of it was impossible due to the large number of dedicated experiments required.
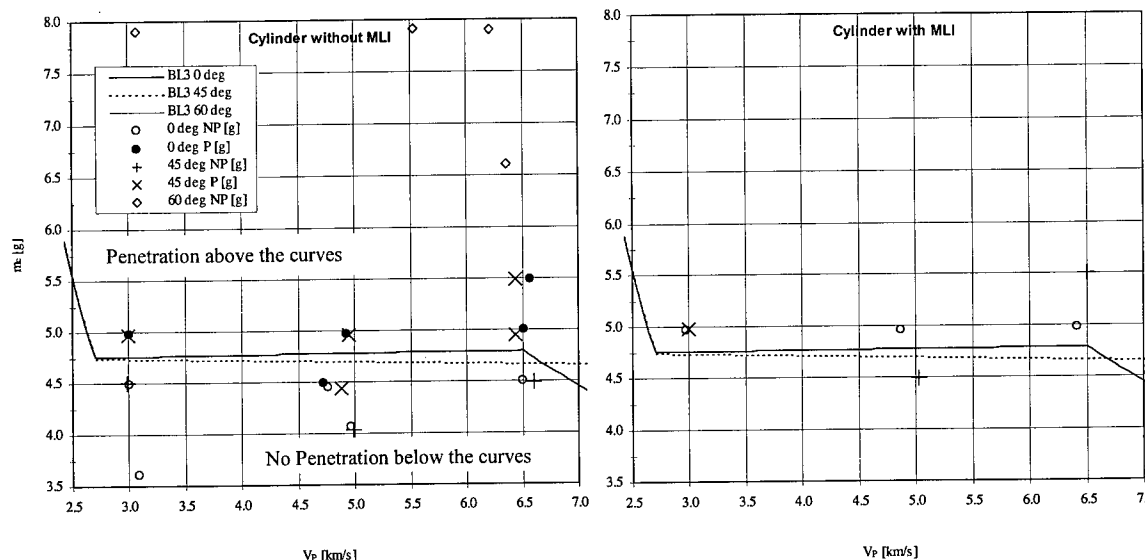
Fig. 5. AS-N4KE6 test data: projectile mass versus projectile velocity. NP is for No Penetration experiments, P is for Penetration. Data for 0, 45, 60-degree impacts without MLI are reported on the left plot, while on the right data for 0 and 45 degrees with MLI are shown. Tentative ballistic limit curves are reported for 0 and 45-degree impacts.

Damage Mechanism Discussion

The results show that the damage on the BW is caused by the addition of two components: the residual solid fragments in the debris cloud and the impulsive load reaching the BW. When the projectile is finely fragmented, only an impulsive load reaches the rear wall, inducing a very large dynamic deformation (the residual plastic BW deformation can be as high as 38 mm, without any perforation). For higher energy loads, the BW fails with large cracks. When fragments are hitting the BW, cracks propagate for much lower energy and the residual plastic deformation is much smaller. Only at low velocity is the BW damage a punched through hole surrounded by small cracks, caused by large chunky fragments. The Advanced Shielding is very effective because the 2nd BS slows down the residual projectile fragments without releasing harmful solid fragments. Therefore, a key feature to understand the overall shielding resistance is the fragmentation process undergone by the projectile upon impact with the 1st bumper. In the following discussion extensive use has been made of the fundamental work (including nomenclature) done by Piekutowsky [5, 6] on the debris clouds. The damage features, from the strike against the 1st BS to the damage on the BW, are discussed using X-ray pictures measurement, evaluation of the damage on Nextel, BW inspection, etc. The measurements on the impacted targets and on the X-ray pictures have not been completed yet and the data reduction is still lacking. The discussion focuses mainly on normal impacts, with a ts/d ratio (i.e., the ratio between the 1st BS thickness and the projectile diameter) ranging from 0.14 to 0.20.

The X-ray pictures of the debris clouds show that for 3 km/s impacts, the projectile is poorly shocked (see Figure 3 right). The mass is concentrated in a central disk-like element composed of large, chunky fragments, with a slow radial expansion during its downrange motion. A rear shell of fragments (spalled from the rear side of the projectile) is clearly visible and the relevant data fit well with the spall failure threshold velocity given by Piekutowsky [6] (see Figure 6). With the increase of the impact velocity to 5 km/s, the projectile fragmentation and spread
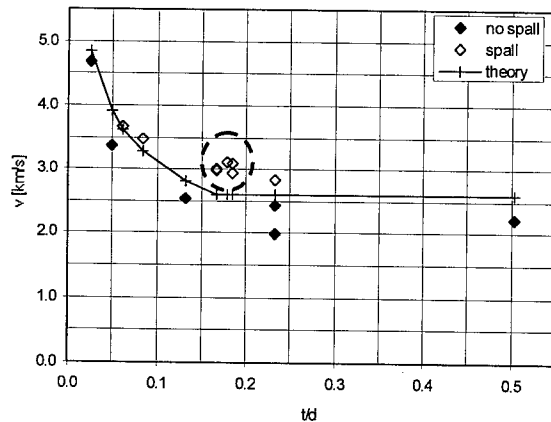
Fig. 6. Impact velocity threshold for projectile spall failure, as a function of the ts/d ratio. Data from this work (within the dashed circle) agree well with the original data [6], even if originated from tests with projectile masses 4 times larger than those used to derive the original data.
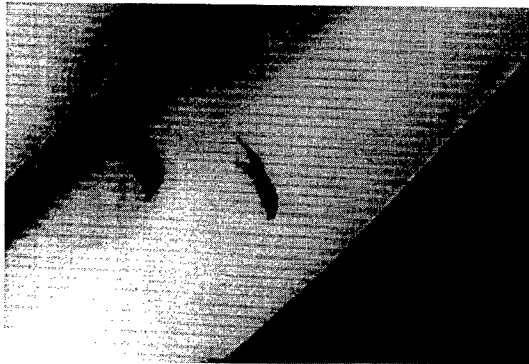
Fig. 7. Triple exposure X-ray picture of experiment 8669, Cone target, 1.60 cm projectile at 6.42 km/s, 45 degrees, ts/d ratio =0.16. Note the ricochet effect.

increases. A front element made of more finely fragmented material starts developing, followed by a denser disk-like element, made of larger chunky pieces. The rear shell is made now of much smaller fragments and is expanding faster. At velocities around 6.5 km/s, the debris cloud has developed a typical "jelly fish" shape (see Figure 3 left). The front element has now a hemispherical shape of molten and finely fragmented material, with some material concentrated in the leading layer. The denser disk-like element is flattened and is bending over during its downrange motion. For oblique angles, the debris cloud emerging from the 1st BS is composed of an outer bubble moving approximately in the direction normal to the bumper and of an internal structure, moving along the flight path of the projectile (see Figure 7). The front element is no longer visible and the center disk-like element is distorted and much less fragmented than for normal impacts. With the increase of the impact angle, the mass seems to be more and more concentrated in the center part made of chunky fragments, the other elements seem to vanish and part of the projectile is ricocheted uprange.

The residual velocities of the front of the cloud between the 1st and the 2nd BS and of the cloud impacting on the BW have been evaluated from the measured X-ray pictures. The residual velocities, normalized with respect to the projectile velocity, VDC1 and VDC3, are plotted as a function of the projectile velocity in Figure 8 for normal impacts. At low velocity, the normalized velocity of the debris cloud front element, VDC1, is around 0.85 and slightly increases with the velocity, up to values around 0.9. The 1st BS is not to slow down the projectile, but acts mostly as a fragmentator. The scattering of the VDC1 values around the regression line is influenced by the ts/d ratio which is not constant for the plotted data, but varies in the range 0.16 – 0.28. The rather high value of the ts/d ratio explains also the lower value of VDC1, when compared to other experiments [6].

The debris cloud fragmentation and composition can be better understood from the analysis of the damage in the Nextel layers. The debris cloud can be divided into two parts: an inner, more massive part able to penetrate the 4 layers of Nextel leaving a through hole and an outer part just able to damage the fibers on the first layer of Nextel leaving a dark trace. The spray angle of the inner (α) and outer (β) parts of the cloud has been reconstructed from the measurements of the through hole and of the dark trace left in the Nextel (see Figure 4). The spray angle for the two parts of the debris cloud is reported as a function of the projectile velocity in Figure 9, for 0-degree impacts on both the Cylinder and Cone configurations. The through hole spray angle (α) and the dark trace angle (β) strongly increase with the impact velocity. From the measurements of the Nextel damage, the average mass density of the inner and outer parts of the debris cloud between the 1st and the 2nd BS can be estimated. The projectile mass has been divided by the area
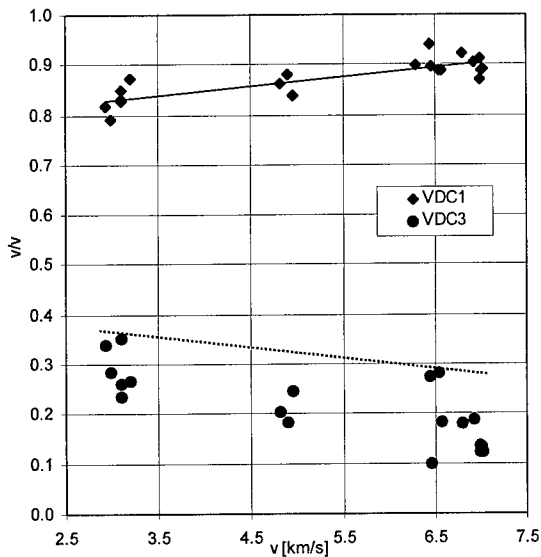
Fig. 8. Residual velocity of the debris cloud between the 1st and the 2nd BS (VDC1, diamonds) and of the cloud impacting on the BW (VDC3, circles) measured from the X-ray pictures. Data for normal impacts, ts/d = 0.16 – 0.28.
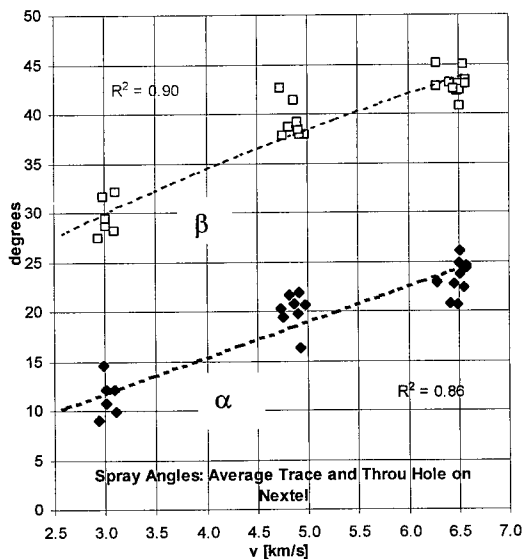
Fig. 9. Spray angle (degrees) for the part of the cloud which penetrates the Nextel mattress (filled diamonds) and for the part which just damages the Nextel external layer (squares) as a function of the velocity (km/s). Cylinder and Cone data, 0 degrees. Scattering of data is enhanced by the ts/d ratio spread from 0.14 to 0.20.

of the dark trace on the Nextel obtaining an estimate of the average mass density of the debris cloud impacting on Nextel. The obtained average mass density per unit area is plotted in Figure 10 as a function of the velocity. In the left graph, only data for the Cylinder configuration, 0-degree impacts are reported. Since most of the tests are close to the ballistic limit, Figure 10 gives an idea of the debris cloud average mass density necessary to perforate the BW. The average mass density decreases sharply with the velocity in the range from 3 to 5 km/s, while from 5 to 6.5 km/s its variation is far less significant. The test data related to impacts causing perforation of the BW are made distinct from the data related to no perforation experiments. The curve fitting the perforation data is slightly above the curve fitting the no penetration data, but the average mass density values of the individual perforation tests do not clearly separate from the no penetration values, as would be expected. Therefore there is no clear difference between the debris cloud with and without enough average mass density to penetrate the complete structure. This means that the penetration is not driven by the average debris cloud density, because a key role is played by the presence of individual solid fragments. In the experimental range, the Nextel and Kevlar layers can greatly reduce the debris cloud velocity, but can not stop all the dangerous fragments. Inspection of the aluminium BW plates shows that when the debris cloud is well fragmented, the BW can be severely deformed but not perforated. Residual plastic deformations in the BW have been measured up to 33 mm (Cylinder) and 38 mm (Cone) without penetration. When fragments are still present in the debris cloud, penetration is obtained with much smaller BW deformations and for much lower debris cloud energy. In the right plot of Figure 10, some data for the Cylinder configuration under oblique impacts are added. The through hole and dark trace in the Nextel are now elliptical. The correlation is worse than 0 degree data alone because of the spread of the data, but the interesting information is that it is even more difficult now to discriminate between perforation and no perforation events. The reason is that for oblique impacts the fragments play an even more important role. Comparing the left with the right plot we can also notice that when oblique angles are inserted, the average debris mass density necessary to penetrate the BW is lower. This is due again to the more important role played by solid fragments for oblique impacts.
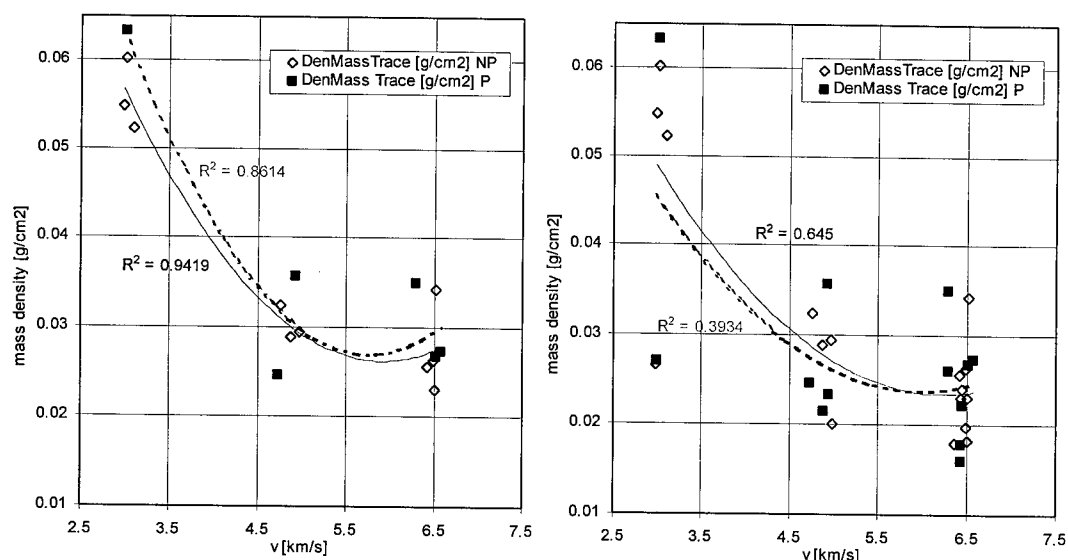
Fig. 10. Debris cloud average mass density between the 1st and the 2nd BS, calculated from the projectile mass and from the damage on the first layer of Nextel. Filled squares are Perforation tests, empty diamonds are No Perforation. The left plot is for normal impacts on the Cylinder; on the right data for oblique impacts have been added.

The velocity of the debris cloud after its impact with the 2nd BS is shown in Figure 8. Since the VDC3 data plotted in Figure 8 are (an estimate of) the lower limit of the velocity, an enveloping curve is drawn in the Figure. The debris cloud velocity drops from 85-95% to less than 35% of the projectile velocity after the impact with the 2nd BS, which acts as an energy absorber, transforming a high velocity impact into a low velocity one and greatly reducing the energy hitting the BW. At 3 km/s, the central larger fragments of the debris cloud hit the 2nd BS (with a normalized velocity of about 0.85), pass through the 2nd BS and hit the BW at very low velocity (below 1 km/s), causing a deep, central crater. These individual fragments can be seen in the X-ray pictures with their effect on the BW. At medium velocity, the cloud is more fragmented, the 2nd BS is strongly delaminated, but some fragments, together with a strong load, pass through it. The impact on the BW is at velocities below 1.5 km/s. Note that the normalized velocity VDC3 decreases with the increase of the velocity: at 5 km/s the fragments are smaller and less concentrated and the 2nd BS is more effective in slowing them down. At higher velocity, the cloud expands and strikes the 2nd BS, causing large holes in the Nextel fabrics and strong delamination in the Kevlar-Epoxy, which are very effective in absorbing the energy and momentum of the well fragmented debris cloud. The BW is impacted by an impulsive load, caused by a finely fragmented/liquid, low density cloud, with velocities below 2 km/s (less than the 30% of the projectile value).

Other Damage Features: Non-monotonic Variation with Impact Angle and Velocity

Analysis has shown that the increase of the projectile velocity increases the debris cloud fragmentation, spread and velocity. For oblique impacts, the projectile shock and fragmentation decreases and the individual fragments become more and more important in the BW damage process. However, this behaviour is not linear and non-monotonic variations of the BW damage with the velocity and the impact angle have been reported. For both the Cylinder and Cone configurations, a "Ballistic Limit interpolation curve" has been built. The masses of projectiles just above and below the penetration threshold (with similar velocity and impact angle) have been added up and averaged. The obtained values have been interpolated to draw a tentative BL curve. This curve is plotted in Figure 11 as a function of the impact velocity, for experiments without MLI. For the Cylinder configuration (left picture), the interpolated BL curve decreases and then increases for 0 and 45-degree impacts, while it increases and then decreases for 30-
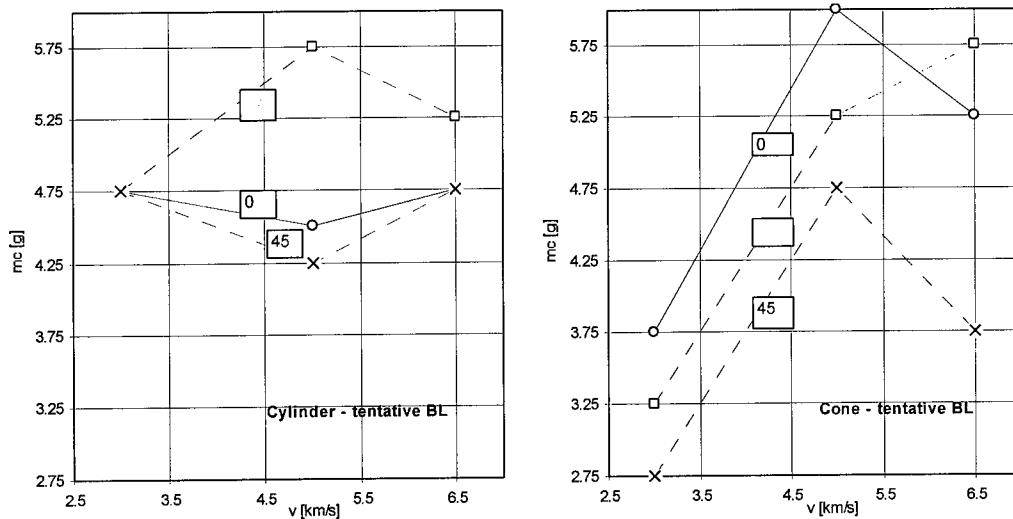
Fig. 11. Interpolated BL curves passing exactly in the middle between Penetration and No Penetration data points. Projectile mass is plotted as a function of the velocity. Circles label 0-degree impacts, squares are for 30 degrees and crosses for 45 degrees. All data are without MLI.

degree experiments. For the Cone configuration, 0 and 45-degree experiments, the curve increases and then decreases, while – for the 30-degree experiments – it increases steadily. Note also that the Cone ballistic capability is worse than the Cylinder at low velocity, while at medium and high velocity it can be worse or better according to the impact angle. This non-monotonic behavior of the ballistic limit is influenced by the data scattering. However, in principle the projectile fragmentation process can explain it: when the impact velocity increases, both the projectile fragmentation (which reduces the projectile lethality) and the fragments energy (increasing the lethality) increase. The effect caused by the impact shock to the projectile is not linear, involving – in sequence – transformations like: beginning of the fragmentation (around 2.6 km/s), incipient melting (around 5 km/s), complete melting (around 7 km/s). Therefore, in the 3 to 6.5 km/s velocity range, the critical mass is expected to show a maximum and a minimum [7]. Oblique impacts are even more complex, because the obliquity modifies both the shock intensity (i.e., the transformation threshold) and the debris cloud spread and trajectory. The maximum and minimum are displaced with respect to the 0-degree experiments and the oscillation of the damage with the velocity seems to be different for every impact angle. Unfortunately, a more detailed description of this phenomenon can be given only with numerous dedicated experiments. Note that the standard ballistic limit equations for Whipple Shields (or for similar structures) [1, 8] give almost invariably a constant increase of the critical diameter with the velocity in the range from 3 to 7 km/s (shatter region).

The non-monotonic variation of the BW resistance with the impact angle is shown in Figure 12, where the projectile momentum is plotted as a function of the impact angle. The curves reported in the figure are tentative damage equations based on simple physical laws, which can not interpolate exactly the experimental data. All the data shown are for the configurations without MLI. For the Cylinder configuration, the ballistic limit is approximately constant in the range 0 - 45 degrees (or better, it seems to improve at 30 degrees for medium and high velocity impact tests). For angles in excess of 45 degrees, the projectile momentum necessary to defeat the structure increases steeply with the angle. For the Cone configuration, the critical momentum decreases with the angle in the range 0 – 45 degrees (with some oscillation) and then increases steeply for 60-degree impacts. The usual ballistic limit curves for Whipple Shields (or for similar structures) [1, 8] predict a steady growth of the critical mass with the increase of the impact angle. The oscillation of the projectile lethality with the angle can be understood in principle considering the variation of the shock pressure induced in the projectile and the projectile fragmentation effects. However, a more detailed explanation cannot be given at present. Note the

excellent resistance of both the configurations against 60-degree impact. At this angle, part of the projectile is ricocheted (see also Figure 7), a smaller amount of mass reaches the 2nd BS and the 2nd BS and the BW have to resist large chunks of material at very low velocity.
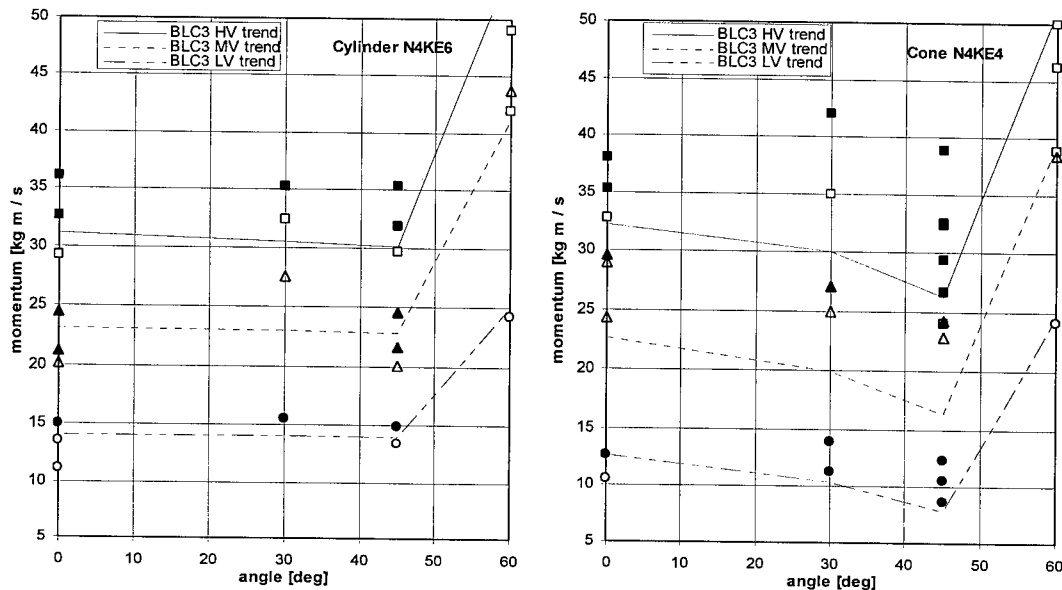
Fig. 12. Critical projectile momentum [kg m/s] as a function of the impact angle [degrees]. Filled symbols are for Penetration experiments, void symbols for No Penetration. Circles are for LV, triangles for MV, Squares for HV. All data refers to tests without MLI. Tentative damage equations based on simple physical laws are plotted.

Comparison with NASA Stuffed Whipple

The development of the Columbus Advanced Shields just followed the development of the Stuffed Whipple Shielding used to protect the American modules [1]. The Columbus configuration, which was at the beginning quite different from the NASA Stuffed Whipple, became quite similar with the increase of the pressure shell thickness and with the introduction of the Nextel fabric. This explains the attention paid to the activities performed in the USA. The damage formulae [1] published for the NASA SW are based on LGG experiments performed at NASA mainly on scaled targets, i.e., experiments performed with smaller projectiles on targets with reduced geometric dimensions. More recent experiments have been performed by NASA (using the LGG available at Ames which is able to fire very large projectiles) on full scale Stuffed Whipple targets [9]. The experimental results obtained are reported in the plot of the projectile momentum versus the impact angle shown in Figure 13: the evolution of the ballistic limit with the impact angle is almost constant from 0 to 45 degrees and then increases from 45 to 60 degrees. This evolution of the damage with the
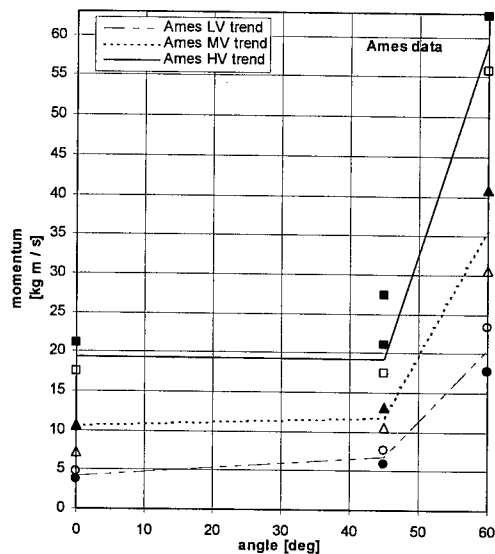
Fig. 13. Ames test data: projectile momentum [kg m/s] versus impact angle [degrees]. The interpolant curves are to show the trend. Circular symbols and da-dotted lines are LV data, triangles and dashed lines are MV, squares and solid lines are HV. Filled symbols are for Penetration, empty symbols are for No Penetration.

angle is very similar to the one reported for the Columbus Advanced Shields AS-N4KE6 in Figure 12. Boeing [9] has proposed modifications to the original SW ballistic curves [1] which make the curves rather conservative. In Figure 14, the Ames test data are plotted together with the SW curves modified by Boeing [9] and the Columbus Cylinder data. The two sets of experimental results seem to be quite similar with a shift towards larger critical masses for the Columbus data points. The AS has a higher areal density than NASA MOD-2, but has better performances (i.e., a large critical mass) in the whole experimental range, from 3 to 6.5 km/s and for 0, 45 and 60 degree impact angles.
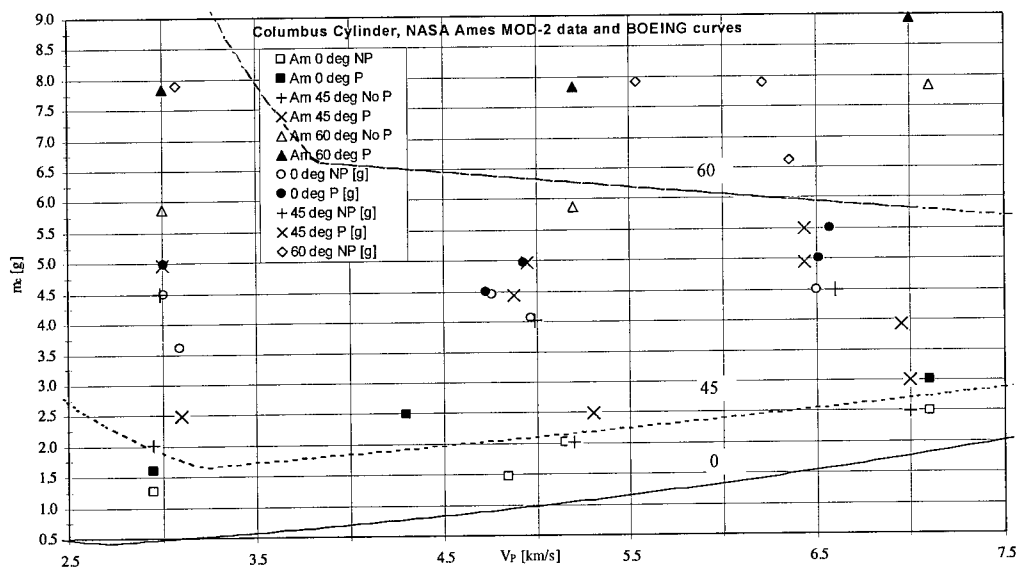
Fig. 14. Test data for the SW obtained at Ames, compared with the Columbus AS-N4KE6 test results. The critical mass [g] is plotted versus the projectile velocity [km/s]. Note that at 6.5 - 7 km/s the Ames ballistic limit is about 2.75 g, while for the AS is around 4.75 g without MLI and above 5.5 g with MLI. The ballistic limit curves for the NASA SW modified by Boeing are also reported for 0, 45 and 60 degrees.

Ballistic Limit Curves for the Columbus Module

Tentative ballistic limit curves have been developed for the Advanced Shields for a preliminary damage assessment. The damage equations have been adapted from NASA Stuffed Whipple curves [1] with some modifications, but are still based on simple laws of physics and are kept as simple as possible. In the following, d_c is the critical diameter [cm], v_p is the projectile velocity [km/s], α is the impact angle from the normal, c_{lv} and c_{hv} are coefficients. The damage equations are based on the following considerations.

- For normal impacts, at low velocity ($v_p < 2.7$ km/s, close to the projectile spall threshold) the damage is proportional to projectile kinetic energy: $d_c = c_{lv} \, v_p^{-2/3}$.
- For normal impacts at high velocity ($v_p > 6.5$ km/s, close to the uni-dimensional complete melting threshold) the damage is proportional to projectile momentum: $d_c = c_{hv} \, v_p^{-1/3}$.
- In the complete velocity range, the damage is assumed to be constant with the impact angle for angles below or equal to 45 degrees (Cylinder configuration). For angles higher than 45 degrees, the damage starts decreasing and a cosine power factor is set to be consistent with 60-degree LGG test data. Note that the oscillations of the damage in the range 0 – 45 degrees could not be modeled.
- In the intermediate velocity range (2.7 - 6.5 km/s) it was not possible to model the oscillations reported in the experiments and therefore the damage is given by a linear interpolation between low and high velocity formulae.
- The threshold between the low and intermediate velocity region shifts with the angle according to the formula $v_{LV} = 2.7 \bullet \cos(\alpha)^{-0.5}$. The threshold between the intermediate and high velocity region

increases with the angle according to the formula $v_{LH} = 6.5 \bullet \cos(\alpha)^{-0.33}$.
- The shifting of the low-high velocity thresholds with the angle make the formulae discontinuous. A correction factor is inserted in both the low and high velocity formulas to re-establish the continuity.

The damage formulae derived with this approach for the Advanced Shields are far from being perfect, as can be seen in Figures 5 and 12, for the Cylinder configuration. The equation fits the low and high velocity data quite well, but is too optimistic at medium velocity: this is due to the impossibility to model the oscillations with the velocity. Also the oscillations with the angle from 0 to 45 degrees are not modeled (see the 30-degree high velocity fit). Note that when the MLI data are considered, the curves are always on the safe side.

CONCLUSIONS

An extensive Light Gas Gun test campaign has shown the 3-wall debris shielding for the European module Columbus to have very good ballistic capabilities. Advanced Shields with an intermediate bumper of Nextel and Kevlar are able to resist impacts with aluminium spheres of 4.5 – 5.0 g with velocities between 3 and 6.5 km/s and impact angles from 0 to 45 degrees. For 60-degree impacts, the ballistic limit is above 8.0 g for all the velocities tested.

The analysis of the impacted targets and of the X-ray pictures taken of the debris cloud has shown that large solid fragments in the debris cloud represent the severer threat to the rear wall integrity. In the velocity range experienced, kinematic quantities describing the average properties of the debris cloud cannot be used to predict the rear wall failure threshold because of the key role played by the individual fragments. As a consequence of this damage mechanism, the ballistic limit shows non-monotonic variations in the 3 – 6.5 km/s range. The impact angle has a strong influence on the projectile shock and fragmentation process, causing oscillations in the rear wall damage in the 0 – 45 degree range. Dedicated, high accuracy experiments are necessary to investigate these mechanisms, which were impossible in the present tests performed to determine the ballistic limit of debris shielding for a space module.

REFERENCES

1. E. L. Christiansen, J. L. Crews, J. E. Williamsen, J. H. Robinson and A. M. Nolen, Enhanced meteoroid and orbital debris shielding. *Int. J. Impact Engng.*, **17**, (1995).
2. E. Schneider and A. Stilp, Meteoroid/debris simulation at Ernst-Mach-Institut (EMI). *Proc. First European Conference on Space Debris*, pp. 401-404, April 5-7, Darmstadt, Germany (1993).
3. R. Destefanis and M. Faraud, Testing of advanced materials for high resistance debris shielding. *Int. J. Impact Engng.*, **20**, 209-222 (1997).
4. E. Beruto, R. Destefanis, M. Faraud and P. Buchwald, High resistance debris shielding development for the Columbus Orbital Facility. *Proc. Second European Conference on Space Debris*, pp. 509-517, March 17-19, Darmstadt, Germany (1997).
5. A. J. Piekutowsky, Characteristics of debris cloud produced by hypervelocity impact of aluminum spheres with thin aluminum plates. *Int. J. Impact Engng.*, **14**, 573-586 (1993).
6. A. J. Piekutowsky, Formation and description of debris clouds produced by hypervelocity impact. *NASA Report 4707* (1996).
7. C. E. Anderson, Jr., T. G. Trucano and S. A. Mullin, Debris cloud dynamics. *Int. J. Impact Engng.*, **9**(1), 89-113 (1990).
8. E. L. Christiansen, Performance equations for advanced orbital debris shielding. *AIAA Paper* (1992).
9. D. R. Williamsen, Structural analysis report: meteoroid and orbital debris protection system performance. Boeing D683-10505-15 (1997).

THE IMPACT OF LONG RODS INTO SPACED-PLATE ARRAYS

DAVID L. DICKINSON and LEONARD T. WILSON

Naval Surface Warfare Center Dahlgren Division, Dahlgren, VA 22448-5100

Summary–The penetration equations of the FATEPEN2 engineering code have been updated to include behavior of large length-to-diameter ratio rods into spaced plate arrays. The changes were validated with light-gas gun experiments conducted at the Naval Research Laboratory to determine the effects of pitch and yaw on long-rod penetration. These experiments were modeled using the CTH hydrocode to simulate rod impact and interaction with the plate array. Numerical and experimental data for three tests were compared directly, and the discrepancies were analyzed. The analysis led to the conclusion that problem resolution is critical to the success of the calculations. © 1999 Elsevier Science Ltd. All rights reserved.

INTRODUCTION

Engineers and scientists use the FATEPEN2 engineering code [1] to predict fragment and projectile penetration into spaced-plate arrays. Because of its wide usage, FATEPEN2 is under almost constant improvement [2]. One of the most recent updates has extended FATEPEN2's penetration equations to include the behavior of large length-to-diameter (L/D) ratio rods. The late Dr. Andrew Williams conducted eight light-gas gun experiments at the Naval Research Laboratory (NRL) in order to validate these new equations with experimental data. The primary objective of these experiments was to determine the effect of rod pitch and yaw on rod penetration.

In these NRL experiments, tungsten alloy rods with L/D ratios of approximately 37.5 were fired into spaced arrays of three 0.635-cm-thick 4140 steel plates. A sabot tip deflector was used to control pitch and yaw of the rods. Pitch and yaw values ranged from 0 to approximately 10°. Impact velocities were on the order of 2.25 km/s. The standard test set-up is shown in Figure 1. Flash radiography was used to track the projectiles as they progressed through the plate arrays, and the data were then used to determine projectile erosion and fracture as the rods penetrated the plates.
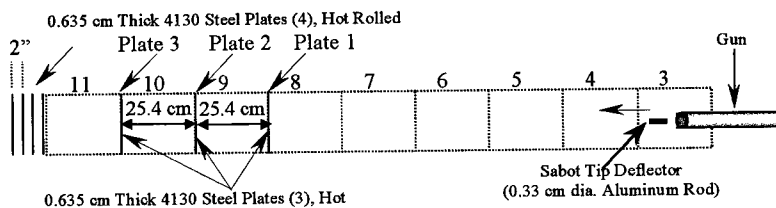
Fig. 1. Experimental Set-up.

In conjunction with the NRL plate array experiments, the CTH hydrocode was used to simulate rod impact and interaction with the plate array [3]. In this modeling effort, the Johnson-Cook constitutive and damage models were used to simulate the rod material.

Parameter values for the models were taken from Table 2 on page 210 of reference 4. The steel plates were modeled using an elastic-perfectly plastic assumption. The Mie-Grüneisen equation of state (EOS) was used to describe the volumetric response of all materials. Because of the three-dimensional nature of the impact conditions, the simulations were primarily performed using a 64-node Origin 2000 system resident at NSWCDD. Problem sizes varied from 13 to 38 million zones. Run times were on the order of 5 to 10 days.

This paper serves two major purposes. First, it presents the results of the eight NRL experiments to provide insight into the penetration of spaced-plate arrays by tungsten alloy long rods. Second, it highlights the difficulty in modeling even relatively simple experiments when material failure is present.

We begin with the NRL experimental data that quantifies projectile erosion and breakup. Following the presentation of the experiments, we will discuss the modeling effort. This discussion will center on three tests, where the experiments and their simulations are compared directly. Finally, we will discuss possible explanations for discrepancies between the experimental and numerical results.

EXPERIMENTAL RESULTS AND THEIR DISCUSSION

Table 1 summarizes the characteristics of the rods in terms of their initial impact conditions, geometries, and break up as they progressed through the target array.

Table 1. Summary of Experiments.

TEST	ROD LGTH.	ROD DIA.	INITIAL PITCH	INITIAL YAW	INITIAL VEL	FRACTURE PLATE 1	PLATE 2	PLATE 3
724	15.10 cm	0.406 cm	3.6° Up	1° Right	2.23 km/s	NO	NO	YES
725	15.05 cm	0.406 cm	9.2° Up	0.3° Left	2.25 km/s	YES	NO	YES
726	15.04 cm	0.404 cm	8.2° Up	0.1° Right	2.23 km/s	NO	YES	YES
727	15.00 cm	0.404 cm	0°	2.6° Left	2.24 km/s	NO	NO	YES
728	15.14 cm	0.406 cm	0.1° Up	0°	2.19 km/s	NO	NO	NO
730	15.15 cm	0.406 cm	4.7° Up	0.6° Left	2.23 km/s	NO	NO	YES
731	15.07 cm	0.407 cm	6.9° Up	1.7° Left	2.27 km/s	NO	YES	YES
732	15.00 cm	0.406 cm	3.5° Up	0.4° Left	2.25 km/s	NO	NO	YES

Looking at Table 1, two observations stand out. First, only one rod fractured as it was penetrating the first plate. This was seen in Test 2-725 (Figure 4) where the rod was pitched up 9.2°. Conversely, only one rod penetrated the entire array without breaking. This occurred in Test 2-728 (Figure 7) where the pitch was less than 0.1°. Note also that in five out of the eight experiments, plate 3 induced the initial fracture in the rods. In the other three cases, plate 3 caused further failure of previously damaged rods. These results are summarized in Figure 2.
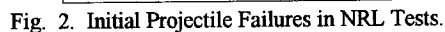
Fig. 2. Initial Projectile Failures in NRL Tests.

Radiographs from the eight experiments are shown in Figures 3 through 10. Note that each figure presents rod residual lengths. Because the target plates were relatively thin, velocity loss as the rods penetrated the array was minimal. Therefore, we have omitted these measurements. Notice in particular Figures 4 and 5 which summarize the results of Tests 2-725 and 2-726. In the first test, the rod had a pitch of 9.2° and broke as it passed through the first plate. In Test 2-726 a pitch of 8.2° resulted in no rod fracture in plate 1. Figures 8 (Test 2-730) and 9 (Test2-731) show similar results for the case of inducing fracture as the rod penetrates plate 2.

Pitch Plane   Yaw Plane
(a) Rod after Plate 1

Pitch Plane   Yaw Plane
(b) Rod after Plate 2

Yaw Plane
(c) Rod after Plate 3

Position in Target Array	Rod Residual Length
Plate 1	143.9 mm
Plate 2	135.0 mm
Plate 3 Piece A	28.4 mm
Plate 3 Piece B	24.8 mm
Plate 3 Piece C	58.0 mm

Fig. 3. Test 2-724.

Pitch Plane   Yaw Plane
(a) Rod after Plate 1

Pitch Plane   Yaw Plane
(b) Rod after Plate 2

Pitch Plane   Yaw Plane
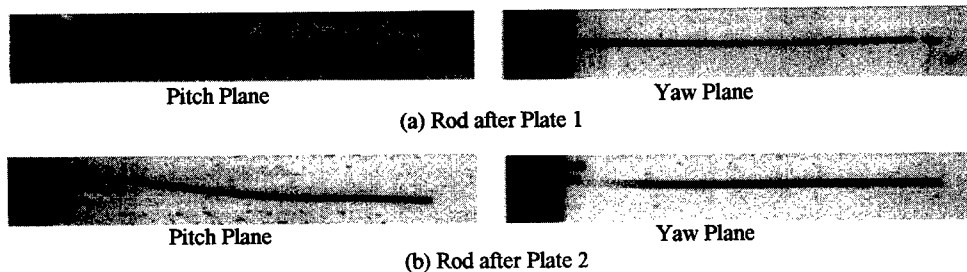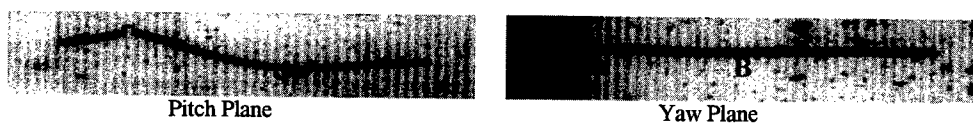
(c) Rod after Plate 3

Position in Target Array	Rod Residual Length
Plate 1 Piece A	137.0 mm
Plate 1 Piece B	7.4 mm
Plate 2	108.4 mm
Plate 3 Piece A	18.2 mm
Plate 3 Piece B	83.1 mm

Fig. 4. Test 2-725.

Pitch Plane   Yaw Plane

(a) Rod after Plate 1

Pitch Plane   Yaw Plane
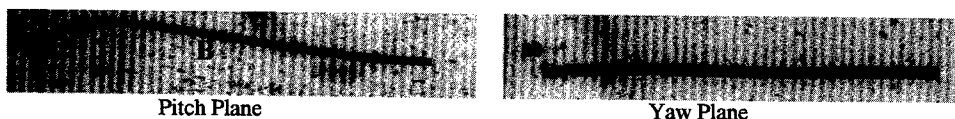
(b) Rod after Plate 2

Position in Target Array	Rod Residual Length
Plate 1	143.0 mm
Plate 2 Piece A	8.7 mm
Plate 2 Piece B	118.8 mm

Fig. 5. Test 2-726.

(a) Rod after Plate 1

Pitch Plane   Yaw Plane

(b) Rod after Plate 2

Pitch Plane   Yaw Plane

(c) Rod after Plate 3

Position in Target Array	Rod Residual Length
Plate 1	143.0 mm
Plate 2	134.9 mm
Plate 3 Piece A	39.5 mm
Plate 3 Piece B	31.2 mm
Plate 3 Piece C	56.8 mm

Fig. 6. Test 2-727.

Pitch Plane
(a) Rod after Plate 1

Pitch Plane
(b) Rod after Plate 2

Pitch Plane
(b) Rod after Plate 3

Position in Target Array	Rod Residual Length
Plate 1	143.8 mm
Plate 2	135.5 mm
Plate 3	127.6 mm

Fig. 7. Test 2-728.

Pitch Plane   Yaw Plane
(a) Rod after Plate 1

Pitch Plane   Yaw Plane
(b) Rod after Plate 2

Pitch Plane   Yaw Plane
(c) Rod after Plate 3

Position in Target Array	Rod Residual Length
Plate 1	143.6 mm
Plate 2	134.0 mm
Plate 3 Piece A	40.4 mm
Plate 3 Piece B	63.9 mm

Fig. 8. Test 2-730.

Pitch Plane   Yaw Plane
(a) Rod after Plate 1

Pitch Plane   Yaw Plane
(b) Rod after Plate 2

Pitch Plane   Yaw Plane

(c) Rod after Plate 3

Position in Target Array	Rod Residual Length
Plate 1	142.1 mm
Plate 2	113.1 mm
Plate 3 Piece A	87.8 mm
Plate 3 Piece B	8.1 mm
Plate 3 Piece C	11.0 mm

Fig. 9. Test 2-731.
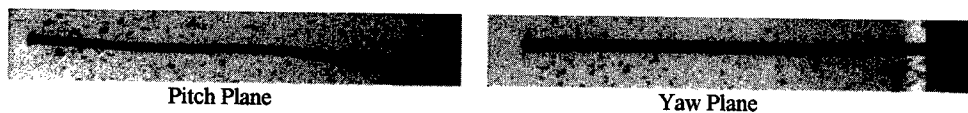
Pitch Plane   Yaw Plane

(a) Rod after Plate 1

Pitch Plane   Yaw Plane

(b) Rod after Plate 2

Pitch Plane

(c) Rod after Plate 3

Position in Target Array	Rod Residual Length
Plate 1	No Data
Plate 2	134.2 mm
Plate 3 Piece A	63.4 mm
Plate 3 Piece B	65.5 mm

Fig. 10. Test 2-732.

As can be seen, the results are quite fascinating.   Although 7 of the 8 experiments resulted in rod fracture, each broken rod remains a potent fragment for subsequent target elements since little shattering occurs. Analysis using FATEPEN2 shows that had these rods been compact fragments (L/D of perhaps 1) it is likely that they would have shattered penetrating the first plate.   Also, even highly deformed rods continued penetrating the plate array without any trajectory instability.

MODELING EFFORTS

Having discussed the experimental results, let's address the modeling effort. Again, as discussed in the introduction, we used the Johnson-Cook constitutive and failure models

for the rods. All eight of the experiments were modeled. However, we will discuss only three: Test 2-728, Test 2-732, and Test 2-731. These three tests were chosen because they demonstrate an increasing level of modeling complexity.

Test 2-728 is instructive because the impact conditions (minimal pitch and yaw of the rod) allowed us to use an axisymmetric assumption for the calculations. This meant we could perform highly resolved calculations-there were 8 cells through the rod for this calculation- using a standard SGI workstation with an R10000 processor. This test was also the only experiment where no fracture occurred. Figure 11 shows the results of our calculation as the rod exits the third plate. The radiograph from the experiment is shown for comparison.

(a) CTH Calculation   (b) Radiograph

Fig. 11. Experiment 2-728 Results.

As can be seen, the calculation suggests that the rod is internally damaged but intact. These results are consistent with the radiographic evidence. Note the calculated residual length was 13.3 cm, and the measured residual length was 12.8 cm; the difference between the experimental and numerical results is about 4%. Thus, the agreement between the simulation and experimental results can be considered reasonably good for this case.

The level of modeling complexity increased for Test 2-732. Due to the 3.5° pitch and 0.4° yaw, an axisymmetric assumption could not be used. Instead, a half plane of symmetry was used since it was assumed that the 0.4° yaw had a negligible effect on the projectile's definition. The validity of this assumption is verified in Figure 10, which shows little deformation occurs in the yaw plane.

Figures 12 through 14 compare radiographs and calculations of Test 2-732. These calculations were performed using 32 nodes of an Origin 2000 system. The problem size was approximately 13 million cells. There were 6 cells through the rod diameter. Looking at Figure 12, we can see that the CTH results qualitatively match the experimental results. However, Figures 13 and 14 show that this agreement lessens with subsequent impacts. At the projectile's exit of the second plate, the simulation shows that the rod has broken into three pieces when, actually, the rod is bent but intact. Referring to Figure 14, fracture does occur after the projectile perforates the third plate, but even here there are only two pieces.

(a) CTH Results   (b) Radiograph
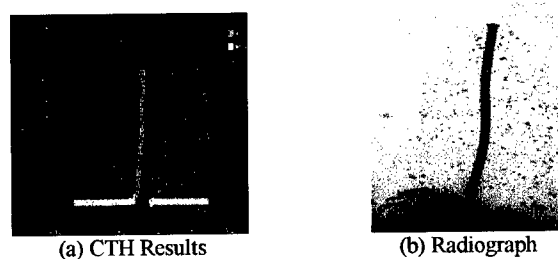
Fig. 12. Test 2-732 - Projectile after First Plate Impact.
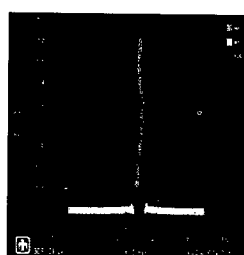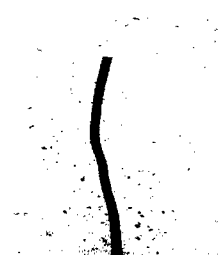
(a) CTH Results   (b) Radiograph
Fig. 13. Test 2-732 - Projectile after Second Plate Impact.
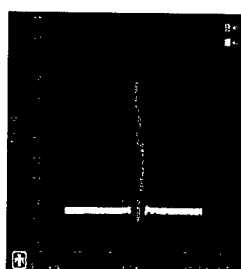
(a) CTH Results   (b) Radiograph
Fig. 14. Test 2-732 - Projectile after Third Plate Impact.

From this discussion, it is clear that our simulations reasonably predicted the outcome of a single plate impact. However, our treatment of multiple plate impacts is less accurate.

The complex impact conditions in Test 2-731 required a fully three-dimensional treatment. Figures 15 through 17 summarize our calculations. Note that the problem resolution was reduced to 4.5 cells through the rod diameter. Note the similarity of the results to those found for Test 2-732. Also note the trend toward decreasing resolution as the degree of freedom increases.
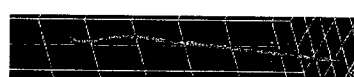
Fig. 15. Test 2-731 - After First Plate Impact.
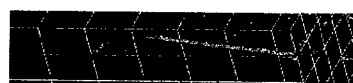
Fig. 16. Test 2-731 – After Second Plate Impact.

Fig. 17. Test 2-731 – After Third Plate Impact.

As is evident from Figures 15 through 17, the quality of the simulation breaks down with each successive plate impact. Each figure shows that the amount of rod bending is under predicted in the CTH calculations. The amount of rod fracture is over predicted in CTH calculations in Figure 16. However, in Figure 17 the shape of the rod is similar for both the experiment and simulation. As was the case for Test 2-732, the modeling results may allow an analyst to make some qualitative predictions of rod performance, but quantitative predictions using CTH would be less dependable.

CORRELATION OF EXPERIMENTAL AND NUMERICAL RESULTS

We will now discuss the discrepancies between the modeling and experimental results. Most of what follows is speculation. Keep this in mind as we "give an air of scientific impartiality to biased judgements"[5].

There are several possible explanations for the discrepancies between the modeling and the experimental results. The first explanation centers on the resolution used in the problem. As we have shown, computer limitations mean that, as geometric degrees of freedom increase, problem resolution decreases. We have examined the effect of resolution for Test 2-732, and the results are shown below in Figures 18 through 20. Hertel of Sandia National Laboratories (SNL), as part of a benchmarking exercise, performed these calculations using 304 processors on an SNL computer [6]. The rod was modeled using 10 zones across the diameter.
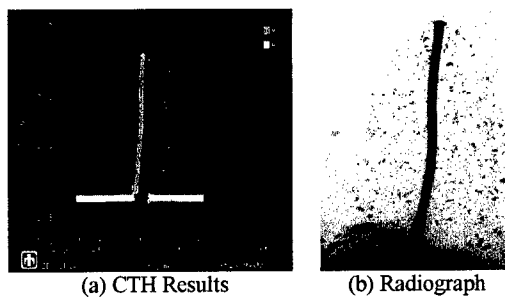
(a) CTH Results   (b) Radiograph
Fig. 18. Test 2-732 – Effect of Problem Resolution (Plate 1).
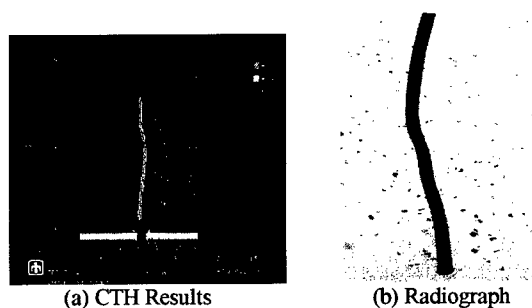
(a) CTH Results   (b) Radiograph
Fig. 19. Test 2-732 – Effect of Problem Resolution (Plate 2).
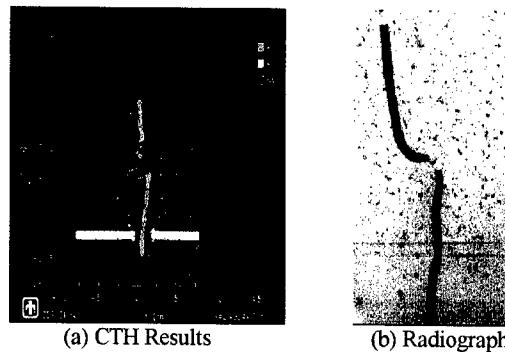
(a) CTH Results   (b) Radiograph
Figure 20. Test 2-732 – Effect of Problem Resolution (Plate 3).

Comparing to the results show in Figures 12-14, it is apparent that using higher resolutions have greatly improved our results, but basic agreement is still lacking. Notice the slope of the rods as they exit the plates in Figure 19. Also, note in Figure 20 that the rod has broken in the wrong place. Therefore, problem resolution alone does not account for all the discrepancies between the calculations and experiments.

The second explanation is that the material parameters used in the analyses are not appropriate for the tungsten alloy used in the experiments. For example, we have used a conservative value for the material spall strength of approximately 1 GPA. We have also used CTH default values for thermal softening. Based upon our interpretation of the results, we do not feel that this is significant. Yet, these properties are unknown. Although similar to alloys for which published data exists, the tungsten alloy used in the experiments is slightly different. More significantly, we have chosen to use the default values for the damage parameters. These have not been measured for this particular tungsten alloy. All in all, we cannot positively state that we have properly treated the rod material.

Accordingly, it was suggested during the peer review process, that we "turn off" the Johnson-Cook damage model and rerun the simulation for Test 2-732. We did this and found that the calculation still did not agree with the experiment. The results for plates 1 and 2 are shown in Figure 21.
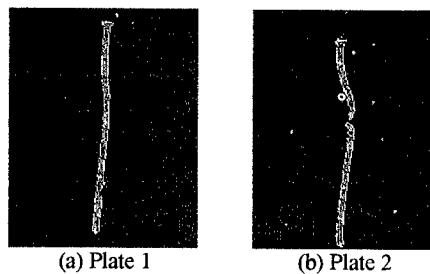
(a) Plate 1   (b) Plate 2
Fig. 21. Test 2-732 Simulation with Damage Model
Not Included in the Calcualtion.

Comparing these results to Figures 12 and 13, as well as to Figures 18 and 19, the reader can see that the damage model has not significantly affected the results.

This result may add credence to our final explanation for the discrepancies between the calculations and test results which is that the Johnson-Cook constitutive and damage models may not be appropriate for modeling the dynamic failure occurring during these experiments. Admittedly, we cannot conclusively prove this assertion. However, light-gas gun and split-Hopkinson Bar experiments conducted at NSWCDD have shed further light on the tungsten rod material properties [2]. Sample results from these experiments are shown in Figure 22.

(a) Specimen from a Flyer Plate   (b) Stress History from a Split Hopkinson
Experiment   Bar Experiment
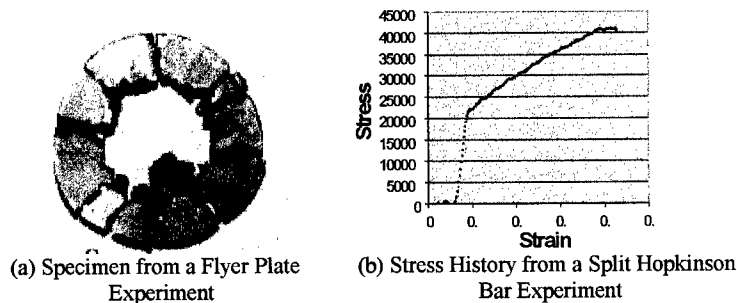
Fig. 22. Flyer Plate and Split Hopkinson Bar Testing Results.

In the flyer plate experiment which produces a state of uniaxial strain, the disk was subjected to a pressure load of 16 GPA at a plastic strain rate of 70,000 s^{-1}. As can be seen in Figure 22 (a), the disk was heavily fractured. The measured strain-to-failure was about 10%. On the other hand, the split Hopkinson bar results shown in Figure 22 (b) indicate a ductility of almost 40% at a strain rate of $6000s^{-1}$. Note, that in the Hopkinson bar experiment a state of uniaxial stress is produced in the material sample. Obviously, loading rate and the state of stress influence the response of the material. Note, in our calculations of the plate impact experiment using published values for the Johnson-Cook constitutive and failure models, the simulation did not predict the failure mode seen in the experiment. Hence, it is not clear that the Johnson-Cook models are allowing us to adequately simulate response of the Tungsten alloy.

Calculations show that loading rates in the rod will vary across a wide spectrum, ranging from several hundred thousand per second at first impact, to several hundred per second at the rear of the rod. In several of the experiments, it is the tip of the rod that breaks. In this area, strain rates exceed those seen in the flyer plate experiment. Since our calculations did not consistently reproduce these failure modes, we feel the Johnson-Cook model is not replicating the loading effects seen in Figure 22 (a). At the same time, it should not be expected to since the model parameters are developed at relatively low strain rates. Another failure model commonly seen in the experiments is breaking at the middle of the rod after a large amount of bending. Here, the loading rates approximate those found in the Hopkinson Bar experiment. Yet, these failures were not reproduced in the model.

CONCLUDING REMARKS

In this paper we have presented the results of eight long rod experiments. The results of these experiments should provide researchers insight into the penetration mechanics that underlie long rod penetration into spaced-plate arrays. We have also presented the results of our modeling effort. From this we have drawn the following conclusion: problem resolution has a dramatic effect upon the outcome of the calculation. Based upon our effort, we would recommend at least 8 cells through the rod in an Eulerian calculation. This level of resolution will require parallel computer architectures for running these calculations. Our efforts have also led us to question the ability of the Johnson-Cook constitutive and failure models to predict the dynamic failure of the rod. However, enough uncertainty exists in the actual rod material properties to prevent us from stating that the discrepancies seen between the calculation and experiments are due to shortcomings in the Johnson-Cook failure model.

REFERENCES

1. J. D. Yatteau; R. H. Zernow; R. F. Recht, Compact Fragment Multiple Plate Penetration Model, *FATEPEN 2 Computer User's Manual*, **2**, Applied Research Associates for Naval Surface Warfare Center, Dahlgren, VA January (1991).

2. L. T. Wilson; E. S. Hertel; D. L. Dickinson, The Impact of Tungsten Long Rod Penetrators into Water Filled Targets, Proceedings of the *17ᵗʰ International Symposium on Ballistics*, Midrand South Africa, March (1998).

3. E. S. Hertel; R. L Bell; M. G. Elrick; A. V. Farnsworth; G. I. Kerley; J. M. McGlaun; S. V. Petney; S. A. Silling; P. A. Taylor; and L. Yarrington, CTH: A Software Family for Multi-Dimensional Shock Physics Analysis, Proceedings of the *19th International Symposium on Shock Waves*, **1**, pages 377-382, Marseilles, France, 26-30 July (1993).

4. J. A. Zukas, Editor, High Velocity Impact Dynamics, John Wiley and Sons, Inc., (1990).

5. G. Orwell, Politics and the English Language, printed in Quaternion Stories, Poems, Plays, Essays; J. M. Mellard, (1978).

6. L. T. Wilson; E. S. Hertel; L. Schwalbe; C. Wingate, Benchmarking the SPHINX and CTH Shock Physics Code for Three Problems in Ballistics, Proceedings of the *17ᵗʰ International Symposium on Ballistics*, Mid Rand South Africa, March (1998).

ABOUT THE STATE OF TWO—METAL CONTACT BOUNDARY AT A HIGH—VELOCITY OBLIQUE IMPACT

OLEG B. DRENNOV

Russian Federal Nuclear Center, All –Russian Scientific Research Institute of Experimental Physics,
Mira ave.37, Sarov, Russia, 607190

Summary – The character of disturbance development on a contact boundary of metal layers at a constant impact angle, γ, but at a varying velocity v_c of a contact point was investigated.

Velocity v_c growth in a subsonic regime leads to a loading pressure and elastic shear deformation intensity increase. Disturbance amplitude grows. At critical velocity v_c values for individual metal pair, characterizing a transition from subsonic to supersonic flux, a disturbance amplitude reaches maximum. A further velocity v_c growth is accompanied by disturbance amplitude decrease. In this oblique impact regime the disturbance are formed under Kelvin – Helmholtz instability development.

An analytical relation for disturbance amplitude on contact boundaries of different metal pairs and their strength properties (dynamic strength yield) was proposed. © 1999 Elsevier Science Ltd. All rights reserved.

INTRODUCTION

In dynamic investigations of solid under high pressures two loading types are usually used – by normal or oblique shock wave. As opposed to the case of normal shock wave loading, the discription of elastic and wave processes under an oblique shock wave is complicated by the necessity of normal as well as tangential components account in stress tensor [1].

Under an oblique impact of metal layers (one of the ways to realise a loading by oblique shock waves) in a contact zone, intensive shearing deformations develop, preboundary layers of materials become strongly heated, cumulative jets might occur. The effects mentioned result in profile deterioration of metal contact boundary after an impact. Regular disturbances (waves), non – symmetric disturbances (distorted waves), melting layers of mixed component originate. In certain cases such disturbances' development result in firm bonding of samples, i.e. explosion welding [2-4].

In special literature a subsonic regime of an oblique impact, $v_c < c_0$, is investigated in detail (v_c – a contact point velocity; c_0 – sound velocity in a given material). Under such loading conditions a cumulative jet is constanly formed in a contact point [2-4]. Well investigated is a coupling of disturbance development character on a contact boundary with the parameters, defining the loading conditions: thickness and material of impacting plates (δ, ρ), thickness and composition of high explosive (HE)(δ_{HE}, ρ_{HE}), collision angle (γ) and so on [2-4].

Sample collision at the velocities, exceeding a sound velocity ($v_c \geq c_0$), is described in analogy with the description of supersonic flux, flowing over a wedge [1]. For a constant collision angle ($\gamma \approx$ const) a critical value of a contact point velocity v_{cr} exists. At $c_0 \leq v_c \leq v_{cr}$, detached shock waves are formed in a flux. Crossing a shock wave front, the supersonic flux transforms into a subsonic one. To a contact point both fluxes (a flying and a fixed plates in a

coordinate system, connected with a contact point) come at a sound velocity, in a collision zone cumulative jet is formed. At $v_c > v_{cr}$, attached shock waves are established in a contact point. They turn the fluxes at an angle, approximately equal to a collision angle. A jet formation is impossible in such a regime, and an explosion welding as well [1, 2]. A contact boundary state of the materials under such supersonic oblique impacts is not investigated practically.

EXPERIMENTAL SCHEME

The present paper is devoted to the experimental investigation of contact boundary state of metal layers under various regimes of oblique impacts (contact point velocities v_c), but at a constant loading angle γ. In the tests a traditional scheme of plate casting was used in the regime of HE charge sliding detonation, see Fig.1.
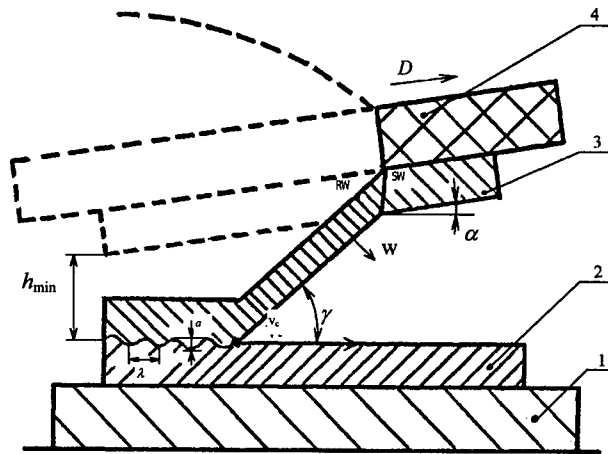
Fig.1. Test arrangment scheme

A fixed plate (2) is mounted on a massive steel base (1). About it, at a given angle α, a casting plate (a striker) (3) is mounted, accelerated by explosion products of HE charge (4), where a plane sliding detonation wave is realized. Minimal distance between the plates, h_{min}, is selected, minding the stationarity of a striker flight before the impact [5]:

$$h_{min} \geq (3\text{-}5)\ \delta_{st} , \tag{1}$$

where:

h_{min} – minimal distans between the plates,

δ_{st} – a striker thickness.

In Fig.1 characteristic parameters, defining an oblique impact, are noted.

D – HE charge detonation velocity;

w – striker flight velocity;

v_c – a contact point velocity;

α – an initial angle of plates' tilting;

γ – an angle of plates' impact;

SW – shock wave front;

RW – head characteristic of a rarefaction wave;

a, λ – amplitude and length of realizing disturbance wave, (welded joint parameters).

After dynamic loading the plates were caught. Out of the sample middles fragments for microsections were cut (usually a fixed plate was used). A section of a contact boundary was studied, which is parallel to the contact point movement. Sample structure in a boundary zone was revealed by etching the surfaces of interest. The most characteristic section parts were investigated and photographed by a metallographic microscope NEOPHOT – 2.

It is known from work [4] that at contact point velocities, v_c<1.5 mm/µs, on a separation boundary of two arbitrary metals the disturbances are not formed. In this case loading pressure P_c is not great. Material strength impedes shear strain strams realization. At v_c > 1.5 mm/µs, on a contact boundary, symmetric wavy disturbances occur (see Fig.2a). With a subsequent velocity v_c growth, the waves lose symmetry, the crests become eddy, the disturbance amplitude increases a bit. The experiments [4] were limited by a range of contact point v_c < 3 mm/µs.

In our tests we obtained that with a further velocity increase v_c a transformation of contact boundary geometry is seen; it becomes a layer of turbulently mixed materials, instead being wavy (see Fig.2b). Then a disturbance amplitude reaches maximum, after that it decreases subsequently (see Fig.2c,d). Such relationships are noted for all metal pairs investigated: aluminium alloy Al Mg Zn (Al– basis; Mg 3.9-4.6%; Zn 2.9-3.6%; Mn 0.6-1.0%; Fe $\leq$ 0.3%; Si $\leq$ 0.2%; Ti $\leq$0.15%; Cu $\leq$ 0.05%), copper M1 (Cu 99.9%; Fe $\leq$ 0.005%; Pb $\leq$ 0.005%; Sn $\leq$ 0.002%; Sb $\leq$ 0.002%), steel St.3(Fe– basis; C$\leq$ 0.04%; Si $\leq$ 0.2%; Mn $\leq$ 0.2%; Cu $\leq$ 0.15%; S $\leq$ 0.03%; P $\leq$ 0.025%).

When analysing the experimental data, we have chosen as the main parameter, characterizing the state of a contact boundary, – the amplitude of realizing disturbances, *a*. Disturbance amplitude was assumed to be a perpendicular distance from a crest peak level up to an ultimate depression of adjacent valley (when wave formation is evident); or a perpendicular distance between the levels of adjacent heaping and valley (if disturbances dramatically differ from regular waves); or the whole width of turbulent mixing zone of contacting materials. In the analysis of experimental data as a disturbance amplitude, an averaged value was accounted after ~ 20 adjacent disturbance were calculated.
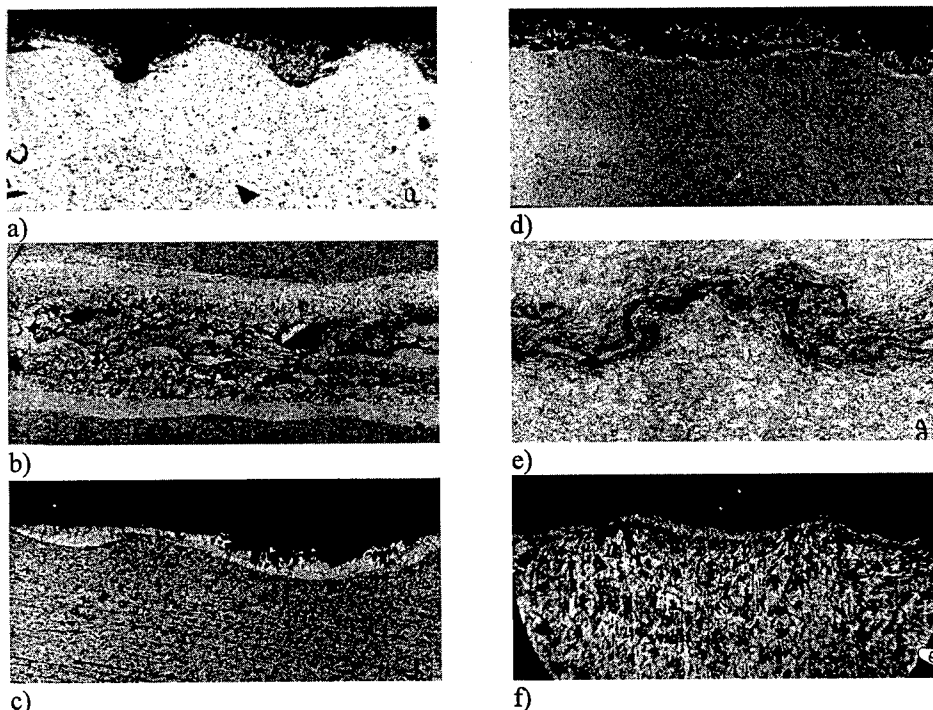
Fig.2. Contact boundary between metals layers after high – velocity oblique collision; γ=12^0 :

a) AlMgZn alloy – AlMgZn alloy, v_c =2.4 mm/μs, $a \approx 0.25$ mm, × 100;

b) AlMgZn alloy – AlMgZn alloy, v_c =6.5 mm/μs, $a \approx 0.43$ mm, × 50;

c) AlMgZn alloy – AlMgZn alloy, v_c =7.8 mm/μs, $a \approx 0.21$ mm, × 50;

d) AlMgZn alloy – AlMgZn alloy, v_c =8.7 mm/μs, $a \approx 0.07$ mm, × 30;

e) copper M1 – copper M1, v_c =2.4 mm/μs, $a \approx 0.2$ mm, × 100;

f) steel St.3 – steel St.3, v_c =6.9 mm/μs, $a \approx 0.15$ mm, × 50.

EXPERIMENTAL RESULTS

In Fig.3 disturbance amplitude dependences at contact boundaries of individual metal pairs on Mach number, $M = \dfrac{v_c}{c_0}$, are presented. We have chosen M – variable to graphically interprete the experimental data, basing on the similiarity for comparison of disturbance amplitudes on contact boundaries of different metals under identical loading conditions (or hydrodynamic flow, v_c/c_0).
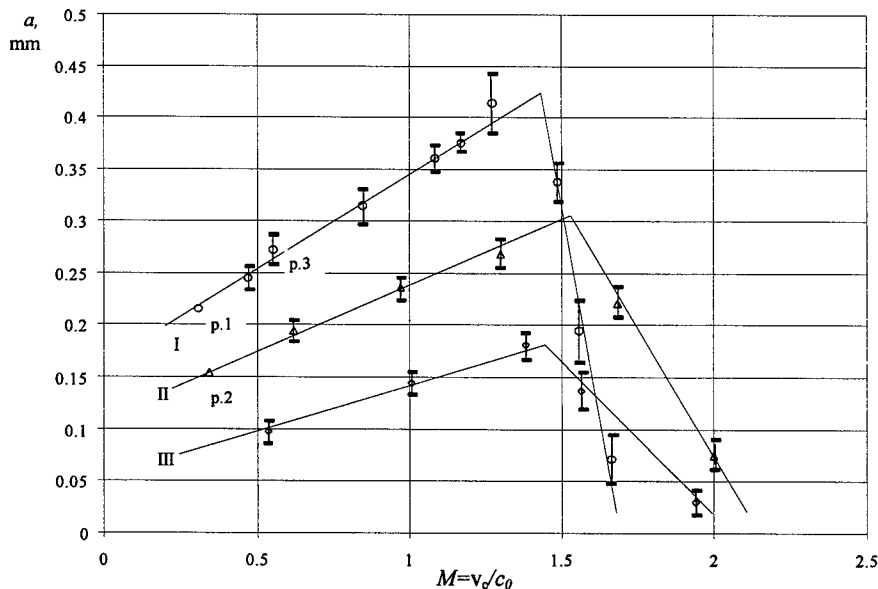
Fig.3. Amplitude of perturbations on contact boundaries between metals layers versus Mach number:

I. Al Mg Zn alloy – Al Mg Zn alloy,

II. Copper M1 – copper M1,

III. Steel St.3 – steel St.3.

Ascending branch of a =f(M) function is determined by a jet formation regime in a contact point (subsonic area of a flux). In Fig.4a a realizing flux pattern near an impact zone in a coordinate system, coupled with a contact point is presented.

Velocity v_c growth results in the increase of loading pressure and elastic shearing deformation intensity in the contact zone. The greater mass of metals is entraped into a jet flux. The disturbance amplitude increases.

Of the three metals investigated, aluminium is the most fusable (see Fig.3). So its melting is explained at a wave formation, which is strengthened with v_c velocity growth and which is

finished by a complete mixing of melted layers on a contact boundary (see Fig.2b). For copper this effect is weaker expressed, however zones are seen, which are enveloped by the intensive melting (see Fig.2e). For steel an intensive warming up was not reached in rather wide pre – boundary areas. However, a state, resembling melting, is denoted in the narrow layers near a contact boundary (recrystalization zone, see Fig.2f).
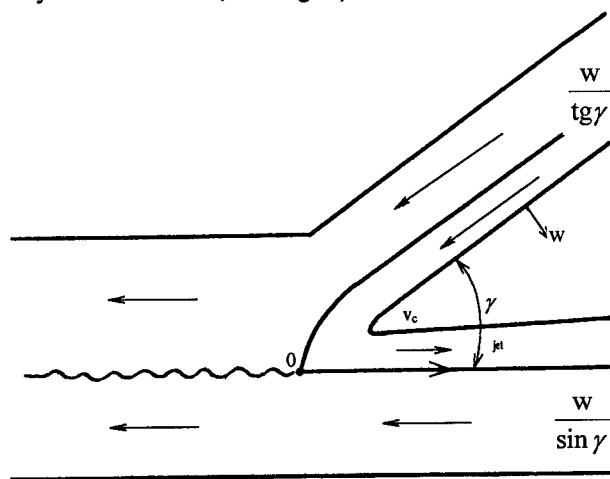
Fig.4a. Scheme of flow realized near the collision zone in the coordinate system, coupled with the contact point, in regime of subsonic oblique collision

In Fig.3 the data, obtained by other authors, are graphically presented. Point 1 for an aluminium – aluminium pair was taken from work [4], point 2 for a copper – copper pair was taken from work [6]. Wave formation parameters, mentioned in these works, agree satisfactorily with our results.

When each metal pair has an individual critical velocity values v_{cr} which characterize the transition from subsonic flow to a supersonic zone, the disturbance amplitude reaches maximum.

A further velocity v_c growth is accompanied by an impacting plates' turn. A jet formation in a contact point is absent (supersonic flux is illustrated in Fig.4b).
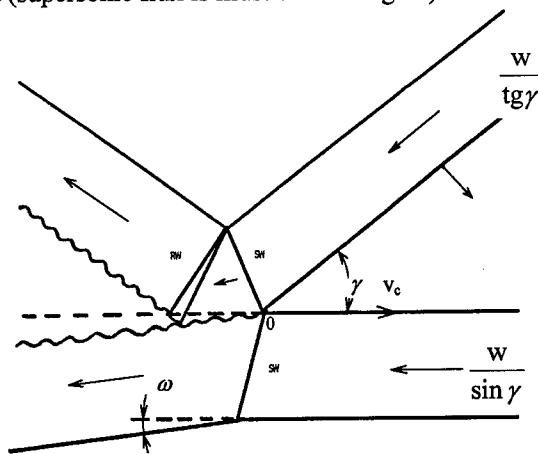
Fig.4b. Scheme of flow realized near the collision zone in regime of supersonic oblique collision with attached shock waves.

In such regime on the contact boundary disturbances are formed under Kelvin – Helmholtz instability development. The plates' turn takes place at a rarefaction wave output on the contact boundary. Contact time of metal layers may be approximately defined as

$$t = \frac{\delta_{st}}{D_s} + \frac{\delta_{st}}{c_0} , \qquad (2)$$

where:

δ_{st} – a striker thickness;

c_0 – sound velocity in a given material;

D_s – a shock wave velocity in a plate material.

The conservation law on an oblique shock wave front testifies that a similar plate impact is accompanied by their turn at an angle ω [4]. Before separation during t period two fluxes (casting and fixed plates) move behind the fronts of oblique shock waves in parallel, touching one another. Their relative sliding takes place. At a wave front a sample temperature rises. In the relative sliding the intensive shearing deformations are realized on the contact boundary; Kelvin – Holmholtz instability is developed , which results in disturbance formation on a separation boundary between two metals. Contact plane melts, that leads to an explosion welding in the thin pre – boundary layers. A rarefaction wave, separating the plates, tears a welded joint. A certain part of a striker metal (up to 0.1 mm in thickness) remains attached to a fixed plate surface in the form of a porous layer (see Fig.2c, d). With velocity v_c growth, a velocity of a relative metal sliding increases as well; simultane onsly, their contact time reduces. The disturbances fail to form completely, their amplitude decreases (a descending branch of $a = f(M)$ function in Fig.3; a photo in Fig.2c,d).

DISCUSSION OF RESULTS

The test results show, that a disturbance amplitude (at equal Mach numbers and a constant impact angle $\gamma \approx$const) is higher for the metals with lower strength characteristics (see Fig.3).

At a high – velocity oblique impact the metal behaviour in the vicinity of a contact point is satisfactorily described from the hydrodynamic point of view [2-4, 7, 8]. In fact, thin pre – boundary metal layers some microns thick transform into a liquid phase. The metal mass remained near a contact point transforms into a somewhat elastic quasiliquid state, which behaviour greatly depends on a shear stress magnitude (τ) that can be estimated as a half – difference between a normal stress (P_n) and a stress tangential (P_τ) to a shock wave front [9].

$$\tau = \frac{P_n - P_\tau}{2} \qquad (3)$$

On the other hand, there is a relation for a dynamic strength yield (Y), which characterizes ability of a material to resist shear deformations [9].

$$Y = 2\tau \qquad (4)$$

In work [10] the experimental functions of a dynamic strength yield values for some metals on a stress are presented.

In work [4] in the analysis of the geometry of metal layers' contact boundaries after an oblique impact the authors showed that a realizing disturbance amplitude is proportional to an equivalent Reynolds number:

$$a \sim Re = \frac{\left(\rho_{st} + \rho_{pl}\right) \cdot v_c^2}{2\left(H_{st} + H_{pl}\right)},\tag{5}$$

where:

a – disturbance amplitude,

Re– equivalent Reynolds number,

v_c – contact point velocity,

ρ_{st}, ρ_{pl} – densities of a striker and a fixed plate, correspondingly,

H_{st}, H_{pl} – microhardness of a striker and a fixed plate, correspondingly.

Rewriting this relation for a case of similar plates' impact and accounting for correspondence of a dynamic yield strength to the physical processes to an even greater degree which occur on a contact boundary, than the microhardness H, introducing the relation $M = v_c / c_0$ and minding that product of $\rho_{pl} \cdot v_c \cdot c_0$ is, in fact a pressure parameter in the vicinity of a contact point P_c, we obtain:

$$a \sim Re = \frac{P_c \cdot M}{Y},\tag{6}$$

where:

a – disturbance amplitude,

Re– equivalent Reynolds number,

P_c – pressure in a contact point,

M – Mach number,

Y – dynamic strength yield.

When the disturbance amplitudes on the contact boundaries of different metals' layers are compared, Mach number M becomes fixed and a loading pressure P_c for it – as well. A particular value Y [10] corresponds to each P_c magnitude. Thus, the relatoin from work [4] transforms into a simple interaction of two parameters:

$$a \sim \frac{1}{Y}\tag{7}$$

That is, the smaller is the value of the dynamic strength yield of the given material, the bigger is the disturbance amplitude on a contact boundary and vice versa. By comparison of the ascending branches of the dependences in Fig.3 one may mention the following:

$$\frac{a_{Cu}}{a_{Al}} \approx \frac{Y\left(P_c\right)_{Al}}{Y\left(P_c\right)_{Cu}}; \ \frac{a_{Cu}}{a_{st}} \approx \frac{Y\left(P_c\right)_{st}}{Y\left(P_c\right)_{Cu}},\tag{8}$$

where:

a_i – disturbans amplitude on a contact boundary of an arbitrary (i) metal,

$Y(P_c)_i$ – dynamic strength yield under pressure P_c of an arbitrary (i) metal,

(at $\gamma \approx$ const; equal M magnitudes and P_c and Y, corresponding to them).

Thus calculated experimental values for the disturbance amplitudes are imposed on the function $a = f(M)$ for copper. A good agreement is evident for three pairs of the metals investigated (see Fig.5).

A reverse operation seems to be possible, i.e. a disturbance amplitude on a metal contact boundary might be an indirect method of dynamic strength yield estimation. In Fig.3 the experimental value of a disturbance amplitude on a contact boundary magnesium – magnesium (p.3) is shown. This point lies practically on a function for aluminium. Dynamic strength yields for aluminium and magnesium might be supposed to be near.

The connection between a disturbance amplitude on a contact boundary and a dynamic strength yield for copper and steel St.3 remains in a supersonic loading regime as well. In this case the wave material properties are dominant (the proximity of the velocity values for a shock wave and sound, the tangential breakage value behind an oblique shock wave front and so on). The preliminary results on the relation between the disturbance amplitude on contact boundaries of various metal pairs are obtained as well. An analytical expression for this relation has a more complex character.
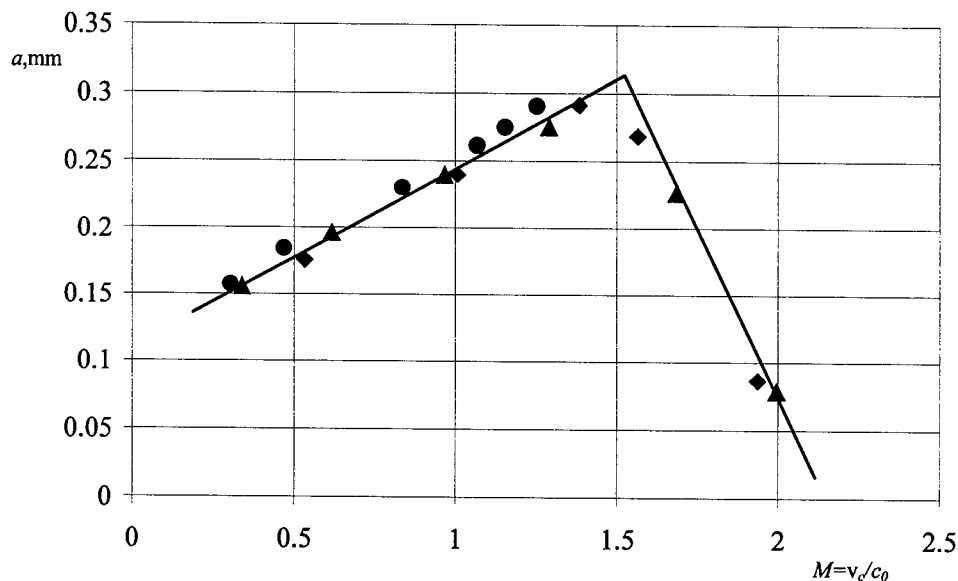
Fig.5. Generalized relation $a(M)$ for three metals (aluminium, copper, steel) at γ=const $\approx 12^0$ (recalculation for dynamic yield strengths Y).

CONCLUSIONS

Thus, the results presented enable us to build a function of a disturbance amplitude on a contact boundary of metal layers on Mach number in a wide range of a contact point velocities. An analytical connection of the disturbance on contact boundaries of different metal pairs with their strength properties (dynamic strength yield) is expected.

Oblique collision of metal layers with supersonic and hypersonic velocities v_c of the contact point was studied experimentally for the first time.

Perturbations growth was recorded on the metals interface boundary in regime with oblique shock waves, joining the contact point.

Results of this work allow to extend understanding of the problem of high—velocity oblique impact and predict state of the collided surfaces.

REFERENCES

1. R.Kurant and K.Fridrikhs, Supersonic flow and shock waves, Moscow, Foreign Literature (1950).
2. G.R.Cowan and A.H.Holtzman, Flow configurations in colliding plates: explosive bonding. *J. Appl. Phys.,* **34**(4), 928-939(1963).
3. A.S.Bahrani, T.J.Black and B.Crossland, The mechanics of wave formation in explosive welding. *Proc. Roy. Soc.* Ser. A, **296**(1445), 123-136(1966).
4. G.R.Cowan, O.R.Bergnrann and A.H.Holtzman, Mechanusm of bond zone wave formation in explosive – clad metals. *Metallurgical Transactions*, **2**(11), 3145-3155(1971).
5. G.E.Kuzmin, V.A.Simonov, I.V.Jakovlev. FGV, **13**(4), 458-461(1976).
6. W. Lucas, Transmission electron microscopy of copper, stainless steel and aluminium explosion welds. *J. Inst. of Metals,* **99**(2659), 335-340(1971).
7. J.N.Hunt, Wave formation in explosive welding. *The Phyl.Mag.,* Ser.8, **17**(148), 669-680(1968).
8. J.H.Robinson, Fluid mechanics of copper:viscaus energy. Dissipation in impact welding. *J. Appl.Phys.*, **48**(6), 2202-2207(1977).
9. F.A.Baum, L.P.Orlenko, K.P.Stanyukovich et al. Fizika vzryva, Moscow, Nauka (1975).
10. Ju.V.Bat'kov, S.A.Novikov, L.M.Sinitsyna, A.V.Chernov. Problemy prochnosti, **5**, 56-59(1981).

HYPERVELOCITY IMPACT TESTING OF THE PRESSURIZED MATING ADAPTERS FOR THE INTERNATIONAL SPACE STATION

BRUCE D. DVORAK

The Boeing Company, ISS Meteoroid/Debris Shielding & Survivability Team,
5301 Bolsa Avenue, Huntington Beach, CA 92647, e-mail: bruce.d.dvorak@boeing.com

Summary—The International Space Station (ISS) has three pressurized mating adapters (PMAs) that are uniquely designed with the latest machining and welding technologies. Each PMA shell consists of five individually machined 2219-T852 ring forgings welded together using a precision variable polarity plasma arc (VPPA) welding process. Low-cost, lightweight metallic shielding is used as on-orbit protection against meteoroid and orbital debris impacts. To determine the adequacy of this shielding at both the weld and nonweld regions, a two-phase hypervelocity impact (HVI) test program was completed at the NASA Johnson Space Center (JSC) Hypervelocity Impact Test Facility (HIT-F). From this test program, it was determined that the shield performance at the PMA pressure shell's critical weld and nonweld regions met and exceeded analysis predictions for the most penetrating threats achievable with no indications of premature through-cracking, perforation, detached spall, or excessive bulging. © 1999 Elsevier Science Ltd. All rights reserved.

INTRODUCTION

When the first element of the ISS is launched in late-1998, it will share near-Earth orbital space with thousands of large and perhaps tens of millions of medium-sized debris objects left from 3,700 previous space missions since 1957. Unlike natural meteoroids, which are much smaller in numbers and pass through and leave the near-Earth area, artificial space debris orbits the Earth and may remain in orbit for long periods of time, posing a significant threat to ISS. According to orbital mechanics, accidental impacts between ISS elements and debris can occur at velocities up to 15 km/s (9.3 mi/s). Less threatening meteoroid impacts can occur at velocities up to 70 km/s (43 mi/s). At these velocities, a piece of debris or meteoroid fragment no larger than a garden pea carries the destructive punch to potentially cripple an entire unprotected spacecraft—even as large as ISS.

To protect against accidental impact with orbiting debris and meteoroids, many of the ISS low-pressure habitable volumes have adopted low-cost, lightweight protective shielding. The majority of these shielded elements include spaced plate (Whipple bumper) passive protection schemes using the structural pressure shell (spacecraft hull) as the inner/rear wall. This shield design differs from a standard Whipple bumper configuration where the rear wall is separated from the structure it is protecting—as in the case of the high-pressure tanks and pumps—in that the rear wall serves two primary purposes: (1) as a structural element and (2) as a protective barrier to defend against incoming ejecta/debris from the impacted shield. Since the rear wall serves as a low-pressure vessel in these instances, high quality precision welds are used to adequately join adjacent machined plates or forgings to make up the structure. This fabrication process combined with the meteoroid/orbital debris (M/OD) shield design introduces legitimate concerns regarding overall shield performance at the weld locations. Premature cracking and perforation of the rear

wall welds once impacted by the debris cloud/ejecta could introduce unacceptable risk in instances where there is high M/OD impact vulnerability.

To ensure safe and continual operation of its three PMAs scheduled to be launched in late 1998 as part of the early ISS assembly sequence, The Boeing Company initiated an HVI test program in 1995 at the NASA JSC HIT-F to determine shield performance at the PMA pressure shell critical weld and nonweld regions. Before that time, no HVI damage assessments for aluminum welds or forgings had been investigated. Before testing, it was believed that shield performance would significantly reduce at the weld locations because of weld mechanical/material property discontinuities while the parent forging material would yield predictable results similar to common plate stock. The results of this test program are discussed herein.

PMA CONFIGURATION AND SHIELD DESIGN

ISS includes three PMAs (1-3) that provide docking ports for the Space Shuttle, with the exception of PMA-1, which provides an adapter between the Russian and United States elements of ISS (Fig. 1). When mated, PMAs 2 and 3 are pressurized and environmentally controlled to accommodate the passage of crew and equipment between the Space Shuttle external PMA and the ISS. Each PMA supports the transfer of utilities to and from the Space Shuttle or connecting elements as in the case of PMA-1. Since a meteoroid or orbital debris collision with the PMA pressure shell could severely endanger the crew and/or ISS survivability, it was judged necessary to include
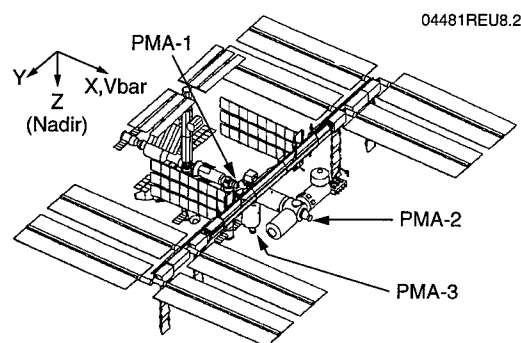
Fig. 1. International Space Station PMAs 1-3 locations.
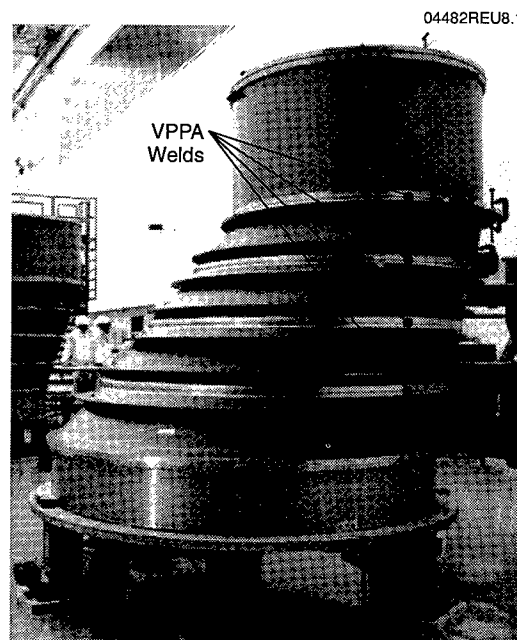
Fig. 2. The completed pressure shell welded assembly stands over 7-ft high and weighs approximately 700 lb.

low-cost, lightweight M/OD shielding as part of the PMA design to minimize risk [1].

The PMA pressure shell assembly is a very unique design incorporating the latest machining and welding technologies. Five individually machined 2219-T852 ring forgings were welded together using a precision VPPA welding process (Fig. 2). It is important to note that the welded assembly is not re-heat treated to recover the strength of the parent material in the weld regions. The M/OD shield design employs a Whipple bumper protection concept that consists of a single thin aluminum shield (Whipple bumper) supported off the surface of the PMA pressure shell 4 to 6.33 in. (Fig. 3). The Whipple bumper is designed to be perforated when impacted by a meteoroid or debris particle while shocking the particle and breaking it into fragments. These fragments disperse in an expanding debris cloud that spreads the impact energy over a much larger area, making it far less damaging to the machined forging pressure shell behind it. If the impacting velocity is high enough, melting or vaporiza-

**Typical Section Cut
Through PMA Shell
and M/OD Shielding**

**PMA 1-3 M/OD
Shielded Surfaces**

04483REU8.3

Welds

Rear Wall
(PMA Shell)

Bumper

(Pressurized Mating Adapter 1-3)

Shield Description	Bumper, in.	Rear Wall, in.	Callout	Standoff, in.
Faceted Side 1	0.063	0.22-0.375	A	4.20-6.33
Faceted Side 2	0.063	0.22-0.375	B	4.40-6.33
Faceted Side 3	0.063	0.22-0.375	C	4.40-6.33
Faceted Side 4	0.063	0.22-0.375	D	4.40-6.33
Faceted Side 5	0.063	0.22-0.375	E	4.40-6.33
Faceted Side 6	0.063	0.22-0.375	F	4.40-6.33
Faceted Side 7	0.063	0.22-0.375	G	4.40-6.33
Faceted Side 8	0.063	0.22-0.375	H	4.40-6.33
All VPPA Welds	0.063	0.375		4.40-6.33
Cylindrical Section	0.063	0.22-0.375	J	4.40
All Close-outs	0.063	0.22	K	4.40

Fig. 3. PMA shield design.

tion will occur, which aids in reducing impact lethality. An increase in the pressure shell thickness has been used to provide the necessary protection against the slower moving particles that penetrate the shield intact. The current shield design has been engineered to provide sufficient protection against impacts covering the entire velocity regime for both small meteoroids and debris [2]. To meet thermal requirements, multilayer thermal insulation blankets are attached to the inner face of the bumper throughout each PMA.

HYPERVELOCITY IMPACT TESTING

Each PMA shield design was qualified for ISS by probability-of-no-penetration (PNP) assessments using the NASA-furnished Bumper Design Analysis Code (Bumper-II, version 1.35) [3,6]. These assessments required that ballistic limit equations (penetration functions) be defined for the shield configuration. Since there was no ballistic limit data available for machined forging or welds, a test program was necessary to determine shield performance for these areas and to support assumptions used in these assessments.

A two-phase HVI test program was completed at the NASA JSC HIT-F in May 1996. The first phase, conducted in April 1995, provided damage tolerance and ballistic limit information that would verify shield design protection capability for shielding at the pressure shell's critical weld region while the second phase, conducted in April 1996, provided the same information that

would verify the shield design protection capability for shielding at the pressure shell's critical nonweld (machined forged) region [4,5].

PHASE I HVI TESTING

Phase I testing was dedicated specifically to shielding at the PMA pressure shell's critical weld region. Since testing would simulate orbital debris impact on flight-representative shield configurations, selecting critical regions was necessary because of the excessive cost of fabricating qualified flight-like VPPA welds that included X-ray and dye-penetrant inspections. A preliminary PNP assessment determined that the weld region with the minimum standoff (4.4-in.—distance between the inside of the bumper and outside of the weld) was critical for all three PMAs. Test specimens representing these critical regions were then fabricated. To define test cases, the most penetrating threats as a function of velocity (V) and obliquity (β) were identified by analysis using the SHVBETA subroutine included in the NASA furnished Bumper Code [6] and the new Cour-Palais penetration functions [7,14]. Since the PMA shields were expected to defeat particles larger than 1mm in diameter and that standard HVI testing is limited to approximately 7 km/s for particles larger than 1mm, the most penetrating threats were narrowed down to "most penetrating threats achievable" for testing. When this analysis was completed, two cases (V = 7 km/s, β = 25 deg and V = 5 km/s, β = 45 deg) were selected for the Phase I testing [8]. With this information, the objective was to determine the ballistic limit (critical particle size, d) for these most penetrating threats and compare with the assumed analytical ballistic limit curves used in overall PNP assessments.

Phase I Test Article

Figure 4 depicts the Phase I test specimen identified as the weld region (WR) configuration. Each specimen consisted of a 0.063-in.-thick 7075-T6 aluminum (Al) clad Whipple bumper with a flight representative multilayer insulation (MLI) blanket attached to the inner face, a 0.375-in.-thick 2219-T851 Al plate VPPA weld (representative of the flight hardware 0.375-in.-thick VPPA forging welds), with a 4.4-in. standoff. A 0.063-in.-thick 7075-T6 Al sheet witness plate was placed 3 in. behind the weld to protect the target chamber and help detect detached spall when the ballistic limit was reached.
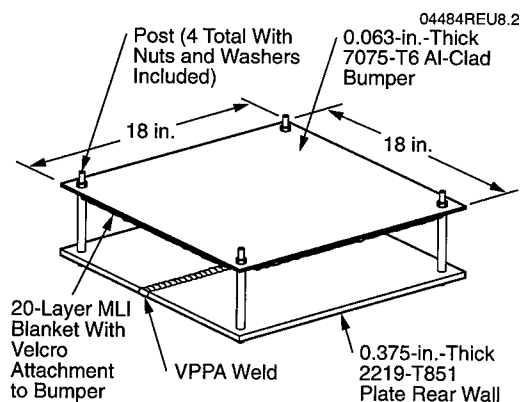
Fig. 4. Phase I test specimen (weld region configuration).

Phase I Test Procedure

Each test specimen was mounted in the HIT-F 12.7-mm-diameter (0.50 caliber) two-stage light gas gun target chamber to accommodate the worst-case impact. The objective here was to orient the test specimen in a way such that the debris cloud density from the impacted bumper was most concentrated on the VPPA weld (Fig. 5) [9]. Once mounted, the test chamber was evacuated and pumped down to approximately 8 to 10 torr just before testing to simulate on-orbit conditions (1 torr is defined as 1/760 of a standard atmosphere). After each test, the impacted specimens were removed from the chamber to be photographed and visually examined for damage. Testing was limited to 2017-T4 Al spherical projectiles. These impacting particles were standard sizes selected from the HIT-F inventory. This inventory included projectiles whose diameters range from 100 μm to 1 cm with a minimum nominal diametrical variance available between projectiles being

0.397 mm (1/64 in.). It was beyond the scope of these tests to have projectiles specially ordered whose diametrical variance was less [10].

Test Results from Phase I Testing

Failure criteria for the WR configuration was defined as detached spall, through penetration (not light tight), and/or excessive permanent deformation (overall bulge) greater than 0.50 in. of the rear wall [9]. This criteria was determined by ISS engineers after a comprehensive examination of possible M/OD impact related catastrophic failure modes for the PMA configurations. Analytical ballistic limit curves based upon the VPPA weld yield strength (σ) were generated and plotted using the new Cour-Palais penetration function listed below to determine what projectile sizes to start with [7,14].
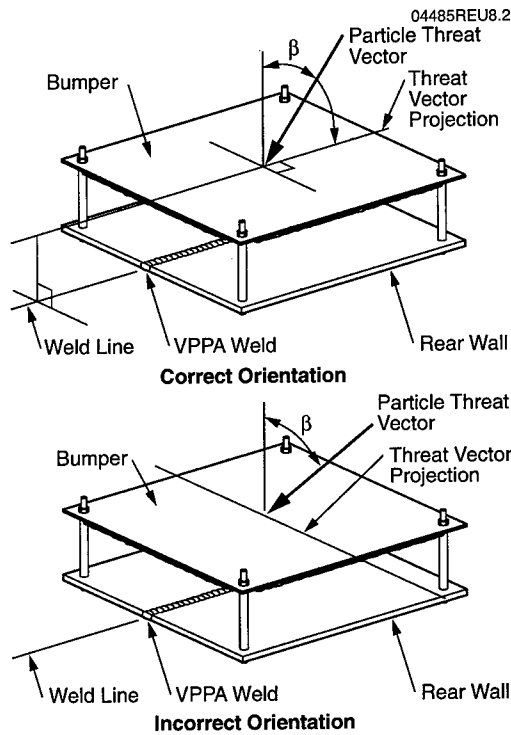
Fig. 5. Phase I target orientations.

For Vn $\geq$ 7 km/sec:

$$dc = 3.918 \cdot tw^{\frac{2}{3}} \cdot \delta p^{\frac{-1}{3}} \cdot \delta b^{\frac{-1}{9}} \cdot (V \cdot \cos\theta)^{\frac{-2}{3}} \cdot S^{\frac{1}{3}} \cdot \left(\frac{\sigma}{70}\right)^{\frac{1}{3}} \tag{1}$$

For 3 km/sec < Vn < km/sec:

$$dc = \left[\frac{tw \cdot \left(\frac{\sigma}{40}\right)^{\frac{1}{2}} + tb}{1.248 \cdot \delta p^{\frac{1}{2}} \cdot \cos\theta}\right]^{\frac{18}{19}} \cdot \left(1.75 - \frac{V \cdot \cos\theta}{4}\right)$$

$$+ \left[1.071 \cdot tw^{\frac{2}{3}} \cdot \delta p^{\frac{-1}{3}} \cdot \delta b^{\frac{-1}{9}} \cdot S^{\frac{1}{3}} \cdot \left(\frac{\sigma}{70}\right)^{\frac{1}{3}}\right] \cdot \left(\frac{V \cdot \cos\theta}{4} - 0.75\right) \tag{2}$$

For Vn $\leq$ 3 km/sec:

$$dc = \left[\frac{tw \cdot \left(\frac{\sigma}{40}\right)^{\frac{1}{2}} + tb}{0.6 \cdot (\cos\theta)^{\frac{5}{3}} \cdot \delta p^{\frac{1}{2}} \cdot V^{\frac{2}{3}}}\right]^{\frac{18}{19}} \tag{3}$$

Testing for the V = 7 km/s, β = 25 deg threat case started with a 7.134-mm (9/32 in.) diameter 2017-T4 Al particle and continued until the critical particle size was determined to be somewhere between 7.94 mm (5/16 in.) and 8.33 mm (21/64 in.), which was well above the analytical ballistic limit curve (Fig. 6). Testing for the V = 5 km/s, β = 45 deg threat case started at a 6.35-mm (1/4 in.) diameter 2017-T4 Al particle and was then concluded based upon examination of the test article that revealed little damage while being above the analytical ballistic curve (Fig. 7). Table 1 outlines the results of the Phase I testing.

The results of the Phase I tests proved to be invaluable. Before testing, there was much speculation that shield performance at the most penetrating threats achievable would significantly reduce at the weld locations because of inherent weld mechanical/material property discontinuities. From a series of pull tests on the PMA VPPA welds before testing, the yield strength (σ) was determined to be approximately 20 ksi while the parent forging material was tested to 38 ksi [11]. Surprisingly, this sharp contrast in yield strengths did not contribute to a premature failure due to an HVI. No premature through-
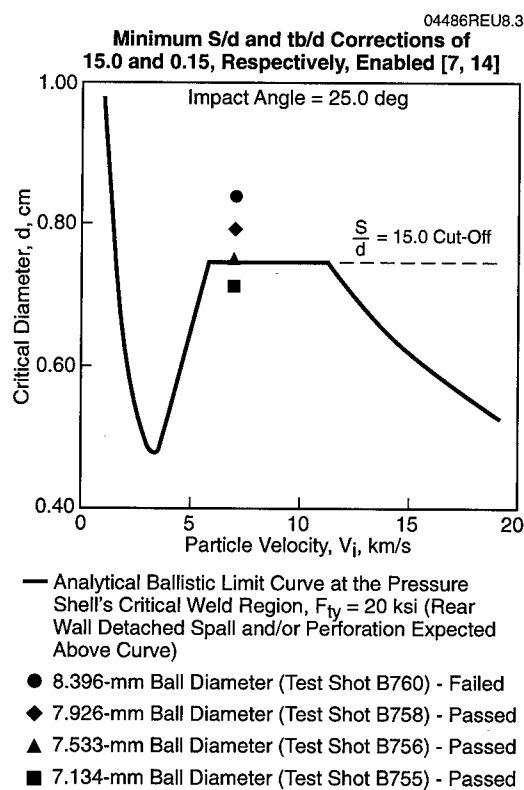
Fig. 6. Analytical ballistic limit curve and test data for shielding at PMA pressure shell's critical weld region.
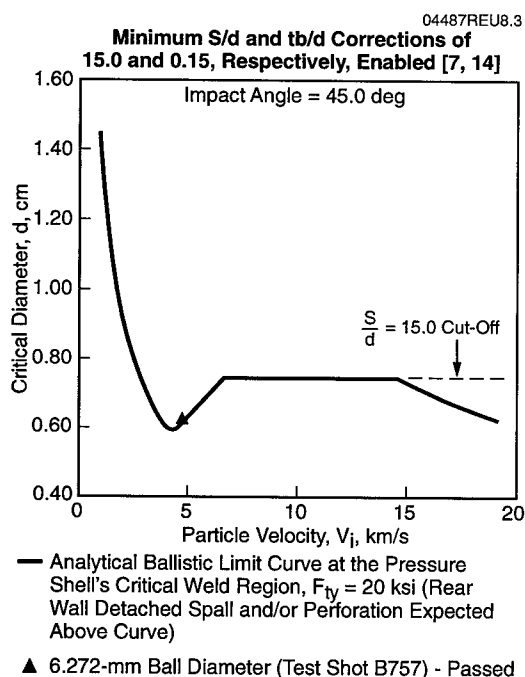
Fig. 7. Analytical ballistic limit curve and test data for shielding at PMA pressure shell's critical weld region.

cracking/penetration was experienced in the heat effected zone (HAZ) or weld itself. Not even the weld bead corrugation on back of the weld, which is characterized as sufficiently weaker and more brittle spalled off the back before spallation of the parent material. The damage typically experienced on the front side of the weld specimens was characterized by deep pitting and melting of both the weld and parent material. No visible damage could be found on the back side of the impacted specimen that successfully defeated the larger projectile (shot B758) while local bulging—attached spall across the weld, HAZ, and parent material—was characteristic for the specimens that successfully defeated the smaller particles (shots B755 and B756). No definite explanation can be offered for this phenomenon other than slight variations in weld thickness or debris cloud impact concentrations between specimens. Examination of the specimens before and after testing, however, revealed no obvious variations in weld thickness or impact concentrations. Additional testing is needed to further explain this seemingly

Table 1. Summary of HVI Phase I test results

Shot pass/fail	Projectile diameter (in.)	Speed, V (km/s)	Impact angle, B (deg)	Rear wall damage	Rear wall hole size*	Rear wall surface crack length†	Witness plate hole size
B755 Pass	9/32 (7.14 mm)	6.95	25	Deep pitting front of rear wall, max. crater depth 4.5 mm. Small bulge across back of weld, no cracks.	None (light tight)	None	No damage
B756 Pass	19/64 (7.54 mm)	6.92	25	Deep pitting front of rear wall similar to previous shot. Microcracks formed in weld HAZ along center of small bulge on back side.	None (light tight)	Not visible to unaided eye	No damage
B758 Pass	5/16 (7.94 mm)	7.00	25	Deep pitting front of rear wall, max. crater depth 4.7 mm. No bulging, visible damage on back side of weld.	None (light tight)	None	No damage
B760 Fail	21/64 (8.33 mm)	7.01	25	Deep pitting on front of rear wall similar to that of previous shot. One large piece of detached spall from across back of weld.	None (light tight)	Detached spall only	Two dents
B757 Pass	1/4 (6.35 mm)	4.74	45	One large crater, several small craters on front side (little damage). No visible damage on back side.	None (light tight)	None	No damage

*Tested specimens were not checked for pressure thightness
†Visual expection only

0000869.2

counter-intuitive behavior. Under adequate magnification of the Shot B756 specimen, small microcracks were found in the HAZ. This was somewhat expected as the critical particle size is approached.

Examination of the failure of the weld region specimen for the $V = 7$ km/s, $\beta = 25$ deg threat showed that detached spall occurred and was characteristic of a homogeneous plate. A single piece from the back of the specimen that included the weld, HAZ, and parent material spalled off the back leaving one large and one very small dent in the witness plate. The spalled piece was recovered in the target chamber afterwards. A representation of the analytical ballistic limits and test data for the $V = 7$ km/s, $\beta = 25$ deg and $V = 5$ km/s, $\beta = 45$ deg threats are illustrated in Figs. 6 and 7, respectively [4].

Conclusions for the Phase I Testing

Results from the Phase I testing determined that the shield performance at the pressure shell's critical weld regions met and exceeded analysis predictions for the most penetrating threats achievable with no indications of premature through-cracking, perforation, detached spall, or excessive bulging [12]. In these regions, HVI failure was identified as detached spall similar to that of homogeneous plate stock of the same material and strength.

Additional strength testing (i.e., pull testing) of the impacted welds has not been conducted. Future test programs may include this work from a fatigue and fracture standpoint.

PHASE II HVI TESTING

Phase II testing was dedicated specifically to shielding at the PMA pressure shell's critical nonweld (machine forging) region that constitutes the vast majority (95%) of the shell's surface.

Procuring flight-like test specimens was heavily constrained by cost and availability of 2219-T852 machined forging leaving a fully assembled PMA weld development unit (similar to that of Fig. 2) from a previous pressure test as an only viable option for sectioning. As in the case of the Phase I testing, selecting critical regions was necessary because of the limited number specimens available. Preliminary PNP assessments determined that the nonweld region with the minimum shield standoff and pressure shell thickness (4.4 in. and 0.22 in., respectively) was critical for all three PMAs. Boeing manufacturing was only able to section a maximum eight panels from the weld development unit in this region. This small number of specimens allowed for only one test case (V = 7 km/s, β = 25 deg) that was determined by the same method outlined in the Phase I testing [8]. As in the case of the Phase I testing, the objective was to determine the ballistic limit for this most penetrating threat and compare with the assumed analytical ballistic limit curves used in the overall PNP assessments.

Phase II Test Article

Fig. 8 depicts the Phase II test specimen identified as the minimum rear wall (MRW) configuration. Each specimen consisted of a 0.063-in.-thick 7075-T6 Al clad Whipple bumper with a flight representative MLI blanket attached to the inner face, a 0.22-in.-thick 2219-T852 machine forging rear wall (sectioned from the PMA weld development unit cylindrical portion), with a 4.4-in. standoff. A 0.063-in.-thick 7075-T6 Al sheet witness plate was placed 3 in. behind the weld to protect the target chamber and help detect detached spall when the ballistic limit was reached.
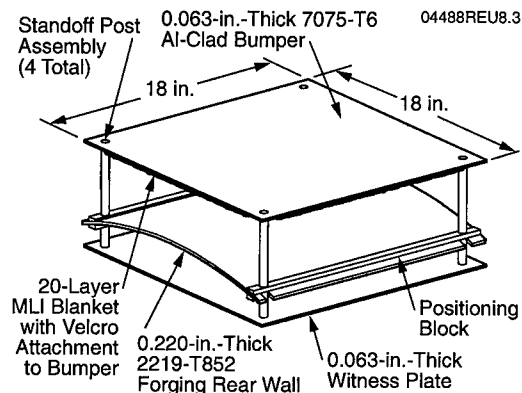
Fig. 8. Phase II test specimen (minimum rear wall configuration).

Phase II Test Procedure

For each test shot, the test specimen was mounted in the HIT-F 12.7-mm-diameter (0.50 caliber) two-stage light gas gun target chamber to accommodate the worst-case impact. The objective here was to orient the test specimen in such a way that the debris cloud density from the impacted bumper was most concentrated on the pressure shell at the minimum standoff. This orientation would seize the greatest amount of damage (Fig. 9) [13]. Once mounted, the test chamber was evacuated and pumped down to approximately 8 to 10 torr just before testing to simulate on-orbit conditions. After each test, the impacted specimens were removed from the chamber to be photographed and visually examined for damage.

Phase II testing also was limited to 2017-T4 Al spherical projectiles as noted in the Phase I test procedure and used the same criteria for size selection from the HIT-F inventory.

Test Results from Phase II Testing

Failure criteria for the MRW configuration was defined as detached spall, through penetration (not light tight), and/or excessive permanent deformation (overall bulge) greater than 0.50 in. of the rear wall [13]. This criteria was determined by ISS engineers after a comprehensive examination of possible M/OD impact related
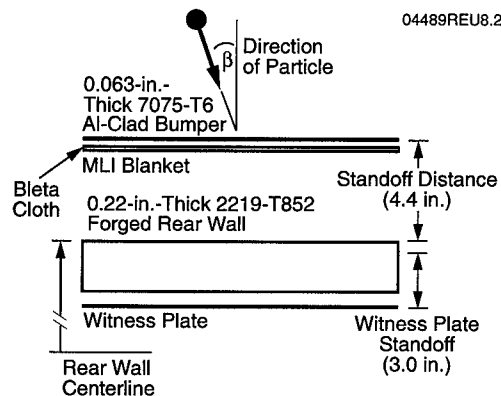
Fig. 9. Phase II target orientation.

catastrophic failure modes for the PMA con-
figurations. Analytical ballistic limit curves
based upon the machined forging rear wall
yield strength (σ) were generated and plotted
using the new Cour-Palais penetration func-
tion [7, 14] to determine what projectile sizes
to start with (reference equations (1), (2), and
(3)). Testing for the V = 7 km/s, β = 25 deg
threat case started with a 6.75-mm (17/64-in.)
diameter 2017-T4 Al particle and continued
until the critical particle size was determined
to be somewhere between 7.14-mm (9/32 in.)
and 7.54-mm (19/64 in.), which was approxi-
mately at the analytical ballistic limit curve
(Fig. 10). Table 2 outlines the results of the
Phase I testing.

As in the case of the Phase I testing,
results from the Phase II testing were signifi-
cant. Prior to testing, there were varying pre-
dictions regarding shield performance in the
critical areas. Most predicted performance
would be considerably better due to the pres-
sure shell forging process which has many
mechanical advantages in strength, fatigue
and fracture. Test results, however, demon-
strated that the machine forging behaved
much like plate or sheet stock during a HVI.
The damage typically experienced on the
front side of the minimum rear wall specimens was characterized by deep pitting and melting.
Local bulging (attached spall) and surface cracking was characteristic on the back side for the
two specimens that passed (shots B-979 and B-980).

04490REU8.3

**Minimum S/d and tb/d Corrections of
15.0 and 0.15, Respectively, Enabled [7, 14]**
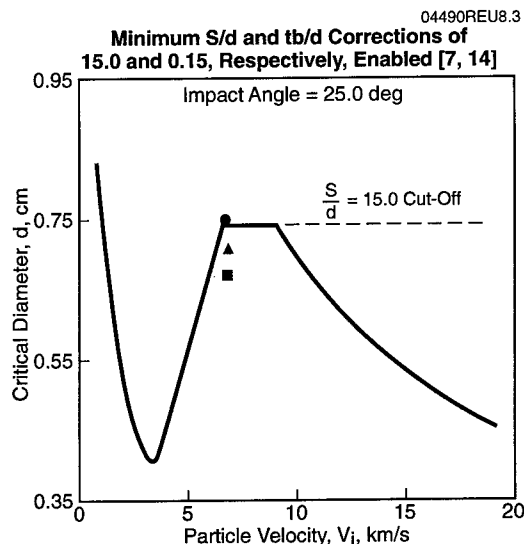
— Analytical Ballistic Limit Curve at the Pressure
Shell's Critical Nonweld Region, F_{ty} = 39 ksi (Rear
Wall Detached Spall and/or Perforation Expected
Above Curve)

● 7.5401-mm Ball Diameter (Test Shot B981) - Failed

▲ 7.1343-mm Ball Diameter (Test Shot B980) - Passed

■ 6.7331-mm Ball Diameter (Test Shot B979) - Passed

Fig. 10. Analytical ballistic limit curve and test data
for shielding at PMA pressure shell's critical
minimum rear wall region.

Table 2. Summary of HVI Phase II test results

Shot pass/fail	Projectile diameter (in.)	Speed, V (km/s)	Impact angle, B (deg)	Rear wall damage	Rear wall hole size*	Rear wall surface crack length†	Witness plate hole size
B-979 Pass	17/64 (6.75 mm)	6.96	25	Deep pitting front of rear wall, max. crater depth 3mm. Largest crater measures 5.5 mm x 2.5 mm. Small bulge across back of rear wall.	None (light tight)	5 mm	No damage
B-980 Pass	9/32 (7.14 mm)	7.00	25	Deep pitting front of rear wall, max. crater depth 2 mm. Largest crater measures 5.0 x 3.0 mm. Small bulge across back of rear wall.	None (light tight)	21 mm	No damage
B-981 Fail	19/64 (7.54 mm)	6.88	25	Deep pitting front of rear wall, max. crater depth 5 mm. Largest crater measures 3.0 x 4.0 mm. Small bulge across back of rear wall, small perforation.	Approx. 1 mm	23 mm	Small particles impingement

*Tested specimens were not checked for pressure thightness
†Visual expection only

A close examination of the minimum rear wall specimen revealed that a large fragment within the debris cloud perforated the rear wall in a single location while local bulging surrounded the area. The witness plate experienced a very small (almost unnoticeable) particle impingement. No fragments were discovered in the target chamber afterwards. A representation of the analytical ballistic limit and test data for the V = 7 km/s, β = 25 deg threat is illustrated in Fig. 10 [5].

Conclusions for the Phase II Testing

Results from the Phase II testing determined that the shield performance at the pressure shell's critical nonweld (machined forged) region met analysis predictions for the most penetrating threat achievable with no indications of premature through-cracking, perforation, detached spall, or excessive bulging [12]. In this critical non-weld region, HVI failure was identified as through penetration (perforation) with a small amount of detached spall surrounding the hole.

FINAL COMMENTS

The testing conducted for the PMA M/OD design is by no means comprehensive. Only critical (worst) cases were investigated to support verification compliance of the PMA M/OD shield design at the pressure shell's weld and nonweld regions to the design requirements as stated in the PMA Prime Item Development Specifications (PIDS) [2]. Additional testing is necessary to fully characterize shield performance of VPPA welds and machined forgings for the entire velocity and impact angle regime. The limited information contained herein provides only a starting point for such studies and should be treated as such.

REFERENCES

1. Boeing Space Station Division, Pressurized Mating Adapter Prime Item Development Specifications (PIDS) S684-10115E (06 Oct 1997) and SP-M-301H (06 Oct 1997), Section 3.3.12.1.16.1.
2. Boeing Space Station Division, Pressurized Mating Adapters Structural Integrity Report (FCA/PCA Submittal). Report No. MDC 95H0336, December 1997, Volume 5, Section 5.0.
3. Boeing Space Station Division, Pressurized Mating Adapter Prime Item Development Specifications (PIDS) S684-10115E (06 Oct 1997) and SP-M-301H (06 Oct 1997), Section 3.3.12.1.3.1.
4. NASA-Johnson Space Center Hypervelocity Impact Test Facility, Phase-I Pressurized Mating Adapter Hyper-velocity Impact Pre-Declared Development, Report No. JSC 27131, (June 1995).
5. NASA-Johnson Space Center Hypervelocity Impact Test Facility, Phase-II Hypervelocity Impact Pre-Declared Development Testing of Pressurized Mating Adapter Meteoroid/Orbital Debris Shield, Report No. JSC 26967, (July 1996).
6. Boeing Space Station Division, BUMPER-II Analysis Tool: Users Manual, Document No. D683-29018-2, (December 1993), Section 6.4.15.
7. Christiansen, Eric L., Shield Sizing and Response Equations, NASA-Johnson Space Center Memorandum SN3-91-42 (15 February 1991).
8. Boeing Space Station Division, Pressurized Mating Adapters Structural Integrity Report (FCA/PCA Submittal). Report No. MDC 95H0336, December 1997, Volume 5, Section 5.9.
9. Dvorak, Bruce D., Pressurized Mating Adapter Phase-I Meteoroid/Orbital Debris Shield Development Test Control Drawing, Drawing No. 1T74802, (30 March 1995).
10. Boeing Space Station Division, Pressurized Mating Adapters Structural Integrity Report (FCA/PCA Submittal). Report No. MDC 95H0336, December 1997, Volume 5, Section 5.0.1.
11. Boeing Space Station Division, Pressurized Mating Adapters Structural Integrity Report (FCA/PCA Submittal). Report No. MDC 95H0336, December 1997, Volume 1, Section 4.2.4.
12. Dvorak, Bruce D., Pressurized Mating Adapter Meteoroid/Orbital Debris Shield Development Test Report, Boeing Space Station Division Memorandum A3-J071 BDD-M-9700558 (11 January 1997).
13. Dvorak, Bruce D., Pressurized Mating Adapter Phase-II Meteoroid/Orbital Debris Shield Development Test Control Drawing, Drawing No. 1T74804, (19 February 1996).
14. Boeing Space Station Division, Pressurized Mating Adapters Structural Integrity Report (FCA/PCA Submittal). Report No. MDC 95H0336, December 1997, Volume 5, Section 5.2.

EFFECTS OF UNCERTAINTY IN HYPERVELOCITY IMPACT PERFORMANCE EQUATIONS AND OTHER PARAMETERS ON VARIANCE IN SPACECRAFT VULNERABILITY PREDICTIONS

HILARY J. EVANS* and JOEL WILLIAMSEN**

*Sverdrup Technology, Inc., Huntsville, AL 35806, USA; **University of Denver Research Institute, Denver, CO 80208-2616 USA

Summary—The increasing man-made debris environment in low-earth orbit (LEO) has prompted NASA to develop new methods for quantifying (and reducing) the risks to spacecraft and crew following hypervelocity penetration by orbital debris. The Manned Spacecraft and Crew Survivability (MSCSurv) computer analysis tool computes the probability of occurrence for seven failure modes which may lead to crew or station loss. The probability of loss, P_{loss}, of station or crew (i.e., its vulnerability) due to impact by one or more orbital debris particles is calculated using three major terms: (a) N_{imp}, the number of impacts on the ISS manned modules, (b) $P_{pen/imp}$, the probability of penetration given that an impact has occurred, and (c) $P_{loss/pen}$, the probability of loss given that a penetration has occurred. MSCSurv was designed to calculate terms (b) and (c). Utilizing MSCSurv, the objective of this study is: (1) to describe briefly the structure of the Manned Spacecraft and Crew Survivability computer code, (2) to detail results from a P_{loss} calculation using baseline penetration, damage, station, and crew-related parameters, and (3) to quantify the variance produced in $P_{pen/impact}$ and $P_{loss/pen}$ associated with each input and modeling parameter used in calculating them. In general, higher uncertainties within Penetration, Damage, Station, or Crew parametric models produced higher uncertainties within the P_{loss} calculation; however, small variances within some models (such as those for hole size following a penetration) produced larger overall P_{loss} variance than large variance within other models (such as the crew movement rate, for example). © 1999 Elsevier Science Ltd. All rights reserved.

NOTATION

PNP	Probability of no penetration.
HVI	Hypervelocity impact.
N_{imp}	Number of impacts by orbital debris particles on the spacecraft surface.
$P_{pen/imp}$	Probability of penetration given orbital debris impact.
$P_{loss/pen}$	Probability of spacecraft or crew loss given orbital debris penetration.
P_{loss}	Probability of spacecraft or crew loss due to orbital debris impact.
R	Ratio of overall spacecraft or crew losses to penetrations, another term for $P_{loss/pen}$.
R-factor	Ratio of overall spacecraft or crew losses to penetrations, another term for $P_{loss/pen}$.
R_5	Ratio of overall spacecraft or crew losses to penetrations considering five factors: (1) manned module critical cracking, (2) critical equipment penetration, (3) thrust-induced loss of control or joint failure, (4) crew hypoxia, and (5) fatal injury to crew.
R_7	Ratio of overall spacecraft or crew losses to penetrations considering seven factors: (1) manned module critical cracking, (2) critical equipment penetration, (3) thrust-induced loss of control or joint failure, (4) crew hypoxia, (5) fatal injury to crew, (6) non-fatal injury to crew, and (7) critical station equipment loss due to module depressurization.

INTRODUCTION

The increasing man-made debris environment in low-earth orbit (LEO) has prompted NASA to develop new methods for quantifying (and reducing) the risks to spacecraft and crew following hypervelocity penetration by orbital debris. Since 1992, NASA has developed and refined the Manned Spacecraft and Crew Survivability (MSCSurv) computer program to determine the likelihood of an orbital debris penetration causing loss of the International Space Station (ISS) or its crew. This Monte-Carlo simulation tool computes the probability of occurrence for seven failure modes which may lead to crew or station loss in the event of an orbital debris penetration: (1) manned module critical cracking, (2) critical equipment penetration, (3) thrust-induced loss of control or joint failure, (4) crew hypoxia during escape or rescue, (5) fatal injury to crew, (6) non-fatal injury to crew, and (7) critical station equipment loss due to module depressurization. The probability of loss (P_{loss}), of station or crew (i.e., its vulnerability) due to impact by one or more orbital debris particles may be computed using the following equation:

$$P_{loss} = 1 - \exp\text{-}\{N_{imp} \times P_{pen/imp} \times P_{loss/pen}\} \tag{1}$$

where N_{imp} is a function of environment flux, surface area and exposure time (this calculation is performed outside the MSCSurv program); $P_{pen/imp}$ is primarily a function of shield ballistic limit; and $P_{loss/pen}$ is a function of both hypervelocity damage prediction equations and other crew and station-related parameters.

MSCSurv calculates the $P_{pen/imp}$ and $P_{loss/pen}$ (which we usually refer to as the R-factor) for all orbital debris particles between 1 mm and 20 cm in size; particles smaller than 1 mm rarely penetrate the station shields, and particles larger than 20 cm can be avoided. [One major assumption used by the ISS Program is that all orbital debris is aluminum. This assumption may be nonconservative.] In order to perform these computations, MSCSurv (a) randomly generates a large number of debris particles (size, velocity, and approach direction) based on one of three NASA orbital debris environment models, (b) selects a space station impact location for each particle generated, based on exposure of the station from this approach direction, (c) determines which of these particles penetrate the station shields based on the interacting particle and shield qualities, (d) predicts the resulting damage from each particle that penetrates the station, (e) compares the predicted damage from the impact to critical levels required to induce loss of the station or crew members, considering the exposure of the crew to these damage levels and their ability to escape from them, and (f) quantifies the final $P_{pen/imp}$ and $P_{loss/pen}$ averaged over hundreds of thousands of simulated impacts.

To perform step (c) above, MSCSurv utilizes selected empirical and analytical ballistic limit relations to determine whether particles penetrate the spacecraft shields. Step (d) requires use of hypervelocity impact damage prediction equations for hole size, crack length, and depth of penetration into the interior of the module. While steps (c) and (d) within the MSCSurv model are related closely to hypervelocity impact phenomenology, step (e) requires other assumptions regarding the capability of the station to tolerate damage as well as the reactions of the crew and its physical capability to withstand and escape harm. The inner workings of MSCSurv Version 4.0 have been thoroughly documented in *MSCSurv Version 4.0 User's Guide* [1].

This paper's objectives are: (1) to describe briefly the function of MSCSurv Version 4.1SE; (2) to quantify the variance produced in $P_{loss/pen}$ (R-factor) associated with each parameter; (3) to examine, through various groupings of parameters, variances and means in $P_{loss/pen}$ (R-factor); and (4) to quantify the variance produced in $P_{pen/imp}$ associated with various uncertainties in the ballistic limit curves. This type of study is critical for identifying those hypervelocity impact modeling parameters where scarce test and analytical resources should be concentrated in order to minimize overall uncertainty within the prediction of P_{loss}.

MSCSURV VERSION 4.1SE

Since its release in September of 1997, two new versions of MSCSurv have been developed: MSCSurv Version 4.1 and MSCSurv Version 4.1SE. The primary difference between MSCSurv Version 4.0 and Version 4.1 is that Version 4.1 has been modified to include the 1996 Orbital Debris environment. This environment is defined in TM 104825 [2]. Version 4.1SE is modified from Version 4.1 to include the capability to assess mean R-factors and the associated variance due to uncertainties in many of the parameters used in the analyses.

Validation of MSCSurv Results Through Comparison to BUMPER

The analysis team used BUMPER (the ISS Program's accepted tool for determining the probability of no penetration [PNP]) to validate the correct implementation of the 1996 NASA orbital debris environment, ISS geometry, shielding placement, and ballistic limit relations within MSCSurv 4.1SE. Figure 1 shows the results of this validation.
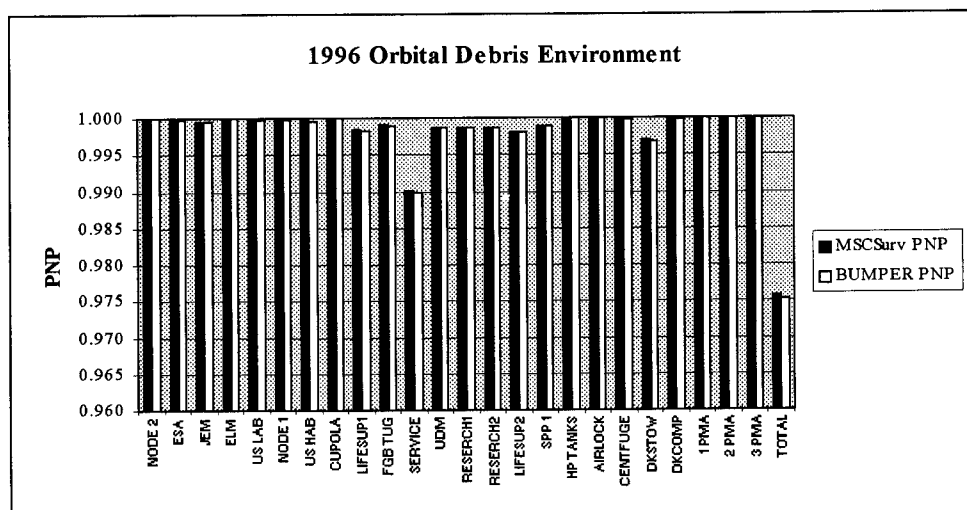
Fig. 1. MSCSurv PNP results compared to BUMPER results (.1cm - 20 cm).

BUMPER and MSCSurv results compare even more closely when MSCSurv environment files include orbital debris as small as .055 cm in diameter as opposed to the typical .1 cm. However, the time required to perform simulations increases by about a factor of six. Consequently, the environment files from .1 cm to 20 cm have been selected for standard use.

Effect of Orbital Debris Environment on Selected Parameters Affecting P_{loss}

Once the 1996 orbital debris environment was properly included in MSCSurv, simulations were performed to compare the 1991 environment [3], the 1994 environment [4], and the 1996 environment [2]. Does the 1996 orbital debris environment result in significantly different R-factors? The answer is "yes." Figure 2 shows the results from three simulations of one million penetrations, each simulation identical in every way except for using a different environment.
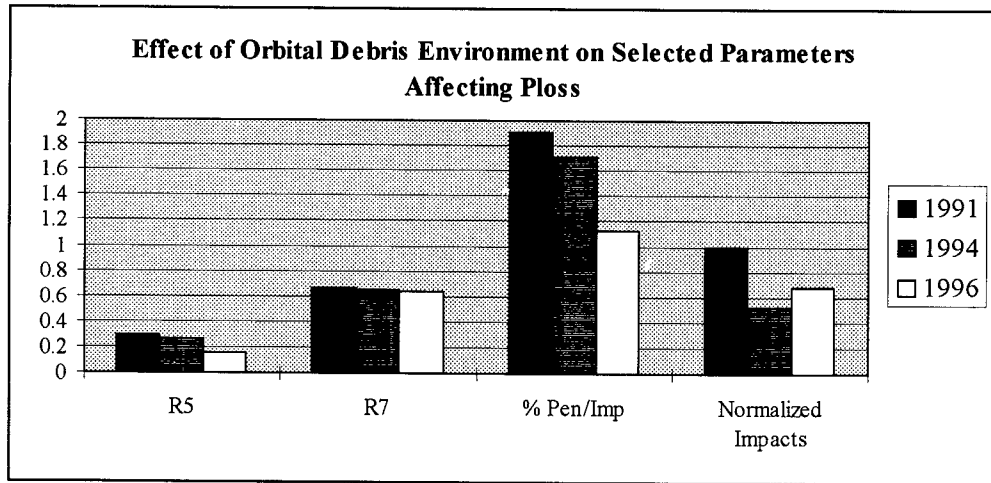
Fig. 2. Effect of orbital debris environment on selected parameters affecting P_{loss}.

The R5 is the R-factor ratio of catastrophic failures to penetrations and includes the failure modes of (1) manned module critical cracking, (2) critical equipment penetration, (3) thrust-induced loss of control or joint failure, (4) crew hypoxia, and (5) fatal injury to crew. R7 is the R-factor ratio of catastrophic failures to penetrations plus two additional failure modes: (6) non-fatal injury to crew and (7) critical station equipment loss due to module depressurization. Thus, R5 is a more immediate, catastrophic measure of loss than R7, and will always be less than R7 in absolute value. The reason for examining both cases is that modes (6) and (7) do not result in immediate loss of the crew; this is seen by some within the NASA safety community as an important distinction worthy of a separate analysis.

As can be seen from Fig. 2, R5 changes significantly from environment to environment ($R5_{91}$ = .29; $R5_{94}$ = .27; $R5_{96}$ = .16). R7 remains fairly constant over all three environments ($R7_{91}$ = .66; $R7_{94}$ = .65; $R7_{96}$ = .63). The probability of penetration given an impact ($P_{pen/imp}$) changes significantly ($P_{pen/imp91}$= .019, $P_{pen/imp94}$=.017, $P_{pen/imp96}$=.011). Using BUMPER, the number of impacts between 1mm and 20 cm (N_{imp}) to ISS was predicted using each of the three environments. These values were normalized to the largest predicted number of impacts. Clearly, the 1991 environment predicts significantly more impacts than the other two environments (N_{imp91}/N_{imp91} = 1.0; N_{imp94}/N_{imp91} = .52, N_{imp96}/N_{imp91} = .68).

MSCSurv also keeps track of the hole-size distribution in the module pressure wall for all penetrations. Figure 3 shows the hole size distribution over the entire space station. Not only do a smaller percentage of particles penetrate with the 1996 environment (as seen in Fig. 2), but the holes produced by penetrating particles are smaller (as seen in Fig. 3). This smaller hole size distribution is the primary reason for the drop in R5 which is seen when using the 1996 environment. The smaller hole size is due primarily to the shift in the velocity distribution of the impacting particles for the 1996 OD environment (lower velocity particles create smaller holes, Schonberg and Williamsen[5]).

Orbital debris environment changes have a triple impact on the overall risk analyses: they affect the number of impacts, the probability of penetration following impact (i.e., more small particles compared to large particles lowers $P_{pen/imp}$), and the probability of loss following penetration (R), as illustrated in the previous discussion involving hole size. Each of these terms can change with changes in the environment. Consequently, uncertainties in environment may be compounded. Uncertainties in the ballistic limit equations affect $P_{pen/imp}$ and R. The parameters used in the parameter study discussed in the following section only affect the R5 portion of Eqn. 1.
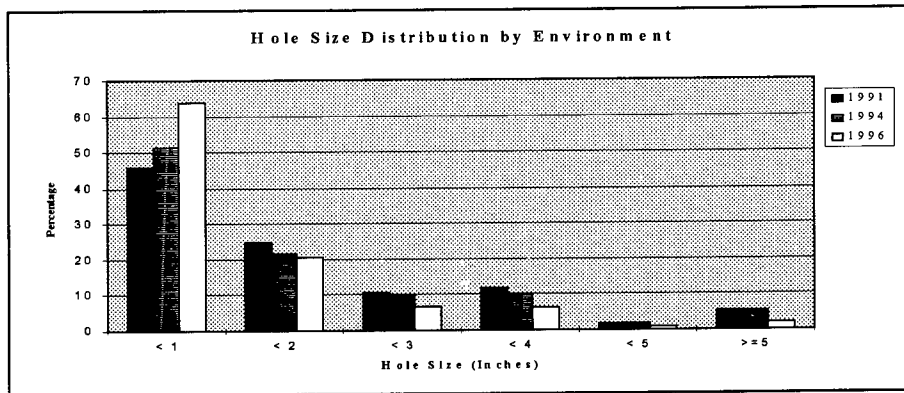
Fig. 3. Hole size distribution by environment.

Computing the Variance in P loss/pen Using MSCSurv

MSCSurv was developed as a trade study tool--i.e., it was used to compare the *relative* improvements in R due to changes in crew protocols, internal designs, and station operations. However, the *absolute* value of R was of little use in quantifying overall P_{loss} without an examination of its associated uncertainty bounds. MSCSurv Version 4.1SE was developed to address this need by allowing the R-factor computed by MSCSurv to be bound in terms of uncertainty. To create Version 4.1SE, the core of Version 4.1 was changed to allow the variation of input and modeling parameters from simulation to simulation.   The flowchart in Fig. 4 represents the flow of MSCSurv Version 4.1SE. An outer loop was added to Version 4.1 so that multiple simulations may be run. After each simulation, particular input or modeling parameter[s] is[are] randomly selected per a specified distribution and range (thus incorporating the uncertainty into the analyses). Certain input or modeling parameters are considered linked, i.e. they move in the same direction. MSCSurv Version 4.1SE outputs nominal R-factors and standard deviations in similar format to the output from MSCSurv Version 4.1. The results from this study of the effect of input parameter variations on R-factor are discussed in the next section.
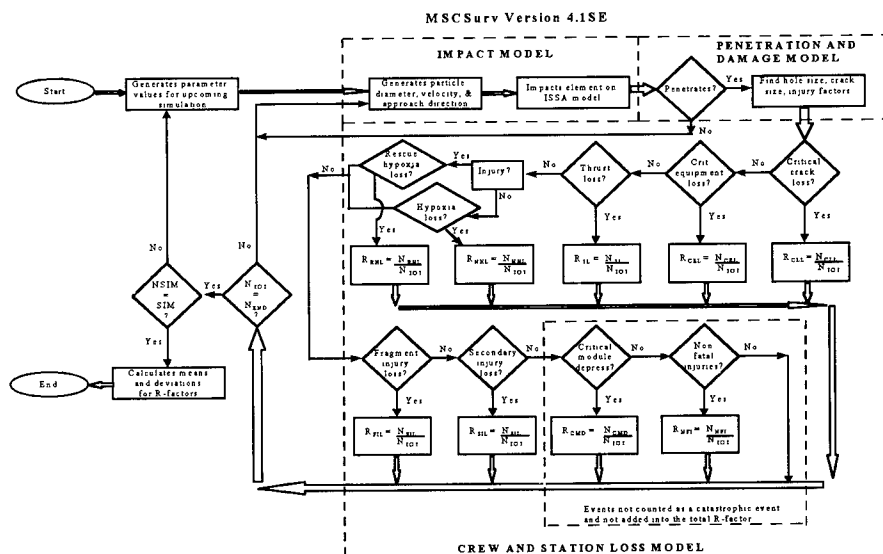
Fig. 4. Flowchart for MSCSurv 4.1SE.

EFFECT OF INPUT AND MODELING PARAMETER VARIATIONS ON $P_{LOSS/PEN}$

Effect of Individual Parameter Variation on Variation of R5 and R7

The overall intent of the parameter study was to determine which input and modeling parameters (and their associated variations) most impact the variation of the R-factors predicted by MSCSurv. The first step toward accomplishing this was to identify all of the parameters used by MSCSurv which have uncertainties associated with them. In doing this, only those parameters associated with the analyses MSCSurv performs AFTER a penetration were considered. These parameters can be broadly categorized as relating to *damage* (hole size, crack length, etc.), *station* (critical equipment protection, critical crack length, etc.), and *crew* (crew rates, hatch closure times, etc.) parameters. The parameters used to determine impacts and penetrations were not considered in this uncertainty analysis; the next section deals with the effects of varying the ballistic limit curves on overall P_{loss}. Tables 1 and 2 , when combined, present a complete list of the parameters considered.

Once the list of parameters was developed, nominal values, two sigma (95% certainty) bounds, and a distribution (uniform, triangular, or normal) were specified for each parameter. For the purposes of this study, reasonable bounds were determined by the authors of this paper--more formal values are being sought from the ISS program to be used to determine a more accurate R-Factor and uncertainty. The values used for this parameter study were judged to be adequate for our stated purpose: to establish which parameters and associated uncertainties most impact the overall R-factors.

Thirty-three parameters or sets of linked parameters were examined. For each run, one parameter or set of linked parameters was allowed to vary according to the pre-defined bounds and distribution. The other parameters were held constant. This exercise points to the parameters which contribute most to the overall variance and consequently points to those parameters where resources might best be applied to improve the overall R-factor accuracy.

Table 1 shows the results of the parameter study by listing the ten parameters (in descending order) which when varied produced the largest variance in R5 (presented in terms of two standard deviations). The results show that the uncertainty in hole-sizing models is by far the largest contributor (more than twice the next largest contributor) to the uncertainty in R-factor calculation. This result strongly indicates that focusing on hole-sizing models will have the largest pay-off in terms of reducing the uncertainty bounds. From Table 1, one can observe that the bounds were set differently according to the hole sizing model used by MSCSurv. MSCSurv primarily utilizes two hole-sizing methods: Burch [6] and Schonberg/Williamsen [7].

For each parameter run, MSCSurv performed 150 simulation of 100,000 penetrations each. The runs took about 13 hours each on a Pentium Pro, 200 MHz machine. The higher the number of simulations performed, the more stable and accurate the results will be. To gain some insight into just how much fluctuation from run to run might be expected, ten identical 50, 100, 150, 300, and 500 simulation runs were performed varying all parameters according to their specified distribution. Figure 5 shows the standard deviations of the mean and two sigma's for R5 and R7 for each set of ten runs. As expected, the larger the number of simulations performed for each run, the smaller the standard deviation in the group of ten runs. Ideally, this deviation would be zero. In cases where the main goal is an accurate mean and two sigma, this chart shows that 500 or more simulations would be desirable. However, for our purposes of grouping parameters, 150 simulations is adequate.

Table 1. Effects of individual input and modeling parameter variation on R5 and R7.

Description	Nominal	Lower bound (Ratio of nominal) (2 sigma)	Upper bound (Ratio of nominal) (2 sigma)	Distribution	R5	Two sigma for R5	% of Two sigma to R5	R7	Two sigma for R7	% of Two sigma to R7
Diameter of hole predicted (in)	Varies/ Equation	.75 (Burch) -1 in (S/W Whipple) -1.2 in (S/W Advanced)	1 (Burch) +1 in (S/W Whipple) +1.2 in (S/W Advanced)	Uniform Normal Normal	0.155	0.075	48.4	0.639	0.134	21.0
Maximum station angular velocity (yaw) above which an EV can not undock from the station (deg/sec)	3.0 deg/s 3.0 deg/s 6.0 deg/s	.3333 .3333 .3333	2 2 1	Uniform Uniform Uniform	0.166	0.033	19.9	0.623	0.008	1.3
Probability that if penetration depth sufficient, critical equipment damage will occur (0-1.0)	Varies/ Input File	.9 (Service Module) 0 (Rest of ISS)	1.1 (Service Module) 3 (Rest of ISS)	Triangular Uniform	0.167	0.028	16.8	0.627	0.021	3.3
Penetration depth of orbital debris particle (cm of AL)	Varies/ Equation	.5	1.5	Uniform	0.156	0.028	17.9	0.618	0.017	2.8
Time required to close a Russian hatch (s)	60 s	1	2	Uniform	0.183	0.027	14.8	0.634	0.014	2.2
Areal density for crew protection (gm/cm²)	Varies/ Input File	.9 (Service Module) 0 (Rest of ISS)	1.1 (Service Module) 3 (Rest of ISS)	Triangular Uniform	0.162	0.022	13.6	0.623	0.014	2.2
Areal density for critical equipment protection (gm/cm²)	Varies/ Input File	.9 (Service Module) 0 (Rest of ISS)	1.1 (Service Module) 3 (Rest of ISS)	Triangular Uniform						
Critical depressurization limit (psi)	9.5 psi	.7895	1	Uniform	0.141	0.019	13.5	0.599	0.024	4.0
Uninhibited crew translation rate (ft/s)	3 ft/s	.3333	2	Triangular						
Translation rate for removal of injured crew member from module (ft/s)	1 ft/s	1	3	Uniform						
Translation rate for searching for injured crew member (ft/s)	1 ft/s	1	3	Uniform	0.160	0.015	9.4	0.622	0.007	1.1
Coefficient of Discharge	.9	.8889	1.1111	Uniform	0.160	0.012	7.5	0.622	0.012	1.9
Time needed for crew to complete checkout procedures to ensure EV's are without damage (s)	300 s	.5	1	Triangular	0.155	0.010	6.5	0.620	0.003	0.5

Table 2. List of other parameters examined

Description	Nominal	Lower bound (Ratio of nominal) (2 sigma)	Upper bound (Ratio of nominal) (2 sigma)	Distribution
Free air volume in module M (ft3)	Input File	.9	1.1	Triangular
Alarm will sound at this pressure (psi)	13.9 psi	.9856	1.0144	Uniform
Pressure at which fog forms (psi)	11.8 psi	.95	1.05	Normal
Time required to determine which side of the PMA/Node 1 the leak is on (s)	120 s	.8	1.2	Uniform
Time required to perform pressure check after each hatch closure (s)	120 s	.8	1.2	Uniform
Time required to stabilize injured crew member prior to removal from a penetrated module (s)	300 s	.5	1.5	Uniform
Delay for crew to put on oxygen masks (s)	30 s	.3333	1	Uniform
Max sustainable arm strength allowing crew to affect movement (lbf)	50 lbf	1	2	Uniform
Length of crack predicted (in)	Equation	.75 (Burch) -2 in (S/W Whipple) -6.4 in (S/W Advanced)	1 (Burch) +2 in (S/W Whipple) +6.4 in (S/W Advanced)	Uniform Normal Normal
Multiplied by hole size to estimate crack size in some instances	2	.75	1	Uniform
Critical crack length for shield PID (cm)	Input File	.8	1.6	Uniform
Minimum size hole detectable by audio/visual means as crew passes hole (in)	.8 in	.5	1.5	Triangular
Time required to prepare EV for launch (s)	300s	.8	1.2	Triangular
Factor by which to multiply travel rates to reduce the rates to account for fog	.5	1	2	Uniform
Mass from rear wall detached by debris	Varies/ Equation	.5	3	Uniform
Mass of hole used in overpressure calculation (gm)	Varies/ Equation	.5	3	Uniform
Debris particle size limit above which all occurrences will be tallied as a critical crack loss (cm)	5.0 cm	1	2	Uniform
Probability an injured crew member is lost immediately or after rescue (0-1.0)	Varies/ Equation	.9	1.1	Triangular
Probability an injured crew member is immediately lost (0-1.0)	Varies/ Equation	.9	1.1	Triangular
Probability crew member in penetrated module is blinded by light flash	.1667	.5	1	Triangular
Minimum time at which the crew gives up all activities and moves to the egress via the EV's	300 s	.9	1.1	Triangular
Delay prior to initiating movement if awake at time ALARM goes off (s)	10 s	.5	1.5	Uniform
Time required to close a NASA hatch (s)	30 s	.9	1.1	Triangular
Delay prior to initiating movement if asleep at time ALARM goes off (s)	30 s	.5	1.5	Uniform
Velocity of rear wall mass (ft/s)	5000 ft/s	.3333	2	Uniform
S3/S4 Interface Allowable (in-lbf)	253 in-lbf	1	2	Triangular
PMA 1/FGB Interface Allowable (in-lbf)	443156 in-lbf	1	2	Triangular
S0/US Lab Interface Allowable (in-lbf)	350000 in-lbf	.5	1.5	Triangular
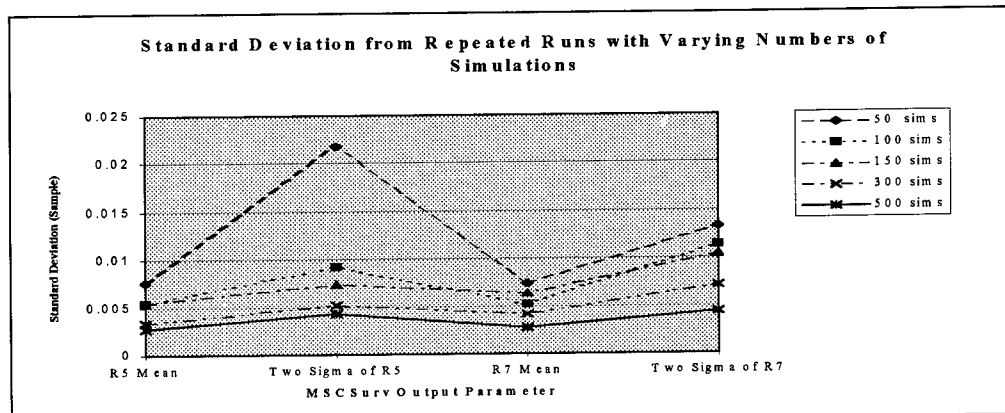
Fig. 5. Standard deviations in R5 and R7 from repeated runs varying numbers of simulations.

Sensitivity of R5 and R7 to Variations within Selected Groups of Input Parameters

Using the results presented in Table 1, those parameters which created the most variance in R5 were identified and grouped together so that runs varying only those parameters resulting in large variances could be performed. Table 3 presents this data. For the first run, no parameters were varied, just to measure background noise. Then a run was performed in which only the parameters which had produced small variances were allowed to vary. Finally, runs were performed in which parameters were grouped by the size of the variances they created in the individual runs. These results indicate that the parameters which cause individual two sigma's of less than .01 contribute very little to the overall two sigma, even when combined, despite the fact that 23 out of 33 parameters were varied in this simulation. One can see that investing resources to better tie down these parameters is probably not worthwhile. On the other hand, the run in which all parameters with 2 sigma's greater than or equal to .02 has about the same variance as the run in which all parameters were varied. These key parameters are (in order of their contribution): 1) hole diameter; 2) maximum allowable station angular velocity prior to causing escape vehicle failure; 3) probability of damaging critical equipment given adequate penetration depth; 4) multi-plate penetration depth equation; 5) time required to close Russian hatch; and 6) internal equipment areal densities (particularly protection for critical equipment).

Again, uncertainty in the hole-size models seems to be the overwhelmingly large contributor to the variance. The second through the sixth parameter in Table 1 would be the next logical parameters to examine, weighing the resources required to narrow the band of uncertainty of a parameter against the variance contributed by that parameter.

Table 3. Parameter groupings based on individual standard deviations

Description of simulation	R5	Two sigma for R5	% of two sigma to R5	R7	Two sigma for R7	% of two sigma to R7
Vary no parameters	0.160	0.002	1.3	0.622	0.002	.3
Vary all parameters with two sigma less than .01	0.158	0.010	6.3	0.618	0.012	1.9
Vary all parameters w/ two sigma >= .03 for either R5 or R7	0.157	0.084	53.5	0.629	0.122	19.4
Vary all parameters w/ two sigma >= .02 for either R5 or R7	0.166	0.121	72.9	.627	0.147	23.4
Vary all parameters w/ two sigma >= .01 for either R5 or R7	0.173	0.129	74.6	0.630	0.137	21.7
Vary all parameters	0.161	0.121	75.2	0.620	0.137	22.1

Grouping $P_{loss/pen}$ Parameters by Damage, Station, and Crew

Another interesting way of grouping the parameters in Tables 1 and 2 is by category. Some of the parameters are used to evaluate the damage the penetrating particle does to the station (hole diameter, penetration depth, crack length, etc.), other parameters specify characteristics of the physical station configuration (critical equipment protection, crew protection, critical crack length, etc.), and a third category of parameters involves the crew and operations (hatch closure times, crew movement rates, bail time, etc.).

Table 4 presents the results of this study. The damage parameters contribute significantly more (about twice as much) to the variance of the R-factors than do either the station or crew-related parameters. Again, this points to devoting resources toward developing more accurate hole-sizing models, the largest single contributor to the variance.

Table 4. Damage, station, and crew parameter results

Description of simulation	R5	Two sigma for R5	% of two sigma to R5	R7	Two sigma for R7	% of two sigma to R7
Damage parameters	0.152	0.084	55.3	0.637	0.148	23.2
Station parameters	0.173	0.048	27.7	0.629	0.027	4.3
Crew parameters	0.157	0.040	25.5	0.607	0.030	4.9

EFFECT OF VARIATION OF BALLISTIC LIMIT CURVES ON $P_{PEN/IMP}$

To this point, only parameters dealing with what happens AFTER a penetration have been varied. Another area of interest is the ballistic limit curves used by MSCSurv (and BUMPER) to predict whether or not a particle penetrates. That is, if the critical diameter causing penetration at a particular velocity and obliquity (i.e., D_{crit}) from a ballistic limit relation was uniformly distributed about the mean with a 2 sigma value of 10% of the predicted D_{crit}, what would be the effect on the variance of the $P_{pen/imp}$? Figure 6 shows a typical ballistic limit curve used by MSCSurv and BUMPER. The dashed lines on the figure show the effect of a 10% variation on ballistic range that was used in the +/- 10% runs. Note that this ballistic limit, like many others, is composed of a low velocity region, a medium velocity region, and a high velocity region. Accordingly, it was of interest to the analysis team to examine the effect on $P_{pen/imp}$ variance due to the variance of each of these individual portions of the ballistic limit curves taken individually.

Table 5 shows the results of several runs. Since changes in the ballistic limit curves would invalidate the hole-sizing models used in MSCSurv, only the penetration model was examined in this study. Looking at the variance in $P_{pen/imp}$ (penetrations/impacts ratio) predicted by MSCSurv by varying the ballistic limit curve, one can see that if the ballistic limit curves' are bounded by +/- 15%, the 2 sigma value of $P_{pen/imp}$ is bounded by +/- 49% of its mean value. Should +/- 10% more accurately bound the uncertainty in the ballistic limit curves, the 2 sigma uncertainty for $P_{pen/imp}$ would then be within 33% of its mean value. *The uncertainties resulting from these minor variances in ballistic limit equations ranks as equal to the highest contributors to uncertainty within the input and modeling parameters affecting $P_{loss/pen}$ (discussed earlier), and is far more important than any crew operation-related parameters used to calculate P_{loss}.*

Clearly, the level of uncertainty in the ballistic limit equations is a crucial factor in the overall level of uncertainty in calculating P_{loss}. While the parameters examined in earlier sections only affect the $P_{loss/pen}$ term in Eqn. 1, the ballistic limit curves affect the $P_{pen/imp}$ and $P_{loss/pen}$ terms. Considering this compounding of uncertainty and the size of uncertainty bounds on $P_{pen/imp}$ created from ballistic limit uncertainties, resources might be well-spent further developing more accurate ballistic limit equations.
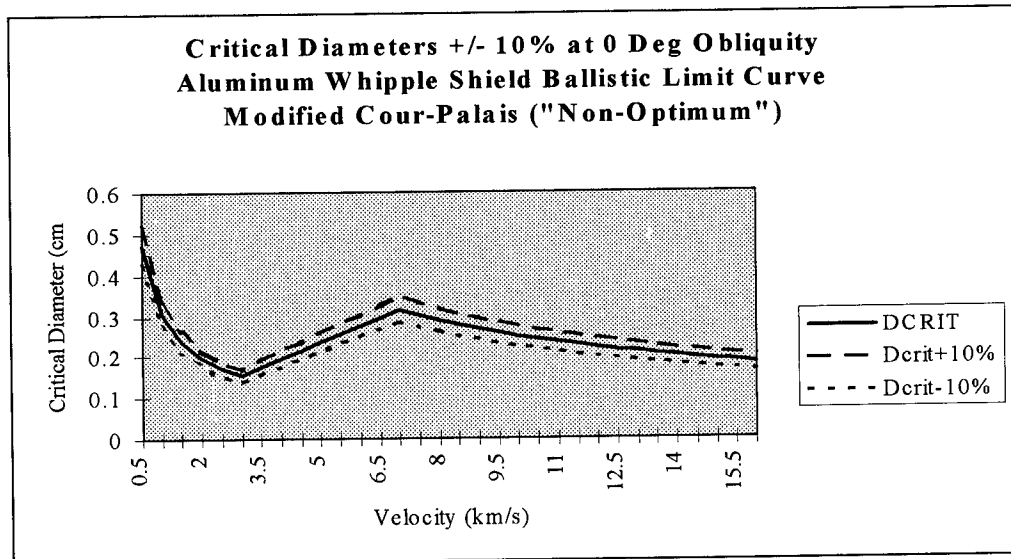
Fig. 6. Critical diameters +/- 10% for a typical spacecraft shield

Table 5. Critical diameter variance runs

Low velocity bounds	High velocity bounds	Velocity criteria (Velocity/ normal velocity)	Pen/Imp	Two sigma	% of two sigma to the whole
.95-1.05	.95-1.05	N/A	0.0127	0.00208	16.3
.9-1.1	.9-1.1	N/A	0.0126	0.00412	32.7
.85-1.15	.85-1.15	N/A	0.0131	0.00641	48.9
.95-1.05	Constant	Velocity	0.0124	0.00084	6.8
.9-1.1	Constant	Velocity	0.0126	0.00165	13.2
.85-1.15	Constant	Velocity	0.0126	0.00262	20.7
Constant	.95-1.05	Velocity	0.0125	0.00135	10.8
Constant	.9-1.1	Velocity	0.0128	0.00279	21.9
Constant	.85-1.15	Velocity	0.0129	0.00390	30.3
Constant	.95-1.20	Velocity	0.0112	0.00242	21.5
.95-1.05	Constant	Normal	0.0124	0.00114	9.1
.9-1.1	Constant	Normal	0.0127	0.00246	19.5
.85-1.15	Constant	Normal	0.0128	0.00389	30.4
Constant	.95-1.05	Normal	0.0125	0.00091	7.3
Constant	.9-1.1	Normal	0.0126	0.00187	14.9
Constant	.85-1.15	Normal	0.0128	0.00285	22.3
Constant	.95-1.20	Normal	0.0116	0.00166	14.3

CONCLUSIONS

The MSCSurv Version 4.1SE spacecraft survivability code allows us to examine for the first time the uncertainties in probability of spacecraft or crew loss (P_{loss}) created by variances in the input or modeling parameters utilized by the code. P_{loss} (and its associated uncertainties) can be traced to three major influences--the number of impacts on the spacecraft (N_{imp}), the probability that the spacecraft is penetrated following an impact ($P_{pen/imp}$), and the probability of spacecraft or crew loss following penetration ($P_{loss/pen}$).

The 1996 orbital debris environment showed fewer penetrations per impacts and fewer losses per penetrations when compared to results from the 1991 and 1994 orbital debris environments.

The holes created by the 1996 orbital debris environment tended to be significantly smaller than either the 1991 or 1994 orbital debris environments which probably accounts for the drop in losses per penetrations. If one assumes that the variances between orbital debris prediction models is anywhere near typical of the uncertainty associated within any of these models, then the effect of uncertainties within the environment on P_{loss} are likely to be of large effect--larger than the effect of variance from $P_{pen/imp}$ or $P_{loss/pen}$.

Using MSCSurv Version 4.1SE, parameters were examined individually to find out which parameters contributed most to uncertainties in predicting R-factors ($P_{loss/pen}$). The uncertainty in predicting the hole sizes resulting from penetrating particles contributed far more to the overall uncertainty variance than any other parameter. Other runs in which parameters were grouped in various combinations further supported this finding. Improving hole-size models is key to reducing uncertainties in MSCSurv analyses. Taken as a group, damage-related parameters had a much higher effect on R (i.e., $P_{loss/pen}$) than did station or crew-related input or modeling parameters. That is, small changes in factors like hole size and depth of penetration models had a far larger effect on $P_{loss/pen}$ than parameters such as crew movement rates, hypoxia limits, or other crew-related factors.

Large uncertainties were introduced into the $P_{pen/imp}$ term when +/- 10% uncertainties were used for predicting critical diameters from the ballistic limit equations. The uncertainties resulting from these minor variances in ballistic limit equations ranks as equal to the highest contributors to uncertainty within the input and modeling parameters affecting $P_{loss/pen}$ (discussed earlier), and is far more important than any crew operation-related parameters used to calculate P_{loss}. Therefore, accuracy in the formation of ballistic limit curves is key to reducing uncertainties in the overall orbital debris risk assessment.

This methodology gives spacecraft designers, NASA safety experts, and program management a method for determining not only the absolute value for P_{loss}, but also the variance associated with it. Additional work is required to determine the effect of simplifying assumptions associated with the orbital debris environment (orbital debris material, shape, and orientation) on overall spacecraft P_{loss}. However, the preliminary analyses here, regarding the effect of variances in the ballistic limit and input and modeling parameters on uncertainties in P_{loss}, indicate that the effect of key environmental assumptions is likely to be very large on predictions of spacecraft P_{loss}.

REFERENCES

1. H. J. Evans, K. Blacklock and J. E. Williamsen, *Manned Spacecraft & Crew Survivability (MSCSurv) Version 4.0 User's Guide* (1997).
2. D. J. Kessler, J. Zhang, M. J. Matney, P. Eichler, R. C. Reynolds, P. D. Anz-Meador and E. G. Stansbery, A computer-based orbital debris environment model for spacecraft design and observations in low-earth orbit, TM 104825 (1997).
3. Space station program natural environment definition for design, SSP 30425, Revision B, NASA-JSC (1994).
4. D. J. Kessler, Update to the orbital debris environment for space station", SN3-94-164, NASA-JSC (1994).
5. W.J. Schonberg and J. E. Williamsen, Empirical models for spacecraft damage from orbital debris penetration and effects on spacecraft survivability, *Second European Conference on Space Debris*, ESOC, March 17-19, Darmstadt, Germany (1997).
6. G. T. Burch, Multiplate-Damage study, Air Force Armament Laboratory, AFATL-TR-67-116 (1967).
7. J. E. Williamsen, D. Grosch and W. J. Schonberg, Empirical prediction models for hole and crack size in space station shielding from 6 to 12 km/s (1996).

A HYBRID PARTICLE-FINITE ELEMENT METHOD FOR HYPERVELOCITY IMPACT SIMULATION

ERIC P. FAHRENTHOLD and BLAISE A. HORBAN

Department of Mechanical Engineering, University of Texas, Austin, TX 78712

Summary—Coupled particle-finite element methods have been suggested as an approach to modeling particular impact problems not well suited to simulation with conventional Eulerian, Lagrangian, or particle codes. An alternative hybrid particle-finite element technique has been developed, in which particles are used to model contact-impact and volumetric deformation while finite elements are employed to represent interparticle tension forces and elastic-plastic deviatoric deformation. The method has been implemented in a three dimensional code and applied to simulate representative hypervelocity impact problems. © 1999 Elsevier Science Ltd. All rights reserved.

INTRODUCTION

Particle-based numerical impact models [1] can offer distinct advantages over Eulerian [2] and Lagrangian [3] hydrocodes in particular hypervelocity impact applications. An example is the design of orbital debris shielding [4, 5], where conventional codes have proven difficult to apply [6, 7, 8]. Particle models avoid certain problems with mesh distortion and debris transport which have hindered the effective use of Lagrangian and Eulerian codes in the simulation of three dimensional impacts on shielded space structures [9]. However particle methods typically incorporate kinematically inexact treatments of material history effects such as plasticity and fracture. Recent research efforts have been directed at the formulation of coupled particle-finite element methods for hypervelocity impact simulation [10], as well as a variety of other new numerical methods [11, 12].

Both particle-in-cell (PIC) methods [13] and smooth particle hydrodynamics (SPH) methods [14, 15] employ particles which are actually moving interpolation points. An alternative particle-based modeling methodology developed by Fahrenthold and Koo [16, 17] offers a fully Lagrangian, energy-based approach to shock physics simulations. This alternative approach, labeled Hamiltonian particle hydrodynamics, avoids the tensile and boundary instabilities associated with some smooth particle hydrodynamics formulations [18, 19] and the potentially diffusive grid-to-particle mapping schemes characteristic of some particle-in-cell methods.

In recent work, the particle method of Fahrenthold and Koo has been extended, by coupling the aforementioned hydrodynamic particle model to a Lagrangian finite element description of material strength in the continuum. The resulting hybrid particle-finite element model retains all of the features (including general contact-impact effects) of Hamiltonian particle hydrodynamics, while in addition accounting for tensile strength, elastic shearing strain, plasticity, and continuum damage effects important in the simulation of some hypervelocity impact problems.

The finite element kinematics used here are similar (not identical) to those employed in existing Lagrangian hydrocodes [20], for example DYNA3D [3]. The coordinates of certain nearest neighbor particles, identified in the reference configuration, determine finite element nodal displacements and hence the local elastic shearing strain, the local plastic strain rate, and interparticle tensile forces. Normal and deviatoric continuum damage variables are introduced to allow for perforation, fragmentation, and fracture in arbitrary geometry's, while no slideline

algorithms [21] are employed. Element failure is based on strictly physical criteria, and is not dependent on any smoothing length or mesh-to-particle mapping scheme. Unlike other particle based strength models, the present formulation incorporates exact Lagrangian finite strain kinematics, which have proven effective in Lagrangian finite element codes in characterizing highly strength dependent features of impact dynamics problems.

A three dimensional, parallel implementation of the hybrid numerical method described here has been coded, with specific interest in the application of orbital debris shielding design. The sections which follow outline the hybrid formulation, and illustrate the method using two example simulations with known experimental results.

MODELING METHODOLOGY

The hybrid particle-finite element model described here is formulated using an energy method, namely Hamiltonian mechanics [22]. Hence the model formulation procedure differs markedly from that used in weighted residual finite element techniques or the finite difference (finite volume) method. It differs also from the model formulation procedure used with many particle methods, which typically rely in part on energy concepts and in part on the differential balance equations for the continuum. As in all discrete Hamiltonian methods, the present model is formulated by assembling kinetic and potential energy expressions for the system, describing the relevant constraint equations, and introducing Lagrange multipliers, in order to arrive at the final first order state (evolution) equations for the system. Unlike the familiar and purely mechanical Hamiltonian models seen often in the literature, the present work employs entropy states to model the thermal dynamics of the system. One result is that the energy dissipation expression normally used to quantify viscous generalized forces is replaced by a set of nonholonomic constraints on the entropy evolution. These and other differences from classical Hamiltonian formulations are discussed in more detail by Fahrenthold and Koo [16, 17], who also employ a Hamiltonian methodology to formulate a particle model of the SPH type.

The sections which follow discuss the particle and element kinematics, the stored energy expressions for the system, and the nonholonomic constraints, and then apply Hamilton's canonical equations to arrive at a state space description of the impact dynamics problem. The particles are used to model kinetic energy effects, contact-impact, and thermomechanical volumetric deformation, while the finite elements represent strength effects (interparticle tension, elastic shear, and plastic deformation). Contact-impact is modeled using penalty forces similar to those employed in DYNA3D. Numerical viscosity is introduced to damp all the elastic modes, and numerical heat conduction serves to diffuse shock heating.

KINEMATICS

This section provides an overview of the particle and element kinematics. The particles of the present model are homogeneously deformed, spherical, Lagrangian control volumes. Hence their motion is described completely by a scalar deformation gradient (F) and a center of mass position vector (c) for each particle. The material time derivatives ($\dot{F}$ and $\dot{c}$) of these generalized coordinates are generalized velocities for the Hamiltonian system. In the reference (undeformed) configuration for the modeled system, the particles are arranged in a body-centered cubic packing scheme.

The Lagrangian finite elements used here incorporate nine nodes: they are eight-noded hexahedra, with a ninth node located (in the reference configuration) at the element centroid. Eight "edge centered" particles define the corners of a hexahedra, while a "body centered" particle locates the interior node. In other words, the particle center of mass coordinates are also nodal coordinates, for intact (uneroded) elements. Each element is subdivided into six separate five-noded subelements, by associating the body centered particle for each element with the six separate sets of four particles which define the faces of the hexahedron. The volumes of the subelements are used in calculating interparticle tensile forces, while the shear deformation of the hexahedron is used to determine the deviatoric strain. The hexahedra are used to describe the following Lagrangian finite strain kinematics for the continuum. The elastic deviatoric strain tensor (E^e) for an element is defined by

$$\mathbf{E}^e = \bar{\mathbf{E}} - \mathbf{E}^p \tag{1a}$$

where $\mathbf{E}^p$ is the plastic strain tensor, and the deviatoric total strain is [23]

$$\bar{\mathbf{E}} = (1/2)\,(\bar{\mathbf{C}} - \mathbf{I}) \quad ; \quad \bar{\mathbf{C}} = J^{-2/3}\,\mathbf{C} \quad ; \quad J = [\,\det(\mathbf{C})\,]^{1/2} \tag{1b,c,d}$$

with J the Jacobian of the hexahedron and $\mathbf{C}$ the right Cauchy-Green strain tensor. Since the edge centered particles define the hexahedra, the center of mass coordinates for those particles are used to calculate the strain tensor ($\mathbf{C}$) and element Jacobian (J). As a result the only new generalized coordinates (internal state variables) introduced by the elements are the six components of the symmetric plastic strain tensor ($\mathbf{E}^p$) for each element.

KINETIC ENERGY

The kinetic energy (T) of the system is a function of the particle translation and deformation, and takes the form [16, 17]

$$T = (1/2) \sum_{i=1}^{n} [\,m^{(i)-1}\,p^{(i)2} + M^{(i)-1}\,H^{(i)2}\,] = T(p^{(i)},\,H^{(i)}) \tag{2a}$$

where n is the number of particles, m is the particle mass, M is the (constant) particle moment of inertia in the reference configuration, p is the particle center of mass momentum, H is the particle distributed momentum, and the superscript "(i)" denotes the ith particle. The generalized momenta are related to the corresponding generalized velocities by

$$\dot{\mathbf{c}}^{(i)} = \frac{\partial T}{\partial \mathbf{p}^{(i)}} = m^{(i)-1}\,\mathbf{p}^{(i)} \quad ; \quad \dot{\mathbf{F}}^{(i)} = \frac{\partial T}{\partial H^{(i)}} = M^{(i)-1}\,H^{(i)} \tag{2b,c}$$

INTERNAL ENERGY

The conserved potential in this Hamiltonian model is the system internal energy (U). The internal energy is partitioned into three parts: (1) a thermomechanical potential (u, an internal energy per unit mass) for each particle which depends on the current particle density (ρ) and entropy per unit mass (s), (2) a deviatoric strain energy which depends on the elastic strain tensor ($\mathbf{E}^e$) and a deviatoric damage variable (d, $0 \le d \le 1$), and (3) an interparticle tensile strain energy which depends on the particle deformation gradients, the subelement volumes, and a normal damage variable (D, $0 \le D \le 1$). Specifically

$$U = \{\,\sum_{i=1}^{n} m^{(i)}\,u^{(i)}(\rho^{(i)},\,s^{(i)})\,\} + \{\,\sum_{i=1}^{n_e} (1 - d^{(i)})\,V_o^{e(i)}\mu^{(i)}\,\mathbf{E}^{e(i)}\!:\mathbf{E}^{e(i)}\,\} +$$

$$\{\,\sum_{i=1}^{n_e} \sum_{j=1}^{6} (1/2)\,(1 - D^{(i)})\,V_o^{e(i,j)}K^{(i)} < V^{e(i,j)} / V_o^{e(i,j)} - \vartheta^{(i,j)} >^2\,\} \tag{3}$$

where n_e is the number of elements, $V_o^{e(i)}$ denotes the reference volume for element "i", $V^{e(i,j)}$ and $V_o^{e(i,j)}$ are the current and reference volume for subelement "j" of element "i", $\mu^{(i)}$ and $K^{(i)}$

are the shear modulus and the reference bulk modulus for element "i", $\vartheta^{(i,j)}$ is the mass weighted average of the particle Jacobians for subelement "j" of element "i", and the notation "< >" represents the Macauley bracket [< x > = x for x > 0, < x > = 0 for x ≤ 0]. In view of the aforementioned particle kinematics,

$$\vartheta^{(i,j)} = \vartheta^{(i,j)} (F^{(k)}) \quad ; \quad u^{(i)} = u^{(i)}(F^{(i)}, S^{(i)}) \quad ; \quad S^{(i)} = m^{(i)} s^{(i)} \qquad (4a,b,c)$$

so that the total particle entropy (S) is a generalized coordinate for the system. Likewise, in view of the aforementioned element kinematics,

$$E^{e(i)} = E^{e(i)} (c^{(k)}, E^{p(i)}) \quad ; \quad V^{e(i,j)} = V^{e(i,j)} (c^{(k)}) \qquad (4d,e)$$

so that the total internal energy has the functional form

$$U = U (F^{(i)}, S^{(i)}, c^{(i)}, E^{p(i)}, D^{(i)}, d^{(i)}) \qquad (5a)$$

The corresponding generalized conservative forces are

$$G^{(i)} = \frac{\partial U}{\partial F^{(i)}} \quad ; \quad \theta^{(i)} = \frac{\partial U}{\partial S^{(i)}} \quad ; \quad g^{(i)} = \frac{\partial U}{\partial c^{(i)}} \qquad (5b,c,d)$$

where $\theta^{(i)}$ is the temperature for particle "i", while

$$\Gamma^{(i)} = - \frac{\partial U}{\partial D^{(i)}} \quad ; \quad \eta^{(i)} = - \frac{\partial U}{\partial d^{(i)}} \qquad (5e,f)$$

are energy release rates associated with normal and shear damage evolution and

$$S^{(i)} = 2\mu^{(i)} (1 - d^{(i)}) \ E^{e(i)} = - (1/V_o^{e(i)}) \ \frac{\partial U}{\partial E^{p(i)}} \qquad (5g)$$

is a deviatoric stress tensor.

PLASTICITY MODEL

The plasticity model used here is a rate independent variation of the isochoric finite strain formulation of Fahrenthold and Horban [24]. The flow rule for the incremental plastic strain is taken as

$$\Delta E^p = \Delta\lambda \ W \qquad (6a)$$

$$\Delta\lambda = < \tau - Y > / \{ 2\mu (1-d) \ [(1/2) \ W{:}W]^{1/2} \} \quad ; \quad \tau^2 = (1/2) \ S{:}S \qquad (6b,c)$$

where τ is the effective shear stress, Y is the yield stress, and

$$W = C^p \ A' + A' \ C^p \qquad (6d)$$

$$A' = A - (1/3) \ \mathrm{tr}(A) \ I \quad ; \quad A = S \ C^p + C^p \ S \qquad (6e,f)$$

$$C^p = I + 2 \ E^p \qquad (6g)$$

In general, the yield stress is taken to be a linear function of J and θ [25]. Here

$$Y = Y(J, \theta) = <\alpha J -1> <1 - \beta (\theta - \theta_0)/(\theta_m - \theta_0)> Y_0 \qquad (7a)$$

where θ_0 and θ_m are a reference and melting temperature, Y_0 is a reference yield stress, and α and β are constants. For use in determining element failure, the effective plastic strain (ε^p) is tracked by integrating

$$\dot{\varepsilon}^p = [(1/2) (\dot{E}^p: \dot{E}^p)]^{1/2} \qquad (7b)$$

It should be noted that the present modeling methodology allows for the introduction of alternative elastic-plastic formulations [26].

DAMAGE EVOLUTION EQUATIONS

The normal and shear damage variables serve to degrade the element moduli in shear and tension, and thereby represent the loss of cohesive strength associated with material failure. The energy released in damage evolution is a source of irreversible entropy production, so that no internal energy is discarded. The simple rate independent damage evolution relations used here are

$$\Delta D = \Delta d = \omega \quad ; \quad \omega = \text{constant (normally 0.1)} \qquad (8)$$

for any time step after an element "fails", due to any one of several effects: (1) the (negative) tensile pressure drops below a specified value, (2) the effective shear stress exceeds a specified value, (3) the maximum eigenvalue of the deviatoric stress tensor exceeds a specified value, or (4) the accumulated plastic strain exceeds a specified value. For $\omega = 0.1$ element failure will occur gradually, over ten time steps [27]. Once the maximum damage value of 1.0 is reached, the element has lost all cohesion and ω is again set to zero.

It should be noted that nothing in the methodology described here precludes the implementation of more complex damage evolution models, like those previously implemented in particle based [28] or Eulerian [29] codes.

NUMERICAL VISCOSITY

Considering the preceding discussion of particle and element kinematics, numerical viscosity [30] is required to damp both relative motion of the particle mass centers and bulk deformation of the individual particles. The damping force on particle "i" due to relative particle motion is taken as

$$f^{(i)} = \sum_{j=1}^{n} v^{(i,j)} \{(\dot{c}^{(i)} - \dot{c}^{(j)}) \cdot (c^{(i)} - c^{(j)})\} (c^{(i)} - c^{(j)}) / (\dot{c}^{(i)} - \dot{c}^{(j)})^2 \qquad (9a)$$

where $v^{(i,j)}$ is the numerical viscosity

$$v^{(i,j)} = c_0 (1/2) (\rho^{(i)} \dot{c}_s^{(i)} A^{(i)} + \rho^{(j)} \dot{c}_s^{(j)} A^{(j)}) \Lambda[\zeta^{(i,j)}] \qquad (9b)$$

$$\zeta^{(i,j)} = (h^{(i)} + h^{(j)}) - |c^{(i)} - c^{(j)}| \qquad (9c)$$

with c_0 a dimensionless viscosity coefficient, $c_s^{(i)}$ the sound speed for particle "i", $A^{(i)}$ the cross sectional area for particle "i", $h^{(i)}$ the radius for particle "i", and $\Lambda[\zeta]$ a step function ensuring that only neighboring particles interact

$$\Lambda[\zeta] = 1 \ \text{ for } \ \zeta \ge 0 \ ; \ \Lambda[\zeta] = 0 \ \text{ for } \ \zeta < 0 \tag{9d}$$

Note that the preceding force depends on the normal component of the relative velocity between two particles. A similar viscous force which depends on the tangent relative velocity component is introduced in each intact element, for relative motion of the edge centered with respect to the body centered particle.

To damp the bulk deformation of individual particles, a viscous pressure is introduced with the functional form

$$P^{B(i)} = - c_1 \, \rho^{(i)} \, c_s^{(i)} \, h^{(i)} \, \dot{F}^{(i)} \tag{9e}$$

where c_1 is a dimensionless viscosity coefficient.

NUMERICAL CONDUCTION

As is standard in impact codes, a numerical heat conduction or artificial viscosity [30] is used in the present model. Given the use of entropy states in the Hamiltonian formulation, it takes the form

$$\dot{S}^{\text{con}(i)} = (1/\theta^{(i)}) \sum_{j=1}^{n} R^{(i,j)} (\theta^{(i)} - \theta^{(j)}) \tag{10a}$$

where $R^{(i,j)}$ is the numerical conduction coefficient

$$R^{(i,j)} = c_2 \, (1/2) \, (\, \rho^{(i)} \, c_s^{(i)} \, c_v^{(i)} \, A^{(i)} + \rho^{(j)} \, c_s^{(j)} \, c_v^{(j)} \, A^{(j)} \,) \, \Lambda[\zeta^{(i,j)}] \tag{10b}$$

with $c_v^{(j)}$ the specific heat for particle "i" and c_2 a dimensionless conduction coefficient.

MECHANICAL AND THERMAL CONSTRAINTS

The energy balance equation used in conventional continuum codes is replaced here by nonholonomic entropy evolution constraints for the particles

$$\dot{S}^{(i)} = \dot{S}^{\text{irr}(i)} - \dot{S}^{\text{con}(i)} \tag{11a}$$

where $\dot{S}^{\text{irr}(i)}$ is the entropy production rate due to viscous dissipation, plastic flow, and damage evolution

$$\dot{S}^{\text{irr}(i)} = (1 / \theta^{(i)}) \, \dot{W}^{(i)} \tag{11b}$$

$$\dot{W}^{(i)} = \mathbf{f}^{(i)} \cdot \dot{\mathbf{c}}^{(i)} - V_0^{(i)} P^{B(i)} \, \dot{F}^{(i)} + \Gamma^{(i)} \dot{D}^{(i)} + \eta^{(i)} \dot{d}^{(i)} + V_0^{e(i)} S^{(i)} : \dot{\mathbf{E}}^P \tag{11c}$$

with $\dot{W}^{(i)}$ and $V_0^{(i)}$ the energy dissipation rate and reference volume for particle "i". As shown by Fahrenthold and Koo [16] in the hydrodynamic case, the Lagrange multipliers associated with

these constraints are known, so that they introduce no new state variables. Similarly, the evolution equations for the plastic and damage variables are constraint equations which can be shown to introduce no new unknown Lagrange multipliers into the formulation.

Additional mechanical constraints are must be introduced to represent particle collisions. They are

$$ |c^{(i)} - c^{(j)}| - \xi \, (h^{(i)} + h^{(j)}) \geq 0 \tag{12a} $$

where the constant ξ allows for close packing of the particles at the reference density. The value of ξ depends on the choice of relative sizes for the edge centered and body centered particles (for equal size $\xi = 0.879$). Since the preceding expression is an inequality constraint, it is represented in the model formulation process using the nonholonomic expressions

$$ [\, (c^{(i)} - c^{(j)}) \, / \, |c^{(i)} - c^{(j)}| \,] \cdot (\dot{c}^{(i)} - \dot{c}^{(j)}) - \xi \, \{ \, h_o^{(i)} \, \dot{F}^{(i)} + h_o^{(j)} \, \dot{F}^{(j)} \, \} \; = 0 \tag{12b} $$

where $h_o^{(i)}$ is the particle radius in the reference configuration. Since the Lagrange multipliers associated with the particle collision constraints are numerous, penalty forces $\lambda^{(i,j)}$ are introduced to impose the latter

$$ \lambda^{(i,j)} = k^{(i,j)} \, [\, \xi \, (h^{(i)} + h^{(j)}) - |c^{(i)} - c^{(j)}| \,] \, \Lambda[\zeta^{c(i,j)}] \tag{12c} $$

where the step function ensures interaction of overlapping particles only

$$ \zeta^{c(i,j)} = \xi \, (h^{(i)} + h^{(j)}) - |c^{(i)} - c^{(j)}| \tag{12d} $$

and $k^{(i,j)}$ is a penalty stiffness. For particles connected by springs in series

$$ k^{(i,j)} = c_3 \, / \, [1.0/(K^{(i)} \, A_o^{(i)2} / \, V_o^{(i)}) + 1.0/(K^{(j)} \, A_o^{(j)2} / \, V_o^{(j)})] \tag{12e} $$

where $A_o^{(i)}$ is the reference cross sectional area for particle "i", and c_3 is a dimensionless penalty stiffness, while for parallel springs (as in DYNA3D)

$$ k^{(i,j)} = c_3 \, (1/2) \, [\, K^{(i)} \, A_o^{(i)2} / \, V_o^{(i)} + K^{(j)} \, A_o^{(j)2} / \, V_o^{(j)} \,] \tag{12f} $$

HAMILTON'S EQUATIONS

The preceding sections have defined the kinematics, stored energy functions, and constraints for the physical system. They lead to Hamilton's equations in the form

$$ \dot{p}^{(i)} = -\, g^{(i)} -\, f^{(i)} + \sum_{j=1}^{n} \lambda^{(i,j)} \, (c^{(i)} - c^{(j)}) \, / \, |c^{(i)} - c^{(j)}| \tag{13a} $$

$$ \dot{c}^{(i)} = m^{(i)-1} \, p^{(i)} \tag{13b} $$

$$ \dot{H}^{(i)} = -\, G^{(i)} -\, V_o^{(i)} P^{B(i)} - \sum_{j=1}^{n} \xi \, h_o^{(i)} \, \lambda^{(i,j)} \tag{13c} $$

Table 1. Oblique Whipple shield impact simulation

Projectile diameter (aluminum 6061-T6 sphere)	=	0.60 cm
Shield thickness (aluminum 6061-T6)	=	0.127 cm
Wall thickness (aluminum 6061-T6)	=	0.3175 cm
Shield-to-wall spacing	=	5.0 cm
Impact velocity	=	7.0 km/sec
Impact obliquity	=	15 degrees
Number of particles	=	207,363
Total simulation time	=	30.7 microseconds
Number of time steps	=	7,000
Wall clock time (2-CPU SGI Octane)	=	60 hours
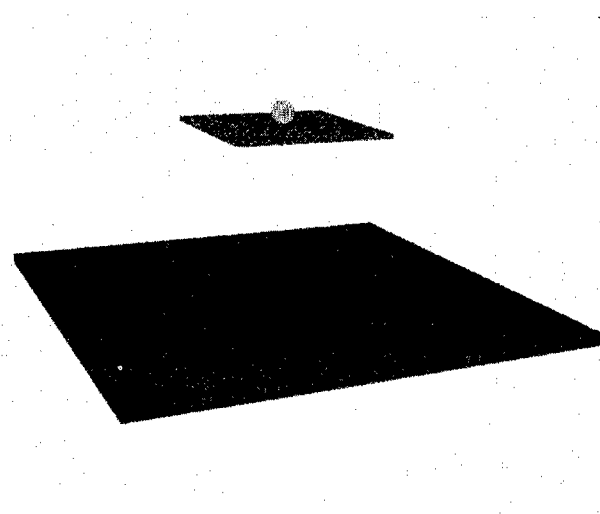
Fig. 1. Oblique Whipple shield impact simulation (t = 0.0 microseconds).

Fig. 2. Oblique Whipple shield impact simulation (t = 30.7 microseconds).

$$\dot{F}^{(i)} = J^{(i)-1} H^{(i)} \qquad (13d)$$

$$\dot{S}^{(i)} = \dot{S}^{irr(i)} - \dot{S}^{con(i)} \qquad (13e)$$

augmented by the evolution equations for the plastic strain and continuum damage variables. Integration of these nonlinear, history dependent relations for a chosen equation of state describes the thermomechanical dynamics of the impact problem of interest.

The state space model described here has been implemented in a three dimensional impact code [31], developed with a particular interest in orbital debris shielding applications. The state equations are integrated using a second order Runge-Kutta method, using time step limits described by Fahrenthold and Koo [16]. Currently Mie-Gruneisen and ideal gas equations of state are employed, and linked lists [32] are used to identify neighbor particles. The code incorporates compiler directives for parallel execution on Cray systems and SGI workstations. A pre-processor is included for model generation, as well as an automated rezoner which deletes particles moving outside a user specified control volume. The latter feature is essential for many orbital debris shielding simulations. Post processing is performed using commercial graphics software. Testing and further code development work is now in progress. The next section presents two example simulations, for which there are known experimental results.

EXAMPLE SIMULATIONS

The simulations discussed in this section employed material property data from Steinberg [25], and the following dimensionless coefficients:

$$c_0 = c_1 = 0.01 \quad ; \quad c_2 = 0.1 \quad ; \quad c_3 = \alpha = \beta = 1.0 \quad ; \quad \xi = 0.900$$

The material failure stress in shear was set to the maximum yield stress, while the failure pressure in tension was set to the spall stress. The effective plastic strain at failure was set to 3.0.

The first example is an oblique Whipple shield impact simulation, at a velocity of seven kilometers per second. The problem parameters are provided in Table 1, and the simulation is depicted in Figures 1 and 2. Automated rezoning was used every 1,000 times steps to delete particles which move outside the modeled region above the wall plate. For the modeled aluminum materials, impact velocity, impact obliquity, shield and wall thickness, and standoff distance, experimental ballistic limit curves [33] predict failure of the wall plate for projectiles over 0.45 cm in diameter. The modeled projectile of 0.60 cm diameter clearly fails the wall plate, as shown in Figure 2, depicting the simulation results at 30.7 microseconds after impact. The required CPU time indicated in Table 1 is reasonable, for a three dimensional simulation. Note that the requirement to model fragmentation of the projectile, as well as contact-impact of all the projectile and shield fragments, presents significant difficulties for conventional Lagrangian codes. On the other hand, tracking small debris fragments requires a relatively fine Eulerian mesh, computationally expensive in three dimensions. Hertel [6] reported a requirement of about 50 CPU hours on a Cray YMP for a three dimensional Whipple shield simulation using CTH, albeit at a standoff distance approximately twice that shown in this example. The latter simulation work incorporated significant user intervention, emphasizing the motivation for considering alternative methods in the simulation of shielding design problems.

The second example involves a highly oblique long rod impact on a flat plate, at projectile and target velocities of 1.21 and 0.217 kilometers per second. The problem parameters are provided in Table 2, and the simulation is depicted in Figures 3 and 4. This problem has been modeled with several codes, including CTH [34]. In the present case, pre-processor limitations did not allow for the hemispherical nose of the experimental projectile to be modeled, so a flat nose was represented. Figure 3 shows the projectile-target configuration at impact, while Figure 4 shows half the physical model (cut along the plane of symmetry) at 100 microseconds after impact. Experimental data at the latter time indicated an eroded rod length of 5.55 cm and a residual velocity of 1.069 kilometers per second. The present work yielded a residual rod length of 4.49 cm and a residual velocity of 0.950

Table 2. Long rod impact simulation

Projectile diameter (DU 0.75% Ti cylinder)	=	0.767 cm
Projectile length	=	7.67 cm
Plate thickness (4340 steel)	=	0.64 cm
Projectile velocity	=	0.121 cm/μsec
Plate velocity	=	0.0217 cm/μsec
Impact obliquity	=	73.5 degrees
Number of particles	=	66,478
Total simulation time	=	100 μsec
Number of time steps	=	5,934
Wall clock time (6-CPU SGI Onyx)	=	7.50 hours
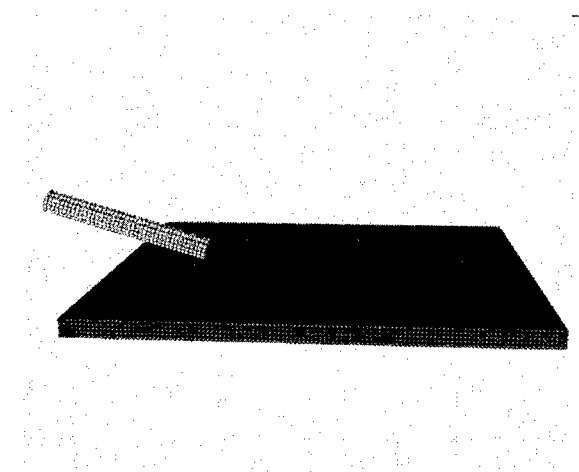
Fig. 3. Long rod impact simulation (t = 0.0 microseconds).
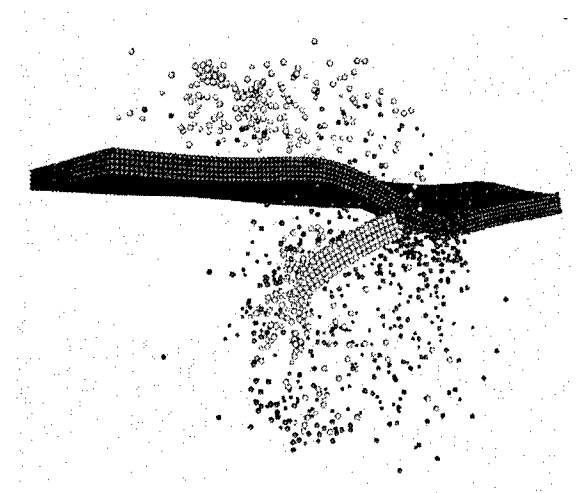
Fig. 4. Long rod impact simulation (half model at t = 100 microseconds).

kilometers per second. The corresponding CTH simulation yielded a better estimate of eroded rod length (6.00 cm) and residual velocity (0.956 kilometers per second). As in the first example, the CPU times reported for a parallel workstation in Table 2 and for a Cray YMP using CTH (4.02 hours) are not directly comparable. However the CPU time reported here is reasonable, for a relatively long (100 microsecond) impact simulation in three dimensions.

CONCLUSION

The present paper has outlined the development of a hybrid particle-finite element modeling approach to hypervelocity impact simulation. The method appears to have certain advantages over pure Lagrangian, Eulerian, and particle methods in the application of orbital debris shielding design. Although further development and testing of the method is in progress, comparisons of simulation results to representative hypervelocity impact problems show reasonable agreement with experiment. Recent research focused on Arbitrary Lagrangian-Eulerian (ALE), element-free Galerkin (EFG), Fluid Implicit Particle (FLIP), and other coupled or hybrid methods suggests that such methods will provide opportunities for the expanded use of simulation in the study of hypervelocity impact problems.

REFERENCES

1. J.J. Monaghan, Particle methods for hydrodynamics, *Computer Physics Reports*, **3**, 71-124 (1985).

2. J.M. McGlaun, S.L. Thompson, and M.G. Elrick, CTH: a three dimensional shock wave physics code, *International Journal of Impact Engineering*, **10**, 351-360 (1990).

3. J.O. Hallquist, Theoretical Manual for DYNA3D, Lawrence Livermore National Laboratories (1983).

4. E.L. Christiansen, J.L. Crews, J.E. Williamsen, J.H. Robinson, and A.M. Nolen, Enhanced meteoroid and orbital debris shielding, *International Journal of Impact Engineering*, **17**, 217-228 (1995).

5. E.L. Christiansen and J.H. Kerr, Projectile shape effects on shielding performance at 7 Km/s and 11 Km/s, *International Journal of Impact Engineering*, **20**, 165-172 (1997).

6. E.S. Hertel, Comparison of Analytic Whipple Bumper Shield Ballistic Limits with CTH Simulations, Sandia Report SAND92-0347 (1993).

7. E.P. Fahrenthold, A Lagrangian model for debris cloud dynamics simulation, *International Journal of Impact Engineering*, **14**, 229-240 (1993).

8. E.P. Fahrenthold, Oblique hypervelocity impact simulation for Whipple shield-protected structures, *International Journal of Impact Engineering*, **17**, 291-302 (1995).

9. R.J. Rabb and E.P. Fahrenthold, Numerical simulation of oblique impact on orbital debris shielding, *International Journal of Impact Engineering*, in press (1998).

10. G.R. Johnson, E.H. Petersen, and R.A. Stryk, Incorporation of an SPH option into the EPIC code for a wide range of high velocity impact computations, *International Journal of Impact Engineering*, **14**, 385-394 (1993).

11. K.G. Budge and J.S. Peery, RHALE: a MMALE shock physics code written in C++, *International Journal of Impact Engineering*, **14**, 107-120 (1993).

12. Y.Y. Lu, T. Belytschko, and M. Tabbara, Element-free Galerkin method for wave propagation and dynamic fracture, Computer *Methods in Applied Mechanics and Engineering*, **126**, 131-153 (1995).

13. D. Sulsky, Z. Chen, and H.L. Schreyer, A particle method for history dependent materials, *Computer Methods in Applied Mechanics and Engineering*, **118**, 179-196 (1994).

14. R.F. Stellingwerf C.A. and Wingate, Impact modeling with smooth particle hydrodynamics, *International Journal of Impact Engineering*, **14**, 707-718 (1993).

15. C.A. Wingate, R.F. Stellingwerf, R.F. Davidson, and M.W. Burkett, Models of high velocity impact phenomena, *International Journal of Impact Engineering*, **14**, 819-830 (1993).

16. E.P. Fahrenthold and J.C. Koo, Hamiltonian particle hydrodynamics, *Computer Methods in Applied Mechanics and Engineering*, **146**, 43-52 (1997).

17. E.P. Fahrenthold and J.C. Koo, Energy based particle hydrodynamics for hypervelocity impact simulation, *International Journal of Impact Engineering*, **20**, 253-264 (1997).

18. J.W. Swegle, D.L. Hicks, and S.W. Attaway, Smooth particle hydrodynamics stability analysis, *Journal of Computational Physics*, **116**, 123-134 (1995).

19. G.R. Johnson and S.R. Beissel, Normalized smoothing functions for SPH impact computations, *International Journal for Numerical Methods in Engineering*, **39**, 2725-2741 (1996).

20. D.J. Benson, Computational methods in Lagrangian and Eulerian hydrocodes, *Computer Methods in Applied Mechanics and Engineering*, **99**, 235-394 (1992).

21. T. Belytschko and J.I. Lin, A three-dimensional impact-penetration algorithm with erosion, *International Journal of Impact Engineering*, **5**, 111-127 (1987).

22. J.H. Ginsberg, Advanced Engineering Dynamics, Harper and Row, Inc., Cambridge (1988).

23. J. Lubliner, Plasticity Theory, Macmillan, New York (1990).

24. E.P. Fahrenthold and B.A. Horban, Thermodynamics of continuum damage and fragmentation models for hypervelocity impact, *International Journal of Impact Engineering*, **20**, 241-252 (1997).

25. D.J. Steinberg, Equation of State and Strength Properties of Selected Materials, Lawrence Livermore National Laboratory, Livermore, CA, UCRL-MA-106439 (1996).

26. L.D. Libersky, A.G. Petschenk, T.C. Carney, J.R. Hipp, and F.A. Allahdadi, High strain Lagrangian hydrodynamics, *Journal of Computational Physics*, **109**, 67-75 (1993).

27. S.A. Silling, CTH Reference Manual: Johnson-Holmquist Ceramic Model, Sandia National Laboratories, SAND92-0576 (1992).

28. W. Benz and E. Asphaug, Simulations of brittle solids using smooth particle hydrodynamics, *Computer Physics Communications*, **87**, 253-265 (1995).

29. E.P. Fahrenthold and C.H. Yew, Hydrocode simulation of hypervelocity impact fragmentation, *International Journal of Impact Engineering*, **17**, 303-310 (1995).

30. W.F. Noh, Errors for calculations of strong shocks using an artificial viscosity and an artificial heat flux, *Journal of Computational Physics*, **72**, 78-120 (1978).

31. E.P. Fahrenthold, User's Guide for EXOS, University of Texas at Austin (1998).

32. R.W. Hockney and J.W. Eastwood, Computer Simulation Using Particles, McGraw-Hill Inc., New York (1981).

33. E.L. Christiansen, Design and performance equations for advanced meteoroid and debris shields, *International Journal of Impact Engineering*, **14**, 145-156 (1993).

34. E.S. Hertel, A Comparison of the CTH Hydrodynamics Code With Experimental Data, Sandia Report SAND92-0347 (1992).

SPH SIMULATIONS OF DEBRIS IMPACTS USING TWO DIFFERENT COMPUTER CODES

MORENO FARAUD*, ROBERTO DESTEFANIS*, DAVID PALMIERI**, and MARIO MARCHETTI**

*Alenia Aerospazio, Divisione Spazio, C.so Marche 41, 10146 Turin, Italy; **University of Rome "La Sapienza," Aerospace Department, v. Eudossiana 16, 00184 Rome, Italy

Summary—This paper reports the results of Smoothed Particle Hydrodynamics (SPH) simulations of debris impact on an all aluminium triple wall system, performed by Alenia Aerospazio using the PAM-SHOCK 3D computer code, and by the University of Rome "La Sapienza" using the AUTODYN 2D hydrocode. The point of view of a user interested in debris shielding design and not that of a software developer or an SPH algorithm expert has been adopted. Comparisons between the results of the two codes at early, mid and late stages of impact are shown. Theoretical predictions are used to evaluate the numerical simulations at early stages of impact. The predictions of the damage induced on the plates are compared with the Light Gas Gun experimental data. X-ray pictures are used to evaluate the simulations of the debris cloud expansion and spalled material detached from the intermediate bumper. Traditional Finite Volume (FV) simulation results are reported and compared with SPH results. The authors do not go into any SPH algorithm details, but using the potentiality of the respective codes show what is the current capability of the hydrocodes to assess the ballistic performance of high resistance debris shielding used to protect space structures.© 1999 Elsevier Science Ltd. All rights reserved.

INTRODUCTION

The European Space Agency has requested from Alenia Aerospazio an innovative debris shielding design able to cope with the severe meteoroid and debris requirement for the Columbus Orbital Facility (COF), the European laboratory to be attached to the International Space Station. The safety requirement demands advanced heavy shield systems to stop debris with a mass that ranges from 1.5 to 3.2 g under normal impacts. The design has been led using a Light Gas Gun firing aluminium spheres up to 6.5 ÷ 7 km/s.

The numerical simulation activity started in late 1996, with the aim to analyse hypervelocity impacts in a velocity range (8 ÷ 16 km/s) not covered by tests. The simulations have been performed at Alenia with the PAM-SHOCK 3D hydrocode, developed by Engineering Systems International (ESI). In mid 1997, a research program on hypervelocity numerical simulations started in cooperation with the University of Rome "La Sapienza", where the simulations have been performed using the AUTODYN 2D hydrocode, developed by Century Dynamics. All the numerical simulations carried out at Alenia are 3D and have been led using the SPH solver. The simulations carried out at the University of Rome are 2D in axial symmetry and have been led using both the SPH solver and the traditional FV technique with the erosion algorithm.

Due to the highly directional debris environment, a directional meteoroid and debris (M/OD) protection system has been selected for the COF module [1]. In the areas more exposed to the M/OD threat, the debris shielding is based on a Whipple structure plus an intermediate wall made of layers of Nextel, placed on top of a Kevlar composite with Epoxy resin. The numerical simulations presented in this paper are relevant to these areas, but, to avoid further complications

and uncertainties, no advanced materials like Kevlar/Nextel are taken into account in these simulations. Therefore the shielding configuration selected as the example for this work is composed of an external bumper (1st BS) 2.5 mm thick, made of aluminium Al 6061 T6, an intermediate bumper (2nd BS) 6.0 mm thick, made of aluminium Al 6061 T6, and a back up wall (BW) 3.2 mm thick, made of aluminium Al 2219 T851 (see Fig. 1). The overall spacing S is 143.5 mm and the internal spacing S2 between the intermediate bumper and the back up wall is 42 mm. This configuration was tested at the Ernst Mach Institute, Germany, in Summer 1995.

PAM-SHOCK 3D AND AUTODYN 2D CHARACTERISTICS

Fig.1. COF shielding configuration.

PAM-SHOCK 3D is a Lagrangian non-linear explicit finite element code. It holds various Equations of State (EOS) like the polynomial EOS, the Sesame library for aluminium and Nextel-Kevlar materials and various constitutive material models including strain rate and temperature effects on the yield stress. A SPH processor is incorporated as a special solver in the PAM-SHOCK software [2]. It is available in one- two- and three-dimensional Cartesian coordinates. Four types of kernel functions are implemented in the current SPH version: the cubic spline W4 (default), the Q-Gaussian, the Quartic as defined by Fulk, and the Quadratic as defined by Johnson and Fulk. The smoothing length is a free parameter which can be given as fixed or variable input. In this last case the smoothing length varies proportionally to the radius of the particles in a range whose limits are fixed by the user. To treat shock fronts, artificial viscosity parameters are given by the user as input. To decrease unphysical particle interpenetration, a particle motion correction can be given optionally by the user as well. Three momentum equation choices are available. Two Normalised Smoothing Functions (proposed by Johnson and Groenenboom, respectively) are implemented as options in the code to treat material boundaries. A SPH sliding interface option prevents SPH particles, belonging to different materials, from interacting as connected elements: the compressive forces are computed only if the distance between the particles is less than the distance equal to the sum of the particles radii multiplied by a factor defined by the user; moreover no shear and tension are transmitted. To reduce the cost of the CPU time, an improved neighbour searching algorithm allows the search for particles belonging to plates not yet impacted to be skipped temporarily. A "rezone" option allows to deactivate selected particles during the restart and to split a complex problem in simpler separated problems. A coupling of SPH particles with finite elements, by means of a contact-like algorithm, also allows to reduce the CPU time consumption, since the finite element model in PAM-SHOCK requires less CPU time than the equivalent SPH model.

The code is still under development as algorithm and pre/post-processors: a lot of input data have still to be introduced by using text editors. The PAM-SHOCK 3D software is installed on a dedicated workstation: a Silicon Graphics Indigo^2 Impact R10000 with a clock speed of 175 MHz and 256 RAM MB.

AUTODYN is a non-linear explicit finite volume code. It is available in both 3D and 2D versions: in the latter planar and axial symmetry options are implemented. Several numerical processors are included: Lagrange, Euler (with first and second order schemes), Arbitrary Lagrangian Euler (ALE), Shell for modelling thin structural elements, and SPH. Individual structured meshes operated on by these different processors can be coupled together in space and time to compute interaction problems efficiently. Many libraries of material data are available for solids, liquids and gases, among which the polynomial shock and the Tillotson EOS, together with constitutive models including rate and temperature effects, that can be used to model the hypervelocity behaviour of solid materials.
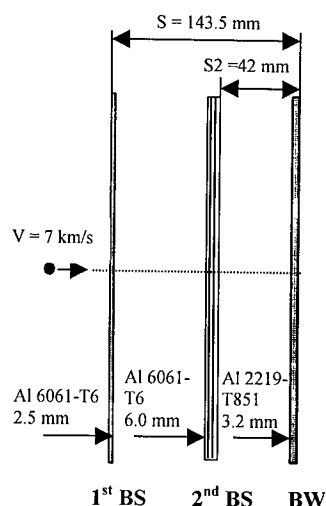
The SPH processor [3] is actually still in a beta-version, and it is implemented only in 2D. The cubic B-spline kernel function is used in the SPH algorithm, while the density can be calculated using both the continuity equation or a corrected kernel sum equation that can be useful in certain cases to improve numerical inconsistencies in the SPH equations. The smoothing length can be kept constant during the calculations or it can be allowed to vary with time depending on the local changes in density: the smoothing length of a particle can be limited to a user specified ratio of the neighbour particles. The values of artificial viscosity coefficients can be chosen as input parameters. The SPH processor can be coupled in the same problem with each of the other Lagrangian grid-based AUTODYN processors: Lagrange, ALE, Shell. The SPH particles which impact on another Lagrangian grid are repelled by means of forces normal to the impact surface, across which there is no tensile or shear material strength: these forces are computed only if the distance between an SPH node and the grid surface is less than the half of the local SPH smoothing length. The current version of AUTODYN is installed on a PC 200 MHz MMX 128 RAM MB.

EARLY STAGES OF IMPACT: ANALYTICAL APPROACH AND HYDROCODE PARAMETER SENSITIVITY

A preliminary study at early stages of impact can be carried out by means of the one-dimensional analysis. Applying the conservation equations (mass, momentum and energy) to the shock, a set of relationships, called the Rankine-Hugoniot equations, is obtained. These equations, together with the impact conditions and a linear shock velocity-particle velocity relationship, called the linear Hugoniot relationship, allow the maximum pressure/density and the particle/shock velocity to be estimated. Assuming that the initial conditions ahead of the shock are zero, the Rankine-Hugoniot jump conditions become:

$$\rho_0\, u_s = \rho(u_s - u_p)$$

$$P_H = \rho_0\, u_s\, u_p$$

$$E_H = p_H\, (V_0 - V_H)/2$$

where ρ is the density, ρ_0 is density at the initial condition, u_s is the shock velocity, u_p is the particle velocity, P_H is the Hugoniot pressure due to shock transition, E_H is the Hugoniot internal energy, V_0 is the initial specific volume, and V_H is the Hugoniot specific volume. The linear Hugoniot relationship has the form

$$u_s = c_0 + K u_p$$

where c_0 and K are experimental coefficients: c_0 is about equal to the speed of sound in the undisturbed material. Pressure, density, internal energy, particle and shock velocity can be evaluated by writing these equations for both the projectile and target material and imposing at the target-projectile interface pressure equilibrium and continuity of the velocity. The study of shock propagation with numerical simulations is faced with unphysical oscillations of the flow variables induced by the shock discontinuity. To cope with this problem, it is usual to introduce extra viscous terms in the differential equations. These terms are an artificial dissipation mechanism that spreads the oscillations over several computational zones, smoothing their amplitude. The user can modify the influence of the viscous terms by means of coefficients α (Alpha) and β (Beta) associated to the linear and quadratic term in velocity, respectively [4].

Several simulations at early stages of impact have been performed in order to analyse the influence of these parameters on various variables, comparing the response of the two codes. The example selected for these analyses involves a spherical projectile with a 10 mm diameter

impacting a target 2.5 mm thick at a normal velocity of 7 km/s. The selected material is Aluminium 6061 for both the projectile and target.

The one-dimensional analysis gives the following results: particle velocity = 3.5 km/s, shock wave velocity = 10 km/s, Hugoniot pressure = 0.95 Mbar and shocked material density = 4.15 gr/cm^3.

Table 1 summarises the characteristics of the cases considered in the numerical simulations: two 3D double symmetric PAM-SHOCK SPH models, which differ in mesh density, and two 2D axial symmetric AUTODYN models obtained using the SPH and FV techniques, respectively. In the PAM-SHOCK models the smooth particles are coupled with a few finite elements localised in the external part of the plate, not involved in large deformations.

Table 1. Simulation cases at early stages

	Case 1 (SPH) *PAM-SHOCK 3D*	*Case 2 (SPH)* *PAM-SHOCK 3D*	*Case 3 (SPH)* *AUTODYN 2D*	*Case 4 (FV)* *AUTODYN 2D*
Sphere	2944 particles 26 particles along the diameter	8000 particles 40 particles along the diameter	610 particles 40 particles along the diameter	600 cells 40 cells along the diameter
Target	4000 particles + 2449 finite elements 5 particles in the thickness	32000 particles + 512 finite elements 10 particles in the thickness	2000 particles 10 particles in the thickness	1200 cells 10 cells in the thickness
EOS	Sesame P_{min} = -0.63 GPa	Sesame P_{min} = -0.63 GPa	Shock P_{min} = -1.2 GPa	Shock P_{min} = -1.2 GPa

Fig. 2 (left) shows the behaviour of the maximum pressure reached during the impact as function of α, keeping β equal to 1.0. The peak of pressure decreases when α increases and in the SPH simulations it is always higher in the projectile than in the target. This difference is strongly evident in the simulations performed with the PAM-SHOCK hydrocode, mainly due to the low mesh density used (5 particles in the thickness) and to the impossibility to get an uniform mesh density in the sphere. This problem is avoided in AUTODYN because the models are in two dimensions and an automatic mesh generator, incorporated in the AUTODYN software, allows a 2D sphere with an uniform mesh density to be created.

For each value of α, the values of pressure obtained with the SPH technique are always higher than the corresponding values of pressure estimated with the one-dimensional analysis. Surprisingly, the results obtained using the AUTODYN FV models are always underestimated
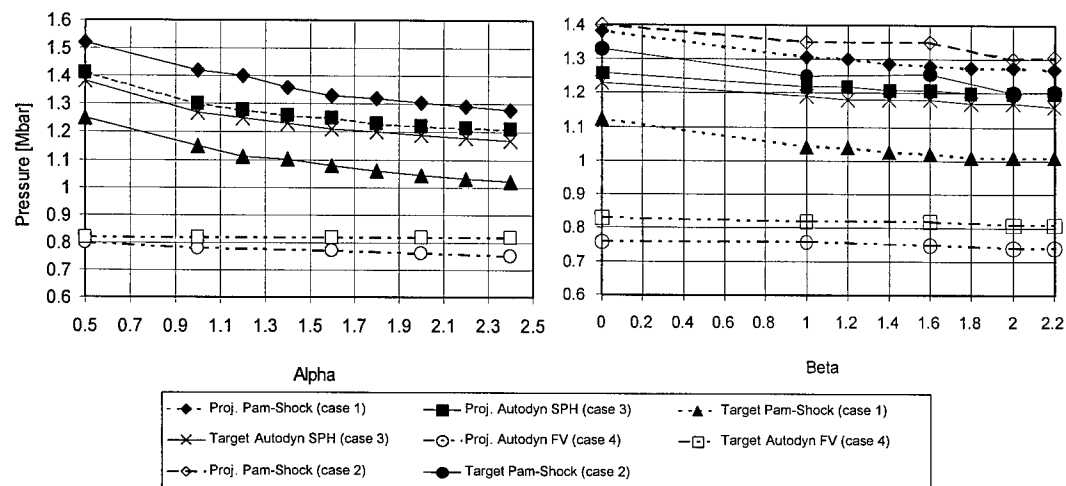
Fig. 2. Shock pressure as function of Alpha with Beta =1.0 (left) and as function of Beta with Alpha = 2.0 (right).

with respect to the analysis, and the peak of pressure in the target is always higher than in the projectile. Moreover, the variation depending on the coefficient α is almost negligible. Fig. 2 (right) shows the maximum pressure as function of β, keeping α equal to 2.0. The behaviour is similar to that reported in Fig. 2 (left), although the decrease of the peaks of pressure with the increase of the value of the coefficient β is lower. The figure shows as well that with a finer mesh density (10 particles in the thickness), the gap in pressure existing between the projectile and target, assessed with PAM-SHOCK, decreases, although the peaks increase (in this case the pressure in the target is overestimated with respect to the analysis performed with AUTODYN). Fig. 2 shows that with a raw mesh density the pressure in the target evaluated with PAM-SHOCK is always underestimated with respect to that evaluated with the AUTODYN SPH technique. Fig. 3 (above) shows the maximum density of the shocked material as function of α, keeping β constant. The behaviour is similar to that of the pressure: the density decreases when the value of α increases. The peaks of density evaluated with the AUTODYN FV technique are always underestimated with respect to the one-dimensional analysis and they are higher

Fig. 3. Shocked material density as function of Alpha with Beta = 1.0 (above) and as function of Beta with Alpha 2.0 (below).

in the projectile than in the target. Higher peaks of pressure and density were obtained when the Mie-Gruneisen and Tillotson EOS were used in the PAM-SHOCK and AUTODYN simulations (not reported here), respectively. Fig. 4 (above) shows the delta energy (total energy increase or decrease with respect to the initial total energy, equal to the kinetic energy of the projectile) as function of α, evaluated 2 μs from the impact. The simulations performed with PAM-SHOCK show a better energy conservation increasing the value of α. The simulations performed with AUTODYN show a more irregular behaviour. However, in the range of 0 ÷ 2 μs, the delta energy is lower in the AUTODYN than in the PAM-SHOCK simulations. Fig. 4 (below) reports the delta energy as function of β. The simulations performed with AUTODYN show that the delta energy has a minimum for β equal to 1. The simulations performed with PAM-SHOCK show that the delta energy decreases when β increases and a better energy conservation is obtained with a finer mesh. In this case the delta energy is lower in AUTODYN until β = 1.8. After that, a better energy conservation is obtained with PAM-SHOCK than with AUTODYN. The results obtained with the FV technique are not reported here because they are not meaningful; in fact the use of the erosion algorithm, removing all the highly distorted cells and the relevant energy, produces an unphysical drop in energy. Fig. 5 shows an example of shock pressure behaviour for three different values of α and β, performed with the PAM-SHOCK hydrocode. With a low value of α (0.5), the peak of pressure is very high; moreover large oscillations occur behind the shock. Increasing the value of α to 2.0, the coefficient β being equal, the peak of pressure gets lower and the oscillations are damped. With respect to this case, using β = 0.0 and α = 2.0, the peak of pressure increases slightly and the oscillations are still
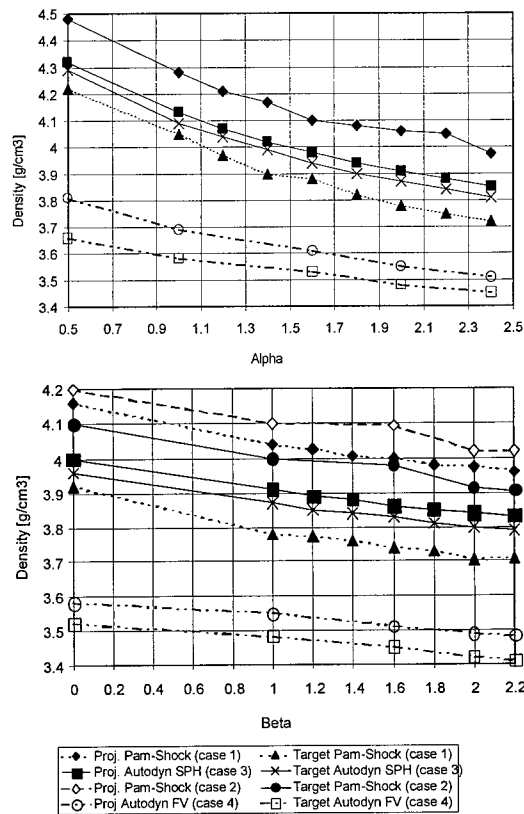
damped. This figure shows that the influence on the results of the coefficient associated to the linear term is greater than that of the coefficient associated to the quadratic term. The same results have been obtained with the AUTODYN SPH and FV technique. The influence of the coefficients α and β is similar to that shown in Fig. 5. However, with the AUTODYN hydrocode, the peak of pressure and the spall threshold are reached earlier (around $0.05 \div 0.1$ and $0.65 \div 0.7$ µs, respectively).

DEBRIS CLOUD EXPANSION

2 µs after the impact the debris cloud is fully formed: all the material (projectile and bumper) inside the cloud has reached the pressure cut off (- 0.63 GPa for the Sesame, -1.2 GPa for the linear shock). Then the tensional failure is set to zero; the debris cloud expansion goes on, since all the failed particles can continue to interact with their neighbours by means of the relevant smoothing lengths. The failed material can still compress but cannot bear any tensile load. A comparison between experiments and numerical simulations of the debris cloud expansion from the 1st BS to the 2nd BS is reported here. The influence of the EOS, mesh density and smoothing length on the results is shown.

The coefficients α, β are kept constant; α = 1.2, β = 1.5 and α = 2.0, β = 2.0 have been selected for the PAM-SHOCK and AUTODYN simulations, respectively. The characteristics of the simulations performed are summarised in Table 2. The examples from 1 to 6 have been drawn out from [5] and are compared here with the simulations performed with PAM-SHOCK. Cases 1 and 2 use the FV technique with an erosion algorithm that removes all the cells which have reached 250% of geometric strain. Cases from 3 to 6 use the SPH technique with a constant smoothing length, equal to twice the particle diameter. Cases from 7 to 12 use the SPH technique with a variable

Fig. 4. Delta energy at 2 µs as function of Alpha with Beta =1.0 (above) and as function of Beta with Alpha = 2.0 (below).

Fig. 5. PAM-SHOCK 3D, SPH simulations: pressure behavior comparison.

smoothing length, proportional to the radius of the particles, whose maximum limit is reported in Table 2. The results of these simulations are reported in Table 3. The values in brackets, corresponding to the debris cloud axial position at 9.3 µs, are relevant to few particles of the debris cloud front.

Table 2. Debris cloud expansion simulation cases

Case	*Equation of State*	*Constitutive Relationship*	*N° of particles in the 1st BS thickness*	*Coefficients α, β*	*Smoothing length*
1 Autodyn 2D, FV	Tillotson P_{min}:-1.2 GPa	Steinberg Guinan	10	2.0, 2.0	Not applicable
2 Autodyn 2D, FV	Shock P_{min}: -1.2 GPa	Steinberg Guinan	10	2.0, 2.0	Not applicable
3 Autodyn 2D, SPH	Tillotson P_{min}: -1.2 GPa	Steinberg Guinan	5	2.0, 2.0	Constant; 2 x (particle diameter)
4 Autodyn 2D, SPH	Tillotson P_{min}: -1.2 GPa	Steinberg Guinan	10	2.0, 2.0	Constant; 2 x (particle diameter)
5 Autodyn 2D, SPH	Shock P_{min}: -1.2 GPa	Steinberg Guinan	5	2.0, 2.0	Constant; 2 x (particle diameter)
6 Autodyn 2D, SPH	Shock P_{min}: -1.2 GPa	Steinberg Guinan	10	2.0, 2.0	Constant; 2 x (particle diameter)
7 Pam-Shock 3D, SPH	Sesame P_{min}: -0.63 GPa	Johnson Cook	5	1.2, 1.5	Variable; max: 0.15 cm
8 Pam-Shock 3D, SPH	Sesame P_{min}: -0.63 GPa	Johnson Cook	5	1.2, 1.5	Variable; max: 0.10 cm
9 Pam-Shock 3D, SPH	Sesame P_{min}: -0.63 GPa	Johnson Cook	10	1.2, 1.5	Variable; max: 0.15 cm
10 Pam-Shock 3D, SPH	Sesame P_{min}: -0.63 GPa	Johnson Cook	10	1.2, 1.5	Variable; max: 0.05 cm

The evaluation of the debris cloud expansion agrees with the experimental measures. In all the cases the materials inside the debris clouds have reached the condition of spalled material at 3.6 µs. Cases 9 and 10, which only differ in smoothing length, give the same results. Also the CPU time necessary for the simulation is equal. The hole diameter increases in size with the expansion of the debris cloud. The values reported for the hole diameter relevant to the SPH simulations are approximate since it is very difficult to find the exact border of the hole. All the material inside the debris cloud is in a spall condition. No influence of the Equations of State and constitutive relationships on the results relevant to the debris cloud evolution has

(a)   (b)   (c)

Fig. 6. Debris cloud shapes; (a): X-ray pictures at 3.6 and 9.3 µs; (b): AUTODYN FV, case 1, at 3.6 µs; (c): AUTODYN SPH, case 4, at 3.6 µs.
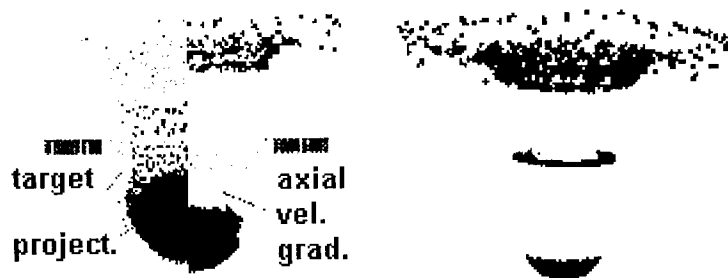
Fig. 7. Debris cloud shapes for case 11, PAM-SHOCK SPH; debris cloud section at 3.6 µs with axial velocity gradient and material distribution (left); debris cloud shape at 9.3 µs with axial velocity gradient (right).

been noted. Fig. 6 shows a double exposure X-ray picture at 3.6 and 9.3 µs, compared with the debris cloud shape at 3.6 µs, simulated with the AUTODYN FV (case 1) and SPH (case 4) technique, respectively. Fig. 7 shows the debris cloud section at 3.6 µs, with the associated axial

velocity gradient and material distribution, and the debris cloud expansion at 9.3 µs, with the associated axial velocity gradient. The simulation has been performed with high mesh density using the PAM-SHOCK hydrocode (case 9).

Table 3. Debris cloud expansion results

Case	Debris cloud axial position [mm] at 3.6 µs	Debris cloud radial position [mm] at 3.6 µs	Hole diam. in the 1st BS [mm] at 3.6 µs	Debris cloud axial position [mm] at 9.3 µs	Debris cloud radial position [mm] at 9.3 µs	Hole diam. in the 1st BS [mm] at 9.3 µs
1	21.3	12.8	20	57.5	28.8	21.6
2	21.2	12.5	19.3	58.3	26.7	20.7
3	21.6	12.5	≈ 23	56.9	27.0	≈ 26
4	21.2	11.7	≈ 22	55.5	24.4	≈ 25
5	22.0	12.9	≈ 24	58.8	29.7	≈ 27
6	22.3	11.6	≈ 23	58.4	23.7	≈ 26
7	23.5	11.6	≈ 21	57.0 (62.5**)	23.8	≈ 23
8	23.7	11.9	≈ 20	57.0 (63.4**)	23.9	≈ 21
9	23.4	11.7	≈ 20	57.0 (62.0**)	23.9	≈ 23
10	23.3	11.6	≈ 20	57.1 (62.3**)	23.9	≈ 23
Exp	23	11	21*	58.7	21	21*

*diameter measured on the plate; **velocity of few particles

PROBLEMS AND DESCRIPTION OF THE MODELS USED TO SIMULATE THE IMPACTS ON THE SECOND BUMPER SHIELD AND BACK UP WALL

Four models pertaining to simulations of damages on the 2nd BS and BW are reported in Table 4. The first simulation has been obtained using the PAM-SHOCK coupling option, which allows to model the problem with particles and finite elements together (see Fig. 8). A whole triple wall model made only of smooth particles would be too demanding for computational power. Therefore a hybrid model made of smooth particles, in the regions where high deformations take place, and finite elements, in the regions where the deformations remain limited, is used. The CPU problems demand using a coarse mesh density: 5 particles in the first bumper thickness, 9 in the second and 5 in the back up wall. The type of mesh density is

Table 4. Plate damage evaluation cases

	1 PAM-SHOCK 3D, SPH (double symmetry)	2 PAM-SHOCK 3D, SPH (double symmetry + rezone option)	3 AUTODYN 2D, FV (axial symmetry)	4 AUTODYN 2D, SPH (axial symmetry)
Projectile: mesh density	2944 particles	2944 particles	600 cells	610 particles
1st BS: mesh density	5760 particles (5 in the thickness); 8208 FE	5760 particles (5 in the thickness); 8208 FE	1200 cells (10 in the thickness)	2000 particles (10 in the thickness)
2nd BS: mesh density	28800 particles (9 in the thickness); 16800 FE	52530 particles (10 in the thickness); 14280 FE	5000 cells (20 in the thickness)	10000 particles (20 in the thickness)
BW: mesh density	16000 particles (5 in the thickness); 8400 FE	17017 particles (5 in the thickness); 96 FE	1200 cells (8 in the thickness)	2000 particles (8 in the thickness)
Equation of State	Sesame P_{min}: -0.63 GPa	Sesame P_{min}: -0.63 GPa	Shock P_{min}: -1.2 GPa	Shock P_{min}: -1.2 GPa
Constitutive relationship	Johnson Cook	Johnson Cook	Steinberg Guinan	Steinberg Guinan
Smoothing length	Variable; max: 0.12 cm	Variable; max: 0.12 cm	Not applicable	Constant; 2 x (particle diameter)
Coefficient α, β	1.2, 1.5	1.2, 1.5	2.0, 2.0	2.0, 2.0

imposed by the second bumper that, owing to its large thickness (6.0 mm), requires a great number of smooth particles (28800). Once the number of particles in the 2nd BS thickness is set, so the mesh density in the other plates is automatically set. In fact the smooth particle density must be as uniform as possible on the whole model. Particles with different mass cause the stopping of the process, according to the maximum number of neighbours defined in the SPH algorithm. Moreover, even if the process can finish correctly, the interaction between small and big particles produces a loss of precision owing to artificial inertia effects. The second simulation has been obtained using, together with the coupling option, the PAM-SHOCK rezone option, that allows selected particles during the restart (see Fig. 9) to be deactivated. In this way it is possible to split a triple wall problem into three simpler simulations. The first one analyses the

Fig. 8. Model used for case 1, PAM-SHOCK SPH.

(a)   (b)   (c)

Fig. 9. Model used in the PAM-SHOCK SPH simulations with the rezone option, case 2: (a), (b) and (c) are the models used in the first, second and third simulation, respectively.

impact of the projectile against the 1st BS; the simulation is stopped when the debris cloud has almost reached the 2nd BS. The particles, defined by the user and belonging to one or more space regions and, optionally, to a velocity field, are dumped in two files. A file contains the particle coordinates, mass, specific internal energy, density and damage. The other contains the velocities. These files are used as input for the second simulation, which analyses the impact against the 2nd BS. In the same way it is possible to evaluate the impact on the BW. The main advantage of this simulation is the drastic reduction of CPU time requested to simulate a triple wall problem, since it is no longer necessary to include the whole model at any time. At present a disadvantage of this option is the great effort requested from the user to generate these models, since a dedicated SPH/rezone pre-processor is still not available.

The third and fourth simulations have been performed using the AUTODYN axial symmetry option, with FV and SPH models, respectively. The two-dimensional approach greatly reduces the computation time with respect to 3D simulations, so that no problems have been found using a complete SPH model. Furthermore no significant differences have been noted in the calculation time for finite volumes and a SPH model with the same spatial resolution. The two-dimensional processor also allows for a higher spatial resolution than the 3D one, keeping an acceptable CPU time. Based on the results found in the relevant literature, ten particles were placed along the first bumper thickness, because this value seems to give a good estimation of the impact features. The spatial resolution for the other bodies has been chosen with the aim of keeping the particle dimension as uniform as possible for the entire problem, because also in AUTODYN this choice gives better results. The possibility exists in AUTODYN to delete some zones that are considered no longer important from the problem at any time, but this option has not been used because no strong requirements on CPU time reduction have been needed.

DISCUSSION OF THE RESULTS

Table 5 shows the results obtained from the simulations compared with those of the experiment. An exact comparison of the results is impossible since it is extremely difficult to make measurements in the plates, owing to the great dispersion of particles around the damage. Only the simulation performed with the FV technique allows an exact measurement, as the damage is well defined. The first hole diameter is well predicted by the FV simulation, while it is
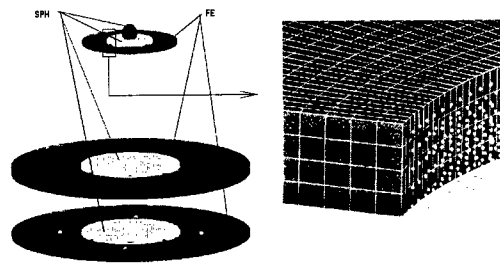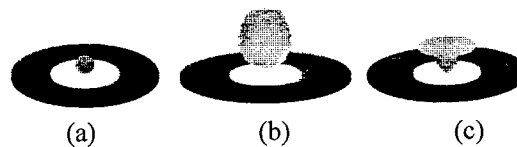
overestimated by all the SPH simulations. The hole in the 2nd BS is not well predicted by any simulation: it is underestimated with the FV technique and overestimated (largely with AUTODYN) with the SPH technique. The spall physical phenomenon is not properly simulated with the FV technique on account of long strips which remain attached to the 2nd BS until they almost reach the BW front surface (see Fig. 10 (left)). The spall area diameter in the 2nd BS is underestimated in case 3 and the spall velocity is higher than the spall velocity inferred by the experiment. The damage in both the 2nd BS and BW obtained in case 3 is not correct: the small central holes are due to an anomalous concentration of eroded cells along the symmetry axis; they have a high axial velocity and perforate the plates at very early stages (see Fig. 11 right). The AUTODYN SPH technique simulates well the spall phenomenon in the 2nd BS only at early stages (see Fig. 10 right), when the spalled fragments detach from the rear face of the intermediate bumper, moving towards the BW. At later stages, part of the material, first attached to the plate, detaches incorrectly and moves toward the BW, producing in it a greatly overestimated hole, whose diameter has not been reported in Table 5 because it is not meaningful. The numerical results give a spall area diameter very close to the experimental measures, while the hole in the front surface of the 2nd BS is totally incorrect.

Fig. 10. Debris cloud between 2nd BS and BW wall; AUTODYN FV simulation at 40 μs, case 3 (left); AUTODYN SPH simulation at 50 μs, case 4 (right).
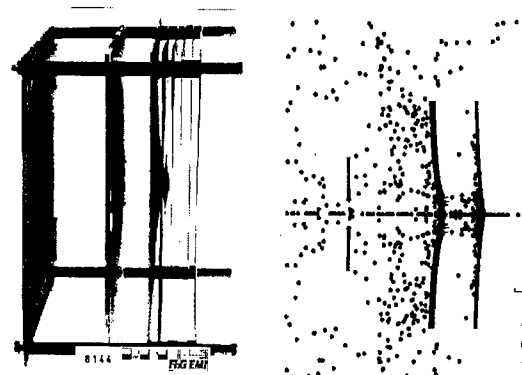
Fig. 11. Impacted target (left) and AUTODYN FV simulation (right), at 363 μs, case 4.

The PAM-SHOCK SPH simulations give a good qualitative representation of the spalled material (see Fig. 12), but the damages on the 2nd BS and BW are generally underestimated and in case 2 not clearly observable. Apart from plastic deformations, no hole has been produced in the BW. That could be due to a low kinetic energy associated to the spalled material; in fact the axial velocity of the mass involved in the impact on the BW is underestimated. The spalled material axial velocity is also underestimated in the AUTODYN SPH simulation, but the large amount of material detached at late stages produces in any case a debris cloud with an energy that causes a very big damage in the BW.

a)   (b)   (c)

Fig. 12. Debris cloud between 2nd BS and BW wall; experiment at 70 μs (a); PAM-SHOCK simulation at 101μs, case 1 (b); PAM-SHOCK simulation with the rezone option at 101 μs, case 2.

Table 5. Plate damage evaluation results

	1 PAM-SHOCK 3D SPH (double symmetry)	*2 PAM-SHOCK 3D SPH (double symmetry + rezone option)*	*3 AUTODYN 2D FV (axial symmetry)*	*4 AUTODYN 2D SPH (axial symmetry)*	*Experiment*
1st BS hole diameter [mm]	≈ 25 at 120 µs	≈ 23 (at 12 µs)	21.6 at 363 µs	≈ 25 at 96 µs	21.6
2nd BS hole diameter [mm]	≈ 10 at 120 µs	not distinguishable	0.3 at 363 µs	≈ 42 at 96 µs	4
2nd BS spall diameter [mm]	≈ 50 at 120 µs	≈ 25 at 80 µs	34.2 at 363 µs	≈ 59 at 96 µs	60
Spalled material velocity [m/s]	500 (max)	500 (max)	970 (max)	600 (max)	860 (max)
BW hole diameter [mm]	No hole	No hole	0.5 at 363 µs	Greatly overestimated	3
CPU time [hours]	450 (Silicon Graphics R10000)	80 (Silicon Graphics R10000)	30 (PC 200 MHz MMX)	20 (PC 200 MHz MMX)	/

The simulation performed with the rezone option gives a debris cloud with a different shape than the simulation with the whole model (see Figs. 12 b and c). In case 1 the SPH plate used for the 2nd BS is too small and tends to be detached at the interface with the finite elements. However, in both case 1 and case 2 the impact effects on the BW are about the same: the damage is underestimated; apart from plastic deformations, no hole has been produced in the BW (at 120 µs). Fig. 13 shows the material evolution at 101 µs. The damage in the BW is produced only by the impact of the 2nd BS material, detached by the rear surface, owing to the impulsive load transmitted by the projectile and 1st BS materials. This phenomenon was confirmed by the experiment. Problems of energy conservation have been partially solved with the PAM-SHOCK simulations. The delta global energy is limited to 5÷7% over an impact period of 120 µs. The momentum continues not to be conserved (the delta momentum is about 35% over a period of 120 µs). Considerable problems of energy and momentum conservation have been found (and not solved yet) in the AUTODYN SPH simulations.
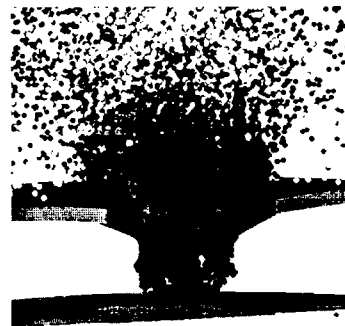
Fig. 13: Material distribution at 101 µs; section of the model. PAM-SHOCK simulation, case 1.

CONCLUSIONS

Hypervelocity numerical simulations are being performed at Alenia to assess the ballistic performance of the high resistance debris shielding designed to protect the Columbus module. The planned activity includes the calibration of the PAM-SHOCK hydrocode, the study of normal and oblique impacts on triple wall systems, with the extrapolation of the experimental results to higher impact velocities. A few problems have been met, delaying the original schedule. The initial calibration of the SPH version was done (in late 1996) with 2D numerical simulations in plane symmetry and in a low impact velocity range (100 ÷ 200 m/s). These simulations showed a few problems like numerical instability, global energy loss or divergence, incorrect plastic strain estimation, maximum pressure overestimation and unphysical row-to-row pressure oscillations between adjacent smooth particles. However, some of these problems are recognised by all the scientists and technicians who deal with SPH algorithms as typical problems affecting the SPH technique. Empirical parameter tuning and algorithm improvements could partially solve these problems.

This paper has shown that a few of the problems, already met in the low velocity impact simulations, are still present in the hypervelocity simulations at early stages of impact, like shock pressure overestimation, with respect to both the one-dimensional analysis and the FV method, and slight energy non-conservation. The cooperation between Alenia and the University of Rome "La Sapienza" has allowed a comparison of the capability of simulating impact problems with two different codes. Both the codes have given a good representation of the debris cloud expansion before the impact on the 2nd BS. The Equations of States and mesh density considerably influence the results at early stages of impact. On the other hand, the comparison with the experimental measures on the debris cloud picture has shown very marginal influence of the Equation of States, constitutive relationships and mesh density on the results. The shock pressure, shocked material density and delta energy heavily depend on the viscous term coefficients. The simulations obtained with the FV and SPH techniques have shown marked discrepancies between them and with respect to the one-dimensional analysis. The simulations of the impact on the 2nd BS and BW have given different results according to the type of code and technique (FV or SPH) used. Both the hydrocodes have been able to predict the spall phenomenon in the rear part of the 2nd BS, but neither has given a good prediction of the damage, also on account of the high level of dispersion of the smooth particles, that makes any measurement of the damage very difficult. The AUTODYN SPH simulations have shown severe problems of energy and momentum conservation. Problems of momentum conservation characterise the PAM-SHOCK simulations as well. The excessive CPU time consumption required by 3D simulations prevents an effective calibration of the PAM-SHOCK hydrocode on triple wall systems. This problem has been partially solved by improving a few algorithms and introducing the rezone option, reducing the CPU time necessary for a typical simulation to about $3 \div 4$ days on a dedicated workstation. However, a disadvantage of this option is the great effort requested from the user to generate these models, since a dedicated SPH/rezone pre-processor is still not available. On account of the axial symmetry, the two-dimensional processor of AUTODYN allows the CPU time to be kept at an acceptable level.

This paper has shown that the SPH technique is not sufficiently mature to support the development of complex debris shielding systems. The two codes cannot completely predict the experiment results and even more so they cannot be used to extrapolate the experimental results to assess the ballistic performance of the Columbus debris shielding. However, considering that the SPH processor in PAM-SHOCK is still a prototype version, and only a Beta version in AUTODYN, the SPH algorithms seem to be very promising for the future. The authors very much hope that further improvements will allow this technique to be used for numerical ballistic assessments.

REFERENCES

1. E. Beruto, R. Destefanis, M. Faraud and P. Buchwald, High resistance debris shielding development for the Columbus Orbital Facility, *Proceedings of the Second European Conference on Space Debris*, Darmstadt, Germany, pp 509-517 (1997)
2. P. H. L. Groenenboom, Numerical simulation of 2D and 3D hypervelocity impact using the SPH option in PAM-SHOCK^{TM}, *Int. J. of Impact Engineering*, Vol 20, pp 309-323 (1997).
3 Hayhurst C.J. and Clegg R.A., Cylindrically symmetric SPH simulations of hypervelocity impacts on thin plates, *Int. J. of Impact Engineering*, Vol. 20, pp. 337-348, 1997.
4. J. J. Monaghan, Smoothed Particle Hydrodynamics, *Ann. Rev. Astron. Astrophys.*, **30**, pp. 550-551 (1992).
5. D. Palmieri, M. Marchetti, R. Destefanis and M. Faraud, Orbital debris impacts against spacecraft multiple shield: comparison of hypervelocity experiments and hydrocode simulations, *Proceeding of the Susi 98 Conference*, Thessaloniki, Greece, pp. 331-340 (1998).

TIME-RESOLVED PARTICLE VELOCITY MEASUREMENTS AT IMPACT VELOCITIES OF 10 KM/S

M. D. FURNISH, L.C. CHHABILDAS, and W.D. REINHART

Sandia National Laboratories
Albuquerque, NM 87185-1168

Summary—Hypervelocity launch capabilities (9 - 16 km/s) with macroscopic plates have become available in recent years. It is now feasible to conduct instrumented plane-wave tests using this capability. Successfully conducting such tests requires a planar launch and impact at hypervelocities, appropriate triggering for recording systems, and time-resolved measurements of motion or stress at a particular point or set of points within the target or projectile during impact. We have conducted the first time-resolved wave-profile experiments using velocity interferometric techniques at impact velocities of 10 km/s. These measurements show that aluminum continues to exhibit normal release behavior to 161 GPa shock pressure, with complete loss of strength of the shocked state. These experiments have allowed a determination of shock-wave window transparency in conditions produced by a hypervelocity impact. In particular, lithium fluoride appears to lose transparency at a shock stress of 200 GPa; this appears to be the upper limit for conventional wave profile measurements using velocity interferometric techniques. © 1999 Elsevier Science Ltd. All rights reserved.

INTRODUCTION

Plane Wave Experiments

Plane-wave impacts have been utilized using explosive or smooth bore systems for many years to measure material properties under shock loading. A suite of diagnostic and experimental techniques [1,2] are used to measure material properties in the high-pressure, high-temperature shocked state induced in materials resulting from impact. These techniques allow measurements of the shock-Hugoniot [3], shock-loading and release behavior [4,5], material strength [3-7], shock-induced melting [5, 8-9], and shock-induced vaporization [8-9] processes in materials. The measurement of these material properties forms a data base to develop constitutive models to represent material behavior in dynamic loading [10].

Until approximately six years ago, the highest pressure and temperature states achieved in material by gun impact loading techniques were restricted to those available with two-stage light-gas guns [11-12]. The most extreme conditions were those produced using high impedance impactor materials such as tantalum or platinum at impact velocities of 8 km/s.

Requirements for stockpile stewardship, meteorite shielding design and other efforts drive a need to determine the equations of state of materials in regimes of extreme high pressures, temperatures and strain rates that are not attainable on current two-stage light-gas guns. These regimes are dominated by phase changes such as melting or vaporization. Some key areas of interest include these transitions, other aspects of the equation-of-state (Hugoniot, thermal properties such as the Grüneisen parameter), and meteorite impact phenomena. Conventional two-stage light-gas guns, however, provide limited access to such extreme thermodynamic states.

Hypervelocity Launcher Experiments

Sandia National Laboratories has developed a hypervelocity launcher (HVL) capable of launching 0.5 mm to 1.0 mm thick by 6 mm to 19 mm diameter plates to velocities approaching 16 km/s. This new launcher complements the available suite of high-pressure, high-temperature loading techniques (which includes radiative sources as well, such as lasers and Z-pinches) currently being used at various laboratories to determine the equation of state (EOS) of weapon and ICF materials at extreme thermodynamic states.

It is the purpose of this paper to report recent results of velocity interferometer (Velocity Interferometry System for Any Reflector, or VISAR [13]) particle-velocity measurements of shock loading and release in aluminum and titanium at impact velocities of ~ 10 km/s using the Sandia HVL. Shock loading and release experiments on aluminum at 1.62 Mbar resulting from symmetric impact at 10 km/s indicate complete melt in the shocked state. This is evidenced both by the lack of shear strength and release wave speed measurement that is indicative of a bulk wave velocity at 1.62 Mbar.

A similar measurement with a symmetric tantalum experiment showed an abrupt loss of returned light to the velocity interferometer, VISAR, upon passage of the shock wave into the lithium fluoride window. Although this experiment failed to return the desired tantalum EOS information, it provided an important indication of the limits of VISAR methods using lithium fluoride as the window material with hypervelocity impact experiments.

HYPERVELOCITY LAUNCHER (HVL)

Basic Operation

The principle of operation of the Sandia HyperVelocity Launcher (HVL) is briefly described here. In its simplest representation, a two stage projectile is impacted on a flyer plate, which is thus launched at a velocity of order twice that of the incident projectile. Very high driving pressures (tens or hundreds of GPa) accelerate flyer plates to hypervelocities. This loading pressure pulse on the flyer plates must be time-dependent to prevent the plate from melting or vaporizing. This is accomplished by using graded-density impactors [6-7,14]. When this graded-density material is used to impact a flyer-plate in a modified two-stage light gas gun, as indicated in Figure 1(a), nearly shockless, megabar pressures are introduced into the flyer plate [7,14-17]. The pressure pulse is tailored to prevent spallation of the flyer-plate.

This technique has been used [16-17] to launch nominally 1-mm-thick aluminum, magnesium and titanium (gram-size) intact plates to 10.4 km/s and 0.5-mm-thick aluminum and titanium (half-gram size) intact plates to 12.2 km/s More recently the technique has been enhanced by
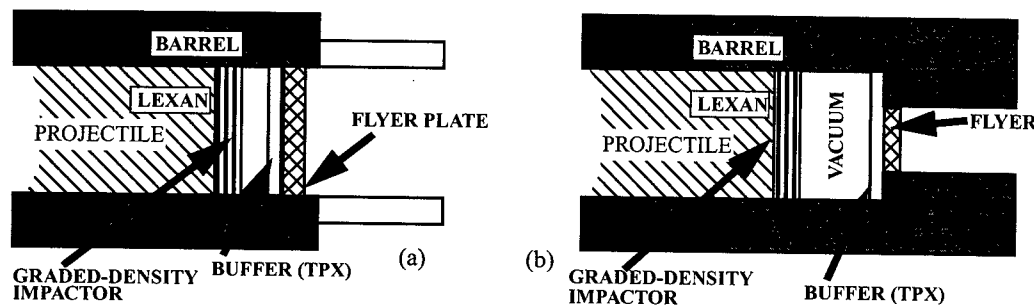
Fig. 1. (a) The Hypervelocity Launcher (HVL). Configuration used to launch flyer plates to hypervelocities. (b) Enhanced HyperVelocity Launcher, (EHVL). Configuration used to launch confined flyer plates in a tungsten barrel to hypervelocities.

using the experimental configuration described in Figure 1(b) to allow the launching of titanium and aluminum plates to velocities approaching 16 km/s [15]. The experimental design shown in Figure 1(b) acts as a dynamic acceleration reservoir which further enhances the flyer plate velocity [15]. This is the highest mass-velocity capability attained with laboratory launchers to date, and therefore should open up investigations into new regimes of impact physics using various diagnostic tools [1-2].

Flyer Plate Issues

Following launch, the flyer plate must be relatively flat and cool for successful planar impact experiments. Due to the severe loading conditions which result from time-dependent megabar loading pressures, the flyer plate achieves peak velocities over acceleration distance of tens of millimeters. The plate appears to be "flat" for approximately the first thirty millimeter flight distances (see Figure 2(a)). Even though shockless loading conditions are used to accelerate the flyer plate, the final temperature of the flyer plate upon acceleration in these studies is approximately 600 K for the geometry used in Figure 1(a) after achieving velocities of 10 km/s. This is "cold" compared to its melt temperature, despite using enormous energy (compared to its melt and vaporization energy) to achieve hypervelocities. Designs using lower-impedance buffers such as foam can further reduce the temperature of the accelerating flyer-plate.

SHOCK LOADING AND RELEASE EXPERIMENTS

We have used the hypervelocity launcher (HVL) to perform one-dimensional plate-impact experiments. To achieve one-dimensional conditions, the target plate is stationed ~ 20 mm from the flyer-plate. This ensures that the flyer plate achieves peak particle velocity prior to impact, and remains relatively flat (see Figure 2) prior to impact. No attempt has been made to date to characterize the *planarity* of the impacting flyer plate. The experimental configuration used to perform shock-loading and release measurements is shown in Figure 2(b)

Recent HVL Experiments - Wave Profile Measurements

Symmetric plate-impact experiments have been performed using aluminum, titanium, and tantalum at impact velocities of ~ 10 km/s. Figure 2(a) shows the radiograph of an experiment in which a 0.56 mm titanium alloy (Ti-6Al-4V) flyer-plate is launched at 9.6 km/s prior to impacting a 2.0 mm thick titanium alloy target. The lithium-fluoride window [18] is clearly seen in the
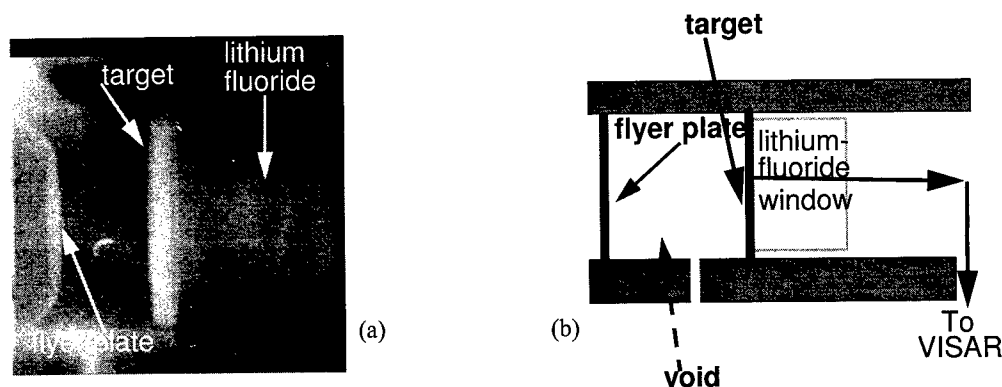
Fig 2. (a) Radiograph of a titanium flyer-plate (prior to impacting a titanium target). The flyer-plate is traveling at 9.60 km/s. (b) HVL configuration for shock-loading and release experiments. Resultant loading and release is measured as particle-velocity history at the target lithium fluoride window interface.
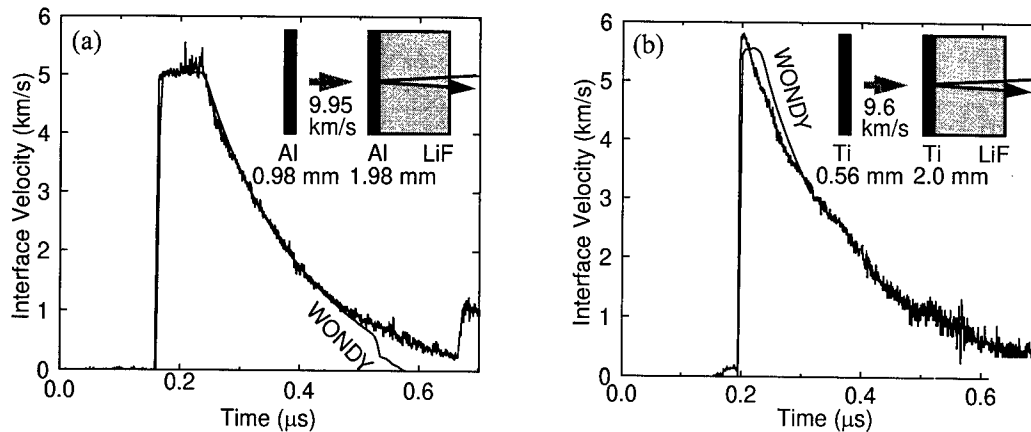
Fig. 3. Measured interface particle velocity history for shock-loading and release experiments in (a) 6061-T6 aluminum at an impact velocity of 9.95 km/s, and (b) Ti-6Al-4V alloy at an impact velocity of 9.6 km/s. Symmetric impact configuration was used in both experiments. An analogous experiment with tantalum did not yield usable particle velocity history data because the LiF window became opaque (see discussion of LiF optical properties in text)

radiograph in Figure 2(a). The flat portion of the flyer-plate prior to impact as observed in the radiograph is 19 mm in diameter. Note that for the full duration of the experiments there is a void behind the flyer-plate; this allows measurements of a complete release from the shocked state. As indicated in Figure 2, a VISAR is used to estimate the particle-velocity history at the sample/lithium-fluoride window interface. The time-resolved particle velocity history measurements at the target/lithium-fluoride window interface are shown in Figure 3(a) and 3(b) for aluminum and titanium, respectively. Since no fiducial was established in these experiments, the shock arrival time at the target/window-interface is determined by impedance-match calculations based on the Hugoniots of Table 1.

Table 1. Aluminum and titanium Hugoniots

Material	C_0 (km/s)	S	ρ_0 (gm/cm^3)	Reference
6061-T6 aluminum	5.386	1.339	2.697	[19]
Titanium - 6Al- 4V	4.99	1.05	4.426	[20]

Wave Profile Interpretations

Figure 3(a) depicts the shock loading and release profile in aluminum shocked to 1.61 Mbar at an impact velocity of 9.95 km/s. In this experiment, a 0.98 mm thick aluminum flyer-plate impacts a 1.98 mm thick aluminum target. Notice that a sustained shock of approximately 80 ns is observed in the figure prior to release. The titanium alloy is shocked to 2.3 Mbar at an impact velocity of 9.6 km/s, and a complete release profile as indicated in Figure 3(b) is measured. A profile resembling wave attenuation is measured in the titanium experiment because a thin flyer plate (0.56 mm) impacts a thick (2.0 mm) target. Both experiments indicate a lack of elastic-plastic release structures—a clear indication of complete melt. These release structures then determine the off-Hugoniot states of materials shocked to extremely high-pressures.

Aluminum Experiments

Results of the aluminum experiment are juxtaposed on those of three analogous lower-velocity experiments [5] in Figure 4. An elastic-plastic signature is visible on the three lower-velocity
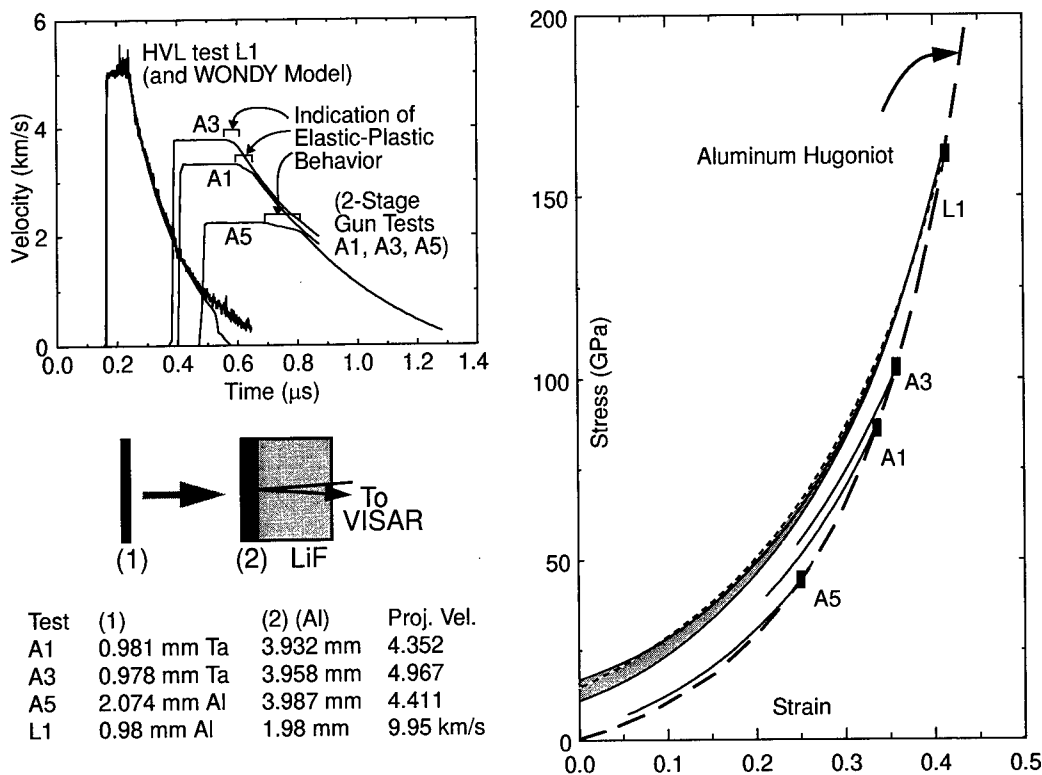
Fig. 4. Wave profiles and results of Lagrangian analysis for four tests with aluminum targets (3 using 2-stage gun, L1 using HVL). All tests yielded Hugoniots lying above the Hugoniot. Shaded area represents uncertainty in L1 release due to uncertainty in LiF $\Delta v/v_0$ (see discussion of LiF optical properties).

wave profiles, but is not visible for the HVL experiment. This is indicated by the double-corner appearance of the beginning of the release in the profiles from tests A1, A3 and A5. Complete melt is indicated for the shocked state at 1.61 MBar. The shock Hugoniot state is based on measurements of the impact velocity and the existing equation of state for aluminum (Table 1) given by the shock-velocity (U_s)-particle (u_p) velocity relation as (U_s = 5.386 (km/s) + 1.339 u_p). Inasmuch as the impact is symmetric, the particle velocity is u_p = 4.975 km/s, giving a shock velocity U_s = 12.05 km/s, a compression ρ/ρ_0 = 1.703 and a stress P = $\rho_0 U_s u_p$ = 161 GPa.

Release paths

We have calculated release paths by several means.

First, the wave profiles were analyzed by an explicit Lagrangian calculation comparing input and output wave profiles for the sample. The incremental form of the release is calculated using $d\sigma = \rho_0 C du$ and $d\varepsilon = du/C$, where C is the Lagrangian wave velocity for the corresponding particle velocity decrement du at particle velocity u. Impedance mismatch calculations are also performed to transform the particle velocity measurement at the window interface to *in situ* material velocity. This analysis yielded tabular relations between wave speed, stress, strain, strain rate, particle velocity, window velocity and time. Here, time is referenced to impact time for loading waves and to the centering time of the release in the sample for unloading waves.

Second, the Lagrangian wavecode WONDY V [21] was used to model the experiment, with the Grüneisen γ adjusted to give agreement between the observed and model waveforms. A second WONDY calculation using a rate-dependent strain-hardening model (Asay and Chhabildas, [4 - 5]) produced comparable results.

Release Wave Velocity in Aluminum

The velocity of the leading edge of the release wave (or equivalently, the sound speed in the shocked state at 1.61 Mbar) can be calculated knowing the sample and impactor dimensions, the dwell time of the shock at the sample-window interface, and the impact velocity. The calculation method is indicated in Figure 5. The calculated Eulerian value of 10.7 ± 0.15 km/s agrees very well with extrapolation of previous sound speed measurements by Asay and Chhabildas [4,5] and McQueen et al [22]. and is shown in Figure 6(b).

$$C_{Lagr} = \frac{a+b}{t_2 - t_3}$$

$$C_{Eulerian} = C_{Lagr} \times \frac{\rho_0}{\rho_{Hugoniot}}$$
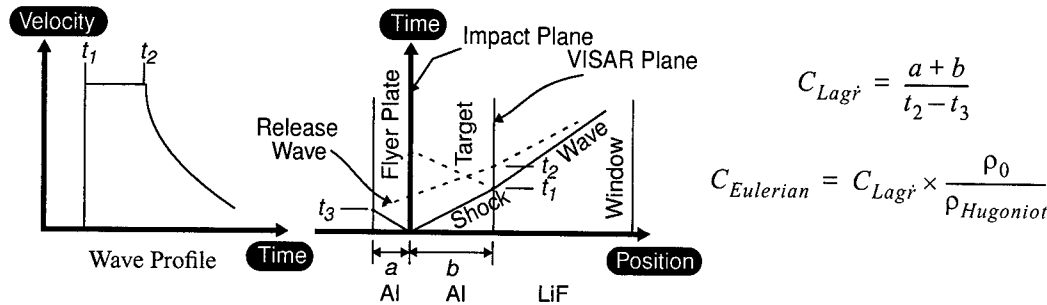
Fig. 5. Method for calculating sound velocities at Hugoniot state. Times t_1 and t_2 are observed; t_3 must be calculated from known flyer plate thickness and Hugoniot shock velocity. Lagrangian sound velocity is referenced to original part dimensions; Eulerian is referenced to compressed part dimensions and corresponds to Fig. 6(b) velocities.

At the onset of the release, the shear stress τ_0 supported by the sample is released and the sample is put under a shear stress τ_c of opposite sign and magnitude equal to the yield strength of the material (Figure 6(a) inset). This shear stress reversal causes the initial portion of the release wave to propagate through the sample with a higher velocity than the subsequent (bulk) release (velocity is equal to $(1/\rho)\sqrt{d\sigma_x/de_x}$, giving a step structure on the velocity profile at the release onset. The total magnitude of the shear stress change may be written [4] as:,

$$\tau_c + \tau_0 = -\frac{3\rho_0}{4} \int_{e_0}^{e_1} (C^2 - C_B^2) de \tag{1}$$

where e_0 and e_1 are the engineering strain (Fig. 4) at the start of the release and the end of the step structure; C is the observed wavespeed, and C_B is the bulk sound speed ($\rho_0 C_B^2 = d\overline{\sigma}/de$).
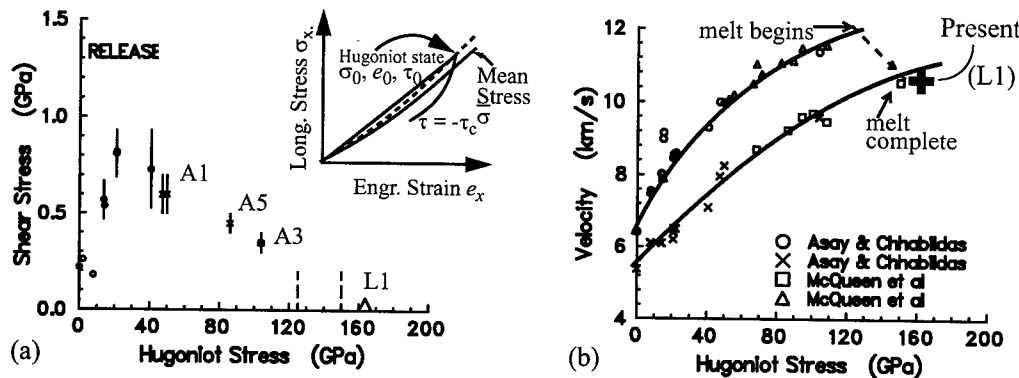
Fig. 6. Measurements of (a) shear stress and (b) sound speed (Eulerian) at 162 GPa in aluminum as determined from the release wave profile indicated in Fig. 4 (a). Comparison with previous studies by Asay and Chhabildas [4,5] and McQueen et al [22] is also indicated.

Titanium Experiment

In this symmetric impact experiment, a thin flyer plate (0.56 mm, vs. 0.98 mm for the above aluminum experiment) impacted a titanium sample 2 mm thick. At the sample/window interface, the leading edge of the release from the back of the flyer plate had overtaken the initial loading wave. Hence an attenuating wave was observed at the window interface. This complicates the process of extracting equation-of-state information from the experiment, such as the release paths and sound velocities deduced above for the aluminum experiment L1.

In retrospect, however, had a thicker flyer plate been used to obtain an unattenuated wave, the experiment would have not yielded release profiles; VISAR fringe contrast would have been lost because of limitations of the LiF window (see discussion in next section).

LITHIUM FLUORIDE WINDOW - OPTICAL PROPERTIES

Transparency

The successful measurements shown in Figure 4 demonstrate the transparency of the lithium-fluoride (LiF) window at much higher pressures (and temperatures) than this window material has ever been subjected to before [18], *i.e.*, to 1.5 Mbar and 2.0 Mbar, respectively, in the aluminum and titanium experiment. A previous study had demonstrated the transparency of LiF windows to stresses of 1.2 Mbar [18]. A symmetric impact experiment at 8.62 km/s using both tantalum as a target and as a flyer plate, however, did not yield a release profile measurement similar to those in Figure 4. Impedance match calculations yield a stress of ~ 6.4 Mbar in the tantalum and ~ 2.4 Mbar in the LiF window. This pressure level causes an apparent transparency loss in the LiF window. This is indicated in Figure 7.
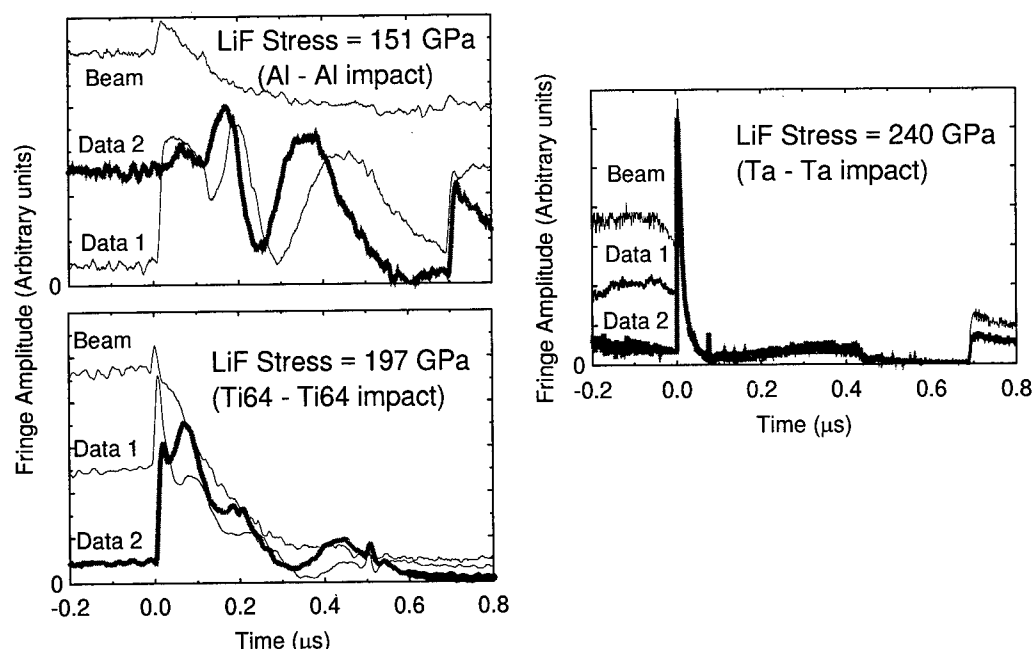
Fig. 7. VISAR interferometer signals from sample/lithium-fluoride window interface suggesting a total loss of beam intensity, fringe data and contrast when the LiF is shocked to 240 GPa. The use of lithium-fluoride window for interferometry is limited up to a shock stress of ~ 200GPa, (lower left) at which fringe information is still available.

The beam intensity monitor suggests that at the 1.6 Mbar stress level there is no loss of transparency, yielding extremely good fringe data for motion at the sample-LiF window interface. As the stress level is increased to 1.97 Mbar in the window there is considerable decrease in the beam intensity signal, but nevertheless reasonable fringe information is obtained at the sample window interface. At a stress level of 2.4 Mbar in the window material there is an abrupt loss of beam intensity and a total loss of fringe information from the sample/window interface. A total loss of contrast suggests a reflection from the shock front or beam absorption behind the shock front. In short, the window interferometry technique using lithium fluoride windows is restricted for use up to shock stresses of 2 Mbar in the window material. These results also point to the need to develop new time-resolved techniques and/or new window materials to allow successful measurements of off-Hugoniot states at extremely high pressures.

Index of Refraction

The calibration of the velocity-per-fringe (VPF) sensitivity of a VISAR depends on the optical properties of the window through the frequency correction $\Delta v/v_0$ [13] according to:

$$VPF = \frac{\lambda_0}{2\tau(1 + \delta)(1 + \Delta v/v_0)}$$

$\delta \equiv$ Etalon dispersion correction

$\tau \equiv$ Relative delay in delay leg   (2)

$\lambda_0 \equiv$ unshifted laser wavelength

The index of refraction of a shock window material may be calculated [18] as:

$$n_H = \frac{1}{1 - \varepsilon_H}[n_0 - \varepsilon_H(1 + \Delta v/v_0)]$$

$\varepsilon_H \equiv$ Strain at Hugoniot

$n_0 \equiv$ Ambient index of refraction   (3)

$\Delta v/v_0 \equiv$ frequency correction

From the aluminum test, $\Delta v/v_0$ may be estimated using the plateau level in the velocity history. An impedance-match calculation, which closely matches a WONDY V modeling using the aluminum EOS from Table 1, gives an expected velocity of 5.035 km/s. The required value of $\Delta v/v_0$ to match this is 0.230 ± 0.047 (this value was used for the HVL plot in Figure 4). Error estimates here include significant uncertainties (2%) for the LiF and aluminum equations of state, and approximately 1% for the projectile velocity. Taking $n_0 = 1.3939$ and $\varepsilon_H = 0.4208$, we conclude that $n_H = 1.513 \pm 0.034$. This is plotted together with earlier data and fits [18] in Figure 8.

Hence, the new data are suggestive of a significant change in the optical behavior of LiF in the hypervelocity impact setting. Experiments which include high precision EOS measurements for the target and window material at these stresses will be necessary to determine this optical behavior to better precision.

CONCLUSIONS

The experiments described here demonstrate the use of the hypervelocity launcher to determine material properties in pressure and temperature regimes not previously accessible in the laboratory in the length scales available in plate impact experiments. These are the first time-resolved wave profile measurements on the hypervelocity launcher at impact velocities of 10 km/s. This has allowed the measurements of time-resolved wave profiles for shock loading and release experiments. The experiments presented here illustrate the use of HVL and time-resolved techniques for material properties measurements. These experiments, due to their plate geometry, allow a determination of the EOS of materials, and also serve to validate hydrodynamic codes in
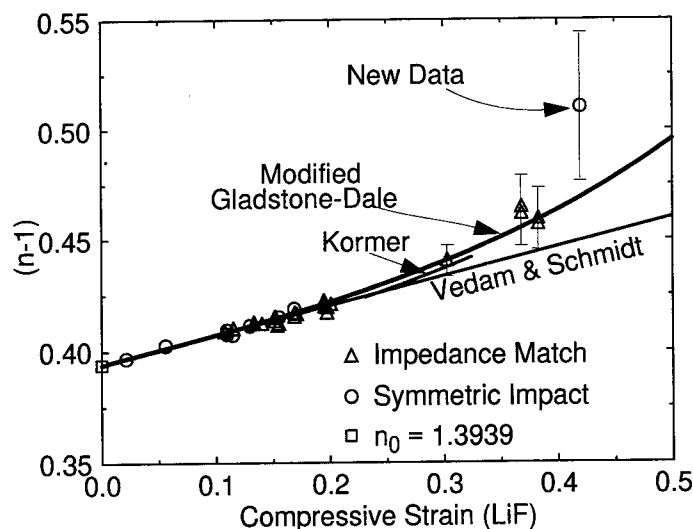
Fig. 8. Index of refraction data for LiF. The HVL aluminum-aluminum experiment (L1) lies significantly above the modified Gladstone-Dale curve, with a $\Delta v/v_0$ value of 0.23 ± 0.047.

the ~10 km/s impact regime (where very few experiments are available). Well-controlled EOS studies are necessary for many applications, including ballistic studies [23-24].

Several technical areas must be further developed to allow expanded use of the HVL in planar impact EOS and constitutive property experiments.

Characteristics of the impact process itself (flatness, flyer temperature, and velocity) must be well controlled for increased accuracy; these changes are amenable to improvement with further HVL development. The experiments discussed here demonstrate the feasibility of such measurements for EOS studies.

Diagnostic issues are also key to experiment usefulness. Window limitations are perhaps the most important barrier for ultra-fast impact experiments if optical probes are to be used. LiF has been seen here to lose transparency at ~200 GPa shock pressure, at least for visible (514.5 nm) light. Whether diamond, post-yield sapphire, other salts, or other optical materials with large band gaps could be used at yet higher shock stresses needs to be determined.

It should be emphasized that most of the diagnostic techniques used here are those that were developed earlier for relatively lower impact studies. They need to be refined to give comparable precision with earlier results at more modest regimes. Future studies may benefit from extensions of these techniques (e.g. miniature VISAR probes, improved time resolution in recording, and better measurement of impact time) and also from the development of new techniques to better study the physical processes accessible with the hypervelocity launcher.

REFERENCES

1. L. C. Chhabildas, Survey of diagnostic tools used in hypervelocity impact studies, *Int., J. Impact Engng.,* **V5**, 205-220 (1987).
2. L. C. Chhabildas, and R. A. Graham, Developments in measurement techniques for shock-loaded solids, in *Techniques and Theory of Stress Measurements for Shock Wave Applications, AMD* **83**, (R. Stout, F. Norwood, and M. Fourney, eds), 1-18 (1987).
3. See for example *LASL Shock Hugoniot Data*, ed., by S. P. Marsh, University of California, Press, (1980).
4. J. R. Asay and L. C. Chhabildas, Determination of the shear strength of shock-compressed 6061-T6 aluminum, in *Shock Waves and High-Strain-Rate Phenomena in Metals* (M. A. Meyers and L. E. Murr, eds.), 417-431, Plenum Publishers, New York (1981).
5. J. R. Asay, L. C. Chhabildas, G. I. Kerley and T. G. Trucano, High pressure strength of shocked aluminum, in *Shock Waves in Condensed Matter-1985* (Y. M. Gupta, ed), pp. 145-149, Plenum Publishers, (1986).
6. L. C. Chhabildas, L. M. Barker, J. R. Asay and T. G. Trucano, Relationship of fragment size to normalized spall strength for materials, *Int. J. Impact Engng.,* **10**, 107-124 (1990).
7. L. C. Chhabildas and J. R. Asay, Dynamic yield strength and spall strength measurements under quasi-isentropic loading, in *Shock Waves and High-Strain-Rate Phenomena in Materials* (M. A. Meyers, L. E. Murr and K. P. Staudhammer, eds.), pp. 947-955, Marcel Decker, New York (1992) 947.
8. J. R. Asay, T. G. Trucano and L. C. Chhabildas, Time-resolved measurements of shock-induced vapor-pressure profiles, in *Shock Waves in Condensed Matter-1987* (S. C. Schmidt, J. W. Forbes and N. C. Holmes, eds.), pp. 159 - 162, Elsevier Science Publishers, (1988).
9. J. R. Asay, T. G. Trucano and R. S. Hawke, The use of hypervelocity launchers to explore previously inaccessible states of matter, *Int. J. Impact Engng.,* **10**, 51-66 (1990).
10. J. R. Asay and G. I. Kerley, Time response of materials to dynamic loading, *Int. J. Impact Engng.,* **5**, 69-99 (1987).
11. A. C. Charters, Development of the high-velocity gas-dynamics gun, *Int. J. Impact Engng.,* **5**, 181-203 (1987).
12. L. C. Chhabildas, Hypervelocity launch capabilities to over 10 km/s, in *Recent Trends in High-Pressure Research, Proceedings of the XIII AIRAPT Conference on High Pressure Science and Technology* (A. K. Singh, ed.), Bangalore, India, 739-746, Oxford & IBH Publishing Co. PVT Ltd. (1992).
13. L. M. Barker and R. E. Hollenbach, Shock-wave studies of PMMA, fused silica, and sapphire, *J. Appl. Phys.,* **43**, 4208-4226 (1972).
14. L. M. Barker, High-pressure, quasi-isentropic impact experiments, in *Shock Waves in Condensed Matter-1983*, (J. R. Asay, R. A. Graham, and G. K. Straub, eds), pp. 217-224, Elsevier Science Publishers (1984).
15. L. C. Chhabildas, L. N. Kmetyk, W. D. Reinhart and C. A. Hall, Enhanced hypervelocity launcher - Capabilities to 16 km/s, *Int. J. Impact Engng.,* **17**, 183-194 (1995).
16. L. C. Chhabildas, L. M. Barker, J. R. Asay, T. G. Trucano, G. I. Kerley and J. E. Dunn, Launch capabilities to over 10 km/s, in *Shock Waves in Condensed Matter-1991* (S. C. Schmidt, R. D. Dick, J. W. Forbes and D. G. Tasker, eds), 1025-1031, Elsevier Science Publishers (1992).
17. L. C. Chhabildas, J. E. Dunn, W. D. Reinhart and J. M. Miller, An impact technique to accelerate flier plates to velocities over 12 km/s, *Int. J. Impact Engng.,* **14**, 121-132 (1993).
18. J. L. Wise and L. C. Chhabildas, Laser interferometer measurements of refractive index in shock-compressed materials, in *Shock Waves in Condensed Matter-1985*, Y. M. Gupta, ed.), 441-454, Plenum Publishers, (1986).
19. G. I. Kerley, Theoretical equation of state for aluminum, *Int., J. Impact Engng.,* **5**, 441-449 (1987).
20. (e.g.) S. P. Marsh, *LASL Shock Hugoniot Data*, Univ. of Calif. Press (1980).
21. M. E. Kipp and R. J. Lawrence, *WONDY V - A one-dimensional finite-difference wave propagation code*, Sandia National Laboratories Report SAND81-0930 (1982).
22. R. G. McQueen, J. N. Fritz, and C. E. Morris, The velocity of sound behind strong shock waves in 2024 Al, in *Shock Waves in Condensed Matter-1983* (J. R. Asay, R. A. Graham, and G. K. Straub, eds), 95-98, Elsevier Science Publishers, (1984).
23. L. C. Chhabildas, Hypervelocity Impact Phenomena, in *Metallurgical and Materials Applications of Shock-Wave and High-Strain-Rate Phenomena*, Elsevier Science Publishers, 245-256 (1995).
24. R. M. Brannon and L. C. Chhabildas, Experimental and numerical investigation of shock-induced full vaporization of zinc, *Int., J. Impact Engng.,* **17**, 109-120 (1995).

NUMERICAL MODELING OF DAMAGE IN VARIOUS TYPES OF HYPERVELOCITY EXPERIMENTS

A.GEILLE

CEA/CESTA, P.O. Box 2, 33114 Le Barp, France

Summary—This paper reviews some applications of numerical methods to predict damage in spalling or fragmentation problems encountered in hypervelocity experiments. After a brief description of these models, some numerical simulations are performed using the HESIONE hydrocode in its Euler and Lagrange versions coupled or not to specific algorithms and some correlations between experiments and calculations are provided when available to help evaluating the limits of the numerical techniques for the given problems. © 1999 Elsevier Science Ltd. All rights reserved.

DESCRIPTION OF THE NUMERICAL MODELS

The numerical approach must be carefully adapted to the requested specifications of the problem in order to perform the most accurate calculation. In the case of damage simulations, this very general rule takes a particular importance since the quality of the estimates is very sensitive to the nature of models.

Spall Models

The spall process, as we understand it in this paper, is an instantaneous process which occurs at a given time, in a specific region of the material, depending only on its thermodynamic status, the organization of unloading waves and a specific value of the negative pressure afordable by the material. The spall geometry can be predicted either by the mean of a characteristic code or using a classical drawing of shocks and releases.

The usual method to model this situation in hydrocodes is to compare the pressure in the cells to a negative threshold value and decide or not the opening of a void inside the material, immediatly returning pressure to zero if the cell is concerned (Fig. 1). Some additional refinements have been implemented (Tuler-Butcher [1],...), correlating the response to the time of application of the release by the way of the strain rate. Nevertheless, none of these models can be considered as damage models because of their non-progressive effect.

Damage Models

In most cases, the physics involved in hypervelocity problems cannot be reduced to the sudden opening of a well-defined spall inside materials under shock. The response of the material is progressive, initiated at randomly distributed micro-cracks locations, very early during the shock and release process. Two different kinds of numerical models are available to perform the simulations.

Porosity Driven Models. These models are based on the replacement of the pressure by a spe-

cific variable called porosity to handle the damage process. This variable contains all the information controling the damage effects inside the cells (nucleation, growth, coalescence of voids), but no real fragment is created. The damage numerical process is initiated by a minimum value of the porosity generally well above the limit negative pressure criterion applied in the spall models. A progressive unloading of the materials is applied which is much closer to the reality than spalling models. These models, well fitted to overall estimates about damage and basic predictions concerning clouds of debris, are usually implemented inside the hydrocodes (Johnson, N.A.G.).

The Johnson model [2] is widely inspired from Carroll and Holt works [3], describing the evolution of spherical microcavities uniformly dispatched inside a non-elastic matrix, starting from a very small initial porosity up to a critical value leading to rupture. The originality of the model is to provide a simple formulation of the local behaviour of materials needing a few parameters to tune, most of them having a good physical connection.

N.A.G.[4, 5], is based on a stastistical approach of the evolution of defaults sizes and locations inside the materials. More than 10 parameters are required to run the model making it very powerful but also very sensitive to the tuning data which are in this case collected from post-mortem analysis of experiments.

Shrapnel Models. A different approach of the fragmentation process must be applied in problems where the composition of the cloud of debris generated in the damage process is the requested result or is the main driver for a subsequent process. For this category of problems, specific models are available to predict shrapnel populations, usually disconnected from the hydrocode because of their very different nature based on statistics. The hydrocode itself becomes a kind of sophisticated preprocessor required to propagate the shocks inside the materials up to the time the direction of computational mass cells are sufficiently established. At this time which must be carefully identified, the required data (strain rate, temperature, density and kinetic variables) are transferred to the fragmentation model and the population distribution is evaluated (Grady [6], Mott [7]). According to the Grady model, each cell potentially contributing to the fragment generation process is associated to a population of debris which are solid, ductile or liquid according to the intensity of the loading. The average size of the fragments is computed using energetic considerations (surface energy for liquid droplets, dynamic fracture for solids). Starting from this value, a Poisson distribution is elaborated with respect to the fundamental conservations, before integrating the contributions to all the generating cells and construction of the debris final distribution.
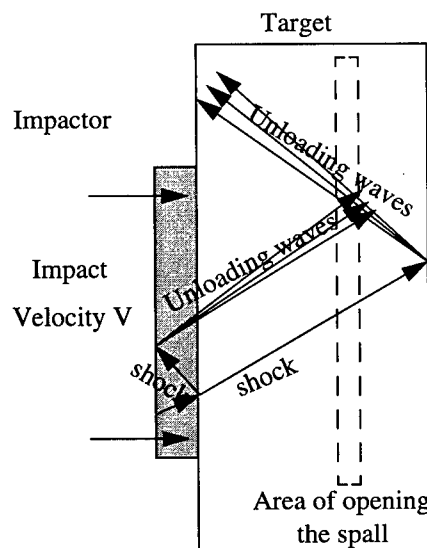
Fig. 1a. Shock-induced spalling mechanism.   Fig. 1b. Spall and damage models.
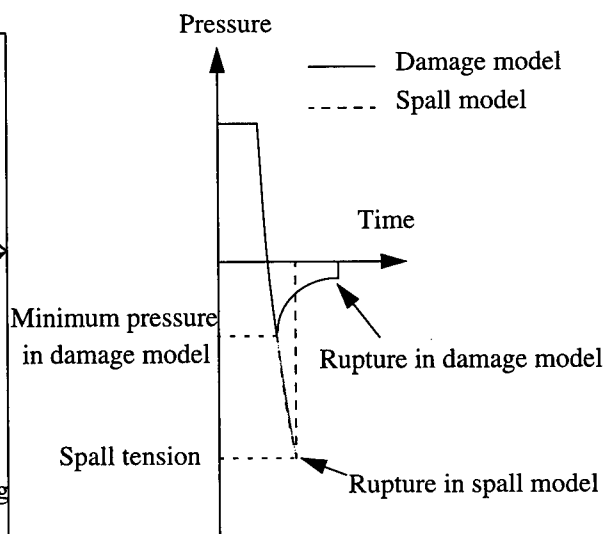
Fig. 1. Fragmentation process.

APPLICATIONS OF THE MODELS

Four examples have been selected in the domains of applications where CEA/CESTA is involved to illustrate the limits of the previously described models.

Simulation of Impact using a Spall Model

This impact experiment (aluminum on titanium), performed at CESTA a few years ago using a high-explosive launcher of flyer plates (velocity 5.3 km/s), provides an efficient way to make a correlation between the experiment and a numerical simulation because of the very clean aspect of the target which has been recovered after the shot.

The simulation required about 20 cells per millimeter in the horizontal direction to handle proper sharpness of the shock inside the materials leading to 200000 cells for the total run. Due to the shock intensity, the Equation of State was a standard Mie-Gruneisen and the target material strength model an Elastoplastic Steinberg one. A spall tension of -37 Kbars was applied.

The comparison is made at Figure 2 after 30 μs, and shows a very good agreement concerning the crater dimensions but also the spall shape, diameter and thickness although the numerical conditions of the simulation are very standard.

Fig. 2a. Schematic drawing.

Fig. 2b. Experiment.

Fig. 2c. Numerics.

Fig. 2d. Overlay of the 2 images.
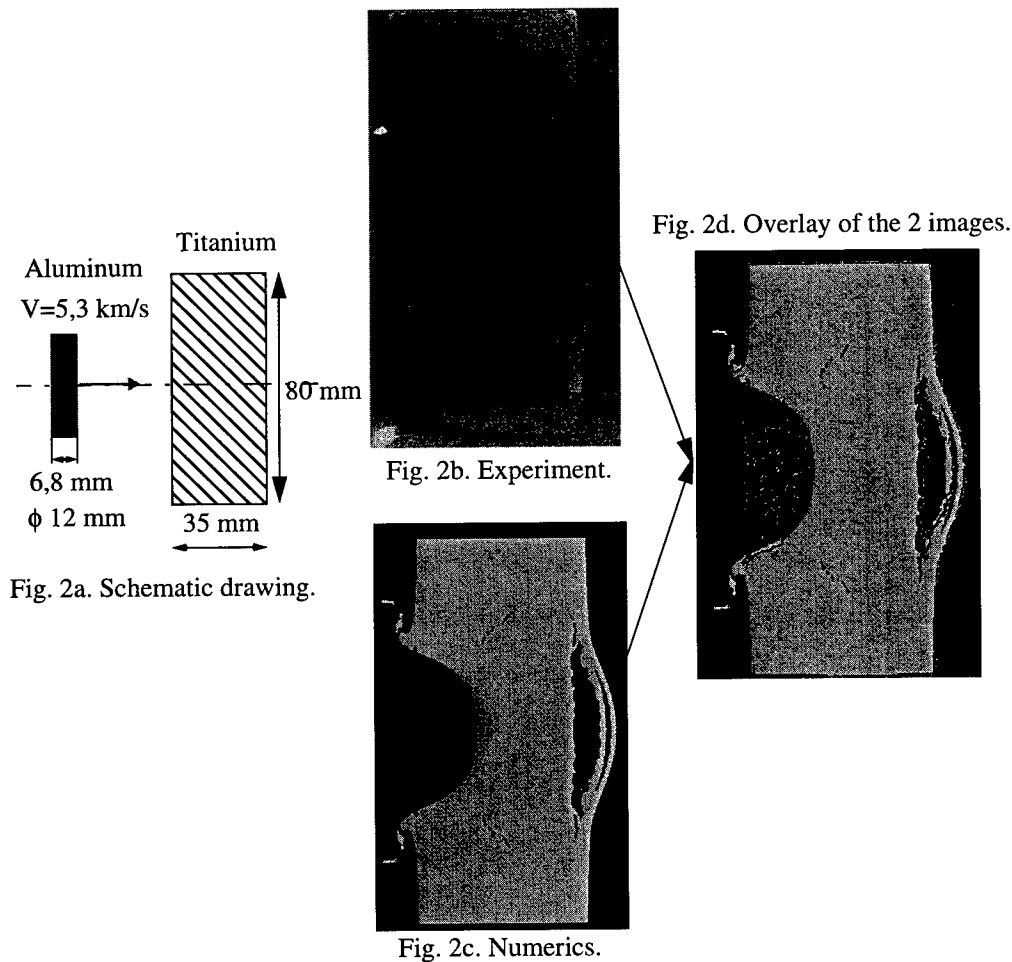
Fig. 2. Comparison between numerics and experiment.

Comparison between a Damage Model and a Spall Model in a Flyer Plate Impact Calculation

The Johnson porosity model and the spall one are compared in the impact of a steel disc 0.2 mm thick flying at 5500 m/s onto a steel target 0.4 mm thick after 200 ns (Fig. 3).

In the two models, the number of debris is so high that most of the fragments occupy a fraction of a cell. This means that the cloud composition is directly driven by the mesh generation procedure and the filling algorithm of the code. In that sense, the 2 models are equally unphysical. Nevertheless, in the Johnson model, behind a front spall much better identified, the density of fragments is continously varying starting from the solid in the back. This model allows to handle a more realistic population of debris, with small softened fragments flying at high velocity in the front part of the cloud and bigger solid ones flying more slowly behind, which is not the case for the simple spall model.
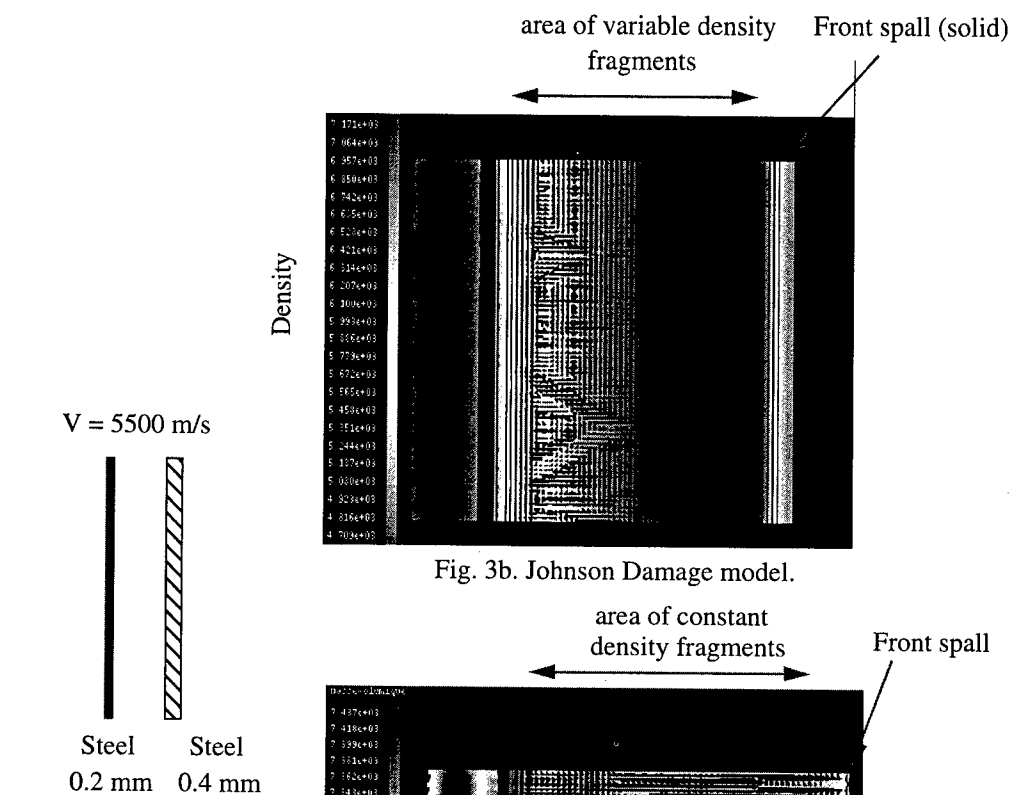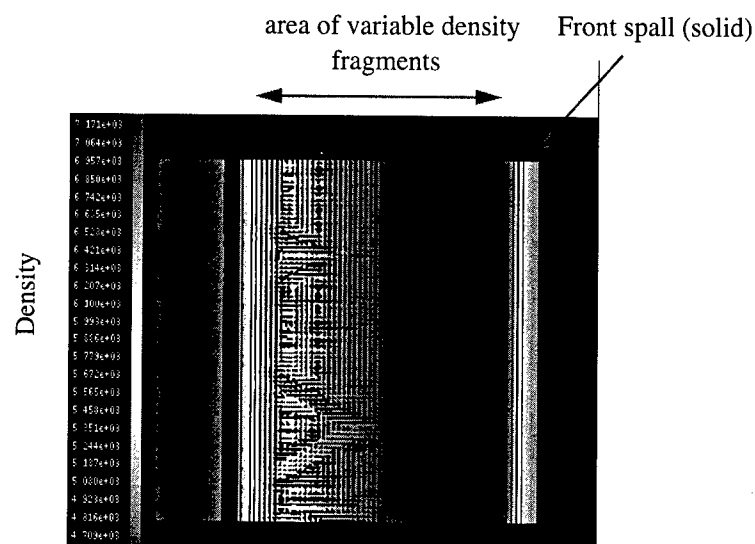
Fig. 3b. Johnson Damage model.

V = 5500 m/s

Steel   Steel
0.2 mm   0.4 mm

Fig. 3a. Schematic drawing.
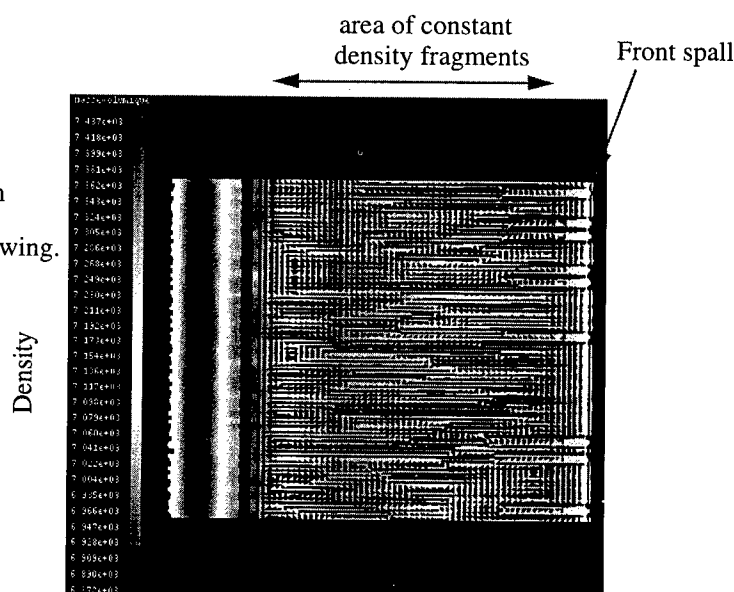
Fig. 3c. Spall model.

Fig. 3. Comparison between Johnson model and a spall model.

Multi-bumper Shields for Space Debris Applications

The shielding technique used to protect spacecraft vehicles from space debris impact is based on the fragmentation of the projectiles impacting multiple walls placed one after the other resulting in a sharp decrease of the kinetic energy applied on the final backwall.

CEA/CESTA recently performed experiments using the multistage active disk launcher of aluminum projectiles (1 gram) developed at CESTA for that purpose at a velocity of 11 km/s according to the schematic drawing described at Figure 4. Two X-Ray images were taken during the flight of the projectile to check its attitude and observe the clouds of debris, and a Fabry-Perot Velocimeter recorded the velocity versus time profile on the back face of the backwall, by the mean of 4 fiber optics.
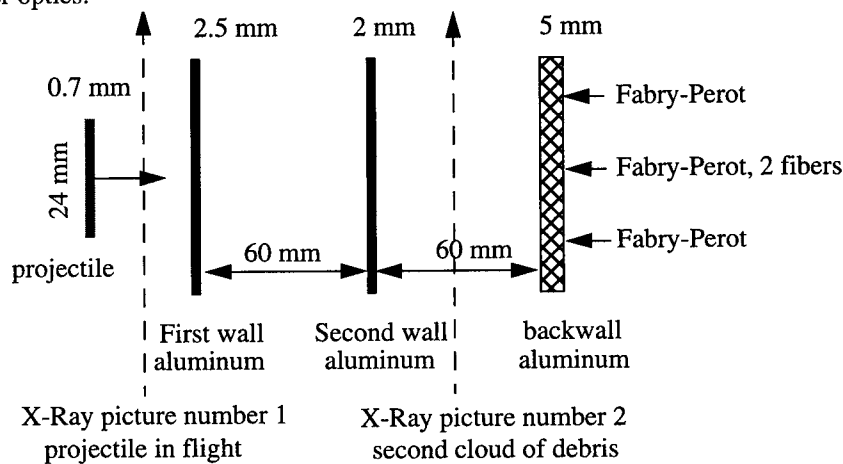
Fig. 4. Schematic drawing of the experiment and diagnostics.

Experimental Results (Fig. 5). The X-ray image of the projectile in balistic flight shows a perfect shape and attitude with no evidence of fracturation or melting before the impact. The X-ray image of the second cloud of debris (snapped a few microseconds before impact on the backwall) needed a reconstruction process because of the very low density of the fragments hardly visible on the original image and not compatible with the printing resolution of this document. The Fabry-Perot record suggests a complete perforation of the backwall since the recorded limit velocity is higher than 1000 m/s.
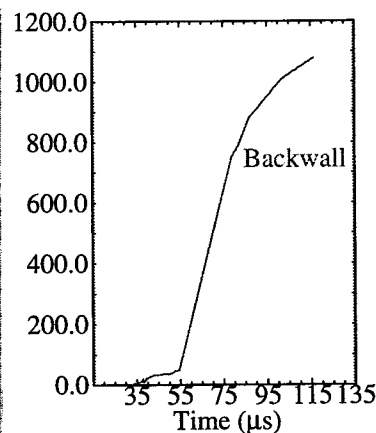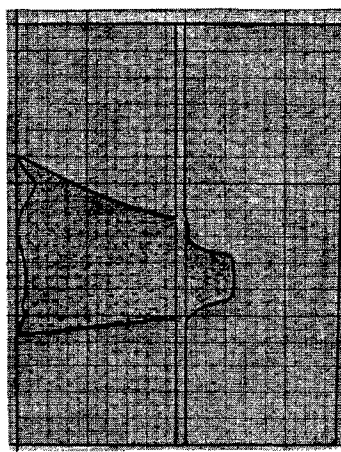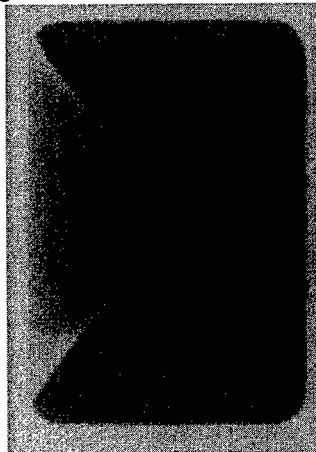
Fig. 5a. First X-Ray picture.   Fig. 5b. Second X-Ray picture.

Fig. 5c. Fabry-Perot velocity profile (m/s).

Fig. 5. Experimental results.

Numerics (Fig. 6). The numerical simulation of this experiment is driven by the 2 clouds of debris generated by the impact of the initial projectile on the 2 intermediate walls. To keep reasonable the cost of this calculation requiring a very refined grid, we selected a spall model to handle damage of the different walls. The comparison with experiment is very good concerning the shape and depth of the cloud, and the limit velocity measured by the Fabry-Perot. The main difference is located in the risetime of the velocity profile which is around 5 μs in the simulation and about 60 in the experiment. This discrepancy illustrates the importance of the fragmentation process to handle proper dislocation of materials and predict the content of each small impact contributing to the acceleration of the backwall. The limit velocity is accurately predicted because it depends only on the correct conservation of momentum and kinetic energy, and, at late time, all the impacts have been collected. A more accurate description of the velocity profile would be obtained using a real damage model, at a more expensive cost.
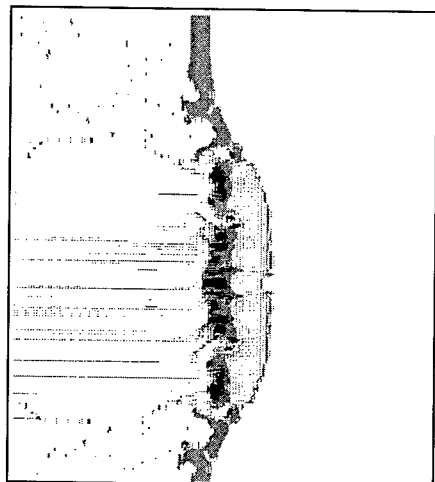
Fig. 6a. Impact of the first cloud on the second wall.
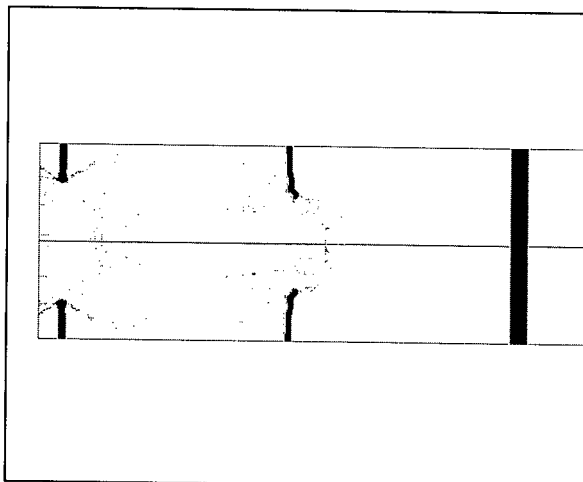
Fig. 6b. Clouds of debris at time of X-Ray snapshot.
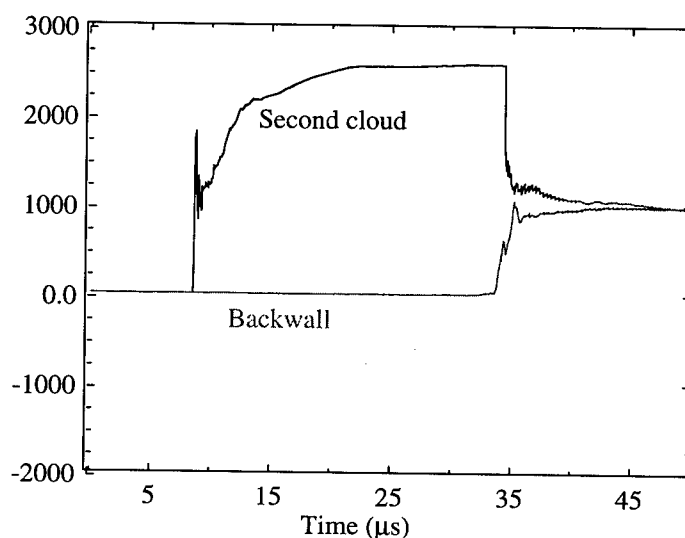
Fig. 6c. Velocity profiles (m/s) versus time.

Fig. 6. Results of the numerical simulation.

Fragmentation of a Steel Tube under High Explosive Loading

The problem of dynamic fracture of tubes and other axisymetrical hollow objects under internal explosive loading is very similar to the previous one in the sense that it needs also a complete understanding of the generation of schrapnels and debris. Some recent experiment has been performed at CESTA [8, 9] to evaluate the debris population generated by a steel cylinder 3 mm thick filled with high-explosive, a Fabry-Perot interferometer recording the velocity of expansion of the cylinder (Fig. 7).

Experiments. The collected debris consists of a large distribution (about 800 fragments) of small to medium-size debris (below 2 mm) rather spherical, combined with some elongated strips of metal having the same thickness as the original tube. The shock-induced debris generated at early time of the simulation are combined with shear effects which can be attributed to the dynamic fracture induced by the mechanical limits of the steel while it is expanding.
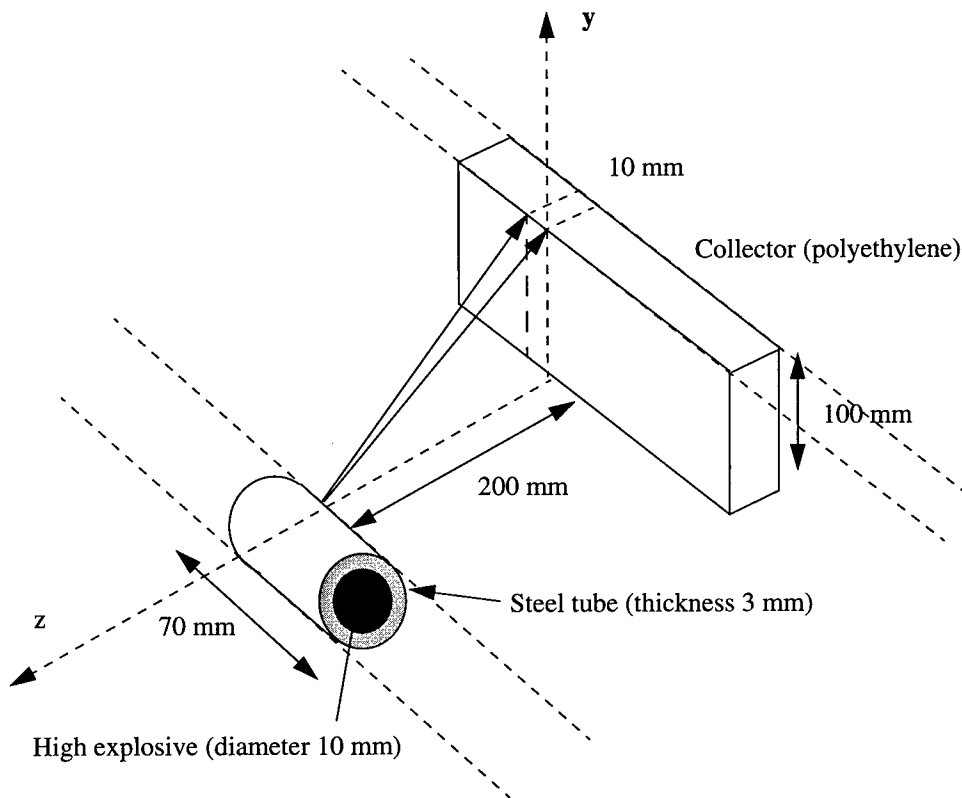
Fig. 7. Schematic drawing of the experiment.

Modeling. The modeling task has be separated in two different analysis to handle the different fragmentation regimes. The first simulation was performed using the Lagrange scheme of HESIO-NE coupled to a separated shrapnel generation algorithm as described previously and the second one a full euler run including a spall model. The 2 simulations were performed in 2D planar geometry, which means that the length of the cylinder is supposed to be infinite for the simulation purpose. The results concerning fragmentation populations are given per centimeter of the tube supposed infinite along its main axis. Figure 8 shows the main results concerning the prediction of fragments size and also a correlation between numerical and experimental free surface velocity.

SIMULATION 1　　　　　　　　　　　　SIMULATION 2
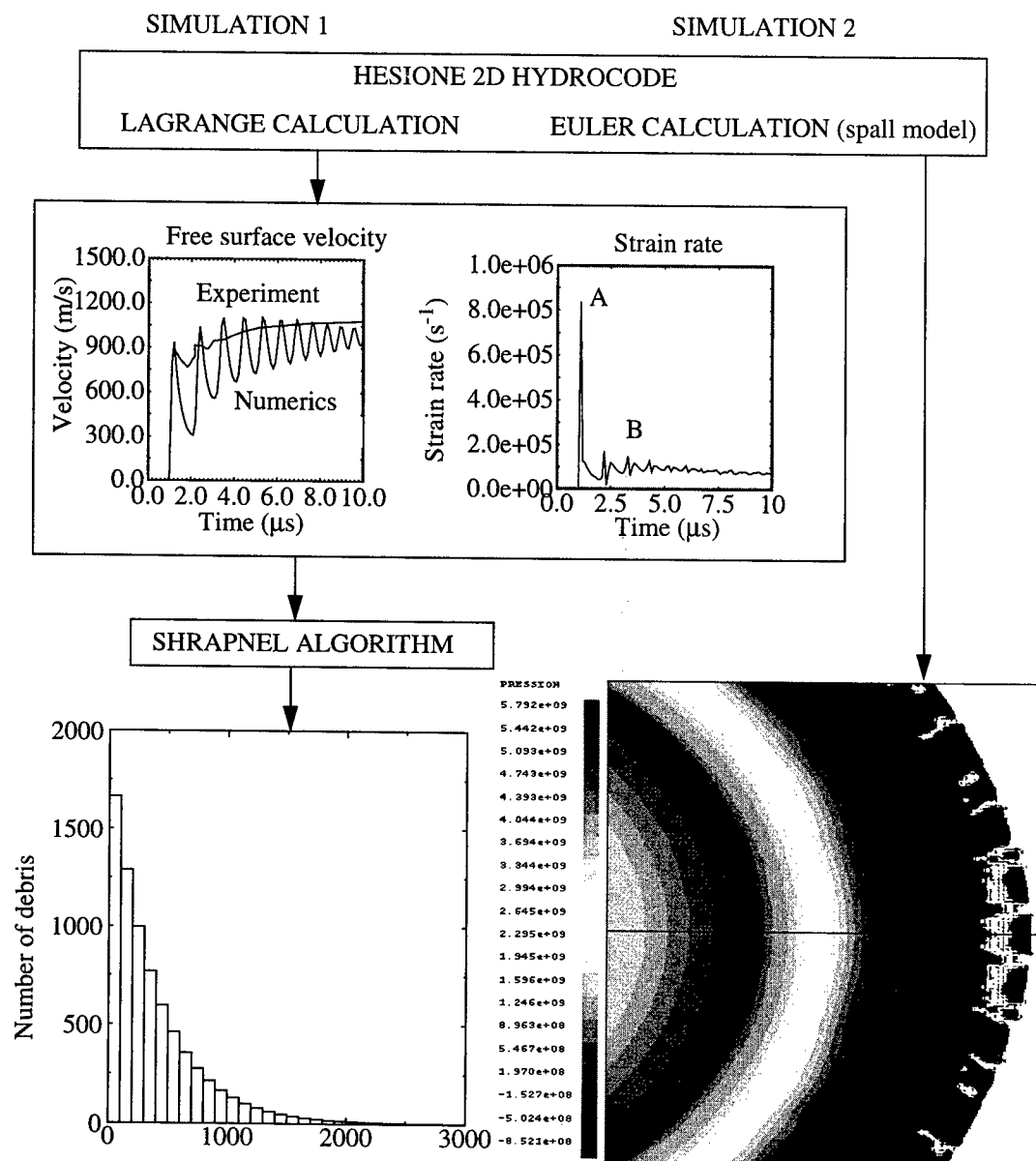
Fig. 8a. Debris size (mm)

Fig. 8b. Surface fragmentation at 2.5 μs

Fig. 8. Schematic diagram of the numerical simulations.

Comments about simulation 1. The velocity and strain rate time profiles have been evaluated in the vicinity of the free surface of the tube. Concerning the velocity profile, the agreement between Fabry-Perot recorded data and calculations is good, despite of some oscillations in the Lagrange run. The strain rate profile exhibits a peak value which is very high (about $10^6 s^{-1}$) for a short period of time («A» on Figure 8). At this time, the first shock reaches the free surface of the steel tube and consequently initiates the shock-induced phase of fragmentation. The second period, much longer, concerns constraints induced by the expansion of the tube under the effect of the explosive pusher and is characterized by a slowly decreasing rate starting from $10^5 s^{-1}$ («B» area on the strain rate profile).

Consequence for the shrapnel populations. As mentioned in the model description part of this paper, the accuracy of the Grady fragmentation analysis depends strongly on the instant selected to stop the hydrocode calculation and activate the method. This time should be long enough to be sure that the interaction between shocks and unloading waves are terminated inside the material and that debris generating cells are in a full balistic flight towards the target. No rigorous criterion can be recommended for its selection which is very dependent on the problem to solve. The observation of the time variation of the thermodynamic and kinetic variables as the simulation proceeds is the only way to minimize the errors. Another possible way is to switch when the geometry of the material has expended a given time its original value. To illustrate the sensitivity of the results versus this selection, we performed the Grady analysis at 2 different instants: 1 and 10 μs. Thermodynamic and kinetic variables have been extracted from HESIONE Lagrange hydrocode run at these instants, and transferred to the shrapnel generation algorithm. The resulting populations are given at Figure 9 in a combined histogram of fragment sizes. The 1 μs simulation does not fully satisfy the previously described requirements since it is performed in the vicinity of the peak shock. The two distributions exhibit an overestimate of the small debris population and a very good fit of the highest range sizes, compared to the experimental results. This trend is general applying the Grady formulation at early time, when the strain rate is too high and not fully stabilized. For the smallest debris, it seems reasonable to assume that most of them have not been collected or identified in the experiment. Another possible explanation of the discrepancy is located in the numerical simulation which is performed in 2D, as the real experiment is at least locally 3D.
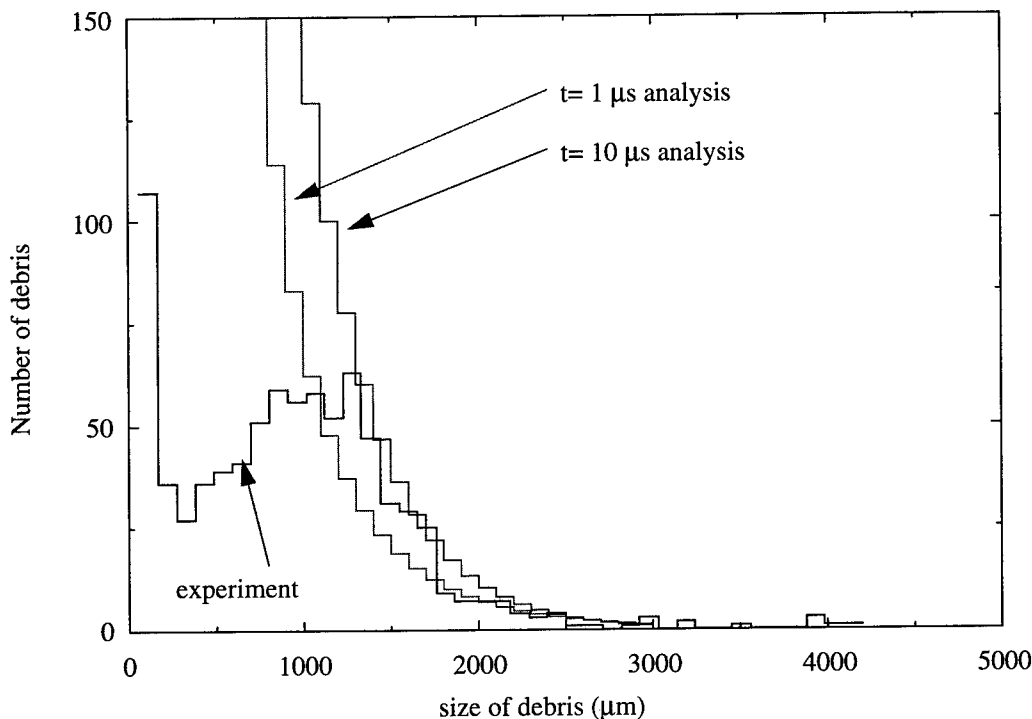
Fig. 9. Distribution of fragments (histogram).

Comments about simulation 2. The Euler simulation provides only global results and does not allow to quantify debris. Nevertheless, the snapshot of the fragmentation process given at Figure 10 after 10 μs confirms the previous results concerning the fragmentation of the ring in a qualitative way. Large fragments supporting (low) positive pressures can be attributed to the dynamic fracture regime, and small fragments surrounded by fully unloaded areas to the shock-induced regime.
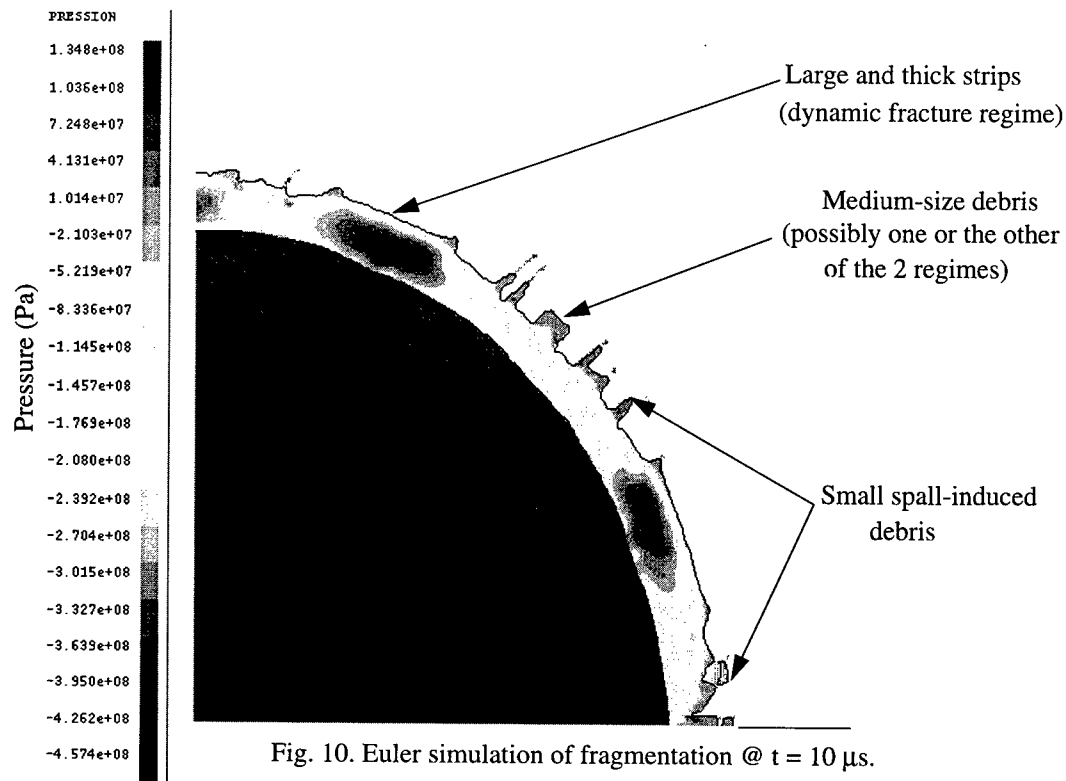
Fig. 10. Euler simulation of fragmentation @ t = 10 μs.

One question is still unsolved about the numerical or physical origin of the radial cracks obser-ved. According to the 1D expanding hypothesis, all the cells located at the same radius are identical and must support the same tensions. Consequently, they must crack at the same time which does not happen. We must consider that some numerical noise initiates the very first cracks at particular locations. The initial crack location is not physical but the subsequent behaviour of the materials under the effect of the unloading process is physically driven. In the real material, the fracturation process is also randomly initiated, due to pre-existing micro-cracks or impurities trapped in the ma-terials. This unexpected numerical noise looks to be an excellent way to introduce a random com-ponent in the simulation.

CONCLUSION

Three different levels of numerical response to a given problem of damage inside shock-loaded materials have been summarized and several applications to experiments performed, allowing a gradual approach to solve the damage problem. The spall models predict fairly well the basic pro-cess caused by unloading waves inside materials but do not allow any sophisticated prediction of fragmentation. The damage models based on porosity control implemented inside hydrocodes al-low a more realistic representation of the debris clouds and reasonable predictions of effects. The specific models usually disconnected from hydrocodes potentially provide the best results for mi-croscopic predictions of the behaviour of materials, fragmentation aspects, and are the only availa-ble models to transport accurately fragments on a long distance of flight.

REFERENCES

1. F.R.Tuler, B.M.Butcher, A criterion for the time dependence of dynamic fracture, *Int. J. Fract. Mech.* (4), pp.431-437 (1968).

2. J.N. Johnson, Dynamic fracture and spallation in ductile solids, *J.Appl.Phys.*, **52**(4) (1981).

3. M.M. Carroll, A.C.Holt, Static and dynamic pore-collapse relations for ductile porous materials, *J.Appl.Phys.*, **43**(4), pp1626-1636 (1972).

4. D.R.Curran, L.Seaman, D.A. Shockey, Computational models for ductile and brittle fracture, *J.Appl.Phys.*, **47**(11), pp 4814-4826 (1976).

5. Lee Davison, Dennis Grady, Mohsen Shahinpoor, *High-Pressure Shock Compression of solids II, Dynamic fracture and fragmentation,* Springer (1996).

6. D.E. Grady, Particle size statistics in dynamic fragmentation, *J.Appl.Phys.,* **68**(12) (1990).

7. N.F.Mott, Fragmentation of Shell Cases. *Proc.R.Soc.*, London A.189, pp.300-308 (1947).

8. Daniel Schirmann, Alan Burnham, LMJ/NIF Project, *Target area development, Tasks 97-3*, Lawrence Livermore National Laboratory (1997).

9. D.Schirmann, L.Bianchi, R.Courchinoux, C.Cordillot, C.Dubern, A.Fornier, A.Geille, F.Jequier, J.C.Gommé, G.Sibille and J.P.Thébault, Engineering physics inside the LMJ target chamber, *Proc. Symposium on Fusion Engineering,* San Diego (1997).

INVESTIGATION OF SHOCK AND DETONATION WAVES BY OPTICAL PYROMETRY

M. F. GOGULYA, A. Yu. DOLGOBORODOV, and M. A. BRAZHNIKOV

Institute of Chemical Physics Russian Academy of Science, Moscow V-334, Russia

Summary — Some aspects of application of optical pyrometry to the investigation of shock and detonation waves in condensed matter are discussed. New results on the chemical interaction of metals with detonation products and oxidizers induced by planar shock wave and the results on shock wave initiation of liquid explosives are presented also. © 1999 Elsevier Science Ltd. All rights reserved.

INTRODUCTION

Shock compression processes in condensed matter has been studied by optical pyrometry for 50 years [1-3]. First works in this area dealt with measurements of the temperatures of detonation products in charges of condensed high explosives. At present, these techniques have been developed further. They stimulated similar studies on shock compression of condensed materials. Thus, during the 1970's, the shock front temperatures were measured for a number of transparent materials [4-6]. Contemporary investigations into detonation of condensed explosives are conducted in the following areas: ascertaining the nature of light emission from detonation waves and measuring the temperature of detonation products of pure and deterred high explosives (HE) [7-9], studying detonation of metallized explosives [10-12], and exploring the initial stage of HE initiation with shock waves [13].

Optical pyrometry allows measurements of pressure profiles with a high resolution both in time and amplitude. This is attained employing the so-called indicator technique, which implies the use of transparent materials with known temperature-pressure dependence placed on samples tested [14]. Optical pyrometry is a non-intrusive method of studying fast processes. Undoubtedly, this beneficially distinguishes it from other techniques.

INDICATOR TECHNIQUE

Indicator technique is based on the property of some materials to lose their transparency immediately upon being shocked and to emit light radiation from thin layer at shock front. Of importance for the purpose of this technique is that previous investigations have shown a direct correlation between the brightness temperature (T) and pressure (p) behind the shock wave front. Thus, shock front radiation in these materials (indicators) may serve as a fast-response pressure gauge capable of monitoring pressure variations at the sample - indicator interface.

Indicator media can be either liquid or solid. However, initially transparent liquids are preferred, because they can no support elastoplastic deformations. In addition, liquids provide better contact with the samples studied, except for samples with an open porosity. In the latter case, one should introduce a thin intermediate medium (foil or films) or use a solid indicator varnished on the side in contact with the sample, in order to cut off radiation from the sample itself.

In the ideal version of the technique, the shock Hugoniot and the pressure dependencies of the intensity of shock front luminosity (temperature) and sound velocity should be known for the indicator media. The indicator medium should not experience marked transformations changing luminosity and sound velocity within the pressure range where this medium is applied.

Indicator materials are applicable within ranges of the parameters where the temperature varies proportionally (or nearly proportionally) to the pressure and where the light absorption of the shocked material is high. Meeting the latter condition provides good time resolution. In other words, a time needed for formation of an equilibrium emitting layer in the shocked indicator, radiation from which corresponds to the thermal shock-compression temperature, must be lower than or equal to the rise time of the leading front of the luminosity signal, i.e. the resolution time of the pyrometric instrument used. At present, the instrumental rise times range between 5 and 20 ns.

The high absorbency of the shocked indicator material allows one to consider radiation of the shocked indicator as that of an opaque material, i.e. as luminosity emitted directly from the shock front. The intensity of shock front radiation follows pressure variations at the boundary with the studied sample, slightly extending the signal in time. This extension enhances the time resolution of the technique. Furthermore, this method for studying shock and detonation waves in condensed materials furnishes continuous information about wave intensity variations in time. One can select an optimal indicator most suitable for a particular study from a set of materials with different initial densities and compressibilities.

Many transparent materials can be used as indicators. Particularly important among them are liquid halogenated methanes. Experimental information available at present on the characteristics and behavior of these liquids under shock compression permit one to use them flexibly as indicators in studies of shock and detonation waves in condensed materials. In our research most frequently used indicators were bromoform and carbon tetrachloride. Bromoform is a transparent liquid with density $\rho_0 = 2.89$ g/cm^3 and sound velocity at $t = 20°$ C equal to 0.928 km/s. Its shock Hugoniot was measured in [15 - 18]. The shock wave velocity (D) as a function of the particle velocity (u) exhibits a kink at $u = 1.29$ km/s ($D = 3.29$ km/s and $p = 12.3$ GPa). The lower section of the plot is described by equation: $D = (0.925 \pm 0.119) + (1.835 \pm 0.135)u$, and the upper line (up to $u = 4.8$ km/s) is specified by equation: $D = (1.546 + 0.061) + (1.354 \pm 0.021)u$.

At pressures of about 10 GPa the compound becomes opaque. Our pyrometric studies demonstrate that the signal rise time at $p = 11.5$ GPa is 150 ns, and at 13 GPa it is less then 20 ns and comparable with the resolution time of the recording instruments. The shock front temperatures had been measured at various pressures [17, 19, 20].

The difference between the temperatures measured at various wavelengths did not exceed 100°K, which allowed us to average the measured parameters over the wavelengths (the pressure values were corrected with due regard for the above-indicated dependences for the shock Hugoniot). The pressure dependence of the shock front temperature for bromoform between 11 and 44 GPa can be written as $T = (237 \pm 26) + (112 \pm 1)p$, here p is in GPa and T in °K. The root mean square deviation of the experimental points from the dependence derived above is 75 °K, which is less than the measurement error. At higher pressures, the temperature deviates from the linear dependence appreciably, which is probably associated with greater degrees of dissociation.

Among other halogenated methane derivatives, the following liquids are of particular interest: carbon tetrachloride, chloroform, dichloromethane, dibromomethane, and diiodomethane. Their detailed shock Hugoniots can be found in [21, 22] and the temperature at the shock front can be written as a linear function of pressure, $T = a + bp$, within certain ranges [14].

First measurements conducted using the indicator technique yielded information on pressures in metal plates in contact with charges of various HE [23] and about the pressure and polytropic indexes of the detonation products. Later on, this technique was successfully employed: to determine the shock wave pressure transmitted through porous plates [24, 25], to study shock wave attenuation in various materials [26, 27], to measure the length of the chemical reaction zone in condensed HE [28], to investigate relaxation attenuation and structure of shock waves in the region of

polymorphic graphite-to-diamond transformation [29], to examine the structure of shock waves in heterogeneous samples consisting of components of different compressibility [30, 31], and so on.

The indicator technique is also used to measure the sound velocity in shocked materials. The feasibility of sound-velocity determination in initially transparent materials from luminosity records was first mentioned in [32]. However this idea was implemented experimentally much later in [33 - 35]. The knowledge of the T(p) dependence may turn out to be unnecessary in this case, because it is time, which is actually measured. However, in order to infer as much information as possible from a single run, this knowledge is very important. In this connection, information about the shock Hugoniot, sound velocities, and structural changes in shock-loaded indicators gained in recent years is also useful. This applies equally to studies in which the velocities of traveling perturbations behind the shock wave fronts have been measured [36].

WINDOW TECHNIQUE

Temperature is one of the most important thermodynamic characteristics of state for a shock-compressed material. Temperature can also furnish information on physicochemical conversions in the course of shock pressurization. The dynamics of temperature variations may provide data on the transformation kinetics. Experimental determinations of temperature at the high pressures and short durations of the processes studied are an extremely difficult problem, which includes not only methodological difficulties of monitoring the parameters, but interpretation difficulties of the measurements as well. Temperature has been measured by various techniques, see e.g. [2, 3, 37], Raman spectroscopy [38-40] and fluorescent probe techniques [41]. Attempts were also undertaken to use film gauges for this purpose [42, 43], the work on which is still being continued. Each of the aforementioned techniques have their own benefits and drawbacks, but the major body of available experimental data on temperatures measured in fast reacting media is obtained for initially transparent materials by optical pyrometry. Its application is based primarily on the hypothesis of the thermal nature of radiation from the object studied and on the assumption that quasi-equilibrium state is established in the shocked material. It is also assumed that radiation from a shock front (or a detonation wave) depends unequivocally on the temperature behind the shock front (or detonation products). Investigations are often performed by means of the technique in which radiation is monitored through another material that retains its transparency within the range of pressures of interest. This material is called a «window». Hence, radiation is recorded from the interface between the tested material and the window. The use of this technique enables one to gain information not only on the temperature at the shock (or detonation) wave front in transparent materials but also to monitor its variations behind the front. Moreover, it makes possible measurement of temperature in opaque materials.

The number of applied window materials is limited, among them are, e.g., sapphire (Al_2O_3), lithium fluoride (LiF), rock salt (NaCl), optical glass, Plexiglas, and some liquids, such as water, glycerol, etc. In the majority of cases, establishing of transparency of a window material is a concomitant result of other optical investigations, e.g., of determination of refractive index of materials and Raman spectroscopy. In this way, determined was transparency of the above-mentioned window materials, namely, of water up to 30 GPa [44], Plexiglas up to 22 GPa [45], sodium chloride up to 46.5 GPa [4], glycerol up to 40.9 GPa [46], lithium fluoride up to 160 GPa [45], and some other materials.

Application of the window technique necessitates assessment of a possible effect exerted by the window material on measurements. This effect arises primarily due to different dynamic compressibilities of the window and the sample tested. If shock impedance of a window material is greater than that of a tested object, a shock wave is reflected back into the tested sample. If this impedance ratio is reverse, a rarefaction wave is reflected into the sample.

In many studies, one needs information about the temperature distribution in the incident wave. However, even for inert materials, it is very difficult to find window materials with compressibilities close to that of the object tested. Using two materials with different dynamic com-

pressibilities (lower and higher than that of the tested material) and assuming a constant composition of the material allows one to determine the temperature profile in the incident wave.

A similar approach can be used in some cases for studying detonation processes. By this way, in [9] a temperature of the detonation products of some explosives (HMX, RDX, and TNT) was determined. The temperature profiles on the shock Hugoniots and isentropes of the detonation products were determined using various window materials differing in their compressibility from the detonation products and original explosive. The temperature of the detonation products in the incident waves was calculated from the measured temperatures assuming a constant ratio of the Gruneisen coefficient to the specific volume.

Investigations of HE-paraffin (HE = RDX and HMX) mixtures [9] have demonstrated that decomposition of the additive and, hence, composition of the products depends upon the relative compressibilities on the window material used. The effect of the window material on the luminosity signal revealed in experiments with RDX - wax explosives is complicated. Paraffin can be considered as an energy-consuming additive. The measured temperature with a glass window is higher than that determined in experiments with a harder window material - lithium fluoride. It is noteworthy that, by and large, the temperature dependencies determined with water and glycerol as window materials lie below the curve determined in experiments with lithium fluoride windows, but the temperatures measured within initial 50 ns are higher when the «softer» the window materials are used (in the series: lithium fluoride, glass, glycerol, and water [47]). Ambiguity of the window material effect manifests itself most profoundly in this case, because the decomposition rate of the energy-consuming additive reduced concurrently with general lowering of the sample temperature.

The window technique enables one not only to measure temperatures but to gain information about the dynamics of its variations in the course of the process as well. Analyzing temperature profiles measured in many shock pressurized reactive systems (e.g. mixtures of sulfur with some metals: magnesium, titanium, tin, etc., of aluminum with sodium perchlorate, and some composite explosives) has revealed a chemical reaction occurring within first microseconds [9, 47- 50].

The measured profiles exhibit a certain peculiarity, namely, the temperature recorded starting with the instant of shock wave arrival at the contact surface first decayed then rose, attaining in some cases the initial measured level. The time to the beginning of temperature rise is identified with the time of a reaction proceeding in the shocked mixture. This time depends not only on the geometry of the experimental assembly and the loading system but on the nature of the physico-chemical processes taking place in the mixture as well. The measured characteristic reaction time depends also on the dynamic compressibility of the window material used.

It is inferred from the investigations performed that, generally, the difference in dynamic compressibilities of the window and sample affects both the characteristic development time of the process and the measured temperatures. Progress of the shock-induced reaction, reacted fraction, and so on depend on many factors, such as particle size of the components, overall density of the sample, intensity and duration of the incident shock wave. This means that there is a threshold pressure for reaction initiation (measurement of which is often one of the objectives of the studies). There are also shock wave amplitudes above which the reactions become unfavorable thermodynamically. Thus, for aluminum mixtures with potassium perchlorate (at one and the same experimental assembly) a pressure was found which was optimal for the reaction [11]. Similar results were obtained in investigations into chemical interaction between tin and sulfur [51].

From the aforesaid, we can infer that the effect of compressibility of the window material on a reacting system is governed by the reflected wave. When the reflected wave is compressive wave (a harder window) the measured temperature may both rise, intensifying the reaction (e.g. in the RDX/Al system [47]), and reduce due to dissociation of the pressurized material, which is insignificant in the incident wave (e.g. in CCl_4 [20]).

To summarize, we would like to emphasize again that attempts to select such an "ideal" window for reacting systems or materials undergoing phase transition always fail, because compressibility of the system tested changes in the course of shock compression and in the post-

shock state; whereas for an inert sample, one can theoretically find a window whose compressibility would be close to that of the tested sample.

TEMPERATURE AND PRESSURE PROFILE MEASUREMENTS

A) BLOCK-DIAGRAM OF THE EXPERIMENTAL SET-UP
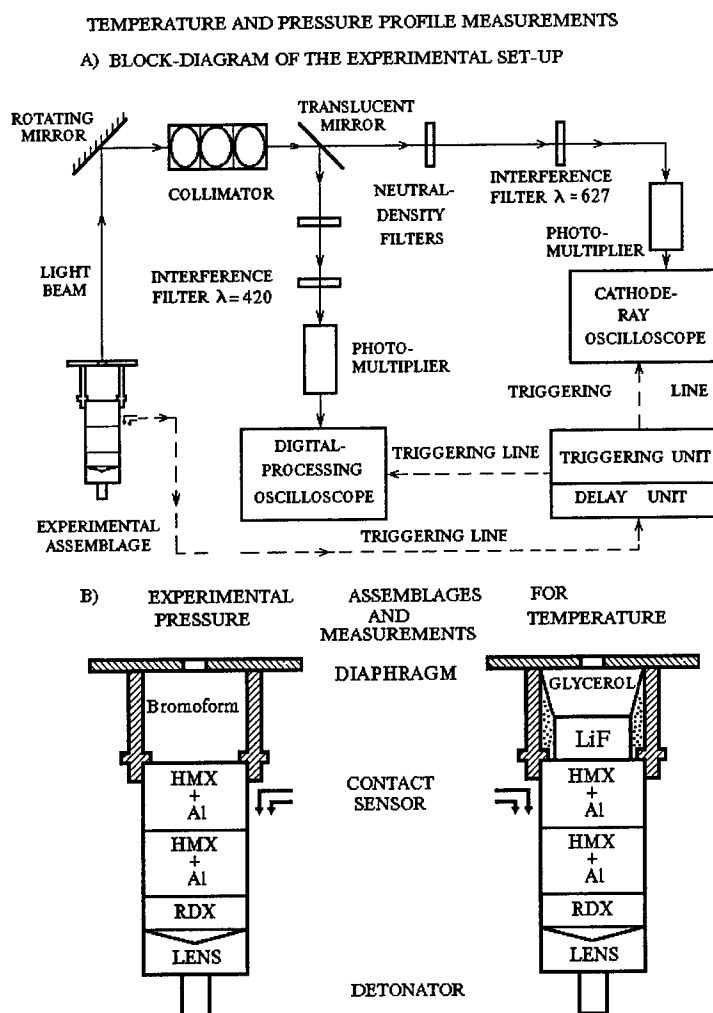
Fig.1. Schematic of (A) dual-channel optical pyrometer and (B) experimental assemblies

Processes taking place in shocked reacting energetic materials are very similar to those occurring in detonation waves. Specifically, this applies to oxidation of metals. Changes in temperature profiles can be used to assess the effect of particle size of the starting components, primarily metals, on the efficiency and rate of reactions and also the characteristic reaction times. In as much as the light emission intensity depends nearly exponentially on the sample temperature, it is these experiments that enable one to detect the beginning of an exothermic chemical reaction even when it affects the kinematics parameters only insignificantly. Exploring compositions containing micron-size metal particles seems to be interesting, because the authors of [10, 52] predict their high conversion degrees both in shock-induced reactions and in detonation waves. Coarser particles in shock-pressurized samples react primarily on their surface. Hence changes in the specific surface area with variation of the reacted fraction and of the mean particle size must be taken into account.

SOME RESULTS ON OPTICAL PYROMETRY APPLICATIONS

Below are presented some experimental data obtained by optical pyrometry techniques. Most of them have been obtained with the aid of a dual-channel pyrometer, schematic of which is displayed in Fig. 1.

Detonation of HMX/Al Mixtures

One of the lines of pyrometry application is the studying of detonation processes and among them the studying of interaction of detonation products with metals behind wave front. Temperature and pressure profiles were measured in HMX/Al mixtures of different composition and Al particle grain of size [53]. Experimental assemblies in which the pressure and temperature profiles have been measured are shown in Fig. 1B. Samples studied were 40 mm in diameter and 44 mm high, they were generated with a plane wave generator made of RDX - wax composition (commonly used for generation in all experiments which results are presented here) supplemented by an intermediate RDX pellet 10 mm high ($\rho_0 = 1.68$ g/cm^3). As an example, the experimental data (pressure and temperature profiles) for HMX mixture with Al 0.5 μm grain of size are shown in Fig. 2. The measured levels of temperatures and the shapes of the profiles (especially for mixture with 25% of Al) uniquely demonstrated occurrence of chemical reaction between Al and detonation products within first microseconds. Additions of Al particles into HMX resulted in pressure level decreasing and pressure profile transformation as can be seen in Fig. 2b. The main peculiarity inferred from the pressure profiles is the two-peak structure exhibited by profiles measured in the majority of mixtures studied, this structure shows up selectively, depending on the particle size. The most plausible explanations for the two-peak structure can be associated with a possible change in the kinetics of HMX decomposition, which is caused by temperature reduction due to heat transfer to cold Al particles and with exothermic chemical reaction between Al and HMX decomposition products.
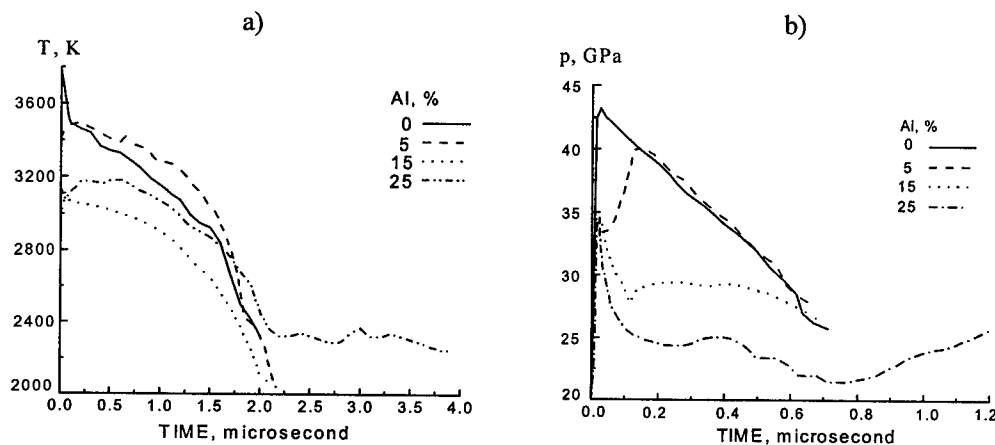
Fig.2. Temperature time histories (a) and pressure profiles (b) in HMX mixtures containing Al 0.5 μm in size

Shock Wave Initiation of Liquid Explosives.

Other perspective line of the optical pyrometry application is investigation of detonation initiation of HE caused by shock wave. Both techniques window and indicator could be applied for this study.

Shock wave initiation of some liquid explosives (LE) bis(2-fluro-2,2-dinitroethyl)formal or (FEFO), isopropylnitrate (IPN) and 1,6-diazido-2-acetohexane (DA)) was studied by indicator

technique. According to the classic model [54], a shock wave initiation in the homogeneous HE occurs through volumetric heating of substance under compression and the macrokinetic of the decomposition obeys Arrenius law. Thus the experimentally determined parameter is the time of delay of adiabatic explosion. The experiments on determination of this parameter were carried out in the following way: the initiating shock wave (ISW) enters LE from liquid indicator (bromoform or tetrachlormethane) with the known Hugoniots and dependencies of radiation intensity on pressure. To prevent LE and indicator mixing, the polypropylene film of 20 microns thickness was located between them. It was expected that first the radiation of SW front in the indicator would be registered, then radiation of the indicator in a wave reflected from LE and, finally, LE detonation product own radiation would be registered. It was supposed that LE would remain transparent up to the moment of sharp intensification of chemical reaction. The results with IPN and DA have shown the close tendencies in behavior of these explosives under ISW. They are something different from the classic model. The profiles of brightness temperature allow allocating area of a supervelocity detonation. At the same time, further we observed the rather delayed site of overdriven detonation formation. For IPN it was determined, that even insignificant decrease of ISW pressure may result in spreading of supervelocity detonation zone. Increase of ISW pressure up to 9,8 GPa results in disappearance of area of gradual radiation increase (including area of supervelocity detonation), instead of it there is an increase of radiation up the moment of formation of a quasi-steady detonation. The change of radiation character for this LE allows receiving only approximate time delays in adiabatic explosion.
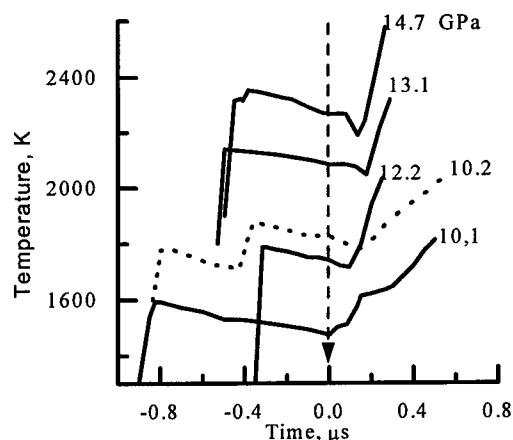
Fig.3. Temperature time histories of FEFO shock wave initiation

Initiation of chemical reaction in FEFO does not correspond to the model of thermal explosion even approximately. After ISW entering into FEFO (in Fig. 3 it is marked by an arrow) at first the plateau is observed. Its duration decreases with growth of ISW pressure. It can indicate that own radiation immediately appears in FEFO. At pressure higher than 10.1 GPa the experimental records do not give the qualitative changes of radiation intensity that could be expected due to the difference of compressibilities of indicator and FEFO. The rate of radiation increase with changing of pressure in the range of 12 - 15 GPa practically does not vary, and at the same time it is mach more than the rate of growth fixed at pressure 10.1 GPa. Possibly, changes in the mechanism of initiation occur in the range of 10 - 12 GPa, i.e. in macrokinetics of observable processes.

Thus, the experiments have shown, that the macrokinetics of process a shock wave initiation in real LE differs from the simplified classical model. Specific features of chemical reactions development, caused by differences in molecular structure of explosives, require a new theoretical model for the description of decomposition a homogeneous HE with a shock wave compression.

Sound Velocities in Shock Compressed Materials

Indicator technique can be applied for measurements of sound velocity in shock compressed material. We calculated the sound velocity behind the shock wave front from the speed of the rarefaction wave, determined by the overtaking-release-wave method with the detection of temporal change in the brightness of the shock front in the indicator [35, 36].

Planar shock waves were generated in the samples by impact of Duralumin plates of different thickness, 40 mm in diameter, driven be expanding detonation products of HE. After the shock wave passed through the rather thin samples into the indicator, we detected the emission, which was constant for some time τ and then drop sharply after the relief wave arrived at the shock front in the indicator from the rear face of the projectile. As the sample thickness was increased, the time τ decreased, and eventually pulse shape became triangular at some thickness of the sample - H. This value (H) was taken as the base line over which the pressure-release wave overtook the shock-wave in the sample. From the values of τ for various sample thickness we constructed a curve which, when extrapolated to $\tau = 0$, determined the value of H. Knowing H for a given material made it possible to calculate the value of sound velocity in shock compressed material.

Table 1. Sound velocities in shock compressed materials

Material	ρ_0, g/cm^3	ε, %	W, km/s	U, km/s	P, GPa	C_l, km/s
Al$_2$O$_3$	3.92	1	3.64	1.36	52.8	16.2 (15.2)
B$_4$C	2.50	1	3.64	1.65	44.4	18.8 (16.4)
SiC	3.09	4	3.64	1.60	46.0	16.6 (13.0)
Al	2.78	0	2.70	1.35	26.8	8.40
			4.48	2.29	53.5	9.70
			5.44	2.72	68.0	10.21
Al$_{por}$	2.17	20	4.80	2.77	44.4	8.30
	1.87	31	4.80	2.98	37.2	7.60
KI	3.08	1	3.20	1.89	26.0	4.20
			4.80	2.72	47.3	5.00
Al/ KI	2.89	0	3.20	1.77	28.9	5.90
50/50			4.80	2.58	51.6	7.10
Cu	8.93	0	1.94	0.97	45.7	6.60
			3.54	1.77	104.4	7.25
			3.66	1.83	109.4	7.55
Paraffin	0.91	0	5.04	3.65	28.1	10.0

Some data on shock compressed solids are given in Table 1. In the Table, there were made the following notations: ρ_0 - material density, ε - sample porosity, W - duralumin plate velocity, p – pressure, u - particle velocity, C_l - calculated sound velocity, Al - Duralumin D 16 (Cu - 4.4% wt; Mg - 1.5% wt; Mn – 0.6% wt), Al$_{por}$ - Al samples pressed from particles of mean grain of size 50 μm, KI - potassium iodide, Al/KI 50/50 - Al and KI mixture with mass ratio 50/50.

The error of sound velocity calculation was estimated to be ~ 0.3 km/s. The data on sound velocity for some ceramic (corundum - Al$_2$O$_3$, boron carbide - B$_4$C, and silicon carbide SiC) are given in the Table 1 as well. For these materials, the error of sound velocity determination could be higher, when utilizing the indicator technique. The error could increase due to the elastic precursor propagating before shock wave in the ceramics at the pressure range studied. It is possible to estimate the maximum error for each measurement introduced by precursor propagation. The values of sound velocities given in brackets were the smallest values calculated taking into account the maximum correction for the influence of the elastic precursor on the detections.

Attenuation of Shock Waves

Indicator technique could be applied to the investigation of shock wave attenuation in solid and mixed materials. Among the data, received by us recently, it is necessary to note interesting results on research of attenuation in mixtures of Al_2O_3 and Plexiglas. Attenuation of plane shock waves in Al_2O_3/Plexiglas mixture was studied experimentally. The mixture specimens were prepared by pressing mixed powders with different content of components. Shock waves were induced by contact detonation of HMX charge (density $\rho_0 = 1.8$ g/cc, 40-mm dia., and 10 mm long). HMX detonation was initiated by low-density explosive charge (TNT 1.35, 50 mm long) and explosive lens. The attenuation rate was determined by measuring pressure change in a wave transmitted through the specimen into liquid indicator (CCl_4) as function of specimen thickness (h). Shock wave pressure was measured by means of indicator technique. Experimental results were analyzed assuming an exponential dependence $P(h)=P(0) \exp(-\alpha\ h)$, where α is the coefficient of wave attenuation with specimen thickness. The comparison of attenuation in mixtures with that for pure ceramic specimen, obtained under similar condition [38], shows, that nonporous ceramic has the most attenuation rate with thickness.

Table 2. Attenuation coefficients.

Material	ρ_0, g/cm^3	ε, %	P_0, GPa	α, 10^{-1} mm^{-1}	α_m, 10^2 g/mm^2
Al_2O_3/Plexiglas					
90/10	2.20	30	21.0	1.26±0.12	0.57
70/30	1.90	18	23.9	1.38±0.13	0.73
50/50	1.58	12	24.2	1.28±0.47	0.81
Al_2O_3	3.92	1	17.6	1.71±0.02	0.44
	2.51	35	20.9	1.40±0.12	0.56
Plexiglas	1.18	0	24.4	0.68±0.07	0.58
	0.83	30	24.1	0.85±0.12	1.03
B_4C	2.50	1	20.0	1.70±0.02	0.68
SiC	3.09	4	18.8	1.39±0.04	0.45
BN	1.57	30	21.8	1.01±0.11	0.64
Al	2.78	0	21.3	0.48±0.06	0.17
Al_{por}	1.89	30	21.4	0.83±0.10	0.44
KI	3.10	0	20.7	0.71±0.09	0.23
	2.17	30	21.3	0.84±0.06	0.39
Al/ KI	2.89	0	21.8	0.65±0.05	0.22
50/50	2.02	30	20.6	0.86±0.13	0.43
Al/Plexiglas					
50/50	1.15	30	22.7	0.82±0.16	0.71

Handling data on attenuation coefficient of some materials are given in the Table 2. The values of initial sample density (ρ_0), sample porosity (ε), and attenuation coefficient per specific weight ($\alpha_m = \alpha/\rho_0$) are given in the Table 2 as well. Solid ceramics (Al_2O_3, B_4C and SiC), as evidenced by the experimental data, have maximum values of attenuation coefficient α. The coefficient (α) in Al_2O_3 decreases by 20 - 25% through porosity increase and plastic introduction, but it still remains much higher than that in non-ceramics. The attenuation coefficient per specific weight (α_m) therewith increases by 80% in comparison with solid ceramics and approaches to the value comparable with that for light organic compounds. It should be mentioned the main peculiarity of the obtained data: in contrast to metals and other materials, a rise of porosity of ceramic layers results in decrease of shock wave attenuation coefficient α. A simple explanation

of this fact could be given in assumption that the chief cause of shock wave attenuation is the interaction of shock waves with overtaking rarefactions.

Thus, the measurements of the sound velocities and attenuation coefficients performed here in samples of corundum, boron carbide, and silicon carbide have demonstrated that they retain high strength properties in the release waves under dynamic loading up to 50 GPa. The rarefaction waves in these materials propagate with the velocities of longitudinal waves, and a significant portion of the pressure decay takes place in elastic waves, making for high values of the shock wave attenuation constants.

REFERENCES

1. R. L. Boyer, Determination of detonation temperature in high explosives. *Phys. Rev.* **74**(9), 1227-1230 (1948).
2. F. C. Gibson, M. L. Bowser, C. R. Summers, et al., Use of an electro-optical method to determine detonation temperatures in high explosives. *J. Appl. Phys.* **29**(4), 628-632 (1958).
3. I.M. Voskoboinikov and A. Ya. Apin, Measurement of detonation fronts temperature for explosives. *Dokl. Akad. Nauk SSSR*, **130**(4), 804-806 (1960).
4. S.B. Kormer, M.V. Sinitsyn, G.A. Kirillov, et al., An experimental determination of the temperatures of shock compressed NaCl and KCl. *Zh. Eksp. Teor. Fiz.* **48**(4), 1033-1049 (1965).
5. S.B. Kormer, Optical studies of shock compressed dielectrics. *Usp. Fiz. Nauk,* **94**(4), 641-687 (1968).
6. I.M. Voskoboinikov, V.M. Bogomolov, A.N. Afanasenkov, et al., Determination of organic matter temperatures under shock wave. *Dokl. Akad. Nauk SSSR,* **182**(4), 807-810 (1968).
7. Y. Kato, N. Mori, H. Sakai, et al., Detonation temperature of nitromethane and some solid high explosives. *Preprint Eight Int. Symp. on Detonation*, N.M., Convention Center, Albuquerque, Conf-85076, V. 1, pp. 314 - 321 (1985)
8. He Hianchu, Han Chengbung, Kang Shufong. The measurement of detonation temperature of condensed explosives with two color-optical fiber pyrometer. *Preprint Eight Int. Symp. on Detonation*, N.M., Convention Center, Albuquerque, Conf-85076, V. 1, pp. 322-329 (1985).
9. M. F. Gogulya and M. A. Brazhnikov. Radiation of condensed explosives and its interpretation (Temperature measurements). *Preprint Tenth Int. Symp. on Detonation*, Boston, Conf-33395-12, pp. 542-548 (1995).
10. Y. Kato and C. Brochet, Detonation temperature of nitromethane aluminum gels. *Dynamics of Shock Waves, Explosion and Detonation.* NY: AIAA, 416-426 (1984).
11. M. F. Gogulya and M. A. Brazhnikov. Investigation of shock-induced chemical reactions in heterogeneous energetic materials. *Proc. of the twenty-first International Pyrotechnics Seminar.* Moscow, pp. 248-262, (1995).
12. . M. F. Gogulya and M. A. Brazhnikov, Investigation of shock-induced chemical reactions in heterogeneous energetic materials by optical pyrometry. *Symposium HDP-95*, Tours, France, pp. 299-307, (1995).
13. Yu. M. Balinets and M. F. Gogulya. Emission from shocked pressed TNT. *Sov. J. Chem. Phys.* **5**(2), 382-386, (1989).
14. M. F Gogulya and A. Yu. Dolgoborodov. Indicator technique for investigation of shock and detonation waves. *Chem. Phys. Rep.* **13**(12), 2059-2069 (1995).
15. J.B. Ramsay. *LASL Shock Hugoniot Data.* (S.P. Marsh, Ed.) Univ. of California Press, Berkeley, 1980, p. 552.
16. S.A. Sheffield. Hugoniot Measurements in Bromoform. *Washington State Univ. Symp. for George Duvall* (1988).
17. I.M. Voskoboinikov and A.Yu. Dolgoborodov. Shock wave propagation in solid mixtures. In *Detonatsiya*, Chernogolovka, pp. 91-94 (1989).
18. G.G. McQueen and D.G. Isaak, Bromoform – a very high-pressure shock-wave analyzer. In *Shock Compression in Condensed Matter-1989*, (S.C. Schmidt, J.N. Johnson, and L.W. Davidson, Eds.), pp. 125-128 (1990).
19. M.F. Gogulya, I.M. Voskoboinikov, The radiation of shocked halogen derivatives of methane, *Fizika. Goreniya i Vzryva*, **24**(6), 127-134 (1988).
20. A.Yu. Dolgoborodov, I.M. Voskoboinikov, I.K. Tolstov, On dissociation of shock-pressurized halogenated methanes, *Sov. J. Chem. Phys.*, **10**(5), 1036-1048, (1992).
21. R.D. Dick. Shock wave compression of benzene, carbon disulfide, carbon tetrachloride and liquid nitrogen. *J. Chem. Phys.* **52**(12), 6021-6032, (1970).
22. R.D. Dick. Shock compression data for liquids. *J. Chem. Phys.* **74**(7), 4053-4061 (1981).
23. I.M. Voskoboinikov, A.N. Kiryushkin, A.N. Afanasenkov, and N.F. Voskoboinikova, Two new techniques for dynamic pressure measuring. *Proc. 1st USSR Symp. on Pulse Pressures*, Moscow, V. 1, pp. 42-49 (1974).
24. I.M. Voskoboinikov, M.F. Gogulya, N.F. Voskoboinikova, et al. The possible description scheme of shock wave compression of porous samples. *Dokl. Akad. Nauk SSSR*, **36**(1), 75-78 (1977).

25. I.M. Voskoboinikov, A.Yu. Dolgoborodov, and M.F. Gogulya, Transfer of dynamic pressures by means of porous samples. *Fizika. Goreniya i Vzryva*, **18** (5), 117-121 (1982).

26. I.M. Voskoboinikov, A.Yu. Dolgoborodov, and A.N. Afanasenkov, Investigation of attenuation of small duration shock waves in condensed matter, *Fizika Goreniya i Vzryva*, **19**(5), 135-138 (1983).

27. I.M. Voskoboinikov and A.Yu. Dolgoborodov, Attenuation of shock waves in heterogeneous matters. *Detonatsiya i Udarnye Volny,* Chernogolovka, pp. 9-13 (1986).

28. I.M. Voskoboinikov and M.F. Gogulya, Luminescence of the shock front in a liquid near the interface with detonating charge, *Khim. Fiz.*, **3**(7), 1036-1041, (1984).

29. M.F. Gogulya, The structure and parameters of shock waves by dynamic loading of natural graphite in the field of polimorphic transformation. *Fizika Goreniya i Vzryva*, **25**(1), 95-104, (1989).

30. A.Yu. Dolgoborodov, I.M. Voskoboinikov, I.K. Tolstov, et al. Characteristic properties of shock waves propagation in mixtures, *Fizika Goreniya i Vzryva*, **28**(3), 106-111, (1992).

31. A.Yu. Dolgoborodov, On propagation of shock waves in liquid solution and mixtures of different solids. *Symposium HDP-95*, Tours, France, pp. 11-16, (1995).

32. L.V. Al'tshuler, S.B. Kormer, M.I. Brazhnik, et al., Isentropic compressibilities of aluminum, copper and iron under high pressure. *Zh. Eksp. Teor. Fiz.* **38**(4), 1061-1070, (1960).

33. R.G. McQueen, J.N. Fritz, and C.E. Morris. The velocity of sound behind strong shock waves in 2024 Al. In *Shock Waves in Condensed Matter-1983,* (J.K. Asay, R.A. Graham, and G.K. Straub, Eds.), pp. 95-98 (1984).

34. A.Yu. Dolgoborodov, I.M. Voskoboinikov, Shock compression of acetonitrile, *Khim. Fiz.*, **8**(8), 1118-1123, (1992).

35. A.Yu. Dolgoborodov and I.M. Voskoboinikov, Sound velocities in shock compressed corundum, boron carbide and silicon carbide, *Technical Physics*, **38**(2), 158-160 (1993).

36. A.Yu. Dolgoborodov, I.M. Voskoboinikov, The Wave Disturbances Rates behind the Shock Wave Front in Aluminium. *Fizika Goreniya i Vzryva*, **25**(1), 88-93 (1989).

37. G. A. Lyzenga, T. J. Ahrens, W. J. Nellis, and A. C. Mitchell. The temperature of shock compressed water. *J. Chem. Phys.*, **76**(12), 6282-6286 (1982).

38. N. C. Holmes, A. C. Mitchell, W. J. Nellis, et al., Raman spectroscopy of shocked water. In *Shock Waves in Condensed Matter-1983,* (J.K. Asay, R.A. Graham, and G.K. Straub, Eds.), pp. 307-308 (1984).

39. A. Delpuech and A. Menil, Raman scattering temperature measurements behind a shock wave. In *Shock Waves in Condensed Matter-1983,* (J.K. Asay, R.A. Graham, and G.K. Straub, Eds.), pp. 309-312 (1984).

40. S. C. Schmidt, D. S. More, and J. W. Shaner. Raman spectroscopies in shock-compressed materials In *Shock Waves in Condensed Matter-1983,* (J.K. Asay, R.A. Graham, and G.K. Straub, Eds.), pp. 293-302 (1984).

41. B. L. Justus, A. L. Huston, and A. J. Campillo, Temperature measurements of shocked water, using fluorescence probe. In: *Shock Waves in Condensed Matter-1985*, (Y. M. Gupta, Ed.), pp. 249-254 (1986).

42. S.S. Batsanov and D.L. Gur'ev, On the sulfur-tin interaction in shock waves. *Fizika Goreniya i Vzryva*, **23**(2), 127-129 (1987).

43. Z. Rosenberg and Y. Partom, Direct measurement of temperature in shock loaded polymethilmetacrilate with very thin copper thermistors. In *Shock Waves in Condensed Matter-1983,* (J.K. Asay, R.A. Graham, and G.K. Straub, Eds.), pp. 251-254 (1984).

44. Ya.B. Zeldovich, S.B. Kormer, M.V. Sinitsin, et al., Investigation of optical properties of transparent materials under super high pressures. *Dokl. Akad. Nauk SSSR,* **138**(6) 1333-1340 (1961).

45. J. L. Wise and L. C. Chhabildas. Laser interferometer measurements of refractive index in shock compressed materials. In: *Shock Waves in Condensed Matter-1985*, (Y. M. Gupta editor), pp. 441-454 (1986).

46. C. F. Petrsen and J. T. Rosenberg, Index of rarefaction of ethanol and glycerol under shock. *J. Appl. Phys.*, **40**(7), 3044-3046 (1969).

47. M.F. Gogulya and M.A. Brazhnikov, Temperatures of the detonation products of condensed explosives. 1. Solid explosives, *Khim. Fiz.*, **13**(1), 52-63, (1994).

48. M.F. Gogulya and M.A. Brazhnikov, On the characteristic times of chemical reactions in heterogeneous systems under dynamic loads. *Chem. Phys. Rep.*, **13**(11), 1887-1901 (1995).

49. M.F. Gogulya, I.M. Voskoboinikov, A.Yu. Dolgoborodov, et al., Interaction of sulfur with metals behind shock waves, *Sov. J. Chem. Phys.*, **10**(3), 634-639 (1992).

50. M.F. Gogulya, I.M. Voskoboinikov, A.Yu. Dolgoborodov, et al., Interaction of sulfur and aluminium behind shock waves, *Sov. J. Chem. Phys.*, **11**(2), 343-348 (1992).

51. S.S. Batsanov, M.F. Gogulya, M.A. Brazhnikov, et al., Investigation of Sn+S reacting system behaviour in shock waves, *Fizika Goreniya i Vzryva*, **30**(3), 107-112 (1994).

52. M. B. Boslough. A thermochemical model for shock induced reaction in solids. *J. Chem. Phys.* **92**(3), 1839-1848 (1990).

53. M.F. Gogulya, A.Yu. Dolgoborodov and M.A. Brazhnikov, Fine structure of detonation waves in HMX – Al mixtures. *Chem. Phys. Rep.*, **17**(1-2), 51-54 (1998).

54. A.N. Dremin, S.D. Savrov, V.C. Trofimov, K.K. Shvedov, Detonation waves in condensed matter. Nauka, Moscow, (1970).

BALLISTIC LIMIT VELOCITY FOR LONG RODS FROM ORDNANCE VELOCITY THROUGH HYPERVELOCITY IMPACT

FRED I. GRACE

U.S. Army Research Laboratory
Aberdeen Proving Ground, MD 21005-5066, USA

Summary—The ballistic limit velocity for long rods impacting targets of finite thickness is explored in a range from ordnance velocity though hypervelocity impact. While several formulas have existed for some time, notable ones of Recht and Ipson, Woodward and de Morton, and Lambert are limited because they either relate primarily to only short rods, bullets, or fragments or apply to long rods but are empirical, as in the case of Lambert's formula. There is, however, a growing need to have a general description of the ballistic limit problem since, today, there is more interest in launching long rods at velocities extending into the hypervelocity range of impact. The current work explores Grace's previous theoretical development of plate penetration/perforation dynamics, providing an iterative solution as well as a derived, approximate, semi-empirical, analytic expression for the limit velocity. Both analyses are applied throughout extended ranges of impact velocity and compared to Lambert's formula and experimental data for long rods of steel and tungsten striking steel armor targets. © 1999 Elsevier Science Ltd. All rights reserved.

NOTATION

D	initial diameter of rod
d_p, d_s	diameter of rod penetrator and target plug
E_f	energy dissipated in the plug fracture process
L	initial length of rod
l_0, l, l_c, l_r	initial, intermediate, specific, and final rod lengths
M, M_p, M_r	initial, intermediate, and final masses of the rod
M_t, M_c, M_{cc}	intermediate target mass and target masses at beginning of target failure
P_s, P_0	penetration into a semiinfinite target and hydrodynamic penetration
S_p, S_t, S_s	strength of rod, target, and target (shear)
$T, T_L, \Delta T$	initial, ballistic limit, and excess target thicknesses
u_0, u, u_c	initial, intermediate, and critical rates of penetration
v_s, v_c, v_e, v_r	initial, critical, intermediate, and residual rod velocity
v_L	ballistic limit velocity
x_0	critical target thickness
z_0, z	initial and intermediate target thicknesses
z_c, z_{cc}	final target thicknesses (plugs) below and above critical thickness
$\alpha, \beta, \kappa, \lambda$	parameters associated with the analysis
ρ_p, ρ_t, γ	densities of rod and target and square root of density ratio

INTRODUCTION AND BACKGROUND

Ballistic limit velocity for long-rod penetrators has been used as a performance measure for both penetrator and target design. Further, the limit and residual rod features that appear behind plate targets at high impact velocity are part of the general penetration/perforation problem. For long rods,

most studies have been limited to impacts in the ordnance range of striking velocity. However, prospects for launching long rods at hypervelocity and use of explosively formed penetrators have created a need to develop analyses in a range significantly above ordnance velocities. The problem has interest since, at very high impact velocity, penetration is considered hydrodynamic so that only material densities are of primary importance, whereas, at ordnance velocity, material properties such as strength substantially influence penetration and ballistic limit behavior. Consequently, any analysis needs to address such material properties and changes in their influences as impact velocity is increased. Also, at the ballistic limit, even at very high impact velocity, processes of failure and fracture depend critically on various properties of the involved materials.

Several formulas exist for the ballistic limit of blunt fragments, short cylinders, and long rods. Of those based on dynamics, Recht and Ipson [1] provided velocity equations for fragments perforating thin and thick target plates and applied these to impacts for limit velocities through 2,300 m/s. In contrast, analyses for medium-length and long rods appear to have been established at a far lower velocity range. For example, Holt *et al.* [2] examined perforation of titanium alloy plates by nondeforming (rigid body) medium-length rods having striking velocities up to 350 m/s. In this work, however, mechanisms for plug failure and both experimental and analytical descriptions of the phenomena were examined. Also, Woodward and de Morton [3] investigated several rod types of medium length; but, again, the velocity range was limited. For long rods, Lambert [4] developed a semi-empirical formula for the ballistic limit velocity for relatively thick targets to include limit velocities up to 2,100 m/s. Of the two analyses that extend to high velocity [1, 4], one is limited to blunt fragments or short cylinders, while the other relates to long rods but is empirical.

While previously cited analyses [1, 4] include general notions of an energy balance at the ballistic limit, several important factors regarding events of the penetration process are unknown. For instance, Recht and Ipson [1] discuss neglected effects of projectile deformation and reduction in plug thickness (mass) as impact velocity is increased together with the need to include such in the analysis. Lambert [4] also pointed out that target mass in front of the penetrator decreases with increased striking velocity but, in lieu of an appropriate relation, assigned that mass to be a constant fraction of target mass based on plate thickness. It is to be noted that the distinction between thin and thick target cases with corresponding different formulas is made by Recht and Ipson [1] on the basis of whether or not the process of target perforation has been accompanied by any penetration into the target. Neither analysis considers rod or target strength, although dynamic shear of target material has been included to account for energy dissipated in the plugging process [1, 2]. Even with these limitations, the formulas have been widely used with success by the ballistics community.

THEORY OF PLATE PENETRATION/PERFORATION

In the theory of penetration dynamics by Grace [5], equations of motion relative to the rod/target interface have been provided for both rod and target masses undergoing simultaneous erosion and acceleration. Results of the dynamics are that both penetrator and target mass are reduced with increased striking velocity. Consequently, this analysis includes the desired reductions in target thickness and rod length as previously discussed [1, 4]. Figure 1a shows an intermediate time, t, in the penetration process [5]. It was assumed that the rod/target interface travels with constant velocity throughout the process at its initial rate, u_0, relative to the laboratory system of coordinates. At time, t, the rod tail has decelerated to velocity, v, from its initial striking velocity, v_s, while target mass in front of the penetrator accelerates from rest to a velocity, w. Noting that reduction rate, u, of the target's thickness is $u = u_0 - w$, then target thickness is reduced in time since $w < u_0$. According to the dynamics, momentum and energy continue to be delivered to the target up to the point when penetration stops (i.e., $u = 0$). At that point, target mass is accelerated to a velocity, u_0, while rod velocity is reduced to v_e. Also, at intermediate times, the rod is reduced to length, ℓ, while the target is reduced to thickness, z, and both are reduced to ℓ_c and z_c at the end of penetration from initial length and thickness, ℓ_0 and z_0, respectively, as shown in Fig. 1. In order for perforation to take
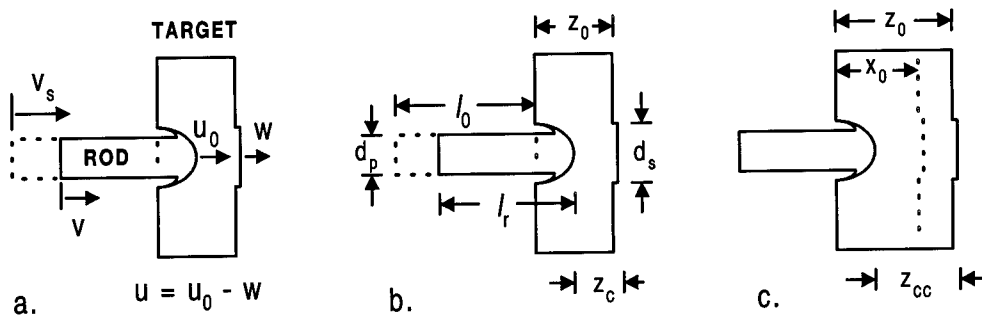
Fig. 1. Impact geometry illustrating (a) penetration variables and (b) target thicknesses below and (c) above the critical target thickness.

place, energy delivered to the target and remaining kinetic energy of the rod must overcome energy required to fracture the remaining target of thickness z_c. In Ref. [5], Grace uses Tate's [6] equation in modified form for rod deceleration, but introduces his own equation for target mass acceleration, based on Newton's law. Thus, target flow rate, u, is obtained without using the modified Bernoulli equation. The following system of equations governs penetration under conditions of rod and target erosion/flow and acceleration

<div align="center">

Rod   Target

</div>

Momentum:
$$M_p \frac{d(v - u_0)}{dt} = -A_p S_p \qquad M_t \frac{du}{dt} = -A_t S_t, \qquad (1)$$

Mass:
$$M_p = \rho_p A_p l \qquad\qquad M_t = \rho_t A_t z, \qquad (2)$$

Erosion/flow:
$$\frac{dl}{dt} = -(v - u_0) \qquad\qquad \frac{dz}{dt} = -u. \qquad (3)$$

Here, rod mass is M_p and target mass is M_t. Densities, designated ρ_p for the penetrator and ρ_t for the target, are assumed to be constant during impact and penetration at ordnance velocity and hypervelocity [7]. Material strength for the rod is S_p, and for the target is S_t.

The first integrals of motion for the system are obtained from Eqns. (1) through (3) for each material body as a function of length, l, for the rod and thickness, z, for the target. Respectively, solutions are

$$v - u_0 = (v_s - u_0) \sqrt{1 + \frac{2 S_p}{\rho_p (v_s - u_0)^2} \ln\left(\frac{l}{l_0}\right)}, \qquad (4)$$

and

$$u = u_0 \sqrt{1 + \frac{2 S_t}{\rho_t u_0^2} \ln\left(\frac{z}{z_0}\right)}. \qquad (5)$$

The initial penetration rate, u_0, was given as a function of rod striking velocity; rod and target material properties; a critical impact velocity, v_c, required to initiate penetration; and a critical

penetration rate, u_c, to initiate rod erosion [8]. With these notions, initial penetration rate, u_0, was given as

$$v_s \leq v_c: \qquad u_0 = 0$$

$$c_0 > v_s > v_c: \qquad u_0 = \frac{v_s}{1 + \gamma} - \frac{\cos Q}{1 + \gamma} \left(\sqrt{\frac{2 S_t}{\rho_p}} - 1.1 \, \gamma \sin Q \sqrt{\frac{2 S_p}{\rho_t}} \right) \qquad (6)$$

$$v_s \geq c_0: \qquad u_0 = \frac{v_s}{1 + \gamma},$$

where

$$\gamma = \sqrt{\frac{\rho_t}{\rho_p}}, \quad v_c = \sqrt{\frac{2 S_t}{\rho_p}}, \quad u_c = \sqrt{\frac{2 S_p}{\rho_t}}, \qquad v_s \geq v_c: \quad Q = \frac{\pi}{2} \left(\frac{v_s - v_c}{c_0 - v_c} \right), \qquad (7)$$

and c_0 is the speed of sound in the target material. The first term in Eqn. (6) is the hydrodynamic penetration rate [7], while the second and third terms subtract and add target and rod strength effects to that rate, respectively [8].

Equation (6) defines two different regimes for perforation of plate targets that are consistent with those of Recht and Ipson [1] (i.e., perforation with penetration, $u_0 > 0$, and perforation without any penetration, $u_0 = 0$). Perforation without penetration occurs when rod impact does not produce target flow (no penetration) but does create a plug whose length is the initial thickness of the plate. For thin plates where bending can occur at relatively low impact velocity, there may be no target flow (no penetration) under the nose of the rod, although the final plate thickness in the general area of impact can be reduced by stretching. The present work does not address these two examples but, rather, only cases where penetration is present. For the case of interest here, the bulge at the target's rear surface results from acceleration of the target mass in front of the rod during penetration.

Penetration/perforation was regarded as a two-stage process wherein rod and target lengths, masses, and velocities after penetration serve as inputs to target failure processes [5]. This notion is depicted in Fig. 1, which also includes attempted perforation of targets whose thickness exceeds a critical amount. The critical thickness, x_0, was defined in terms of the rod's semi-infinite penetration into similar material, P_s, where both are functions of striking velocity, v_s. Thus,

$$x_0 = \frac{P_s}{1 - \exp\left[-\frac{\rho_t}{2 S_t} u_0^2 \right]}. \qquad (8)$$

Both Eqns. (4) and (5) indicate that, for high striking velocity (large v_s and u_0), penetration is hydrodynamic with $v = v_s$ and $u = u_0$ throughout. For lower striking velocities, a solution for target thickness remaining after penetration was obtained from Eqn. (5) at the point at which penetration stops within the target (i.e., $u = 0$). Two possibilities, as noted in Fig. 1, depending upon whether the plate thickness, z_0, is greater or less than the critical target thickness, x_0, are

$$z_0 \leq x_0: \quad z_c = z_0 \exp\left[-\frac{\rho_t}{2 S_t} u_0^2 \right], \quad z_0 \geq x_0: \quad z_{cc} = x_0 \exp\left[-\frac{\rho_t}{2 S_t} u_0^2 \right] + \left(z_0 - x_0 \right). \qquad (9)$$

Equation (9) indicates that the target's initial thickness is not reduced completely during penetration. The exponential term tends toward zero at high impact velocity wherein target thickness is reduced

penetration rate, u_c, to initiate rod erosion [8]. With these notions, initial penetration rate, u_0, was given as

$$v_s \le v_c : \qquad u_0 = 0$$

$$c_0 > v_s > v_c : \qquad u_0 = \frac{v_s}{1+\gamma} - \frac{\cos Q}{1+\gamma}\left(\sqrt{\frac{2\,S_t}{\rho_p}} - 1.1\,\gamma \sin Q \sqrt{\frac{2\,S_p}{\rho_t}}\right) \qquad (6)$$

$$v_s \ge c_0 : \qquad u_0 = \frac{v_s}{1+\gamma},$$

where

$$\gamma = \sqrt{\frac{\rho_t}{\rho_p}}, \quad v_c = \sqrt{\frac{2\,S_t}{\rho_p}}, \quad u_c = \sqrt{\frac{2\,S_p}{\rho_t}}, \qquad v_s \ge v_c : \quad Q = \frac{\pi}{2}\left(\frac{v_s - v_c}{c_0 - v_c}\right), \qquad (7)$$

and c_0 is the speed of sound in the target material. The first term in Eqn. (6) is the hydrodynamic penetration rate [7], while the second and third terms subtract and add target and rod strength effects to that rate, respectively [8].

Equation (6) defines two different regimes for perforation of plate targets that are consistent with those of Recht and Ipson [1] (i.e., perforation with penetration, $u_0 > 0$, and perforation without any penetration, $u_0 = 0$). Perforation without penetration occurs when rod impact does not produce target flow (no penetration) but does create a plug whose length is the initial thickness of the plate. For thin plates where bending can occur at relatively low impact velocity, there may be no target flow (no penetration) under the nose of the rod, although the final plate thickness in the general area of impact can be reduced by stretching. The present work does not address these two examples but, rather, only cases where penetration is present. For the case of interest here, the bulge at the target's rear surface results from acceleration of the target mass in front of the rod during penetration.

Penetration/perforation was regarded as a two-stage process wherein rod and target lengths, masses, and velocities after penetration serve as inputs to target failure processes [5]. This notion is depicted in Fig. 1, which also includes attempted perforation of targets whose thickness exceeds a critical amount. The critical thickness, x_0, was defined in terms of the rod's semi-infinite penetration into similar material, P_s, where both are functions of striking velocity, v_s. Thus,

$$x_0 = \frac{P_s}{1 - \exp\left[-\dfrac{\rho_t}{2\,S_t}\,u_0^2\right]}. \qquad (8)$$

Both Eqns. (4) and (5) indicate that, for high striking velocity (large v_s and u_0), penetration is hydrodynamic with $v = v_s$ and $u = u_0$ throughout. For lower striking velocities, a solution for target thickness remaining after penetration was obtained from Eqn. (5) at the point at which penetration stops within the target (i.e., $u = 0$). Two possibilities, as noted in Fig. 1, depending upon whether the plate thickness, z_0, is greater or less than the critical target thickness, x_0, are

$$z_0 \le x_0 : \quad z_c = z_0 \exp\left[-\frac{\rho_t}{2\,S_t}\,u_0^2\right], \quad z_0 \ge x_0 : \quad z_{cc} = x_0 \exp\left[-\frac{\rho_t}{2\,S_t}\,u_0^2\right] + \left(z_0 - x_0\right). \qquad (9)$$

Equation (9) indicates that the target's initial thickness is not reduced completely during penetration. The exponential term tends toward zero at high impact velocity wherein target thickness is reduced

by penetration (z_c approaches zero for $z_0 < x_0$). At the other limit, when impact velocity is so low that $u_0 = 0$, the exponential term equals one. Thus, at very low impact velocity, no penetration occurs so that the target remains at its initial thickness, z_0. When the target fails by plugging, thickness z_c or z_{cc} is taken as the plug thickness to be sheared out of the target surrounds.

As a result of rod erosion, there are two rod lengths of interest. The first length, l_c, occurs when penetration ceases within the target ($u = 0$), while the second length, l_r, is the final rod length when rod erosion stops ($v - u_0 = 0$), from Eqn (4). These lengths were given previously [5] as

$$l_c = l_0 \exp\left[-\frac{\rho_t}{2\,S_t}\,u_0^2\right], \quad \text{and} \quad l_r = l_0 \exp\left[-\frac{\rho_p}{2\,S_p}\,(v_s - u_0)^2\right]. \tag{10}$$

An inelastic collision between the remaining rod and target (plug) masses gave an energy balance from which the velocity of the residual rod, v_r, was derived [5] as

$$v_r = \sqrt{\frac{M_r\,v_e^2 + M_c\,u_0^2 - 2\,E_f}{M_r + M_{cc}}} \tag{11}$$

where E_f is the energy required for plug fracture. For impacts at the ballistic limit condition, energy delivered may not necessarily be translated into kinetic energy of the target material, as included in Eqn. (11), for more than a momentary period since there is ultimately no motion behind the target. Nonetheless, the process must absorb significant amounts of energy to prevent breakout. A measure of the imparted energy is taken to be that acquired by the plug mass during the penetration process. In Eqn. (11), kinetic energy of the plug mass is based on z_c since $1/2 M_c u_0^2$ is the maximum energy attainable [5], while actual plug mass and thickness contributing to the energy of failure is based on z_c or z_{cc}, as indicated by Eqn. (9). Energy dissipated during plug failure, E_f, is that of Holt *et al.* [2] and Woodward and de Morton [3]. In current notation, E_f has two possibilities

$$z_0 \le x_0: \quad E_f = \frac{\pi}{2}\,d_s\,S_s\,z_c^2, \quad \text{and} \quad z_0 > x_0: \quad E_f = \frac{\pi}{2}\,d_s\,S_s\,z_{cc}^2, \tag{12}$$

where d_s is the diameter of an assumed cylindrical plug, S_s denotes shear strength of the target material, and either z_c or z_{cc} is the thickness to be sheared out of the target.

The ballistic limit velocity is defined as the condition where the residual rod velocity just equals zero. Using $v_r = 0$ in Eqn. (11) gives the condition to be met at the ballistic limit as

$$\frac{1}{2}\,M_r\,v_e^2 + \frac{1}{2}\,M_c\,u_0^2 - E_f = 0. \tag{13}$$

Equation (13) is evaluated by iteration using Eqns. (4) through (12) to give theoretical results for the ballistic limit velocity above the critical impact velocity after penetration into the target occurs.

ANALYTIC EXPRESSION FOR BALLISTIC LIMIT VELOCITY

The development of an analytical expression starts with Eqn. (13), with substitution of quantities for rod and target masses and velocities based on cited theory of the previous section. However, since the aforementioned theory does not have closed solutions, some simplifying expressions and empirical factors must be introduced. For masses having cylindrical shapes, Eqn. (13) becomes

$$\frac{\pi\,e}{4}\,\rho_p\,d_p^2\,l_c\,v_e^2 + \frac{\pi}{4\,k}\,\rho_t\,d_s^2\,z_c\,u_0^2 - \pi\,d_s\,S_s\,z_{cc}^2 = 0, \tag{14}$$

where d_p is rod diameter, and targets thicker and thinner than the critical one can be included in the E_f term. The thicker target case will be important at hypervelocity since the initial plate thickness,

z_0, is relatively large and can exceed the rod's hydrodynamic penetration capability. An empirical factor, k, is introduced to adjust the energy acquired by the target mass at the ballistic limit, as discussed previously. Further, a factor, e, to be discussed later, is included as the ratio of rod lengths, l_t/l_c, so that all exponentials are expressed in similar terms. Now, rod kinetic energy includes rod velocity, v_e, which according to the dynamics of Eqn. (4), decelerates toward u_0 as rod erosion approaches termination (i.e., $v - u_0 = 0$). Thus, $v_e = u_0$ will be used. Also, plug diameter and target shear strength are related to rod diameter as $\alpha = d_s/d_p$ and nominal strength as $\beta = S_s/S_t$, respectively. Initially, target thickness, z_{cc}, is used, but the result also suffices for z_c as well. Using Eqns. (9), (10), and (15) and $v_e = u_0$ in Eqn. (14) gives

$$k \frac{e}{\alpha^2 \gamma^2} \frac{l_0}{z_0} u_0^2 + u_0^2 - 4 k \frac{\beta}{\alpha} \frac{S_t}{\rho_t} \frac{z_{cc}^2}{d_p z_0} \exp\left[\frac{\rho_t}{2 S_t} u_0^2\right] = 0. \tag{15}$$

The exponential terms shown and that for z_{cc} are expanded in series, but only two terms are retained so that all u_0 terms in the expression are of second order. Inaccuracies that result are addressed later. Also, the hydrodynamic relation, $u_0 = v_L/(1 + \gamma)$, is used to express results in terms of the ballistic limit velocity, v_L, so that

$$\left[1 + k \frac{e}{\alpha^2 \gamma^2} \frac{l_0}{z_0} - 2 k \frac{\beta}{\alpha} \left(\frac{z_0 - 2 x_0}{d_p}\right)\right] \frac{v_L^2}{(1 + \gamma)^2} - 4 k \frac{\beta}{\alpha} \frac{S_t}{\rho_t} \frac{z_0}{d_p} = 0. \tag{16}$$

In Eqn. (16), the solution for E_f, when based on z_c, is obtained also when x_0 is replaced by z_0. Equation (8) indicates that critical target thickness, x_0, increases with striking velocity until the hydrodynamic limit is reached and, at that point, it becomes a maximum and is equal to the hydrodynamic penetration, p_0. So when $z_0 > p_0$, its equivalent, $z_0 > x_0$, represents the case of z_{cc} in Eqn. (16) and is associated with hypervelocity impact. The situation for lesser target thickness is not so clear, but the iterative solution based on the previous section indicates that $z_0 < x_0$. Thus, $z_0 < x_0$ is taken to represent the case of z_c in Eqn. (16) for the lower range of impact velocity (ordnance velocity).

For the z_c case, Eqn. (16) gives the proper trend only over a small range of target thickness beyond $z_0 = 0$. This response arises from the second and third terms within the bracket, which contains inverse and direct functions of z_0. Initially, at low values of z_0, the second term is relatively large but decreases with increased z_0, while the third is small but increases. Thus, initially, the bracketed term is a slowly varying function of z_0 so that v_L has a near square root dependence on z_0, as experience indicates it should. The limited range of z_0 results from the coefficients for these terms being too large. Thus corrections need to be introduced. To get an estimate for e, it is noted by Eqn. (6) that, at low impact velocity, u_0 is small relative to $v_s - u_0$, while the two tend toward each other at high impact velocity. This comparison means that l_t/l_c is small initially but increases with impact velocity. Now, for the z_c case, the limit thickness, z_0, is small at low impact velocity relative to p_0. So, e is structured to contain z_0/p_0 and strength effects as suggested by Eqn. (10). Thus,

$$e = \gamma \frac{S_p}{S_t} \frac{z_0}{l_0}, \tag{17}$$

where p_0 is related to initial rod length by $p_0 = l_0/\gamma$. When e is introduced into Eqn. (16), the second term of interest previously loses its dependance on z_0. Then, since the third term can no longer be offset by the second and a near square root dependance on z_0 is desired, the third term, which needed to be small, in any event, is now set to zero for the low impact velocity case.

Experience with Eqn. (16) at high impact velocity suggests that the factor of 2 that results from the exponential expansion and appears in the $(z_0 - 2 x_0)$ term is too large. Therefore, $2 x_0$ is

multiplied by an empirical parameter λ. When $\lambda = 1/2$, Eqn. (16) satisfies the previously discussed desire to eliminate the third term for the low impact velocity case. Now, p is used to represent either z_0, when $z_0 < x_0$, or p_0, when $z_0 > x_0$, in Eqn. (16). Further, k turned out to be close to the density ratio, so $k = \kappa \gamma^2$ was used. Finally, using these discussed notions, Eqn. (16) becomes

$$
\begin{array}{c} z_0 \le p_0, p = z_0: \\ z_0 > p_0, p = z_0: \end{array}
\left[1 + \kappa \frac{\gamma}{\alpha^2} \frac{S_p}{S_t} - 2 \kappa \gamma^2 \frac{\beta}{\alpha} \left(\frac{z_0 - 2 \lambda p}{d_p} \right) \right] \frac{v_L^2}{(1 + \gamma)^2} - 4 \kappa \frac{\beta}{\alpha} \frac{S_t}{\rho_p} \frac{z_0}{d_p} = 0. \quad (18)
$$

Introducing more traditional notation such as $T = z_0$, $D = d_p$, and $L = l_0$ and letting $P = p$ and $P_0 = p_0$ in Eqn. (18) provide an approximate solution for the ballistic limit velocity as

$$
\begin{array}{c} T \le P_0, P = T: \\ T > P_0, P = P_0: \end{array}
v_L = \sqrt{4 \kappa (1 + \gamma)^2 \frac{\beta}{\alpha} \frac{S_t}{\rho_p}} \left[\frac{\dfrac{T}{D}}{1 + \kappa \dfrac{\gamma}{\alpha^2} \dfrac{S_p}{S_t} - 2 \kappa \gamma^2 \dfrac{\beta}{\alpha} \left(\dfrac{T}{D} - 2 \lambda \dfrac{P}{D} \right)} \right]^{\frac{1}{2}}. \quad (19)
$$

The conditions on target thickness, T, in Eqn. (19) reflect the departure point where target thicknesses greater than P_0 exceed the critical target thickness. When $T > P_0$, the denominator of the second term becomes increasingly small with further increases in thickness, T, causing the limit velocity to approach extremely high values. It is in this regime of the phenomena that consequences of hypervelocity impact of long rods are demonstrated.

Limit thickness can be derived from Eqn. (19) by substituting limit thickness, T_L, for target thickness, T, and striking velocity, v_s, for limit velocity, v_L. The limit thickness has two solutions depending on whether $T_L \le P_0$ or $T_L > P_0$. These solutions are

$$
\begin{array}{c} T_L \le P_0, q = 1: \\ T_L > P_0, q = 0: \end{array}
T_L = \frac{1}{g^2} \left[\frac{\left(1 + \dfrac{\kappa \gamma}{\alpha^2} \dfrac{S_p}{S_t} \right) D + 4 q \kappa \gamma^2 \lambda \dfrac{\beta}{\alpha} P_0}{1 + 2 \dfrac{\kappa \gamma^2}{g^2} \dfrac{\beta}{\alpha} [1 - 2 \lambda (1 - q)] v_s^2} \right] v_s^2, \quad (20)
$$

where g is equal to the first term on the right hand side of Eqn. (19). In addition, for very thick targets $(T > P_0)$, Eqn. (19) or (20) can be used to estimate limit thickness, T_∞, for a given penetrator as its striking velocity approaches infinity. This condition occurs when the denominator of the second term in Eqn. (19) equals zero or at extreme striking velocity so that the factor of 1 in the denominator of Eqn. (20) can be neglected. Thus,

$$
T_\infty = 2 \lambda P_0 + \frac{1}{2 \beta} \left(\frac{\alpha}{\kappa \gamma^2} + \frac{1}{\alpha \gamma} \frac{S_p}{S_t} \right) D. \quad (21)
$$

From Eqn. (21), the ultimate excess thickness, ΔT_∞, beyond hydrodynamic penetration, P_0, is

$$
\Delta T_\infty = (2 \lambda - 1) P_0 + \frac{1}{2 \beta} \left(\frac{\alpha}{\kappa \gamma^2} + \frac{1}{\alpha \gamma} \frac{S_p}{S_t} \right) D. \quad (22)
$$

Since the ultimate excess thickness is that beyond P_0, then the coefficient associated with P_0 in Eqn. (22) might be expected to be zero. If so, then $\lambda_\infty = 1/2$, so that the ultimate excess thickness is a function of rod diameter only. This point lends additional impetus for examining $\lambda = 1/2$ as a starting point throughout the analysis. It is of interest to compare present results for the limit velocity with Lambert's expression, given as

Table 1. Material properties and geometries for penetrators and targets [9, 10, 11]

Material	Density (g/cm^3)	L/D	Length/Thickness (cm)	Diameters (cm)	Hardness (BHN)
Rod: C110W1 Steel	7.85	10	2.5, 4.3, 5.4	0.25, 0.43, 0.54	230
Rod: D17 WHA	17.0	10	2.8, 6.0	0.28, 0.60	294
Rod: X27 WHA	17.2	19.6	15.14, 19.07	0.773, 0.974	354
Target: St37/52 Steel	7.85	—	0.2 - 6.03	—	135, 180
Target: GerArmSt	7.85	—	0.64 - 4.15	—	426 - 298
Target: RHA	7.85	—	20.3 - 25.4	—	269

Table 2. Material properties and coefficients used in present calculations

Material Combination	Nominal strengths (GPa)	c_0 (m/s)	α	β	κ	λ
C110W1/St37/52	1.27/1.00	5,170	1.3	0.465	1.00	1/2
D17/GerArmSt	1.18/1.59 - 1.28	5,170	1.3	0.465	1.00	1/2
X27/RHA	1.29/0.993	5,170	1.3	0.465	1.00	1/2
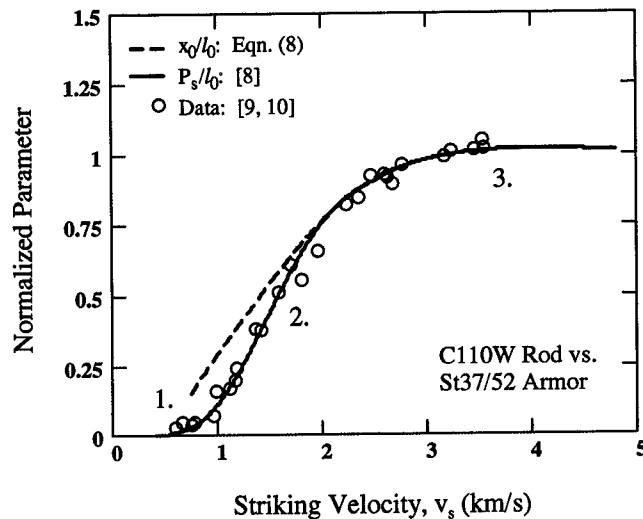
Fig. 2. Normalized semi-infinite penetration and critical thickness versus rod striking velocity.

presently when $\beta = 0.465$. The latter value can be compared to an inferred value of 0.356 from Holt et al. [2] for titanium alloy having an ultimate tensile strength (UTS) of 941 MPa, where it was believed that lower shear strength was due to thermal softening in localized shear zones during plugging. For German armor steel (GerArmSt), a linear decreasing strength beginning at 1.59 GPa for thin targets with a reduction to 1.28 GPa was used to represent strengths over the range of thickness indicated in Table 1.

Calculated results for rod-target combinations listed in Table 2 are shown in Figs. 3 and 4. As shown, the iterative solutions (dotted lines) of Eqn. (13) display trends of the experimental data for C110W1 rods against St37/52 steel targets and X27 rods against RHA. While data for D17 rods
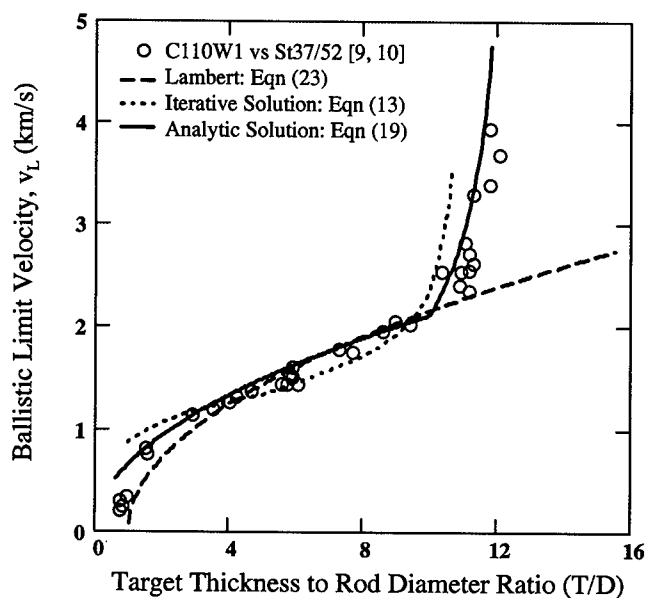
Fig. 3. Calculated and experimental ballistic limit velocity for steel rods striking steel targets.
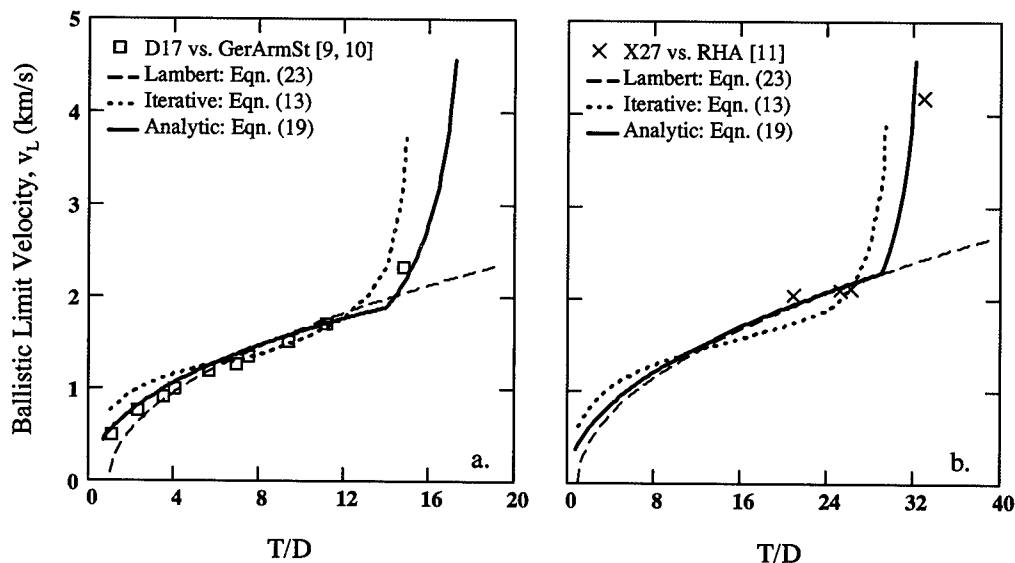
Fig. 4. Calculated and experimental ballistic limit velocity for tungsten alloy rods striking targets of (a) German armor steel and (b) RHA steel.

striking German armor steel is not extensive, the iterative solution agrees with data at ordnance velocities and suggests that the data point at 2,300 m/s in Fig. 4a might lie at the beginning of the hypervelocity impact range. The iterative solution predicts the observed transition in limit velocity with increased target thickness from ordnance velocity into hypervelocity range of impact.

Analytic results to include the present expression (solid lines) and that of Lambert (dashed lines) are also shown in Figs. 3 and 4. For calculations involving tungsten alloys, a value of a = 4,500 m/s was used in Lambert's equation. The present results of Eqn. (19), show reasonable agreement with experimental data over the entire range of target thicknesses for each rod/target combination. Equation (19) also displays the transition event as increased target thickness drives limit velocities

from the low slope portion of the curve just below the hypervelocity point of departure into the hypervelocity region. Lambert's expression of Eqn. (23) matches the data reasonably well for intermediate target thickness but is not designed to represent hypervelocity phenomena that occur for relatively thick targets. Results for ballistic limit thickness and excess target thickness that can be perforated as a function of striking velocity may be seen in Fig. 5. These calculations are obtained from differences between limit thicknesses of Eqn. (20) and a calculation of semi-infinite penetration as shown. Figure 5 also shows a nearly monotonic increase (ignoring the cusp due to the bifunctional relation for T_L) in excess thickness with striking velocity, starting at about 1/2 rod diameter at 500 m/s and increasing to about 1 3/4 rod diameters at 5,000 m/s. The ultimate excess thickness, ΔT_∞, is given by Eqn. (22) to be 2.45 rod diameters for these steel rods striking steel armor.
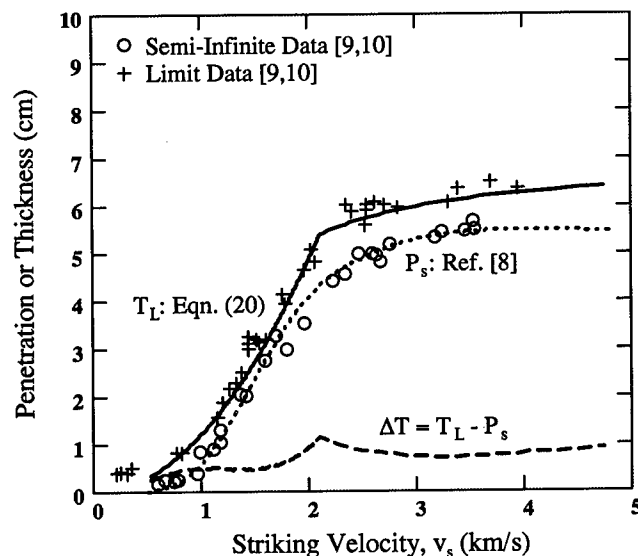
Fig. 5. Comparison of ballistic limit thickness, semi-infinite penetration, and excess target thickness for steel targets impacted by steel rods (L/D = 10, L = 5.4 cm).

DISCUSSION AND SUMMARY

The penetration dynamics for eroding rods striking targets of finite thickness, as described by the author previously [5], have been useful for determining ballistic limit velocities and limit thicknesses. It was found that thick and thin targets can be defined respectively in terms of whether or not any penetration takes place. When penetration occurs, the target's ability to withstand impact decreases since its initial thickness is reduced by penetration and less material is involved in the target failure process.

For a fixed penetrator, three different responses are seen for the limit velocity as target thickness is increased. These responses appear for small, intermediate, and very thick targets, and reflect the functional relationship for depth of penetration into semi-infinite targets as striking velocity is increased. The responses correlate with changes in the slope of the penetration curve as shown in Fig. 2 (regions labeled 1, 2, and 3). At the lower end of target thickness, striking velocity must be increased substantially as plate thickness is increased since penetration is not increasing much with increased impact velocity (region 1). For intermediate target thickness, small increases in thickness are more easily offset by increased penetration resulting from small increases in striking velocity. This response is related to the very steep slope of the penetration curve (region 2) and is responsible for the low slope regions of the data in Figs. 3 and 4. For thick targets, further increases in target

thickness are not offset by increased penetration since the limit of penetration is being reached (region 3). When the target thickness is increased beyond the rod's maximum penetration capability, the rod's energy is expended in obtaining this maximum, and little energy is available to perforate the excess thickness. Eventually, as thickness is increased still further, impact velocity would have to become infinite to reach the ballistic limit velocity (region 3).

There is a transition in the ballistic limit velocity as target thickness is increased beyond the rod's penetration capability. In the ordnance range of impact velocity, limit velocity appears to vary with the square root of target thickness. However, beyond the transition, and into hypervelocity impact, limit velocity increases dramatically with further increases in target thickness. While it has been known that long rods can perforate armor thicknesses that exceed their semi-infinite penetration capability, the present analysis quantifies this excess thickness.

The dynamics of penetration/perforation that contains a notion of critical target thickness appears to have captured some important physical phenomena related to the ballistic limit problem. Thus, results can be obtained for quantities such as limit velocity, limit thickness, and excess target thickness based on penetrator and target geometries and respective material properties. The analyses should further the ability to generate good engineering estimates of ballistic limit phenomena for long-rod penetrators from ordnance velocity through hypervelocity impact.

REFERENCES

1. R. F. Recht and T. W. Ipson, Ballistic perforation dynamics. *J. Appl. Mech. Trans. ASME* **30**, 384–390 (1963).
2. W. H. Holt, W. Mock, Jr., W. G. Soper, C. S. Coffrey, V. Ramachandran, and R. W. Armstrong, Reverse-ballistic impact study of shear plug formation and displacement in Ti6Al4V alloy. *J. Appl. Phys.*, **73**, 3753–3759 (1993).
3. R. L. Woodward and M. E. de Morton, Penetration of targets by flat-ended projectiles. *Int. J. Mech. Sci.*, **18**, 119–127 (1976).
4. J. P. Lambert, A residual velocity predictive model for long rod penetrators. ARBRL-MP- 02828, U.S. Army Ballistic Research Laboratory, Aberdeen Proving Ground, MD (1978).
5. F. I. Grace, Long-rod penetration into targets of finite thickness at normal impact. *Int. J. Impact Engng.*, **16**, 419–433 (1995).
6. A. Tate, A theory for the deceleration of long rods after impact. *J. Mech. Phys. Solids*, **15**, 387–399 (1967).
7. G. Birkhoff, D. P. MacDougall, E. M. Pugh, and G. Taylor, Explosives with lined cavities. *J. Appl. Phys.*, **19**, 563–582 (1948).
8. F. I. Grace, Nonsteady penetration of long rods into semi-infinite targets. *Int. J. Impact Engng.*, **14**, 303–314 (1993).
9. V. Hohler and A. Stilp, Hypervelocity impact of rod projectiles with L/D from 1 to 32. *Int. J. Impact Engng.*, **5**, 323–331 (1987).
10. C. E. Anderson, Jr., B. L. Morris, and D. L. Littlefield, A penetration mechanics database. SwRI Report 3593/001, Southwest Research Institute, San Antonio, TX (1992).
11. G. Silsby, unpublished data. U.S. Army Research Laboratory, Aberdeen Proving Ground, MD (1997).

IMPACT FAILURE AND FRAGMENTATION PROPERTIES OF TUNGSTEN CARBIDE

DENNIS GRADY

Applied Research Associates, Inc., 4300 San Mateo Blvd. NE, Suite A-220, Albuquerque, NM, 87110, USA,
phn 505-883-3636, fax 505-872-0794, email dgrady@swd.ara.com

Summary — Samples of a liquid-phase sintered tungsten carbide were prepared in the form of solid spheres and launched with a light-gas gun facility to impact velocities ranging over about 2-4 km/s. Spherical samples were caused to impact thin plates of low density non-metallic material (fused silica glass and PMMA plastic in the present tests) and undergo failure and dynamic fragmentation due to the impulsive load. Impulse intensities led to incipient failure at the lowest impact velocities to extremely intense particulation and debris dispersion at the highest impact velocities. Flash radiography was used to image the failed specimens in flight at several stations. Only the ceramic debris was imaged in the radiographs because of the low density of the impact plate materials. From the onset and extent of fragmentation and the velocities of debris dispersion, failure and fragmentation properties of the test ceramic were inferred. Supporting shock Hugoniot and tensile spall data were also acquired on the same tungsten carbide material, providing a broad base of dynamic properties data for analysis purposes on this solid (Grady [1]). Results of the dynamic tests and material properties acquired on the present tungsten carbide ceramic are presented in this report. © 1999 Elsevier Science Ltd. All rights reserved.

INTRODUCTION

Dynamic failure of solids and the subsequent treatment of failed material in the computational simulation of the high velocity interaction of structures is probably the most poorly modeled material response in such events. Tungsten carbide is a high-density ceramic used in both military projectile and armor applications. In this report, we present data for the purposes of examining the mechanisms of dynamic failure in tungsten carbide ceramic and deriving material response properties appropriate to computational models. The sphere impact method previously pursued on metals (Grady and Kipp [2]) was used to perform a series of dynamic failure tests on tungsten carbide from near-threshold failure to very intense fragmentation. In addition, complementary dynamic compression (shock equation-of-state and Hugoniot elastic limit) and dynamic tension (spall) experiments were performed to provide necessary material response data. Those principally experimental results are described and used to examine features of the sphere-impact test method and a theory of dynamic failure and fragmentation in solids.

Test Method and Material Characterization

Materials. The principal material tested in the present study was a pressureless liquid-phase sintering tungsten carbide (WC) ceramic extracted from 14.5 mm AP (BS-41) rounds. The material contains 3-4% Ni, 0.4-0.8% Fe and 0.05-0.2% Co. The Rockwell-A hardness is 86-92. Static compressive strength for this material is 4.4 GPa and split cylinder test results provided a tensile strength of 240-270 MPa (Holmquist [3]).

Because of the very small sample sizes that could be prepared from the BS-41 round tungsten carbide for equation-of-state (EOS) studies, a second comparable tungsten carbide ceramic was selected to supplement the testing. The second material was a fully dense tungsten carbide provided by Kennametal, Inc. The Kennametal tungsten carbide contains 5.7% Co, 1.9% Ta, and less than 0.3% Nb and Ti. The reported Rockwell-A hardness is 93, and the static compressive strength is 5.9 GPa. Density and elastic properties for the two ceramics are provided in Table 1 and compared with a fully dense monolithic WC prepared by Cercom.

Table 1. Elastic properties of tungsten carbide

Material	Density (kg/m^3)	c_l (km/s)	c_s (km/s)	c_o (km/s)	Bulk Modulus (GPa)	Poisson's Ratio
KM[1]	14930	6.895	4.165	4.941	364.5	0.213
AP[1]	14910	6.918	4.149	4.991	371.4	0.219
Cercom[2]	15560	7.040	4.300	4.960	383.0	0.200

[1]KM refers to the K68 material obtained from Kennametal, Inc., whereas AP identifies the tungsten carbide extracted from 14.5 mm (BS-41) armor piercing rounds.

[2]A fully dense monolithic tungsten carbide prepared by Cercom, Inc.

Equation-of-State and Dynamic Strength Tests. Uniaxial strain compressive shock and release waves were produced in the tungsten carbide with a single stage powder gun facility (Grady [4]). The gun used for these experiments has an 89 mm bore diameter and is capable of achieving a maximum impact velocity of 2.5 km/s. A disc of impactor material (either tungsten carbide or aluminum in the present tests) is mounted in the projectile and is backed by a disc of polymethyl-methacrylate (PMMA). An aluminum ring encloses the ceramic disc and provides a coplanar impact surface for electrically shorting the various diagnostic pins.

For the target, a disc of the ceramic is mounted in a stationary supporting target fixture. An optical quality disc of single crystal lithium fluoride is intimately bonded with epoxy to the back of this ceramic sample. All critical surfaces are lapped and polished, and are typically flat to within a few bands of sodium light. The bonded lithium fluoride surface is first lightly diffused and vapor-deposited with about 100 nm of aluminum. The ceramic-lithium fluoride epoxy bond thickness is approximately 10 to 20 μm.

The planar impact produces a compressive wave of uniaxial strain which propagates across the stationary ceramic specimen and through the ceramic-lithium fluoride interface. The compression and release wave behavior is measured by monitoring the time-resolved longitudinal motion at the center of the ceramic and lithium fluoride interface with laser velocity interferometry (VISAR) techniques (Barker and Hollenbach [5]). Measurements are recorded on transient digitizers with a sampling period of 0.742 ns per data point.

The interference fringes measured with the VISAR system are converted to a time-resolved history of the velocity at the interface. The amplitude resolution is approximately 2% per fringe and typically two to three fringes are achieved in the interface acceleration through the compressive shock front.

Sphere Impact Test Method. The experimental configuration for investigating the fragmentation properties of solids has been reported by Grady and Kipp [2]. Briefly, spheres of the test material, mounted in lexan sabots, were launched at velocities between about 2 to 4 km/s with a two-stage light-gas gun system. The diameter of the launch tube used was 12 mm. Plastic sabots were separated from the ceramic spheres through forces produced by a rarified atmosphere in the gun range section. Sabot segments were trapped upstream and did not reach the target impact chamber. Velocity of the sample spheres was measured to ±1% accuracy by recording of the time interval during passage between two magnetic coils of known separation. Normal impact occurred in the target chamber at the center of a 75 mm by 75 mm square thin

target plate. Target plates were of both plastic and glass. The plastic was PMMA Rohm and Haas Type II UVA, and had a nominal density of 1186 kg/m^3. GE dynasil 1000 with a density of 2201 kg/m^3 provided the higher impedance glass targets. In this series of experiments, tungsten carbide spheres 6.45 ±0.03 mm in diameter were used. The measured mass was 2.07 ±0.01 grams. Fragment debris was diagnosed at two stations (approximately 80 mm and 250 mm) downstream from the input point. Two 150 kev flash x-ray tubes, placed approximately 400 mm from the line of debris travel, provided orthogonal shadow-graphs of the fragment debris. Appropriate delay times were calculated from the predicted impact velocity and the x-ray tubes were independently triggered from the second magnetic velocity coil. The x-ray film cassette, using Kodak Direct Exposure film backed by a Quanta Fast Detail screen, was stationed about 100 mm from the centerline of the debris trajectory. The fragment debris impacted aluminum witness plates, which in some cases provided an independent measure of particle size and velocity statistics (Kipp et al. [6]).

Hugoniot Properties

Hugoniot states for the present tungsten carbides were determined assuming a precursor velocity equal to the longitudinal ultrasonic elastic velocity of 6.90 km/s (Table 1). Hugoniot states are shown in a shock velocity versus particle velocity plot in Fig. 1 and compared with the data of McQueen et al. [7, 8]. The two higher amplitude states (KM material) are in reasonable agreement with the data of McQueen. The relatively broad shock wave for the lowest amplitude test (AP material) lends some ambiguity to the experimental shock velocity at this amplitude. Nevertheless, this data point cannot be fully reconciled with the measurements of McQueen, although the trend of the lower three or four data points of McQueen tend to fall above the linear shock velocity versus particle velocity expression for tungsten carbide (Steinberg [9]).
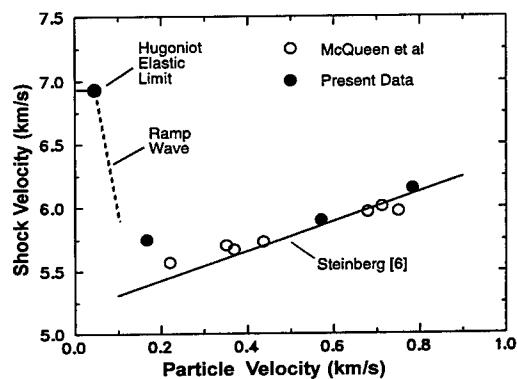
Fig. 1. Shock velocity versus particle velocity data for tungsten carbide, including precursor elastic limit and ramp wave region.
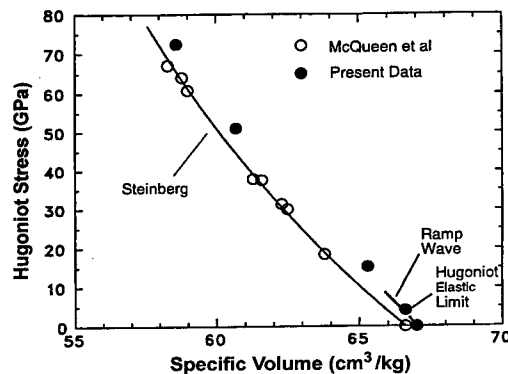
Fig. 2. Hugoniot stress versus specific volume for tungsten carbide.

Precursor Hugoniot elastic limit states and ramp region for these data are also indicated in Fig. 1. Corresponding Hugoniot pressure versus specific volume states for the present tungsten carbide ceramics are provided in Fig. 2.

The tungsten carbide tested by McQueen and coworkers was also approximately 5% cobalt by weight, comparable to the Kennametal material; however, the reported density of 15,013 kg/m^3 is about 1/2% higher than the present Kennametal material. This density difference accounts for about half of the discrepancy between the McQueen and coworkers Hugoniot and the present Hugoniot data in Fig. 2. Since the present Hugoniot states were calculated based on an ultrasonic velocity for the elastic precursor (a lower limit), it appears that the present

Hugoniot is slightly stiffer than that reported by McQueen and coworkers. More recent unpublished Hugoniot data (Grady [10]) for the Cercom WC is only slightly stiffer than that reported by McQueen and coworkers.

Dynamic Strength

The 6.5 mm thickness Kennametal tungsten carbide samples reveal in Fig. 3 a fairly distinct transition from the elastic precursor rise to the transition ramp region at approximately 70 m/s. Based on an acoustic impedance calculation, this leads to a Hugoniot elastic limit of 4.1 GPa. The thinner AP samples tested did not provide as distinct a transition level; however, a yield at about 70 m/s was not inconsistent with the behavior of this material, and indicates similar yield characteristics for both materials.

Material behavior within the transition ramp regime was analyzed in two ways. First, computational simulations of the precursor and transition ramp portions of the wave profile were performed using the one-dimensional Lagrangian wave code WONDY-IV (Kipp and Lawrence [11]). With this technique, empirical parameters for the longitudinal modulus as a function of amplitude were adjusted until a best fit to the wave profile in the region of interest was achieved. The stress-strain relation derived from this fit was then accepted as the dynamic response of the tungsten carbide. The experimental profiles are shown with the one-dimensional wave code solution in Fig. 3. An analytic solution was also performed assuming a linear rising velocity versus time behavior within the region of the ramp (Fig. 3) along with centered self-similar wave propagation.

Results of the stress-versus-strain behavior within the ramp region determined from both the computational simulation and the analytic solution for the axial behavior are provided in Fig. 4. Comparisons are made with linear mean stress curve calculated from the ultrasonic bulk modulus and corresponding responses based on ideal elastic-plastic behavior.

If there is onset of an inelastic deformation mechanism at the 4 GPa break in the measured wave profile in tungsten carbide, as common understanding of the process tends to support, then the ramp structure in the profile cannot be described with simple von Mises plasticity as indicated in Fig. 4. Several hardening mechanisms may potentially explain the observed
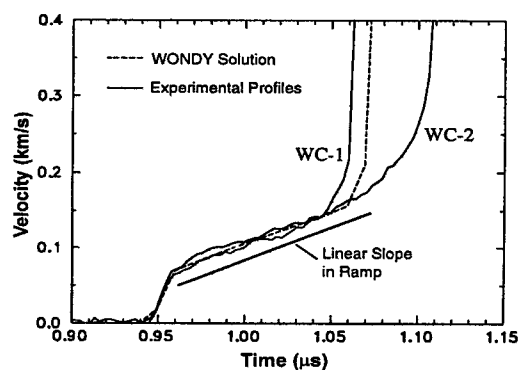
Fig. 3. Compression shock profiles and WONDY computational solution emphasizing the ramp region of the elastic precursor.
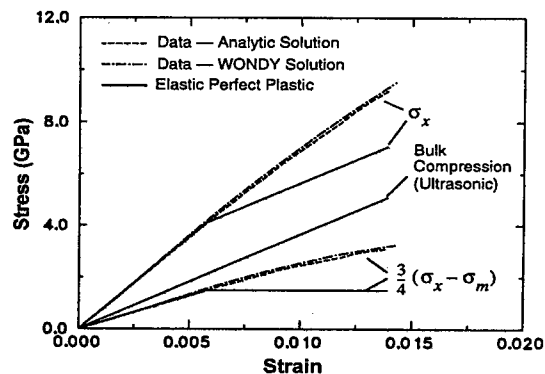
Fig. 4. Stress versus strain behavior in ramp region of the wave profile.

behavior. The elastic loading path could contact a pressure-hardening yield surface at the Hugoniot elastic limit (HEL). Subsequent loading would lead to increased stress rise due to the increasing shear stress with confining pressure on the pressure-hardening yield surface.

Alternatively, the HEL may correspond to the intersection of the elastic loading path with a deformation-hardening yield surface. Due to post-yield deformation in the shock wave, the initial yield surface would evolve through a succession of states to a final yield surface consistent with later states in the ramp wave. Evolution of the yield surface would be determined by a deformation-hardening law and could account for the ramp behavior characteristic of the early inelastic deformation.

There is a further, less commonly considered mechanism for hardening which could account for the observed wave profile structure. Rather than an increase in the stress deviator with inelastic deformation, an increase in the mean stress state above that predicted by compressibility of the fully dense solid could account for the observed behavior. Such an elevated mean stress versus volume curve is possible if dilatant void volume is generated during the shear deformation process.

Of course, all three of the hardening mechanisms proposed could be operating collectively, and rate dependence of these effects may also be playing a role. Of the three hardening mechanisms, pressure hardening is the most difficult to reconcile with the second order character of the elastic-to-inelastic deformation transition. (The transition to a ramp wave represents a discontinuous jump in the curvature of the stress-versus-strain curve and not the slope.) In principal, deformation hardening or dilatancy hardening laws could be constructed which could simulate the observed transition to ramp wave structure.

Spall Strength

In experiments designed to test spall stress of the tungsten carbide, ceramic release waves originating from the rear of the aluminum impactor and from the lithium fluoride window interface interact within the tungsten carbide samples carrying the material rapidly into tension. The dynamic tensile strength (spall strength) of tungsten carbide was exceeded in the present tests and the time history of the spall process was imaged in the measured spall pullback signal within the velocity profile recorded at the window interface. Interface velocity profiles for three tests in which spall occurred, are shown in Fig. 5.

The spall strength of tungsten carbide can be calculated from the spall pullback signal identified in Fig. 5. The present data provide an opportunity to compare two methods for determining the spall strength when an interferometer window is used. The appropriate velocity levels are identified for Test WC-6 in Fig. 5 for the spall analysis. First, if the full amplitude of the pullback is used, then the appropriate relation for the spall strength is,

$$\sigma_{sp} = \frac{1}{2}(Z_s + Z_w)(u_{max} - u_{min}) - Z_w u_{max}.$$ (1)

In Eqn. (1), Z_s and Z_w are the shock impedance of the sample material and window material, respectively. This equation assumes linear behavior of stress-strain response of the sample and window material, and ignores the complications of corrections for wave dispersion and elastic-plastic behavior which have been discussed in the literature (e.g., Grady and Kipp [12]). The down side of Eqn. (1) is that it can be a difference of two large quantities, each of which may have uncertainties. This is not a serious problem with the present data, however.

An alternative expression for the spall stress is provided by the relation,

$$\sigma_{sp} = \frac{1}{2}(Z_s + Z_w)(u_o - u_{min})$$ (2)
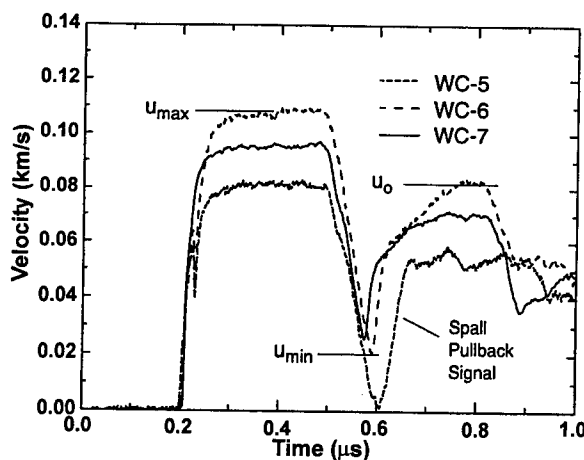
Fig. 5. Wave profiles emphasizing spall pullback signals in tungsten carbide.

Equation (2) does not suffer from the differencing problem of Eqn. (1). On the other hand, it assumes that stress at the spall plane has relaxed to zero before the reflected wave has returned to the recording interface. This depends on experiment design and the time history of the spall process, but often this relaxation is not complete and the spall strength calculated from Eqn. (2) is a lower bound. With the present data, spall strengths have been calculated with both Eqn. (1) and Eqn. (2). Results are plotted in Fig. 6.

Sphere Impact Fragmentation

Testing of the failure and fragmentation properties of tungsten carbide extracted from 14.5 mm armor piercing (AP) rounds was performed using the sphere impact test method described in the test method section. Pertinent experimental parameters are provided in Table 2. Impact velocities ranged from a little over 2 km/s to about 4 km/s. Target barrier materials of both plastic and glass were used. Targets were squares 3 inches on a side and 1/8-inch thick. Aluminum witness plates 1-foot square and 1/4-inch thick were placed 295 mm downstream from the target plate. Residual velocity of the tungsten carbide fragment debris provided in Table 2 was determined from radiographs at each test. Radial expansion velocity of the packet of fragments was determined from both radiographs and the size of the witness plate hole. Values provided by both methods in Table 2 are in reasonable agreement.
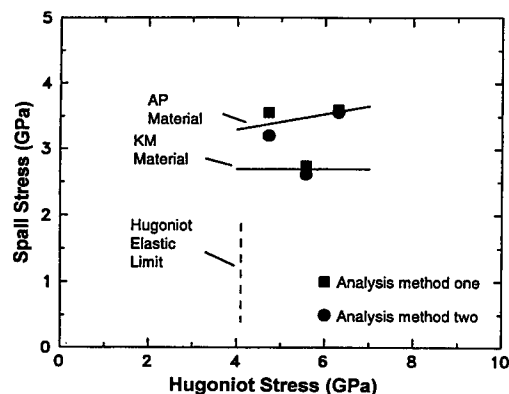
Fig. 6. Spall strengths determined from the present tests on tungsten carbide.

Radiographic records for seven of the eight tests are provided in Figs. 7 and 8. Records provide a shadow graph of the fragment debris at two stations downstream from the impact point. Timing for each x-ray image after impact is provided in Table 2.

Table 2. Tungsten carbide sphere impact tests

Test No.	Barrier Material	Impact Velocity (km/s)	Residual Velocity (km/s)	Expansion Velocity (x-ray) (m/s)	Expansion Velocity (W.P.) (m/s)	Witness Plate[4] Hole Size (mm)	X-Ray #1 Time (μs)	X-Ray #2 Time (μs)
1	Plastic[1]	2.44	2.35	0	—	8	27.7	97.3
2	Plastic[1]	2.90	2.79	21	24	11	26.5	85.6
3	Plastic[1]	3.43	3.30	50	62	17	21.2	71.4
4	Glass[2]	2.13	1.94	76	80	30	28.2	113.3
5	Glass[2]	2.70	2.47	137	142	40	27.1	87.0
6	Glass[2]	3.09	—[3]	—[3]	157	39	—	—
7	Glass[2]	3.55	3.30	185	190	40	20.9	70.8
8	Glass[2]	4.05	3.73	261	259	47	17.7	64.6

[1]Polymethyl-Methacrylate (PMMA), 3.12 mm.
[2]Fused Silica (GE Dynasil 1000), 3.12 mm.
[3]X-rays failed on Test #6.
[4]Separation of target and witness plate was 295 mm.

Radiographs for three normal impacts on PMMA barriers are provided in Fig. 7. These data have previously been examined by computational simulation (Hertel and Grady [13]). At the lowest impact velocity, the impulsive load is just sufficient to spall segments off both the front and back of the test sphere. The major central segment remains intact. At higher impact velocities, the spherical samples of tungsten carbide are fully fragmented and the packet of debris is expanding as it travels away from the point of impact. Radial expansion of the debris tends to be somewhat faster toward the back of the sample.

Test 1 (2.44 km/s)

Test 2 (2.90 km/s)

Test 3 (3.43 km/s)

Fig. 7. Radiographs for three tests of tungsten carbide spheres undergoing high-velocity normal impact on plates of PMMA plastic.

Test 4 (2.3 km/s)

Test 5 (2.70 km/s)

Test 7 (3.55 km/s)

Test 8 (4.05 km/s)

Fig. 8. Radiographs for four tests of tungsten carbide spheres undergoing high-velocity normal impact on plates of glass.

Comparable impact fragmentation experiments on glass barriers are shown in Fig. 8. Some interesting differences are observed. The two lower impact velocity tests show similar features with the sphere separating axially into two reasonably distinct regions. The forward section suggests relatively large fragments undergoing little radial expansion. The rearward section indicates more intense fragmentation and radial kinetic energy. The separation into a front and back cloud of fragments continues to be suggested in the two higher impact velocity tests on glass in Fig. 8. The samples are fully fragmented, however, and only slight differences in the expansion kinetics at the front and back regions are noted.

In earlier, similar fragmentation studies on metals, the radial expansion velocity of the packet of fragment debris was found to be a useful interpretive experimental observable. The radial expansion velocity was readily normalized to the impact shock pressure where different barrier materials were used (Grady and Kipp [2]). This convenient normalization of the data does not appear to hold for the present tungsten carbide experiments. Radial expansion velocity is plotted as a function of impact velocity in Fig. 9. As expected, glass barriers at similar impact velocities lead to more intense fragmentation and higher debris expansion velocities than do plastic barriers

because of the higher shock impedance of the former material. Some scatter in the measurement of impact velocity is suspected considering the reasonably close comparison of expansion velocity determined by x-ray and by witness plate hole diameter.
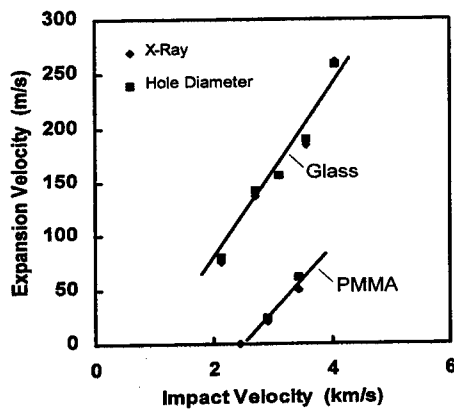
Fig. 9. Expansion velocity versus impact velocity for tungsten carbide
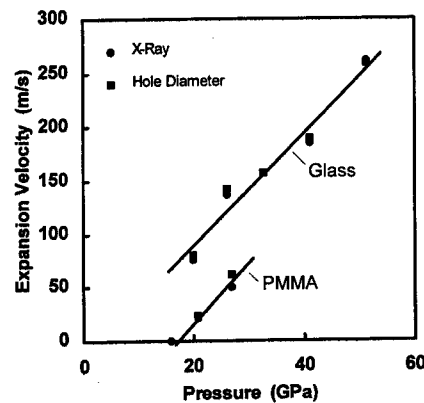
Fig. 10. Expansion velocity versus impact shock pressure for tungsten carbide

Expansion velocity versus impact shock pressure determined by impedance match solutions between the tungsten carbide and barrier material for the same data are plotted in Fig. 10. Linear shock-velocity-versus-particle-velocity parameters for the participating materials are provided in Table 3. In contrast to previous experience with metals (Grady and Kipp [2]), impact pressure apparently does not normalize the expansion velocity data. It is unfortunate that overlap of the data for the two barrier materials occurs only at the lower end of the glass barrier experiments. The trend for the two tests in this lower range is for the expansion velocity to emphasize the radial motion of fragment debris from the rearward end of the sphere. Thus, the expansion velocity may not adequately characterize the overall radial kinetic energy of the sample. The glass data are particularly suspicious in that a linear extrapolation to zero expansion velocity indicate a negligible threshhold pressure. Clearly, radial expansion velocity in the present tungsten carbide fragmentation tests is more sensitive to details of the impact interaction than in previous metal tests (Grady and Kipp [2]). Consequently, it may be less useful as an experimental observable in the sense of previous attempts to extract global material failure properties.

Table 3. Shock parameters

Material	ρ_o kg/m³	C_o km/s	S
WC	14930	5.19	1.16
PMMA	1190	2.60	1.52
FS	2220	1.18	1.58

Discussion

The rather complete set of dynamic data for tungsten carbide ceramic presented here provides a unique opportunity for examining some of the factors governing impact failure and fragmentation of this material. Particularly intriguing are comparisons of the spall failure data from the plate impact experiments and the sphere impact fragmentation results. An energy-based theory has previously been proposed which provides predictive expressions for spall strength and fragment size (Grady [14]). They can be written, respectively, as

$$\sigma_s = \left(3\rho c K^2 \dot{\varepsilon}\right)^{1/3},$$	(3)

$$s_f = \left(\sqrt{24} K / \rho c \dot{\varepsilon}\right)^{2/3},$$	(4)

Parameters $\rho, c,$ and $\dot{\varepsilon}$ are the material density, wave speed, and the loading strain rate, respectively. The property K with dimensions of fracture toughness characterizes the dynamic fracture and fragmentation resistance of the material. In principle, K is the same fracture toughness relating spall strength and fragment size through the expressions above.

This correspondence can be tested for the present tungsten carbide. Equations (3) and (4) will be written as,

$$K_s = \left(\frac{\sigma_s^3}{3\rho c \dot{\varepsilon}}\right)^{1/2},$$	(5)

$$K_f = \frac{\rho c \dot{\varepsilon} \, s_f^{3/2}}{\sqrt{24}},$$	(6)

where the subscripted K_s and K_f correspond to the fracture resistance property determined empirically from the spall data and the fragment size data, respectively. Based on a spall strength of 3.5 GPa for the AP material and an estimated strain rate of 10^5/s, a resistance of $K_s = 37$ MPa·m$^{1/2}$ is obtained from Eqn. (5). The value is comparable to numerous metals and is not unexpected considering the liquid-phase sintered nature of this material. On the other hand, estimates of fragment size and fragmentation strain rates from the sphere impact data, and through the use of Eqn. (6), lead to a $K_f = 3$-5 MPa·m$^{1/2}$, nearly an order of magnitude lower. The value is more consistent with fracture resistance characteristics observed on other engineering ceramics. Static fracture toughness data for the present materials were not found. A monolithic WC prepared by CERCOM exhibits a toughness of about 6-7 MPa·m$^{1/2}$.

Reasons for the discrepancy are not understood, but tungsten carbide may be a material where conditions necessary for energy-limited spall and fragmentation are not met (Grady [14]). Limited spall nucleation sites may lead to a large level of tensile elastic strain energy before activation and spall failure. In contrast, later time growth and coallescense leading to fragmentation may experience significantly lower fracture resistance, leading to crack branching and the smaller fragment size. Such dependence of fracture and fragmentation on details of the microstructure would negate applicability of the energy-based expressions for this material.

CONCLUSIONS

The first failure and fragmentation data on a ceramic material using the sphere impact technique have been performed and presented here. These data are nicely complemented by both dynamic compression (Hugoniot elastic limit and shock EOS) and dynamic tension (spall) test data. These new data have raised both experimental and theoretical concerns. Normalization simplifications readily achieved for test data on metals using the sphere impact method are not realized for the present material and test conditions. A dynamic theory of failure which relates spall strength and the characteristic size of fragments has not been supported by the present data.

REFERENCES

1. Grady, D.E., *Dynamic Properties of Ceramic Materials*, Sandia National Laboratories Technical Report, SAND94-3266, February 1995.
2. Grady, D.E. and M.E. Kipp, *Experimental Measurement of Dynamic Failure and Fragmentation Properties of Metals*, Int. J. Solids and Structures, 20, pp. 293-308, 1997.
3. Holmquist, T.J., *Tungsten Carbide Quasistatic Strength*, Unpublished Technical Correspondence, June, 1994.
4. Grady, D.E., *Shock Compression Properties of Ceramics*, in High Pressure Research, A.K. Singh, ed., Oxford and IBH Publishing, pp. 641-650, 1992.
5. Barker, L.M., and R.E. Hollenbach, *Laser interferometer for measuring velocities of any reflecting surface*, J. Appl. Phys. 43, 4669, 1972.
6. Kipp, M.E., D.E. Grady, and J.W. Swegle, *Experimental and Numerical Studies of High-Velocity Impact Fragmentation*, Sandia National Laboratories Technical Report, SAND93-0773, August 1993.
7. McQueen, R.G., *The equation of state of mixtures, alloys, and compounds, in seismic coupling*, G. Simmons, ed., Proceedings of a meeting sponsored by the Advanced Research Projects Agency at Stanford Research Insititute, Menlo Park, California, January 15-16, 1968.
8. McQueen, R.G., S.P. Marsh, J. W. Taylor, J.N. Fritz, W.J. Carter, *The equation of state of solids from shock wave studies*, in High-Velocity Impact Phenomena, R. Kinslow, ed., Academic Press, pp. 293-417 and 521-568, 1970.
9. Steinberg, D.J., *Equation of state and strength properties of selected materials*, Lawrence Livermore National Laboratories Report, UCRL-MA-106439, 1991.
10. Grady, D.E., Unpublished Technical Memorandum, 1996.
11. Kipp, M.E. and R.J. Lawrence, Sandia National Laboratories Technical Memorandum, SAND81-0930, July 1982.
12. Grady, D.E. and M.E. Kipp, *Dynamic fracture and fragmentation*, in High-Pressure Shock Compression of Solids, J.R. Asay and M. Shahinpoor, eds., Springer Vergal, pp. 285-322, 1993.
13. Hertel, E.S., Jr., and D.E. Grady, *Tungsten Carbide Fragmentation: Experimental Characterization and Numerical Modeling*, Proceedings of the International Symposium on Ballistics, Jerusalem, Israel, May 21-24, 1995.
14. Grady, D.E., *The Spall Strength of Condensed Matter*, J. Mech. Phys. Solids, 36, pp. 353-384, 1988.

NATURAL AND SIMULATED HYPERVELOCITY IMPACTS INTO SOLAR CELLS.

G.A.Graham[*,***], A.T.Kearsley[**], M.M.Grady[***], I.P.Wright[*],
M.K.Herbert[****], and J.A.M.McDonnell[****].

[*]Planetary Sciences Research Institute, The Open University, Walton Hall, Milton Keynes MK7 6AA, U.K.,
[**]Geology, Oxford Brookes University, Headington, Oxford OX3 7AB, U.K., [***]Mineralogy Department, The
Natural History Museum, Cromwell Road, London SW7 5BD, U.K., [****]Unit For Space Sciences and Astrophysics,
The University Of Kent at Canterbury, Canterbury CT2 7NR, U.K.

Summary-The solar array which was returned to Earth from the Hubble Space Telescope (HST) in 1993, after 3.62 years of space exposure in low Earth orbit (LEO), has offered the opportunity to document populations of natural micrometeoroids and artificial "space debris". Residues from the hypervelocity impact (HVI) of material deposited in 25 individual solar cells from the array have been investigated herein by scanning electron microscopy. The observations have been compared with the results of simulated HVIs into solar cells using known meteorite mineralogies. This has permitted assessment of the probability of retention for residue materials derived from HVI by well-characterised mineral species. The simulation experiments have thus far suggested that some of the textural features observed in impact residues are dependent on the nature of the individual mineral components within the original impactor. Furthermore it transpires that compounds containing volatile elements, such as Ca (from calcium carbonate), can be preserved as near-intact fragments explosively emplaced in an impact crater. Such unusual particles should not always be dismissed as simply contamination products if observed in LEO-derived HVIs. © 1999 Elsevier Science Ltd. All rights reserved.

INTRODUCTION

The presence of hypervelocity micro-particles in low earth orbit (LEO) has been a long standing concern, due to the impact damage hazard these particles present to space hardware such as satellites, e.g. Drolshagen [1]. The particles can be divided into two populations: natural micrometeoroids, e.g. Laurance and Brownlee [2] and artificial 'space debris', e.g. Bernhard *et al.* [3]. The hypervelocity impact (HVI) of particles from either population leaves little evidence of the original impactor, although occasionally near pristine materials are observed, Rietmeijer and Blandford [4]; Hörz *et al.* [5]. As such while it is relatively easy to constrain the physical nature of the impact damage in space hardware, it is usually difficult to assess exactly what caused it. As only traces of material, usually a complex melt derived from residues of the impactor and the target material are identified, e.g. Zolensky *et al.* [6]. Much of the previous work on HVI onto space hardware was focussed upon the returned Solar Maximum Mission spacecraft, e.g. Warren *et al.* [7], and the Long Duration Exposure Facility (LDEF), e.g. McDonnell *et al.* [8]. Much of the investigation centred on impacts into ductile surfaces such as Al-clamps and Au-foils, Rose *et al.* [9]; Hörz *et al.* [10], which generated simple, bowl-shaped crater morphologies, Melosh [11]; Hörz *et al.* [10]. The chemical analysis of residual material from the impactor deposited in the craters was difficult since in most cases the material was vaporised and lost during the impact process, e.g. Brownlee *et al.* [12].

The Hubble Space Telescope (HST) solar array which was returned to Earth in 1993, after 3.62 years of space exposure, has offered an opportunity to document further the LEO environment and gain a better understanding of HVIs upon space-hardware. The surfaces

returned from the solar array, unlike many of the previous studies already mentioned, are brittle in nature. Thus, instead of simple crater morphologies, they produce complex radial and conchoidal fractures with extensive spallation zones (Fig.1) during the crater forming process, Rival et al. [13]. The previous investigations of impacts into brittle targets have focussed on the crater morphologies, e.g. Mandeville [14] and impact dynamics, e.g. Taylor et al. [15]. The possible retention of impactor material has not been assessed extensively, as it has been presumed that, as with LDEF craters, much of the material would be lost. Recent work employing analytical microscopy techniques has been successful in both the location and identification of residue material in the solar cells, Graham et al. [16]. A programme of light-gas-gun shots that have produced similar impact features in the laboratory has now extended this work. Although many craters from LEO exposure have proved to contain very distinctive residue 'fingerprints' of the impactor mineralogy, some are not so easy to tie unambiguously to original mineralogy, and some were clearly due to polymineralic grains. The laboratory experiments were thus designed to discover what happens to impactors of well-characterised mineralogy during HVI in terms of chemistry and the amount of material retained. Herein we discuss the observations made on both simulated and LEO micro-particle impacts, and their implications for the ability of solar cells to retain residue material.
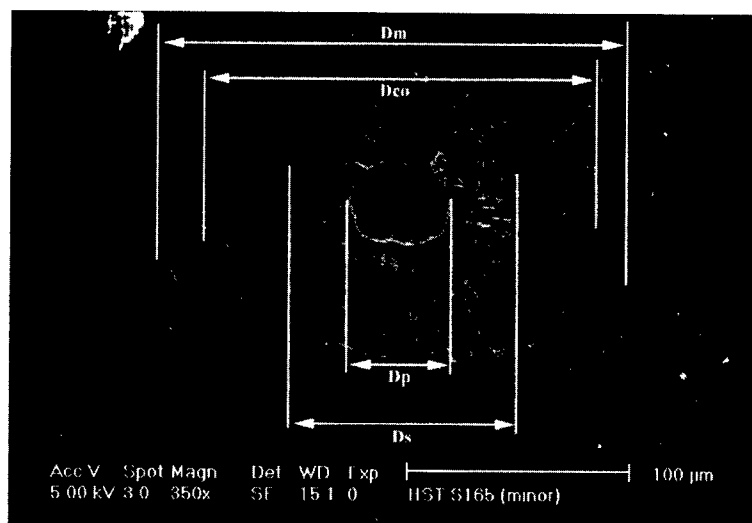
Fig.1 Secondary electron images (SEI) of an impact crater. The crater terminology can be described as the following: D_p = central pit (melt pit), this may contain debris in the form of melt residues; D_s = Shatter zone, this area is highly fragmented; D_{co} = Conchoidal spallation; D_m =Maximum damage detected at an impact site.

SAMPLES AND METHODS

Solar Cells

The samples of flight hardware from LEO used in this study were individual solar cells removed from the upper blanket of the solar array assembly from the HST, which was returned to Earth after the 1993 service mission. Prior to recovery, the array had been exposed to LEO for 3.62 years, at an operational altitude of approximately 600km, Drolshagen [1]. Upon return and de-integration the array was transported to a clean-room facility at ESTEC (the Netherlands), where it underwent post-flight investigation, Drolshagen [1].

The 25 individual solar cells (Fig.2) requested for the residue studies were specially selected on the basis that they contained class I and II impact craters, as defined by Herbert and

McDonnell [17], rather than holes (class V). The analysis of the impact holes had shown that little or no impactor material is retained, whereas class I and II craters appear to offer the potential to retain material as the impact had only penetrated the upper layers of the cell and a melt pit is generated.
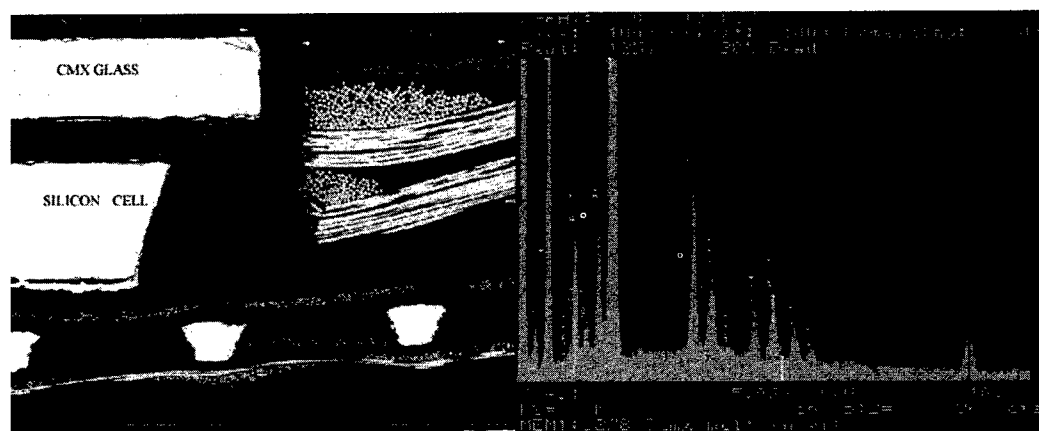
Fig.2 A cross-section of a solar cell and supporting stiffener and EDS spectra of the CMX glass. The solar cells are composed of a top protective layer (150μm thick) of CMX borosilicate glass coated with a Mg + F layer. A layer of silicone resin (70μm thick) on the underlying silicon solar cell (250μm thick) bonds the CMX layer. Below the silicon cell is a silver connector strip running through the cell (approximately 900 nm thick). Under the connector is a second layer of silicon resin (70μm thick). This composite structure is supported by a fibre-glass backing tape (100μm thick).

Scanning Techniques

The analytical protocols are described more fully in Graham et al. [16]. The chemical compositions and debris morphology associated with the impact features were determined using a JEOL JSM 840 SEM fitted with an Oxford Instruments e-XL X-ray energy dispersive spectrometer. The analytical work was carried out at an accelerating voltage of 20kV with a beam current of 2nA at a working distance of 32mm. Back-scattered electron images (BEI) and X-ray maps were digitised for analysis and storage. High-resolution imaging of selected craters was carried out on a Philips XL FEG-SEM fitted with a Robinson back-scattered electron detector, using an accelerating voltage of 5kV and a working distance of 15mm. All the samples were given an ultra-thin carbon coat to reduce the effects of charging during analysis.

Simulated Shots Program

Sabot-mounted impactor samples were individually accelerated in a light-gas-gun (LGG) at the University of Kent (U.K.), using the buck-shot technique described in Taylor et al. [18]. Grains were impacted on solar cell targets at velocities around 5 km/s (calculated from time-of-flight measurements using piezo-electric transducer sensors).

The first laboratory HVI were designed to demonstrate whether or not it is relatively easy to find and characterise different residues from LGG impacts, as had already been demonstrated for LEO-exposed materials, Graham et al. [16]. The first projectiles (up to 400μm in diameter) were composed of soda-lime glass (as an analogue of natural silicates) and stainless steel AISI 420 ball-bearings (as an analogue of space debris). Distinctive, unambiguous residues were found in a number of craters in each case.

Following this success, the programme was extended to a suite of high purity natural minerals (determined to be homogeneous in composition by examination under the SEM). The selected minerals included olivine (Mg-silicate); calcite (Ca-carbonate); pyrrhotite (Fe-sulfide); feldspar

(Ca-aluminosilicate) and pyroxene (Ca- + Mg- silicate). Projectiles of 125-250μm diameter were employed to provide simple, yet realistic, analogues of individual components of natural micrometeoroids. When a range of minerals may be intimately associated at the scale of micrometres, as seems to be the case in interplanetary dust particles (IDPs), e.g. Bradley [19] and probably in micrometeoroids, their impact may produce complex polymineralic residues that are difficult to assign to precise, individual mineral compositions. The use of well-characterised samples in a relatively simple experimental environment was therefore an essential first step to enable positive and unambiguous identification of impactor mineralogy before attempted interpretation of more complex, mixed-mineralogy HVI, such as those observed in polymineralic residues as seen by Graham et al. [16].

In particular, these impacts permitted an analysis of the degree to which samples undergo alteration during the impact process at 5 km/s, such as loss of volatile elements or chemical fractionation of the residue between different components such as the melt glasses and vapour. The textural characteristics of the residue were also noted as a further potential indicator of impactor mineralogy and were very similar to those seen on space exposed surfaces where impact velocities may range to 70 km/s, Hörz et al. [10].

In practice, LGG HVI residues needed to be interpreted with care, as the apparatus may create a number of contamination problems. It proved common place to identify finely-dispersed particles containing Fe, Al, S and Cu strewn across the surface of the target in every LGG shot. Energy-dispersive spectra (EDS) micro-spot analysis of gun components revealed that these contaminant elements are almost certainly derived from parts of the gun and chamber, including the Fe particle-bearing, Al-Cu alloy 'burst-disk'. The contaminants do not, however, resemble true impact residues in texture or grain size, and it can be easily demonstrated that they are not mixed with the solar cell glass melt. They can, therefore be reliably distinguished from impact residue. Previously the LGG has been used to model crater morphologies and impact processes, e.g. Taylor et al. [18], not to investigate chemical variations of residues, and the presence of such contaminants has been relatively unimportant.

OBSERVATIONS

Chemical Analysis

Experience suggests that morphological studies of craters, e.g. McDonnell et al. [8], are unlikely to yield sufficient information on the origin of an impactor to allow the broad classification in terms of space debris (SD) versus micrometeoroid (MM). Such a classification can only be achieved through chemical studies. Herein the residues identified in the HST solar cells have been classified as SD or MM using the previous schemes of Graham et al. [16] and those which arose during the post-flight studies of LDEF hardware, e.g. Zolensky et al. [20]; Bernhard et al. [3].

SD material is basically considered to be anything that is not from a natural MM source. SD-derived residues are classified based upon energy dispersive spectra (EDS) of characteristic X-ray emission, showing combinations of elements such as: Ti, C, N and O (possible paint fragments); Fe, Cr, Mn and possibly Ni (in the correct ratio for specialised steels); Sn and Cu (printed circuit board electronics); Al, Cl, O, Cr (possibly solid rocket motor components); C, Na, K, Cl, Ca (urine). The MM-derived residues may not retain the stoichiometric chemical signature of their parent mineral compositions. It is nevertheless possible from EDS spectra to assume that the following indicate MM origins: Mg, Fe, Ca, Si (olivine or pyroxene mafic silicates); Fe, S (Fe-sulfides); Fe, Ni, S (Fe-Ni sulfides); Fe-Ni metal (in the range of kamacite, a metal identified in meteorites); further more complicated elemental chemistries indicative of MM origins are also possible.

The analysis of 29 residues in the 25 solar cells exposed to LEO indicated 3 of the residues

were artificial in origin, 20 were natural in origin and 6 were unclassified (due to spalled melts, where it is assumed the residue was lost during the impact process). The amount of residue material identified in the solar cell craters is in stark contrast to LDEF studies where up to 73% of the impact craters into the Al and Au targets from various experiments on LDEF were unclassified, e.g. Brownlee *et al.* [12]; Zolensky *et al.* [6]. This contrast in residue abundance could be due to a number of reasons: 1) the analytical methods and detectors employed in the LDEF studies were insufficiently sensitive to identify discrete residues within the craters; 2) the impact process into Al and Au surfaces caused much of the material to be lost; 3) sample bias: the number of impact craters investigated was much higher for LDEF than HST (e.g. in the micrometeoroid chemistry experiment of LDEF, the number of impacts in the high-purity Au-targets was 199 and 415 impacts in the high-purity Al-targets, Bernhard *et al.* [21]); (this is substantially more than the 29 impacts observed herein); 4) the impact features identified in craters on LDEF do not represent average conditions, i.e. we might expect different features on different space hardware, Bernhard *et al.* [21].

Notwithstanding the high number of unclassified impacts (48%), for the trailing and leading edge surfaces of LDEF in the dedicated chemistry experiment, Bernhard *et al.* [21], the majority of impacts identified were classified as natural (39%) compared to artificial (13%). In the HST solar cell impacts, the number of unclassifed impacts are considerably lower, 6 out of 29 (21%); the rest are dominated by MM-derived residue (68%) (their detailed classification was discussed in Graham *et al.* [22]). This observation raises the possibility that LEO may harbour a previously under-estimated population of micrometeoroids, Graham *et al.* [23], as well as space debris. Further work is required to substantiate this observation.

Textural Observations Of Residues

The physical appearance of the impact residues identified within the craters (D_{CO} 100-1000μm) were highly variable in both concentration and composition; a similar conclusion was previously made in LDEF studies concentrating on micrometeoroid residues in Al and Au substrates, Brownlee *et al.* [12]. Our data however, especially that from the LGG experiments, suggest that apart from the velocity dependent factors, there may also be a strong link between residue texture and the original mineralogy of the impactor. Although the processes of formation and retention of residues are undoubtedly extremely complex, it is unlikely that the textural variations observed in our LEO HVI are due to differing types of interaction between a single composition of impactor particle and different components of the host substrate. It seems likely that variations in the degree of impactor vaporisation and fragmentation, the viscosity and miscibility of melt components (and therefore the intimacy of their mixing) together create residue textures that may be diagnostic of the impacting mineralogy. This may prove to be important in distinguishing silicates of differing crystal structure and volatile content (e.g. orthosilicates such as olivine, framework silicates such as pyroxene, and hydrous phyllosilicates such as saponite). EDS spectra of embedded particles sometimes clearly revealed Mg+Fe to Si ratios directly comparable to those of specific mafic silicates; however, many residues showed much greater interaction with the host melt and cannot be assigned so simply to mineral groups on chemistry alone. Combined chemical and textural distinction might allow direct comparison of impactors with the recognised classes of interplanetary dust particles (mafic silicates; phyllosilicate and refractory phases, e.g. Bradley [19]). The textural features of the 20 residues identified as MM in origin in the solar cell craters can be defined as: surface glass (2), sub-surface glass (10); surface globules (13) and near-intact particles (2). The impact residues rarely contained only the individual textures, a typical residue would consist of more than one of the different textural variations. To allow comparisons between LDEF observations and those herein, LDEF terminology, Brownlee *et al.* [12] is used where appropriate in the description of the glass residues.

Vesicular Glass Residues. Vesicular melt residues usually have a distinctive 'ropy' appearance in BEI. They appear as networks on the surface of the melt pit, and occasionally as detached strings in the shattered surroundings. In some cases these melts demonstrate a degree of volatile retention during their deposition, in the form of possible gas bubbles, (dark areas in BEI, Fig.3a). The residues are usually enriched significantly in Mg, Ca and Fe above the solar cell composition, an assemblage suggestive of origin from a mafic silicate, such as pyroxene as previously suggested in the preliminary investigation of the solar cells, Graham *et al.* [24]. Vesicular residues were previously identified in LDEF craters on pure Al and Au substrates by Brownlee *et al.* [12], who also suggested that the vesicular nature was a product of the volatile content within the impactor. The HVI residues of soda-lime glass (Ca-bearing silicate), selected as a micrometeoroid analogue, also showed a characteristic ropy texture (Fig.3b) similar in appearance to those which we consider to be a result of impact by natural particles. It is noteworthy that the vesicular texture was enriched in Ca and Na (i.e. high volatile content within the projectile).
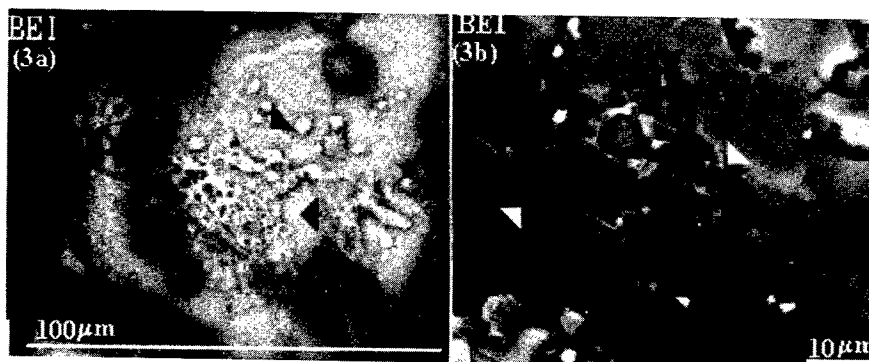
Fig.3a A BEI of a vesicular residue (black arrows highlight the area of interest) observed in LEO-derived impact crater generated by a micrometeoroid. **Fig.3b** A BEI of a vesicular residue (white arrows highlight the area of interest) observed in impact crater generated in the laboratory using soda-lime projectiles.
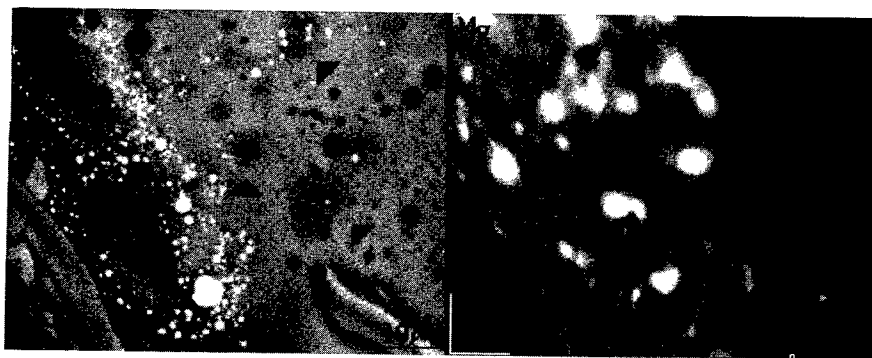
Fig.4a A BEI of an embedded residue observed in a LEO-derived impact crater. The residue is identified by the dark grey patches within the melt glass (the black arrows highlight the patches). The melt also contains bright globules, which are Fe-Ni metal melt droplets. The impact melt has been generated by a polymineralic micrometeoroid impactor. **Fig.4b** Shows the Mg elemental x-ray map for the melt glass. The Mg concentration directly corresponds to the embedded patches in the BEI.

Glass-embedded, concentrated residues. In Fig.4 the Mg- and Si-rich residue from a LEO impactor is an embedded patch within the melt pit. Where the patch derived from thermal melting of the impactor, or a condensate from gas, it might be expected that such residue would show a high degree of elemental mixing with the solar cell substrate. The ED X-ray spectra from

the residue (Fig.5a) were, however, very similar to those from a meteoritic silicate grain (olivine from CM2 Murchison - Fig.5b). This suggests that the patch may be a concentrated Mg+Si glass within the melt glass of the host, with almost no elemental mixing (i.e. immiscibility), or it is a surviving, shocked, solid particle beneath the melt surface. It was not possible to be certain whether the spectra from the residue patch showed the pristine composition of an end-member olivine or whether some degree of elemental fractionation had occurred during the impact process, although the former seems more likely. If the residue is a shocked solid particle it is unlikely that significant elemental fractionation would have occurred.
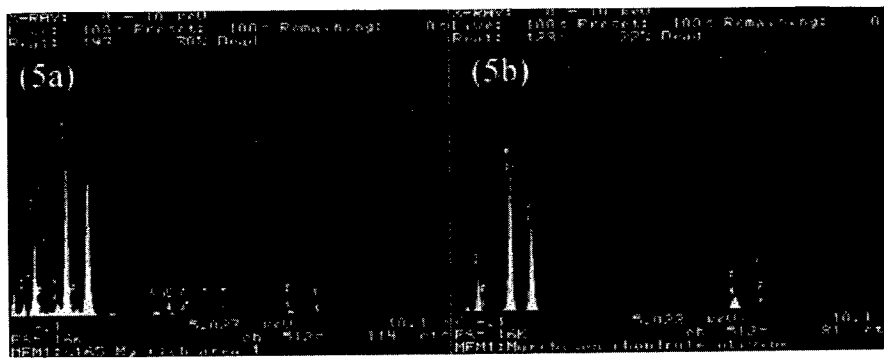
Fig.5a ED spectrum obtained from the analysis of the embedded residue. **Fig.5b** ED spectrum obtained from the analysis of an olivine grain in the Murchison meteorite. Although the ED spectrum for the residue is enriched in Si compared to the olivine from the meteorite the general pattern is comparable.
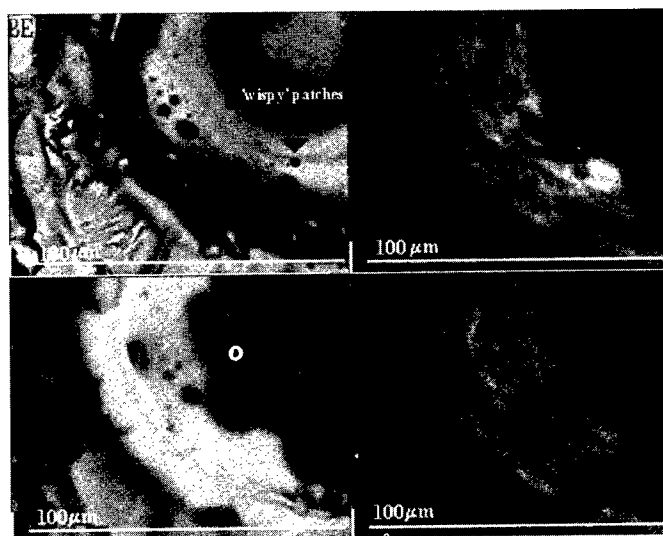
Fig.6 A BEI of a thin glass 'wispy' residue (highlighted by the black arrows) observed in a LEO generated crater. The discrete patches in the BEI correspond to enrichments in both the Mg and Fe elemental x-ray maps.

Thin Glass And 'Wispy' Residues. The textures described above show only limited interaction with the host melt during the impact process, indicated by the clear compositional contrast in BEI between vesicular or embedded glass and the melted borosilicate substrate. The 'thin glass' residue in some LEO HVIs is much more difficult to see, with only a slightly darker tone in BEI, and the texture could easily be overlooked. The texture is seen most easily in X-ray maps that enable the location of enrichment in Mg to be identified (Fig.6). The lack of fluorine in these areas indicates the magnesium is not derived from the CMX layer of the cell. We tentatively

suggest that this marked difference in texture (compared to vesicular and embedded residues) may be indicative of different silicate mineralogy, probably a hydrous phyllosilicate component. If a LGG impactor of heterogeneous origin, e.g. Orgeuil (CI carbonaceous chondrite meteorite) matrix (phyllosilicate dominated) is added to the shot program above, it may well elucidate these preliminary findings.
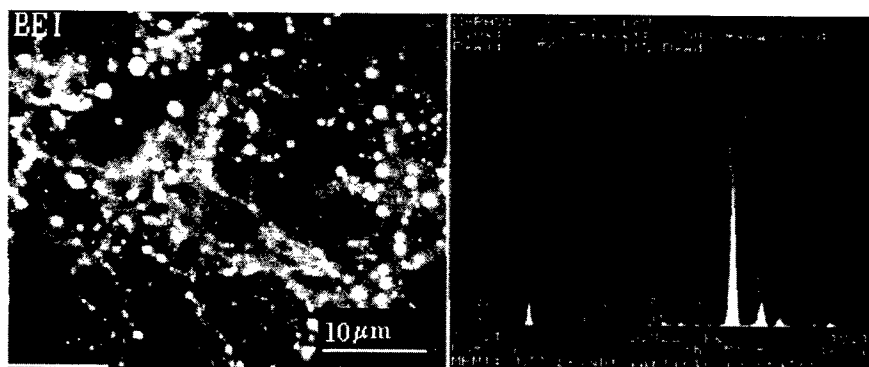
Fig.7 A BEI of the metallic surface melt droplets observed in a LEO-generated impact crater. The ED spectra obtained from the analysis of an individual droplet shows the enrichment in Fe and Ni.

Surface Globules. In low magnification BEI, several craters contained remarkably bright patches, showing strong compositional contrast between the host and the discrete residue chemistry (Fig.4a). At high magnification these patches reveal myriad separate, 1 - 10μm-sized hemispherical globules on the surface of the melt-pit or shallowly embedded within the melt glass (Fig.7). X-ray maps showed that the residue had not mixed with host melt in the way that silicates sometimes did mix. The globules were composed of Fe-Ni metal (Ni = 5-7.5 weight %, i.e. kamacite ratios) and metal sulfides (Fe-Ni sulfides and Fe-sulfides); similar globules were identified in a crater on Al from LDEF, Brownlee *et al.* [12] and it is assumed that they form by very rapid quenching. There appears to be no loss of volatile sulfur during the process, suggesting that the droplets were immiscible liquid melt droplets, rather than condensates from a gaseous phase. The pyrrhotite (FeS) impactor in the LGG produced very similar textural features (Fig.8) on a variety of scales although, some melt surfaces showed amalgamation of globules into broader surface patches or stretching of sulfide residue into streaks and curls. There was no evidence of mixing with the borosilicate melt.
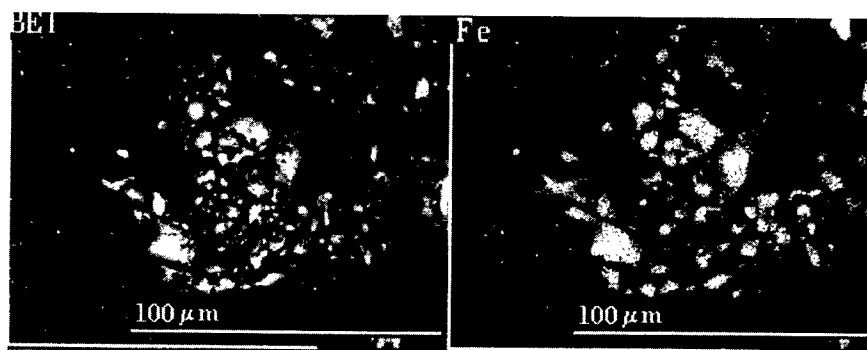
Fig.8 A BEI of the impact residue derived from an LGG-generated shot using pyrrhotite (FeS). The melt droplets in the BEI correspond to the enrichments in the Fe elemental x-ray map.

Near-intact Particulate Residue Material. The preservation of near-pristine particles in HVIs is extremely rare, Rietmeijer and Blandford [4]; Brownlee *et al.* [12], yet the identification of

such material clearly offers the best opportunity to classify impactor origin. The steel projectiles fired during the LGG program revealed that residue material is not only deposited in the melt-pit, but that it is also possible to locate material in both the conchoidal fractures and the underlying spall zone. Therefore, there exists the probability that in certain craters, especially when the zone of conchoidal fractures does not show complete detachment of fragments around the entire circumference of the crater, residue or even debris from the impactor may be retained. The evaluation of the LEO-exposed impact craters identified one with calcium-rich material ($<8\mu m$ diameter) as near-intact particles located in the spall zone and radial fractures (Fig.9a).
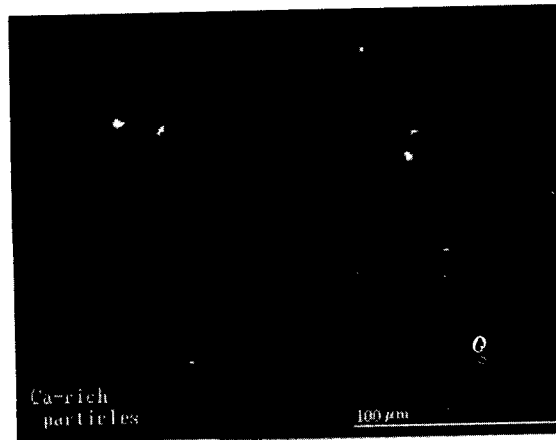
Fig.9a A BEI of an impact crater generated in LEO, which contains Ca-rich particles in the spall zone. The lack of the particles in the surrounding area would suggest that they are not simply contamination products.
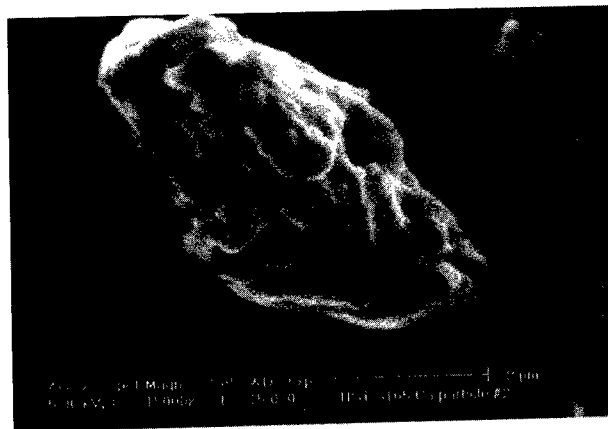
Fig.9b A secondary electron image (SEI) of a Ca-rich particle located in the LEO derived crater. The surface texture of the particle indicates that it has undergone a degree of melting that would suggest that it is not contamination.

These fragments appeared not to be simply contamination at some later stage, as they showed evidence of surface melting (Fig.9b). We conclude that such debris was emplaced explosively. EDS X-ray microanalysis showed abundance of mainly calcium with no silicon, giving a spectrum remarkably like that of the carbonate mineral calcite. Calcite is a common constituent of altered refractory inclusions and veins in hydrated carbonaceous chondrite meteorites, e.g. Grossman [25]. It might be expected that explosive fragmentation on emplacement would result in the complete destruction and loss of such volatile-rich compounds rather than retention.

To evaluate whether such a volatile chemistry would survive HVI, calcite grains ($125-250\mu m$ in diameter) were fired into a solar cell target using the LGG. Subsequently, fragments were

observed to be retained in the spall zone of several craters.
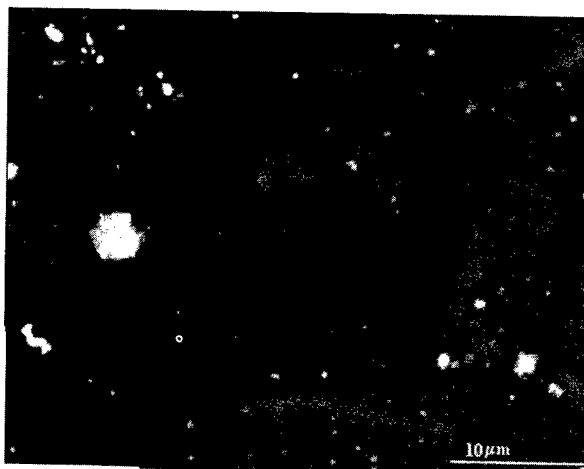
Fig.10 A BEI of Ca-rich fragments retained in the spall zone of a impact crater generated by the calcium carbonate LGG shot. The fragments are comparable to those observed LEO impact craters (Fig.9b).

These fragments (Fig.10) were demonstrably not simply original mineral grains (i.e. artefacts of the experiment, accreted after formation of the craters), as they showed evidence of surface alteration and were mantled in a thin coat of borosilicate host glass melt. The LGG shot of $CaCO_3$ has indicated that calcite can survive HVI.

It is clear that an EDS spectrum from a LEO-generated particle could be ambiguous if only Ca is observed since this could either be due to minerals of micrometeoroid origin (calcite in this case) or space debris (Ca-rich particles from urine). However we contest that, remnants of urine solids would be accompanied by other volatile elements (e.g. Na and K). Areas rich in sodium and chlorine have been found on the surface of some of the cells, probably as the result of contamination after recovery, but these are distinct in texture from impact residues. The techniques utilised in this study do not produce substantial volatile loss during analysis and the presence of some sodium or chlorine would be expected in urine-derived solids given the very substantial enrichment of these elements in urine when compared to calcium.

The scanning techniques employed in this investigation were not able to yield information on the crystallographic structure of the fragments. It is hoped that using the established techniques of residue extraction, Teetsov and Bradley [26], appropriate particles can be removed, and any surviving crystal structure be determined by transmission electron microscopy.

Debris Retention in HVI craters

The rigorous interpretation of HVI-derived residues in space hardware is a complex task. Crater size, penetration depth and accompanying degree of damage to the host can vary to a great extent (e.g. for the HST sample, crater diameters range from approximately 50 to 3000µm D_{CO}). There is potentially a strong bias to the population of impacting particles that can be recognised by residue studies, particularly if the host is only efficient at collecting the smaller particles, Graham et al. [24]. To date we have not yet seen a sufficiently large number of craters on solar cells to be able to assess whether residue can be routinely found in craters greater than 1500 µm in diameter. In this study a further limitation lies in the relatively small number of individual samples yet examined, and it is therefore very important to establish an efficient sampling method for a larger survey. To yield the maximum information on the LEO environment, it is essential to understand the likelihood of debris retention within a given crater size.

The pyrrhotite (FeS) LGG experiment, due in part to the buck-shot technique used in firing,

produced a large number of impact craters. Approximately 200 were of diameters comparable to those common in HVI from LEO (D_{CO} 100-2000 μm). The large number of craters, and the appropriate variation in crater diameter, offered the opportunity to quantify retention of residue in the crater size range that previous work, Graham et al. [24] had suggested would be the most effective at trapping material in brittle targets. 116 craters (D_{CO} 100-1700μm) were examined for residue: 111 (96%) contained FeS residue, 3 were unclassified (spalled melt) and 2 were contamination from the LGG. The results indicate that FeS is highly likely to survive HVI into a brittle target and should be adequately represented in a sample of natural impactors. This supports the observation that in the HVIs identified in solar cells from LEO as natural, 13 out of the 20 (65%) retained metal sulfide residues. Clearly we would like to extend this work to residue material from all of the other types of mineral shots employed herein. Furthermore to allow direct comparison with the retention of debris in LDEF craters, e.g. Bernhard et al. [21] laboratory HVI must use similar ductile targets (e.g. Al-blocks). Such experiments would form a logical extension of the present study, to be followed by a similar SEM survey of the craters.

SUMMARY AND CONCLUSIONS

Previous investigations of HVIs in space hardware have focused on ductile target surfaces, e.g. Al and Au, Bernhard et al. [21]. The analysis of such surfaces highlighted the complexity of these studies, as the location of residue material was rare, Brownlee et al. [12]. The investigation herein has focussed on solar cells (brittle surfaces) returned from the HST after 3.62 years of space exposure in LEO. Detailed analytical scanning electron microscopy has enabled the identification of extraneous residue material in impact craters (D_{CO} = 100-1000μm). The residue material was initially classified in terms of either space debris or micrometeoroid in origin. The latter has been sub-classified using chemistry and textural observations, e.g. embedded and vesicular glass melts identified as mafic silicates in origin.

The use of a LGG to simulate similar impacts has enabled critical evaluation of the nature of the LEO HVI derived-residues. Although the simulated residues are produced at lower velocities (~5 km/s) than compared to LEO derived residues (11-68 km/s for micrometeoroids) it appears that similar textures and chemical effects are produced.

REFERENCES

1.   Drolshagen, G., HST meteoroid and debris impact analysis: Overview, *Proc. Hubble Space Telescope Array Workshop*, ESA WPP-77, 295-300 (1995).
2.   Laurance, M.R. and Brownlee, D.E., The flux of meteoroids and orbital space debris striking satellites in low Earth orbit, *Nature*, **323**, 136-138 (1986).
3.   Bernhard, R.P., Durin, C. and Zolensky, M.E., Scanning electron microscope / energy dispersive x-ray analysis of impact residues in LDEF Tray clamps, *LDEF 69 Months in Space - 2nd Post-Retrieval Symp.*, 541-550 (1993).
4.   Rietmeijer, F.J.M. and Blandford, G.E., Capture of an olivine micrometeoroid by spacecraft in low Earth Orbit, *J. Geophys. Res.*, **93**, 11943-11948 (1988).
5.   Hörz, F., Zolensky, M.E., Cress, G., Bernhard, R.P., See, T.H., et al., ODC: Aerogel particle capture during 18 months exposure on Mir, *Lunar Planet. Sci* XXIX, (CD-ROM abstr.), (1998).
6.   Zolensky, M.E., Hörz, F., See, T.H., Bernhard, R.P., Dardano, C., Barrett, R.A., Mack, K., et al., Meteoroid Investigations Using The Long Duration Exposure Facility, In *Analysis Of Interplanetary Dust Particles* (eds M.E. Zolensky, T.L. Wilson, F.J.M. Rietmeijer and G.Flynn), AIP Conf. Proc. 310, AIP Press, Woodbury New

York, 291-304 (1994).

7. Warren, J.L., Zook, H.A., Allton, J.H, Clanton, U.S., Dardano, C.B., Holder, J.A., et al., The detection and observation of meteoroid and space debris impact features on the solar max satellite, *Proc. 19th Lunar and Planet. Sci. Conf.*, 641-657 (1989).

8. McDonnell, J.A.M., and the Canterbury LDEF MAP TEAM, Impact cratering from LDEF's 5.75 year exposure: decoding of the interplanetary and earth-orbital populations, *Proc. 22nd Lunar and Planet. Sci.*, 185-193 (1992).

9. Rose, M.F., Best, S., Chaloupka, T., Stephens, B. and Crawford, G., Hypervelocity impact facility for simulating materials exposure to impact by space debris, *LDEF 69 Months in Space - 2nd Post-Retrieval Symp.*, 479-492 (1993).

10. Hörz, F., Cintala, M., Bernhard, R.P., and See, T.H., Penetration experiments in aluminum and teflon targets of widely variable thickness, In *Analysis of Interplanetary Dust Particles* (eds. M.E.Zolensky, T.L.Wilson, F.J.M.Rietmeijer and G.Flynn), AIP Conf. Proc. 310, AIP Press, Woodbury New York, 329-344 (1994).

11. Melosh, H.J., *Impact cratering. A geologic process*, Oxford University Press, Oxford 1996.

12. Brownlee, D.E., Joswiak, D., Bradley, J.P. And Hörz, F., Interplanetary meteoroid debris in LDEF metal craters, *LDEF 69 Months in Space - 2nd Post-Retrieval Symp.*, 577-584 (1993).

13. Rival, M., Mandeville, J.C. and Durin, C., Impact phenomena on brittle materials: analysis of 1μm to 1mm impact features on solar arrays, *Adv. Space Res.*, (In press) 1998.

14. Mandeville, J.C., Profile and depth of microcraters formed in glass, *Earth and Planet Sci. Lett.*, **15**, 110-112 (1972).

15. Taylor, E.A., Hayhurst, C.J. and Tsembelis, K., Hydrocode modelling of space debris - Hypervelocity impact on soda-lime glass using the Johnson-Holmquist Brittle Material Model, *Proc. 2nd European Conf. On Space Debris*, ESA SP-393, 449-454 (1997).

16. Graham, G.A., Kearsley, A.T., Grady, M.M. and Wright, I.P., The rapid identification of impact residues in solar array panels of the HST by digitised back-scattered electron and x-ray elemental imaging, *Proc. 2nd European Conf. On Space Debris*, ESA SP-393, 183-189 (1997).

17. Herbert, M.K. and McDonnell, J.A.M., Morphological classification on the EuReCa and Hubble Space Telescope solar arrays, *Proc. 2nd European Conf. On Space Debris*, ESA SP-393, 169-175 (1997).

18. Taylor, E.A., Kay, L., and Shrine, N.R.G., Hypervelocity impact on semi-infinite brittle materials: fracture morphology related to projectile diameter, *Adv. Space Res.*, (In press) (1998).

19. Bradley, J.P., Mechanisms of grain formation, post-accretional alteration, and likely parent body environments of interplanetary dust particles (IDPs), In *Analysis of Interplanetary Dust Particles* (eds. M.E.Zolensky, T.L.Wilson, F.J.M.Rietmeijer and G.Flynn), AIP Conf. Proc. 310, AIP Press, Woodbury New York, 291-304 (1994).

20. Zolensky, M.E., Zook, H.A., Hörz, F., Atkinson, D.R., Coombs, C.R., Watts, A.J et al., Interim Report Of Meteoroid and Debris Special Investigation Group, *LDEF 69 Months in Space - 2nd Post-Retrieval Symp*, 277-302 (1993).

21. Bernhard, R.P., See, T.H. and Hörz, F., Projectile compositions and modal frequencies on the "Chemistry of micrometeorites" LDEF experiment, *LDEF 69 Months in Space - 2nd Post-Retrieval Symp.*, 551-574 (1993).

22. Graham, G.A., Kearsley, A.T., Grady, M.M., Wright, I.P. And McDonnell, J.A.M., Micrometeoroid residue collected in low earth orbit, *Lunar Planet. Sci.*, XXIX, (CD-ROM abstr.) (1998).

23. Graham, G.A., Kearsley, A.T., Grady, M.M., Hough, R.M., Wright, I.P. and McDonnell, J.A.M., Populations of low earth particles: Significant other or simply space junk?, *Meteoritics Planet Sci.*, **33**(4), A61 (abstr. suppl.), (1998).

24. Graham, G.A., Sexton, A., Grady, M.M. And Wright, I.P., Further attempts to constrain the nature of the impact residues in the HST solar array panels, *Adv. Space Res.*, **20**(8), 1461-1465 (1997).

25. Grossman, L. Petrography and mineral chemistry of Ca-rich inclusions in the Allende meteorite, *Geochim. Cosmochim. Acta*, **39**, 433-454 (1975).

26. Teetsov, A. and Bradley, J.P., Micromanipulation of extraterrestrial particles, *Lunar Planet. Sci.* XVII, 883-884 (Abstr.) (1986).

EVALUATING THE EVOLUTION OF PROCESS SPECIFIC DEGRADATION SIGNATURES AROUND IMPACT CRATERS

JOHN A. GRANT

SUNY College at Buffalo, Earth Sciences, 1300 Elmwood Ave, Buffalo, NY, 14222, U.S.A.

Summary—The pristine morphologies created during an impact event comprise a template for constraining how various environmental parameters influence the mechanics of crater formation. Identification of pristine morphologies used in defining and/or evaluating models of crater formation can be complicated or precluded, however, by the effects of post-formation degradation. Field and/or remote examination of simple, unglaciated impact craters on the Earth (*e.g.*, Meteor Crater, Arizona, and Roter Kamm crater, Namibia) can yield results that help to define characteristic degradation signatures for use in placing first-order constraints on the number and intensity of processes that have been active. In turn, the presence of a suite of these degradation signatures can be used to define the amount and style of crater degradation that has taken place, thereby providing a tool for possible distinction between pristine versus secondary, post-formation characteristics. © 1999 Elsevier Science Ltd. All rights reserved.

INTRODUCTION

Impact craters on the Earth and other solar system bodies comprise an important database for evaluating the mechanics of crater formation [*e.g.*, 1-5]. Study of the varying morphology of pristine impact craters occurring in a wide range of planetary settings can yield information for use in relating the formation of certain characteristics to the influence of key environmental parameters (*e.g.*, the role of atmospheric density in the formation of ejecta ramparts, see [1-2]). Interpreting possible mechanisms responsible for the evolution of pristine crater morphology can be complicated, however, by the superposition of secondary, post-formational degradation characteristics.

Examination of simple, unglaciated impact craters on the Earth [6-8] helps to define characteristic degradation signatures for use in placing first-order limits on the number and intensity of processes that have been active. In turn, the presence of a suite of these degradation signatures can be used to constrain the amount and style of crater degradation that has taken place, thereby providing a tool for distinguishing pristine versus secondary, post-formation characteristics.

A summary of the field methods used to quantify the degradation history of Meteor Crater, Arizona [*e.g.*, 6, 9], and Roter Kamm crater, Namibia [8] is followed by presentation of the results from field and remote analysis of other crater structures. These results, in turn, are used to develop a first-order sequence for crater degradation by several processes.

DEGRADATION STATE OF METEOR CRATER, ARIZONA

Meteor Crater, Arizona (35°1'N, 111°1'W, Fig. 1), has long been recognized as one of the best preserved, naturally formed impact craters on the Earth [*e.g.*, 10-14]. The 1.2 km in diameter crater was formed into nearly flat-lying sedimentary target rocks [10] ~50,000 Ka [15, 16] and preserves a ~300 m wide raised-rim reaching 30-60 m above the level of the surrounding plain.

Nevertheless, a comprehensive, quantitative assessment of crater degradation occurring since formation has only recently been completed [6, 9].
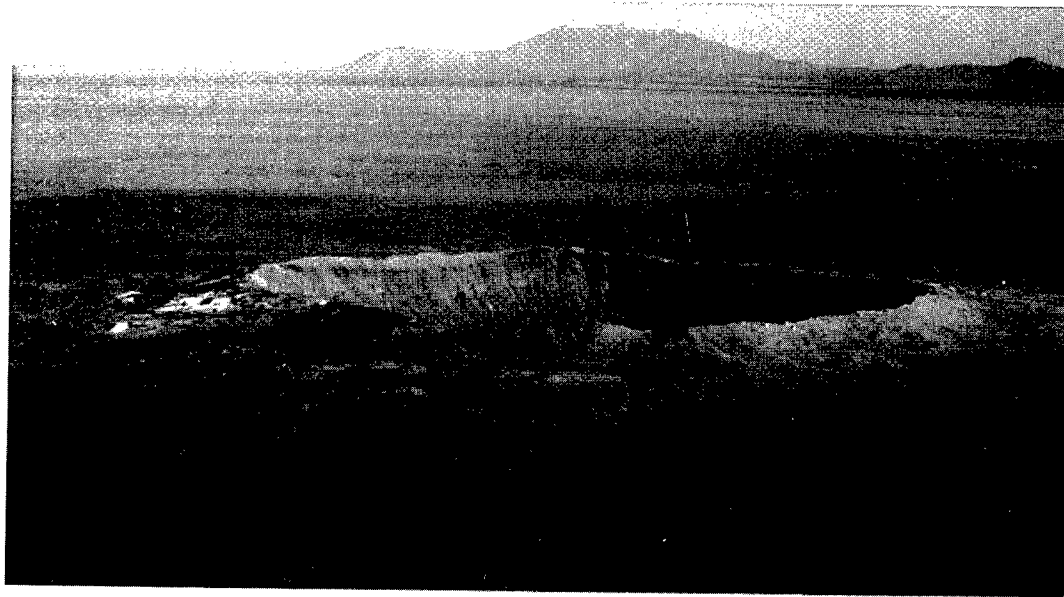
Fig. 1. Air photo of the relatively pristine 1.2 km in diameter, 50,000 year old [15, 16] Meteor Crater in north central Arizona ($35°1'N$, $111°1'W$). View is from the east towards the west. The crater was formed into flat-lying sedimentary rocks and has not been modified by glacial activity.

As summarized from Grant and Schultz [6, 7, 9], traditional field and depositional environment mapping together with remote investigations with a ground penetrating radar (GPR) yield results that help to constrain post-formation crater degradation. Specifically, estimates of the amount of erosion responsible for modification of the continuous ejecta surrounding the crater were based upon: A) evaluation of surface vs. sub-surface concentration of coarse fragments (>4 mm in diameter) created by erosional transport of surface fines; B) the volume of erosionally transported sediments contained within a semi-enclosed drainage basin on the western flank of the crater; and C) the radial extent of preserved ejecta as delineated using a GPR. Evaluation of surface coarsening was based upon grain size analysis of more than 100 samples collected mostly in surface (<10 cm depth) and subsurface (>30 cm depth) pairs and included corrections for possible ambiguities arising from eolian deposition, weathering, and surface wash. Results reveal that *in situ*, pristine ejecta grain size properties are relatively uniform and that low relief surfaces have been subjected to mostly vertical denudation. The volume of sediments within the semi-enclosed depositional basin was constrained by field mapping, excavation, and ground penetrating radar. The total calculated sediment volume includes corrections for possible sediment losses or gains related to more regional-scale alluvial, mass-wasting, and/or eolian activity. Efforts demonstrate that the basin is occupied largely by sediments derived from erosion of ejecta from intrabasin surfaces and subsequent redistribution into local alluvial, colluvial, and eolian sinks/deposits. Finally, an impulse GPR configured with 500 MHz and 100 MHz transducers was deployed along radial and circumferential transects crossing the medial and distal portion of the ejecta. These data confirm that much of the low relief topography on the distal ejecta surface is created by draping over buried, pre-crater topography typical of that on exposed regional surfaces and that the true extent of the ejecta is often masked by minor accumulations of alluvium and/or colluvium (generally less than 50-100 cm thick).

Each of the approaches outlined yields an independent, but similar estimate of the amount of vertical denudation affecting the ejecta and indicate that much of the crater exterior beyond the immediate near-rim has experienced an average of ~1m or less erosion [6, 7, 9]. Slightly greater degradation of up to 10-15 m affected the higher relief near-rim areas (within ~100-200 m of the rim-crest) and the interior walls [6, 9, 13, 14] and is responsible for increasing the diameter of the vertically undulating rim-crest by 2.5%.

As reported in Grant and Schultz [6, 7], the volume of deposits within the various depositional sinks surrounding the crater confirm that primary degradation was accomplished by

alluvial/colluvial and lesser eolian activity. Secondary deflation of fine sediment from these alluvial/colluvial deposits, however, coupled with primary deflation of small ejecta fragments accounts for redistribution of up to 2/3 of all sediment eroded around the crater.

As might be expected, the signatures associated with the limited overall denudation of the crater exterior are subtle (*e.g.*, crater flank incisement is generally less than 5 m) and difficult to detect remotely using data possessing resolution lower than ~1-2 m/pixel (*e.g.*, see Fig. 1). By contrast, the steep interior walls of the crater (30^0-90^0 slopes) reflect active backwasting and alluvial processes. Resultant infilling, accompanied by some eolian deposition, buries the original crater floor beneath ~30 m of fill [11]. Signatures associated with degradation of the crater interior include walls that remain sloped at or above the angle of repose and incised debris chutes that are detectable in images possessing a resolution of ~30 m/pixel or better.

The conclusion that Meteor Crater retains a remarkably pristine form [6, 9] is consistent with the results of alternate studies [17, 18] and requires that nearly all of the subtle topography associated with the continuous ejecta deposit at Meteor Crater is pristine, thereby reflecting the influence of conditions present when the crater formed. Such information is invaluable for investigators attempting to relate various aspects of crater formation models to observational field data [*e.g.*, 4, 19, 20]. For example, the distribution of several distal ejecta lobes superposing a low butte ~2.0R north of the crater must be pristine and do not reflect local differences in erosion intensity. Hence, their occurrence can be used be used to help constrain processes of distal ejecta emplacement [4].

DEGRADATION STATE OF ROTER KAMM CRATER, NAMIBIA

The Roter Kamm impact crater in Namibia ($27^0$46'S; $16^0$18'E) is ~2.5 km in diameter (Fig. 2) and was formed into crystalline target rocks [21] approximately 3.7 Ma ago [22]. Roter Kamm retains a raised-rim extending 40 to 90 m above the surface. Eolian sands associated with an up to 10 m thick regional sand sheet [21, 23] bury all but the highest portions of the rim and are responsible for ~500 m of fill within the crater [8, 24]. Sediments associated with eolian infilling limit the present depth of the crater to ~50 meters below the surrounding plain. An impact origin for Roter Kamm was first proposed by Dietz [25] and Fudali [24] and confirmed by Miller and Reimold [26], Reimold and Miller [27], and Reimold *et al.* [28, 29]. Evaluation of the preservation state of the crater was more recently accomplished via interpretation of topographic information, GPR data, and analysis of sediment samples from around the crater [8].
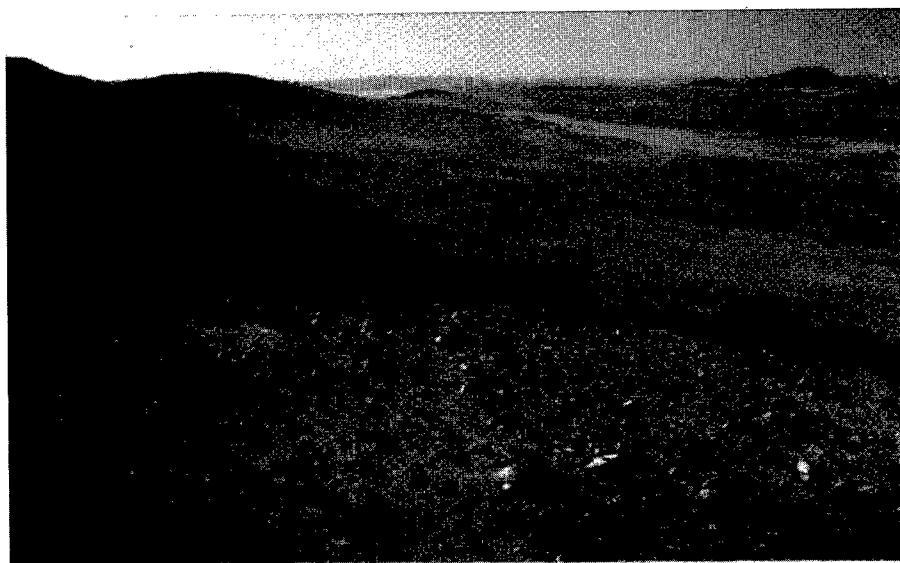
Fig. 2. View of a portion of the exposed rim and interior of the 2.5 km in diameter, ~3.7 million year old [22] Roter Kamm crater in the Namib Desert, Namibia ($27^0$46'S; $16^0$18'E). View is from the north rim-crest towards the southeast and illustrates the subdued, incised form of the exposed upper rim-crest and extensive infilling of the crater by sediments associated with the regional sand sheet. The crater was formed into mostly crystalline rocks and has not been modified by glacial activity.

As summarized from Grant *et al.* [8], topographic data reveal that Roter Kamm presents a subdued form relative to Meteor Crater. Gradients on the exposed interior walls of the crater range between $8°-22°$ and the rim presents a broader, more rounded expression that is locally incised by up to 30 m. Interpretation of topographic information was assisted by collection of GPR data (using an impulse GPR system configured with 500 MHz and 100 MHz transducers) from within and around the crater along transects totaling 15 km in length. These GPR data typically delineate reflections beneath the sand sheet to depths of 3-5 m and help define the nature and extent of near-surface stratigraphic and/or pedogenic horizons. GPR data also assisted in identifying locations where ground truth and samples were obtained for evaluation of grain size and textural properties (*e.g.*, shape and sorting).

Exposed portions of the crater rim are relatively limited in areal extent and are characterized by heavily fractured bedrock. GPR data from along the upper interior wall of the crater defines a reflection corresponding to the crater wall and/or alluvium mantling the crater wall that can be traced beneath the sand fill and confirm that slopes on exposed wall surfaces persist beneath at least the upper portions of the fill. By contrast, GPR and sedimentologic data collected along transects descending the exterior flank of the crater distinguish a deposit beneath the sand sheet whose radar and sedimentologic properties are most consistent with an origin related to alluvial transport from higher on the rim (Fig. 3). The thickness of this alluvium exceeds the penetration depth of the GPR.
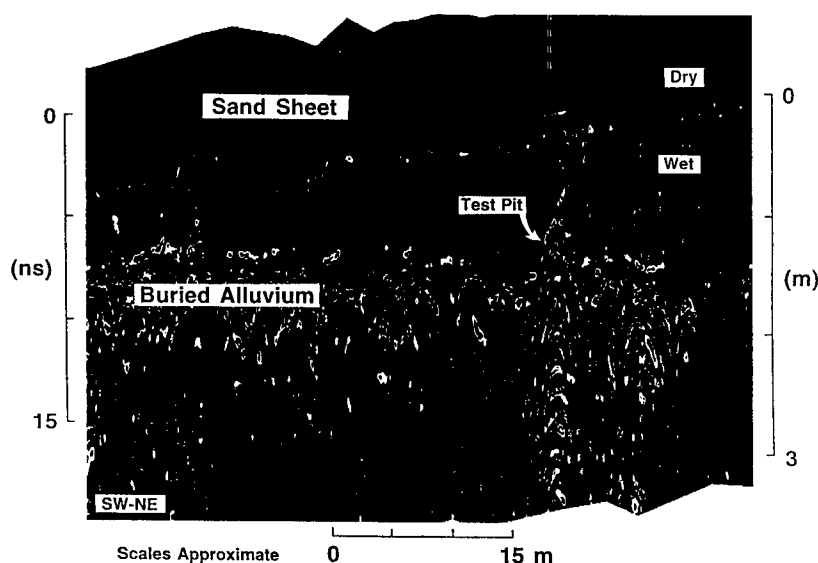
Fig. 3. Portion of a ground penetrating radar (GPR) transect completed down the eastern outer flank of Roter Kamm. Data delineate a reflection beneath the regional sand sheet sediments corresponding to the top of extensive alluvium whose thickness exceeds the penetration depth of the GPR. Comparable accumulations of alluvium occur on at least the east and south flanks of the crater [8]. The reflection within the sand sheet marks the transition from dry to damp sand and highlights the sensitivity of the GPR to changing moisture.

With only one exception, all GPR reflections delineated beyond the base of the exterior flank of the crater are created by nodular to massive pedogenic calcrete horizons and/or bedrock. An isolated GPR reflection identified on a slightly elevated surface 2.4 crater radii north of the rim, however, corresponds to a deposit of coarse, unsorted, angular-to-subangular fragments that are supported in a finer-grained matrix. These fragments are coarser, more poorly sorted, and more angular than the fragments comprising either the alluvial deposits on the crater flank and the pedogenic calcretes noted above. Moreover, grain mounts of constituent fragments display abundant planar deformation features and confirm their involvement in the impact event. On the basis of these attributes, the deposit is identified as preserved ejecta that have been modified by colluvial and pedogenic processes, but remained largely *in situ*. The isolated deposit comprises the only ejecta identified to date at Roter Kamm.

Interestingly, the properties of the Roter Kamm ejecta [8] are remarkably similar to those at Meteor Crater [6] for the range of sizes evaluated despite differences in involved target rocks. The

moderate to high rates of surface infiltration and hydraulic conductivity indicated by these ejecta size distributions [30] likely plays an important role in controlling the amount of runoff on the ejecta that is available for development of fluvial degradation signatures.

Topographic, GPR, and sedimentologic data from in and around Roter Kamm assist in distinguishing deposits preserving at least a partial record of crater degradation [8]. Although well-preserved from a structural standpoint, these data reveal that erosion accounts for nearly complete removal of the continuous ejecta deposit, approaches 50 m in higher relief near-rim areas, and accounts for an increase in the diameter of the crater by ~10%.

As discussed in Grant *et al.* [8], several factors indicate that degradation of ejecta at Roter Kamm resulted from mostly fluvial and lesser eolian activity: A) the broad extent and sedimentologic properties of alluvium within and around the crater; B) deep incisement of the crater rim; and C) nearly complete redistribution of coarse ejecta fragments that are too large for transport by eolian processes. Stratigraphic and climatic data [31, 32] reveal that alluvial activity would have been most important during the pre-Pleistocene history of the crater and was followed by more recent eolian modification associated with arrival of the regional sand sheet. It is likely that mass wasting played an important role in early degradation of the crater interior when the gradients on the walls were much higher than at present [*e.g.*, see 14, 20, 33]. Any deposits associated with such activity, however, remain undetected. The low slope presently characterizing the crater walls together with the inability to detect these deposits through thick overlying alluvium and eolian fill imply significant mass wasting was mostly confined to the earliest history of crater modification.

Significant denudation at Roter Kamm has been accomplished by mass wasting, fluvial, and eolian activity whose relative importance likely varied in chronological order [8]. Significant mass-wasting probably characterized early back-wasting of the crater wall and colluvial redistribution of ejecta fragments, but became less important as wall slopes were reduced by runoff. Fluvial activity accounts for most of the erosion at the crater and has accomplished nearly complete removal of the continuous ejecta deposit. Ongoing eolian redistribution of sediments associated with the regional sand sheet effectively mask many of the older mass-wasting and fluvial signatures evolved at the crater. Nevertheless, diagnostic evidence of the importance of fluvial processes persists in the form of a deeply incised rim and low wall slopes. The absence of preserved ejecta and the modified form of Roter Kamm suggest that cratering models would be of limited usefulness as tools for understanding anything more than the first-order formation mechanics.

The preceding discussion of Meteor Crater and Roter Kamm serve to illustrate the ability to constrain the amount and processes of degradation affecting impact craters. Results from Meteor Crater and Roter Kamm together with data collected from field and/or remote evaluation of other simple, unglaciated craters permit definition of a general evolutionary sequence for terrestrial crater degradation.

A FIRST-ORDER DEGRADATION SEQUENCE FOR SIMPLE TERRESTRIAL CRATERS

The degradation state of several other terrestrial craters/structures has also been investigated. This ongoing effort includes field work at the Odessa Craters ($31^\circ45$'N, $102^\circ29$'W), Texas [34] and the results of remote investigation of Lonar Crater (20°N, 76.5°E) and the Ramgarh Structure ($25^\circ20$'N, $76^\circ37$'E), India, the Pretoria Saltpan ($25^\circ34$'S, $28^\circ5$'E), South Africa, and Talemzane Crater (33.3°N, 4.0°E), Algeria [7, 35] All of these craters are formed into nearly flat-lying sedimentary and/or volcanic and/or crystalline rocks.

The Odessa Craters consist of a main depression that is ~0.17 km diameter and several smaller depressions that were formed simultaneously ~25,000 Ka [36, 37]. Lonar Crater is 1.8 km in diameter and was formed 62 Ka [38, 39], whereas the Ramgarh structure is 4.1 km in diameter and of unknown age [40]. The Pretoria Saltpan is 1.13 km in diameter and approximately 200 Ka [41]. Talemzane Crater is 1.75 km in diameter and formed sometime between 0.5-3.0 Ma [42, 43]. Comparative analysis of the degradation signatures at these structures permits definition of a sequence of diagnostic morphologic characteristics that may accompany advancing crater degradation by fluvial, mass wasting, and eolian processes (see Grant and Schultz [7, 8, 35]).

For example, analysis of evolved degradation signatures reveals that mass wasting on interior crater walls is typically most important during early crater modification. Mass-wasting is then superseded by fluvial activity as unconsolidated and fractured debris is shed from the crater walls and slopes are reduced to and then below the angle of repose (Fig. 4). Modification of the exterior of the craters by mass wasting is limited primarily to local redistribution of fragments by colluviation. Once important, fluvial degradation of crater interiors proceeds rapidly as a result of the initially higher slopes and low infiltration rates characteristic of the crater walls. Resultant high

stream power within the craters leads to rapidly evolving systems that initially incise increasingly inactive debris chutes and quickly erode headward to first notch and then incise the crater rim (Fig. 4). Eventually, the interior drainages breach the rim and begin to capture the headward reaches of basins draining the crater exterior, thereby leading to further crater infilling, steady reduction in wall slopes, and crater enlargement (Fig. 4). By contrast, the drainages evolving outside of the craters steadily increase in size and density as they strip most or all of the continuous ejecta, but they do not achieve the scale of the systems within the craters. One factor important in controlling the scale of exterior drainages is the high infiltration rate and hydraulic conductivity within the ejecta that impedes runoff. The larger scale and increasing density of the interior systems (Fig. 4) means that they are more readily detected and measured than the smaller scale systems evolving around the craters. Wall slopes, drainage density, and drainage scale (or degree of incisement) all change systematically with increasing fluvial degradation and are relatively easy to measure. These parameters, therefore, are considered to be the least ambiguous indicators of increasing stages of fluvial degradation. Eolian erosion of craters is mostly limited to primary and secondary deflation of fines from exposed ejecta, colluvial, and alluvial surfaces, and development of small-scale ventifacts and yardangs. Although potentially responsible for transport of significant material derived from erosion of ejecta by a range of processes, primary eolian erosion is typically subordinate to modification by alternate processes. Eolian erosion may be briefly more important for a short period following crater formation when surfaces are not yet stabilized by the effects of alternate, more competent processes. Significant eolian deposition can be responsible for considerable crater infilling and masking of many signatures evolved by the action of alternate processes. Nevertheless, the higher relief associated with crater rims inhibits burial and frequently enables measure of wall slope, rim incisement, and drainage density to assess the degree of fluvial modification.
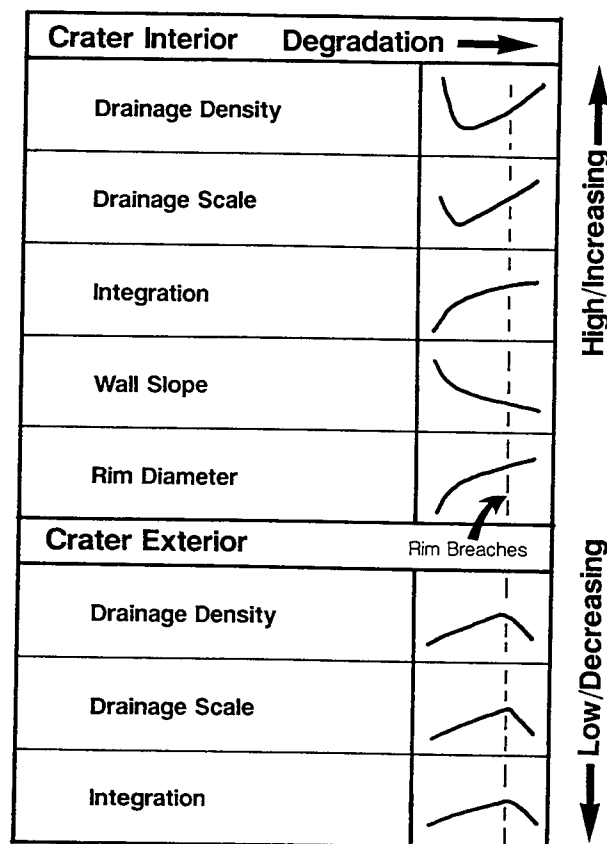
Fig. 4. Qualitative illustration of characteristic signatures associated with advancing fluvial degradation of simple, unglaciated impact craters on the Earth.

SUMMARY

Based on the preceding discussion, the craters/structures examined to date can be placed in order of increasing degradation state (Fig. 5): Meteor Crater, Lonar Crater, Ramgarh Structure, Pretoria Saltpan, Odessa, Talemzane, and Roter Kamm. Although largely qualitative, the first order sequence presented in figure 5 does permit assignment of processes most responsible for modification and, in many instances, places broad limits on the scale and degree to which primary formational characteristics of impact craters can be resolved. Such information can also be useful for evaluating the amount and process(es) of degradation operating on other planets.

Stages of Crater Degradation
Simple, Unglaciated Craters

Immediate Post–Formation
0 Years

Incised Debris Chutes

Small Gullies

Fans

◀── **Meteor Crater**
50,000 Years
1.2 km Diameter
Exterior Drainage Density = 8.6 km/km² (Mapped)
3.4 km/km² (Air Photo)
Interior Drainage Density = 13.7 km/km²
Interior Slope = 30°-49°

Incised Rim

Continued Incisement

Fans?

◀── **Lonar Crater**
62,000 Years
1.8 km Diameter
Exterior Drainage Density = 4.3 km/km²
Interior Drainage Density = 4.6 km/km²
Interior Slope = 35°-36°

◀── **Ramgarh Structure**
◀── **Pretoria Saltpan**

Patchy Ejecta

Captured Drainage

Low Gradient Drainage

Fans?

◀── **Talemzane Crater**
0.5-3.0 Million Years
1.75 km Diameter
Near-Rim/Interior Drainage Density = 6.5 km/km²
Interior Slope = 22°-35°

◀── **Roter Kamm**

▦ Ejecta

▦ Crater Fill

All Target Rocks Flat-Lying
(Not to Scale)

Fig. 5. Graphic illustration of a first-order degradation sequence for simple, unglaciated impact craters on the Earth. The relative degradation state of craters discussed in the text is indicated along with characteristic variations in drainage density, scale, and interior wall slope. Further definition of signatures evolved around other terrestrial craters should help to place more quantitative limits on the degradation stages, thereby enabling better resolution of pristine versus degradational characteristics associated with craters on the Earth and planets.

For example, Martian impact craters display a tremendous range in morphology. Some (Fig. 6) reveal evidence of extensive crater wall incisement, rim breaching, and reduction of wall slopes below the angle of repose [*e.g.* 44]. Although the size/type of the Martian crater illustrated in Figure 6 (complex versus simple) and associated geologic and climatic setting may not be directly analogous to those discussed for the terrestrial craters examined so far, cited degradation characteristics appear indicative of considerable fluvial modification. Refinement of terrestrial crater degradation sequences may eventually permit more quantitative evaluation of this and other Martian craters and help to confirm the possible role of running water in crater degradation.

Further, results might assist in assessment of the amount and source of any water involved in the development of observed features (*e.g.*, runoff vs. groundwater sapping vs. mass wasting or other source, see [45-49]).
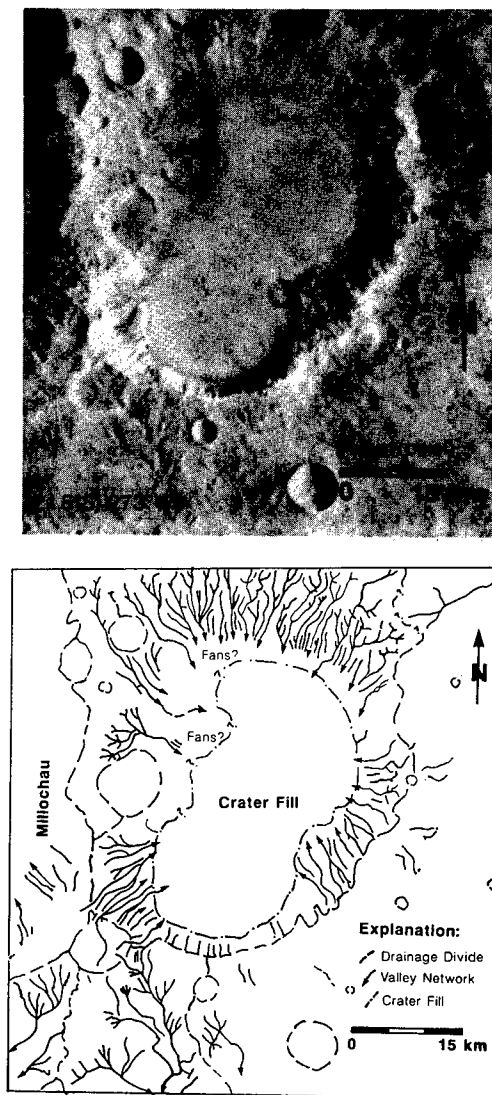
Fig. 6. Viking Orbiter image and geomorphic map of a degraded impact crater located east of Crater Millochau in Terra Tyrrhena, Mars [44]. While perhaps not directly analogous to the terrestrial craters discussed, the Martian crater displays an incised rim, low sloping walls, and significant infilling that may reflect modification by running water. Better definition of the characteristic signatures associated with increasing degradation by mass-wasting, fluvial, and eolian processes could eventually enable constraint of the amount and source of any water involved in development of the observed morphology.

Knowledge of degradation state and the history of active erosional processes can enable distinction between pristine and degradational characteristics of craters on the Earth and planets, thereby assisting in definition of ground truth for efforts geared towards modeling crater formation and understanding the influence of environmental variables on resultant crater morphology.

REFERENCES

1. P.H. Schultz, Atmospheric effects on cratering efficiency. *J. Geophys. Res.*, **97**, 975-1005 (1992).
2. P.H. Schultz, Atmospheric effects on ejecta emplacement. *J. Geophys. Res.*, **97**, 11,623-11,662 (1992).
3. P.H. Schultz and D.E. Gault, Atmospheric effects on Martian ejecta emplacement. *J. Geophys. Res.*, 84(B13), 7669-7687 (1979).
4. P.H. Schultz and J.A. Grant, Styles of ejecta emplacement, Meteor Crater. *Lunar and Planet. Sci. XX*, pp. 972-973, LPI, Houston, TX, March (1989).
5. O.S Barnouin-Jha and P.H. Schultz, Ejecta entertainment by impact-generated vortices: Theory and experiments. *J. Geophys. Res.*, **101**, 21,099-21,116 (1986).
6. J.A. Grant and P.H. Schultz, Erosion of Ejecta at Meteor Crater, Arizona. *J. Geophys. Res.*, **98**, 15,033-15,047 (1993).
7. J.A. Grant and P.H. Schultz, Degradation of selected terrestrial and Martian impact craters. *J. Geophys. Res.*, **98**, 11,025-11,042 (1993).
8. J.A. Grant, C. Koeberl, W.U. Reimold, and P.H. Schultz, Gradation of the Roter Kamm impact Crater, Namibia. *J. Geophys. Res.*, **102**, 16,327-16,388 (1997).
9. J.A. Grant and P.H. Schultz, Erosion of ejecta at Meteor Crater: Constraints from ground penetrating radar. *Proc. 5th Int. Conf. on Ground Penetrating Radar (GPR '94)*, pp. 789-803, June 12-16, 1994, Kitchener, Ontario, Canada, June (1994).
10. E.M. Shoemaker and S.E. Kieffer, *Guidebook to the geology of Meteor Crater, Arizona:*. Arizona State Univ. Cent. Meteorite Stud. Pub. **17**, Tempe, AZ, 66pp. (1974).
11. E.M. Shoemaker, *Impact mechanics at Meteor Crater, Arizona:*. Ph.D. Dissertation, Princeton Univ., Princeton, NJ, 55pp. (1960).
12. E.M. Shoemaker, Meteor Crater, Arizona. In *Centennial Field Guide, v. 2, Rocky Mountain Section of the Geological Society of America* (edited by S.S. Beus), pp. 399-404, Geol. Soc. Am., Boulder, CO (1987).
13. D.J. Roddy, J.M. Boyce, G.W. Colton, and A.L. Dial, Jr., Meteor Crater, Arizona, rim drilling with thickness, structural uplift, diameter, depth volume, and mass-balance calculations. *Proc. 6th Lunar and Planet. Sci. Conf.*, pp. 2621-2644, LPI, Houston, TX (1975).
14. D.J. Roddy, Pre-impact geologic conditions, physical properties, energy calculations, meteorite and initial crater dimensions and orientations of joints, faults, and walls at Meteor Crater, Arizona. *Proc. 9th Lunar and Planet. Sci. Conf.*, pp. 3891-3930, LPI, Houston, TX (1978).
15. S.R. Sutton, Thermoluminescence measurements on shock-metamorphosed sandstone and dolomite from Meteor Crater, Arizona: 2. Thermoluminescence age of Meteor Crater. *J. Geophys. Res.*, 90(B5), 3690-3700 (1985).
16. K. Nishiizumi, C.P. Kohl, E.M. Shoemaker, J.R. Arnold, D. Lal, J. Klein, D. Fink, and R. Middleton, In Situ Be[10]-Al[26] exposure ages at Meteor Crater, Arizona. *Lunar and Planet. Sci. XX*, pp. 792-793, LPI, Houston, TX (1989).
17. J.A. Pilon, R.A.F. Grieve, and V.L. Sharpton, The subsurface character of Meteor Crater, Arizona, as determined by ground-probing radar. *J. Geophys. Res.*, **96**, 15,563-15,576 (1991).
18. F.M. Phillips, M.G. Zreda, S.S. Smith, D. Elmore, P.W. Kubik, R.I. Dorn, and D.J. Roddy, Age and geomorphic history of Meteor Crater, Arizona, from cosmogenic ^{36}Cl and ^{14}C in rock varnish. *Geochim. Cosmochim. Acta*, **55**, 2695-2698 (1991).
19. D.J Roddy, S.H. Schuster, K.N. Kreyenhagen, and D.L. Orphal, Computer code simulations of the formation of Meteor Crater, Arizona: Calculations MC-1 and MC-2. *Proc. 11th Lunar and Planet. Sci. Conf.*, pp. 2275-2308, LPI, Houston, TX (1980).
20. J.B. Garvin, J.L., Bufton, B.A., Campbell, and S.H. Zisk, Terrain analysis of Meteor Crater ejecta blanket. *Lunar and Planet. Sci. XX*, pp. 333-334, LPI, Houston, TX (1989).
21. R.McG. Miller and K.E.L. Schalk, *Namibia Geological Map.* Geological Survey of Namibia, Windhoek, Namibia (1980).
22. C. Koeberl, J.B. Hartung, M.J. Kunk, J. Klein, J.I. Matsuda, K. Nagao, W.U. Reimold, and D. Storzer, The age of the Roter Kamm impact crater, Namibia: Constraints from ^{40}Ar-^{39}Ar, K-Ar, Rb-Sr, fission-track, and ^{10}Be-^{26}Al studies. *Meteoritics*, **28**, 204-212 (1993).
23. E.D. McKee, Sedimentary Structures in Dunes of the Namib Desert, South West Africa. *Geol. Soc. Am. Spec. Paper* **188**, Geol. Soc. Am., Boulder, CO, 64pp. (1982).
24. R.F. Fudali, Roter Kamm: Evidence for an impact origin. *Meteoritics*, **8**, 245-257 (1973).
25. R.S. Dietz, Roter Kamm, Southwest Africa: Probable meteorite crater. *Meteoritics*, **2**, 311-314 (1965).
26. R.McG. Miller and W.U. Reimold, Deformation and shock deformation in rocks from the Roter Kamm crater, SWA/Namibia. *Meteoritics*, **21**, 456-458 (1986).
27. W.U. Reimold and R.McG. Miller, The Roter Kamm impact crater, SWA/Namibia. *Proc. 19th Lunar and Planet. Sci. Conf.*, pp. 711-732, LPI, Houston, TX (1989).

28. W.U. Reimold, R.McG. Miller, R.A.F. Grieve and C. Koeberl, The Roter Kamm impact structure in SWA/Namibia. *Lunar and Planet. Sci. XIX,* pp. 972-973, LPI, Houston, TX (1988).

29. W.U. Reimold, C. Koeberl and J. Bishop, Roter Kamm impact crater, Namibia: Geochemistry of basement rocks and breccias. *Geochim. Cosmochim. Acta,* **58,** 2689-2710 (1994).

30. W.K. Summers and P.A. Weber, The relationship of grain-size distribution and hydraulic conductivity - an alternate approach. *Groundwater,* **22,** 474-475 (1984).

31. Cooperative Holocene Mapping Project (COHMAP) Members, Climatic changes of the last 18,000 years: Observations and model simulations. *Science,* **241,** 1043-1052 (1988).

32. P.B. deMenocal, Plio-Pleistocene African climate. *Science,* **270,** 53-59 (1995).

33. R.A.F. Grieve and J.B. Garvin, A geometric model for excavation and modification at terrestrial simple impact craters. *J. Geophys. Res.,* **89,** 11,561-11,572 (1984).

34. J.A. Grant and P.H. Schultz, Characteristics of Ejecta and Alluvial Deposits at Meteor Crater, Arizona and Odessa Craters, Texas: Results from Ground Penetrating Radar. *Lunar and Planet. Sci. XXII,* pp. 481-482, LPI, Houston, TX (1991).

35. J.A. Grant and P.H. Schultz, Gradational Evolution of Young, Simple Impact Craters on the Earth. *Lunar and Planet. Sci. XXII,* pp. 483-484, LPI, Houston, TX (1991).

36. E.H. Sellards and G.L. Evans, *Statement of Progress of Investigation at Odessa Meteor Craters:* Univ. of Texas, Bur. Econ. Geol., 12pp. (1941).

37. G.L. Evans, Investigations at the Odessa meteor craters. *Proc. Geophys. Lab./Lawrence Rad. Lab. Cratering Symp.,* Wash., D.C., March 1961 (edited by M.D. Nordyke), 11pp., Paper D, Univ. Calif. Livermore Rad. Lab. Rept. UCRL-6438, Livermore, CA (1961).

38. K. Fredriksson, A. Dube, D.J. Milton, and M.S. Balasundaram, Lonar lake, India: An impact crater in basalt. *Science,* **180,** 862-864 (1973).

39. R.A.F. Grieve, C.A. Wood, J.B. Garvin. G. McLaughlin, and J.F. McHone, Jr., *Astronaut's Guide to Terrestrial Impact Craters.* LPI Tech Rpt. **88-03,** LPI, Houston, TX, 89pp. (1988)

40. A.V. Murali and K.P. Lulla, Ramgarh Crater, Rajasthan, India: Study of multispectral images obtained by Indian Remote Sensing Satellite (IRS-IA). *Geocarto International,* **7,** 75-80 (1992).

41. W.U. Reimold, C. Koeberl, T.C. Partridge, and S.J. Kerr, Pretoria Saltpan crater: Impact origin confirmed. *Geology,* **20,** 1079-1082 (1992).

42. R. Karpoff, The meteorite crater of Talemzane in southern Algeria. *Meteoritics,* **1,** 31-38 (1963).

43. P. Lambert, J.F. McHone, Jr., R.S. Dietz, and M. Houfani, Impact and impact-like structures in Algeria, Part 1. Four bowl-shaped depressions. *Meteoritics,* **15,** 157-179 (1980).

44. J.A. Grant and P.H. Schultz, Early fluvial degradation in Terra Tyrrhena, Mars: Constraints from styles of crater degradation on the Earth. *Lunar and Planet. Sci. XXV,* pp. 457-458, LPI, Houston, TX (1994).

45. M.H. Carr, *The Surface of Mars.* Yale University Press, New Haven, CT, 232pp. (1981).

46. V.R. Baker, *The Channels of Mars.* University of Texas press, Austin, TX, 198pp. (1982).

47. Mars Channel Working Group, Channels and valleys on Mars. *Geol. Soc. Am. Bull.,* **94,** 1035-1054 (1983).

48. M.H. Carr and F.C. Chuang, Martian drainage densities. *J. Geophys. Res.,* **102,** 9145-9152 (1997).

49. J.A. Grant, 1997, Geologic mapping and drainage basin analysis in Margaritifer Sinus, Mars. *Lunar and Planet. Sci. XXVIII,* pp. 451-452, LPI, Houston, TX (1997).

SHOCK HUGONIOT AND RELEASE IN CONCRETE WITH DIFFERENT AGGREGATE SIZES FROM 3 TO 23 GPa

C.A. HALL, L.C. CHHABILDAS, and W.D. REINHART

Sandia National Laboratories[*]
Albuquerque, NM 87185-1181

Summary- A series of controlled impact experiments has been performed to determine the shock loading and release behavior of two types of concrete, differentiated by aggregate size, but with average densities varying by less than 2 percent. Hugoniot stress and subsequent release data was collected over a range of approximately 3 to 25 GPa using a plate reverberation technique in combination with velocity interferometry. The results of the current data are compared to those obtained in previous studies on concrete with a different aggregate size but similar density. Results indicate that the average loading and release behavior are comparable for the three types of concrete discussed in this paper. Residual strain is also indicated from these measurements. © 1999 Elsevier Science Ltd. All rights reserved.

INTRODUCTION

Considerable interest in characterizing the dynamic response of concrete under impact or explosive loading exists because it is used extensively as a structural material. Concrete is a heterogeneous composite, typically consisting of quartz aggregate and cement grout, which makes it difficult to characterize its dynamic loading behavior to the same degree of accuracy as for a homogeneous material. Local variations in the shock and particle velocities due to impedance differences within the material cause fluctuations in the measured particle velocity profiles. A deliberate attempt to average these local variations was made in this study by using "thick" copper and tantalum plates. Plate thickness was controlled, however, to also allow determination of isentropic decompression states. The plate reverberation technique has been used to determine the shock loading and release states in which the plate response is strictly elastic (1,2). The technique was extended for use at high pressures to determine the dynamic re sponse of quartz (3) and concrete (4). In the latter configurations, as well as in this investigation, the dynamic response of the plate was no longer elastic.

MATERIAL DESCRIPTION

The concrete used in the present study had two distinct aggregate size distributions. The concrete referred to as large aggregate had an ASTM aggregate size number of 57 (5). This implies that 5% of the material by weight is between 25 mm and 37.5 mm, 40% to 75% is between 19 mm and 25 mm and the balance is 4.75 mm or smaller (6). The concrete referred to as small aggregate had an ASTM aggregate size number of 7 (5), which means 10% of the material by weight is 12.5 mm, 30% to 60% is 9.5 mm and the balance is 4.75 mm or smaller (6). Cores were taken from large castings in both cases to ensure representative responses. Samples were obtained from each core by grinding to precise dimensions and measurements made to determine the density of each sample. Results are listed in Table 1.

Ultrasonic measurements of longitudinal, C_L, and transverse, C_S, sound speeds were made on each concrete core and individual sample prior to use. A group of samples was selected for use in the experiments that had fairly consistent sound speeds. From the samples selected, an average value for the longitudinal and transverse sound speed was determined for each aggregate size. The bulk sound speed, C_o, and Poissons ratio, v, were calculated from these averages for each concrete type using equation 1. These values are also listed in Table 1.

$$C_0 = \left[C_L{}^2 - \frac{4}{3}\left(C_S{}^2\right) \right]^{\frac{1}{2}} \quad \text{and} \quad v = \frac{C_L{}^2 - 2C_S{}^2}{2\left(C_L{}^2 - C_S{}^2\right)} \tag{1}$$

The concrete previously tested (4,7,13) is referred to as SAC-5. The largest percentage of aggregate present in the mix had a maximum size of approximately 10mm with finer aggregates present in lesser amounts (8). Ultrasonic measurements and calculated values of sound speeds for SAC-5 concrete (4) are also listed in Table 1 for comparison.

Table 1: Characteristics of Large and Small aggregate concrete used in present studies

Concrete Type	Average Density (kg/m³)	Longitudinal Wave Speed C_L (km/s)	Shear Wave Speed C_S (km/s)	Bulk Wave Speed C_0 (km/s)	Poissons Ratio v
Large Agg	2357.4	5.057[a] / 4.983[b]	2.991	3.694	0.231
Small Agg	2334.3	4.555[a] / 4.685[c]	2.657	3.367	0.241
SAC-5 (4)	2313.1	5.06 / 4.45	2.68	3.20	0.22

a: average sample thickness, approximately 30mm
b: average sample thickness, approximately 90mm
c: average sample thickness, approximately 60mm

EXPERIMENTAL TECHNIQUE

The experiments were performed on an 89mm diameter, smooth bore powder gun which is capable of generating impacts in the 0.5 km/s - 2.4 km/s range. The tilt between impactor and target plate, exit velocity of the projectile, and particle velocity from the rear surface of the metallic target plate were measured during each experiment.

The configuration used for this experimental series is shown in Figure 1. The projectile consisted of a concrete sample attached to the aluminum projectile nose plate and phenolic body.

This projectile assembly traveled through the launch tube of the gun and exited with velocity V_i. The target was a thin metal plate which was inserted into an aluminum target holder. A series of four coaxial shorting pins were mounted into the target plate and preset to be flush with the impacting surface. The time between impact of each pin was measured and related to the angle, or tilt, between the two impacting surfaces. Typical tilt measurements in this experimental series were between 0.5 and 2 milliradians. A series of three shorting pins were set at various known heights based on expected impact velocity. The time interval between impact on each of these pins was measured to provide impact velocity, V_i, within 0.5%.

Two beams of 514.5nm laser light were diffusely reflected from the rear surface of the metallic target plate. The velocity of this free surface, resulting from projectile impact, was measured with velocity interferometers referred to as VISARs (9). Two VISARs were used on each of the large aggregate experiments to determine the magnitude of local velocity variations within the concrete. By collecting information from multiple points, variations in velocity profiles that result from heterogeneous aggregate distributions can be used as an indication of the amount of local variations expected within a given concrete sample experiencing identical loading conditions. This provides a baseline range of variation in particle velocity profiles and is particularly useful when comparing the response of different types of concrete. The diameter of the smaller aggregate samples allowed only one VISAR measurement. The laser beam from the VISAR was placed in the center of these smaller diameter samples to obtain a maximum reading time before release waves influenced the data.
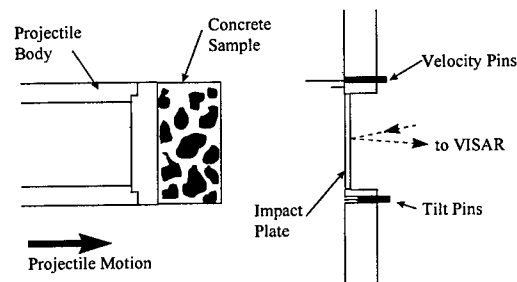
Fig. 1. Experimental configuration for plate reverberation experiments.

As shown in Figure 1, a sample whose Hugoniot and release characteristics are being investigated (concrete), impacts a thin, high impedance plate (tantalum or copper). Upon impact, a shock wave propagates into both the concrete and metal. The resulting stress state is indicated as 1 in the stress (P) versus particle velocity (u_p) diagram of Figure 2. When this stress wave reaches the free surface of the metal, a left going release wave travels back into the metal plate as a release fan, while accelerating the plate to a velocity indicated by state 2. This is shown schematically in the X-t diagram of Figure 3. As the waves reverberate between the impact and free surfaces of the metallic plate, they incrementally relieve the stress in the concrete sample by alternately satisfying the free and impact surface boundary conditions. Continuous measurements of particle velocity in the metallic plate were made using the velocity interferometer. The resulting velocity profiles are shown in Figure 4. These records show incremental velocity steps which at times are not easily distinguishable due to material nonlinearities, but correspond to the even numbered, 2,4,6, etc., states. The odd numbered release states, 3, 5, 7, etc., of the concrete can be inferred by knowledge of the Hugoniot and release adiabat of the metallic plate material. In an isentropic release process approximation, an approach

using stress and particle velocity decrements can be employed to calculate the release path. This technique will satisfy the simple wave approximations until the first attenuating release wave from the concrete arrives at the impact surface. Sample dimensions are optimized to ensure attenuating shock reflections do not occur during times of interest.
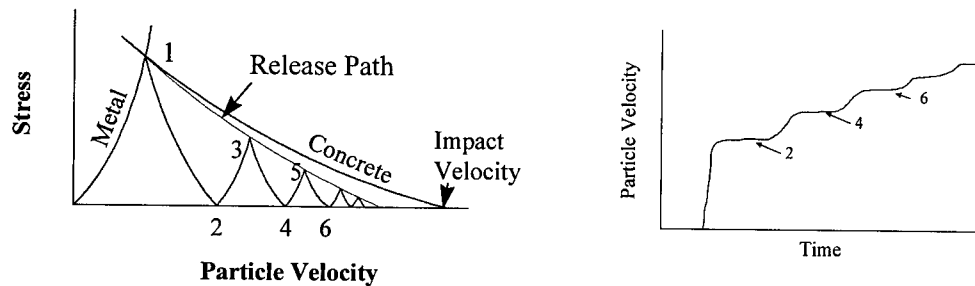
Fig. 2.   P-u_p diagram of concrete impacting a metallic plate with expected (corresponding) particle velocity trace
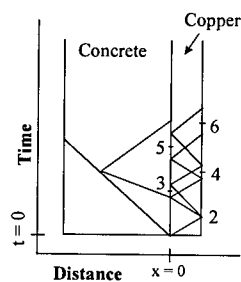
Fig. 3.   X-t diagram of concrete impacting a metallic plate

EXPERIMENTAL PARAMETERS AND VELOCITY PROFILES

The experimental parameters used in this investigation are given in Table 2.   The parameters were intended to closely match those used during the SAC-5 work (4) to make meaningful comparisons.   Metallic target plates used in this experimental investigation were increased in thickness due to the larger aggregate sizes within the concrete.   This allowed local variations that existed due to the heterogeneous nature of the concrete to converge to a magnitude representing an average response. Both copper and tantalum were used as target plates.   Since tantalum has a higher shock impedance, a higher Hugoniot stress state is obtained in the concrete for a given impact velocity.   Results for the experiments using copper and tantalum as target plates are shown in Figure 4.

HUGONIOT PROPERTIES

In this experimental investigation, shock waves are introduced into both the target plate and impactor by way of a high velocity, planar impact between the two materials. In typical experiments, measurements of shock velocity and particle velocity are made directly on the sample of interest.   For a highly heterogeneous material such as concrete, however, the

measurements of these parameters are best made through an averaging medium such as a homogeneous metallic plate. Therefore, the concrete becomes the impactor and particle velocity measurements are made on the rear free surface of the metallic plate. Upon impact, the plate achieves a common Hugoniot stress state which is inferred from the measured free surface particle velocity data. Using the free surface velocity approximation of equivalent loading and release behavior, the particle velocity in the metallic plate at the Hugoniot state 1 is one half the particle velocity measured with the VISAR at state 2; or $u_2/2$. The stress is then given by $\sigma_m = \rho_{0m}U_m\,(u_2/2)$ where the subscript m refers to the metallic plate. U_m is the corresponding shock velocity in the metallic plate for a particle velocity of $u_2/2$.

Table 2. Experimental parameters for large and small aggregate concrete

Shot Number	Aggregate Type	Concrete Density (kg/m^3)	Concrete Dimensions (Dia x thk)	Target Material	Target Thickness* (mm)	Impact Velocity (km/s)
LC-1	Large	2353.9	87.45 x 30.03	copper	3.51	0.464
LC-2	Large	2356.1	87.44 x 30.03	copper	3.52	0.797
LC-3	Large	2356.1	87.44 x 30.01	copper	3.52	1.34
LC-4	Large	2363.4	87.44 x 30.00	copper	3.50	1.74
LC-5	Large	2356.7	87.44 x 30.01	copper	3.50	2.15
LC-7	Large	2354.0	87.44 x 30.02	tantalum	1.85	2.14
SC-1	Small	2340.2	59.61 x 30.00	copper	3.50	2.143
SC-2	Small	2347.9	59.61 x 30.01	copper	3.50	1.748
SC-3	Small	2321.6	59.64 x 30.01	copper	3.50	1.33
SC-4	Small	2340.6	59.62 x 30.01	tantalum	1.86	2.175
SC-5	Small	2327.7	59.62 x 30.01	copper	3.52	0.83
SC-6	Small	2327.5	59.63 x 30.00	copper	3.52	0.451

* Nominal target plate diameter of 73.7 mm in all experiments

Table 3. Hugoniot parameters for copper and tantalum

Material	Density kg/m^3	Co km/sec	S
Copper	8924	3.91	1.51
Tantalum	16656	3.43	1.19

The stress and particle velocity in the concrete and metallic plate are continuous at the impact interface as indicated in the P-u_p diagram of Figure 2, i.e. $\sigma_m = \sigma_c$. The particle velocity in the concrete is given by the relation $u_c = V_i - u_2/2$. The corresponding shock velocity U_c and strain can be obtained using $U_c = \sigma_c/(\rho_{0c}u_c)$ and $\varepsilon_c = u_c/U_c$. Hugoniot results for the large and small aggregate concrete are given in Table 4. A "b" on the end of a shot number refers to data obtained from a second VISAR on the same experiment. The results, including some lower pressure data on SAC-5 (12, 13), are plotted as stress vs. particle velocity and stress vs. strain in Figure 5. As can be seen, the results are tightly grouped in the P-u_p plane. Quadratic curve fits

through the data points, listed in Table 5, lie within an area bounded by scatter bars representing stress deviations due to local variations in the measured particle velocity at the Hugoniot state for each experiment.

Table 4. Hugoniot properties for large and small aggregate concrete

Shot Number	u_2 (km/s)	$u_2/2$ (km/s)	σ_h (Gpa)	u_c (km/s)	U_c (km/s)	ε_c
LC-1	0.15	0.075	2.79	0.387	3.06	0.13
LC-2	0.32	0.16	5.97	0.637	3.98	0.16
LC-2b	0.30	0.15	5.58	0.647	3.66	0.18
LC-3	0.59	0.295	11.43	1.048	4.63	0.23
LC-3b	0.53	0.265	10.26	1.075	4.05	0.27
LC-4	0.79	0.395	15.86	1.368	4.98	0.27
LC-4b	0.76	0.38	15.29	1.36	4.76	0.29
LC-5	1.00	0.50	20.92	1.65	5.38	0.31
LC-5b	0.89	0.445	18.29	1.71	4.55	0.37
LC-7	0.70	0.35	22.17	1.833	5.12	0.36
SC-1	0.95	0.475	19.71	1.668	5.05	0.33
SC-2	0.77	0.385	15.52	1.363	4.85	0.28
SC-3	0.60	0.30	11.75	1.030	4.91	0.21
SC-4	0.71	0.355	22.70	1.820	5.33	0.34
SC-5	0.32	0.16	6.01	0.669	3.86	0.17
SC-6	0.12	0.06	2.07	0.394	2.26	0.17
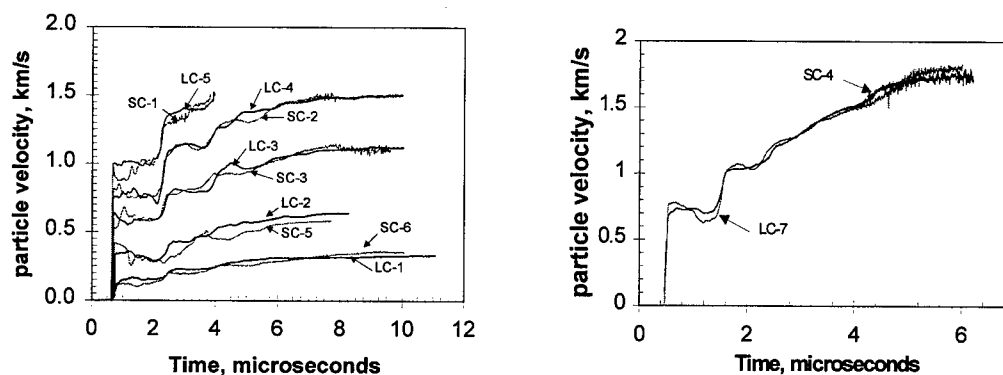
Figure 4. Particle velocity profiles for the Large and Small aggregate concrete experiments.
Figure (a) are experiments with copper target plates, and Figure (b) use tantalum plates.

This indicates that the loading response of concrete is somewhat independent of aggregate size at these stresses. Greater dispersion of the data is seen in the stress-strain plot. This is expected

since the strain varies as the square of the particle velocity. Any variations in the measured particle velocity profiles are therefore greatly magnified.

The shock velocity, U_s, versus particle velocity, u_p, Hugoniot data for the concrete, which is tabulated in Table 4, has been plotted in Figure 6. Also shown in the figure are the results of previous studies on other concrete both above (4) and within (13) the elastic regime. There appears to be a definite slope change in the concrete behavior above the initial elastic regime. A linear least squares fit to the large aggregate, small aggregate, and corresponding SAC-5 data yields $U_c = 2235 + 1.75u_c$. For comparison, the fit for the lower stress data is given by $U_c = 551 + 4.52u_c$. This behavior can be attributed to both the porosity and heterogeneous nature of the material. The large slope, S, indicated for the elastic behavior suggests that relatively large compressions are occurring in this pressure regime. As the stress increases beyond this point, considerably stiffer compaction behavior is indicated by the lower slope value. This phenomenon is also seen in the stress-strain response shown in Figure 5.

Table 5. Quadratic Curve Fits to Hugoniot Data Sets

Concrete Type	Quadratic Curve Fit
Large Aggregate	$\sigma = 2.361u_p^2 + 7.832u_p$
Small Aggregate	$\sigma = 2.731u_p^2 + 7.516u_p$
SAC-5	$\sigma = 3.411u_p^2 + 5.977u_p$
All Data Points	$\sigma = 2.925u_p^2 + 6.916u_p$

RELEASE STATES

As in determining Hugoniot states in this experimental configuration, the concrete decompression must be inferred using the measured particle velocity and calculated stress of the metallic plate at each release state. Once the Hugoniot point is established in the P- u_p plane, subsequent release stress states 3, 5, 7, etc can be determined within the metallic target plate through $\Delta\sigma_m = \rho_0 C_m \Delta u_m$ where ρ_0 is the initial density, C_m is the average unloading wave speed, and Δu_m is the change in particle velocity between states of interest. Both C_m, and Δu_m are determined from the experimental data. The time, Δt, between arrival of subsequent release fan midpoints represents the two way transient time within the metallic target plate, and is used to obtain the wave velocity. In a Lagrangian coordinate frame, $C_m = 2h/\Delta t$, where h is the plate thickness. Since stress and particle velocity are continuous for all release states across the impact interface, the change in stress and particle velocity in the concrete at any odd numbered unloading state in the P-u_p diagram is the same as that calculated for the metallic plate, or $\Delta\sigma_m = \Delta\sigma_c$ and $\Delta u_m = \Delta u_c$. Using the free surface velocity approximation between successive even numbered states shown in the P-u_p diagram of Figure 2, Δu_c, the particle velocity within the concrete, can be obtained from $\Delta u_c = \Delta u_m = 0.5(u_{x+2} - u_x)$, where x is states 2,4,6,8,etc. The corresponding average wave velocity within the concrete, C_c, can be estimated from $C_c = \Delta\sigma_c / (\rho_{0c}\Delta u_c)$. In this relation, $\Delta\sigma_c$ represents the difference in stress, ρ_{0c} is the initial density of the concrete, and Δu_c the difference in particle velocity between successive unloading states 1,3,5,7 etc in the concrete. The corresponding change in strain between states can be obtained through the relation $\Delta\varepsilon = \Delta u_c / C_c$. The stress and strain at each unloading state can be determined once the Hugoniot state is fixed from the relations $\sigma_{k+2} = \sigma_k - \Delta\sigma$ and $\varepsilon_{k+2} = \varepsilon_k - \Delta\varepsilon$, where k is the odd numbered release states 3,5,7, etc within the concrete. These results are shown in Figure 9. The

quadratic curve fits to the release data in the concrete are tightly grouped in the P-u_p plot. As with the Hugoniot curves, this would indicate that the release response of the concrete does not exhibit a great dependence upon aggregate size at these stress levels. Larger deviations are seen in the stress-strain plot. This can be partly attributed to the difficulty in determining an average particle velocity and two way transit time within the metallic plate as the steps become less discernible late in time. Also, the change in strain between release states is dependent upon the square of the corresponding change in particle velocity. This tends to amplify the dispersion in the strain states.
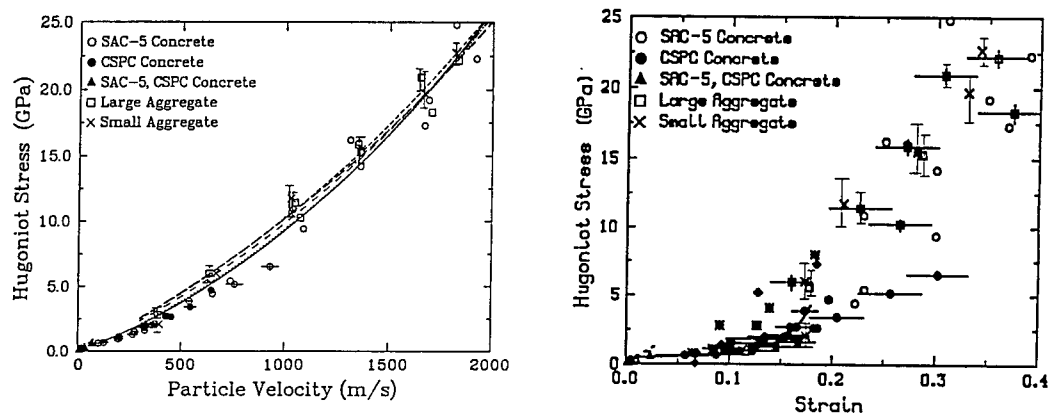
Fig. 5. Stress vs. particle velocity and Stress-strain graphs for Large aggregate, Small aggregate, SAC-5 and low stress concrete Hugoniot data.
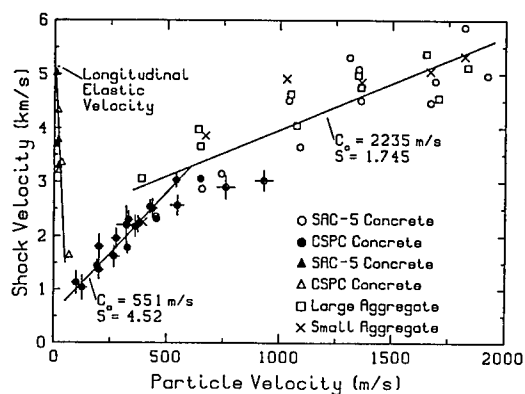
Fig. 6. Shock velocity vs. particle velocity for Large aggregate, Small aggregate, SAC-5 and low stress concrete Hugoniot data.

An indication of residual strain exists in each of the particle velocity records. In the latter part of each trace where discreet velocity steps are not easily distinguishable, the change in particle velocity per two way transit time in the target plate approaches zero. Consequently, $\Delta\varepsilon$ will be quite small. This implies that the value for strain will not vary greatly from that

calculated for the last detectable velocity step. Therefore, it appears that residual strain is present within the concrete samples in the latter stages of the unloading process. This is also indicated in Figure 7 where permanent compaction is indicated by the release curves in the stress-strain plot.

Additional insights into the release behavior of concrete beyond the domain of easily identifiable particle velocity steps can be gathered by assuming rigid body response of the target plate. This technique has been used by Grady on concrete (4), and Chhabildas on fused silica (3). Using this approach, target plate velocity measurements can be directly correlated to pressure using

$$P = \rho(x)(dV/dt) \tag{2}$$

where ρ is target plate density, x is plate thickness, and dV/dt is the local acceleration. Thus the measured particle velocity history and calculated pressure history allow determination of sound speed, and strain in the concrete due to continuity of pressure and particle velocity across the impact interface. Results of this form of analysis are shown in Figures 7 and agree well with results obtained using the incremental "reverberation" technique. One advantage of this additional form of analysis is that it extends the release to lower pressure states than before. These results agree with the previous indications that residual strain is present in the concrete samples.

COMPARISON WITH PREVIOUS STUDIES

In order to obtain a measure of the variations in particle velocity that can be expected within a particular type of concrete, two VISAR signals were recorded at separate locations on the same experiment. Results from experiments where both signals could be analyzed are shown in Figure 8. The largest deviation in local particle velocity is seen in shot number LC-3. As much as 29% deviation in local particle velocity is seen between the maximum and minimum values during initial loading. An approximate 5% deviation between average values can be observed as it converges towards a steady state Hugoniot response. These estimates provide an indication for the magnitude of particle velocity deviations at a particular state resulting from the heterogeneous nature of the concrete. One objective of this study is to compare the loading behavior of concrete with different aggregate sizes at these stress levels. One method for comparison is to overlay the particle velocity profiles obtained from corresponding experiments. To make these types of comparisons more meaningful, each profile should be normalized to obtain similarity in both time and velocity if the experimental parameters are not identical. Figure 9 shows the normalized velocity profiles for large aggregate, small aggregate, and the SAC-5 (4) concrete. The time axis is divided by the corresponding plate thickness in millimeters to obtain the transit time per unit thickness for each experiment. The velocity axis was not normalized since variations in impact velocity were small; less than 1% for the high velocity set, and 1.5% for the medium velocity set. These are well within the 5% variations observed from the two particle velocity profiles recorded on the same sample.

The average value for particle velocity at state 2, i.e. the Hugoniot state, in both the high and medium velocity experimental sets varies by no more than 5%. The average value for the lower velocity set varies by as much as 25% between the two particle velocity records which had the two larger aggregate sizes even though they differed by only 2% in impact velocity. This indicates that the material characteristics such as aggregate size are more significant at lower stress levels. These results suggest that the three concrete types do behave similarly at stress levels between approximately 2.5 Gpa and 25Gpa.
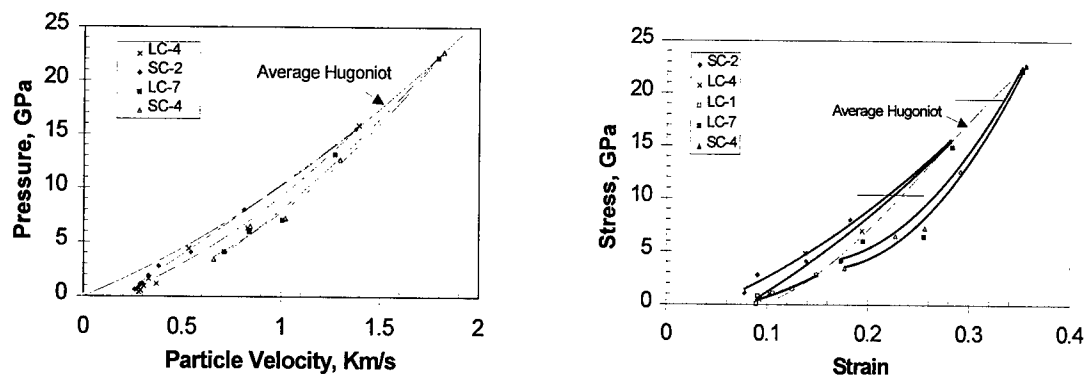
Fig. 7. Stress vs. particle velocity and Stress vs. Strain release curves for large and small aggregate concrete for high, medium and low stress regimes.
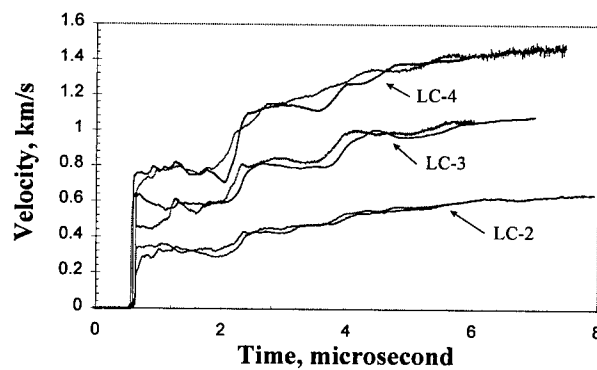
Fig. 8. Particle velocity profiles from two locations on the same experiment
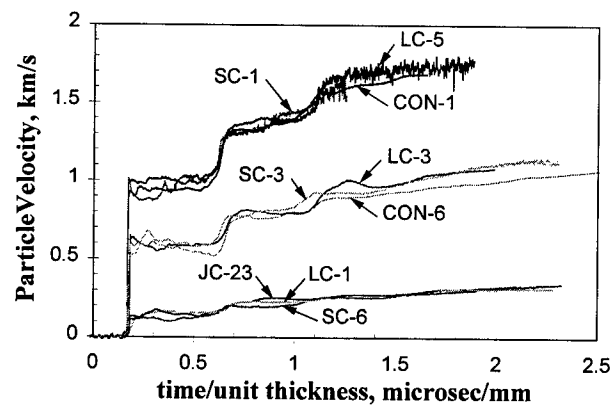
Fig. 9. Normalized particle velocity profiles for large aggregate, small aggregate, and SAC-5 concrete.

SUMMARY

In summary, a series of controlled impact experiments has been performed to determine the shock loading and release behavior of two types of concrete, differentiated by aggregate size, but with average densities varying by less than 2 percent. Hugoniot stress and subsequent release data was collected over a range of approximately 3 to 25 GPa using a plate reverberation technique in combination with velocity interferometry. This data set was compared in several ways to data obtained in previous studies on SAC-5 concrete (4), which has a different aggregate size but similar density. In one comparison, the particle velocity profiles were normalized with respect to plate thickness and overlaid on the same graph. Also, derived quantities such as stress and strain for both the Hugoniot and subsequent release states were plotted and compared. Results indicate that the average loading and release behavior of the three types of concrete discussed in this paper are grouped within scatter bars derived from particle velocity variations due to the heterogeneous nature of the material. Therefore, it appears that concrete does not exhibit a strong dependence upon aggregate size in the 3 to 25 GPa stress range.

REFERENCES

1. Rosenberg, J.T., and Ahrens, T.J., ASME Paper No. 66-WAPT-7, *American Society of Mechanical Engineers*, N.Y., December (1966)
2. Lysne, P.C., Boade, R.R., Percival, C.M., Jones, O.E., *Journal of Applied Physics* **40**, 3768 (1969)
3. Chhabildas and D.E. Grady, "Dynamic Material Response of Quartz at High Strain Rates", *Material Response Symposium Proceedings*, Elsevier 22, pp 147-150 (1984)
4. Grady D.E., "Dynamic Decompression Properties of Concrete From Hugoniot States 3 to 25 Gpa", *Sandia National Laboratories Technical Memorandum* - TMDG0396, February (1996)
5. Phillips, B., Waterways Experimental Station, Biloxi, Mississippi, private communication, April (1997)
6. American Society for Testing and Materials, C33-93 Standard Specifications for Concrete Aggregates, pp 3, (1993).
7. Grady D.E., "Shock and Release Data for SAC-5 Concrete to 25 GPa", *Sandia National Laboratories Technical Memorandum* - TMDG0595, October (1995).
8. Grady, D.E., Applied Research Associates, Albuquerque, New Mexico, private communication, June (1997)
9. Barker L.M., and R.E. Hollenbach, "Laser Interferometer for Measuring High Velocities of any Reflecting Surface", *Journal Applied Physics* **43**, 4669, (1972)
10. Asay, J.R., Shahinpoor, M., "High Pressure Shock Compression of Solids", New York, Springer-Verlag, (1993), pp 11.
11. Marsh, S.P., "LASL Shock Hugoniot Data", Los Angeles, University of California Press, (1980).
12. Grady, D.E., "Impact Compression Properties of Concrete", *Proceedings of the Sixth International Symposium on Interaction of Nonnuclear Munitions with Structures*, Panama City Beach, Florida, pp 172-175, May 3-7 (1993).
13. Kipp, M.E., Chhabildas, L.C., Reinhart, W.D., "Elastic Shock Response and Spall Strength of Concrete", *Proceedings of the American Physical Society Topical Conference*, (1997).

JET PENETRATION FOR A CLASS OF CUMULATIVE MASS PROFILES

STEVEN L. HANCOCK

Consultant, Primex Technologies, 2700 Merced St., San Leandro, CA, 94577, USA

Summary—An analytical model of jet penetration is developed using a power law mass distribution and a simplified Walsh breakup model. The model describes a wide variety of jets, including jets which break up at a constant time and jets which break up at a constant distance. The model yields an expression for the maximum possible continuous penetration, as a function of the jet energy and standoff distance. It also yields an upper bound for breakup length as a function of the jet energy and velocity ratio. © 1999 Elsevier Science Ltd. All rights reserved.

NOTATION

A	normalization const., Eqn. 18	t	time since virtual origin
c_b	breakup parameter, r_b/t_b	$T(v)$	hole-bottom time
C	hole energy/volume	$t_b(v)$	breakup time, Eqn. 23
$E(v)$	cumulative kinetic energy, Eqn. 22	U	penetration rate, Eqn. 7
$F(\xi; p)$	Power-law integral, Eqn. 21	v	jet velocity
$L_b(v)$	cumulative breakup length, Eqn. 29	v_{min}	jet cutoff velocity
$M(v)$	cumulative mass, Eqn. 20	v_0, v_1	jet tip, tail velocity
P	penetration	Y	jet flow stress
$\mathcal{P}(v)$	cumulative momentum	z	distance from virtual origin
q	mass shape factor, Eqn. 18	$Z(v)$	hole bottom coordinate
r	jet radius at any time, Eqn. 2	$z_b(v)$	breakup coordinate, Eqn. 25
$r_j(v)$	jet radius at hole bottom	γ	$(\rho_t/\rho_j)^{1/2}$
$r_b(v)$	jet radius at breakup, Eqn. 24	ξ	v_0/v
R_h	hole radius, Eqn. 8	ρ_j	jet density
S	standoff distance	ρ_t	target density
$0, 1$	subscripts for values at $v = v_0, v_1$	σ_b	ductility parameter, $= \pi \rho_j c_b^2 \simeq Y/40$

INTRODUCTION

A shaped-charge device can produce a rapidly stretching, high velocity jet with great penetrating capability. This stretching jet will eventually break into a stream of particles, so that two different modes of penetration are possible. If a jet element reaches the bottom of the hole before breakup, it penetrates in the continuous mode, and otherwise it penetrates in the particulated mode. The total penetration will be the sum of the contributions of each of these modes, although, depending upon the standoff distance and mass distribution, only one mode may be present. Typically, at short

standoff distances, most of the contribution to penetration is from the continuous mode, while at long distances, most or all of the contribution is from the particulated mode. These two modes of penetration produce very different hole profiles in metal targets. The continuous mode typically makes a smooth hole, while the particulated mode makes a scalloped hole with a smaller minimum diameter. For this reason, penetration made in the continuous mode is generally more robust in the presence of perturbations.

The model presented here began as an attempt to find a theoretical upper bound on continuous penetration, as a function of jet energy and standoff distance. To solve this problem, one must find jets for which each element of the jet particulates at the same instant that it arrives at the hole bottom, because if it broke up any later it would not be fully stretched, and if it broke up any earlier, it would not be continuous. An analytical solution was found by employing a simple breakup model described by Pearson, *et al.* [1]. Further work with this breakup model produced additional interesting results; eventually these results were unified into a single model by introducing a power law mass distribution. This general model is the subject of this paper, but before describing it, a brief review will be made of the basic jet penetration theory to be used.

REVIEW OF JET PENETRATION THEORY

A review of jet penetration theory can be found in Walters and Zukas [2]. Another standard reference is DiPersio, Simon, and Merendino (DSM) [3]. Here, the relevant equations are summarized and the notation to be used is introduced. A one-dimensional model of a stretching jet is adopted, with tip velocity v_0 and tail velocity v_1. For much of this paper, it does not matter if this velocity range represents the entire jet or a subsection of it. A useful dimensionless velocity ratio is $\xi = v_0/v$.

It is assumed that a jet with density ρ_j emerges from a virtual origin at time $t = 0$ and travels in the direction z, and that it encounters a monolithic target layer, of density ρ_t, at some distance Z_0. For any jet element, the two most significant z coordinates are the coordinate at which it breaks into particles, which will be denoted by $z_b(v)$, and the coordinate at which it arrives at the instantaneous hole bottom, which will be denoted by $Z(v)$. The times corresponding to these events will be denoted as $t_b(v)$ and $T(v)$; by the virtual origin assumption, they are $t_b(v) = z_b(v)/v$ and $T(v) = Z(v)/v$.

It will be assumed that jet penetration continues until either there is no more jet material or until a cutoff velocity, v_{min}, is reached; penetration then terminates abruptly. For the continuous mode of penetration in hard targets, a constant v_{min}, whose value depends upon the target strength, will often give acceptable results; in the particulated mode, the cutoff velocity is known to also depend upon particle spacing and alignment. No specific cutoff model will be assumed here.

The virtual origin assumption implies a relationship between the radius of the jet, the time, and the slope of the cumulative mass distribution. Consider an element of jet, before breakup, with a mass increment dM, a length increment dL, and a velocity increment dv. Since v decreases from the tip to the tail of the jet, it is assumed that dM and dL are positive when dv is negative. Its length at time t is $dL = -t\,dv$, and if it is idealized as an incompressible cylinder of radius r, then $dM = -\rho_j \pi r^2 t\,dv$. Rearranging gives

$$r^2 t = \frac{-1}{\pi \rho_j} \frac{dM}{dv}.$$

(1)

Since the right hand side is independent of time, this equation holds at breakup time, and it follows that

$$r(v,t)^2 = \begin{cases} r_b(v)^2\,(t_b(v)/t) & \text{if } t < t_b(v), \\ r_b(v)^2 & \text{otherwise.} \end{cases}$$

(2)

According to the assumptions of incompressible, hydrodynamic flow, the relationship between incremental penetration and jet length consumption during continuous penetration is $dZ = dL/\gamma$,

where $\gamma = (\rho_t/\rho_j)^{\frac{1}{2}}$. The integral of this equation is the well-known formula for the hole bottom location as a function of velocity,

$$Z(v) = Z_0 \left(\frac{v_0}{v}\right)^{1/\gamma} = Z_0 \xi^{1/\gamma}. \tag{3}$$

After breakup, it is assumed that a jet element stops stretching, so that its length remains constant at the breakup value,

$$dL_b = -t_b(v)\,dv, \tag{4}$$

and the penetration law is taken to be $dZ = dL_b/\gamma$. Integration yields the location of the penetration front for particulated penetration, starting with velocity v_0 at location Z_0,

$$Z(v) = Z_0 + L_b(v)/\gamma, \tag{5}$$

where the cumulative breakup length is

$$L_b(v) = -\int_{v_0}^{v} t_b(v)\,dv. \tag{6}$$

The minus sign is required because, as with all cumulative quantities, the integral runs in the negative dv direction. The average penetration rate, which is needed for some cutoff models, is

$$U = \begin{cases} v/(1+\gamma) & \text{if } t < t_b(v), \\ v/(1+\gamma t/t_b) & \text{otherwise.} \end{cases} \tag{7}$$

In order to estimate hole size, the constant energy/volume assumption will be made, which implies an average hole radius given by

$$R_h^2 = \left(\frac{\gamma \rho_j v^2}{2C}\right) r_j^2, \tag{8}$$

where C is a constant. This equation holds for both continuous and particulated penetration.

BREAKUP MODEL

The breakup model to be used can be expressed as a proportionality between the local breakup radius and breakup time,

$$t_b(v) = r_b(v)/c_b, \tag{9}$$

where c_b is a constant with units of velocity. Pearson, *et al.* [1] show that this assumption is equivalent to a simplified version of the Walsh breakup model [4], and they interpret c_b as an average neck formation rate. If a radiograph of a jet is available, it may be possible to estimate the value of c_b directly by measurement of the breakup radius and breakup time. For example, the copper jet produced by the standard shaped charge used in the DSM report had a nearly constant breakup time of 103 μs and a radius of 1 mm, so $c_b \approx 10$ m/s for that jet. Other methods for estimating c_b can be developed based upon measurements of cumulative breakup length and cumulative mass.

It might seem at first that Eqn. 9 is not deterministic, since it involves both $t_b(v)$ and $r_b(v)$, but these quantities are also related by Eqn. 1. Eliminating $r_b(v)$ gives a relationship between the breakup time and the slope of the cumulative mass curve,

$$\frac{dM}{dv} = -\sigma_b t_b(v)^3, \tag{10}$$

where $\sigma_b = \pi \rho_j c_b^2$ is a convenient parameter with units of stress.

Establishing the relationship of this model to other breakup models is of interest. Many existing models are expressed in the form $\bar{t}_b = \bar{t}_b(\bar{\eta}_0)$, where $\bar{t}_b = C_p t_b/r_0$ is a dimensionless breakup time,

and $\bar{\eta}_0 = (\Delta v/\Delta L_0) r_0/C_p$ is a dimensionless initial strain rate. Here, to follow conventional notation, subscript 0 temporarily denotes values at the birth of a jet element. The symbol ΔL_0 denotes the initial length of an element; Δv is its velocity range; r_0 is its initial radius; $C_p = (Y/\rho_j)^{1/2}$; and Y is the flow stress. The model used here can be put into this form as follows. From the virtual origin assumption, $\Delta L_0 = t_0 \Delta v$, so $\bar{\eta}_0 = r_0/(C_p t_0)$. It can then be shown that $\bar{t}_b{}^3 \bar{\eta}_0 = (C_p/c_b)^2$ if use is made of the incompressible assumption, $r_b^2 t_b = r_0^2 t_0$, and Eqn. 9. This result can be written

$$\bar{t}_b = \alpha/\bar{\eta}_0{}^{1/3}, \tag{11}$$

where $\alpha = (C_p/c_b)^{2/3}$. This functional form has been recommended by Chou, *et al.* [5], who attribute it to unpublished work of Nellums in 1991. They suggest $\alpha \simeq 5$. A model presented earlier, by Grady [6], also has this form; Grady showed graphically that $\alpha \simeq 4.3$ produces an approximate lower bound on a set of data collected by Chou. For $\alpha \simeq 5$ we have $C_p = \alpha^{3/2} c_b \simeq 11.2 c_b$ and $\sigma_b = \pi Y/\alpha^3 \simeq Y/40$. To summarize, then, the simplified Walsh breakup model used in the present work, Eqn. 9, is equivalent to the more familiar form given by Eqn. 11.

OPTIMAL BREAKUP LENGTH

Since, by Eqn. 10, the breakup time can be computed from the slope of $M(v)$, we can make penetration predictions if we have an $M(v)$ curve along with material properties and a cutoff model. Thus, this breakup model puts us in a position to study the general relationship between $M(v)$ curves and the penetration they produce, without reference to the details of the jet formation. In order to proceed with such a study, a source of $M(v)$ curves is required; a suitable family of curves will be introduced in the next section.

Before doing so, it will be useful to pursue an optimization problem that can be addressed immediately. We can find $M(v)$ curves which maximize breakup length. Assume initially that a fixed amount of jet mass, $M_1 - M_0$, is available to be distributed between velocities v_0 and v_1 in such a way as to maximize cumulative breakup length. That is, we wish to find the $M(v)$ curve which maximizes the integral

$$\Delta L_b = -\int_{v_0}^{v_1} \left(\frac{-1}{\sigma_b} \frac{dM}{dv} \right)^{1/3} dv, \tag{12}$$

which is the result of combining Eqns. 6 and 10. This is a problem in the calculus of variations. For an integrand of this form, which is dependent upon dM/dv, but not explicitly dependent upon v and $M(v)$, the extremum condition is simply that $dM/dv = $ constant (e.g. Weinstock, [7]). The optimal mass distribution is, therefore,

$$M(v) = M_0 + (M_1 - M_0)\frac{v - v_0}{v_1 - v_0} = M_0 + (M_1 - M_0)\frac{\xi^{-1} - 1}{\xi_1^{-1} - 1}. \tag{13}$$

Now consider a situation of perhaps greater interest, in which, rather than mass, a certain total energy, $E_1 - E_0$, is available to be optimally distributed along the jet. The solution can most readily be seen if Eqn. 12 is transformed into

$$\Delta L_b = \int_1^{\xi_1} \left(\frac{2}{\sigma_b} \frac{dE}{d\ln\xi} \right)^{1/3} d\ln\xi, \tag{14}$$

where use has been made of $dE = \frac{1}{2}v^2 dM$, $v = v_0\xi^{-1}$, and $dv = -v_0\xi^{-2} d\xi$. Using the same result from the calculus of variations, the extremum condition is $dE/d\ln\xi =$ constant, so the solution is

$$E(v) = E_0 + (E_1 - E_0)\ln\xi/\ln\xi_1. \tag{15}$$

Using this solution in Eqn. 14, and simplifying, gives the corresponding maximum breakup length possible for a jet with energy $\Delta E = E_1 - E_0$,

$$\Delta L_b = [2\Delta E/\sigma_b]^{1/3} [\ln(v_0/v_1)]^{2/3}. \tag{16}$$

Note the energy/ductility equivalence implied by the appearance of energy and σ_b only in a ratio. This shows that, as far as maximum breakup length is concerned, an improvement in the ductility of a jet material, through a reduction in σ_b, is equivalent to an increase in jet energy.

Using the same methods, it can be shown that the jet which optimizes breakup length, for a given total momentum, has the momentum distribution

$$\mathcal{P}(v) = \mathcal{P}_0 + (\mathcal{P}_1 - \mathcal{P}_0)\frac{\xi^{-1/2} - 1}{\xi_1^{-1/2} - 1}. \tag{17}$$

These optimal jets are special cases of the family of mass distributions to be introduced next. Their properties will follow from an analysis of the properties of the entire family.

MASS DISTRIBUTION FUNCTION

The mass distributions to be considered are defined by the power law

$$\frac{dM}{dv} = -\frac{A}{v_0}\xi^q, \tag{18}$$

where parameter A is a normalization constant, and q is a shape parameter which plays an important role in all that follows. Multiplying by $dv = -v_0\xi^{-2}d\xi$ gives

$$dM = A\xi^{q-2}\,d\xi. \tag{19}$$

Integration gives the cumulative mass distribution,

$$M(v) - M_0 = \int_{v_0}^{v} dM = A \int_1^{\xi} x^{q-2}\,dx = AF(\xi; q), \tag{20}$$

where the following auxiliary function has been defined to represent the integral,

$$F(\xi; p) = \int_1^{\xi} x^{p-2}dx = \begin{cases} \ln\xi & \text{if } p = 1, \\ (\xi^{p-1} - 1)/(p - 1) & \text{otherwise.} \end{cases} \tag{21}$$

Some cumulative mass profiles based upon this distribution are shown in Fig. 1. A linear distribution is described by $q = 0$, and as q increases above 0, the mass distribution becomes increasingly concave as the center of mass moves toward the tail. The cumulative momentum and kinetic energy distributions are found, using Eqn. 19 and $v = v_0\xi^{-1}$, to be

$$\mathcal{P}(v) - \mathcal{P}_0 = \int_{v_0}^{v} v\,dM = Av_0 \int_1^{\xi} x^{q-3}\,dx = Av_0F(\xi; q - 1),$$

and

$$E(v) - E_0 = \int_{v_0}^{v} \frac{v^2}{2}\,dM = \frac{Av_0^2}{2} \int_1^{\xi} x^{q-4}\,dx = \frac{Av_0^2}{2}F(\xi; q - 2), \tag{22}$$

where $\mathcal{P}_0$ and E_0 are the cumulative momentum and kinetic energy at velocity v_0. In the special case that v_0 is the jet tip and M_0 represents a tip particle, we have $\mathcal{P}_0 = M_0v_0$ and $E_0 = M_0v_0^2/2$. This result shows that the normalized cumulative momentum and energy distributions are mathematically similar to the cumulative mass distribution; their normalized shapes are therefore also illustrated in Fig. 1, except that their shape factors are $q - 1$ and $q - 2$, respectively.

Using these results, it can be verified that the three jets found in the previous section to optimize breakup length, under conditions of constant mass, momentum, and energy (Eqns. 13, 17, and 15) are contained in this family of mass distributions as jets with $q = 0$, $3/2$, and 3, respectively. In a later section it will be shown that jets which maximize continuous penetration are also contained in this family. Therefore, this family seems ideally suited to studying the properties of the simplified Walsh breakup model.
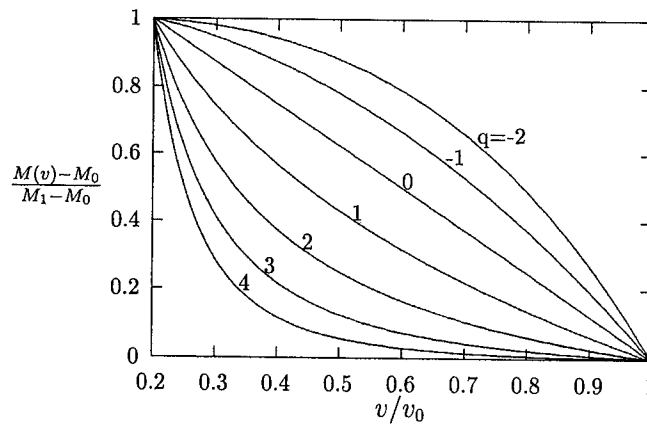
Fig. 1. Normalized cumulative mass curves, shown for $v_1/v_0 = 0.2$.

JET BREAKUP PROPERTIES

The distribution of breakup properties along the jet can now be evaluated. The breakup time distribution is found by eliminating dM/dv between equations 10 and 18, giving

$$t_b(v) = t_{b0}\xi^{q/3}, \qquad (23)$$

where $t_{b0} = [A/(\sigma_b v_0)]^{1/3}$. From this, it can be seen that breakup will occur simultaneously along the jet, at time t_{b0}, when $q = 0$, which corresponds to a linear mass distribution. When $q > 0$, the jet will break up first at the tip and last at the tail, and conversely, when $q < 0$, breakup will occur first at the tail and progress toward the tip. The breakup radius distribution is

$$r_b(v) = c_b t_b(v) = r_{b0}\xi^{q/3}, \qquad (24)$$

where $r_{b0} = c_b t_{b0}$. The location of the breakup point in space is, by the virtual origin assumption,

$$z_b(v) = v t_b(v) = v_0\xi^{-1} t_b(v) = z_{b0}\xi^{(q-3)/3}, \qquad (25)$$

where

$$z_{b0} = v_0 t_{b0} = \left(A v_0^2/\sigma_b\right)^{1/3}. \qquad (26)$$

The exponent on ξ indicates that the breakup location will be constant, z_{b0}, when $q = 3$. This model, then, includes jets with a constant breakup time and jets with a constant breakup distance, as well as a complete spectrum of intermediate jets, and it can shed some light on the debate over a constant breakup time versus a constant breakup distance approximation. In the DSM work, the assumption of simultaneous breakup was made, and this was both analytically convenient and also a good approximation for the standard charge used in that study. Occasionally, however, it has been suggested that a constant breakup distance assumption may be more appropriate (e.g. Mayseless, et al. [8]). According to the present model, the key issue is the curvature of the cumulative mass profile. The proponents of a constant breakup time model may be working with mass profiles closer to linear, with $q = 0$, while those who favor a constant breakup distance may be working with profiles closer to the $q = 3$ distribution.

The location of the breakup point as a function of time can be found by substituting $v = z_b/t$, with the result

$$z_b/z_{b0} = \left(v_0 t/z_{b0}\right)^{(q-3)/q}. \qquad (27)$$

The sign of the exponent determines the direction of motion of the breakup point in space. When $0 < q < 3$ it moves backward, and when $q < 0$ or $q > 3$ it moves forward.

A useful alternative expression for the jet energy distribution can be derived by eliminating the constant A between Eqn. 26 and Eqn. 22, with the result

$$E(v) - E_0 = \frac{1}{2}\sigma_b z_{b0}^3 F(\xi; q - 2). \tag{28}$$

The cumulative breakup length is found by integration to be

$$L_b(v) = -\int_{v_0}^{v} t_b(v)\, dv = \int_{1}^{v_0/v} (t_{b0}\xi^{q/3})(v_0\xi^{-2}\, d\xi) = z_{b0} F(\xi; q/3). \tag{29}$$

The distribution of the jet radius, at any time, can be obtained by combining Eqns. 2, 23, and 24, with the result

$$r(v,t)^2 = \begin{cases} r_{b0}^2 (t_{b0}/t)\xi^q & \text{if } t < t_b(v), \\ r_b(v)^2 & \text{otherwise.} \end{cases} \tag{30}$$

The variation of the jet radius as a function z and t can found from this by the substitution $\xi = v_0 t/z$.

In order to evaluate the depth of penetration, it is necessary to find the locations of any transitions between the two possible modes of penetration. A transition point occurs whenever the breakup time of a jet element is the same as its hole-bottom time, or equivalently, whenever Eqn. 25 equals either Eqn. 3 or 5, as appropriate. A detailed analysis shows that the transition points depend upon a critical value, $q_c = 3 + 3/\gamma$. When $q < q_c$, there may be one transition from continuous to particulated penetration, and when $q > q_c$, there may be one transition from particulated to continuous penetration. The transition points are given in the next section. When $q = q_c$, and when in addition $z_{b0} = Z_0$, Eqns. 25 and 3 indicate that $Z(v) = z_b(v)$. This corresponds to optimal continuous penetration, and is discussed in detail in a later section.

PENETRATION HISTORY

The penetration history can be summarized in a computationally convenient form. It will be assumed that the contributions to penetration of any previous sections of the jet, including any tip particle, have already been accounted for. The solution can be constructed by performing the following computation for a sequence of velocities between v_0 and v_1, stopping if a cutoff criterion has been exceeded or if the hole bottom location, $Z(v)$, exceeds the end of the target layer.

- If $Z_0 < z_{b0}$ the penetration is initially continuous. The point of transition to particulated penetration is:

$$\xi_* = (v_0/v_*) = \begin{cases} (Z_0/z_{b0})^{3/(q-3-3/\gamma)} & \text{if } q < 3 + 3/\gamma, \\ \infty & \text{otherwise.} \end{cases}$$

The hole bottom location is:

$$Z(v) = \begin{cases} Z_0\xi^{1/\gamma} & \text{if } v > v_*, \\ Z_0\xi_*^{1/\gamma} + [L_b(v) - L_b(v_*)]/\gamma & \text{otherwise.} \end{cases}$$

- If $Z_0 \geq z_{b0}$ the penetration is initially particulated. The point of transition to continuous penetration is, with $p = (q - 3)/3$:

$$\xi_* = (v_0/v_*) = \begin{cases} \left(\frac{\gamma p Z_0/z_{b0} - 1}{\gamma p - 1}\right)^{1/p} & \text{if } \gamma p > 1, \\ \infty & \text{otherwise.} \end{cases}$$

The hole bottom location is:

$$Z(v) = \begin{cases} Z_0 + L_b(v)/\gamma & \text{if } v > v_*, \\ [Z_0 + L_b(v_*)/\gamma]\, (v_*/v)^{1/\gamma} & \text{otherwise.} \end{cases}$$

With the location of the hole bottom defined, the time for a particle to reach the hole bottom can be found using $T(v) = Z(v)/v$; the corresponding jet radius can be found by using this time in Eqn. 2. The hole radius is given by Eqn. 8, and the penetration rate is given by using the hole-bottom time $t = T(v)$ in Eqn. 7.

JET AND HOLE DIMENSIONS

The variation of the jet and hole dimensions with depth of penetration can now be examined. For initially continuous penetration, the hole-bottom time is found from Eqn. 3 to be $T = (Z_0/v_0)\xi^{1+1/\gamma}$. Substituting this into Eqn. 30 gives the jet radius at the hole bottom,

$$r_j^2 = r_{b0}^2 \frac{z_{b0}}{Z_0} \xi^{q-1-1/\gamma}. \tag{31}$$

Since larger values of ξ always correspond to greater depths of penetration, the exponent indicates that r_j increases or decreases with depth according to whether q is greater than or less than $1 + 1/\gamma$. Using this jet radius in Eqn. 8 gives the hole radius,

$$R_h^2 = r_{b0}^2 \frac{z_{b0}}{Z_0} \left(\frac{\gamma \rho_j v_0^2}{2C} \right) \xi^{q-3-1/\gamma}. \tag{32}$$

The exponent indicates that the hole widens or narrows with depth depending upon whether q is greater than or less than $3 + 1/\gamma$. To find the actual hole profile in space during continuous penetration, we can substitute $\xi = (Z/Z_0)^\gamma$, which gives

$$R_h^2 = r_{b0}^2 \frac{z_{b0}}{Z_0} \left(\frac{\gamma \rho_j v_0^2}{2C} \right) (Z/Z_0)^{\gamma(q-3)-1}.$$

One case of interest is the optimal continuous jet, with $q = 3 + 3/\gamma$, for which this equation shows R_h increasing linearly with Z; this indicates a hole which is a frustum of a cone centered at the virtual origin. For short standoff distances, the entrance diameter to this hole will be very small, so a clearance problem is to be expected for this jet at short standoff. The question of jet/hole clearance will be considered in more detail in the next section.

During particulated penetration, the jet radius is simply the breakup radius, $r_j = r_b(v) = r_{b0}\xi^{q/3}$, which shows that the jet radius at the hole bottom increases with depth when $q > 0$. With this jet radius, the average hole radius during particulated penetration is, from Eqn. 8,

$$R_h^2 = r_{b0}^2 \left(\frac{\gamma \rho_j v_0^2}{2C} \right) \xi^{2(q-3)/3}. \tag{33}$$

The exponent indicates that a jet with $q = 3$ creates a constant average hole radius during particulated penetration. A jet with $q < 3$ creates a narrowing hole, and one with $q > 3$ creates a widening hole.

JET/HOLE CLEARANCE

Although many jet asymmetries can lead to interference between the jet and target during penetration, we can check for a geometrical situation in which even a perfectly aligned jet could not fit in the hole that it created. We will do this only for the continuous mode of penetration, since a particulated jet creates a ragged hole which is not well described by an average radius. Experimental evidence that such interference can occur for sufficiently concave mass distributions has been presented by Miller, *et al.* [9]. They developed the following formula for the radius of a jet element with velocity v' passing by the portion of the cavity wall created by an element with $v > v'$:

$$(r'/R_h)^2 = \left(\frac{2C}{\gamma \rho_j v^2} \right) \left(\frac{v'\, dM/dv'}{v\, dM/dv} \right). \tag{34}$$

The first factor in this expression is, by Eqn. 8, $(r_j/R_h)^2$. The second factor is $(r'/r_j)^2$; this can be shown by applying Eqn. 1 at the common coordinate $Z = vt = v't'$. Substituting the value of dM/dv given by Eqn. 18 gives

$$(r'/R_h)^2 = \left(\frac{2C}{\gamma \rho_j v^2}\right)\left(\frac{v}{v'}\right)^{q-1}.$$

If we assume that an equilibrium hole radius has been reached by the time of passage of the jet element v', and ignore the volume occupied by debris from preceding jet material, then the jet makes contact with the cavity wall when $r' \geq R_h$, and disruption is expected. We are interested in the first cutoff point, or in other words the maximum value of v', for any v in the range $v' < v \leq v_0$, for which $r'/R_h = 1$. Analysis reveals that the non-local cutoff mechanism of interest occurs when $q > 3$, for $v = v_0$, and is:

$$\frac{v'_{max}}{v_0} = \left(\frac{2C}{\gamma \rho_j v_0^2}\right)^{1/(q-1)}. \tag{35}$$

As a very rough check on this result, approximate q values for three jets described by Miller, *et al.* [9] are shown in the table below along with the experimental results regarding jet/hole interference. These jets cannot be accurately described with a single q value; the range of q values shown are for fits starting from the tip and ending in the range 3–5 km/s. The method of fitting was to adjust q to match the total jet mass and energy variation over the selected velocity interval.

Case	q	v_0, km/s	Observed Jet/Hole Interference
A	2.3–2.7	8.9	sometimes none, sometimes below 2.6 km/s
B	2.9–3.3	8.45	always below 3.9 km/s, sometimes higher
C	5.6–6.7	9.5	always severe interference

Since jet A appears to be below the threshold, and jet B is above it, this table is consistent with the result that $q = 3$ is the threshold of the jet/hole interference mechanism for continuous penetration. However, the minimum disruption velocity of jet B, at 3.9 km/s, is much higher than estimates made with Eqn. 35. Therefore, it should be emphasized that Eqn. 35 represents a limiting geometrical condition, for which interference is definitely expected, but that actual interference might occur before this criterion is reached.

OPTIMAL CONTINUOUS PENETRATION

For an optimal continuous jet, in which breakup and penetration occur simultaneously, it was shown that $z_{b0} = Z_0$ and $q = 3 + 3/\gamma$. The tip mass will be assumed to be zero, because otherwise it represents a significant amount of unstretched energy. Let S denote the standoff distance to the target; using $E_0 = 0$ and $z_{b0} = S$ in Eqn. 28, the energy in the jet at some still unspecified tail velocity v_1 can be written

$$E_1 = \frac{1}{2}\sigma_b S^3 F(\xi_1; 1 + 3/\gamma).$$

Using the definition of $F(\xi; p)$ in Eqn. 21, we can solve for ξ_1, and get

$$\xi_1 = \frac{v_0}{v_1} = \left[1 + \left(\frac{P_0}{S}\right)^3\right]^{\gamma/3}, \tag{36}$$

where

$$P_0 = \left(\frac{6E_1}{\gamma \sigma_b}\right)^{1/3}.$$
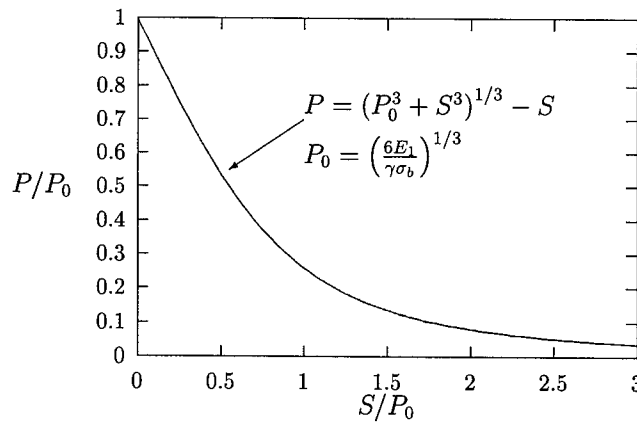
Fig. 2. Maximum continuous penetration as a function of standoff.

The penetration is $P = z_b(v_1) - S$ which, using Eqn. 25, gives

$$P = \left(P_0{}^3 + S^3\right)^{1/3} - S. \tag{37}$$

This is the desired theoretical upper bound on continuous penetration, for a given amount of kinetic energy, a given standoff distance, and given material properties. Fig. 2 shows this function.

It has been tacitly assumed in the derivation of Eqn. 37 that all elements of the jet down to velocity v_1 contribute to penetration. If premature cutoff does occur, then the penetration will be less, in which case Eqn. 37 is still an upper bound, even though it cannot be physically realized. In fact, it would be difficult to produce functional jets similar to those described by this solution because of the jet/hole cutoff effect discussed in the previous section. To avoid this cutoff condition, the value of ξ_1 of Eqn. 36 must not imply a tail velocity below the value implied by Eqn. 35. At short to moderate standoff distances, this requirement turns out to imply jet tip velocities much greater than sound speed limits of typical materials would allow.

CONCLUSION

This work has shown that a power law mass distribution, when combined with the simplified Walsh breakup model, plus some standard jet penetration assumptions, leads to a comprehensive mathematical model of one-dimensional jet penetration. Fig. 3 summarizes many of the relationships which have been found with the model. The range of q of greatest practical interest is probably that bounded on the low end by the simultaneous breakup jets, with $q = 0$, and on the high end by jets with a constant breakup distance, with $q = 3$. The maximum possible breakup length, for a given energy, occurs at $q = 3$, but $q = 3$ is also the lower bound of the jet/hole interference problem. The empiricism of a cutoff model needs to be introduced into the model at this point in order to make further progress.

Many simplifying assumptions have been made in the development of this model, and in any real jet all of them will be violated to some extent. Numerical modeling can avoid many of these limiting assumptions, and therefore achieve more accurate results for specific jets, but this model provides a global perspective which is difficult to obtain with isolated numerical results.

				Eqn.
Breakup Sequence along Jet	Tail to Tip	Tip to Tail		23
Breakup Point Motion in Space	Forward	Backward	Moves Forward	27
Jet Radius at Hole Bottom: Continuous	Decreases with Depth $1+1/\gamma$		Increases	31
Jet Radius at Hole Bottom: Particulated	Decreases	Increases with Depth		24
Hole Radius: Continuous	Narrows with Depth $3+1/\gamma$		Widens	32
Hole Radius: Particulated	Narrows with Depth	Widens		33
Jet/Hole Geometric Overlap? (Continuous)	No	Yes		35
Particulated-->Continuous Possible?	No		$3+3/\gamma$ Yes	

-2 -1 0   1   2   3   4   5   6   7

Simultaneous breakup

Constant breakup distance

Shape Factor, q
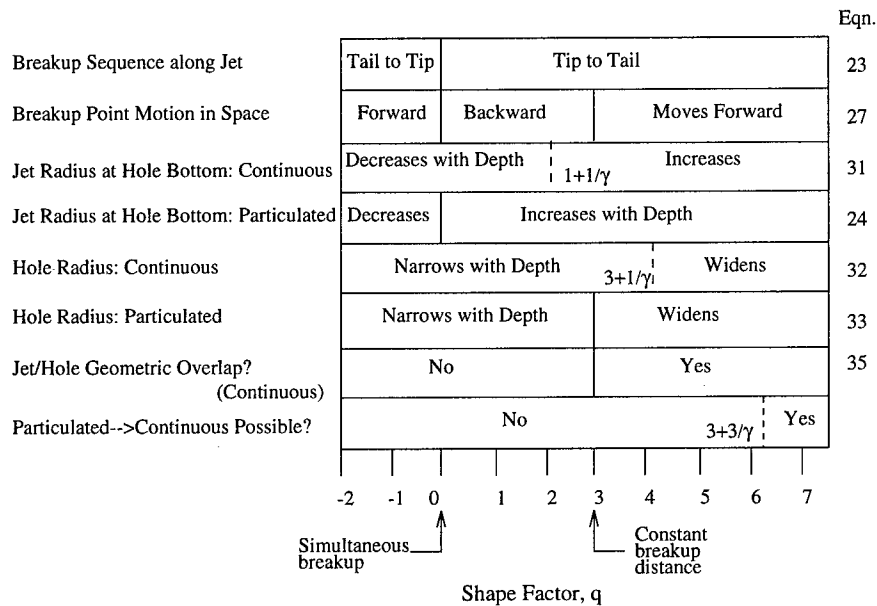
Fig. 3. Influence of shape parameter q on jet and hole properties. The dashed vertical lines depend upon γ; the chart is drawn for $\gamma = 0.94$.

REFERENCES

1. J. Pearson, E.L. Baker, and R. Campbell, Experimental Confirmation for the Walsh Jet Breakup Theory. *46th Annual Bomb and Warhead Technical Meeting*, 14-15 May (1996).
2. W.P. Walters and J.A. Zukas, *Fundamentals of Shaped Charges*, John Wiley (1989).
3. R. DiPersio, J. Simon, and A. Merendino, Penetration of Shaped-Charge Jets into Metallic Targets. BRL Report No. 1296 (1965).
4. J.M. Walsh, Plastic instability and particulation in stretching metal jets. *J.Appl.Phys.*, **56**, 1997-2006 (1984).
5. P.C. Chou, M.Grudza, Y-F.Liu, and Z.Ritman. Shaped-Charge Jet Break-Up Formula with Metal Anisotropy. *Proc. 13th Int. Symp. Ballistics*, vol. 2, paper WM-23, June 1-3, Stockholm, Sweden (1992).
6. D.E. Grady, Fragmentation of Rapidly Expanding Jets and Sheets. *Int. J. Impact Engng.* **5**, 285-292 (1987).
7. R. Weinstock, *Calculus of Variations*, Dover Publ., New York, (1974).
8. M. Mayseless, E. Marmor, S. Miller, and B. Zommer, A New Approach in Characterizing the Breakup Phenomenon of a Shaped Charge Jet. *Proc. 11th Int. Symp. Ballistics*, vol. 2, pp WM-6/1-7, May 9-11, Brussels, Belgium (1989).
9. S. Miller, S. Konfino, E. Arad, and M. Avinor, Mass Distribution Factors Which Dominate Jet Penetration into RHA Steel. *Proc. 14th Int. Symp. Ballistics*, vol. 2, Paper WM-20, pp 183-192, Sept. 26-29, Quebec City, Canada (1993).

DEVELOPMENT OF MATERIAL MODELS FOR NEXTEL AND KEVLAR-EPOXY FOR HIGH PRESSURES AND STRAIN RATES

COLIN J. HAYHURST*, STEFAN J. HIERMAIER†, RICHARD A. CLEGG* WERNER RIEDEL† and MICHEL LAMBERT#

*Century Dynamics Ltd., Dynamics House, Hurst Road, Horsham, West Sussex, England, RH12 2DT
†Ernst Mach Institute, Fraunhofer Institut fur Kurzzeitdynamik, Ecker Str. 4, 79104 Freiburg, Germany
#ESTEC, Postbus 299, 220 Noordwijk, Keplerlaan 1, AZ Noordwijk, The Netherlands

Summary—Material models suitable for Nextel cloth and Kevlar-epoxy in bumper shield systems are being developed. The paper describes the current status of a project aimed at developing such material models for usage in hydrocode simulations. The starting assumption was that the model should be suitable for implementation in existing hydrocodes and it should aim to simulate the main system phenomena rather than the detailed microscopic response of the material under hypervelocity impact loading.

It is shown how the anisotropic behaviour, of these materials, leads to a coupling of the volumetric and deviatoric response. This creates a difficulty in combining conventional equation of state behaviour with the anisotropic constitutive model. We have implemented an approach based on that by Anderson [1] to overcome this difficulty. Further development of this approach, to include non-linear constitutive behaviour and in particular porous compaction effects, is in progress.

An overview of the material characterisation tests being conducted is given with details, and results, presented for confined static compression, inverse flyer plate and hypervelocity impact tests. The confined static compression tests have enabled the definition of a porous compaction model. This compaction model has been used in simulations of the inverse flyer plate tests and has led to much improved correlation. Results of micro- and meso- mechanical simulations of Nextel cloth under confined compressive loading are also presented. Finally, we show details of three preliminary simulations of a hypervelocity impact test on a multi-shock shield. The results of these simulations emphasise the importance of compaction and anisotropic response to the system behaviour. © 1999 Elsevier Science Ltd. All rights reserved.

INTRODUCTION

Project Overview

Protective design for space vehicles against hypervelocity impacts requires the development of new techniques for structures and materials. The typical approach for this aim is to use bumper shields made of one or more layers. Impacting particles are fragmented into solid particles and at higher velocity these particles may also be partly melted and vaporised. Thus debris clouds behind each layer develop and a reduction of the momentum density per unit area is achieved. Experimental work has shown that the use of a multi-shock shield concept [2], incorporating materials like Nextel cloth and Kevlar-epoxy in second and subsequent bumpers, can improve the efficiency of a space debris shield. The limitations of performing controlled experiments at higher velocities means that there is a need to study impact events at higher velocities using numerical simulations, as is the case for conventional aluminium bumper shields. Whilst material models for aluminium, under conditions of high pressure and strain rates, have been successfully developed and used in numerical simulations of hypervelocity impacts this is not the case for Nextel and Kevlar-epoxy. Previous attempts to model these materials have applied

isotropic models using equation of state data for similar materials; for instance in [3] alumina data with a modified density was used to represent Nextel. More recently, some initial work was performed, using flyer plate tests, in an attempt to characterise some equation of state data for Nextel [4].

The work described in this paper is aimed at developing a material model for Nextel cloth and Kevlar-epoxy, which is suitable for usage in numerical simulations of hypervelocity impact scenarios. The objective is to develop a macro-mechanical model that simulates the main phenomena of relevance in the hypervelocity impact event. We are not attempting to model the detailed microscopic behaviour of the materials: This would require a level of model resolution which would render any numerical simulations, of bumper shield systems, far too expensive to compute on any current or foreseeable type of computer system. Nevertheless we are conducting micro- and meso-mechanical simulations of small sub-volumes of the Nextel cloth, as a means of trying to understand the material behaviour at this small scale.

MATERIAL MODEL

Phenomena to Simulate

The behaviour of Nextel and Kevlar-epoxy under hypervelocity impacts is assumed to be more complex than that of aluminum bumper shields. Additional effects that need to be considered, which are normally assumed negligible in aluminum, include anisotropy, porosity and more complex failure mechanisms. In addition, there is little existing material data for these materials over and above the usual range of handbook/supplier data.

Initial material and hypervelocity impact tests and simulations performed, some details of which are in the following sections, have led us to formulate a strategy for further testing and simulation. This is aimed at developing and characterising the data for a model that will incorporate the following phenomena, which we believe are of primary interest:

- Shock response
- Material compaction (particularly in Nextel) which is macroscopically porous
- Phase changes, in particular epoxy vaporisation which has been observed to occur at impact velocities below 500 m/s
- Material anisotropy
- Anisotropic strength degradation
- Coupling of volumetric and deviatoric response

Proposed Material Models

No model, which incorporates combinations of many of the above effects, has to our knowledge been developed although individual effects can be simulated with existing techniques. The challenge is to develop a model which couples these behaviours and to obtain the required material data. Our main concern is to develop a practical formulation which combines what is normally deemed the equation of state and constitutive strength. The problem is that in anisotropic materials these two sub-models are strongly coupled as volumetric strain leads to deviatoric stress, and similarly deviatoric strain leads to spherical stress. Anderson [1] has proposed a theoretical approach for coupling together these responses in an orthotropic material. This methodology has previously been applied to high velocity impacts on graphite/epoxy composite laminates [5]. We are also, at least initially, using this approach as a basis for the model to be developed. The existing model and our proposed adaptations are summarised below.

Consider a linearly elastic orthotropic material for which the total stress-strain relationship can be expressed as:

$$
\begin{bmatrix} \sigma_{11} \\ \sigma_{22} \\ \sigma_{33} \\ \sigma_{23} \\ \sigma_{31} \\ \sigma_{12} \end{bmatrix} =
\begin{bmatrix}
\dfrac{1-v_{23}v_{32}}{E_2E_3\Delta} & \dfrac{v_{21}+v_{31}v_{23}}{E_2E_3\Delta} & \dfrac{v_{31}+v_{21}v_{32}}{E_2E_3\Delta} & 0 & 0 & 0 \\
\dfrac{v_{21}+v_{31}v_{23}}{E_2E_3\Delta} & \dfrac{1-v_{13}v_{31}}{E_1E_3\Delta} & \dfrac{v_{32}+v_{12}v_{31}}{E_1E_3\Delta} & 0 & 0 & 0 \\
\dfrac{v_{31}+v_{21}v_{32}}{E_2E_3\Delta} & \dfrac{v_{32}+v_{12}v_{31}}{E_1E_3\Delta} & \dfrac{1-v_{12}v_{21}}{E_1E_2\Delta} & 0 & 0 & 0 \\
0 & 0 & 0 & 2G_{23} & 0 & 0 \\
0 & 0 & 0 & 0 & 2G_{31} & 0 \\
0 & 0 & 0 & 0 & 0 & 2G_{12}
\end{bmatrix}
\begin{bmatrix} \varepsilon_{11} \\ \varepsilon_{22} \\ \varepsilon_{33} \\ \varepsilon_{23} \\ \varepsilon_{31} \\ \varepsilon_{12} \end{bmatrix}
$$

where σ_{ij} is total stress tensor

ε_{ij} is total strain tensor

E, v, G are the orthotropic elastic constants

$$
\Delta = \frac{1-v_{12}v_{21}-v_{23}v_{32}-v_{31}v_{13}-2v_{21}v_{32}v_{13}}{E_1E_2E_3}
$$

For Nextel and Kevlar-epoxy, and tests thus far support this, we may not be able to consider the response as linearly elastic; for instance, Nextel exhibits a non-linear elastic response due to decrimping effects. We therefore propose to replace the constants in the above stiffness matrix with non-linear functions C_{ij} which might depend on, for instance, strain. Further so that the deviatoric and volumetric components can be coupled it is necessary to decompose the total strain tensor into volumetric (ε_v) and deviatoric (ε_{ij}^d) components.

$$
\begin{bmatrix} \sigma_{11} \\ \sigma_{22} \\ \sigma_{33} \\ \sigma_{23} \\ \sigma_{31} \\ \sigma_{12} \end{bmatrix} =
\begin{bmatrix}
C_{11} & C_{12} & C_{13} & 0 & 0 & 0 \\
C_{21} & C_{22} & C_{23} & 0 & 0 & 0 \\
C_{31} & C_{32} & C_{33} & 0 & 0 & 0 \\
0 & 0 & 0 & C_{23} & 0 & 0 \\
0 & 0 & 0 & 0 & C_{31} & 0 \\
0 & 0 & 0 & 0 & 0 & C_{12}
\end{bmatrix}
\begin{bmatrix} \varepsilon_{11}^d + \dfrac{1}{3}\varepsilon_v \\ \varepsilon_{22}^d + \dfrac{1}{3}\varepsilon_v \\ \varepsilon_{33}^d + \dfrac{1}{3}\varepsilon_v \\ \varepsilon_{23}^d \\ \varepsilon_{31}^d \\ \varepsilon_{12}^d \end{bmatrix}
$$

Since the pressure is the average of the three direct stresses, from above we can obtain:

$$
P = -\frac{1}{9}\left(C_{11}+C_{22}+C_{33}+2C_{12}+2C_{23}+2C_{31}\right)\varepsilon_v
$$

$$
-\frac{1}{3}\left(C_{11}+C_{21}+C_{31}\right)\varepsilon_{11}^d - \frac{1}{3}\left(C_{12}+C_{22}+C_{32}\right)\varepsilon_{22}^d - \frac{1}{3}\left(C_{13}+C_{23}+C_{33}\right)\varepsilon_{33}^d
$$

For an isotropic Hookean material the first term on the right-hand side is equivalent to a linear equation of state, whilst the remaining deviatoric strain terms would be zero. Thus for an orthotropic material we can replace the first term with a Mie-Gruneisen equation of state and the remaining terms act as a correction due to deviatoric strains [1].

$$
P = P_r(\varepsilon_v) + \frac{\Gamma(v)}{v}\left[e - e_r(\varepsilon_v)\right] - \frac{1}{3}\left(C_{11}+C_{21}+C_{31}\right)\varepsilon_{11}^d - \frac{1}{3}\left(C_{12}+C_{22}+C_{32}\right)\varepsilon_{22}^d - \frac{1}{3}\left(C_{13}+C_{23}+C_{33}\right)\varepsilon_{33}^d
$$

The parameters $P_r(\varepsilon_v)$ and $e_r(\varepsilon_v)$ respectively define the material pressure-volume and energy-volume relationship along a reference curve, usually taken to be the shock Hugoniot. The Gruneisen gamma, $\Gamma(v)$, allows extrapolation to material states off the reference curve and is a thermodynamic property of the material.

The model in the above form has been incorporated into the AUTODYN hydrocode. Currently, linear orthotropic strength and failure can be combined with solid equations of state. Further work is now being carried out so that compaction and non-linear strength effects can be incorporated into the above approach. In addition the model will be combined with existing orthotropic failure models so that failure modes such as delamination and fibre failure can be detected. The detected failure modes will be used as criteria for degrading the material strength, which will be achieved by reducing the terms in the stiffness matrix above.

CHARACTERISATION TESTS AND SIMULATIONS

A range of material tests are being carried out at Ernst Mach Institute (EMI), and The Netherlands Organisation of Applied Scientific Research (TNO) where indicated, to characterise the material model input data and to provide data for comparison with simulations. The range of tests being conducted is listed below. Details of the last three types of test, and corresponding simulations, are given in the remainder of the paper.

- Uniaxial static tensile tests
- Uniaxial dynamic tensile tests
- Biaxial static tensile tests
- Biaxial dynamic tensile tests
- Surface wave propagation tests
- Triaxial static compression tests
- Hypervelocity flyer plate tests (up to 10km/s) using the TNO Mega Ampere Pulser
- Confined static compression tests
- Inverse flyer plate tests (up to 1.2km/s)
- Hypervelocity impact tests up to 7km/s on multi-shock bumper shield systems

Confined Static Compression Test (CSCT)

The purpose of these tests is to characterise the static compaction data for the materials. Whilst dynamic compaction occurs in flyer plate tests the problem is that the compaction response is not directly measured and is heavily coupled with other responses. Static compression tests have been used in the past to obtain compaction data for heat shielding material and for subsequent usage in hydrocode simulations [6]. A schematic of the test rig developed is shown in Fig. 1 together with a sample load-displacement curve obtained for 22 layers of Nextel AF62 cloth mounted perpendicular to the load direction. The curve shown includes five unload-reload cycles with the peak load being increased in steps of 20% of the maximum. Similar tests are being carried for Nextel cloth in transverse directions by rolling the cloth and also for Kevlar-epoxy and Kevlar cloth. By confining the macroscopic lateral displacement we are thus able to obtain information about the compaction relationships on the leading diagonal of the anisotropic stress-strain relationships; that is C_{11}, C_{22} and C_{33}. A porous compaction model has been fitted to the experimental compaction data as shown in Fig. 1. For this model the solid density of the Nextel is assumed to be 2.7 g/cc, this being the density of the constituent filaments of Nextel 312. The model has been subsequently used in simulations of the flyer plate tests that are described next.
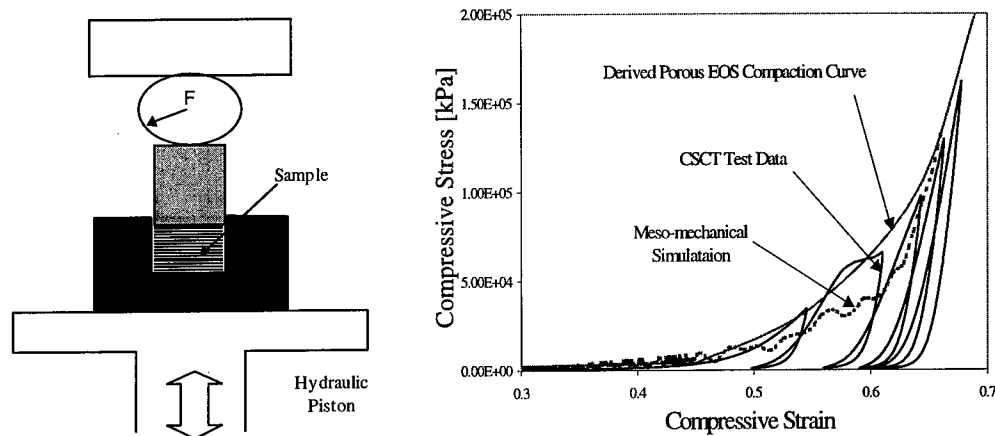
Fig. 1. Confined static compression test set-up and sample results for Nextel cloth together
with fitted porous compaction curve and meso-mechanical simulation results.

Numerical simulations of a typical woven Nextel fabric subjected to confined compressive
loading have been conducted. These simulations have been carried out at two levels: Micro-
mechanical simulations of a single Nextel yarn and meso-mechanical simulations of a typical
repeating weave in Nextel cloth. Reflective electron microscopy (REM) images of a sample of
Nextel AF62 cloth are shown in Fig. 2 along with corresponding numerical models.
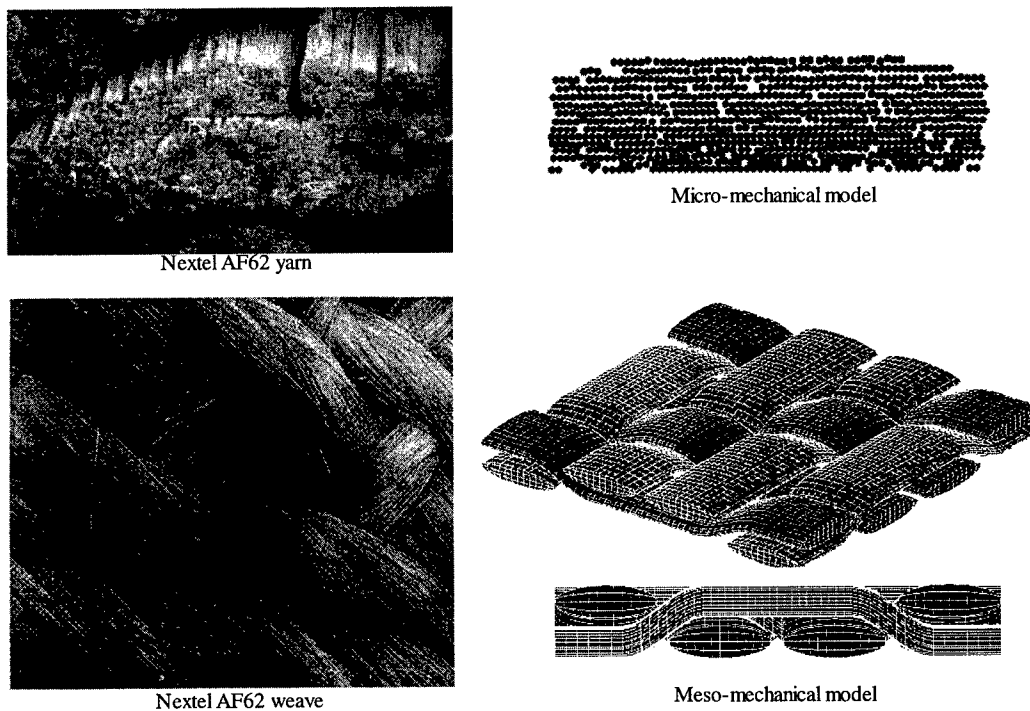
Fig. 2. Nextel AF62 REM images and micro- & meso-mechanical models.

The micro-mechanical model of a single Nextel yarn includes an explicit representation of
each filament of Nextel. In-plane loading is applied in the simulation to investigate the

compressive load deflection behaviour (yarn compaction) for different filament arrangements. The resulting load displacement (stress-strain) curves provides input to a non-linear orthotropic material model for each yarn in the Nextel cloth modelled in the meso-mechanical model. Each yarn is assumed to have non-linear orthotropic tensile and compressive properties which can vary independently with the corresponding orthotropic strain state. Coupling between the yarn orthotropic material directions is assumed negligible; that is C_{12}, C_{13}, and C_{23} are assumed to be zero. Application of confined compressive loading in the meso-mechanical simulation results in qualitatively similar compaction behaviour to that observed in the tests (Figure 1).

One important feature of the response of Nextel to confined compressive loading is fracture and breakup of the filaments at relatively small load. The meso-mechanical simulations show how breakup occurs in the weave.

Inverse Flyer Plate Test (IFPT)

Data on uniaxial compression at higher strain rates is being obtained by use of the inverse flyer plate test. The flyer consists of the Nextel or Kevlar-epoxy backed by a metallic plate (either C45 steel or aluminum) whilst the target witness plate is C45 steel. A laser velocity interferometer VISAR is used to record the rear side velocity of the target plate. Sample target plate velocity time histories from two tests are shown in Fig. 3, together with details of the flyer plate set-up.
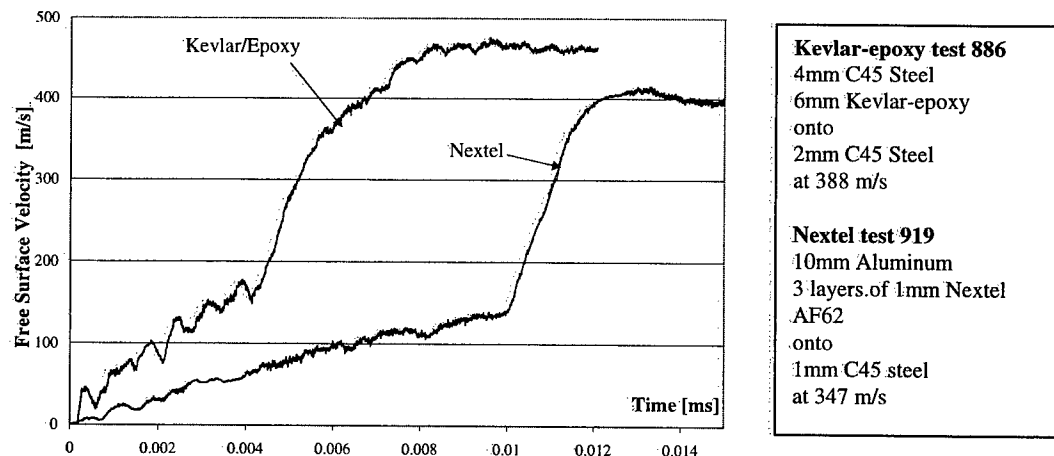
Fig. 3. Inverse flyer plate back surface velocity histories for Kevlar-epoxy and Nextel.

The Kevlar-epoxy velocity time-histories exhibit velocity reductions, which at this stage are assumed to be due to release waves being generated inside the Kevlar-epoxy during compression. These could be due to impedance mismatches between the Kevlar and epoxy constituents and/or vaporisation of the epoxy. Post-impact examination of the specimens shows that epoxy vaporisation is taking place at this range of impact velocities. Another related effect, which may be being observed, is the coupling of blast effects with the fabric deformation, where the epoxy vapour is confined between the steel plates and within the Kevlar fabric. Such hypotheses will be examined in further physical and numerical experiments.

The Nextel time-history exhibits a similar trend but with much less pronounced velocity reductions. Both tests exhibit a rapid rise in velocity (at 4.5μs for Kevlar-epoxy and 10.5μs for Nextel) which is due to the compression wave being reflected from the backing plate of the projectile. Velocity time-histories taken from simulations of the flyer plate test on Nextel are shown below and compared with the experimental result. The two simulation results show the dramatic difference that is obtained when porous compaction is included in the Nextel material

model. The match between the porous model case and the experiment is encouraging. The material model in this case consists of a porous equation of state for the Nextel with no shear strength. In the porous equation of state the reference curve, $P_r(\varepsilon_v)$, was derived directly from the confined static compression test result shown in Fig. 1. The energy dependence, $\Gamma(v)$, and deviatoric contribution to pressure was assumed to be zero. It is expected that further refinement of this model by incorporating anisotropic dynamic strength and energy effects will lead to a further improvement in the correspondence between simulation and experiment.
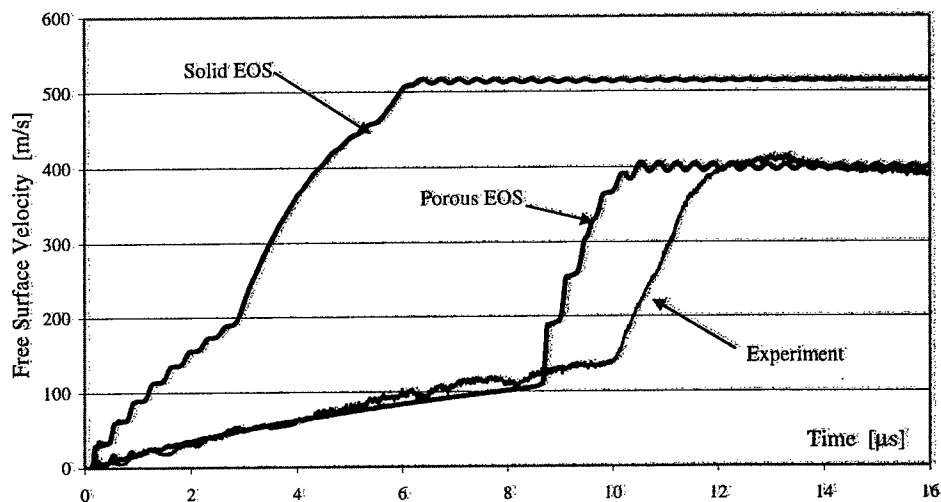
Fig. 4. Comparison of Nextel experimental and simulated flyer velocity histories for solid [from 4] and porous [Fig. 1] equation of state data.

HYPERVELOCITY IMPACT TESTS AND SIMULATIONS

Hypervelocity Tests of Multi-Shock Shield

Hypervelocity impact tests on multi-shock shields have been conducted at EMI for Alenia/ESA [7]. Test case 8656 was chosen for detailed comparison with the simulations described below and has details as follows:

- Impact velocity 6290 m/s at 0 degrees
- Projectile is 16mm diameter Aluminum 207 sphere, density 2.85g/cc
- Bumper is 2.5mm Aluminum 6061-T6
- The second bumper consists of 4 layers of Nextel AF62 fabric with 12 layers of Kevlar 129-812 plates bonded with Brochier 914 epoxy (<40% by mass)
- Backwall is 3.8mm Aluminum 2219-T851
- Spacing between front of bumper and rear of backwall is 170mm
- Spacing between rear of Kevlar-epoxy and front of backwall is 42mm
- 5 aluminum 2024-T3 witness plates were placed behind the backwall at 25mm spacings

Side view of all shields
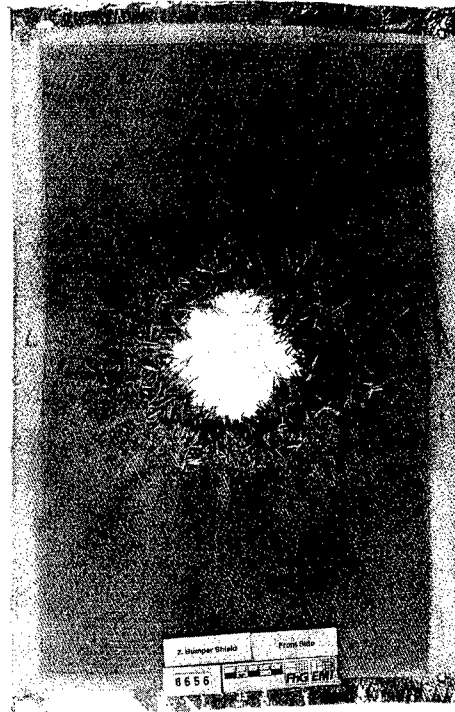
Nextel front surface
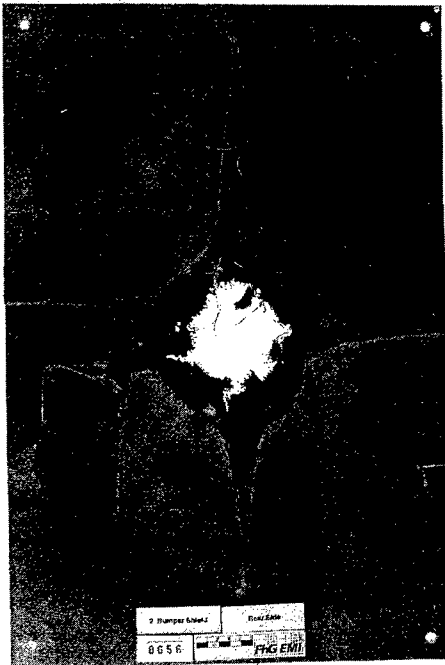
Kevlar-epoxy rear surface

Backwall rear surface

Fig. 5. Alenia/ESA test 8656 [7] post-test images of the damaged multi-shock shield.

Images of the resulting targets after impact are shown in Fig. 5. Features of note are the approximately circular perforation and response of the Nextel, with fibre tensile failure occurring around the edge of the central hole. The Kevlar-epoxy exhibits extensive delamination and in-plane cracking/petalling particularly towards the back surface. The central perforation is approximately circular and around this central hole there is evidence that the epoxy has vaporised. The backwall shows large plastic deformation due to bending together with extensive petalling.

Simulations of Multi-Shock Shield Hypervelocity Tests

Two-dimensional cylindrically symmetric AUTODYN hydrocode simulations have been conducted of test 8656. The experimental results suggest that the cylindrical approximation is reasonable except that the petalling behaviour of the Kevlar-epoxy and the aluminum backwall will not be well represented. The two-dimensional models enable simulation using much finer resolution of the materials than would be possible with a full three-dimensional analysis. The Smooth Particle Hydrodynamics (SPH) technique was used to model all materials. Previous detailed comparisons of experiments by Piekutowski and 2D SPH simulations using AUTODYN indicate a good degree of confidence in this simulation approach [8]. Fig. 6 shows a comparison of the experimental and simulated debris cloud at a time just before impact with the multi-shock shield.
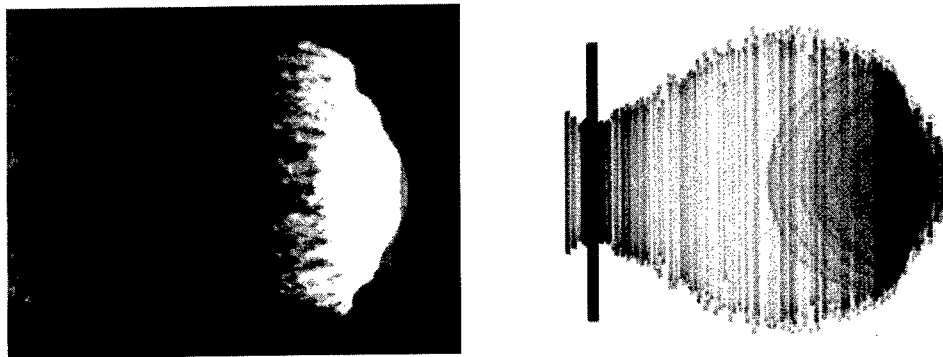
Fig. 6. Experimental and simulated debris clouds in test 8656.

The particle size was set at 0.25mm throughout so that, for instance, the bumper was modelled using 10 SPH particles through thickness. In the simulations conducted the 5 rear witness plates were not included. The aluminum plates and projectile were modelled using a "Shock" equation of state and Johnson-Cook strength model. The data was based on that for aluminum 2024-T351 [9] but with the density modified to represent the particular alloy; 2.85g/cc for the projectile, 2.785g/cc for bumper and backwall. In addition, a principal tensile stress failure model was included with the failure stress in all cases being set at 1.2GPa.

Three simulations consisting of different material model cases for the Nextel and Kevlar-epoxy have been conducted, as follows.

- Non-porous, isotropic, with no strength for Nextel and Kevlar-epoxy (Model 11)
- Non-porous, anisotropic, with strength for Nextel and Kevlar-epoxy (Model 12)
- Porous, isotropic, with no strength for Nextel combined with a non-porous, anisotropic, with strength model for Kevlar-epoxy (Model 14)

Material location plots from these three simulations are shown in Fig. 7.
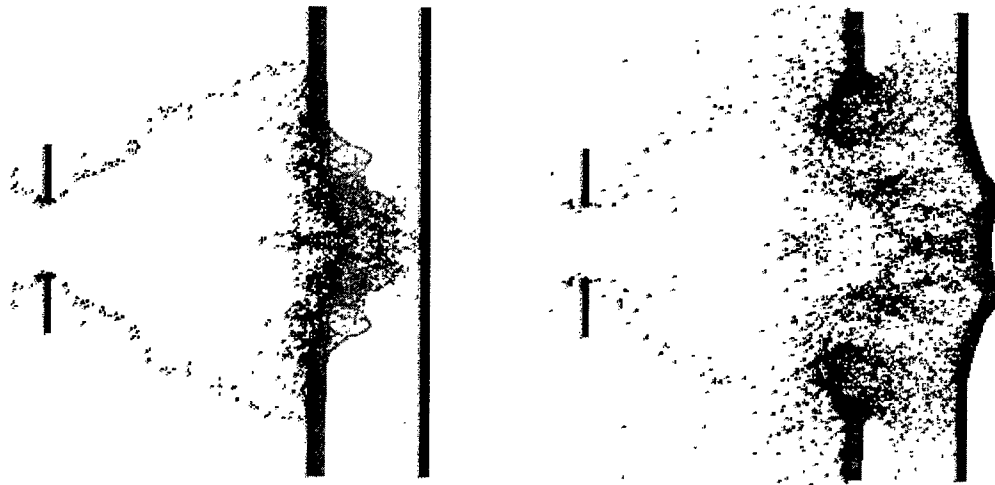
Model 11: Non-porous, isotropic, no strength for Nextel and Kevlar-epoxy
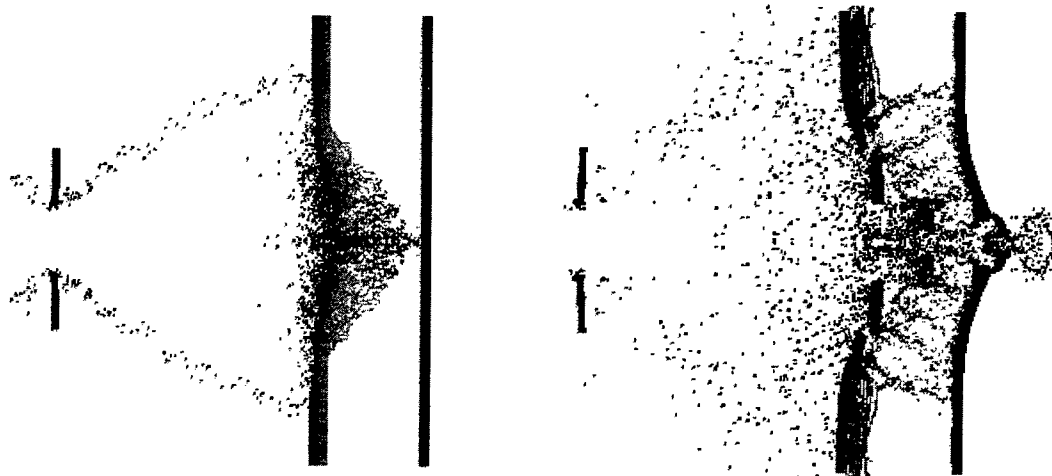
Model 12: Non-porous, anisotropic, with strength for Nextel and Kevlar-epoxy
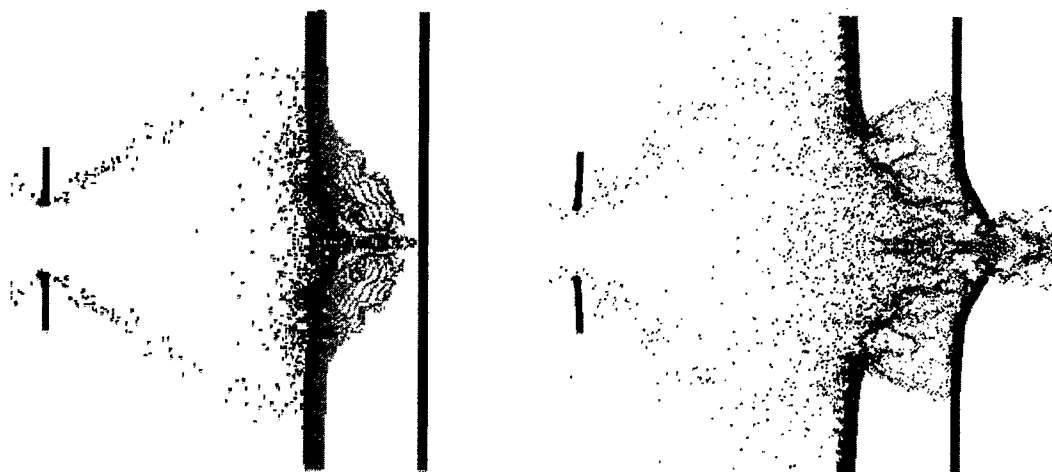
Model 14: Porous, isotropic, no strength for Nextel & non-porous, anisotropic, with strength for Kevlar-epoxy

Fig. 7. Material locations at 34μs & 76μs from AUTODYN-2D simulations of test 8656.

The anisotropic models use an orthotropic linear elastic model with elastic constants based on measured or calculated values. They also include orthotropic brittle failure criteria to detect directional failure such as delamination. The isotropic models include a minimum tensile pressure failure criterion.

A comparison of the experimentally measured hole sizes with those obtained in the simulations is given below:

Table 1. Hypervelocity test 8656, experiment and simulation hole sizes

Bumper material	Perforated Diameter (mm)			
	Test 8656	Model 11	Model 12	Model 14
Nextel	103	136	80	99
Kevlar-epoxy	56	146	108	95

The model 11 case results in hole sizes in the Nextel and Kevlar-epoxy which are much too large as might be expected in this simple hydrodynamic model. The backwall deformation is reasonably represented although the perforated diameter of 42mm is larger than indicated in the experiment.

Model 12, which includes anisotropic linear elastic behaviour before failure, predicts much smaller perforation diameters than model 11, although the hole size in the Kevlar-epoxy is still too big. The hole in the Nextel is now too small indicating perhaps that the representation of the Nextel is too strong. This might also cause the very extensive delamination in the Kevlar-epoxy, which appears to be much greater than that evident in the test. The backwall deformation is generally consistent with the test, within the limitations of the cylindrically symmetric simulation, and the perforation diameter is more representative of the experimental observations.

Model 14, which includes a porous model for the Nextel, better predicts the hole sizes in the Nextel. The hole size in the Kevlar-epoxy, although closer to the test, is still too large. The porous model used in this case is the same as that used in the earlier flyer plate simulations, and as derived from the constrained static compression test results. The backwall deformation is again consistent with the test.

The total elapsed time to run each of the above simulations to 76µs on a dedicated Pentium 2 300MHz PC was approximately 16 hours. The simulations were carried out, without user intervention, using AUTODYN-2D. No attempt was made to optimise the computer time required for these analyses.

DISCUSSION

The work described here is aimed at developing a material model for Nextel and Kevlar-epoxy multi-shock shields. The aim is not to simulate the detailed micro-mechanical behaviour of such materials but rather to develop a macro-mechanical model, which represents the main phenomena of relevance. As such, the model is intended to be applicable to existing continuum-based techniques in hydrocodes. Whilst the work is at an early stage of model development and material characterisation, some promising results have already been obtained and project completion is expected in the first half of 1999.

The proposed model is intended to couple together the effects of compaction, anisotropy and strength degradation. To achieve this, a means of coupling together spherical and deviatoric response is required and this will be based on the approach proposed by Anderson [1]. Current work is extending this approach for the case of non-linear behaviour, in particular by incorporating porous compaction effects.

Ten different types of experimental tests are being conducted as a means of characterising the material behaviour and to provide data for comparison with corresponding simulations of these tests. Confined static compression test results have enabled the quantification of a simple porous compaction model for the Nextel. This porous model has been applied to simulations of inverse flyer plate tests that have been conducted. This resulted in much improved simulation results when compared with simulations conducted using conventional Nextel shock data. Further improvement is expected, as more complex material responses are included in the flyer plate simulations. Work in the near future will also focus on the response of Kevlar-epoxy as well as Nextel.

Hypervelocity impact tests previously conducted on multi-shock shields [7] have been used to assess the status of the developing material model. SPH simulations of the three material model variations shown above indicate the sensitivity to the assumed material behaviour. These simulations indicate the importance of the anisotropic response of the Nextel and Kevlar-epoxy and the macroscopic compaction behaviour of the Nextel. Work in the near future will concentrate on performing simulations that incorporate both of these effects.

REFERENCES

1   C.E. Anderson, P.A. Cox, G.R. Johnson, P.J. Maudlin, "A Constitutive Formulation for Anisotropic Materials Suitable for Wave Propagation Computer program-II", Comp. Mech., vol. 15, p201-223, 1994

2   B.G. Cour-Palais, J.L. Crews, "A Multi-Shock Concept for Spacecraft Shielding", Int. J. Impact Engng., 10, 135-146, 1990

3   E. Cykowski, "Hydrocode Modelling of Cadmium and Aluminum Projectile Impacts into Whipple Shields", JSC 32311, May 1994

4   J.H. Kerr, J.L. Crews, E.L. Christiansen, L.C. Chabildas, "Evaluating the Equation of State for Nextel AF62", 1996 Hypervelocity Impact Symposium, Freiburg, Germany, October 1996

5   J.K. Chen, F.A. Allahdadi, T.C. Carney, "High-velocity Impact of Graphite/Epoxy Composite Laminates", Comp. Sc. and Tech.. 57, 1369-1379,1997

6   C. Loupias, J.M. Sibeaud, P.L. Hereil, "Hypervelocity Impacts of Orbital Debris on an Advanced Heat Shielding Material: Comparison of Ouranos Computations to Experimental Results", Int. J. Impact Engng., 20, 545-556, 1997

7   F. Schafer, E. Schneider, "Hypervelocity Impact Test Campaign, Columbus APM-COF", Phase 2 Report No. 1, EMI-HVITC 003, Ernst Mach Institut, October 1997

8   C.J. Hayhurst, R.A. Clegg, "Cylindrically Symmetric SPH Simulations of Hypervelocity Impacts on Thin Plates", Int. J. Impact Engng., 20, 337-348, 1997

9   G.R. Johnson, W.H. Cook, "A Constitutive Model and Data for Metals Subjected to Large Strains, High Strain Rates and High Temperatures", 7th Int. Symp. on Ballistics, The Hague, 1983

CHARACTERISATION OF REAR INCIDENT HYPERVELOCITY IMPACT PHENOMENA ON HUBBLE SPACE TELESCOPE SOLAR ARRAYS

M. K. HERBERT

Unit for Space Sciences & Astrophysics, University of Kent at Canterbury, Canterbury, Kent CT2 7NT, U.K.

Summary—Impact damage on glass faced HST solar cells generated by rear-incident impactors represent over one-third of the total damage on the retrieved solar array. Analysis of such space and laboratory generated morphologies has revealed a means of discriminating between front and rear incident impact sites and enabled characterization through either impactor energy or a simplified indentation fracture model. Morphology is seen to evolve with impactor energy and incidence. Onset of rear incident penetration occurs at one-third of the particle size necessary for front incident. Calibration of rear incident particle flux-size is possible using this approach. © 1999 Elsevier Science Ltd. All rights reserved.

NOTATION

d	projectile diameter [mm]	Subscripts:	
D	diameter of impact feature [mm]	co	conchoidal
E	impactor energy [J]	hf	hole front
s	semi-breach distance [mm]	hr	hole rear
ρ	density [g/cm^3]	is	inner spallation
t	target thickness [mm]	os	outer spallation
t_x	cumulative target depth for class x [mm]	p	projectile
V	velocity [km/s]	pro	silicon protrusion
θ	projectile incidence angle relative to apex [°]	rtv	room temp. vulcanised rubber (silicon based)
2α	cone crack angle [°]	x	morphology class

INTRODUCTION

On retrieval from Low Earth Orbit (LEO), solar arrays provide a routine and cost-effective means of monitoring change to the space particulate environment. Their large area-time product and pointing stability make them suited to detect small changes in directional particle flux. The retrieved Hubble Space Telescope (HST) Solar Array (SA) has demonstrated solar cells to be effective particle detectors. Despite 2700 impact sites in the one hundred micron to centimetre size range [1], HST solar cells have shown an ability to function without impact attributed power loss [2]. The second set of HST solar arrays provides current in-situ monitoring and the next opportunity of space retrieval to verify the predicted increase in untrackable orbital debris [3] and enhanced Leonid meteoroid stream activity [4]. (The latter assumes no in-plane slew of the arrays with the stream radiant.) Ability to decode hypervelocity impact signatures on HST solar cells into particle flux-size distributions is of fundamental importance, enabling a continuous monitoring capability. To this end, this paper presents how we may utilise discrete impact morphologies to i) discriminate between front and rear incident impact sites, and ii) characterise the rear incident space impactors.

CLASSIFICATION OF IMPACTS

Much of the research to date has focused on interpreting impact data produced by particles incident on the array's glass face (defined as *front-top* impacts). Rear incident impact phenomena on glass faced HST solar cells (defined as *front-back* impacts) has, up to now, been relatively unexploited. The latter represent in excess of one third of the impact damage on HST consistently generating the largest singular surface areal damage. Given the relatively thin (705μm) and 'finite' thickness of the composite solar cell, *front-back* damage is unique to the HST solar array enabling an improved front-to-rear flux-size comparison than offered by the retrieved EURECA solar arrays [5]. Earlier detailed analysis of space impacts on solar cells identified significant morphological differences between *front-back* and *front-top* impacts suggesting that the physical impact processes may vary considerably. Therefore, the impact parameters for *front-back* and *front-top* morphologies change according to the differing directional response of the cell to hypervelocity impact. A classification of all commonly observed impact morphologies on solar cells has been produced by the author [6].

A summary definition of *front-back* morphologies is now described (in order of increasing damage) based on observations of high resolution imagery from space generated impacts [7]. **Class Pre-A** is characterised by an irregular crimson edged spallation zone (D_{os}) raised slightly from the undisturbed surface (Figure 1)[1]. No radial cracks are visible. No central hole exists, though often there is evidence of central spall denoting pre-hole formation (D_{hf}). This class marks the threshold at which a rear-incident particle is on the verge of penetrating a solar cell or ballistic limit.

Space Generated Class Pre-A
[impact ref. F_A_O8pF41].

Lab. Generated Class Pre-A
[impact ref. RITP-1 20_f1].
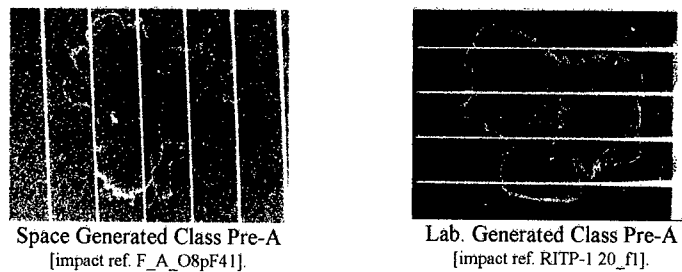
Fig. 1. Class Pre-A Morphology.

Class A is characterised by a central hole through a retained and raised cover glass (D_{hf}) as in Figure 2. The glass has radial cracks bound by annular spall (D_{is} and D_{os}). Cracks in the raised cover glass are most likely to have been initiated by lifting of the deformed silicon beneath.

Space Generated Class A
[impact ref. F_A_I8pV25]

SCALE (IN MICRONS)
0   500   1000   1500

Vp

UNDISTURBED
FRONT SURFACE
Dos
Dis
Dhf

ANTI-SUN FACE
CMX COVER GLASS
BSFR SOLAR CELL
RTV ADHESIVE
GLASS FIBRE SUBSTRATE

Lab. Generated Class A
[impact ref. RITP-1 08_f1]

Fig. 2. Class A Morphology.

Class B is characterised by a central silicon protrusion (D_{pro}) evolving from the exposed silicon layer, through which a hole (D_{hf}) can sometimes be observed (Figure 3). Occasionally,

---

[1] the distance between two parallel solar cell collector lines is 1.25mm

part of the cover glass is not always thrown off indicating a potential progression between Class A and B. Usually, the cover glass is not retained. The inner silicon wall of the crater appears excavated (D_{is}) and is surrounded by outer spall in the cover glass (D_{os}).

Space Generated Class B
[impact ref. F_AA_7pM15].

Lab. Generated Class B
[impact ref. RITP-1 13_f2]
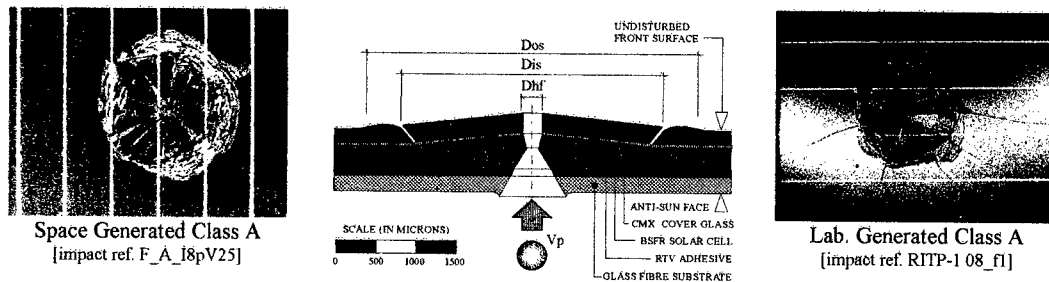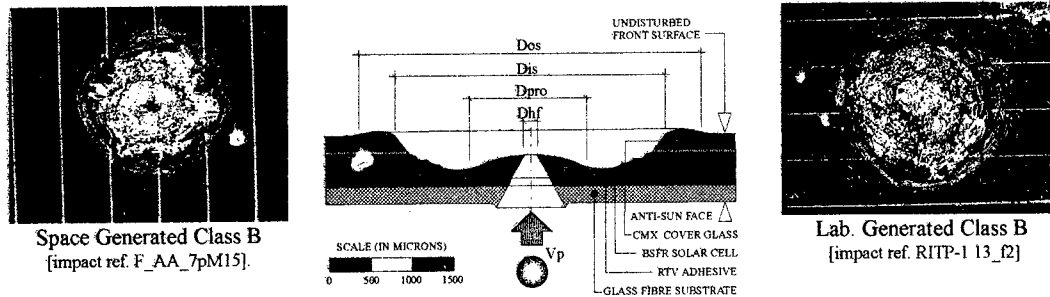
Fig. 3. Class B Morphology.

Class C is characterised by a central hole through the entire cell structure (D_{hf}) around which is an exposed layer of RTV (D_{rtv}) shown in Figure 4. It has been suggested that the central protrusion visible in Class B is displaced at a critical energy, exposing the RTV layer beneath. The exposed RTV, bound by a silicon lined crater wall (D_{is}), has a terraced appearance. At the periphery, outer spall (D_{os}) comprising finely shattered cover glass surrounds the crater wall.

Space Generated Class C
[impact ref. F_A_7pJ37].

Lab. Generated Class C
[impact ref. RITP-1 15_f5f6].
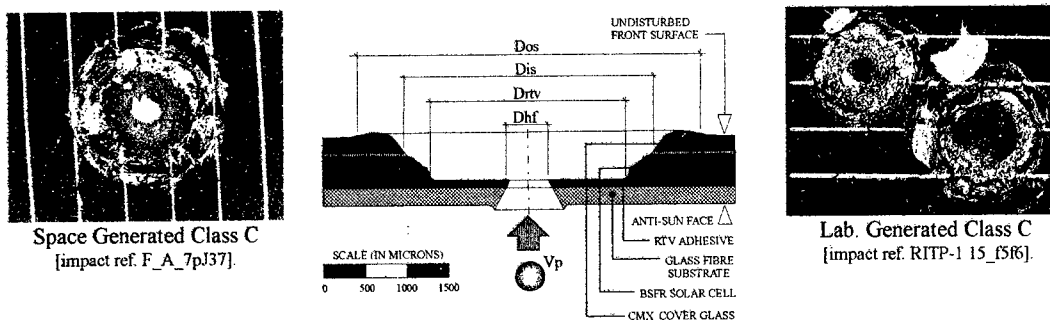
Fig. 4. Class C Morphology.

Yano *et al* suggested that each of the four *front-back* morphologies were discrete states in a progressive evolutionary impact process [8]. Detailed examination of space generated impacts revealed the existence of intermediate morphological states denoted Pre-A/A, A/B and B/C; the observational evidence given and their relatively low frequency of occurrence (Table 1), established a link between each morphology. Clearly, experimental proof was required to substantiate any evolutionary impact process and establish its most likely dependencies.

Table 1. Summary of HST Front-Back Impacts

Morphology Class/State	No. Observed	Relative Proportion
Pre-A	10	5%
Pre-A/A	8	4%
A	60	28%
A/B	12	5%
B	71	33%
B/C	8	4%
C	46	21%
Total Impacts:	215	100%

EXPERIMENTAL PROGRAMMES

In response to the need for calibration of the space generated *front-back* impacts, two Rear Impact Test Programmes (RITP) were performed; the first by the author [9] and the second by a contract consortium (including the author) [10]. The first test programme (RITP-1) was devised in an attempt to reproduce the space generated *front-back* morphologies with the purpose of satisfying the following key objectives: i) verify the predicted *front-back* morphologies, ii) substantiate the hypothesised progressive evolution of *front-back* morphologies, iii) calibrate the *front-back* impact parameters to derive suitable damage equation(s) and, iv) determine the rear-incident ballistic limit of an HST solar cell. Space flown 'damage-free' (defined as having no visible impacts to the unaided eye, ie.$\geq$100μm) HST solar cells retrieved from Solar Panel Assembly (SPA) B (SPA nomenclature defined in [1]) were provided as target material. The array's structural composition and maximum thicknesses (t_{MAX}) are shown in Figure 5.
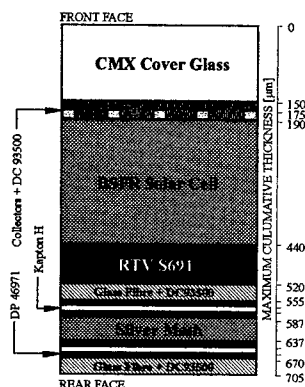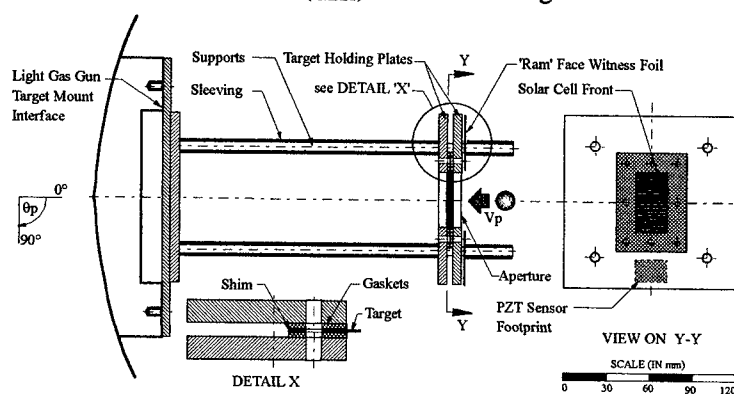

Fig. 5. HST Solar Cell Structure.

Fig. 6. RITP Test Configuration.

Figure 6 illustrates the RITP test configuration. Each solar cell, measuring 40.2 mm x 20.8mm was secured around its periphery between two 120mm x 120mm aluminium plates with a central 39mm x 19mm aperture. To assist attenuation and avoid catastrophic shock damage of the entire cell, each cell was sandwiched between 2mm rubber gaskets. An interchangeable aluminium witness foil of thickness 30$\pm$2mm was mounted on the 'ram' face of the top plate to monitor the in-plane rear face ejecta cloud. Projectiles were accelerated normal to the target assembly by the two stage Light Gas Gun (LGG) facility at the University of Kent at Canterbury (UKC) using 10.10$\pm$0.05g of R19 or R22 shotgun powder. The working gas was either hydrogen or nitrogen (depending on the velocity required) at an initial pressure of 42.5 $\pm$ 1.0bar. The projectiles were loaded individually into 4.3mm diameter long nylon sabot (split into 4 parts). Sabot stripping was accomplished by way of the rifled launch tube and a stop plate at 2.71m from the target. Velocity measurement was performed by determining the flight time using Piezoelectric Transducer (PZT) sensors on the stop plate and target. Laser light curtains were also used to complement the projectile flight time measurements. Signal timing was performed using a digital storage oscilloscope recording 10[8] samples per second. The error on the velocity measurements was $\pm$2%. Details of the projectile materials/sizes used and velocity regimes achieved are presented in Table 3.

Morphological class was largely considered to be a function of impactor energy. Limited availability of projectile materials and sizes required impact generation at both relatively low (2km/s) and high (5km/s) velocity regimes. A programme of 15 rear incident shots was undertaken, of which 6 shots were duplicated for repeatability. In addition, 3 front incident shots were performed with identical projectile parameters used in RITP-1; these shots would

enable comparison of the relative amounts of damage and morphologies for both front and rear incident impacts at a given projectile energy level.

Table 3. RITP-1 Projectile Parameters

Projectile Material	d_p [mm]	ρ_p [g/cm³]	V_p [km/s]	θ_p [°]
St. Steel 420	0.400	7.75	2.0±0.10	0.0
			5.0±0.40	0.0
Soda Glass	0.390	2.30	2.0±0.05	0.0
			4.7±0.60	0.0
Soda Glass	0.293	2.30	2.0±0.05	0.0
			5.0±0.30	0.0
Soda Glass	0.195	2.30	-	-
			4.8±0.05	0.0
Nylon 66	1.200	1.15	-	-
			2.2±0.05	0.0

Table 4. RITP-2 Projectile Parameters

Projectile Material	d_p [mm]	ρ_p [g/cm³]	V_p [km/s]	θ_p [°]
Soda Glass	0.098	2.45	5.0±0.10	0.0
Soda Glass	0.151	2.45	5.3±0.05	0.0
			5.0±0.10	30.0
			5.1±0.05	45.0
			5.1±0.05	60.0
Soda Glass	0.178	2.45	5.1±0.05	0.0
Soda Glass	0.225	2.45	5.1±0.05	0.0
Soda Glass	0.264	2.45	4.9±0.05	0.0
Soda Glass	0.320	2.45	5.1±0.05	0.0
Soda Glass	0.389	2.45	4.8±0.05	0.0

Given the limitation of RITP-1's angular range, a smaller second programme of rear impact testing (RITP-2) was required to fulfil the following objectives: i) assessment of morphology sensitivity and impact parameter dependence with impactor angle of incidence and, ii) enhancement of the RITP-1 data set with intermediate data points. For consistency, the UKC LGG was re-employed to undertake further *front-back* calibration shots (using the technique described for RITP-1) in accordance with the projectile parameters defined in Table 4. Only glass projectiles of between 98 to 389μm in diameter were fired at a velocity of 5.0±0.3km/s over a 0 to 60° angular range (for one size only) onto 'damage-free' HST solar cells retrieved from SPA-D. The RITP-1 target configuration was modified to suit the revised incidence range.

Laboratory generated impact sites on each solar cell were digitally scanned at a wide range of magnifications using HIROX HI-SCOPE KH-2200 Video Microscope facilities at CERT-ONERA. This approach was chosen to ensure compatibility of impact resolution and illumination conditions associated with the scanned space generated impacts performed during post-flight investigations. Images were displayed on a 20" 'Applevision' monitor using a Power Macintosh (8300) running Adobe Photoshop software. Digitisation at 768 x 512 pixels provided the most useful resolution. *Front-back* impact parameters were directly measured from enlarged colour prints using high magnification images via a steel scale calibrated to 0.5mm. This reliable measurement technique (previously verified [11]) permitted a large sample of impacts to be processed and was also used to measure the 215 high resolution space generated impact images having an outer spallation diameter range of 1.88mm to 6.07mm.

RESULTS & ANALYSIS

The resultant 74 *front-back* morphologies produced by both test programmes were integrated and compared with the 215 space generated impacts. A consolidated appraisal of the results and data analysis is now presented.

Space Morphologies Reproduced

Both test programmes successfully reproduced all classes of *front-back* impact morphology observed on the HST solar array; examples of space and laboratory generated impacts are presented in Figs 1-4, 7, 8, & 17. On comparison, the space and laboratory impacts demonstrate excellent correlation of morphologies. A summary of morphology classes and intermediate states produced is defined in Table 5.

Morphology Progression

The production of a number of intermediate morphology states (given in Table 5) assisted in verifying the *front-back* morphology progression.

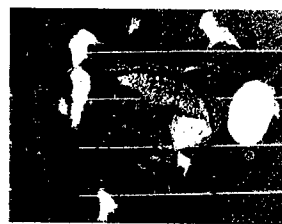Table 5. Summary of RITP Morphologies

Fig. 7. Class A/B Intermediate State [impact ref. RITP-1 06_f8].

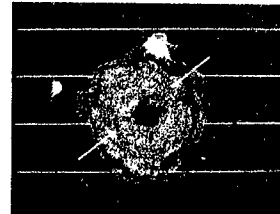| Morphology	Number of Impacts Produced		
Class/State	RITP-1	RITP-2	TOTAL
No Penetration	7	0	7
Pre-A	3	1	4
A	3	8	11
A/B	1	5	6
B	6	2	8
B/C	5	1	6
C	23	9	32
Total Impacts:	48	26	74

Fig. 8. Class B/C Intermediate State [impact ref. RITP-1 06_f4].

Figure 7 identifies the Class A/B intermediate state; 50% of the petals from the cover glass have been displaced, partially revealing the inner silicon layer. An unfolding Class C morphology is shown in Figure 8; note that the silicon protrusion (arrowed) has not fully displaced and the exposed RTV has formed within its envelope and not at its boundary. Despite the belief that the protrusion and exposed RTV features are inherently linked, no evidence for this has been firmly established. Comparison of D_{pro} with D_{rtv} for a large sample of space generated impacts, shows that D_{rtv} is consistently larger than D_{pro} (by a factor of 1.3) and that consequently the protrusion never achieves the size of the exposed RTV.

Morphology Ellipticity

The degree of ellipticity of each *front-back* morphology was investigated for its potential as an indicator of impactor incidence. In contrast with smaller size space generated *front-top* impacts, *front-back* impacts showed little evidence of pronounced spallation ellipticity. Contrary to this, non-normal incident impacts generated in the laboratory demonstrated a tendency towards high ellipticity, although these are not deemed to be of sufficient quality to provide a meaningful assessment. However, caution must be exercised as experimentation has sometimes shown ellipticity to be an unreliable measure of impactor incidence. This is evident from Figures 7 & 8, both of which resulted in differing degrees of ellipticity but were produced from normal impacts.

Impactor Energy

Impactor energy levels in the range of 0.06 to 3.51J were required to reproduce *front-back* space generated impacts. These energy levels were considered relatively low, possibly one to two magnitudes lower than an encounter with a meteoroid or debris particle in LEO; energies equate to impact damage from either a 0.1mm sporadic at 15km/s or 0.5mm aluminium debris at 7km/s. Figure 9 illustrates that *front-back* morphology progression is partially a function of impactor energy.

Discrete impactor energy levels are required to create morphology states up to and including Class A. Thereafter, with the cover glass displaced, morphology dependence on impactor energy alone appears to break down as the 0.8J plateau is reached. Clearly, an impactor of up to 0.8J could form any one of three morphologies. Therefore, the fundamental parameters from which impactor energy is derived (ρ_p, V_p^2 & d_p^3) appear to have limited influence on the morphologies generated beyond that of Class A.
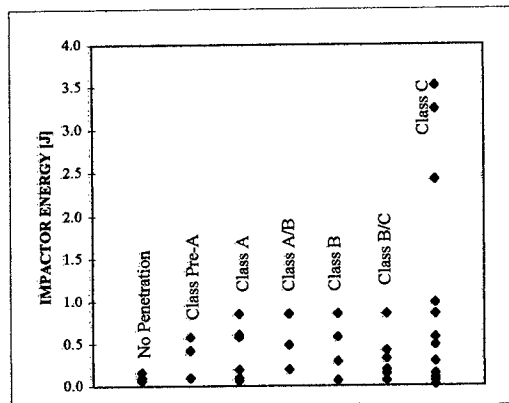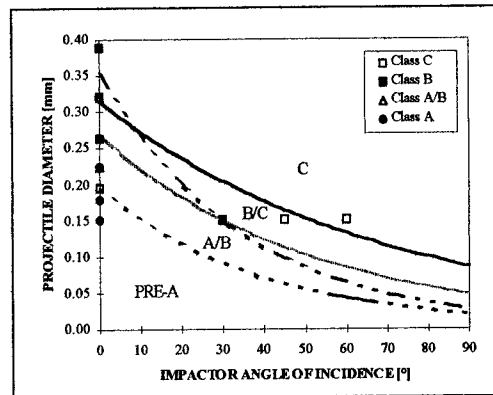
Fig. 9. Impactor Energy - Morphology Regimes.

Fig. 10. Morphology-Incidence-Size Diagram
(for ρ_p = 2.45g/cm^3 and V_p = 5.1km/s).

Morphology Sensitivity to Impactor Incidence

Data analysis of soda glass projectiles at the high velocity regime (ie. for a constant ρ_p and V_p) was performed to investigate any dependence of impactor incidence on *front-back* morphology. These data comprised a limited number of data points at non-normal angles (2 at 30°, 2 at 45° and 1 at 60°) in addition to 35 points at normal angles. Impactor angle of incidence (θ_p) was plotted against d_p for a given morphology class; the following morphologies at non-normal angles were available for plotting - 3 Class C, 1 Class B and 1 Class A/B. The resultant plot (Figure 10) combines and relates the three variables d_p , θ_p and morphology for a given ρ_p and V_p, and hereafter, is referred to as a Morphology-Incidence-Size (MIS) diagram.

An exponential decay function extrapolated over a full angular range best fitted the Class C data points. Given that Class C yielded the most reliable data set, a similar function was applied to Class B and also assumed to fit Class A, which was without non-normal data points. The MIS diagram tentatively indicates that, i) morphology is sensitive to both θ_p and d_p , ii) the same impact morphology can be generated by either a particle with high incidence-small size or low incidence-large size, iii) evidence of a morphology evolution that progresses with θ_p and d_p and iv) given any two variables, the third can be determined. Equivalent MIS diagrams can also be produced for other values of ρ_p and V_p. Packaging d_p and θ_p in terms of ρ_p and V_p provides a means of isolating particle source; ie. for a known meteoroid stream or orbital debris population. The experimental data at non-normal angles is currently insufficient to confirm any of these interpretations with a high degree of confidence. However, if further experimentation finds this relationship to hold true, morphology becomes a key factor not only to define particle size but also the spatial direction from whence they originated. To utilise the MIS diagram, a means of solving for d_p or θ_p from *front-back* impact parameters is required. Given the uncertainty of any relationship between θ_p and morphology, deriving damage laws from impact parameters in terms of d_p was considered more reliable.

Ballistic Limit

The rear-incident ballistic limit of an HST solar cell has been defined by the minimum impactor energy required to generate a Class Pre-A morphology. Experimentation has determined this threshold in terms of projectile parameters (Table 6). The projectile parameters necessary to generate no penetration are also tabulated; the variation in onset of penetration may be attributed to the non-homogenous nature of the cell. The ballistic limit has not yet been detected at impacts other than those at normal incidence; the MIS diagram establishes the size-incidence envelope at which Pre-A is predicted to occur.

Table 6. HST Solar Cell Rear & Front Incident Ballistic Limit

| Ballistic Limit	d_p [mm]	ρ_p [g/cm³]	V_p [km/s]	θ_p [°]	E [J]
Rear Incident : Pre-A (E_{MIN})	0.195	2.30	4.78	0.0	0.102
Rear Incident : No Penetration (E_{MAX})	0.389	2.30	2.11	0.0	0.159
Front Incident : Class III (E_{MIN})	0.400	7.75	4.60	0.0	2.747

In addition, data from *front-top* laboratory generated impacts were used to compare the front and rear incident ballistic limits (Table 6); limited experimentation has shown onset of penetration to occur at D_{co} = 2.36mm (Class III morphology). Analysis of space generated *front-top* data has identified front incident onset of penetration to occur at D_{co} = 2.28mm (Class IV morphology) [6]. In terms of solar cell performance, the front to rear impactor energy ratio at the ballistic limit shows the solar cell to be 27 times less resilient to rear incident impact; thus exposed to a particle stream (at a constant ρ_p and V_p) within the ballistic energy regime, rear incident penetration will result at one-third of the particle size necessary for front incident penetration.

Outer Spallation

The outer spallation diameter is the largest and most indisputable glass face impact feature common to all *front-back* morphologies and therefore, a useful parameter to; i) compare the relative damage between front and rear incident impactors and, ii) universally inter-relate all morphology classes. Data from laboratory generated impacts were used to determine the relative areal damage of front and rear incident impactors at a given energy level, defined by the ratio of maximum areal rear to front impact parameters A_{rf} Eqn.(1);

$$A_{rf} = (D_{os} / D_{co})^2$$ (1)

Application of the most reliable data consistently determined A_{rf} to fall in the range 4.6 to 12.4; the implications are that rear incident impacts yield the largest areal damage and are the most significant contributor to surface degradation of the solar array's front face.   As Figure 11 illustrates, D_{os} does not significantly vary with morphological class unlike the *front-top* impact equivalent (D_{co}) [6].   Space generated *front-backs* yield a weighted mean for D_{os} of 4.0±1.2mm; 95% of laboratory produced *front-backs* fall within the space generated D_{os} envelope.   Hence, outer spallation diameter remains constant with morphology.
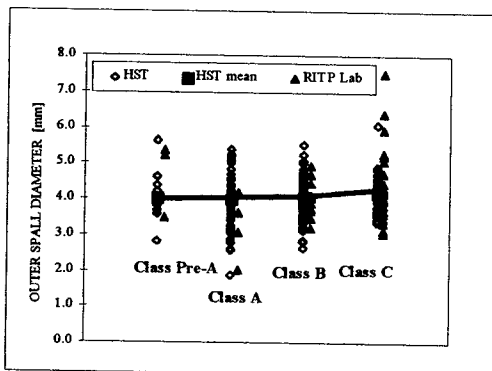
Fig. 11. Variation of D_{os} with Morphology Class.
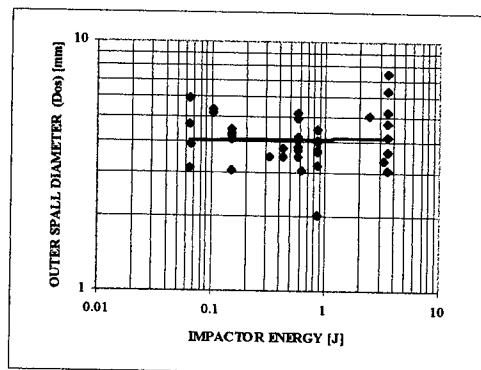
Fig. 12. Independence of D_{os} with Impactor Energy.

During the exploratory search for a universal damage law, D_{os} demonstrated independence of projectile size, density and velocity for all morphologies as illustrated in the $\log_{10}$ -$\log_{10}$ plot (Figure 12) reducing its characterising potential. However, an explanation for the poor response of spallation to impactor energy is offered by indentation fracture mechanics theory. Previous

morphological analysis of hypervelocity impact on free and composite brittle material surfaces shows evidence of cone cracks [12]. Under static loading, the angle subtended by the cone is related to the target thickness and indentor diameter. Results from previous static loading of glass [13] yielded the following relationship:

$$(90 - \alpha) = 21 + 1.65t \tag{2}$$

Re-application of Eqn.(2) for the front two consecutive elements of the solar cell ($t = 0.440$mm) resulted in a semi-cone crack angle range of 68.3 to 78.4°. Therefore, given an elemental thickness of solar cell, any variation of cone angle will be potentially due to projectile size. Figure 13 demonstrates that α for Class C morphology falls within the limits predicted by Eqn.(2) for the equivalent thickness of soda-lime plate glass and shows dependence with spallation.
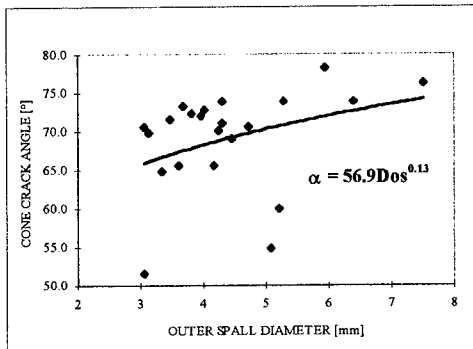

Fig. 13. Variation of Cone Crack Angle with D_{os} & D_{rtv} for RITP Class C Morphology.

Table 7. Morphology - Impact Parameter Applicability Matrix

Morphology Class	Impact Parameter Applicability					
	D_{hr}	D_{hf}	D_{pro}	D_{rtv}	D_{is}	D_{os}
Pre-A	√					√
A	√	√			√	√
B	√		√		√	√
C	√	√		√	√	√

With a link between spallation and cone crack geometry established, a means of resolving projectile size (d_p) would enable a MIS diagram solution. In the pursuit of damage laws, two different approaches were used to characterise *front-back* data, based on exploratory searches for; i) specific damage equations for A, B and C morphologies, and ii) a 'universal' damage equation, relating cone crack parameter to spallation. Both approaches are examined in turn.

Specific Morphology Damage Laws

The simplest relationship between a spherical impactor and target is to assume that the volumetric impact damage is proportional to the kinetic energy (E), resulting in Eqn.(3),

$$E = \pi(\rho_p V_p^2 d_p^3)/12 \tag{3}$$

With D_{os} ineffective with impactor energy, attention was focused on examining the energy dependence of alternative front face impact parameters applicable to each *front-back* morphology (defined in Table 7). Neither, D_{hf}, D_{is} or D_{pro} demonstrated any meaningful trend with energy disabling any progress of finding a function to relate Class A and B morphologies. Furthermore, the calibration of Pre-A morphology was only possible via the ballistic limit criteria. Advancement in damage law development was achieved by examining Class C morphology; by assuming that front hole diameter (D_{hf}) is the nearest size to the projectile (as is pit diameter for *front-top* impacts), it is expected to respond well with impactor energy. The $\log_{10}$ -$\log_{10}$ plot (Figure 14) demonstrates the relationship. As a first approximation, a power law fit to front hole diameter and impactor energy has been produced resulting in the simple damage equation Eqn. (4), from which d_p can de determined.

$$d_p = (D_{hf}/0.286)^{0.606} (\rho_p^{-0.33} V_p^{-0.66}) \tag{4}$$

The exposed RTV is a unique feature to Class C morphology and offers further opportunity to compare D_{rtv} with the fundamental projectile parameters. The results are also encouraging despite the data points being more widely scattered as illustrated in the $\log_{10}$ -$\log_{10}$ plot (Figure 15).   Applying a power law assumption to the data yields an additional damage equation to complement hole calibration Eqn.(5).

$$d_p = (D_{rtv} /1.13)^{1.512} (\rho_p^{-0.33} V_p^{-0.66}) \tag{5}$$
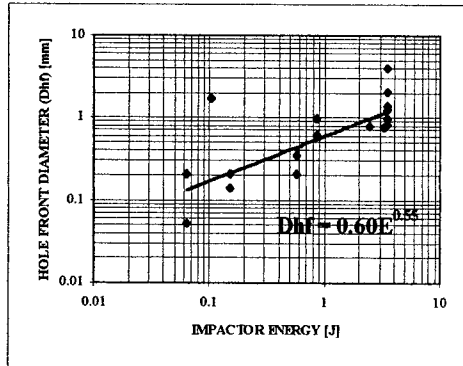

Fig. 14. Dependence of D_{hf} with Impactor Energy.
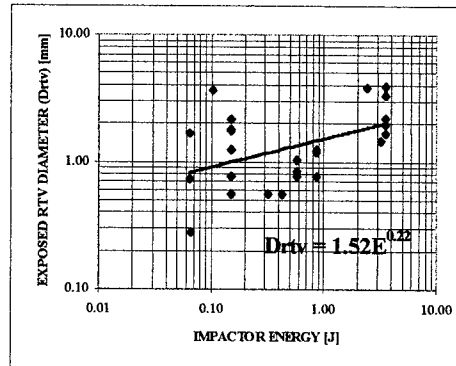
Fig. 15. Dependence of D_{rtv} with Impactor Energy.

In summary, only Class C morphology has demonstrated a potential for calibration via D_{hf} and D_{rtv}. This approach has shown Eqns.(4) & (5) to be valid for a d_p not exceeding 500µm; thereafter, Eqn.(4) and Eqn.(5) have a tendency to under-predict and over-predict respectively. The main limitation of this approach is the inability to unify all morphologies and therefore benefit from a wider and consolidated examination of the data set.

Cone Cracks : 'Universal' Damage Law

Cone cracking phenomena, as produced during the indentation fracture of brittle materials, offers an alternative approach of solving for d_p using a variety of front-back morphology characteristics. In order to proceed, a series of simplifying assumptions were made; i) the dynamic conditions for cone crack propagation are not unlike those for quasi-static projectile loading of the rear substrate, ii) the high speed projectile behaves as a blunt (cylindrical) indentor initiating cone crack propagation at its periphery as opposed to that of a point contact indentor, iii) the cone crack angle remains constant across the entire solar cell thickness and, iv) only the behaviour of normal impacts are considered in which the cone and impactor vertices are co-axial.

Fig. 16. Cone Crack - Projectile Geometrical Configuration.

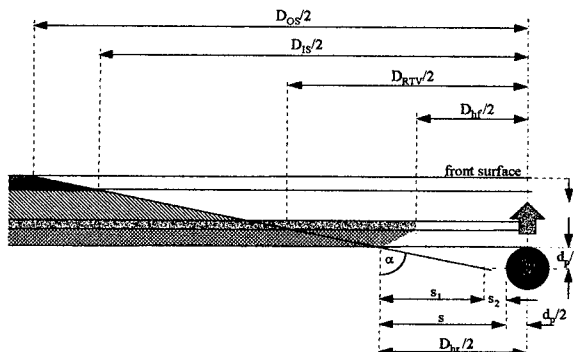The cone crack - projectile geometry illustrated in Figure 16 was assumed to prevail given that the initial projectile and final target damage geometries were known; a spherical projectile of diameter d_p (shown at first contact with the rear substrate) has a relation with D_{os} and D_{hr} subtending a cone angle 2α over solar cell thickness t_{max}. Analysis of the experimental data has consistently shown D_{hr} to be larger than D_{hf}; the inequality of the front and rear hole parameter is believed to be real evidence of negative hole growth in the direction of flight and not due to unreliable measurement. An example of a paired hole illustrating the extent of D_{hf} and D_{hr}, is defined by the central opaque regions of Figure 17. It is uncertain which hole parameter is most representative of d_p.
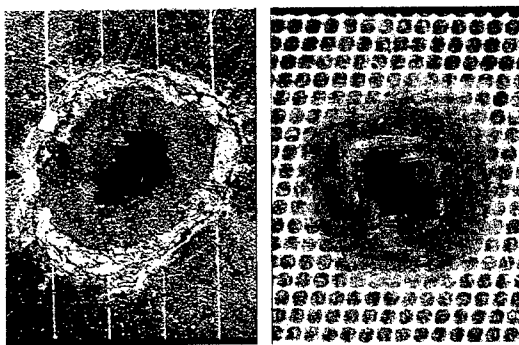

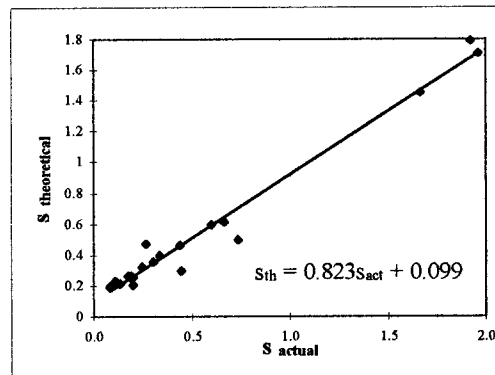Fig. 17. Class C Front-Rear Impact Pair
[impact refs. RITP-1 10_f1/r1]

Fig. 18. Correlation of Measured & Theoretical Semi-Breach Distance.

Simple geometrical relationships were developed on the basis of two known boundary conditions; i) measurement of laboratory impacts always shows D_{hr} to be greater than d_p by an annular breach of semi-distance s Eqn.(6) and, ii) as a result of the blunt form of impactor, s will never be less than s_1 Eqn.(7).

$$s = (D_{hr} - d_p)/2 \tag{6}$$

$$s_1 = (d_p \tan \alpha / 2) \tag{7}$$

In the limiting case, where s_2 is zero, it follows that,

$$s = (D_{hr}/2)(1 - (1/(1 + \tan \alpha))) \tag{8}$$

Pre-determination of the semi-cone angle (α) and rear hole diameter (D_{hr}) permits solution of the theoretical semi-breach distance Eqn.(8); these are achieved by applying Eqn.(9) & (10), substituting the correct parameters for the morphology under consideration,

$$\tan \alpha = 2t_x / (D_{os} - D_x) \tag{9}$$

$$D_{hr} = D_x - [(D_{os} - D_x)((t_{max}/t_x) - 1)] \tag{10}$$

where, (i) for Class C : $D_x = D_{rh}$ and $t_x = t_C$; (ii) for Classes A & B : $D_x = D_{is}$ and $t_x = t_A$ or t_B. Cumulative target depth for morphologies (t_x) are $t_A = 0.15$mm, $t_B = 0.19$mm and $t_C = 0.52$mm.

Correlation between measured and calculated values of s produces linearised scatter as shown in Figure 18; this result further demonstrates evidence of a cone cracking characteristic and validates the geometrical model as a good approximation. The amount of scatter may be indicative of two factors; i) the cone angle constant does in fact change at each material interface and, ii) the cone angle shows subtle variations with impactor incidence. These factors aside, acceptable correlation has resulted in a means for solving for d_p Eqn.(11).

$$d_p = D_{hr} [1 - (k / 0.8219)] + 0.241 \tag{11}$$

$$\text{where } k = 1 - (1 / (1 + \tan \alpha)) \tag{12}$$

An expression utilising both D_{os} and D_{hr} (parameters common to all *front-back* morphologies) permits 'universal' application to rear incident impact phenomena. This approach has shown Eqn.(11) to be valid for a d_p not exceeding 400μm; thereafter it has a tendency to under-predict.

DISCUSSION

The rear incident morphologies produced on HST solar arrays are complex and unlike the impact response of any other material. The finite and brittle multi-layer structure of HST solar cells is able to record the varying target response to impact by producing discrete damage forms which differ in visual appearance over a relatively small impactor energy range. Extensive analysis of nearly 1350 space impacts has revealed repetitive glass faced impact morphologies. Visual classification has reduced these data into 4 classes of rear incident and 6 classes of front incident phenomena [6]. Tentative explanations for the meaning of the variety of morphologies are becoming apparent as the experimental knowledge base broadens. The consistent and reproducible occurrences of morphology are a significant means of 'fingerprinting' the impactor in terms of its direction, size and perhaps origin.

The front and rear impact morphology classification systems are the means of discriminating between front and rear incident impactors; moreover, these permit impactor incidence identification requiring access to the front face of the solar array only. The most notable implications and differences between *front-back* and *front-top* morphologies, influencing design considerations for solar array space survivability are; i) rear incident impactors are the most significant contributor to the total front face areal damage (representing 83% of 0.0036m^2), ii) the array offers significantly less resistance (by 27 times) to a rear incident impactor at a given energy than for a front incident and, iii) morphologies generated by front incident impactors retain a significant proportion of their cover glass, whereas a rear incident impact site has a greater than 60% chance of shedding its cover glass to the orbital debris population.

The laboratory generation of both *front-top* and *front-back* impacts verified the classified means of discriminating between front and rear incident impactors. Experiment has also provided visibility of the intermediate morphological states which link together the hypothesised morphology progression. A direct relationship of morphology evolution with impactor energy has only been found in morphologies characterised by cover glass retention. Limited testing at non-normal incidence has shown morphology to be sensitive to impactor incidence and size; relating morphology-size-incidence has indicated that each morphology state can be produced at an infinite number of incidence-size conditions. A greater number of non-normal incidence data points will eventually allow: i) both particle size and spatial direction to be mapped and enveloped more accurately and, ii) a re-visit of impact site ellipticity as a reliable indicator of impactor incidence.

Development of empirically based damage equations and their extrapolation to LEO impact conditions, provides the means of calibrating the rear incident space flux on the HST solar array. An energy based equation unifying all *front-back* morphologies was impossible to produce. An alternative 'universal' equation, developed on the basis of quasi-static particle indentation fracture, was able to reproduce the experimental data within the calibration regime. As a result, confidence was gained in the cone crack model devised and its simplifying assumptions. Damage equations based on specific morphologies had a limited application, demonstrating calibration potential with Class C morphology only. Therefore, the equations must be considered as approximations until a larger data set comprising a wider range of impact conditions validates their reliability.

CONCLUSIONS

In summary, the following key conclusions have been drawn from this research:

- space generated *front-back* impacts are reproducible in the laboratory.
- all space generated morphology classes predicted as *front-back* impacts (Pre-A, A, B & C) have been confirmed; thus verifying that 36% of the impacts ($\geq 1200\mu m$ D_{os} or D_{co}) observed on the HST solar array front face are attributed to impactors entering from the rear substrate.
- existence of progressive evolution of *front-back* morphologies was verified to be partially dependent on energy and tentatively sensitive to impactor size-incidence conditions.
- rear-incident ballistic limit of an HST solar cell has been defined in terms of critical projectile parameters to generate a Pre-A morphology; comparison with the front incident ballistic limit has shown the solar cell to be 27 times less resilient to rear incident impact.
- rear incident impacts contribute the largest areal damage to the HST solar array.
- outer spallation remains independent of morphology and impactor energy but demonstrates dependence with cone crack angle showing relevance to indentation fracture mechanics.
- morphology specific damage equations could only be developed for Class C.
- a 'universal' damage equation relating cone crack to outer spallation successfully reproduced the experimental data within the calibration regime, validating the cone crack model.

REFERENCES

1. Herbert, M.K., Hubble space telescope solar array #1 : impact damage - the first post-flight survey. *Proc. HST Solar Array Workshop*, ESA WPP-77, pp. 301-314, 30-31 May, ESTEC Noordwijk, The Netherlands (1995).
2. Gerlach, L., Robben, A & Fromberg, A., HST-SA1 : electrical performance evaluation. *Proc. HST Solar Array Workshop*, ESA WPP-77, pp. 257-264, 30-31 May, ESTEC Noordwijk, The Netherlands (1995).
3. Rex, D., The role of the scientific and technical subcommittee of UN-COPUOS for the space debris work of the United Nations. *Proc. 2nd Euro. Conf. on Space Debris*, ESA SP-393, pp. 759-762, 17-19 March, ESOC Darmstadt, Germany (1997).
4. Mason, J.W.,The leonid meteors & comet 55/P Tempel-Tuttle. *J.Br.Astron. Assoc.* **105**(5), pp. 219-235 (1995).
5. McDonnell, J.A.M., Meteoroid & debris flux and ejecta modelling - WP1 image products resolution, ESA Contract. No. 11887/96/NL/JG, p.14 (1996).
6. Herbert & McDonnell, J.A.M., Morphological classification of impacts on the EURECA & Hubble space telescope solar arrays. *Proc. 2nd Euro. Conf. on Space Debris*, ESA SP-393, pp. 169-175, 17-19 March, ESOC Darmstadt, Germany (1997).
7. Unispace Kent, HST and EURECA meteoroid & debris post-flight analysis results. CD-ROM, ESA Contract No. 11887/96/NL/JG (1996).
8. Yano, H., The physics & chemistry of hypervelocity impact signature on spacecraft : meteoroid & space debris. University of Kent at Canterbury, PhD Thesis, pp. 190-194 (1995).
9. Herbert, M.K., Kay, L. & McDonnell, J.A.M., Decoding the evolution of rear impact morphologies on the Hubble space telescope solar array. *Proc. 7th Int. Symp on Materials in a Space Environment*, ESA SP-399, pp. 461-468, Toulouse, France (1997).
10. Unispace Kent, Meteoroid & debris flux and ejecta modelling - WP3 additional impact simulations. ESA Contract. No. 11887/96/NL/JG (1997).
11. Carey, W.C., MDFEM WP1- analysis of impact data from optical surveys - technical note. ESA Contract 11887/96/NL/JG, SAS-MADFEM-TN-001-97, p.6 (1997).
12. Lawn, B., Indentation fracture. In *Fracture of Brittle Solids (2nd Ed.)*, Cambridge Solid State Science Series, pp. 249-257 (1993).
13. Woodward, R.L., Some aspects of cone crack propagation in finite thickness glass plates. *Material Wealth of the Nation*, **1**, Sydney, Australia, pp. 111-118 (1988).

HYPERVELOCITY IMPACT FRAGMENT CLOUDS IN HIGH PRESSURE GAS NUMERICAL AND EXPERIMENTAL INVESTIGATIONS

STEFAN HIERMAIER and FRANK SCHÄFER

Fraunhofer Institut für Kurzzeitdynamik, Ernst-Mach-Institut, Eckerstr. 4, 79104 Freiburg, Germany

Summary—Space debris poses a threat to vehicles in near earth orbits. Due to the potential risk of catastrophic bursting under hypervelocity particle impact, pressurized vessels have been identified as high risk components. During recent experimental studies the principle failure mechanisms were investigated that lead to qualitative descriptions of the phenomenology. First experimental results from different studies showed that a strong interaction between cloud fragments and pressure gas occurred. In some cases the fragments were completely ablated inside the vessel.

The aim of this study was the numerical simulation of the complex interaction between fragments and gas. The numerical work was performed in parallel to experiments, where hypersonic fragment clouds in pressure gas were photographed. The pictures obtained in the experiments showed black regions behind the leading edge of the cloud which are assumed to be filled with ablation products. A distinct blast wave formation behind the fragments was observed in the surrounding gas. Also, particularly at high pressures, a size dependent deceleration of the fragments leads to the formation of a jet-like spike along the impact axis.

SPH hydrocode methods turned out to be an adequate tool for the simulation of the complex interaction mechanisms. Particularly the high density gradients and the fragment-gas interaction requires a flexible and robust simulation method. Despite some specific problems gridless methods proofed to be a promising discretization tool for the simulation of the mentioned experiments. A beta SPH version of AUTODYN-2D was used to simulate hypervelocity impact on a vessel pressurized to 10.5 bar. As a result a good correlation between experimental and numerical results was obtained. Features like the blast wave propagation and the formation of the jet-like spike at the tip of the fragment cloud compared well to the experimental results. © 1999 Elsevier Science Ltd. All rights reserved.

INTRODUCTION

Space debris represents a threat to any space mission, particularly to missions in Low- and Medium Earth Orbits (LEO and MEO). During the past years increasing attention has been given to the problem of debris particle impacts on pressurized modules. Such modules are habitated space stations, pressure vessels used in attitude control systems, pressure tubes and pipes, or any other pressurized spacecraft component.

In recent experimental studies [1-4], the structural behaviour of unshielded and shielded pressurized components to hypervelocity impact was investigated. A great variety of parameters were investigated, among them projectile parameters, vessel materials and -geometries, and various vessel pressures. The damage ranged from simple front wall perforation to complete

rupture of the pressure vessels. In further basic research programs the various mechanisms involved were studied [5-7].

However the number of tests that can be performed in experimental programs is limited, and thus numerical techniques that are capable to deal with the complex processes that are involved in hypervelocity impacts on pressure containers are needed. Up to date neither pure Langrangian or Eulerian nor combined Lagrange-Euler formulations were able to simulate numerically the processes. The problems encountered with these types of code were overcome by application of the SPH formulation to the problem. In this paper, numerical simulation results are compared to experiments.

EXPERIMENTAL SET-UP AND TEST PARAMETERS

The test chamber (Figure 1) consists of a cylindrical pressure container that was made of high-strength steel. Planar steel caps are welded to the tube ends. In the vessels front end, a borehole was drilled that serves as an impact channel for the projectile. The borehole was closed by the thin aluminium bumper plate. The vessel's side walls were made of thick plexiglas windows to allow for shadowgraph photography. The container can be pressurized up to about 25 bar. Nitrogen was used as a pressurant. The schematical set-up is shown in Figure 2. The impact flash triggers the image converter camera and the flashlight source. The fragment cloud is then photographed with a frame separation of 5 or 10 µs on a path of 200 mm.
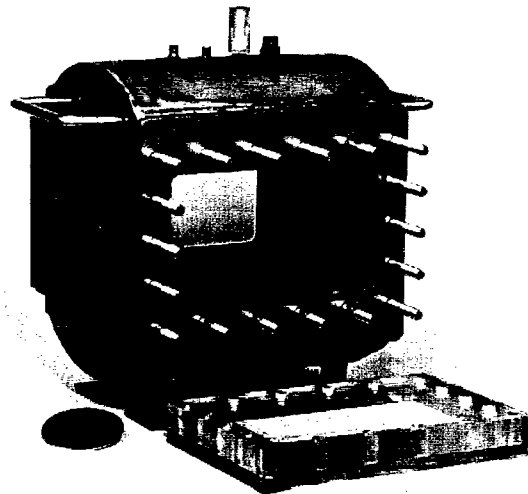

Figure 1   Pressure Container

Two experiments were performed. Projectile was a 5 mm diameter aluminium sphere, impact velocity was 5.2 km/s, and bumper plate material was Al 5754, with a thickness of 1.5 mm. The operation pressures were 0.1 bar (forevacuum) and 10.5 bar.
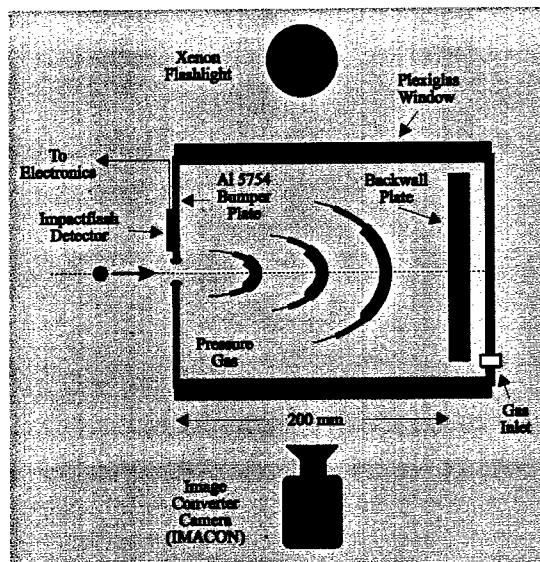
Figure 2   Schematic test set-up

NUMERICAL SIMULATION

As repeatedly pointed out in literature [10-12] the numerical simulation of hypervelocity impacts requires special types of discretization, the gridless methods, in order to handle the occurring large deformations. For applications like hypervelocity impacts the originally by astrophysicists invented method of smooth particle hydrodynamics (SPH) was improved by the implementation of strength models [9]. Amongst other gridless approaches like Moving Least Squares (MLS) [16] or Element Free Gallerkin (EFG) [17] SPH is a meshless Lagrange method to discretize structures or fluids. The main problem of SPH, it's instabilities under certain conditions [13,14], lead to several different approaches to improve the method between 1996 and 1998 [15-17].

In the case of an impact on gas filled vessels, there is a significant influence of the gas pressure on the formation of the fragment cloud as will be shown below. Therefore a simulation of this kind of impact must of course also describe the gas and its interaction with the fragment cloud. This can be done in different ways. Commonly a fluid like the pressurized gas would be described by an Euler grid. This would however mean to use a single Euler grid for the whole system. A coupled Euler-Lagrange or Euler-SPH method would need some type of polygon to describe the interaction zone between solid material and the fluid. Due to the fragmentation of the impacting sphere and the target material it is impossible to use standard polygon type interaction methods between Euler and Lagrange or SPH. According to the experience with other hypervelocity impact simulations the whole system was described using SPH particles. The disadvantage of that solution is that the SPH method is computationally much more expensive than standard Lagrange or Euler methods.

In advance of the pressure vessel impact a 2D axisymmetric test simulation of an unfilled vessel was done to check the quality of the calculated fragment cloud. Figure 3 shows that the material model used together with the AUTODYN SPH discretization delivers very reliable results in case of a (near-)zero pressure vessel impact. The shape of the cloud as well as the fragment velocities match the experimental data.
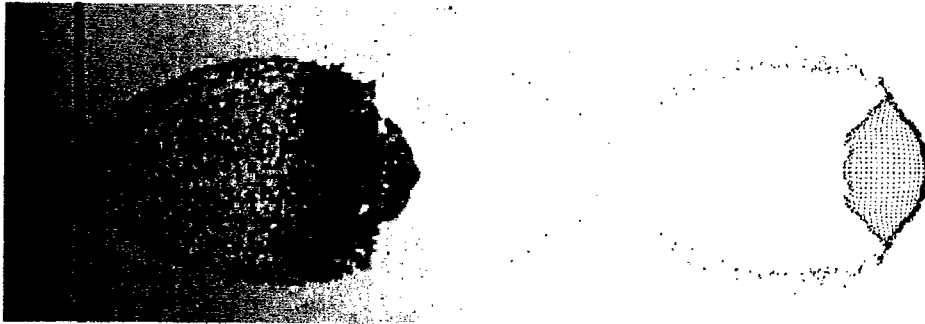
Figure 3   Shadowgraph and AUTODYN-2D SPH simulation of zero pressure impact

A direct comparison of experimental and numerical results for the fragment clouds expansion in longitudinal and lateral directions is shown in figure 4.
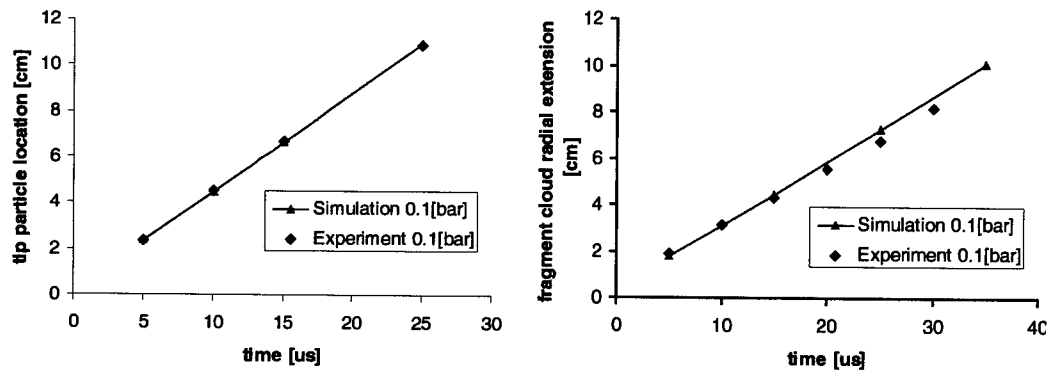
Figure 4   Comparison of fragment cloud expansion in longitudinal and lateral direction

For the simulation of a 5.2 km/s impact on a vessel filled with gas pressurised to 10.5 bar the aluminium material model consisted of a Johnson-Cook strength model and a Tillotson equation of state whereas air was described via a ideal gas EOS. The vessel casing off the penetration zone was described using shell elements. For the penetrated front wall SPH particles were applied.

SPH particles have a characteristic size. The interpolation length h is given by its mass and density. Where the particle mass is constant in time the density changes of course. The interaction between particles of highly different h values can cause instabilities which then lead to unphysical stresses, velocities etc. To avoid this it is important to use an initial particle discretization with equal or similar h values and thus with particles of comparable size. Thus if there are structural elements of different geometrical dimensions within the system that is to be discretized, a high resolution of the smaller elements means a very high number of particles in the larger elements. In our case a good representation of the small projectile means a huge amount of particles in the vessel. As mentioned before SPH calculations tend to be more time consuming than standard Lagrange. Thus a particle size was chosen that allowed a calculation of the process in a time scale of up to 10 days. The used SPH model contains about 45.000 particles. A simulation with 10.000 time steps takes about 180 hours on a 300 MHz Pentium processor.

RESULTS

Fragment cloud pictures from experiments and numerical simulation are presented in Figure 5. At 0.1 bar forevacuum pressure, the well-known undisturbed drop-like cloud shape is formed. In the center of the cloud's leading edge, a large fragment particle is visible in the 25 μs picture. Piekutowski [8] pointed out that this large central fragment originates from the center of the spherical projectile. At later stages of the impact process, a gray fog-like dust becomes visible behind the leading edge of the cloud. This dust is most likely due to a small amount of ablation products which are generated from the interaction of the hypervelocity fragments with the residual atmosphere in the target chamber.

Shadowgraphs 0.1 bar   Shadowgraphs 10.5 bar   Simulation 10.5 bar
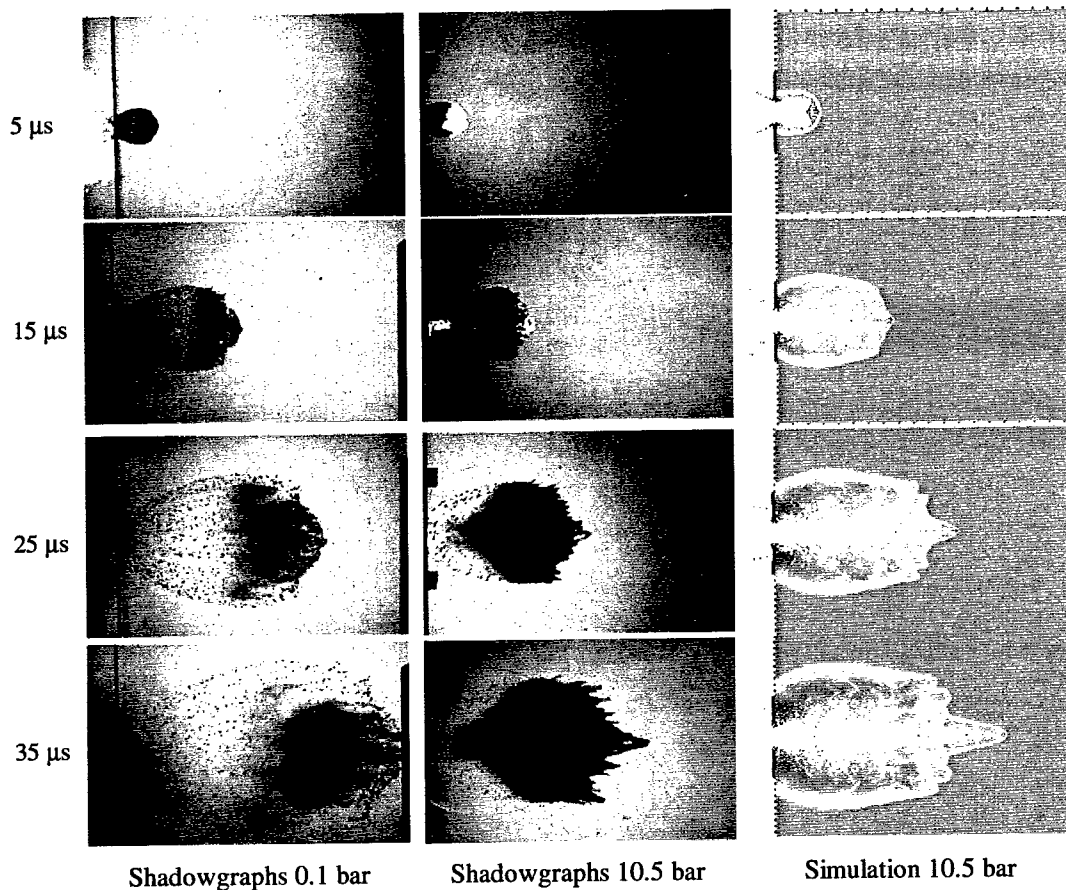
Figure 5   Shadowgraph pictures of fragment cloud at different pressures and numerical results

At 10.5 bar during the first microseconds the cloud still has a drop like shape. The light emission from the leading edge of the cloud can be related to radiation of the hot nitrogen gases behind the individual bow shockwave layers of the fragments and radiation of fragments that were heated by frictional forces. Chemical gas reactions and reactions between the gas molecules and the aluminium of the fragments are not likely to occur, because firstly the dissociation temperature for nitrogen is not yet attained at these impact velocities, and secondly the high ambient pressure inhibits such reactions. At some 15 to 25 microseconds after impact, light emission from the leading edge of the cloud stops. The space behind the leading edge is not transparent to light any more. Most likely, this space is filled with ablation products. Also, turbulent flow in the wake of

each fragment scatters the light. As shown in figure 6 the longitudinal and lateral expansion of the fragment cloud is slowed down due to the increased pressure.

About 25 microseconds after impact, a spike forms at the tip of the fragment cloud. This spike is related to the large central fragment, that has a higher ballistic coefficient than the small fragments that surround it and thus is less decelerated from aerodynamic drag. The cone behind the tip particle is not transparent to light which has to be attributed to the same phenomena as listed above. At later times, spikes can be observed off-axis, which are related to larger fragments. Although the experimental set-up was not initially designed for the visualization of gas density gradients, the formation and propagation of a pure gas shockwave was captured in the photographs. Approximately 25 microseconds after impact the shockwave detaches from the fragment cloud hull and propagates laterally into the gas. In axial direction the shockwave remains attached to the leading edge of the cloud respectively the large central fragment.
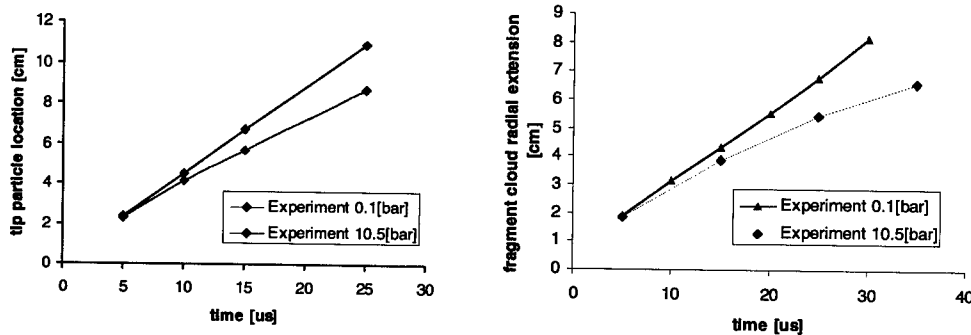
Figure 6   Longitudinal and lateral expansion of fragment clouds
as a function of time at 0.1 and 10.5 bar

For increasing pressure, the tip particle velocity decreases gradually. Figure 8 shows position and velocity of the fragment cloud tip. The radial velocity of the fragment cloud is constant at forevacuum pressure, but decreases strongly as the pressure is increased (Figure 9).

Compared to the experimental results the SPH simulation shows very similar phenomena:
a) After the initial formation of a drop like fragment cloud a spike is built out in the front centre area of the bubble
b) Bigger fragments are less decelerated in the whole cloud and build additional spikes in the outer regions
c) The individual fragments initiate shock waves in the surrounding gas. From figure 10 it is visible that the expansion of the radial gas shock wave is very well represented by the numerical simulation.

The simulation shows quite good accordance with the experiments concerning the bubble shape and velocities as also shown in figure 5. The spike formation starts at approximately 20μs in the simulation. The resulting jet like tip grows very similar to the experimentally observed process. One big fragment on the centre axis and about five smaller ones in the outer front region characterise the cloud's appearance from then on.

The number of used particles influences of course the results. In order to discretize an arrangement where the fragment cloud can expand up to 65 μs we reduced the resolution in a way that the number of particles through the vessel's wall thickness was 6 instead of 8. The

cloud's resulting expansion velocity in both directions was unchanged by this. However the front lateral fragments are worse represented as to be seen in figure 7.

b)

c)
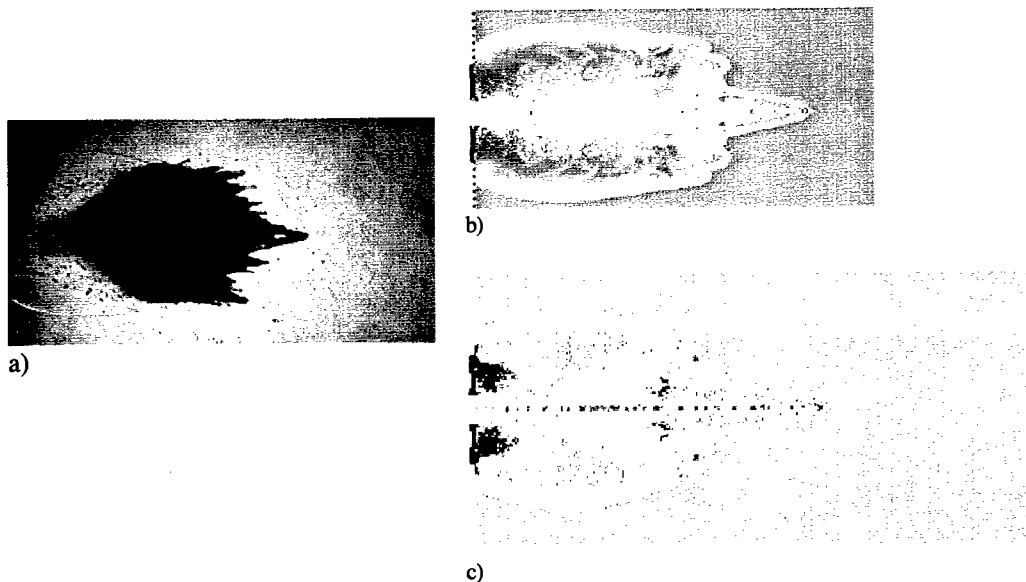
Figure 7   Computed fragment clouds for different resultions in comparison to experiment
a) Shadowgraph
b) High resolution simulation result (8 particles through vessel wall thickness)
c) Lower resolution simulation result (6 particles through vessel wall thickness)

Currently the simulation doesn't include any model that describes the formation of jet like spikes in front of the fragment clouds in pressurised gas. The information from both the experiments and the simulation shows that bigger fragments are less decelerated than smaller ones. Further more the experiments show that ablation takes place due to friction between fragments and air. This ablation shrinks the fragments and thus enhances the effect of size dependent deceleration. It is uncertain how big the effect of ablation influences the resulting fragment sizes and velocities.

Up to now the simulation does not account for friction. However it is possible to calculate the temperatures due to the enhanced internal energy in the deformed fragments. The implementation of an algorithm that erodes particles if they reach a threshold temperature, i.e. the vaporization temperature, showed that the resulting fragments become smaller and stronger decelerated than in the case shown above, where no ablation was simulated. However this first step numerical ablation model is too course. The whole physical process must be better understood to develop threshold values for temperature and exposition times to establish a better ablation model. In this context it is then necessary to calculate friction terms in the stress tensor and the corresponding change in temperature.

Figure 8   Position and velocity of tip particle of the fragment cloud
as a function of time at 10.5 bar

Figure 9   Radial extension and velocity of the fragment cloud
as a function of time at 10.5 bar

Figure 10   Radial extension of the shock wave
as a function of time at 10.5 bar

CONCLUSIONS

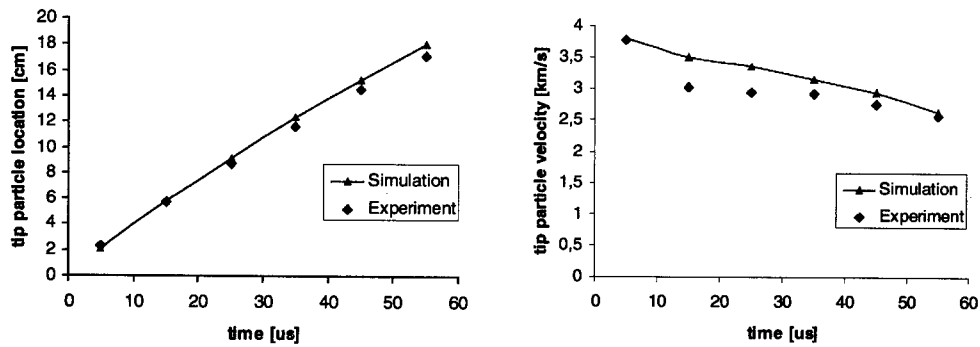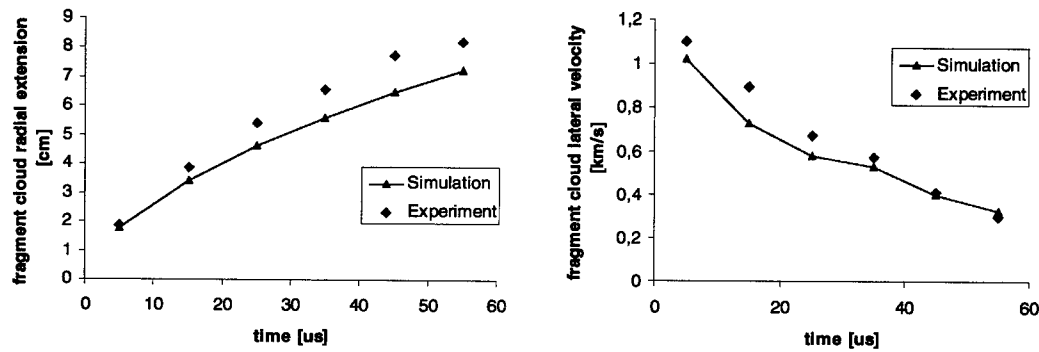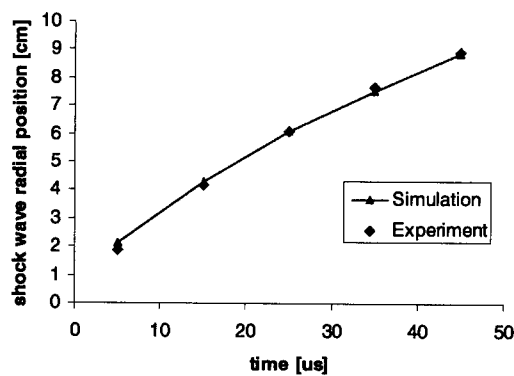Aerodynamic drag reduces strongly the radial and axial velocity of the fragment cloud. A spike forms at increased chamber pressures. This spike is produced by the large central fragment in the center of the fragment cloud's leading edge. Its occurrence is due to the fact that fragments with a large ballistic coefficient are less decelerated than those with a small ballistic coefficient. The non-transparent area behind the leading edge of the cloud contains the ablation products of the fragments. On the photographs, a radial gas shockwave was observed. This shockwave was detached from the fragment cloud. In axial direction the gas shockwave remains attached to the fragment cloud.

The numerical simulation showed a good representation of the basic effects like the formation of a spike in the front part of the fragment cloud. Also the shock wave resulting from the fragments can be observed and is calculated very exactly concerning it's propagation velocity in the pressurised air. The fact that the development of a jet like formation in the front region of the cloud could be simulated encourages further investigations on parameter studies of hypervelocity impacts on pressure vessels. An ablation model that describes the shrinkage of fragments due to temperature rises will be developed and implemented in order to estimate the influence of ablation effects with numerical simulation. A preliminary ablation model with estimated threshold values showed positive results. Further investigations will be made to better understand the ablation process and the physical effects that are responsible for it.

REFERENCES

1. F. Schäfer, E. Schneider, M. Lambert, "An Experimental Study to Investigate Hypervelocity Impacts on Pressure Vessels", ESA SP-393, pp 435 - 443, Proc. Second European Conference on Space Debris, ESOC, Darmstadt, 17. - 19.03.1997

2. F. Schäfer, E. Schneider, M. Lambert, "Hypervelocity Impacts on Cylindrical Pressure Vessels - Experimental Results and Damage Classification", PVP-Vol. 351, Structures under Extreme Loading Conditions, Proc. 1997 ASME Pressure Vessels and Piping Conference, Orlando, FL, USA, 28. - 31.07.1997

3. J.P. Whitney, Hypervelocity Impact Tests of Shielded and Unshielded Pressure Vessels, NASA JSC, JSC 32294, 1993

4. L. J. Friesen, "Hypervelocity Impact Tests of Shielded and Unshielded Pressure Vessels, Part II", NASA Johnson Space Center, JSC 27081, July 1995

5. F. Schäfer, E. Schneider, M. Lambert, "Impact Fragment Cloud Propagating in a Pressure Vessel", Acta Astronautica, Vol. 40, Number 1, pp 31-40, Pergamon 1997

6. F. Schäfer, E. Schneider, M. Lambert, M. Mayseless, "Propagation of Hypervelocity Fragment Clouds in Pressure Gas", Proc. 1996 Hypervelocity Impact Symposium, Int. J. Impact Engng., Vol. 20, pp 697-710, Pergamon 1997

7. E. L. Christiansen, J. H. Kerr, J. P. Whitney, "Debris Cloud Ablation in Gas-Filled Pressure Vessels", Int. J. Impact Engng., Vol. 20, Pergamon 1997

8. A. J. Piekutowski, "Formation and Description of Debris Clouds Produced by Hypervelocity Impact", NASA Contractor Report 4707, Contract NAS8-38856, February 1996

9. L.D. Libersky, A.G. Petschek, "High Strain Lagrangian Hydrodynamics, Journal of Computational Physics", 109 (1993), pp. 67.75

10. Hiermaier S., "Numerische Simulation von Impaktvorgängen mit einer netzfreien Lagrangemethode (Smooth Particle Hydrodynamics)", Mitteilungen des Instituts für Mechanik und Statik 8, Universität der Bundeswehr München, 1996, ISSN 0944-8381

11. Hiermaier S., Könke D., Stilp A.J., Thoma K., "Computational Simulation of the Hypervelocity Impact of Al-Spheres on Thin Plates of Different Materials", Int. J. of Imp. Engineering, 20, 1997

12. Hayhurst C.J., Clegg R.A., "Cylindrically Symmetric SPH Simulations of Hypervelocity Impacts on Thin Plates", Int. Journal of Impact Engineering, 20, 1997

13. Swegle J.W., Hicks D.L., Attaway S.W., "Smooth Particle Hydrodynamics Stability Analysis", Journal of Computational Physics 116 (1995), pp. 123-134

14. Balsara, D.S., "Von Neumann Stability Analysis of Smooth Particle Hydrodynamics - Suggestions for Optimal Algorithms", Journal of Computational Physics, 121, pp. 357-372, 1995
15. Randles P.W., Libersky L.D., "Smooth Particle Hydrodynamics: Some recent improvements and applications", Computer Methods in Applied Mechanics and Engineering, 139, 1996, pp. 375-408
16. Oñate E., Idelsohn S., Zienkiewicz O.C., Taylor R.L., "A Finite Point Method in Computational Mechanics. Applications to Convective Transport and Fluid Flow", Int. Journal for Numerical Methods in Engineering, 39, (1996), pp. 3839-3866
17. Belytschko T., Lu Y., Gu L., "Element Free Galerkin Methods", Int. Journal for Numerical Methods in Engineering, 37, (1994), pp. 229-256

MASS SPECTROMETER CALIBRATION OF HIGH VELOCITY IMPACT IONIZATION BASED COSMIC DUST ANALYZER

G. JYOTI*, SATISH C. GUPTA*, THOMAS J. AHRENS**, DMITRI KOSSAKOVSKI*** AND J. L. BEAUCHAMP***

*now at: High Pressure Physics Division Bhabha Atomic Research CentreTrombay, Bombay-400 085 INDIA; **Lindhurst Laboratory Of Experimental Geophysics, Seismological Laboratory, California Institute Of Technology, Pasadena CA 91125; ***Arthur Amos Noyes Laboratory of Chemical Physics, California Institute of Technology, Pasadena CA 91125.

Summary —We are calibrating the time of flight mass spectrometer of the Cosmic Dust Analyzer (CDA) instrument aboard the Cassini spacecraft. The CDA measures the flux of particles in the 10^{-15} to 10^{-9} g range at intersection velocities of up to 100 km/s. Of special interest are the chemical composition of the particles in orbit about Saturn and/or its satellites that are expected to be captured by CDA during ring plane crossings and upon close encounter with the satellites. Upon impacting a rhodium plate, particles are expected to partially ionize and their chemical composition is expected to be determined from mass analysis of the positive ions. In order to optimize impact ionization calibration experiments using a light gas-gun launched microspheric particles, we have done initial testing with a short duration pulsed laser (4 ns duration nitrogen laser (337 nm)). The beam is focused to deliver the 300μJ energy per laser pulse onto a 33 μm². The laser power density (~10^{10} W/cm²) simulates the impact of particles with various combinations of density and velocities, e.g., 8 g/cm³ (Fe) projectile at 23 km/s or 1 g/cm³ projectile at 65 km/s. The CDA spectrometer will operate in the near vacuum of Saturnian zone environment is housed in a laboratory chamber at 10^{-6} mbar. The ions and electrons are separated by 680 V between target and grid. The laser ionization produces charge of 4.6pC (mostly Al^{+1}) in aluminum and 2.8pC (Fe^{+1}) in stainless steel. Estimating that each Al^{+1} and Fe^{+1} ion requires an energy of 5.98 and 7.90 eV/ion implies that ~10^{-5} % of the laser pulse energy produces ions and the present system has a 10% detection efficiency. Using multi-channel plate detector to detect ions from aluminum alloy and kamacite yields well defined peaks at 24(Mg^{+1}), 27(Al^{+1}) and 64 (Cu^{+1}) and, 56(Fe^{+1}), 58(Ni^{+1}) and 60(Ni^{+1}) amu, respectively. Also contaminant ions at 23 (Na^{+1}) and 39(K^{+1}) amu are detected. © 1999 Elsevier Science Ltd. All rights reserved.

INTRODUCTION

One of the objectives of the Saturn orbiter, Cassini spacecraft is to characterize the dust/meteoroid environment of the Saturnian ring and satellite system. For this purpose the orbiter is equipped with a Cosmic Dust Analyzer (CDA) instrument[1]. The CDA measures the charge, the impact speeds, the mass and composition of these dust particles. The micrometeoroid mass measurement range is 10^{-15} to 10^{-9} g and the speed measurement range is 1 to 100 km/s. The initial (usually positive) charge on the particles is measured upon their passage through the two inclined grids at the entrance of the sensor housing, Fig.1a. The speed and the mass of the particles is determined from the rise time and the amplitude of the integrated charge pulse upon impact on the impact ionization detector (IID), Fig.1a. Upon impact single and multiple ionization occur depending upon particle material and velocity. Electrons are collected on the impact plate of the detector. An integrated time-of-flight impact ionization mass spectrometer provides constraints on the particle chemical composition. Particles impacting onto the Rh target plate (Fig 1a), and a lesser mass of the Rh target, get vaporized and partially ionized. The positive ions (mostly singly charged) so produced get accelerated to 10^3 eV energy. Providing no equi-dalton interference exists, the time of arrival of ions provides mass spectra for each dust particle in the above mass range.
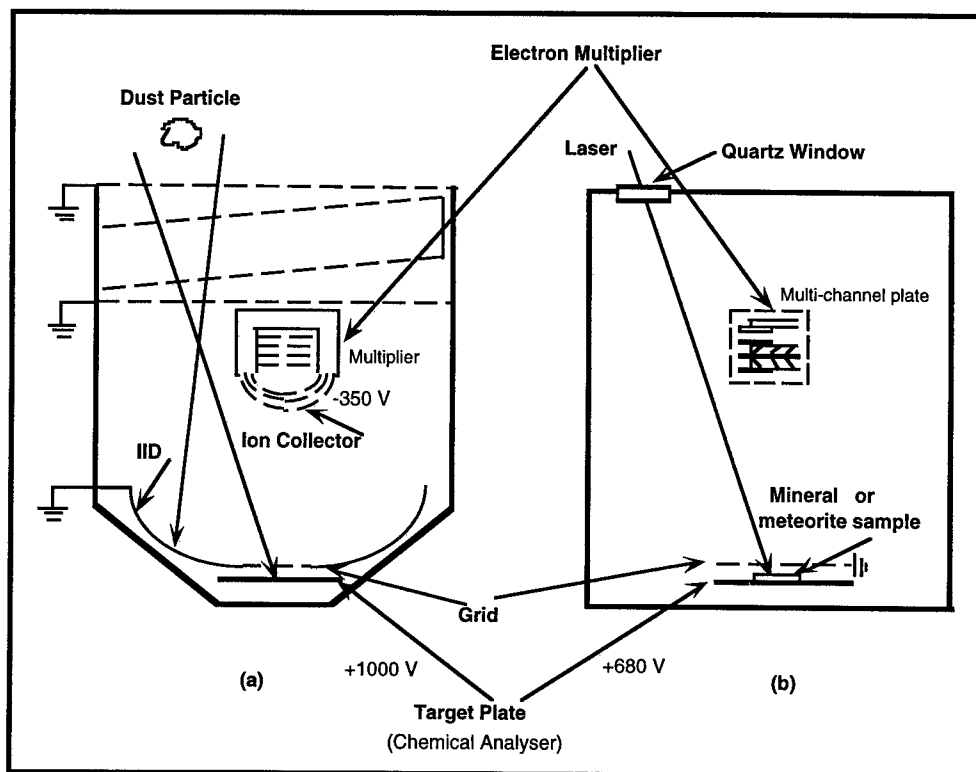
Fig 1. Schematics of (a) the CDA instrument aboard Cassini mission which is simulated by the (b) laser ionization time of flight mass spectrometer at our laboratory.

The dust analyzer has two types of ion detection systems, one is a charge sensitive amplifier (CSA) that measures the ions collected at the ion collector and the other is an electron multiplier[2]. The multiplier (Johnston, type MM1) consists of stacked dynodes that provides upon electrostatic capture of positive ions, a high electron current gain and time resolutions of 10^{-8} s.

The output of the CSA is in the form of an integrated charge pulse. The pulse has steps that correspond to the arrival time of different ionic species, whereas the output signal of the electron multiplier is in the form of separate (differentiated) peaks.

BACKGROUND

Impact ionization experiments that determine the species type have been carried out previously with dust particles with diameters in the range 0.2 μm to 20 μm that have been electrostatically accelerated[3] to velocities in the range of 1 to 70 km/s and in the mass range 10^{-15} to 10^{-10} g. The particles normally used were iron, or metal coated carbon and silicate spheres. These experiments were limited by the commercial availability of conducting particles. For larger particles having diameters of the order of 100 μm, we expect to employ a light gas gun for launching a wide range of projectiles of cosmochemical importance. Particles with velocities of the order of 6 km/sec are expected to be launched. These velocities are comparable to the circular orbit speeds around Saturn, the larger Saturnian satellites, and ring-plane particles (5-10 km/s). The CDA is expected to characterize the environment at each object for which a close encounter is conducted during this part of the Cassini tour.

Because of the difficulty in launching a single microspheric projectile with a light gas gun, and also to provide the pulsed ion source for setting up the calibration electronics, a crucial
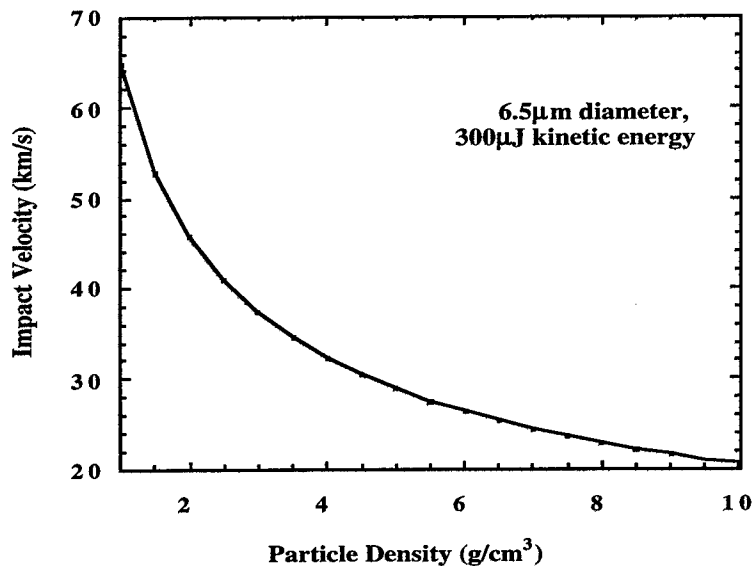

Fig. 2   Velocity of the 300 μJ kinetic energy, 6.5 μm diameter impacting particle as a function of particle density.

calibration program was initiated using a commercial pulsed laser.   Fig.1 shows the correspondence between the laser ionization time of flight mass spectrometer (on mock-up instrument) in our laboratory and the CDA instrument now aboard the Cassini spacecraft. Detection methods for the micro-particle impact experiments to be conducted at F. Hörz's 4 mm diameter, two stage light gas gun (NASA/ Johnson Space Center), are now being developed using the laser source as a proxy for the impact of a dust particle. Since the particle-target interaction occurs over a short interval (~10 nanoseconds) and the impact energies of dust particles are comparable to the duration and energy deposition achievable with commercial pulsed lasers[4], laboratory laser ionization experiments are useful to optimize the instrumentation for impact experiments.

We employ a 4 ns pulsed nitrogen laser with an energy of 300 μJ, a power density of ~2.25 $\times 10^{11}$ W/cm^2 and a laser focal spot diameter of ~6.5 μm. The incident laser energy density simulates the impact of particles with various combinations of density and velocity. For example, it simulates an Fe-Ni projectile having a density of ~8 g/cm^3, impacting at 23 km/s (the projectile footprint is taken to be 6.5 μm). The particle velocities as a function of various particle densities in the range 1.0 to 10 g/cm^3, so as to produce the energy density of our laser experiment are plotted in Fig. 2. The velocities, V, are calculated using E= 0.5 ρ_p v_p V^2 where ρ_p, v_p are the particle density and total volume, respectively, and E= 300 μJ. Normally, particles having initial densities in the ~0.01 to 5 g/cm^3 range are expected to be encountered in space. They could range in composition from those similar to carbonaceous chondrites that are of low density and possibly correspond to the Brownlee particles[5] collected in the Earth's atmosphere to differentiated metal silicate asteroid fragments.

EXPERIMENTAL METHOD

The schematic of the experiments carried out with a nitrogen laser (Laser Science, VSL337ND-S model #337201) on a mock-up instrument of the CDA is shown in Fig. 3. The 337 nm, 300 µJ energy laser beam enters the chamber through a quartz window (MDC, quartz Viewport no. 450020). The beam is directed into the chamber by two beam steerers (Newport, model BSD-1). The mirrors used in these beam steerers have a dielectric coating to give 99% reflectivity in the UV region. The laser is focused onto the target with a 2.54 cm diameter plano-convex fused silica lens (Newport, SPX022AR10) having anti-reflection coating in the UV region. The focal length of the lens is 10 cm. The ions are formed in the short source region between the target plate and the grid. The target plate, here, is ~17.5 cm in diameter, made of commercial aluminum alloy on which samples of a few mm diameter and 0.10 to 0.15 mm in thickness are mounted. The grid parallel to and in front of the target is made of copper.
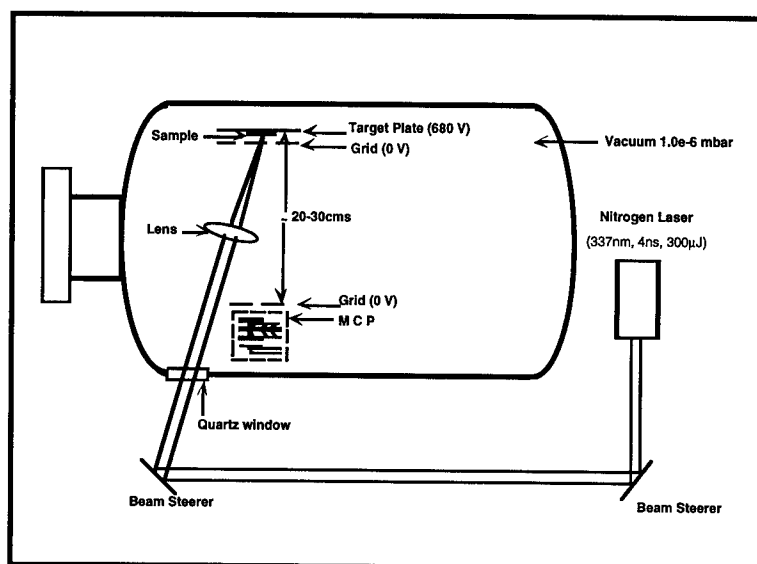
Fig. 3. Schematic of the optical set-up for the instrument.

This grid has a transmission of 66%. The nominal distance between the grid and the target plate was kept at 6 mm. A voltage (680 V) impressed on the target accelerates the positive ions towards the detector which is at ground potential. The distance between the target and the detection system can be varied between 20 to 30 cm. The chamber pressure was maintained below 1.0×10^{-6} mbar with a 1500 l/s diffusion pump. We have also employed two kinds of ion detection systems in two series of experiments described below. In Experiment Run #1, the detector consists of a copper collector plate (at ground potential), shielded in an aluminum enclosure to suppress electromagnetic noise. The side of the detector facing the target is constructed of 78% transmission aluminum mesh. The collection area was limited to a central zone (~6.8 cm diameter) of the 15 cm diameter copper collection plate. The charge on the copper electrode is monitored by a charge sensitive amplifier (CSA, EG &G, ORTEC model 142A) and a 500MHz, HP54540 digital storage oscilloscope. The laser is triggered externally. The oscilloscope is triggered by the optosynchronous signal provided by the laser (Fig. 4).
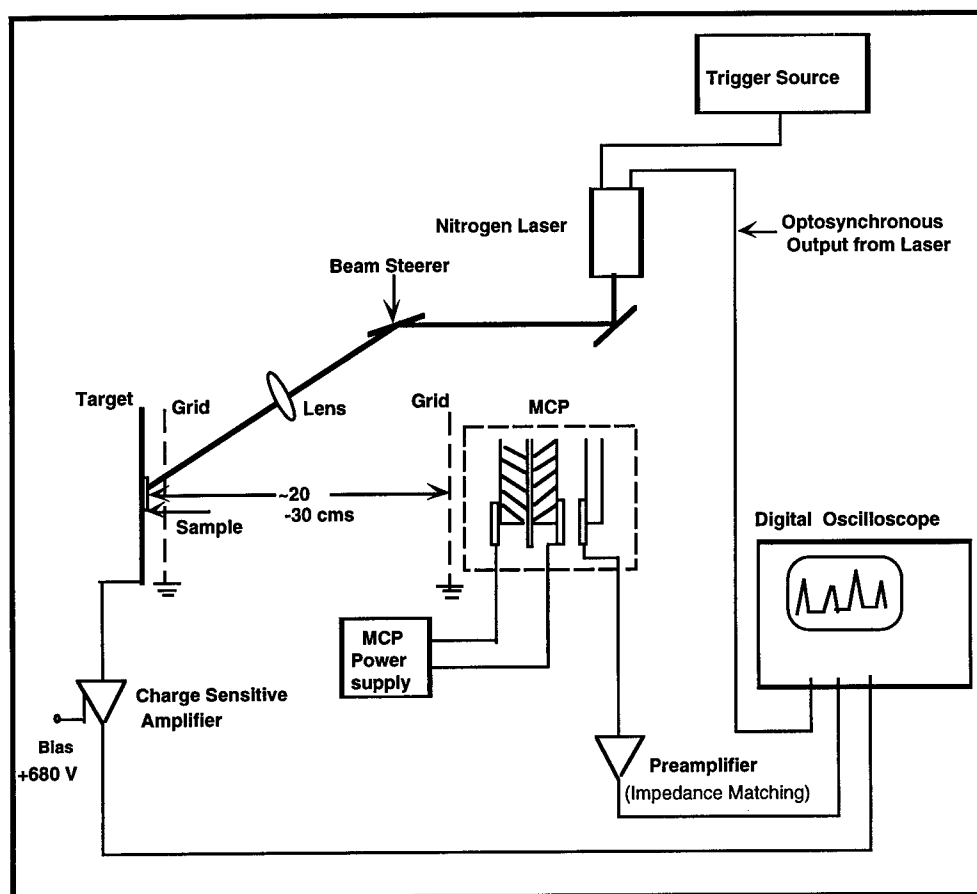
Fig. 4. Experimental set-up for the signal recording system.

For Experiment Run #2, the collector plate is replaced by a multichannel plate detector (MCP) (Galileo Corp., part no. 1397-0050). The MCP consists of an array of miniature high-gain electron multipliers oriented parallel to one another. The time resolution of the MCP is comparable to the MM1 multiplier used in the CDA (Fig. 1). The active detection diameter of the MCP used here is 18mm and its operating voltage is kept at -1800V. A preamplifier (EG&G, ORTEC model VT120C) is used to couple the MCP signal to the oscilloscope.

RESULTS

Charge Sensitive Amplifier

For Run #1A experiments, where charge is measured by a CSA, the first sample material was an aluminum alloy target plate. Here, initially at low laser power densities, we observed a two-step pulse corresponding to Na^+ and K^+ each with an approximately 350 ns rise time. The presence of contaminant alkali salts on material/sample surfaces is well known in laser desorption mass spectrometry. Although impurities, the known mass of the Na^+ and K^+ ions is advantageously used for calibrating the instrument. With higher laser power density, we observed a high-amplitude, long duration (~ 800 ns) pulse at the times corresponding to arrival of $^{23}Na^+$ and $^{27}Al^+$ (Fig. 5a). No further steps were observed.

For Run #1B, stainless steel was used, and we found Fe, Cr and Ni at 56, 52 and 58 amu to be merged into a single pulse, Fig. 5b. The electron charge collected (at the target end) is estimated

to be around 4.7 pC and 2.8 pC for the aluminum alloy and stainless-steel samples, respectively. The ion charge collected at the collector plate was estimated to be 0.23 pC and 0.15 pC for these two samples. This corresponds to an ion detection efficiency of 4-5% over a ~0.09 sr collection solid angle.

(a)
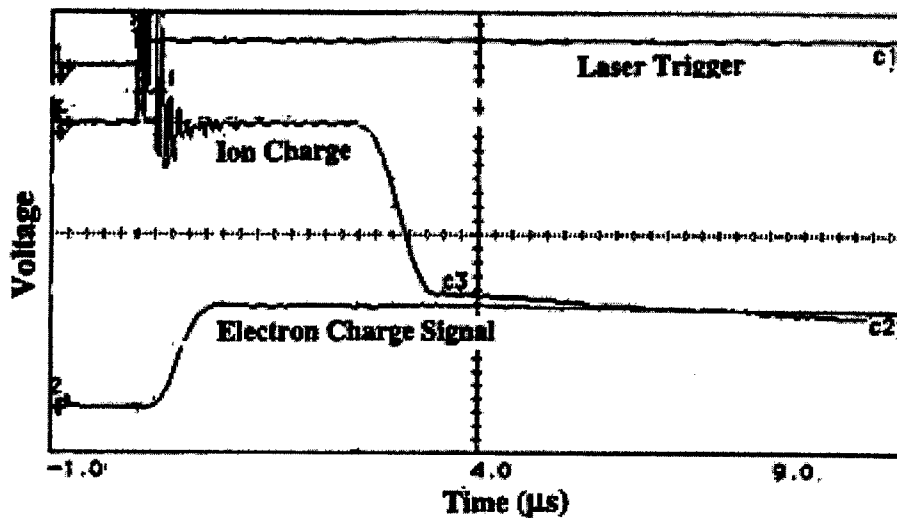
(b)
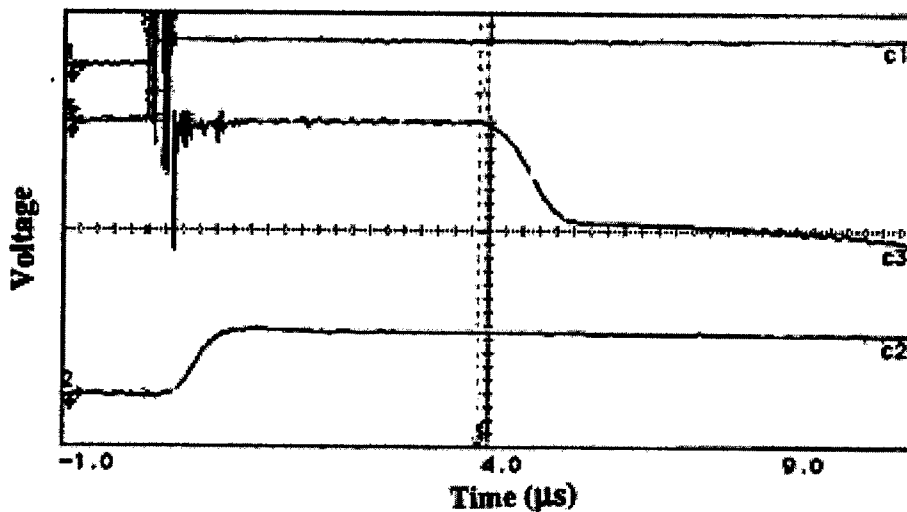
Fig. 5. Single shot time of flight spectra recorded using charged sensitive amplifier: (a) from Al sample, (b) from stainless steel sample, (c1 is the optosynchronous output due to laser trigger (5V/div), c2 is the integrated electron charge signal at the target end (200m V/div), c3 is the ion signal at the collector plate (75mV/div)).
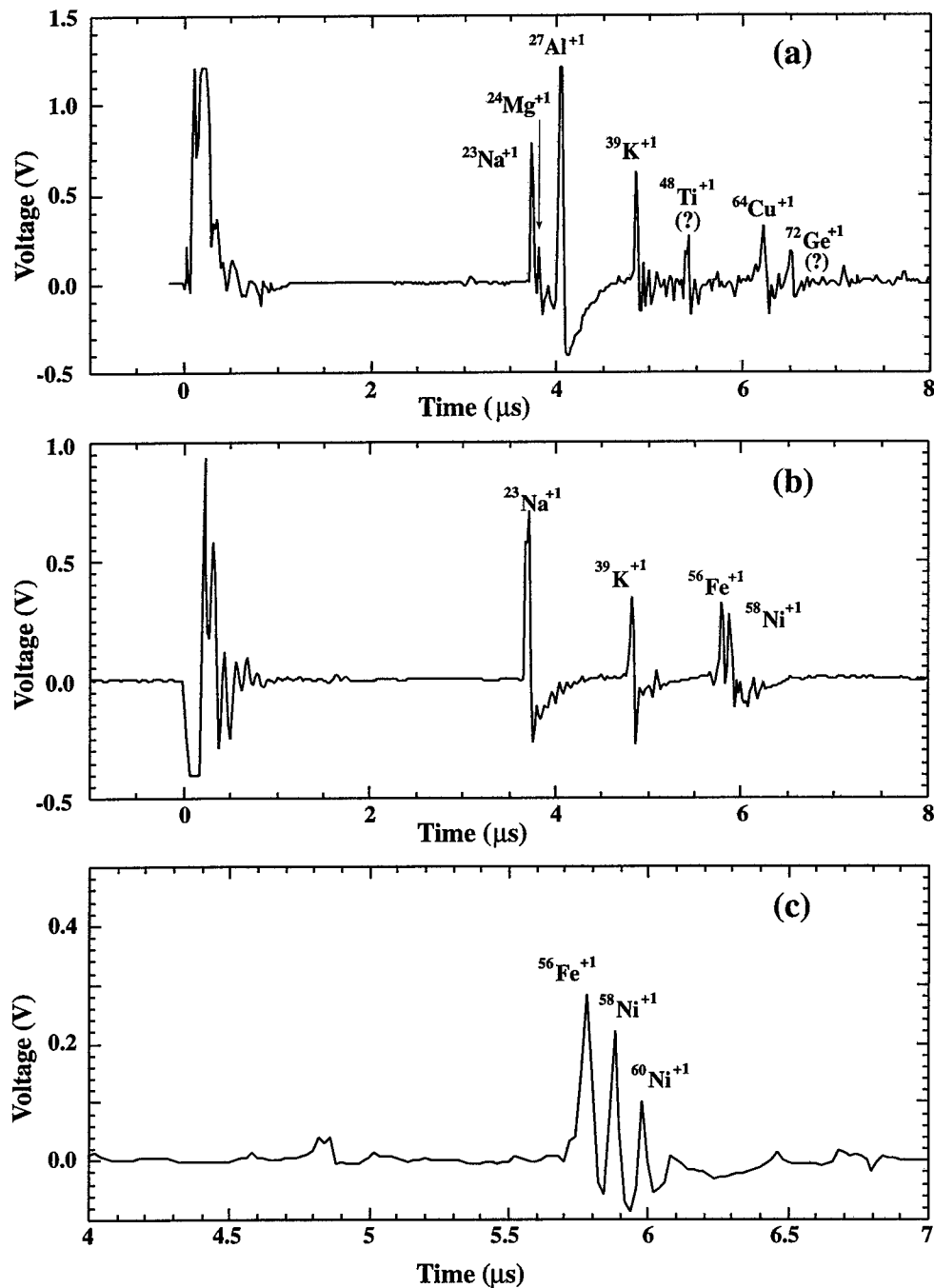
Figure 6. Single N_2 laser pulse, time-of-flight spectra recorded using multi-channel plate detector: (a) from Al sample (b) from kamacite, at laser power density of 3.45 x 10^9 W/cm² (c) from kamacite, at laser power density of 4.5 x 10^9 W/cm².

Multichannel Plate Detector

In the second category of experiments, we employed a MCP. Experiments were repeated, first on the aluminum alloy target plate and on the mineral, kamacite. Kamacite[6] (94.5% Fe and 5.5% Ni) is the principal mineral in Fe-Ni meteorites. The Gibeon meteorite was the source of our sample. Fig. 6a displays the spectrum recorded with the Al target. It shows a well defined singly charged aluminum peak. The Na^+ and K^+ peaks observed from the surface impurities are used to calibrate the mass spectra. Peaks corresponding to Cu^{+1} and Mg^{+1} present at low levels are aluminum alloying elements. Fig. 6b shows the spectrum recorded for kamacite. Here too, apart from well separated Na^+ and K^+ peaks, we observe well-resolved peaks for $^{56}Fe^+$ and $^{58}Ni^+$. Yet another spectrum from this mineral at slightly higher laser density (laser density was varied with the help of neutral density filters) is shown in Fig. 6c. Here, we see an additional peak corresponding to ^{60}Ni. Further systematic study with varying laser energy density from 1.0 $\times 10^2$ W/cm^2 to 9.0 $\times 10^2$ W/cm^2 is in progress.

SUMMARY AND CONCLUSIONS

In our first set of experiments using a 300 μJ, 4 ns, 337 nm laser pulse and a charge sensitive amplifier as a detector, the elements with masses differing by 4 amu (e.g. ^{23}Na and ^{27}Al) could not be distinguished. In the second set of experiments with the multi-channel plate detector (similar to the multiplier on CDA), we observed well defined peaks of Fe and isotopes of Ni. We also could observe ion signals from several elements that are present at low levels in the sample, e.g. Cu and Mg in the case of commercial aluminum sample. We are now conducting additional pulsed laser experiments on pyrrhotite (FeS), olivine (Mg_2SiO_4), serpentine ($Mg_3Si_2O_7 \cdot 2H_2O$) and Murchison meteorite prior to studying ionic spectra on these same materials at the light gas-gun facility at the NASA/Johnson Space Centre (operated by Dr. F. Hörz). In addition we expect to study $^{13}C/^{12}C$ ratio in a series of terrestrial coal, petroleums, the tissue of plant eating bovine and other carbon bearing meteorites besides Murchison to verify that we can detect a wide range in $^{13}C/^{12}C$ ratio, previously reported. We also expect to determine the ratio of D/H for ices. Because of the enhancement of D/H in comets, these data can be applied in measurement of D/H for ring particle ices. Finally, we expect to obtain mass spectra of volatized ilmenite $FeTiO_3$ and GeO_2 in order to attempt to verify the occurrence of Ti^{+1} and Ge^{+1} observed in spectra shown in Fig. 6a.

REFERENCES

1. L. J. Spilker, Passages to a Ringed World, NASA Report #SP533 (1997).
2. S. Ralf and E. Grün, Private communication, Germany (1997).
3. E. Grün, H. Fechtig, M. S. Hanner, J. Kissel, B.-A. Lindblad, D. Linkert, D. Maas, G. E. Morfill and H. A. Zook, The Galileo Dust Detector. *Space Science Reviews*, **60**, 317-340 (1992).
4. J. Kissel and F. R. Krueger, Ion formation by impact of fast dust particles and comparison with related techniques. *Appl Phys A*, **42**.1, 69-85 (1987).
5. D. E. Brownlee, Cosmic dust: Collection and research. *Ann. Rev. Earth Planet. Sci.*, **13**, 147-173 (1985).
6. B. Mason, Meteorites, (New York and London: Wiley, 1962)

HIGH PRESSURE SOLID STATE EXPERIMENTS ON THE NOVA LASER

**D. H. KALANTAR*, B. A. REMINGTON*, E. A. CHANDLER*, J. D. COLVIN*,
D. M. GOLD*, K. O. MIKAELIAN*, S. V. WEBER*, L. G. WILEY*, J. S. WARK**,
A. A. HAUER***, AND M. A. MEYERS******

*Lawrence Livermore National Laboratory, Livermore, CA 94550; *Department of Physics,
Clarendon Laboratory, University of Oxford, Oxford, UK OX1 3PU; *** Los Alamos National Laboratory,
Los Alamos, NM 87545; ****University of California at San Diego, La Jolla, CA 92043

Summary — An x-ray drive has been developed to shock compress metal foils in the solid state in order to study the material strength under high compression. The drive has been characterized and hydrodynamics experiments designed to study growth of the Rayleigh-Taylor (RT) instability in Cu foils at 3 Mbar peak pressures have been started. Pre-imposed modulations with an initial wavelength of 20-50 μm, and amplitudes of 1.0-2.5 μm show growth consistent with simulations. In this parameter regime, the fluid and solid states are expected to behave similarly for Cu. An analytic stability analysis is used to motivate an experimental design with an Al foil where the effects of material strength on the RT growth are significantly enhanced. Improved x-ray drive design will allow the material to stay solid under compression throughout the experiment, and dynamic diffraction techniques are being developed to verify the compressed state. © 1999 Elsevier Science Ltd. All rights reserved.

INTRODUCTION

In a classical fluid model, when a light fluid accelerates a heavier fluid, the interface is Rayleigh-Taylor (RT) unstable. As a result, any mass modulation at the embedded material interface is unstable, and can grow when accelerated. However, when the material is in the solid state, the strength of the material can counter the effect of the RT instability. The parameters that define whether a material is stable or unstable to instability growth in the solid state depend on the wavelength and amplitude of the modulation, the acceleration, foil thickness, and material properties, such as yield stress, shear modulus, and the acceleration history.

Solid state instability growth will occur in the plastic flow regime. Plastic behavior is described by a semi-empirical constitutive model [1] that has been developed for phenomena that occur at strain rates $<10^5$ s^{-1}. Such plastic flow has been characterized either microscopically by the theory of lattice dislocations, or macroscopically by an effective lattice viscosity [2]. The best approach to describe the plastic flow of a material may depend on the specifics of the particular experiment. Neither approach has been well tested experimentally.

Analytically, stability boundaries can be defined, as described by Lebedev *et al* [3, 4], which can be used to determine whether material strength is sufficient to inhibit plastic deformation, completely stabilizing growth of a modulation. Outside the stability boundary, the material may undergo plastic deformation, and the modulated interface may grow. This has been demonstrated by Barnes *et al* [5] using Al plates with a preimposed surface modulation that are driven with a high explosive drive, and also by Lebedev *et al*, [3, 4] using Al and Ti plates in similar experiments.

We are conducting experiments on the Nova laser [6] to study the plastic flow of metals at high pressure and very high strain rates. Metal foils of copper are compressed by a factor of 1.5-2.0 with staged shocks reaching peak pressures of about 3 Mbar. The Rayleigh-Taylor instability is the observable "probe" in this experiment, with departures from classical (liquid) behavior characterizing the material strength properties at high pressure and compression.

We present details in this paper of the hohlraum target design and x-ray drive characterization for a Cu foil experiment. We also present calculations of the material state with this drive, and results from instability growth experiments using thin Cu foils. We discuss the stability boundaries for solid state plastic flow for the Nova experiments, and conclude with a discussion of an improved experimental design using an Al foil where the foil remains solid throughout the experiment and strength effects should be considerably enhanced.

EXPERIMENTAL DETAILS

The hydrodynamics experiments are conducted using an x-ray drive created in a cylindrical gold hohlraum. This x-ray drive accelerates a metal foil payload by ablation of a brominated polystyrene ablator layer. A preimposed sinusoidal modulation is located on the metal foil at the embedded interface. The growth of this RT unstable interface is then diagnosed by face-on x-ray radiography using a gated x-ray framing camera. [7]

The target geometry is shown in Fig. 1. The hohlraum (Fig. 1a) is cylindrically symmetric with internal shielding to prevent hard x-rays from preheating the Cu foil due to M-band emission coming from the laser spots on the inner hohlraum wall. The hohlraum is 3.44 mm in diameter, and 5.75 mm long. The laser entrance holes are 1.2 mm in diameter, and the holes in the internal shields are 1.6 mm in diameter.

The hydrodynamics package (Fig. 1b), consisting of a 20 μm thick brominated polystyrene (CH(Br)) foil pressed in contact with the metal foil, is mounted on the side of the hohlraum. The CH(Br) ablator has a 3% atomic Br fraction to enhance the opacity to the soft x-rays. We typically use 18-19 μm thick oxygen-free high conductivity Cu foils that have been rolled and then machined to have a sinusoidal modulation.
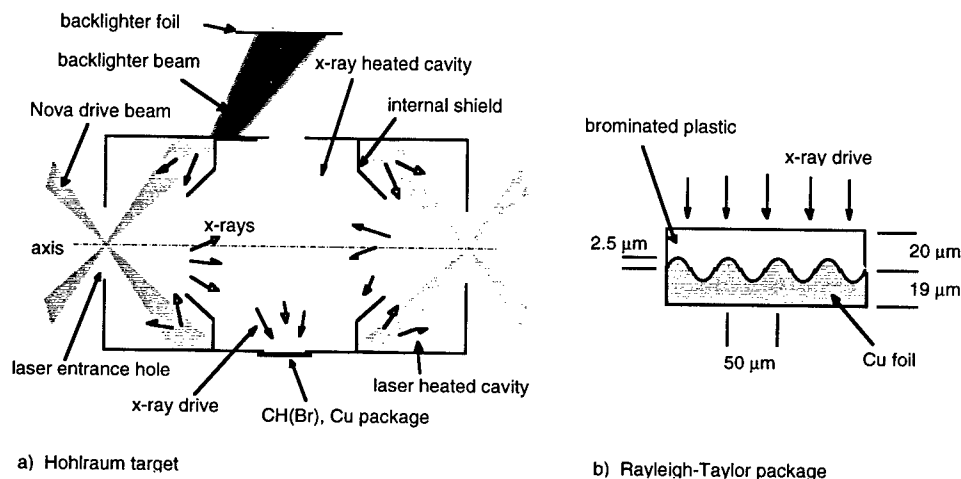

Fig. 1. (a) Schematic showing the internally shielded hohlraum and geometry for face-on radiography. (b) Modulated foil package mounted on the side of the hohlraum.

Eight Nova beams generate an x-ray radiation environment in the two laser heated cavities of the target. Re-emitted x-rays that pass through the holes in the internal shields heat the central (x-ray heated) cavity and ablate material from the CH(Br) ablator, launching a series of shocks into the package. Without the internal shields, the 2-4 keV Au M-band component of the spectrum of emission from the laser plasmas would be absorbed throughout the full volume of the package, potentially preheating the Cu foil causing it to melt and decompress. With the internal shielding, the x-rays incident on the ablator are generated by re-emission from the regions of the wall that are not directly illuminated by the laser beams, and the spectrum of these x-rays is nearly Planckian without a significant M-band component.

The x-ray drive ablates the brominated plastic, launching a series of shocks into the metal foil, compressing and accelerating it away from the hohlraum. We diagnose the growth of the perturbed unstable embedded interface by x-ray radiography using a large area (0.7 mm diameter focal spot) backlighter generated with two additional Nova beams aligned to a separate Fe backlighter foil generating He_α x-rays at 6.7 keV. A 2-3 ns square laser pulse shape was used for these backlighter beams, and delays relative to the drive beams ranged from 5-14 ns.

X-RAY DRIVE MEASUREMENT

The laser pulse shape is designed to generate an x-ray drive to launch 2 shocks, compressing the Cu foil to a peak pressure of about 3 Mbar while maintaining the metal foil in the solid state. This pulse shape is shown in Fig. 2. It has an intensity ratio in the peak vs. the foot of about 30. We have characterized the x-ray drive using the Dante diagnostic [8] and side on foil trajectories.

The Dante diagnostic is a filtered array of absolutely characterized x-ray diodes. These are positioned to view the spectral soft x-ray emission from the inner wall of the central section of the hohlraum through a beryllium-lined diagnostic hole. With the high contrast shaped laser pulse, only the lowest energy channels of the Dante detected signals starting at about 1.0 ns. The absolute signal levels from these diodes were used to estimate the Planckian drive temperature, which started at about 15 eV and rose to 40 eV at 3.5 ns. Above 40 eV, enough channels recorded signals that a spectral unfold could be performed. The measured radiation temperature rose from 40 eV at 4.0 ns to 90 eV at the end of the laser pulse at 6.5 ns, and then slowly decayed as energy was lost into the hohlraum walls and through the laser entrance holes.

The measured drive temperature is shown overlaid with the laser pulse shape in Fig. 2. Note that the measured drive is the re-emission from the wall of the hohlraum at the midplane. The package experiences the x-ray drive that is incident on the wall, the incident flux temperature (T_I),
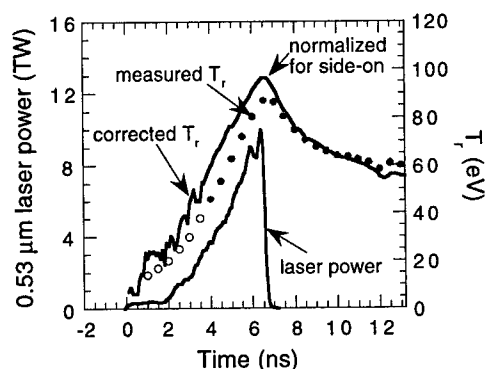

Fig. 2. Laser pulse shape and x-ray drive temperature for the low isentrope drive.

which is related to the measured re-emission flux temperature (T_R) by the albedo (α) [9] of the wall by the equation:

$$T_l = T_R / \alpha^{1/4} \tag{1}$$

We calculated the albedo correction using the LASNEX computer code [10], incorporating a view-factor analysis where the flux incident on the wall at the midplane of the target is calculated from the view of the different regions of the hohlraum. We also performed a full simulation of the hohlraum target including the laser power incident in the laser heated regions to estimate the drive temperature at the package. The resulting corrected drive is shown overlaid in Fig. 2. As a consistency check for the low temperature foot portion of the pulse, we analytically solve the power balance prescription from Rosen and Lindl [11]. We consider the power flow in the laser heated and x-ray heated cavities of the internally shielded hohlraum. The laser power that enters the laser heated cavities is equal to the sum of the losses through the laser entrance hole, losses into the wall, and power flow into the x-ray heated cavity. Similarly, the power flow into the x-ray heated cavity is equal to losses to the hohlraum wall and losses out to the laser heated cavities. Incorporating the temporal scaling of the wall albedo from high power 1 ns drive experiments, we estimate that the temperature of the foot at 1 ns is about 24 eV. The LASNEX albedo corrected drive is in good agreement with this scaling at 20-25 eV.

The peak portion of the drive is verified with a side-on foil trajectory measurement. For this, we mounted a package consisting of 22 µm CH(Br) with 13 µm Cu on the side of the hohlraum. We recorded an x-ray shadow image of the foil as it was accelerated away from the hohlraum using a high magnification (55X) x-ray streaked imager. In order to match the overall motion of the foil, the albedo corrected drive is reduced in the simulations by only about 2% in radiation temperature, T_R, for times t>5 ns. This adjustment is interpreted as a correction due to the uncertainty in the opacity of the ablator at low drive temperatures, and in the initial Dante drive measurement itself.

Using the albedo corrected x-ray drive in the hohlraum, we model the conditions in the foil package with 1-D LASNEX. The calculated temperature and pressure at the embedded ablator/Cu interface are shown in Fig. 3. The x-ray drive ablatively launches two shocks into the copper. The first shock due to the low foot is about 0.4 Mbar in the Cu, and the second is 3 Mbar. There are subsequent reflected shocks that maintain the high pressure until about 8 ns. At about this time, the material temperature at the interface exceeds the melt temperature, which we calculate by the Lindemann law:

$$T_m = T_{mo} exp\{2a(1 - 1/\eta)\}\eta^{2(\gamma_o - a - 1/3)} \tag{2}$$

where T_{mo} is the melt temperature at constant volume, η is the compression of the sample, γ is the Grüneisen gamma, and a is the coefficient of volume dependence of γ, as defined by Steinberg *et al* [1].

The low isentrope drive is calculated to keep the foil very near an adiabat throughout the experiment. In Fig. 4 we show the internal energy at the Cu interface plotted as a function of density (compression) from t=0 to t=15 ns. Note that this trajectory is sensitive to the temperature of the foot of the shaped drive pulse. If the albedo correction for the foot is incorrect, the timing of the first shock may be off. In particular, if the foot drive is much lower then the second shock may catch up before it reaches the interface, placing the metal foil on a higher adiabat and potentially melting it. For the case of this drive, the shocks overlap about half way through the foil, melting the back side. The interface then melts with the rarefaction.
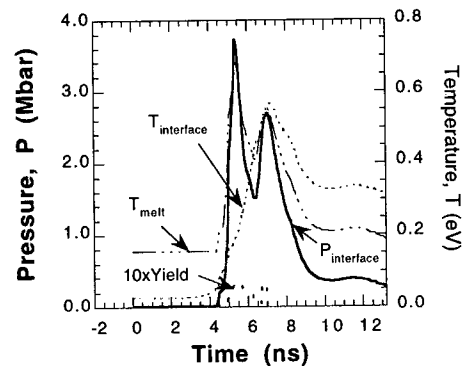
Fig. 3. Pressure and temperature calculated at the CH(Br)/Cu interface with the
low isentrope drive.

Adjusting the level of the foot somewhat higher is one way to keep the temperature at the interface below the melt curve for longer, as is discussed later.

Experiments to characterize the foot drive were done using both active shock breakout [12, 13] and dynamic Bragg diffraction techniques [14, 15] to measure shock timing. For the case of the active shock breakout measurement, we use a displacement Michaelson interferometer to measure motion of the back surface of a 17 μm thick Al flat target mounted on the side of the hohlraum. Motion of the back surface due to the shock transit and breakout through the foil is evident by a shift in the fringe pattern, as shown in Fig. 5. The streaked interferometer data is shown in Fig. 5a, and the analyzed position as a function of time for the back surface is shown in Fig. 5b. This measurement is done with an interferometer that operates at a wavelength of 400 nm, so a full fringe shift corresponds to one half wavelength (0.2 μm) of motion at the back surface.

The interferometer data shows motion that may be due to the breakout of the elastic precursor wave or due to some amount of preheat at the back surface of the Al foil, and then the rapid motion and disappearance of the fringes as the main shock breaks out. We show simulated position as a function of time for the back surface with some imposed preheat to illustrate how this measurement is affected by low preheat levels.

For the case of Bragg diffraction, we use a CH(Br) ablator with a 40 μm thick Si crystal as a
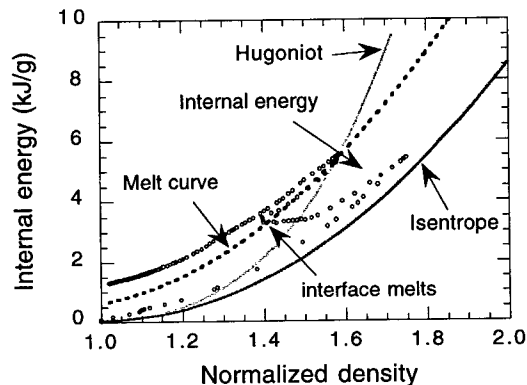
Fig. 4. Internal energy trajectory of the Cu at the CH(Br)/Cu interface
for the low isentrope x-ray drive.

a)

b)

Fig. 5. (a) Streaked displacement interferometer data showing the fringes move due to motion of the back surface of a 17 μm Al foil. (b) Back surface position plotted as a function of time, overlaid with simulation results.

surrogate for the Cu foil mounted on the side of the hohlraum. A vanadium backlighter generates x-rays at 5.3 keV, diffracting off the crystal through the brominated plastic ablator. When the shock transits the ablator and reaches the interface, it compresses the Si lattice. This is observed as a shift in the Bragg diffraction angle of th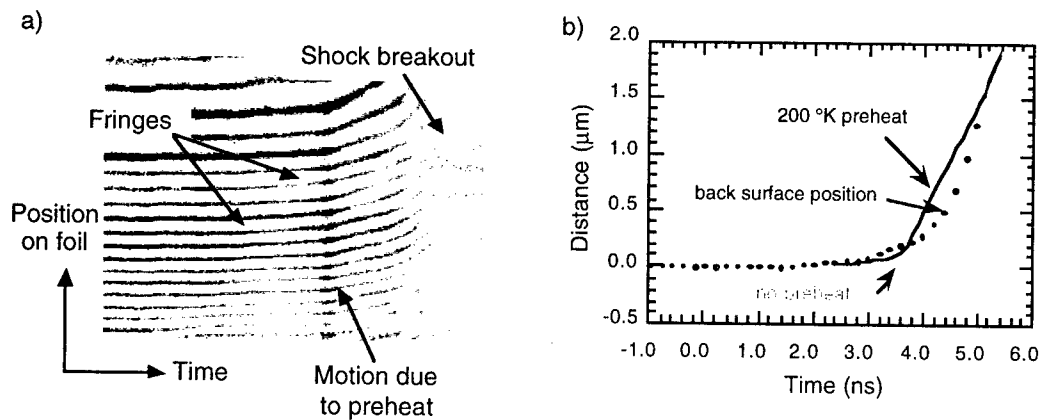e backlighter x-rays. Data obtained using this technique with a square laser pulse shape is shown in Fig. 6 to illustrate the technique. [14-16] The estimated shock strength in the Si for this experiment was 350 kbar, compared to the calculated 650 kbar first shock strength in Cu for this shaped x-ray drive. Note that the presence of the diffraction signal under shock compression is consistent with the assumption that the Si remains solid under compression.

INSTABILITY GROWTH EXPERIMENTS

Sinusoidal modulations are machined in the Cu foils with amplitudes of 1.0-2.5 μm, and wavelengths of 20 and 50 μm. A 20 μm thickness of brominated plastic ablator is pressed onto the modulated foils, and then the package is mounted over a hole in the side of the hohlraum. The x-ray drive ablatively launches a series of shocks to compress and accelerate the metal foil away from the side of the hohlraum.

Radiographic images of the foil are recorded using 6.7 keV Fe x-rays. Up to 16 images are recorded on 4 independently timed microchannel plate striplines on each laser shot, using the Flexible X-ray Imager [17] with a 230 ps gate pulse. The modulation amplitude in optical depth is calculated by Fourier analysis at each time. The Fourier amplitude is normalized to the initial contrast in optical depth, which we measured on a separate shot.

The growth factors for λ=50 μm, 2.5 μm amplitude modulations are shown in Fig. 7a, and for λ=20 μm, 1.0 μm amplitude modulations are shown plotted in Fig. 7b. In these experiments, the ablator/metal interface moves only about 40 μm during the time the measurements are made and the overall growth factors are small, which means the modulation remains nearly linear. As a result, when we normalize the measurements with the initial (measured) contrast at that wavelength (x-ray mean free-path and instrument resolution function), the instrument resolution (MTF~0.65 at 8X instrument magnification for λ=50 μm and 0.6 at 12X for λ=20 μm) is removed from the measurement.

Overlaid on the graphs in Fig. 7, we have plotted the growth factors simulated with LASNEX using both a fluid model, and the constitutive material strength model described by Steinberg *et al.*

shock arrival at interface

x-ray backlighter turns on

Increasing
compression

unshocked Si

shock
compressed Si
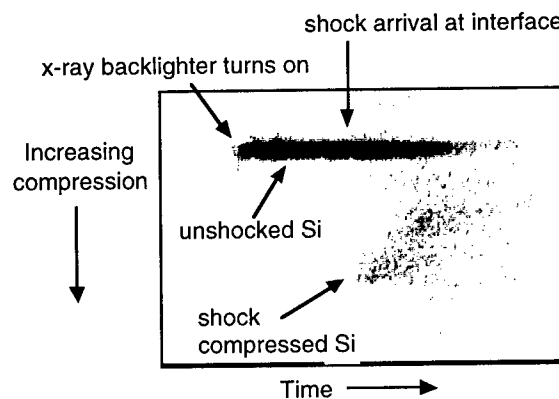
Time ⟶

Fig. 6. Streaked diffraction pattern from the CH(Br)/Si embedded interface showing a shift in the diffraction peak at the time the shock reaches the interface.

We show separate calculations in Fig. 7 for experiments where the peak portion of the laser pulse shape was reduced by about 20% (indicated on the figure by 'low drive') since the growth is sensitive to the actual drive history. The difference between the fluid and material strength simulations for λ=20 μm and 50 μm is small. For the 50 μm wavelength case, the simulations are nearly identical. For the 20 μm wavelength case, material strength leads to about 20% less growth, but the difference due to variation in the laser power history for the different shots is about this order, making it difficult to confirm that reduced growth is due to the material strength at λ≥20 μm with these Cu foils.

Extending the simulations to shorter modulation wavelengths, λ<20 μm, we observe a greater effect due to material strength. The calculated growth factors for a range of wavelengths from 5 to 50 μm are shown in Fig. 8, plotted after the interface has moved a distance of 20 μm. The enhanced difference between fluid and strength modeling at λ≤20 μm suggests that with some modifications we should be able to observe the effect of strength stabilization in the Nova experiments. Measuring perturbation growth factors at λ=5-10 μm with gated pinhole imaging is problematic due to reduced exposure levels and diffraction effects with apertures smaller than 5 μm. As a result, this experiment would be improved with a design where longer wavelengths would be stabilized.

a)

b)
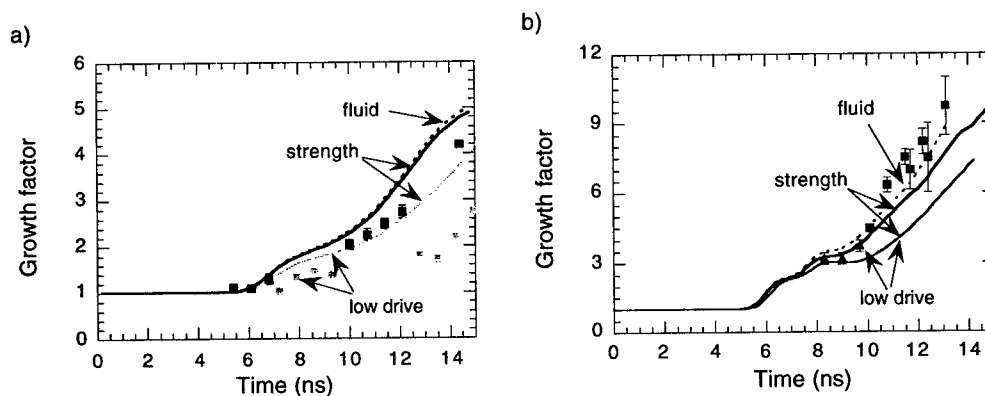
Fig. 7. Instability growth factors for a) 50 μm and b) 20 μm wavelength modulation at the embedded CH(Br)/Cu interface. LASNEX simulations were done with and without strength.
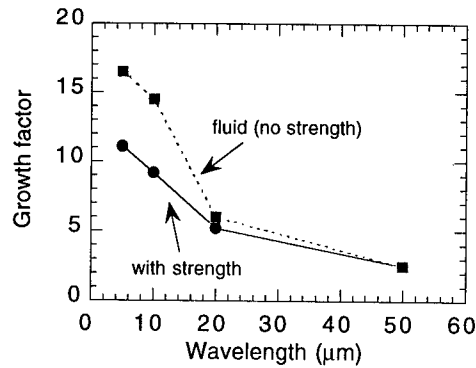
Fig. 8. Growth factor as a function of wavelength for a modulated Cu foil, plotted for a distance moved of 20 μm.

STRENGTH STABILIZATION

The pressure enhanced yield strength and shear modulus are given in the strain-rate independent constitutive model by Steinberg *et al* as

$$Y(P,T) = Y_o[1 + \beta(\varepsilon + \varepsilon_i)]^n \left[1 + \left(\frac{Y_P'}{Y_o}\right)\frac{P}{\eta^{1/3}} - \left(\frac{G_T'}{G_o}\right)(T - 300)\right] \tag{3a}$$

$$G(P,T) = G_o\left[1 + \left(\frac{G_P'}{G_o}\right)\frac{P}{\eta^{1/3}} - \left(\frac{G_T'}{G_o}\right)(T - 300)\right] \tag{3b}$$

where the Y is the yield strength, and G is the shear modulus, ε is the strain, and η is the compression. In this formulation, the pressure (P) and temperature (T) dependence and the effect of work hardening (β) are included. The initial value for yield strength is $Y_o=1.2\times10^{-3}$ Mbar and the initial value for shear modulus is $G_o=0.477$ Mbar for a Cu foil.

At a shock pressure of 3 Mbar, the Cu foil is compressed by about a factor of >1.5, at which point the yield strength is 50 kbar, enhanced by a factor of about 40 over the nominal value, Y_o. The shear modulus is about 3.6 Mbar. Under these conditions, the yield strength is exceeded by more than an order of magnitude, putting the foil into the plastic flow regime and allowing for instability growth in the solid state.

Estimates can be made as to whether the modulation on the Cu package grows or not, based on a stability boundary analysis assuming steady-state conditions. The Miles criterion, based on linear theory, [18] assumes a modulation amplitude, η_o, much smaller than the wavelength. It establishes that for a semi-infinite slab with a modulated surface, the modulation is stable if its wavelength is shorter than the cutoff wavelength,

$$\lambda_\infty = 4\pi G \big/ \rho g \tag{4}$$

where g is the acceleration. Including the finite thickness of the foil, Lebedev *et al* extend Miles' theory and predict this cutoff is at

$$\lambda_c = \frac{2\lambda_\infty}{1+\sqrt{1+8\sqrt{3}c^2/gH}} \tag{5}$$

where c is the speed of the shear wave, and λ_∞ corresponds to the Miles cutoff wavelength, Eqn. (4). For the conditions of this experiment, λ_c=30 μm. Therefore, at λ=20 μm, we are below the cutoff wavelength, suggesting that perturbations with very small initial amplitude under steady state conditions should not grow.

We observe, however, the λ=20 μm modulation grows in both the experiment and the simulation. This is because the amplitude exceeds the critical amplitude given by Lebedev et al. This amplitude cutoff is given by the expression:

$$\eta_c = \eta_c(Druc\,ker)\left[1-0.86e^{\left(2\pi H/\sqrt{3}\lambda\right)}\right]\left\{\left[1-e^{\left(-2\pi H/\sqrt{3}\lambda\right)}\right]^2 - \left(\frac{\lambda}{\lambda_\infty}\right)^2\right\} \tag{6}$$

where

$$\eta_c(Druc\,ker) = \frac{2Y}{\rho g} \tag{7}$$

is the wavelength independent critical amplitude threshold to instability growth from Drucker [19]. For these experiments, at λ=20 μm, the amplitude threshold is <1 μm, which is much too small to diagnose by x-ray backlighting using a hard x-ray backlighter at 6.7 keV.

In order to design an experiment in a regime where there is a much greater reduction in growth due to material strength, we consider a material with a lower density and a larger value for the derivative of the yield strength with pressure to maximize the effect of strength on the R-T instability growth. Aluminum is one such metal with a pressure derivative of the yield strength that is a factor of 2 larger than for Cu. For 7075 (or 6061) Al, which has an initial yield strength of 4.2 kbar, we calculate the growth of 20 μm wavelength with and without strength using an initial amplitude of 0.5 μm. The case with strength grows less than a factor of 2 while the fluid case shows a growth factor of about 5 at t=12 ns (Fig. 9a). Note that in order to time the shocks so that they do not overlap in the metal foil, the foot portion of the drive is raised (Fig. 9b). With this design, the peak pressure in the Al is 1.4 Mbar, and the foil is calculated to remain solid throughout, as indicated by a plot of the internal energy trajectory (Fig. 10).
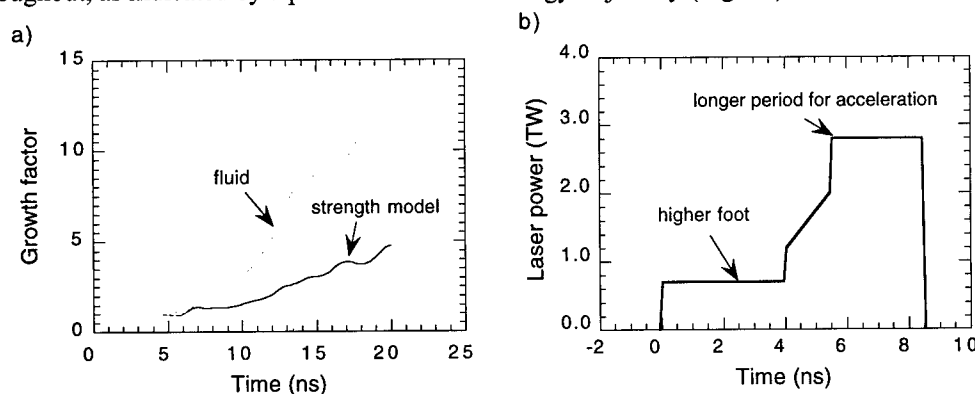
Fig. 9. (a) Growth factor as a function of time calculated for a modulated Al foil with a perturbation wavelength of λ=20 μm and initial amplitude of 0.5 μm. Simulations were done with and without material strength. (b) Laser pulse shape for the Al instability experiment.
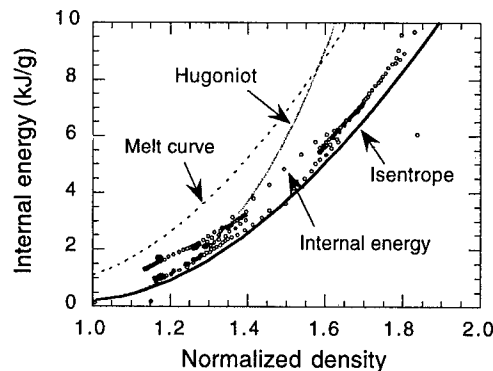
Fig. 10. Internal energy trajectory calculated for an Al foil at the CH(Br)/Al interface. The modified drive is expected to shock the foil without melting it.

SUMMARY

We have developed an x-ray drive to shock compress metal foils in the solid state using an internally shielded hohlraum with a high contrast shaped laser pulse. We use a combination of Dante measurements, side-on foil trajectories, and shock timing measurements to develop an understanding of the x-ray drive. Hydrodynamic experiments that are designed to study growth of the RT instability in the plastic flow regime have been started. Measurements of initial 20-50 μm wavelengths, and 1-2.5 μm amplitude perturbations are presented and compared with simulations in this paper. In this experiment, the growth of the instability in fluid and solid state are calculated to be nearly the same. Analytic stability analysis is consistent with the instability growing in the plastic flow regime. However, by re-designing the experiment to use an Al foil, the foil will remain in the solid state throughout, and the effect of material strength may be enhanced considerably, allowing us to conduct experiments on either side of the stability boundary.

REFERENCES

1.   D. J. Steinberg, S. G. Cochran, M. W. Guinan, J. Appl. Phys. **51**, 1498 (1980).
2.   L. C. Chhabildas, J. R. Asay, J. Appl. Phys. **50**, 2749 (1979).
3.   A. I. Lebedev, P. N. Nizovtsev, V. A. Rayevsky, in the Proceedings of the 4th International Workshop on the Physics of Compressible Turbulent Mixing, 29 March - 1 April, Cambridge, England (Cambridge University Press, 1993), p. 81.
4.   A. I. Lebedev, P. N. Nizovtsev, V. A. Rayevsky, V. P. Soloviov, in the Proceedings of the 6th International Workshop on the Physics of Compressible Turbulent Mixing, 17-21 June, 1997, Marseille, France (I.U.S.T.I./C.N.R.S., Marseille, 1997).
5.   J. F. Barnes, P. J. Blewett, R. G. McQueen, K. A. Meyer, D. Venable, J. Appl. Phys. **45**, 727 (1974).
6.   E. M. Campbell, J. T. Hunt, E. S. Bliss, D. R. Speck, R. P. Drake, Rev. Sci. Instrum. **57**, 2101 (1986).
7.   P. M. Bell, J. D. Kilkenny, G. Power, R. Bonner, D. K. Bradley, in Ultrahigh Speed and High Speed Photography, Photonics, and Videography '89 (SPIE, Bellingham, WA, 1989), Proc. SPIE Vol. 1155, pp. 430-444.
8.   H. N. Kornblum, R. L. Kauffman, J.A. Smith, Rev. Sci. Instrum. **57**, 2179 (1986).

9.   R. L. Kauffman, H. N. Kornblum, D. W. Phillion, C. B. Darrow, B. F. Lasinski, L. J. Suter, A. R. Theissen, R. J. Wallace, F. Ze, Rev. Sci. Instrum **66**, 678 (1995).
10. G. B. Zimmerman, W. L. Kruer, Comments Plasma Phys. Controlled Fusion **2**, 51 (1975).
11. J. Lindl, Phys. Plasmas **2**, 3933 (1995).
12. K. S. Budil, P. Celliers, G. W. Collins, L. B. DaSilva, R. Cauble, R. J. Wallace, G. Chiu, A. Ng, in the Inertial Confinement Fusion Quarterly Report **7** (1), UCRL-LR-105821-97-1, 11 (1997), copies available from the National Technical Information Service, Springfield VA.
13. G. W. Collins, P. Celliers, L. B. Da Silva, R. Cauble, D. Gold, M. Foord, K. S. Budil, R. Stewart, N. C. Holmes, M. Ross, B. A. Hammel, J. D. Kilkenny, R. J. Wallace, A. Ng, Phys. Plasmas **5**, 1864 (1998).
14. Q. Johnson, A. Mitchell, R. N. Keeler, L. Evans, Phys. Rev. Lett. **25**, 1099 (1970).
15. J. S. Wark, *et al*, Phys. Rev. B **35**
16. D. H. Kalantar, *et al*, to appear in Rev. Sci. Instrum.
17. K. S. Budil, *et al*, Rev. Sci. Instrum. **67**, 485 (1996).
18. J. W. Miles, Technical Report No. GAMD-7335 (General Dynamics, San Diego, 1966).
19. D. C. Drucker, Ingenieur-Archiv **49**, 361 (1980).

APPLICATIONS OF THE ION BEAM TECHNIQUE FOR INVESTIGATIONS OF HYPERVELOCITY IMPACTS

**G.I. KANEL[*], J.R. ASAY[±], K. BAUMUNG[+], H. BLUHM[+], L.C. CHHABILDAS[±],
V.E. FORTOV[*], B. GOEL[+], P. HOPPÉ[+], T. MEHLHORN[±], S.V. RAZORENOV[**],
D. RUSCH[+], and A.V. UTKIN[**]**

[*] High Energy Density Research Center, Izhorskaya 13/19, Moscow 127412 Russia;
[±] Target & Z-Pinch Theory Department, Sandia National Laboratories, Albuquerque, NM 87185-1187, USA;
[+]Forschungszentrum Karlsruhe, P.O. Box 3640, D-76021 Karlsruhe, Germany.
[**]Institute for Chemical Physics Research, Chernogolovka, 142432, Russia

Summary— In the presentation we report on experiments at the Karlsruhe Light Ion Facility KALIF employing high-resolution laser-Doppler velocimetry. The schemes of possible EOS experiments using interferometry and the dynamics and the limiting factors of the ablative hypervelocity launching are discussed as well as advantages of the ion beam technique for investigations in the field of hypervelocity impacts and equations of state. So far, we have accelerated aluminum foils of 10 to 30 µm thickness to velocities beyond 12 km/s. Besides the beam power, the limiting factors for the launching are melting of the accelerated flyer plate as a result of shock-wave heating and the heat transfer from the energy deposition zone. The experiments considered include the Hugoniot measurements and measurements at unloading of shock-compressed state down to the vaporization region. Parameters of shock waves that cause melting of aluminum, copper, molybdenum and titanium in release have been measured with a pulse proton beam on KALIF. A way of measurements in the vaporization region has been tested with explosive facilities. © 1999 Elsevier Science Ltd. All rights reserved.

INTRODUCTION

Pulse power machines, which were developed for their potential applications in inertial confinement fusion, are available now for experiments in high pressure physics and material response phenomenology related to hypervelocity impact events. Possible ways to utilize the pulse power capabilities in shock wave and hypervelocity impact physics were discussed in 1996 in a meetings of members of the KALIF team of Forschungszentrum Karlsruhe, the pulse power team of Sandia National Laboratory, and the shock-wave physics groups of the High Energy Density Research Center and Institute of Chemical Physics of Russia Academy of Sciences. The meetings and the experience of shock-wave research work with Karlsruhe Light Ion Facility (KALIF) have stimulated some ideas which are discussed herein.

At KALIF high-power proton beams with power densities up to ~1 TW/cm² are generated depositing up to 40 kJ of ion energy in a focal spot of 6-8 mm diameter. With peak proton energies of ~1.7 MeV, specific power densities of up to 200 TW/g and energy densities of several MJ/g can be realized at ~40 ns fwhm. The massive energy deposition in a zone of 5-10 mg/cm² leads to fast vaporization and ablation of the material and causes intense compression waves to propagate into the residual part of the target. In this way thin foil plates with a thickness of several tens of micrometers can be accelerated to velocities larger than 10 km/s. This is a regime in which hypervelocity impact experiments are of particular interest. For the shock wave

experiments, an ORVIS-type laser-Doppler-velocimeter was set up allowing us to measure the velocity of the rear surface of thin (10 μm -1 mm) targets with a 200 ps temporal resolution. The experience of research work carried out on KALIF during the years 1991 to 1996 was discussed in review papers [1,2]. During these years investigations of the equation of state, dynamic failure of solids under nanosecond load duration, phase transitions, and viscosity at strain rates up to 10^8 s^{-1} were performed. The shock-wave diagnostics was applied also to study hydrodynamics of the ion beam interaction with solid targets and to investigate the beam structure. The main objective of this paper is to consider advantages and promising experimental arrangements for hypervelocity impact investigations using ion beam sources.

HYPERVELOCITY LAUNCHING WITH ION BEAMS

Figure 1 demonstrates the flyer velocities over the whole acceleration process measured with the ORVIS-type laser Doppler velocimeter [3] for metal and polymer foils of different initial thickness. The final velocity of heavy tantalum flyer is much smaller than the velocity of light flyers. The final kinetic energy of the flyers launched with $B_\ominus$ diode is estimated as $(1.3-1.8) \times 10^6$ J/m^2, independently of the flyer material.

A maximum velocity of 12.5 km/s was reached but, obviously, it is not an absolute upper limit of the particle beam drivers. Using more powerful sources we can hope to increase the velocity. One of the physical limitations on this way is caused by the necessity to keep the flyer plate unmelted and smooth. Meanwhile the velocity histories measured in the experiments with the $B_\ominus$ diode contain a steep velocity rise in the initial phase of the acceleration. For thicker flyer plates this rise is certainly transformed to a discontinuity which is an evidence of formation of a shock wave. The shock-wave compression is accompanied by irreversible heating of the flyer matter. At a certain peak pressure the entropy increase in the shock wave results in melting of the solid flyer which leads to the appearance and development of instabilities. Therefore, the formation of a shock wave with an intensity high enough to heat the flyer up to the melting point limits the launching capabilities of the beam drivers. Melting is not expected in the case of smooth compression.

The structure of the compression wave generated by the ion beam interaction with a condensed target can be varied by adjusting the beam structure. If the beam energy, E_b, is deposited instantaneously in a condensed target, the pressure in the energy deposition zone just
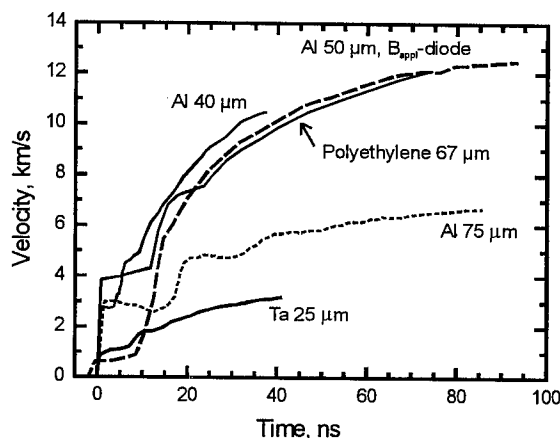

Fig. 1. Ablative acceleration of foils of different materials with the $B_\ominus$-diode (0.15 TW/cm^2) and the appl-B diode (1 TW/cm^2, mentioned velocity history). Measurements with the ORVIS-type [3,4] laser Doppler velocimeter.

after deposition would be compressive with an amplitude of

$$p = \Gamma \rho E_b,$$

where Γ is the Grüneisen parameter. Actually, because the front surface is a free surface, the stress must be zero for all time at the surface. On the facilities operating today the time of energy deposition exceeds the acoustic relaxation time in the energy deposition zone, $\tau_a \approx \delta/c$, where δ is the zone thickness. This means that pressure in the energy deposition zone is a result of two competing effects: energy deposition and unloading by volume expansion. The effects of variations in the pulse structure and duration as compared to the acoustic transit time across the penetration depth of the incident energy have been analyzed in a frame of acoustic approach by Bushell and McGloskey [5] for laser-driven compression waves and by Utkin et al. [6,7] for the ion beam driven processes. Roughly, the pressure generated under these conditions is proportional to the power density, and with an appropriate power history the shock wave formation can be avoided. Fig. 1 shows that the B_{appl} diode provides a smooth acceleration of a flyer without velocity jumps, that means without a shock wave formation.

The residual flyer thickness derived from different types of experiments reduces with time as a result of vaporization in the energy deposition zone and in the nearby layer. Simulations show a great contribution of the heat transfer and vaporization of the residual part as a result of the heat conductivity which also imposes a certain limit on the ratio of minimum flyer thickness to the energy deposition range. The conditions in the boundary layer between the energy deposition range and the adjacent cold matter are not quite clear. Probably the heat transfer, melting and vaporization are accompanied with the development of an instability in the boundary layer between the heated and cold matter. However, the ORVIS interferograms show that the foil rear surface keeps a high reflectivity and, consequently, smoothness during a relatively long time.

ADVANTAGES OF THE TECHNIQUE

Like lasers, ion beam sources can be used for hypervelocity launching of very thin plates only and for simulating hypervelocity impacts of microparticles. However, it seems more useful to apply the technique to investigate properties of matter under hypervelocity impact conditions and to use this information in a following analysis. The properties of material which control its response to the hypervelocity impact should be described by the equation of state over a wide range of pressures and temperatures and by the constitutive relationships accounting for resistance to inelastic deformation and fracture over a wide range of strain rates.

An important issue is the domain where beam-driven shock wave measurements compete with more conventional techniques. In many cases the small load duration in the beam experiments is an advantage when studying time-dependent properties of materials. There is evidence, for example, that thermal destruction of polymers occurs under shock compression in the vicinity of 20 GPa and higher. Since any chemical process is time-dependent, Hugoniots of polymer materials can be different depending on the duration of the process considered or the space scale of the target. Perhaps the most promising feature of thin foil impactors is that they provide a possibility to investigate time-dependent elastic-plastic and strength properties of materials at extremely high strain rates.

The energy delivered by the ion beam is distributed over a relatively large focal spot on the target surface. As a result of the power density profile of the beam, the radial distribution of the shock pressure in a massive target or of the velocity of a flyer plate is bell-shaped. This means that a range of impact conditions can be covered in one shot. The nonuniformity of the load caused by the radial beam profile is usually considered as a disadvantage of the method. However, since the characteristic radius of curvature is much larger than any longitudinal
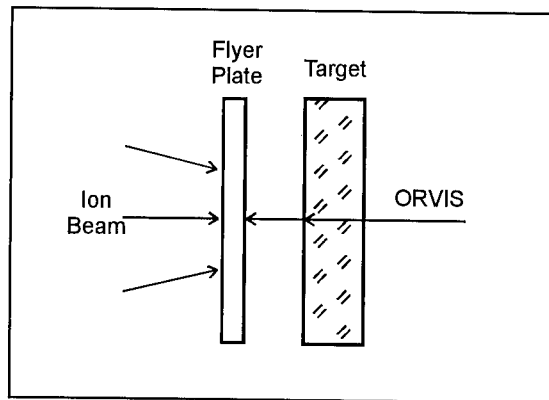
Fig. 2. Schematic of experiments for the shock compressibility measurement
using transparent target and the ORVIS velocimeter.

characteristic dimension of the phenomenon, the shock-wave process can be still considered as
one-dimensional. The line-imaging laser velocimeter [4] provides a possibility to utilize the
impact velocity distribution and to make a continuous series of shock-wave measurements in one
shot.

THE MODERN AND POTENTIAL EQUATION OF STATE EXPERIMENTS

When the Hugoniot of matter is determined experimentally, the measurable parameters most
often are the shock velocity, U_s, and the particle velocity, u_p. Techniques for measuring the shock
wave velocity with an accuracy of ±1% are well developed for shock pressures up to several
Mbar generated by explosive facilities and gas guns; the velocities are calculated from the times
taken for shocks to transit known distances. Particle beam as well as the laser driven shock
waves have to be examined on a nanosecond time scale at micrometer propagation distances.
Using conventional velocity measurement methods at these time and distance scales increases the
uncertainty up to ~4-5% [8] that reduces significantly the value of the data obtained. Obviously,
we have to look for other capabilities for measuring Hugoniots under conditions of very short
load pulses.

A more appropriate method for diagnosing proton beam-driven shock waves is the laser
Doppler velocimeter [3,4]. The measured quantity with this method is the phase of interference
of reflected light inside the interferometer, so precise knowledge of the sample thickness and the
transit time are not necessary. The accuracy of instrumentation is estimated [9] as 0.2% to 1% of
the peak velocity. High accuracy of measurements is provided by their differential character. The
time resolution of such velocimeters can be ~100 ps or better; the space resolution reaches ~10
μm in a lateral direction. A demonstration of capabilities of this diagnostic in measuring the
shock compressibility has been done in preliminary experiments with laser [10] and proton [2, 11]
beams. The main idea is based on the use of a transparent barrier on the way of flyer plate
accelerated by the beam as it is shown in Fig. 2. One of the colliding pieces, the flyer plate or the
barrier, has to be the standard with known Hugoniot. If the barrier material keeps its
transparency under shock compression, the flyer velocity and the impact surface velocity can be
measured simultaneously in the same experiment. It is sufficient to calculate all shock-wave
parameters for both colliding pieces.

As an example, figures 3 and 4 show results of an experiment in which we recorded the
acceleration of a polyethylene foil, and the impact on a LiF barrier which is also an optical
window in this case. The measurement provides the impact velocity $u_i = 10.01$ km/s, and the
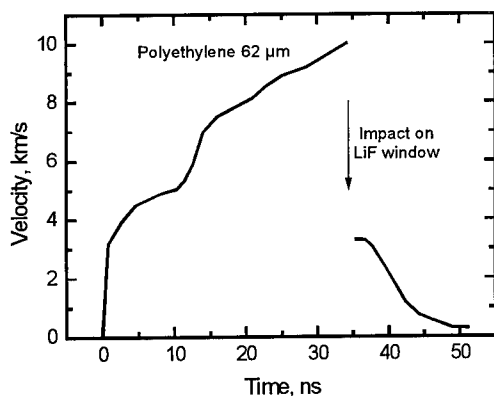
Fig. 3. Velocity history of a polyethylene film ablatively launched by the ion beam and impacted on a LiF window.
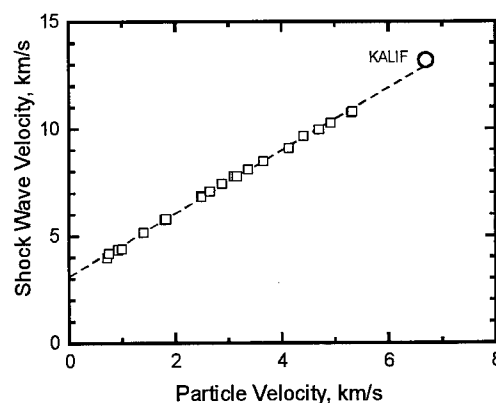
Fig. 4. Comparison of the Hugoniot point measured in the KALIF experiment with data published by Marsh [12].

velocity of the interface between polyethylene and LiF after impact, $u_t = 3.32$ km/s. Hence, the jump in the particle velocity of polyethylene is $u_p = 6.70$ km/s. Since the Hugoniot of LiF is well known, the measured interface velocity gives the pressure $p_1 = 84.4$ GPa in both shock-compressed materials. The shock front velocity, U_s, and the specific volume of the shock compressed polyethylene are calculated using the conservation laws.

Figure 4 shows the Hugoniot point obtained in comparison with data published by Marsh [12]. Our new point at 84.4 GPa is situated above the extrapolation of data at lower pressure. It is not quite clear whether or not an equilibrium state of the shock-compressed polyethylene is reached on the nanosecond time scale. It is known that thermal destruction of many organic materials occurs at shock compression above 20 GPa. Since the nature and kinetics of these chemical reactions are not well understood, we cannot exclude the possibility that actually the shock compressed state of polyethylene encountered in our experiment is some intermediate state which is quickly passed through during experiments on a microsecond time scale. Since the shock compression can be accompanied with relaxation processes, the problem of equilibrium becomes especially important for hypervelocity impact conditions where the time scale is changed by several orders of magnitude. Another reason for the discrepancy could be heating of the polyethylene film by heat transfer from the ablation zone. However, with preheated material of reduced density we should expect a lower shock pressure.

At high shock pressures transparent materials become opaque. In this case, the shock front velocity can be measured in a continuous manner with the laser interferometer. The idea is based on monitoring the laser light reflection from the shock front [11]. For transparent materials the shock front reflectivity as a result of the jump in the refractive index [13] amounts for only few percent or less. However, at high pressure a transition of some transparent dielectrics, such as sulfur [14, 15], and others into the metal phase occurs. It has been shown in experiments with static compression [15], the reflectivity of sulfur has a sudden increase at 95 GPa and reaches 62% in the infrared range at 121 GPa. If the dielectric-to-metal transition occurs rapidly enough, the shock front will become reflective like a metal mirror. Experiments with ion crystals at shock pressures up to 380 GPa have shown a maximum shock front reflectivity of about 8% observed for NaCl [13]. Such materials can be used as standards for the Hugoniot measurements with the laser interferometer technique.

At present, numerous Hugoniots over a wide pressure range have been measured for different classes of materials. To fill the gap between the guns and nuclear methods of shock wave generation, the impact velocity in beam-driven experiments should exceed ~15 km/s. Such high velocities are easier obtained with lower-density flyers. Since the shock pressure is less sensitive to the impactor material when the target impedance is less than the impedance of impactor, we

may compete with gun facilities in measurements of Hugoniots of low-density materials such as polymers or light metals.

Besides the determination of Hugoniots, the experimental basis for EOS includes isentropes corresponding to unloading of shock-compressed states. Shock compression is accompanied by heating of the medium. At a certain peak pressure, the entropy increase in the shock wave results in melting and vaporization of solids at isentropic unloading (Fig. 5). Experimental isentrope data are especially important in the region of vaporization and in the vicinity of the critical point.
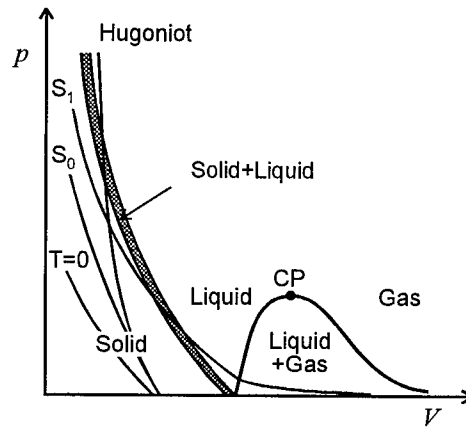
Fig. 5. Schematic phase diagram of matter.

With guns or explosive facilities, the unloading isentrope is recovered from a series of experiments where the shock wave parameters in the plates of standard low-impedance materials placed behind the sample are measured [16, 17]. The experimentally found $p(u)$ relationship corresponds to the Riemann integral

$$u = u_0 \pm \int_{p_s}^{p} \frac{dp}{\rho c}.$$

The specific internal energy and specific volume are calculated from the measured $p(u)$ release curve. Low-density foams and gases at different initial pressures are used in these experiments as standards to provide measurements of unloading down to the low-pressure region of vaporization. This technique is not quite suitable for experiments with ion beams where we have to deal with micrometer-thick targets and not well reproducible incident shock wave parameters.

The thick foil method [18] provides a few experimental points on the isentrope in one shot. When a higher shock impedance foil is placed on the surface of the material studied, the release phase occurs by steps, whose durations correspond to the time needed for the shock wave to go back and forth in the foil. The velocity during the different steps, connected with the knowledge of the Hugoniot of the foil, allows us to determine a few points on the isentropic unloading curve. However, the method becomes insensitive when the low pressure range of vaporization is reached in the course of the unloading. The isentrope in this region can be measured by recording the smooth acceleration of a thin witness plate foil. With the mass of the foil known, measurements of the foil acceleration will give us the vapor pressure.

The thin foil acceleration method was tested in explosive experiments with shock compressed PMMA. Earlier [19], evidence was found that vaporization of PMMA occurs at unloading after the shock compression to 40 GPa peak pressure. Fig. 6 presents the results of measurements of the unloading isentrope [19] which demonstrate that the particle velocity increment in the
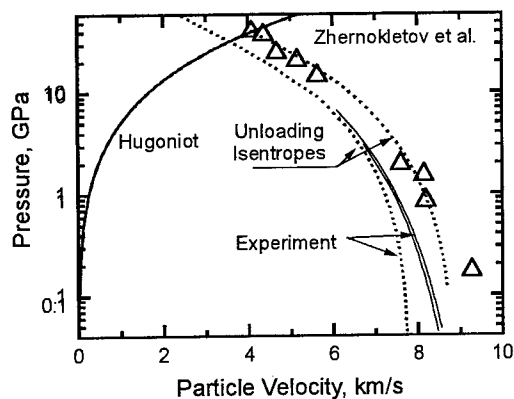
Fig. 6. Unloading data for the shock-compressed PMMA. Triangles present the data from ref. [19], the short-dashed lines were calculated using EOS [19], the thin lines at low pressures present the results of our experiments.
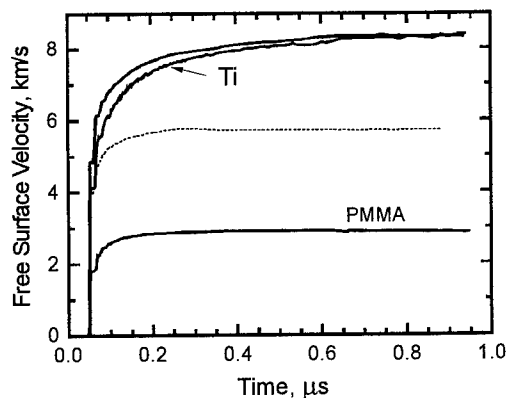
Fig. 7. The velocity histories of the aluminum and titanium (mentioned) foils 50 μm thick covering PMMA sample plates. The peak shock pressures in the PMMA samples were 33.9 GPa.

unloading wave much exceeds that in the shock wave. Fig. 6 also shows that an empirical equation of state does not describe the lowest experimental point of the release isentrope.

In the experiments performed the shock compression of 1.8 mm thick PMMA samples up to a peak pressure of 34.5 GPa was realized by impacting 2 mm thick aluminum plates at a velocity of 5.3 km/s. The sample rear surfaces were covered by 50 μm thick aluminum or titanium foils. The velocity history of the foil surface was recorded with a VISAR velocimeter. The experiments have been carried out in vacuum. Figure 7 shows the foil velocity histories measured in these experiments. Additionally, two experiments at lower pressure have been done. According to computer simulation, the final constant velocity of the covering foil should be established after ~200 ns of the wave reverberation process. This was certainly observed in the experiments at lower shock pressures. However, the results of measurements at maximum peak pressure demonstrate a much longer time of the velocity increase and some higher final velocity. Obviously, an explanation is that the finding is an evidence of vaporization of the shock-heated PMMA at 34.5 GPa peak pressure.

Fig. 8 illustrates the interpretation of the measured velocity histories. The upper parts of the velocity profiles have been approximated by a smooth function $u_a(t)$ with monotonous decrease of the first and second derivatives. After that, with the foil mass known, the vapor pressure was evaluated using Newton's law as $p(t)=\rho\cdot\delta\cdot du_a(t)/dt$, where ρ and δ are the foil density and
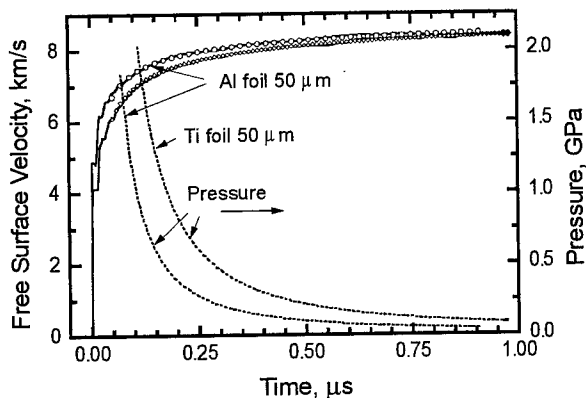
Fig.8. Interpretation of the measured velocity history. The points are the approximation; the dashed lines show the pressure histories calculated from the foil acceleration.

thickness. The values of the pressure, p, and the particle velocity, $u=u_a$, taken at the same time moment t correspond to a point on the unloading isentrope of the shock-compressed PMMA.

The results of this treatment are shown in Fig. 6 by thin lines in the low pressure part of the p-u diagram. It is seen that the experiments with aluminum and titanium witness foils of different mass are in a good agreement. Compared with the data of ref. [19] in this pressure range, our preliminary results can be considered quite reasonable. The next steps in this direction should be the modification of the EOS model and the adjustment of the model parameters by means of computer simulations.

It is evident from the launching capabilities illustrated in Fig. 1, that the experiment can be reproduced with KALIF. In this case the Al flyer plate thickness can be about 50 µm at the instant of impact, the polymer target thickness should be within a range of 50 to 100 µm, and the covering foil thickness should be a few µm. Under these conditions, the expected acceleration time is several tens of nanoseconds. All of these quantities are reasonable for the planned experiments at KALIF. Covering a range of impact velocities of 4.5 to 6 km/s we hope to make measurements for an essential part of the vaporization region of polymers in a few planned shots on the KALIF.

Vaporization of condensed matter can not occur instantaneously and has some kinetics which is controlled by a rate of bubble formation and growth. This means that in some energy range the matter response to a rapid energy deposition can differ from the equilibrium state. In this sense the planned experiments with particle beams coupled with measurements made with explosive or gun facilities will provide a wide range of controlled unloading rates and, therefore, the possibility to examine the vaporization kinetics.

The problem that can be expected for measurements using laser velocimeters is that the reflection of strong shock waves from the surface of a solid body leads to the ejection of material and a drastic drop in the reflectivity when approaching post-shock melting at release [20 to 23]. Parameters of shock waves that cause melting of aluminum, copper, molybdenum and titanium in release have been measured with a pulse proton beam on KALIF [22, 23]. The beam was focused in a spot of ~8 mm diameter on the surface of 40 to 70 µm thick aluminum flier plate. The residual cold part of the flyer plate was accelerated by the ablation pressure to velocities of 5 to 10 km/s. As a result of the power density profile of the beam, the radial velocity distribution of the flier was bell-shaped and, as a consequence, a range of shock pressures was covered in each shot at the flyer collision with the target placed 0.06 to 0.2 mm away from the initial flyer position. In the experiments, the acceleration of the flier and the sample free surface velocities were recorded along a measuring line on the target surface using the line-imaging version of the ORVIS laser velocimeter. An example of experimental interferogram is shown in Fig. 9.

Fig. 9. Line-imaging ORVIS interferogram of an experiment with an aluminum flyer plate launched by the ion beam (upper part of the interferogram) and impacting a titanium foil target (lower part of the interferogram). A downward shift of the fringes corresponds to a velocity increase. The impact velocity ranges from ~5.2 km/s on the periphery of the field of view to 6.3 km/s near the center. The reflectivity of the titanium target disappears in the impact velocity range of 5.6 to 6 km/s. The clearly recorded velocity pullback in the impact velocity range < 5.6 km/s indicates that titanium maintains a high dynamic tensile strength.

The loss of the intensity of the reflected laser light was considered indicative of material ejection and instability processes related to melting. Within an uncertainty of ~5%, the threshold pressure for the onset of melting in the release wave was found to be 64 GPa for aluminum, 136 GPa for copper, 86.5 GPa for titanium, and 252 GPa for molybdenum. For aluminum, copper and molybdenum these results are in a good agreement with the equation of state by McQueen and Marsh [24]. The large discrepancy for titanium is obviously due to phase transition under pressure. These measurements give the upper shock pressure limit above which the movement of a metal free surface can not be recorded with the interferometer technique.

The results obtained are related to beginning of melting. Experimental interferograms show that there is not a sharp drop of reflectivity at melting. Some progressive reduction of the reflectivity and the interference contrast were observed at lower shock pressures, and a small short-time residual reflectivity at the destroyed interference was observed when the shock pressure exceeded the melting threshold in release. These details should be still analyzed.

CONCLUSION

Our experiments with KALIF have demonstrated that the pulsed high-power light-ion beam is a promising and well-controlled tool for the impact and shock-wave experiments. The velocity of 12.5 km/s realized so far matches the ultimate velocity obtained with two-stage gas guns and explosive facilities, both using multi-layer systems that cumulate the kinetic energy of thick projectiles into thin flyer plates. However, an absolute upper limit on particle beam drivers has not been reached yet. With increasing the beam power we hope to increase the impact velocity range. The main limitation on this way is the flyer melting as a result of both the heat transfer from the energy deposition zone and the irreversible shock-wave heating.

We have a good basis to be optimistic about future applications of high-power ion beams in impact physics and physics of matter at high energy density. So far, the capabilities of the ion beam technique in measurements of shock compressibility, polymorphous transformations, elastic-plastic and strength properties have been demonstrated. To exhaust the potential, new experimental arrangements should be tested. The measurement of the threshold shock pressure that cause melting in release we consider as an example of effective use of the beam driver properties and the line-imaging laser Doppler velocimetry. We are planning to continue the beam experiments in this arrangement for measuring the unloading isentropes in the vaporization region. The preliminary experiments made with explosive facilities have provided a new measurement technique that can be used with the beam drivers.

The problem of equilibrium of the shock-compressed states obtainable at nanosecond load durations should be analyzed in future. For complex chemical compositions the problem of equilibrium can be actually important and requires special analysis. On the other hand, the capability to generate very short load pulses and to investigate the matter behavior in the nanosecond load duration range is one of the apparent advantages of the technique.

REFERENCES

1. K. Baumung, H.J. Bluhm, P. Hoppe, H.U. Karow, D. Rush, O. Stoltz, J. Singer, G.I. Kanel, A.V. Utkin, S.V. Razorenov and V.E. Fortov. Hypervelocity Launching and Impact Experiments on the Karlsruhe Light Ion Facility KALIF. *Int. J. . Impact Engng*, **17**(1-6), 37-46 (1995).

2. K. Baumung, H. Bluhm, B. Goel, et al. Shock-wave physics experiments with high-power proton beams. *Laser and Part. Beams* **14**(2), 181-209 (1996).

3. D.D. Bloomquist and S.A. Sheffield. Optically recording interferometer for velocity measurements with subnanosecond resolution. *J. Appl. Phys.* **54**(4), 1717 (1983).

4. K. Baumung, J. Singer, S.V. Razorenov, and A.V. Utkin. Hydrodynamic proton beam - target interaction experiments using an improved line-imaging velocimeter. In *Shock compression of Condensed Matter - 1995"*, (edited by S.C. Schmidt and W.C. Tao), pp, 1015-1018, AIP Conference Proceedings 370, Woodbury, New York (1996).

5 J.C. Bushell and D.J. McGloskey. Thermoelastic Stress Production in Solids. *J. Appl. Phys.* **39**(12), 5541-5546 (1968)

6 K. Baumung, H.U. Karow, D. Rusch, H.J. Bluhm, P. Hoppe, G.I. Kanel, A.V. Utkin, V. Licht. High-power proton beam-matter interaction diagnostics by analysis of the hydrodynamic response of solid targets. *J. Appl. Phys.*, **75**(12), 7633-7638 (1994).

7 A.V. Utkin, G.I. Kanel, S.V. Razorenov, K. Baumung, D. Rush. Diagnostics of high-power ion beam interaction with composite targets. - *J. Appl. Phys.*, **79**(5), 2180-2185, (1996).

8. A.M. Evans, N.J. Freeman, P. Graham, et al. Hugoniot EOS measurements at Mbar pressures. *Laser and Part. Beams* **14**(2), 113-123 (1996).

9. L.M. Barker. The accuracy of VISAR instrumentation. In *Shock Compression of Condensed Matter - 1997* (edited by S.C. Schmidt, D.D. Dandekar, J.W. Forbes), AIP Conference Proceedings 429, pp. 833-836 (1998).

10. D.L. Paisley. Laser-driven miniature plates for one-dimensional impacts at 0.5-≥6 km/s. In *Shock-Wave and High-Strain-Rate Phenomena in Materials*, (edited by M.A. Meyers, L.E. Murr, K.P. Staudhammer), pp. 1131-1141, Marcel Dekker, Inc., New York (1992).

11. G. Kessler, H.U. Karow, K. Baumung, V.E. Fortov, and G.I. Kanel. High-power light ion beams and intense shock waves. In *High-Pressure Science and Technology - 1993* (edited by S.C. Schmidt, J.W. Shaner, G.A. Samara, and M. Ross), pp. 1887-1890, AIP Conference Proceedings, **309** (1994).

12. S.P. Marsh. *LASL shock Hugoniot data*. Univ. of California Press, Berkeley, (1980).

13. S.B. Kormer. Optical studies of properties of shock-compressed condensed dielectrics. *Usp. Fiz. Nauk (USSR)*, **94**(4), 640-693 (In Russian) (1968).

14. S.S. Nabatov, A.N. Dremin, V.I. Postnov, V.V. Yakushev. Measurements of electrical conductivity of sulfur at superhigh dynamic pressures. *Letters to J. Exp. and Theor. Phys. (USSR)*, **29**(7), 407-410 (In Russian) (1979).

15. H. Luo, S. Desgrenies, Y.K. Vohra, and A.L. Ruoff. High-pressure optical studies on sulfur to 121 Gpa: optical evidence for metallization. *Phys. Rev. Letters*, **67**(21), 2998-3001 (1991).

16. J.C. Skidmore and E. Morris. Experimental equation of state data for uranium and its interpolation in the critical region. *Proc. Symposium on Thermodynamics of Nuclear Materials*, pp.173-187, May 1962, Vienna, (1962).

17. A.V. Bushman and V.E. Fortov. Equations of state models of the matter. *Usp. Fiz. Nauk (USSR)*, **140**(2), 177-232 (1983).

18. C. Remiot, J.M. Mexmain, and L. Bonnet. Precise method to determine points on isentropic release curve on copper. In *Shock compression of Condensed Matter - 1995"*, (edited by S.C. Schmidt and W.C. Tao), AIP Conference Proceedings **370**, Woodbury, New York, pp. 955-958 (1996).

19. A.V. Bushman, M.V. Zhernokletov, I.V. Lomonosov, et al. Investigations of Plexiglass and Teflon in waves of secondary shock compression and isentropic unloading. The equation of state of polymers at high energy densities. *Academy of Sciences USSR: Doklady*, **329**(5), 581-584 (1993).

20. J.R. Asay, L.P. Mix, and F.C. Perry. Ejection of Material from Shocked Surface. *Appl. Phys. Lett.*, **29**, 284-287 (1976).

21. P. Chapron, P. Elias, and B. Laurent. Experimental Determination of the Pressure Inducing Melting in Release for Shock-Loaded Metallic Samples. In *Shock Waves in Condensed Matter - 1987* (edited by S.C. Schmidt and N.C. Holmes), Elsevier Science Publishers B.V. 171-173 (1988).

22. K. Baumung, G.I. Kanel, S.V. Razorenov, D. Rush, J. Singer, and A.V. Utkin. Shock-Melting Pressures from Non-Planar Impacts. *Int. J. Impact Engng*, **20**(1-5), 101-110 (1997).

23. G.I. Kanel, K. Baumung, D. Rush, J. Singer, S.V. Razorenov, and A.V. Utkin. Melting of shock-compressed metals in release. In *Shock Compression of Condensed Matter - 1997* (edited by S.C. Schmidt, D.D. Dandekar, J.W. Forbes), AIP Conference Proceedings 429, pp. 155-158 (1998).

24. R.G. McQueen and S.P. Marsh. Equation of State for Nineteen Metallic Elements from Shock-Wave Measurements to Two Megabars. *J. Appl. Phys.*, **31**, 1253-1269 (1960).

CONCEPT OF ULTIMATE FRACTURE VELOCITY IN THE ANALYSIS OF SPHERICAL CAVITY EXPANSION IN BRITTLE MATERIALS: APPLICATION TO PENETRATION PROBLEMS

V. V.KARTUZOV, B. A. GALANOV, and S. M. IVANOV

Institute for Problems in Materials Science National Academy of Science of Ukraine, Kiev 252142, Ukraine

Summary — A new model of dynamic spherical cavity expansion with constant velocity in a brittle material has been developed on the basis of the hypothesis of an ultimate fracture front velocity proposed by Nikolayevskii. With the use of this model, the Alekseevskii-Tate model is modified for long-rod penetration into brittle materials. The ultimate fracture front velocities relative to the material moving before this front are considered as a physical characteristic specific to every material and fracture mode. Therefore, fracture front velocities (as well as crack propagation velocities) relative to unperturbed material depend on the cavity expansion velocity and can exceed the Rayleigh wave velocity. Unlike the models based on the hypothesis of an ultimate fracture stress, this proposed model explains the possibility of short term "dynamic overloads" of the material: tensile in elastic precursor and shearing in the cracked material zone. © 1999 Elsevier Science Ltd. All rights reserved.

NOTATION

t time;

$h = h(t)$ cavity radius, $h(0) = 0$;

V impact velocity or velocity of penetrator;

$V_c = \dot{h}$ constant cavity expansion velocity;

V_c^τ velocity of spherical cavity expansion, above which shear saturation appears in the pulverized zone ($|\sigma_{r3} - \sigma_{\theta 3}| = 2\tau$);

$V_c^{\sigma f}$ velocity of cavity expansion, above which model formulae exhibit "dynamic overload" of the elastic precursor material under tensile stresses, i.e. $\sigma_{\theta 1} \geq \sigma_f$ (defined from the necessary fracture condition $\sigma_{\theta 1 b} = \sigma_f$). The value of this overload is determined by the difference ($\sigma_{\theta 1} - \sigma_f$);

V_c^Y cavity expansion velocity, above which model formulae exhibit "dynamic overload" of cracked region "2" material in shear stresses, i.e. $\tau_c = |\sigma_{r2}|/2 \geq Y/2$ (defined from the necessary fracture condition $\sigma_{r2a} = -Y$). The value of the overload is determined by the difference ($\tau_c - Y/2$);

V_c^N velocity of cavity expansion, above which the cavity expansion is governed by the condition of ultimate fracture front velocities $N_1, N_2, V_c^N = \max\left(V_c^{\sigma f}, V_c^Y\right)$;

u contact surface velocity of rod and target (taken from approximation of [1,2], i.e. $u = 2V_c$);

$r = a$ fracture front formed by shearing mode cracks and radial opening mode cracks;

$r = b$ fracture front formed by radial opening mode cracks;

$r = d$ shock wave front or elastic precursor;

$r = l$ boundary of shear saturation region, $h \leq r \leq l$;

ξ velocity of boundary $r = l$;

N_1 velocity of front $r = b$ relative to the material moving before it (ultimate fracture velocity);

N_2 velocity of front $r = a$ relative to the material moving before it (ultimate fracture velocity);

D velocity of shock wave front $r = d$;

C_{F1} velocity of front $r = b$ relatively to coordinate origin;

C_{F2} velocity of front $r = a$ relative to coordinate origin;

p depth of rod penetration in target;

Y_p strength resistance of rod material;

τ shearing stress corresponding to shear saturation in failed material (material constant);

ρ_p rod density;

ρ_i density of material in i zone ($i = 0, 1, 2, 3$);

V_i radial material velocity in i zone;

σ_{ri} radial stresses in material of i zone;

$\sigma_{\theta i} = \sigma_{\varphi i}$ hoop stresses in material of i zone;

$\rho_{i\eta}, V_{i\eta}$ values of ρ_i, V_i at $r = \eta$;

$\sigma_{ri\eta}, \sigma_{\theta i\eta}$ values of stresses $\sigma_{ri}, \sigma_{\theta i}$ at $r = \eta$;

$\sigma_c = \sigma_{r3h}$ radial stresses on cavity surface;

$P_c = -\sigma_c$ pressure on cavity surface;

R_t target materials resistance in quasi-static penetration regime [1-3];

R_u target material resistance to penetration. $R_u = -\sigma_x(V_c)$;

Y static compressive strength of target material [1-3];

σ_f static tensile strength of target material [1-3];

HEL Hugoniot elastic limit ("dynamic strength");

E Young's modulus;

ν Poisson's ratio;

K bulk modulus;

C, C_R velocities, respectively, of longitudinal and Rayleigh's waves in zone "0";

μ friction coefficient;

α, m coefficients, $\alpha = 6m/(3+4m)$, $m = 3\mu/(3-4\mu)$ [1-3].

INTRODUCTION

At present, simplified models with a small number of principal initial physical data are widely used to study the regularities of penetration problems. These models are rather good in determination and forecasting of the principal physical parameters of the penetration process which can be measured during shock resistance tests.

Models using the solution of problem of spherical and cylindrical cavity expansion in infinite media of different reology belong to these models. Works [1-3] comprise a full review and analysis of such models. Authors propose the model of spherical and cylindrical cavity expansion in brittle materials which presents a new approach to the solution of penetration problems in such materials. The focus is also on unsolved problems and the necessity of future investigations of the penetration processes in brittle materials.

Unlike [1-3], this investigation is based on the concept of an ultimate fracture front velocity, N, moving relative to the material before this front (N is considered a material physical characteristic (constant) specific for each material and fracture mode [4]). The review and thorough analysis of a large number of works, supporting this concept, are given in reference [4], and the case of plane waves in ceramic materials is studied in [5]. Here, the case of constant spherical cavity expansion velocity (steady regime) is examined. A spherical coordinate origin (r, θ, φ) system (Figure 1) is assumed from the center of the cavity and as defined in references [1 - 3], four zones with different material states exist: zone "0", $r > d$ (unperturbed material); zone "1", $b \leq r \leq d$

(elastically deformed material, elastic precursor); zone "2", $a \le r \le b$ (material fractured by radial opening mode cracks); and zone "3", $h \le r \le a$, (material, comminuted by shearing mode cracks and radial opening mode cracks). Zone "3" can contain subzone of shear saturation $h \le r \le l$. Spherical surfaces $r = a$ and $r = b$, which are the boundaries of zones 3-2 and 2-1 accordingly, are considered as fracture fronts moving with different velocities C_{F2} and C_{F1} relative to the coordinate origin. The spherical surface $r = d$ (boundary of zones 0-1) is considered as a shock wave front (or the front of the elastic precursor) moving with the velocity D. The value $N = N_1$ is connected with front $r = b$, and with front $r = a$, $N = N_2$. The values N_1 and N_2 ($C_R \ge N_1 \ge N_2$) are assumed to be dependent on the crack propagation velocity and fracture mode. Parameters N_1 and N_2 are the principal parameters of the proposed model, implementing the concept of an ultimate fracture front velocity. Quantitative data on material characteristics N_1 and N_2 are not readily available in the literature and only estimates exist [4]. For calculations, $N_1 = C_R$, and $N_2 = 0.71C_R$ are accepted, where the coefficient 0.71 is stipulated by the assumption that shear cracks grow at the angle of 45° to the direction of front motion [4].
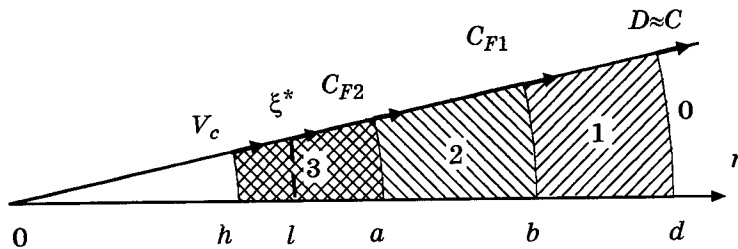
Fig.1. Scheme of zones with different material states ($V_c \le C_{F1} \le C_{F2} \le C$)

Thus, in the proposed model shock wave has a three-front structure. At the fronts, where material density, velocity and stress in the material are discontinuous, dynamic compatibility conditions (Hugoniot conditions) are assumed to hold true. To these conditions, the conditions of an ultimate fracture front velocity are added: $C_{F1} - V_{1b} = N_1$, $C_{F2} - V_{2a} = N_2$, where V_{1b}, V_{2a} are velocities of the material before these fronts. At $C_{F1} = C_{F2}$, the shock wave has a two-front structure. The necessary condition of this structure is the condition $N_1 = N_2$.

The proposed modifications of the Alekseevskii-Tate penetration model [6,7] are based on the solution of the problem of spherical cavity expansion and on the approximations introduced in [1,2] coupling the cavity expansion velocity with penetration velocity. Other model hypotheses are introduced during the analysis of the problem.

DYNAMIC SPHERICAL CAVITY EXPANSION IN A BRITTLE MATERIAL – FORMULATION OF THE BOUNDARY VALUE PROBLEM AND ITS SOLUTION

Elastic Region (Elastic Precursor, $b \le r \le d$)

For this region, in Eulerian coordinates, the following equations are defined:

$$\frac{\partial \rho_1}{\partial t} + \frac{\partial}{\partial r}(\rho_1 V_1) + \frac{2}{r}\rho_1 V_1 = 0 \qquad \text{(mass conservation),} \qquad (1)$$

$$\frac{\partial \sigma_{r1}}{\partial r} + 2\frac{\sigma_{r1} - \sigma_{\theta1}}{r} = \rho_1\left(\frac{\partial V_1}{\partial t} + V_1\frac{\partial V_1}{\partial r}\right) \quad \text{(equation of motion).} \qquad (2)$$

From the approximations in references [4,5], the elastic precursor front in the steady state regime is assumed to be moving at a velocity $D \approx C$. In this area $\rho_1 = constant$, and $\rho_1 \ne \rho_0$ is also

assumed. Equations (1) and (2) are completed by the following boundary conditions. The boundary conditions of dynamic compatibility at $r = d = Ct$:

$$\rho_1(V_{1d} - C) = -\rho_0 C \qquad \text{(mass balance)}, \qquad (3)$$

$$V_{1d}\rho_1(V_{1d} - C) = \sigma_{r1d} \qquad \text{(impulse balance)}. \qquad (4)$$

The boundary conditions of dynamic compatibility at $r = b$:

$$\rho_{2b}(V_{2b} - C_{F1}) = \rho_1(V_{1b} - C_{F1}) \qquad \text{(mass balance)}, \qquad (5)$$

$$\rho_{2b}V_{2b}(V_{2b} - C_{F1}) - \sigma_{r2b} = \rho_1 V_{1b}(V_{1b} - C_{F1}) - \sigma_{r1b} \quad \text{(impulse balance)}, \qquad (6)$$

$$C_{F1} - V_{1b} = N_1 \qquad \text{(condition of ultimate fracture velocity)}. \qquad (7)$$

From accepted hypotheses and equations (1), (3), (4) we have:

$$V_{1d} = (1 - \rho_0/\rho_1)C = const, \qquad (8)$$

$$\sigma_{r1d} = -\rho_0(1 - \rho_0/\rho_1)C^2 = const, \qquad (9)$$

$$V_1 = V_{1d}(Ct/r)^2, \qquad b \le r \le d. \qquad (10)$$

Using the condition of ultimate fracture velocity (7) and ratio (10), the following non-linear integral equation for the fracture front velocity $C_{F1}(t)$ is obtained:

$$C_{F1}(t) - V_{1d}\left(Ct \Big/ \int_0^t C_{F1}(\tau)d\tau\right)^2 = N_1.$$

This equation has only one solution $C_{F1}(t) = C_{F1}(0) = C_{F1} = const > 0$, which is time-independent and is a root of the cubic equation:

$$C_{F1}^3 - N_1 C_{F1}^2 - V_{1d}C^2 = 0. \qquad (11)$$

With the help of equation

$$(\sigma_{r1} + 2\sigma_{\theta1})/3 = -K(1 - \rho_0/\rho_1) \qquad (12)$$

$\sigma_{\theta1}$ can be eliminated from (2), and substituting (10) into the right-hand side of (2), the following automodel solution of equation (2) can be obtained:

$$\sigma_{r1}(r,t) = A/3 + \hat{C}_1(t/r)^3 + B(t/r)/2 + Q(t/r)^4,$$

where

$$A = -3K(1 - \rho_0/\rho_1),$$

$$\hat{C}_1 = \sigma_{r1d}C^3 - AC^3/3 - BC^2/2 - Q/C,$$

$$B = 2V_{1d}\rho_1 C^2,$$

$$Q = 2V_{1d}^2 \rho_1 C^4 \qquad \text{(see (8), (9))}.$$

Thus, the solutions $V_1(r,t)$, $\sigma_{r1}(r,t)$, $\sigma_{\theta1}(r,t) = -\sigma_{r1}/2 - 3K(1-\rho_0/\rho_1)/2$ are completely defined by the value of ρ_1 (which will be shown later to be the root of equation (29)).

At the front $r = Ct$, the magnitude of stresses $\sigma_{r1d} = -\rho_0 V_{1d}C$, $\sigma_{\theta1d} = \sigma_{r1d}\nu/(1-\nu)$ fully coincides with the values obtained by S. C. Hunter [8, p.87] and from Hook's law the radial displacement $u(r,t)$ at $r = Ct$ naturally results:

$$u(Ct,t) = \left((1 - \nu)\sigma_{\theta1d} - \nu\sigma_{r1d}\right)r/E = 0$$

Note also, that inside zone "1" stresses σ_{r1} and $\sigma_{\theta1}$ differ from corresponding values obtained by Hunter. In particular, in this zone, stress $\sigma_{\theta1}$ changes sign and at $r = b = C_{F1}t$ the stress is tensile (see Fig. 6), while according to Hunter it is compressive everywhere [8, pp. 90,91].

Cracked Region ($a \le r \le b$)

This region is considered as a continuum with density $\rho_2 = constant$, and from references [1-3],

$\sigma_{\theta 2} = 0$ is assumed. By integrating the mass conservation equation, equation (13) can be obtained:

$$V_2 = V_{2b}\left(C_{F1}t/r\right)^2, \qquad a \leq r \leq C_{F1}t. \tag{13}$$

In Eulerian coordinates, the equation of motion is:

$$\frac{\partial \sigma_{r2}}{\partial r} + \frac{2}{r}\sigma_{r2} = \rho_2\left(\frac{\partial V_2}{\partial t} + V_2\frac{\partial V_2}{\partial r}\right), \tag{14}$$

which is completed by the boundary conditions (5), (6).

Since $\sigma_{r2b} = -3K(1-\rho_0/\rho_{2b})$, the system of (5), (6) defines the values V_{2b} and ρ_{2b} as functions of density ρ_1 in accordance with the following formulae:

$$V_{2b} = \left[3K\left(\rho_0 C_{F1} - \rho_1 N_1\right) - \rho_1^2 N_1^2 V_{1b} - \rho_1 N_1 \sigma_{r1b}\right] / \left(3K\rho_0 - \rho_1^2 N_1^2\right), \tag{15}$$

$$\rho_{2b} = \rho_1 N_1 / \left(C_{F1} - V_{2b}\right).$$

The accepted hypotheses and (13) allow the integration of equation (14). The result is:

$$\sigma_{r2}(r,t) = \hat{C}_2\left(t/r\right)^2 + F(t/r) - H\left(t/r\right)^4\big/2, \tag{16}$$

where

$$F = 2V_{2b}\rho_2 C_{F1}{}^2$$

$$H = -2V_{2b}{}^2 \rho_2 C_{F1}{}^4$$

$$\hat{C}_2 = C_{F1}{}^2 \sigma_{r2b} - FC_{F1} + H\big/\left(2C_{F1}{}^2\right).$$

If (15) is taken into account, (13) and (16) are completely defined by the density ρ_1 (which will be shown later to be the root of equation (29)).

Comminuted (Pulverized) Region ($h = V_c t \leq r \leq a$)

In Eulerian coordinates, the equation of motion is:

$$\frac{\partial \sigma_{r3}}{\partial r} + 2\alpha\frac{\sigma_{r3}}{r} = \rho_3\left(\frac{\partial V_3}{\partial t} + V_3\frac{\partial V_3}{\partial r}\right), \tag{17}$$

where, from references [1-3], $\alpha = 6m/(3+4m)$ is assumed. By integrating the equation of mass conservation, where ρ_3 is taken to be constant, equation (18) is obtained:

$$V_3 = V_c\left(V_c t/r\right)^2, \qquad V_c t \leq r \leq a. \tag{18}$$

By inserting (18) to (17) and integrating (17), equation (19) is obtained:

$$\sigma_{r3}(r,t) = \hat{C}_3\left(\frac{t}{r}\right)^{2\alpha} + \frac{L}{(2\alpha - 1)}\left(\frac{t}{r}\right) - \frac{M}{(4 - 2\alpha)}\left(\frac{t}{r}\right)^4, \tag{19}$$

where

$$L = 2V_c{}^3 \rho_3,$$

$$M = -2V_c{}^6 \rho_3,$$

$$\hat{C}_3 = \sigma_{r3a}C_{F2}^{2\alpha} - \frac{L}{2\alpha - 1}C_{F2}^{2\alpha - 1} + \frac{M}{4 - 2\alpha}C_{F2}^{2\alpha - 4}.$$

For the conditions of dynamic compatibility at the fracture front $r = a$:

$$\rho_{3a}\left(V_{3a} - C_{F2}\right) = \rho_{2a}\left(V_{2a} - C_{F2}\right) \quad \text{(mass balance)}, \tag{20}$$

$$\rho_{3a}V_{3a}\left(V_{3a} - C_{F2}\right) - \sigma_{r3a} = \rho_{2a}V_{2a}\left(V_{2a} - C_{F2}\right) - \sigma_{r2a} \quad \text{(impulse balance)}, \tag{21}$$

$$C_{F2} - V_{2a} = N_2 \quad \text{(condition of ultimate fracture velocity)}. \tag{22}$$

From the accepted hypotheses, $\rho_{3a} = \rho_3 = constant$, $\rho_{2a} = \rho_2 = constant$ and from (20) and (22), the equation for the unknown velocity C_{F2}, similar to equation (11), can be obtained:

$$C_{F2}^3 - N_2 C_{F2}^2 - V_{2b}C_{F1}^2 = 0. \tag{23}$$

Since V_{2b} and C_{F1} are functions of ρ_1, C_{F2} depends only on ρ_1.

Analyzing the system of (20) - (21), and using (22), equations (24),(25) are obtained:

$$\rho_3(C_{F2} - V_{3a}) = \rho_2 N_2, \tag{24}$$

$$\rho_2 N_2 V_{3a} + \sigma_{r3a} = \rho_2 N_2 V_{2a} + \sigma_{r2a}. \tag{25}$$

The values on the right-hand side of (24) and (25) depend only on one unknown value ρ_1. The left-hand parts of (24) and (25) contain the unknowns ρ_3, σ_{r3a}, and ρ_1 because C_{F2} and $V_{3a} = V_c^3/C_{F2}^2$ depend on ρ_1 (see (23)). Therefore, this system can be closed by the equation of state:

$$\sigma \equiv (\sigma_{r3a} + 2\sigma_{\theta3a})/3 = -K(1 - \rho_0/\rho_3), \tag{26}$$

which, from plate impact tests, is true under the condition:

$$-\sigma \leq \mathrm{HEL}(1+\nu)/(3(1-\nu)). \tag{27}$$

For cases of violation of (27) at high velocities V_c, equation (26) should be replaced with the non-linear case $\sigma = f(\rho_0/\rho_3)$ relative to the compressibility value (ρ_0/ρ_3). Since $m = 3(\sigma_{r3} - \sigma_{\theta3})/(2(\sigma_{r3} + 2\sigma_{\theta3}))$, equation (26) can be transformed to the form of (28):

$$\sigma_{r3a} = -K(3 + 4m)(1 - \rho_0/\rho_3)/3 = -3K(1 - \rho_0/\rho_3)/(3 - 4\mu). \tag{28}$$

Equations (24), (25) and (28) form the closed system of equations which defines ρ_3, ρ_1 and σ_{r3a}. Separating the unknowns in this system, the non-linear equation which defines density ρ_1, depending on V_c can be obtained:

$$\Phi(\rho_1) \equiv \frac{\rho_0 C_{F2}}{\rho_2 N_2} - \frac{(3-4\mu)}{3K}\rho_2 N_2 V_{2a} + \left(\frac{3-4\mu}{3K}\rho_2 N_2 - \frac{\rho_0}{\rho_2 N_2}\right)\frac{V_c^3}{C_{F2}^2} - \frac{\sigma_{r2a}}{3K}(3-4\mu) - 1 = 0, \tag{29}$$

where values ρ_2, C_{F2}, V_{2a}, σ_{r2a} depend on ρ_1.

After the solution of equation (29), ρ_3 can be found by the formula $\rho_3 = (\rho_2 N_2 C_{F2}^2)/(C_{F2}^3 - V_c^3)$, and then from (28), the value of σ_{r3a} can also be found.

Finally, using (19) at $r = C_{F2}t$, the stress at the cavity boundary can be found:

$$\sigma_c = \sigma_{r3a}\left(\frac{C_{F2}}{V_c}\right)^{2\alpha} + \left(\frac{3}{(2-\alpha)(2\alpha-1)} - \frac{2}{2\alpha-1}\left(\frac{C_{F2}}{V_c}\right)^{2\alpha-1} - \frac{1}{2-\alpha}\left(\frac{C_{F2}}{V_c}\right)^{2\alpha-4}\right)\rho_3 V_c^2. \tag{30}$$

Shear Saturation in Failed Material of Zone "3"

If shear saturation is present ($|\sigma_{r3} - \sigma_{\theta3}| = 2\tau = const$), equation (17) can be replaced by the following equation of motion:

$$\frac{d\sigma_{r3}}{d\xi} - \frac{4\tau}{\xi} = L\xi^{-2} + M\xi^{-5}, \quad \xi = r/t, \quad L = 2V_c^3\rho_3, \quad M = -2V_c^6\rho_3, \tag{31}$$

and the region of failed material "3" can be subdivided into two sub-regions (see Fig. 1): a saturated area ($h \leq r \leq l$) with equation of motion (31) and an unsaturated area ($l < r \leq a$) with equation of motion (17). The velocity ξ_* of the boundary $l = \xi_* t$ can be defined by the equation

$$-\tau = \alpha\sigma_{r3}(\xi_*)/2, \quad V_c \leq \xi_* \leq C_{F2},$$

where $\sigma_{r3}(\xi) = \sigma_{r3}(r/t)$ is given by formula (19). For stresses in the shear saturated area, the following expression can be obtained from (31):

$$\sigma_{r3}(\xi) = -\frac{2\tau}{\alpha} + 4\tau \ln\frac{\xi}{\xi_*} - L(\xi^{-1} - \xi_*^{-1}) - M(\xi^{-4} - \xi_*^{-4})/4, \quad V_c \leq \xi \leq \xi_*,$$

from which, for $\xi = V_c$, the stress σ_c at the cavity boundary can be defined:

$$\sigma_c = \sigma_{r3}(V_c) = -\frac{2\tau}{\alpha} + 4\tau\ln\frac{V_c}{\xi_*} - \left[\frac{3}{2} - \frac{2V_c}{\xi_*} + \frac{1}{2}\left(\frac{V_c}{\xi_*}\right)^4\right]\rho_3 V_c^2 \qquad (32)$$

If, from formula (30), values for $\sigma_c < (-2\tau/\alpha)$ are obtained, a saturation area exists and the calculation should be made by formula (32).

The graph of σ_c dependence on V_c, as calculated by formulae (30) and (32) for a Coors AD995 99.5% aluminum oxide ceramic is given in Figure 2. All calculations were made for AD995 with the following mechanical characteristics from references [1-3]: E= 373.14 GPa, K= 231.8 GPa, Y= 2.62 GPa, σ_f= 0.462 GPa, m = 0.273, ρ_0= 3.89 g/cm^3 and τ = 1.5 GPa. N_1= C_R= 5600 m/s, and N_2= $0.71C_R$= 3980 m/s. For the value of τ, no substantiated value exists, so the calculation results depend on the accepted τ value.

Since the limit condition $\lim\limits_{V_c\to 0}\sigma_c = 0$ can be proven, the model makes sense only for velocities where $V_c \geq V_c^N$ (see notations and Figure 2). For the condition $V_c < V_c^N$, the authors consider the cavity expansion to be quasi-static ($\sigma_c = -R_f =$ $-Y\left[E\Big/\left(3Y\left(1-(1-\nu)\sqrt{\sigma_f/(2Y)}\right)\right)\right]^{2\alpha/3} \approx -Y\left(E/(3Y)\right)^{2\alpha/3}$) or in accordance with the dynamic model of references [1-3].

P_c= $-\sigma_c$, GPa
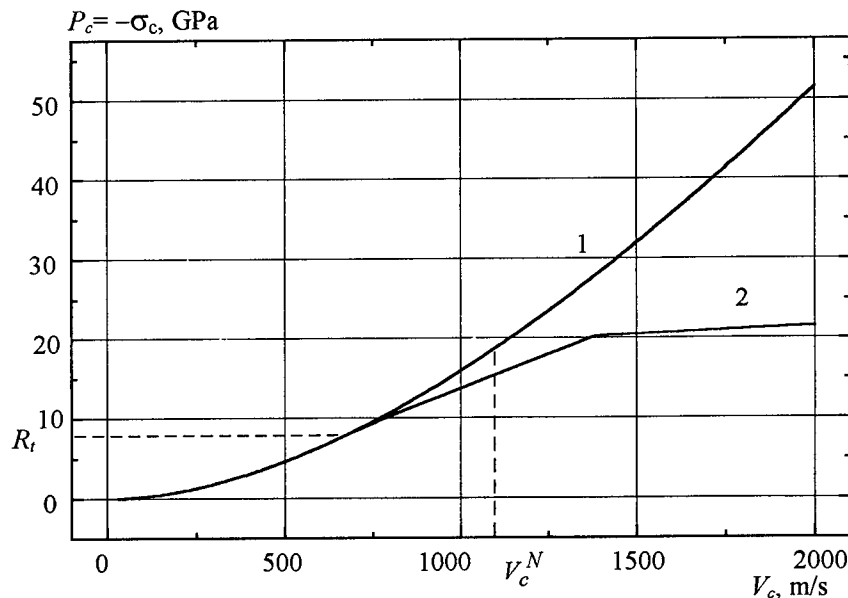
Fig. 2. Dependence of pressure at the cavity surface P_c on the cavity expansion velocity V_c for AD995 aluminum oxide ceramic. 1 - without saturation; 2 - with saturation.

MODIFICATIONS OF ALEKSEEVSKII-TATE MODEL FOR STATIONARY PENETRATION OF LONG PLASTIC RODS

Principal Hypotheses

The modification of the Alekseevskii-Tate model [6,7] for stationary penetration of long rods into the target of brittle materials is examined in this section. Only the principal relation at the contact surface of penetrator and target is modified:

$$Y_p + \frac{1}{2}\rho_p(V - u)^2 = R_{tr}. \tag{33}$$

Here, the penetration resistance of the brittle target, R_{tr}, corresponds to the pressure at the contact surface. Previously obtained solutions of the problem on dynamic spherical cavity expansion without shear saturation (30) and with shear saturation (32) are used for R_{tr}:

$$R_{tr} = -\sigma_c(V_c), \quad V_c \geq V_c^N, \tag{34}$$

where, in accordance with approximations of [1,2] in formula (34), it is assumed that $V_c = u/2$ (u - rod – target contact surface velocity).

In Figure 3, the case of penetration of long rod into a brittle material is shown, in which a shock wave with a three-front structure is formed. The fronts split the material into 4 zones with different material states: zone "0" (unperturbed material); zone "1" (elastically deformed material); zone "2" (material fractured by radial cracks); and zone "3" (material, comminuted (pulverized) by both shear mode cracks and radial opening mode cracks). Zone "3" as in the previous section can be subdivided into two sub-zones: with and without saturation. The zones here are listed in the order, opposite to the rod penetration direction (see Fig. 3).
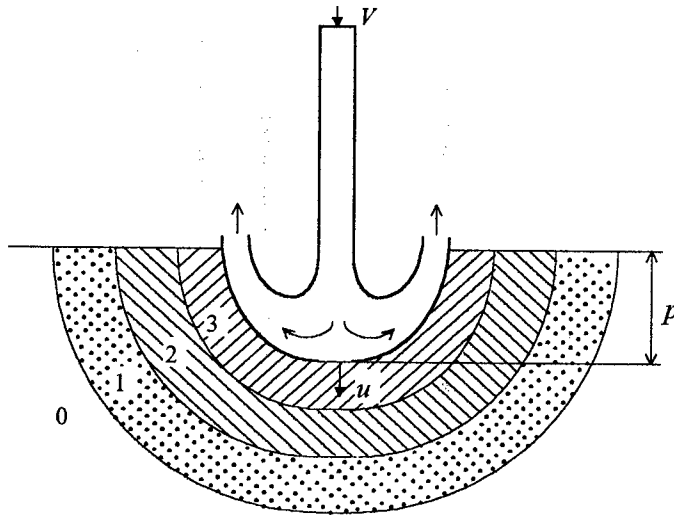
Figure 3. Scheme of penetration into target.

Equation (33) in the model [6,7] is only a quadratic equation in u; in the model considered here, it is transcendental. Therefore, the dichotomy method is used for the solution.

The dependence of the penetration velocity, u (which is the root of equation (33)), on impact velocity V is shown in Figure 4 for the target material - Coors AD995 and a tungsten alloy penetrator ($Y_p = 2$ GPa, $\rho_p = 17.3$ g/cm^3). Figure 4 shows the strong dependence of u on τ. For the comparison the plot of $u(V)$ dependence for Alekseevskii-Tate model is also included.

Figures 5, 6 illustrate target material state (stresses, densities, and mass velocity) at $V = 3600$ m/s, $\tau = 1.5$ GPa at time moment $t = 10^{-6}$ s. Fig. 6 is enlarged part of stress graph in Fig. 5 illustrating change of sign of σ_θ.

Penetration velocity u, m/s

Figure 4. Graph of functions $u(V)$, $u^N = 2V_c^N$. 1 - without saturation, 2 - with saturation ($\tau = 1.5$ GPa), 3 - Alekseevskii-Tate model ($R_{tr} = R_t + 0.5\rho_0 u^2$)

Density, kg/m³

Radial distance r, m

Mass velocity, m/s

Radial distance r, m

Figure 5. Graphs of radial and hoop stresses, density and material velocity at t= 10^{-6} s along the shock direction. V_c= 1156 m/s, u= 2312 m/s, V= 3600 m/s.

Stress, GPa

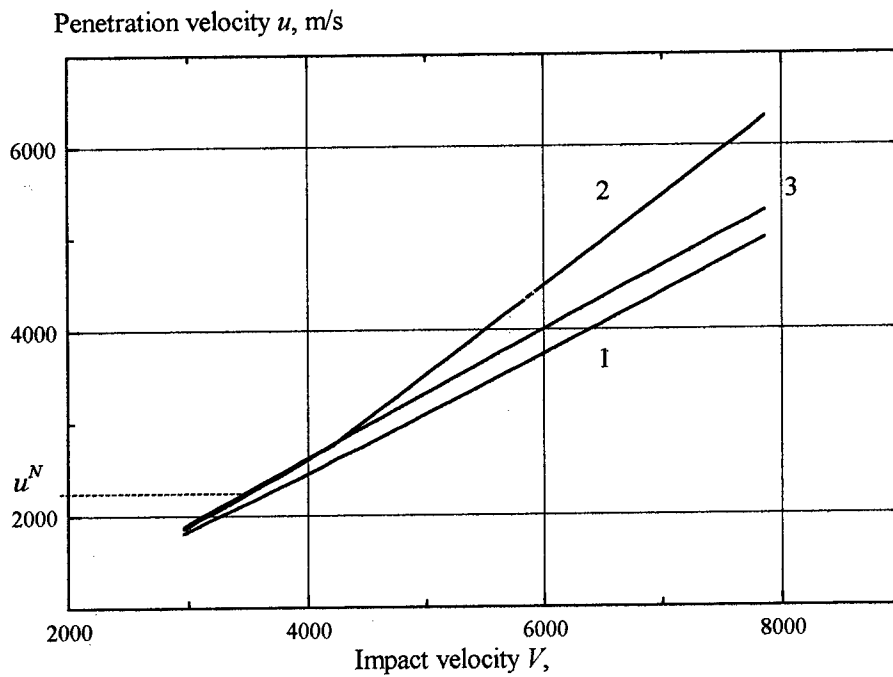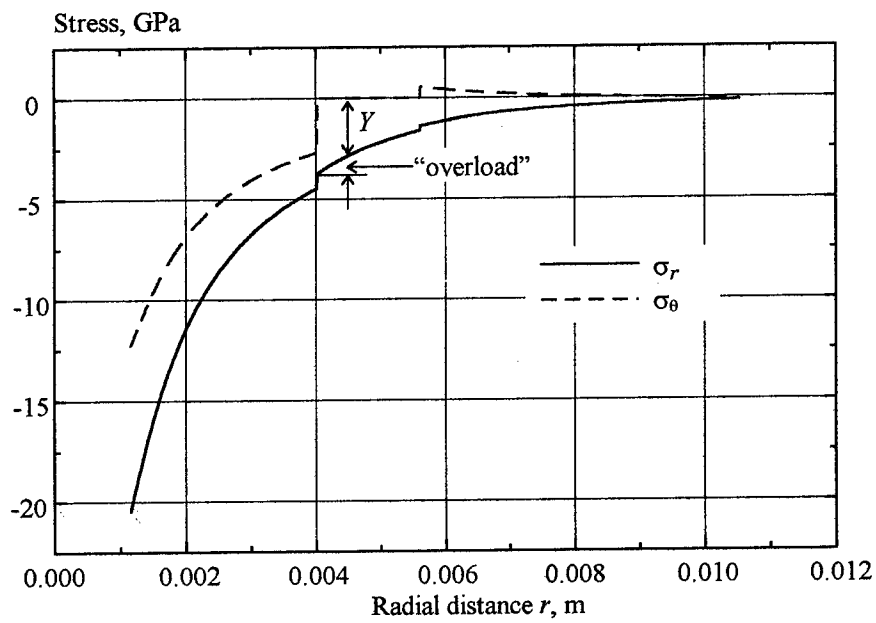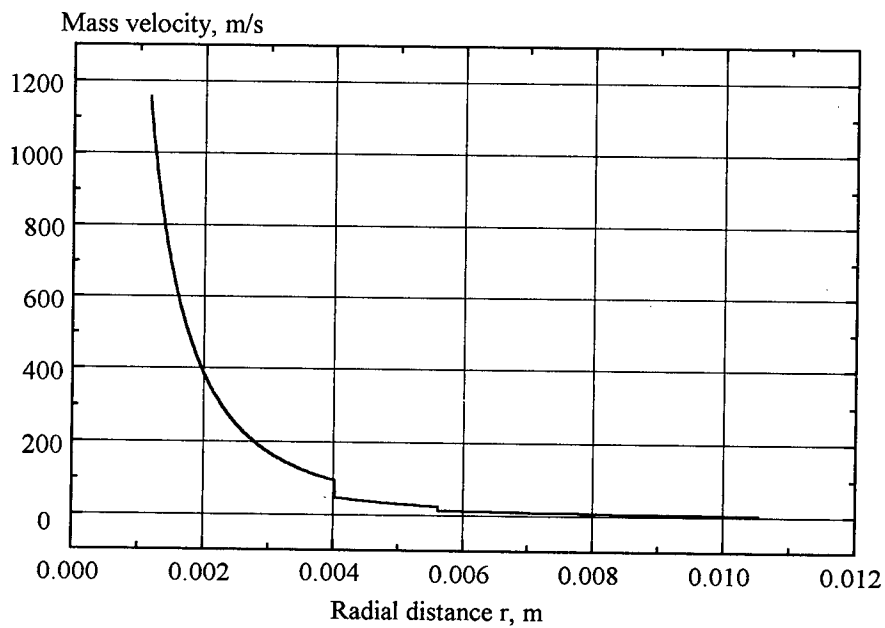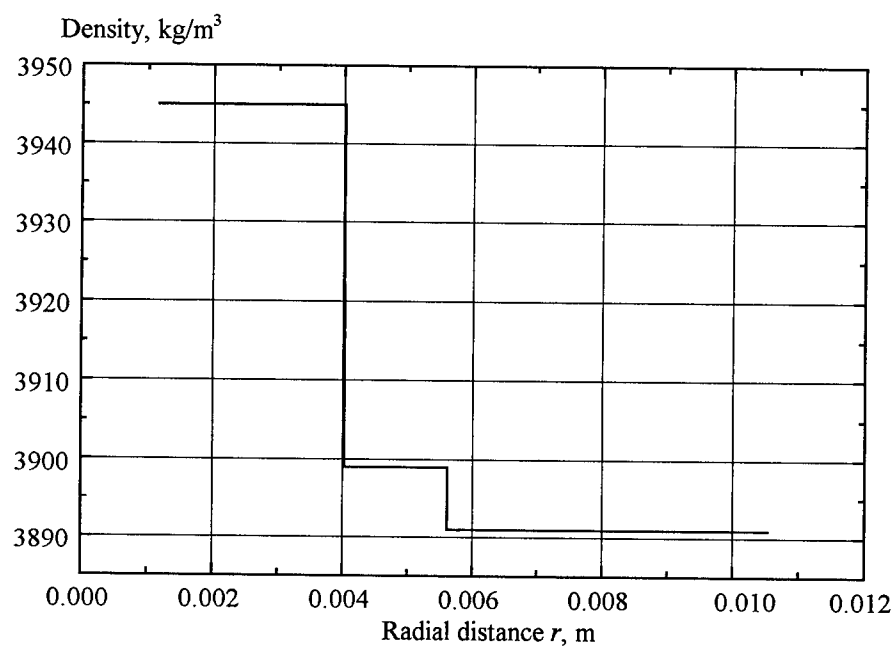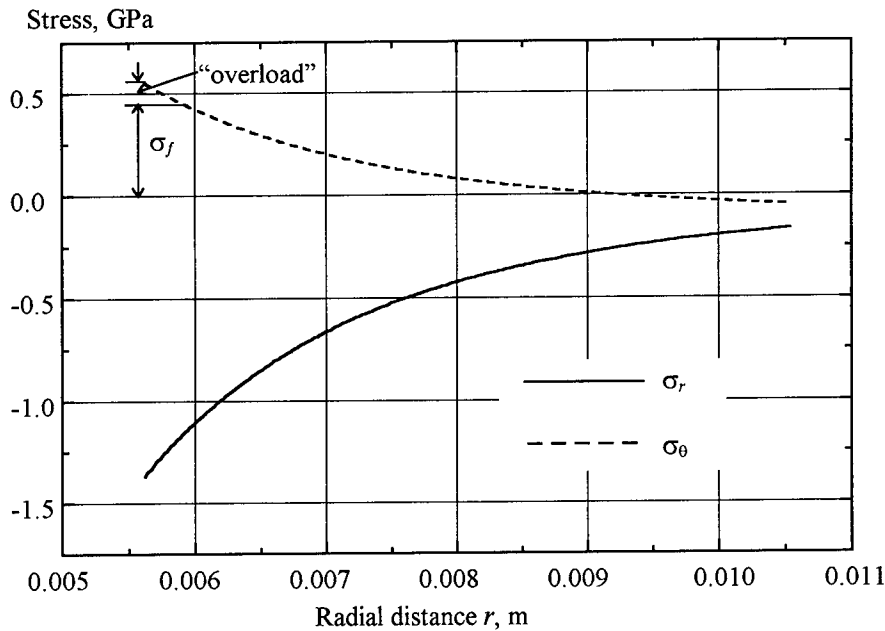Figure 6. Graph of stresses in elastic precursor.

CONCLUSION

A new model of spherical cavity dynamic expansion in a brittle material based on the hypothesis of an ultimate fracture front velocity (proposed in [4]) has been developed. This model was used to modify Alekseevskii-Tate model for penetration of long rods into brittle materials. The ultimate fracture front velocities N_1, N_2 relative to the material moving before this fronts are considered a physical characteristic specific to each material and fracture mode. Therefore, in the proposed model, the fracture front velocity (as well as crack propagation velocity) relative to the unperturbed material depends on the cavity expansion velocity and can exceed Rayleigh's velocity. Unlike the models using the hypothesis of an ultimate fracture stress, the proposed model explains the possibility of short term "dynamic overloads" of the material: tensile in the elastic precursor ($\sigma_{\theta 1} \geq \sigma_f$) and shearing in the cracked material zone ($2\tau_c \geq Y$, τ_c - tangential stress in zone 2, see Fig. 1).

The analysis of the models has shown that they are valid only for sufficiently high velocities V_c of cavity expansion and penetration $u = 2V_c \geq u^N = 2V_c^N$ ($u^N \approx 2190$ m/s for ceramics AD995). At these velocities, material dynamic overload takes place and stresses σ_r, σ_θ are discontinuous at the fracture fronts. For $V_c < V_c^N$, the authors consider the cavity expansion to be quasi-static ($\sigma_c = -R_t$) or in accordance with the dynamic model of references [1-3]. The velocity V_c^N is sensitive to the values of static ultimate fracture stresses σ_f and Y.

The principal parameters of the brittle material in the proposed model affecting its penetration resistance are: elastic constants (Young's modulus E, Poisson's ratio ν), ultimate fracture front velocities N_1 and N_2, angle coefficient m in linear dependence (Mohr - Coulomb) of shear stresses on the pressure for fractured material. At sufficiently high velocities of penetration when $u \geq u^\tau = 2V_c^\tau$ the shear saturation stress τ is added to these parameters. For the ceramic AD995, the calculations show a strong dependence of penetration velocity u on τ (see Figure 4).

As mentioned above, the principal model parameters are the ultimate fracture front velocities

N_1 and N_2, $N_1 \geq N_2$. There are no well-grounded quantitative data for these values at present [4] and the values N_1 and N_2 depend on the crack propagation velocities (i.e. upon fracture mode: fracture by opening cracks or by shearing cracks) and show a weak dependence upon strong changes of the stress state of the material across which cracks propagate within the shock wave [4]. Therefore, the conditions for dynamic cavity expansion may be possible when a cracked zone or pulverized zone is absent.

In the opinion of the authors, shear saturation of the pulverized zone at $V_c > V_c^\tau$ is possible only at a rather high degree of comminution by shear cracks. There are a limited number of experiments, suggesting that this saturation is achieved at compressive stresses on the order of the HEL and complete material failure. At the same time, there are experimental evidences of fragmentation and partial material comminution in the pulverized zone and, accordingly, the degree of its comminution in this zone changes.

Thus, preliminary investigations of the proposed model have shown, that these investigations should be complemented by experimental verification of the principal model hypotheses and compared with the other models as well as calculations for different materials.

REFERENCES

1. S. Satapathy, Application of Cavity Expansion Analysis to Penetration Problems. *IAT.R 0136*, Institute for Advanced Technology, University of Texas at Austin (1997).
2. S. Bless, S. Satapathy and C. H. M. Simha, Response of Alumina Ceramics to Impact and Penetration. *Preprint SVSF 96*, Udine, Italy, July 3-5 (1996).
3. S. Satapathy and S. Bless, Calculation of Penetration Resistance of Brittle Materials Using Spherical Cavity Expansion Analysis. *Mech. Materials*, 23, 323-330 (1996).
4. V.N. Nikolaevskiy, O dinamike frontov razrusheniya v hrupkih materialah. *Izv. AN SSSR. Mehanika tverdogo tela*, 5, 106-115 (1980). (in Russian)
5. B.A. Galanov, O.N. Grigor'ev, V.V. Kartuzov, V.I. Kovtun, V.N. Ostapenko and V.I. Trefilov, Shock Failure of Ceramic Plates. *Poroshkovaja Metallurgiya*, 4, 63-71 (1989). (in Russian).
6. V.P. Alekseevskii, Penetration of a Rod into a Plate at High Velocity. *Fizika Goreniya i Vzryva*, 2, 99-106 (1966). (in Russian).
7. A. Tate, A Theory for the Deceleration of Long Rods after Impact. *J. Mech. Phys. Solids*, 15, 387-399 (1967).
8. G. Gopkins, Dinamicheskiye neuprugie deformatsii metallov. Moscow, Mir Publishers, (1964). (in Russian). Translated from: H.G. Hopkins, Dynamic Expansion of Spherical Cavities in Metals. *Progress in Solid Mechanics*. 1, 84-164 (1960); H.G. Hopkins, Dynamic Anelastic Deformations of Metals. *Applied Mechanics Reviews*, 14(6), 417-431 (1961).

ANALYSIS OF JET FORMATION AND PENETRATION BY CONICAL SHAPED CHARGE WITH THE INHIBITOR

MASAHIDE KATAYAMA*, ATSUSHI TAKEBA*, SUSUMU TODA† and SEISHIRO KIBE†

*Structural Engineering Department, CRC Research Institute, Inc., 2-7-5, Minamisuna, Koto-ku, Tokyo 136-8581, Japan; †National Aerospace Laboratory, 7-44-1 Jindaiji Higashi-machi, Chofu-shi, Tokyo 182-8522, Japan

Summary ——This paper proposes a numerical method to simulate not only the jet formation process of the conical shaped charge with the inhibitor: approximately 11 km/s aluminum jet, but also the succeeding flight and impact processes onto the target plates. The method is demonstrated by performing a series of numerical analyses with a multi-processor type hydrocode: AUTODYN-2D™ and is successfully verified by comparing with the experiment conducted by National Aerospace Laboratory of Japan to assess the protection of orbital space debris impacts on the spacecraft in the low earth orbit (LEO). In the numerical model the shock-induced vaporization is taken into account by applying the Tillotson equation of state to the liner and the target materials. We can visually know the distribution of various field variables in the jet formed from the liner and in the jet and target after the impact: contour plots of velocity, temperature, density, energy, etc. Besides they are useful for understanding the mechanism of the phenomenon, it is truly interesting to see what physical phase the jet is in, especially by the phase indicator. The decrease effect of the jet mass during travel to the target is investigated, as well as the density and shape effect of the jet on the size of the crater formed on the target. The investigation is useful for the calibration of the jet mass and jet velocity, because it is difficult to know the accurate information on them by the experimental measurement. These numerical results are discussed over the comparison with the corresponding experimental results in the jet shape, the crater shape, the jet mass and the jet velocity.© 1999 Elsevier Science Ltd. All rights reserved.

INTRODUCTION

A cylinder of chemical high explosive with a hollow cavity in one end and a detonator at the opposite end is used in order to obtain hypervelocity metal jet up to approximately 12 km/s. The hollow cavity of conical shape, called "liner", causes the gaseous products formed from the initiation of the explosive at the end of the cylinder opposite the hollow cavity to focus the energy of the detonation products. This acceleration method is referred to "shaped charge", and its phenomenon is known as the Munroe effect mainly in US and UK, while Neumann or Foerster effect in the other countries. In order to assess the protection of orbital space debris impacts on the spacecraft, a series of hypervelocity impact tests have been conducted by using a conical shaped charge (CSC) equipment with the inhibitor in National Aerospace Laboratory of Japan (NAL), which can accelerate an aluminum liner up to approximately 11 km/s jet [1]. At present, since no experimental methods are available which can accelerate a solid projectile with a gram-order mass and above 10 km/s velocity in the laboratory on the ground, the shaped charge employing the inhibitor can be regarded as the most effective method to simulate experimentally the orbital space debris impact against the spacecraft in the low earth orbit (LEO). The aluminum liner is used for the space application in order to obtain the higher velocity jet, at the same time because it is a very populous material in the LEO. The same method has been studied from both the experimental and numerical standpoints by Walker, et al. [2], Bol and Fucke [3]. However, the method has difficulty in the reproducibility to simulate the mass and velocity of space debris with

accuracy, from the standpoint of determination of the ballistic limit curve for the protection structure on the spacecraft. The extremely high pressure and temperature cause the phase change of the liner material, at the same time the shape of the jet becomes hollow in its tip because it is subjected to seriously complicated deformation by the existence of the inhibitor. These facts make it difficult to know the density and velocity distributions in the jet only by the experimental measurement. In order to cope with this problem, it is indispensable to make use of the numerical simulation method.

For the purpose of investigating the Munroe effect numerically, some hydrocodes have been utilized by applying several numerical models. In the case of 'self-forging-fragment' analyses, of which liner angle is fairly greater than the shaped charge, since the liner material is not subjected to much serious deformations, conventional Lagrangian hydrocodes enable us to make numerical simulations up to some advanced time stages [4]. On the other hand, in the case of shaped charge analyses it has been indispensable to adopt some special numerical methods as to cope with the complicated liner deformations. As an analytical theory of jet formation [5] is known to be effective which calculates the jet and slug masses and the velocity as functions of the liner collapse velocity and the liner angle at the axis, it is sufficient to estimate the liner collapse velocity from the engineering viewpoint in the case of the non-inhibited CSC. Another is the direct solution method by using Lagrangian rezoning technique applied to the complicated liner deformations as to improve the numerical grids [6], although it is a considerably troublesome method for researchers.

For all the various efforts, these methods are not robust enough to solve the jet formation process of the inhibited CSC.

It has rarely been attempted to solve the overall jet formation process of the shaped charge jet by using the Eulerian method, because the thickness of liner is too thin to solve with enough numerical meshes. However, as the computer memory and CPU performance have remarkably improved in recent years, we tried to apply the Eulerian method even to the liner material and demonstrated that the method is applicable to the analysis of the overall jet formation process of the shaped charge in our previous work [7]. In the analysis the multiple material Eulerian processor was used to solve all the components: a liner, chemical high explosive, targets, etc., and obtained the maximum jet velocity of approximately 12 km/s for the aluminum liner.

In this study the jet formation and its penetration processes into the targets, formed by the CSC with the inhibitor, is simulated by a hydrocode, and the numerical analysis includes 1) phase changes of the liner material, 2) the decrease of jet mass during the flight and 3) the hollow and low-density effect of the jet. The simulated results are compared with the experimental results conducted by NAL, and they are investigated and discussed from the viewpoint as to enhance the experimental accuracy of the hypervelocity impact tests by the inhibited CSC method. The present approach also makes for the elucidation and comprehension of physical mechanism of the jet formation and penetration processes by the inhibited CSC impact test facility.

IMPACT TEST FACILITY OF THE INHIBITED CSC

Fig. 1 shows the impact test facility of the conical shaped charge with the inhibitor and its schematic, denoting notation and indicating the dimensions, is shown in Fig. 2. And the configuration of the inhibited CSC is shown in Fig. 3 with the nomenclature in each part. The liner, the
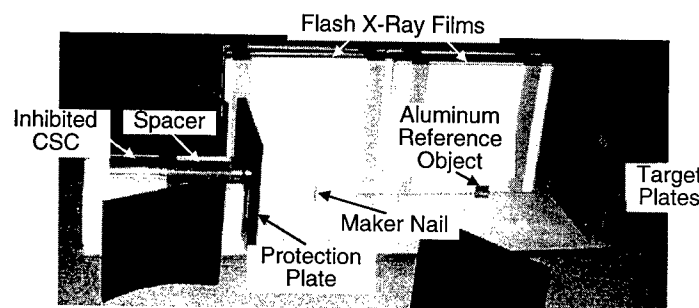

Fig1. Photograph of the test facility of the inhibited conical shaped charge (CSC).
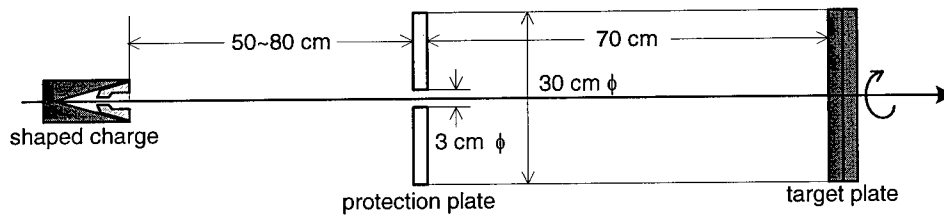
Fig.2 Schematic of the hypervelocity impact test facility using CSC with the inhibitor.

high explosive, the inhibitor and the case are made of aluminum, OCTOL, copper and aluminum respectively. The diameter and the longest length of the explosive cylinder are 70 mm and 147 mm. The thickness and inclination angle of the liner are 2.1 mm and 15 degree. The double-sheet target and protection plate are made of mild steel, and the spacer is made of vinyl chloride. The annular protection plate was employed in order to trap the inhibitor, the liner slug and the blast of the products generated by the detonation of the chemical high explosive, so it is as not to simulate the Whipple bumper in the experiment. The thicknesses of two target plates are 2.5 cm equally. An aluminum reference object is placed in order to calibrate the mass of the jet by comparing both images of the flash X-ray photograph.

NUMERICAL MODELING

Fig. 2 also indicates the whole calculational system to simulate the present experiment. Two-dimensional hydrocode: AUTODYN-2D™ was applied for the numerical simulation. All the calculations were made in the axisymmetric geometry. Though this hydrocode is a fully coupled (multi-processor type) computer program, only the multiple material Eulerian processor was utilized all the time in this study. The case and inhibitor of the shaped charge were assumed to be perfectly rigid, because the liner is destined at the early stage how to deform hereafter and the reflection of the shock wave by those components is not to be dominant factors in this problem, especially from the viewpoint of the tip jet formation.

We applied the JWL equation of state (E.O.S.) to OCTOL proposed by E. L. Lee [8], and using 'on-time burning' model. The equation of the state and its properties are shown in Eqn. (1) and Table 1.

$$P = A_{JWL}\left(1 - \frac{\omega\eta}{R_1}\right)\exp\left(-\frac{R_1}{\eta}\right) + B_{JWL}\left(1 - \frac{\omega\eta}{R_2}\right)\exp\left(-\frac{R_2}{\eta}\right) + \omega\eta\rho_{ref}e \qquad (1)$$

where P is the pressure, η is ρ/ρ_{ref}, ρ is the current density, ρ_{ref} is the reference density, e is the specific internal energy, A_{JWL}, B_{JWL}, R_1, R_2, ω are the material properties of the chemical high
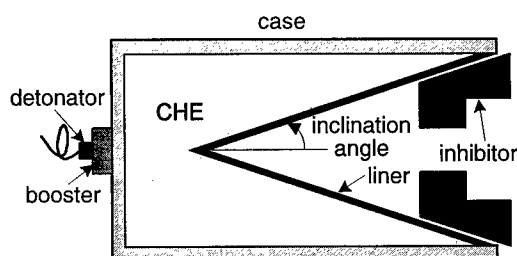
Fig.3 The nomenclature for a conical shaped charge (CSC) configuration.

Table 1. Material properties of OCTOL

Variable	Properties	(Unit)
ρ_{ref}	1.821	(g/cm^3)
A_{JWL}	7.486	(Mbar)
B_{JWL}	1.338×10^{-1}	(Mbar)
R_1	4.5	(—)
R_2	1.2	(—)
ω	3.80×10^{-1}	(—)
V_{det}	8.48×10^{-1}	(cm/µs)
e_0	9.60×10^{-2}	(Terg/cm^3)

1 Mbar = 10^{11} Pa, 1 Terg = 10^5 J

explosive. And the variables denoted as V_{det} and e_0 in the table are the detonation velocity and the initial internal energy of the high explosive respectively. The constitutive model of OCTOL was neglected, namely assumed to be hydrodynamic.

For the aluminum liner the Tillotson equation of state [9] and the Johnson-Cook constitutive model [10] were applied, because the liner is subjected to the extreme condition: the high pressure, high temperature, high strain rate, severe deformation, etc. The Tillotson E.O.S. can take account of the shock-induced vaporization. This E.O.S. is equivalent to the Mie-Grüneisen type shock-Hugoniot E.O.S. [11] in the lower pressure region (below 1 TPa order), and adopts the Thomas-Fermi's semi-classic quantum statistic theory [12] in the higher pressure region. The Tillotson E.O.S. is divided into the following four regions according to the compression μ $=\rho/\rho_{ref}-1$ and the specific internal energy (energy per unit mass) E.

I) In the region 1 (if $\mu \geq 0$), the pressure is calculated by Eqn. (2).

$$P_1 = \left(a_{Til} + \frac{b_{Til}}{1 + \frac{E}{E_0 \eta^2}} \right) \eta \rho_{ref} E + A_{Til} \mu + B_{Til} \mu^2 \tag{2}$$

II) In the region 2 (if $\mu < 0$, $E \leq E_s$), the pressure (P_2) is calculated by the equation substituted $B_{Til}=0$ to Eqn. (2).

III) In the region 3 ($\mu < 0$, $E_s < E < E'_s$), the pressure is calculated by Eqn. (3).

$$P_3 = P_2 + (P_4 - P_2)\frac{E - E_s}{E'_s - E_s} \tag{3}$$

IV) In the region 4 ($\mu < 0$, $E \geq E'_s$), the pressure is calculated by Eqn. (4)

$$P_4 = a_{Til}\eta\rho_{ref}E + \left[\frac{b_{Til}\eta\rho_{ref}E}{1 + \frac{E}{E_0\eta^2}} + A_{Til}\mu \times \exp\left\{\beta\left(1 - \frac{1}{\eta}\right)\right\}\right]\exp\left\{-\alpha\left(1 - \frac{1}{\eta}\right)^2\right\}, \tag{4}$$

where E is the current specific internal energy, E_s and E'_s is the specific internal energy with relation to the sublimation point. E_0 is the specific internal energy at 0 °C. The variables indicated by a_{Til}, b_{Til}, A_{Til}, B_{Til}, α, β are the properties characteristic of the materials introduced in Ref. [9].

In the Johnson-Cook constitutive model applied to the aluminum liner the yield stress (Y) is estimated by the function of strain (ε), strain rate ($\dot{\varepsilon}$) and homologous temperature (T^*) by Eqn. (5).

$$Y = (A_{J-C} + B_{J-C}\varepsilon^n)(1 + C_{J-C}ln\dot{\varepsilon}^*)(1 - T^{*m}), \tag{5}$$

where $\dot{\varepsilon}^* = \dot{\varepsilon}/\dot{\varepsilon}_0$ is the dimensionless plastic strain rate for $\dot{\varepsilon}_0 = 1.0$ s^{-1}, and T^* is defined by

Table 2. Material properties of aluminum

Eqn.	Variable	Properties	(Unit)
	ρ_{ref}	2.70	(g/cm³)
	A_{Til}	7.52×10^{-1}	(Mbar)
E.	B_{Til}	6.50×10^{-1}	(Mbar)
	a_{Til}	5.00×10^{-1}	(—)
O.	b_{Til}	1.63	(—)
	α	5.00	(—)
S.	β	5.00	(—)
	E_0	5.00×10^{-2}	(Terg/g)
	E_s	3.00×10^{-2}	(Terg/g)
	E'_s	1.50×10^{-1}	(Terg/g)
	G	2.76×10^{-1}	(Mbar)
C.	A_{J-C}	2.65×10^{-3}	(Mbar)
	B_{J-C}	4.26×10^{-3}	(Mbar)
M.	C_{J-C}	1.50×10^{-2}	(—)
	m	1.00	(—)
	n	3.40×10^{-1}	(—)
	T_{melt}	7.75×10^{2}	(K)
	C_{cv}	8.75×10^{-6}	(Terg/g·K)

E.O.S.: equation of state,
C.M.: constitutive model,
G: shear modulus, C_{cv}: constant volume specific heat,
1 Mbar = 10^{11} Pa, 1 Terg = 10^5 J

Table 3. Material properties of protection plate and target plates

Eqn.	Variables	Properties	(Unit)
	ρ_{ref}	7.86	(g/cm³)
	A_{Til}	1.279	(Mbar)
E.	B_{Til}	1.05	(Mbar)
	a_{Til}	5.00×10^{-1}	(—)
O.	b_{Til}	1.63	(—)
	α	5.00	(—)
S.	β	5.00	(—)
	E_0	9.50×10^{-2}	(Terg/g)
	E_s	2.44×10^{-2}	(Terg/g)
	E'_s	1.02×10^{-1}	(Terg/g)
	G	8.18×10^{-1}	(Mbar)
	A_{J-C}	3.50×10^{-3}	(Mbar)
C.	B_{J-C}	2.75×10^{-3}	(Mbar)
	C_{J-C}	2.20×10^{-2}	(—)
M.	m	1.00	(—)
	n	3.60×10^{-1}	(—)
	T_{melt}	1.81×10^{3}	(K)
	C_{cv}	4.52×10^{-6}	(Terg/g·K)

E.O.S.: equation of state,
C.M.: constitutive model,
G: shear modulus, C_{cv}: constant volume specific heat,
1 Mbar = 10^{11} Pa, 1 Terg = 10^5 J

$$T^* = \frac{T - T_{room}}{T_{melt} - T_{room}} ,$$

(6)

and T_{room} and T_{melt} are the room temperature and melting temperature, respectively. A_{J-C}, B_{J-C}, C_{J-C}, m and n are determined by an experimental procedure [10].

The material properties of the Tillotson E. O. S. and the Johnson-Cook constitutive model used for the aluminum liner are shown in Table 2. And as a fracture condition we used the value of spall strength (negative maximum hydrostatic pressure) of 0.0 Pa, not as to affect the expansion after the liner becomes hydrodynamic.

Equally, the Tillotson E.O.S. and the Johnson-Cook constitutive model were applied to the steel protection plate and the two plates of steel targets. The material properties used for them are shown in Table 3. To the rear target the Mie-Grüneisen shock Hugoniot E.O.S. was applied instead of the Tillotson E.O.S., because the shock-induced vaporization was not to occur in this component: U_S = $4.57+1.49u_p$ km/s, Γ = 2.17, where U_S is the shock velocity, u_p is the particle velocity and Γ is the Grüneisen coefficient. As fracture conditions, both the spall strength and the ultimate strain were applied to them by which the numerical cell is triggered to be fractured instantaneously. The value of spall strength used in the calculation is -2.0 GPa and that of the ultimate strain is 25 %.

RESULTS AND DISCUSSIONS

Jet Formation Analysis

Fig. 4 indicates the early stages of aluminum jet formation processes, comparing the non-inhibited jet formation with the inhibited jet formation. In the case of the inhibited CSC, the tip

of the jet is hollow but separated from the aluminum slug efficiently. These plots are useful to comprehend the effect of inhibitor on the separation of the tip jet from the slug. The fact is also ascertained experimentally that the conical shaped charge using the inhibitor forms a hollow jet.

Fig. 4 also shows the contour plots of the region number mentioned in the description on the Tillotson E.O.S. In the case of the inhibited CSC, a portion of the region 4 (completely vaporized phase) is estimated in the lateral part of

Fig.4 Inhibitor effect on the initial jet formation and the phase change.

the tip jet, while other dark colored regions are corresponding to the region 3 (solid-vapor-multiphase) in both cases. On the other hand, no completely vaporized regions are calculated in the case of the non-inhibited CSC. The region number for the chemical high explosive has no meanings in these plots.
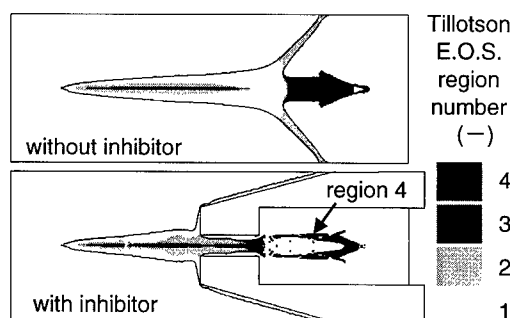
Jet Flight and Impact Analysis

Fig. 5 shows the material fraction contour of the inhibited CSC at 20 ms. From this figure we can see that the tip region of the jet has a complicated distribution of the mass density. In order to investigate the mass and velocity distribution in the tip jet, we introduce the effective mass and the effective average velocity of the tip jet. Generally, if all the mass and all the kinetic energy of the jet included in the region Ω_i are denoted by $\overline{M}_i$ and $\overline{E}_i$ at a time index i, respectively, the axial average velocity $\langle \overline{V}_i \rangle$ in the same region may be defined by
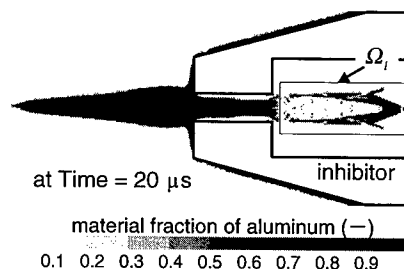

Fig.5 Mass fraction distribution and jet mass sampling area.

$$\langle V_i \rangle = \sqrt{\frac{2\overline{E}_i}{\overline{M}_i}} \tag{7}$$

Referring to the mass and its velocity vector in an Eulerian cell in the region Ω_i as $m_{i,j}$ and $v_{i,j}$, respectively, and noting that the radial velocity components are far smaller than the axial ones, $\overline{M}_i$ and $\overline{E}_i$ are given by

$$\overline{M}_i = \sum_j^{\Omega_i} m_{i,j}, \qquad \overline{E}_i = \sum_j^{\Omega_i} \frac{1}{2} m_{i,j} \left| v_{i,j} \right|^2 \tag{8}$$

According to the above notation and Eqn. (8), $\overline{M}_i$ and $\overline{E}_i$ in the region Ω_i are calculated as shown in Table 4. Then we continued the numerical simulation to advanced time stages.

Fig. 6 and 7 depict the overall phenomena of the jet flight and its impact on two plates of targets after the jet formation in the case of the inhibited CSC. The calculated profile of the tip jet at 40 μs shown in Fig. 6 (b) is similar to the experimental result in Fig 6 (a), although it should be noted that two figures have some different points because of their expression methods: the

Table 4. Summary of the typical jet properties in the numerical simulation

Region Symbol	Time (μs)	Mass: $\overline{M}_i$ (g)	Kinetic Energy: $\overline{E}_i$ (kJ)	Axial Momentum (N·s)	Radial Momentum (N·s)	Average Velocity: $\langle \overline{V}_i \rangle$ (km/s)
Ω_1	20	3.17	1.54	31.0	0.66	9.85
Ω_2	40	3.24	1.55	31.4	0.71	9.77
Ω_3	50	2.97	1.44	29.1	0.65	9.97
Ω_4	100	1.79	0.94	18.3	0.29	10.25
Ω_5	150	1.19	0.64	12.3	0.14	10.37

three-dimensional projection view and the two-dimensional slice view. We can visually see the process of jet's expanding to the target plates in the velocity distribution plots at 50 through 150 μs shown in Fig. 7. Consequently the jet forms a crater with a depth (2.5 cm) just same as thickness of the front target, as shown in the material distribution profile at 250 μs in Fig. 8 (a). Fig. 9 shows an example of the experimental results about the front target plate. The sectional view tells us that a petal about 5 cm in height was formed on the front side and no significant deformation is observed on the rear side. The comparison of crater-size parameters between the calculation and the experiment is summarized in the lower part of Fig. 9. The average value of the crater depth was obtained from ten experimental shots, and the crater diameters are shown in their value range, because they have larger deviations among ten cases than the crater depths, including a directional difference in diameter. The calculational result has a fairly good agreement with the experimental result. In the numerical analysis the drag effect by the atmosphere was neglected, because the experimental tests were performed at low pressure (about 0.01 MPa).

These results were obtained by using the Eulerian rezoning technique, that is, deleting numerical meshes backward when they are no longer required to be included in the calculational system and adding new Eulerian meshes forward gradually. This method does not burden us so much, as compared with the Lagrangian rezoning method. We carried out several times Eulerian rezoning

(a) 3D X-ray photograph (experiment)

Jet tip profile

Ω_2

(b) 2D slice material fraction at 40 μs (calculation)
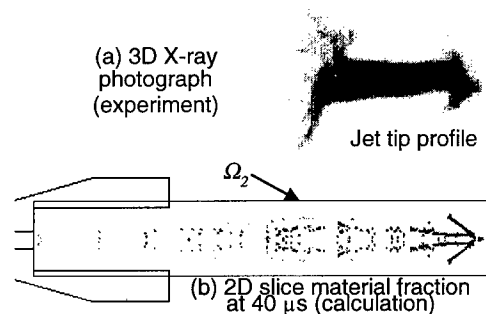
Fig.6 Comparison of the jet profiles between the experiment and the calculation.

Ω_3

0 — 5 cm

(a) Velocity distribution at 50 μs (calculation)

Ω_4

0   10 cm

(b) Velocity distribution at 100 μs (calculation)

Ω_5

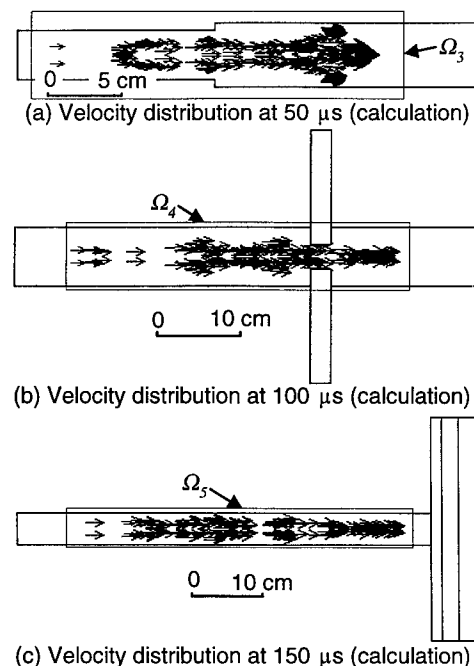0   10 cm

(c) Velocity distribution at 150 μs (calculation)

Fig.7 Jet's flying process in the simulation.

procedures to accomplish the whole calculation by using any current typical engineering workstation or personal computer.

In Table 4, the calculated jet parameters described above are summarized again for the regions $\Omega_2 \sim \Omega_5$ shown in Fig. 7. From the figure, noting that different scales are used for each drawing time, we can see that the length of the jet becomes long as time goes by, because the velocity at the tip is higher than at the tail. Considering that the decrease of the mass by the genuine numerical error based upon the advection calculation of the Eulerian method has been ascertained to be less than 0.1 % in this whole simulation, we can conclude that the decrease of the jet mass indicated in Table 4 was caused by the neglect of the delayed jet. This effect makes its appearance as an increase of the effective average velocity as the jet flies far away.

As shown in Fig. 7 (b), the protection plate traps the jet that has expanded to the radial direction. We can also realize the same effect from the decrease of the radial momentum between 50 and 150 µs in Table 4. That is, the ratio of the axial momentum in the region Ω_5 to Ω_3 is 0.423, while that of the radial momentum is 0.215. Therefore, the jet is collimated effectively by the protection plate.

Fig. 10 indicates the comparison of the relation of the jet mass decrease as the function of the flight distance among the calculational and three experimental results. The calculated jet masses indicate a little bit smaller than the experimental results, except for the data point of about 90-cm flight distance of the experiment C. This is because the region (Ω_i) used for the summation of the jet mass in the calculation is wider than in the experiment, i.e. the region Ω_i includes too much delayed jet. It is coincident with the fact that the velocities of the jet in the calculation are a little bit lower than in the experiment: the average velocities between the two plotting points in Fig. 10
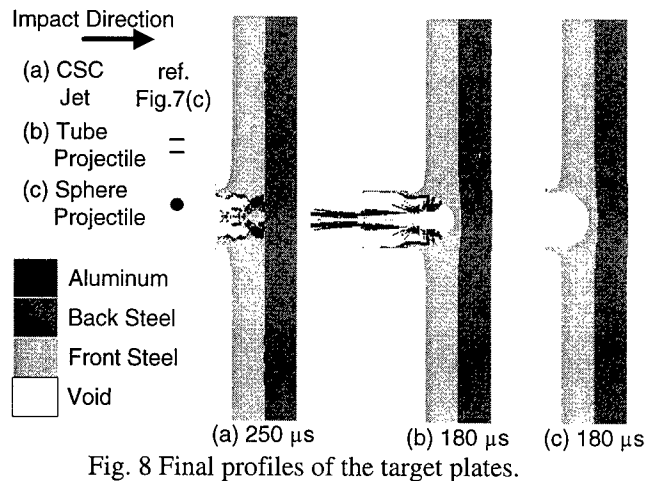

Impact Direction

(a) CSC Jet   ref. Fig.7(c)

(b) Tube Projectile   —

(c) Sphere Projectile   ●

Aluminum
Back Steel
Front Steel
Void

(a) 250 µs   (b) 180 µs   (c) 180 µs

Fig. 8 Final profiles of the target plates.

front side view

0   5 cm

Test No. H10. 2-2

sectional view

front petal

front side

rear side

Test No. H10. 2-2

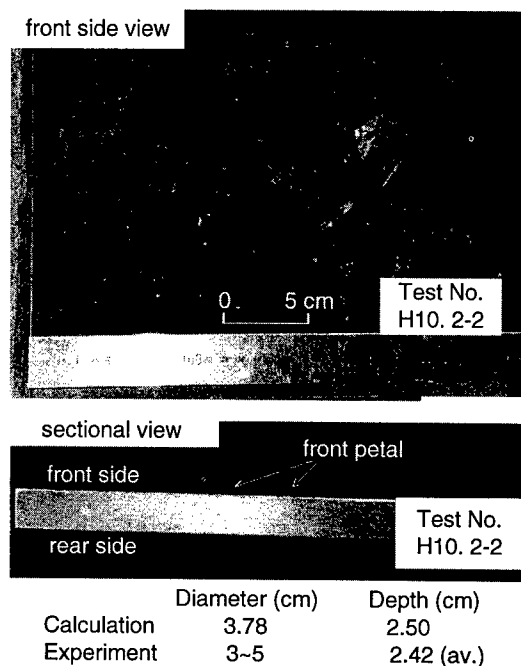|	Diameter (cm)	Depth (cm)
Calculation	3.78	2.50
Experiment	3~5	2.42 (av.)

Fig. 9 A photograph of the front target plate obtained by the CSC test.
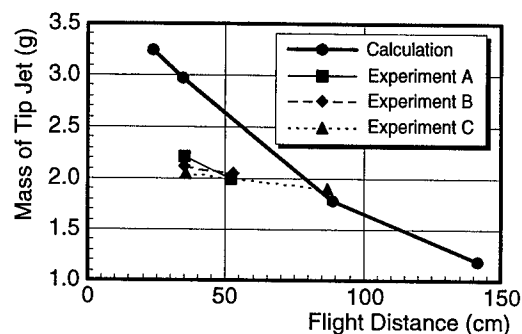

Fig. 10 The relation of the jet mass to the flight distance.

for the experiment A and B [1] are 10.49 and 10.96 km/s, respectively. The calculated velocity corresponding to these values is approximately 10 km/s.

The jet masses in the experiment were estimated by a computer-aided image processing method. In the procedure an image scanner (ScanJet3P/C2570A, resolution: 250 dpi, Hewlett-Packard) and an image analysis software (Image-Pro Plus™ Ver.2.0 for Power Mac, Media Cybernetics) were utilized.

Shape Effect of Jet

Now we have the information on the effective mass and average velocity of the jet formed numerically just before impacting on the target plates. According to these data, we modeled three shapes of projectiles that have the same mass and velocity as the jet at 150 μs in the previous calculation. First is just same as the jet obtained by the calculation. Second is a cylindrical tube with the 1.40-cm length, the 0.9-cm inner diameter and the 1.1-cm outer diameter. Third is a sphere with the 0.94-cm diameter. Every projectile has the mass of 1.19 g and the average velocity of 10.37 km/s. The tube and sphere projectiles are, equally, assumed to have a uniform velocity distribution and the initial specific internal energy of 0.0 J/kg. The same material model and data were applied to the cylindrical tube and sphere projectiles as the aluminum liner summarized in Table 2.

The sizes of the tube and sphere projectiles shown in upper left-hand side of Fig. 8 are drawn by using nearly same scale by which the target deformations are drawn in the right-hand side of the figure. The diameters of the craters for the cases of the jet, tube and sphere projectiles are 3.88, 3.78 and 4.14 cm; the depths of the craters are 25.0, 22.6 and 20.6 cm, respectively. The crater shape of the front target formed by the jet is more similar to that by the tube projectile than to that by the sphere projectile. However, both the impacts by the tube and sphere projectiles overestimate the crater diameter and the deformation of the front target in the rear side as compared with the jet case. It should be noted that the result of the jet projectile shown in Fig. 8 is at 250 μs, while the other results are at 180 μs. Furthermore, we can see much projectile material (aluminum) in the vicinity of the original impact faces for the cases of the jet and tube projectiles, whereas almost nothing for the case of the sphere projectile.

We are able to obtain more information about the projectile and target materials by the numerical examination in various parameters in detail. Fig. 11 shows the distribution of the velocity vector at 180 μs for the three cases. We can clearly understand that it takes much more time for the jet to make its crater completely than for the tube and sphere projectiles. In the case of the jet penetration, the considerable delayed jet has not reached the target at 180 μs. On the other hand, all the velocity vectors in the target plates have already decreased below 100 m/s at the same moment in the cases of the tube and sphere projectiles. As almost all the velocities of the projectile material in Fig. 11 (b) are negative to the impact direction, they are not to make any significantly thicker crater after this moment.

Fig. 12 shows the distribution of the region number of the Tillotson E.O.S. (phase indicator). In the cases of the jet and tube projectiles, the projectiles are vaporized almost completely by the shock compression and the succeeding rarefaction. It seems that the hollow space of the projectile plays an important part in the appearance of the rarefac-

Scale of Velocity Vector: ⟶ 10 km/s

boundaries of Eulerian grids
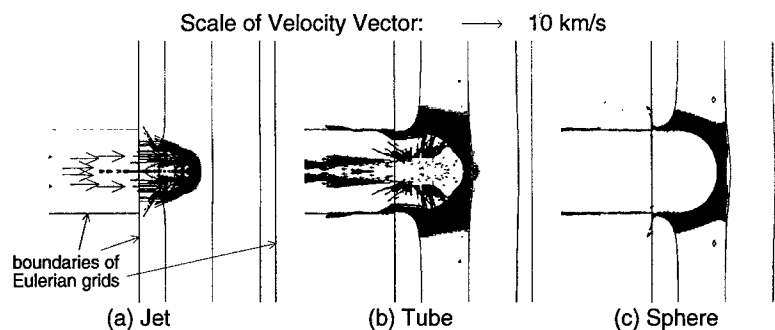
(a) Jet   (b) Tube   (c) Sphere

Fig. 11 Velocity vector distributions at 180 ms.

tion, and consequently in the occurrence of the shock-induced vaporization. The front side view of the target plate shown in Fig. 9 is similar to an internal crater in a volcano. This is coincident with the fact that a similar lump can be observed only in the case of the jet impact as shown in Fig. 12 (a).

CONCLUSIONS

We have come to the conclusions through the present study as follows:

1) The calculated jet mass, the jet velocity and the target crater formed by the conical shaped charge with the inhibitor were compared successfully with those of experimental results, for the time range from the formation of the jet to its penetration into the target. The multiple material Eulerian method is proved to be sufficiently applicable to such a big scale and/or long term problem, as hypervelocity impact phenomena.

2) The effect of the inhibitor upon the jet formation process in the conical shaped charge launcher is demonstrated visually at the early stage in the present numerical simulation.

Fig. 12 The status of the projectile and the front target standing for their phase change.

3) The physical phase of the jet created by the shaped charge was made clear, although on the assumption that the liner material should be subject to the Tillotson E.O.S.

4) The present numerical simulation method enables us to estimate not only the mass and velocity of the jet right after its formation, but also the decrease of the jet mass and the change of the jet velocity during the flight which cannot be estimated easily by experimental methods. And such information provides us important data on the projectile in order to assess the protection of the spacecraft from the orbital space debris.

5) It was successfully demonstrated numerically that the shape and mass distribution of the jet are of great importance for its penetration mechanism into the target. And it was clarified that the shape of projectile plays an important role in the vaporization of the projectile material accompanied with the hypervelocity impact over 10 km/s.

We applied the present analysis method only to the simulation of the CSC jet impact against two plates of steel targets. However, since one of the authors has already ascertained that the multiple material Eulerian method is applicable to the hypervelocity (6~14 km/s) impact problem against the stuffed Whipple bumper shield (stuffed with Nextel™, Kevlar™, MLI, etc.) [13], the numerical simulation of the shaped charge jet impact on the stuffed Whipple bumper shield might be performed by using a similar procedure.
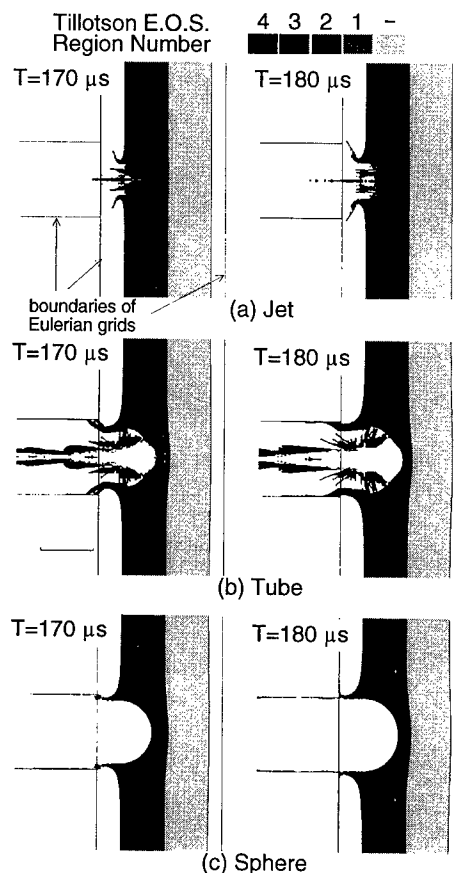
In a previous paper [14], the authors investigated the density and shape (L/D) effect of the projectile on the crater size. The conclusion was that a high-density projectile forms a larger crater than a low-density projectile, and that a long-rod projectile makes a deeper but smaller diameter crater than a sphere projectile. The conclusion on the projectile's density and shape effect upon the crater

Table 5. Crater sizes of the front target for each projectile in the calculation

Parameter (Unit)	Jet	Tube	Sphere
Diameter (cm)	3.88	3.78	4.14
Depth (cm)	25.0	22.6	20.6

size derived from the present study may be comparable with that of the previous study, but a little bit more complicated. The conclusion of the present study on this point can be summarized again as shown in Table 5. Considering that the jet created by the CSC has the small value of the compression (μ) and is partially vaporized, it might be said that the jet is nearly equivalent to a long-tube projectile with the low-density. At the same time, as the jet has a long mass distribution in space, it also corresponds to a long tube. According to our previous study, the density of the projectile works on both diameter and depth of the crater as a positive factor, while the length of the projectile acts on the depth as a positive factor but on the diameter as a negative factor. Therefore, in the case of the jet impact, it can be said that the crater was made by overlapping of the L/D effect and the density effect, judging from the crater sizes in Table 5.

As many studies on the segmented penetrator, including the telescope-type penetrator [15], have been performed, we should conduct our study referring to these important works. However, their purposes are not to investigate the density effect and not to attempt to apply to the impact at over 10 km/s: i.e. the impact to be accompanied with the shock-induced vaporization.

The authors investigated the material models and properties to be applied to the aluminum alloys, and demonstrated that the numerical analysis, in which they were used for the materials consisting of the Whipple bumper shield, is in fairly good agreement with the experimental results [16]. However, its verification is also limited to the impact velocity below 8 km/s.

Therefore, it is highly expected to continue the present study by using the conical shaped charge with the inhibitor, and to enhance the accuracy and reliability on the mass and velocity of the jet by the collaboration between the experiment and the numerical simulation.

REFERENCES

1. M. Hikiji, H. Miyoshi, T. Yamamoto, M. Kobayashi, A. Kunoh, S. Toda and S. Kibe, Study of hypervelocity impact testing with shaped charge (Part4). *Proc. Symp. on Shock Wave Japan FY'97*, pp. 671-674, March 20-22 (1998), in Japanese.
2. J. D. Walker, D. J. Grosch and S. A. Mullin, A hypervelocity fragment launcher based on an inhibited shaped charge. *Int. J. Impact Engng.*, **14**, 763-774 (1993).
3. J. Bol and W. Fucke, Shaped charge technique for hypervelocity impact tests at 11 km/s on space debris protection shield. *Proc. 2nd Eur. Conf. on Space Debris*, pp. 405-411, ESA SP-393, ESOC, Darmstadt, Germany, 17-19 March (1997).
4. R. G. Whirley and B. E. Engelmann, DYNA2D a nonlinear, explicit, two-dimensional finite element code for solid mechanics User Manual. UCRL-MA-110630, Lawrence Livermore National Laboratory (1992).
5. E. M. Pugh, R. J. Eichelberger and N. Rostoker, Theory of jet formation by charges with lined conical cavities. *J. App. Phys.*, **23**(5), 532-536 (1952).
6. S. Hancock, H. Hancock and L. Behrmann, Full Lagrange and Lagrange-Euler shaped charge jetting calculation. PIIR-3-82, Physics International Company, CA, January (1982).
7. M. Katayama, A. Takeba, S. Toda and S. Kibe, Numerical simulation of jet formation by shaped charge and its penetration into bumperd target. *Proc. 2nd Eur. Conf. on Space Debris*, pp. 411-416, ESA SP-393, ESOC, Darmstadt, Germany, 17-19 March (1997).

8. E. L. Lee, F. H. Helm, M. Finger and J. R. Walton, Equations of state for detonation products of high energy PBX explosives. UCID-17540, Lawrence Livermore Laboratory, CA, August (1977).

9. J. H. Tillotson, Metallic equations of state for hypervelocity impact. GA-3216, General Atomic, CA, July (1962).

10. G. R. Johnson and W. H. Cook, A Constitutive Model and Data for Metals Subjected to Large Strains, High Strain Rates and High Temperatures. *Proc. 7th Int. Symp. on Ballistics*, pp. 541-547, The Hague, The Netherlands (1983).

11. R. G. McQueen, S. P. Marsh, J. W. Taylor, J. N. Fritz and W. J. Carter, The equation of state of solids from shock wave studies. In *High-Velocity Impact Phenomena*, (edited by R. Kinslow), pp. 294-299, Academic Press, New York (1970).

12. R. D. Cowan and J. Ashkin, Extension of the Thomas-Fermi-Dirac statistical theory of the atom to finite temperatures. *Phys. Rev.*, **105**, 144 (1957).

13. K. Shiraki, S. Terada, N. Noda and M. Katayama, Hydrocode Simulation for the JEM pressurized module structure performance for space debris impact. *Proc. 7th ISCOPS*, C-8-6, July (1997).

14. M. Katayama, S. Toda and S. Kibe, Numerical study on density and shape effects of projectiles for hypervelocity impact. *Proc. 2nd Eur. Conf. on Space Debris*, pp. 445-448, ESA SP-393, ESOC, Darmstadt, Germany, 17-19 March (1997).

15. C. E. Anderson, Jr., R. Subramanian, J. D. Walker, M. J. Normandia and T. R. Sharron, Penetration mechanics of Seg-Tel penetrators. *Int. J. Impact Engng.*, **20**, 13-26 (1997) .

16. M. Katayama, S. Toda and S. Kibe, Numerical simulation of space debris impacts on the Whipple shield. *Acta Astronautica*, **40**(12), 859-869 (1997).

SHOCK-DATA CONSTRAINTS ON INTERATOMIC POTENTIALS FOR CONDENSED MATTER

THOMAS KING* and **JON SHIVELY

Air Force Research Laboratory, Phillips Research Site, Kirtland AFB, NM 87111; **CME Department, California State University, Northridge, CA 91330

Summary — It is customary to represent the shock Hugoniot as a linear relation between shock velocity and the particle velocity behind the shock. It has been recently shown that the coefficients appearing in the general expansion of shock velocity as a power series in particle velocity can be calculated, to arbitrary order, from the derivatives of the shock pressure with respect to volume, evaluated at the initial state. The first two coefficients in the expansion have a simple relation to the interatomic potential describing the material. Most such potentials contain just two parameters (roughly, a "strength" parameter and a "shape" parameter), which can be conveniently extracted from the shock parameters. We present results for the values of the potential parameters, for several commonly-used forms of potential, determined by least-squares fitting of the shock data to nonlinear Hugoniots. The results obtained sometimes differ from those obtained on the assumption of a linear Hugoniot. © 1999 Elsevier Science Ltd. All rights reserved.

INTRODUCTION

We shall consider four potential energy functions that are frequently used in scattering and condensed-matter calculations: the Lennard-Jones Potential [1], the Buckingham 6-Exp Potential [2], the Morse Potential [3], and the Rose (aka Universal) Potential [4,5].

The Lennard-Jones potential was originally obtained by considering the equation of state of real gases, and later was applied to the potential-energy surface of cubic crystals [ref. 1, op.cit.]. It contains an attractive term and a repulsive term, each proportional to a (different) inverse power of the atomic (or molecular) spacing, written as:

$$\phi(r) = \frac{E_0}{m-n}\left(\frac{m}{r^n} - \frac{n}{r^m}\right) \tag{1}$$

where E_0 is the well depth and r the (dimensionless) pair separation, normalized to the equilibrium spacing. In its familiar form, the Lennard-Jones 6-12 potential, it incorporates an induced-dipole attractive term (m = 6), but the dependence of the repulsive part (n = 12) was chosen for convenience. Repulsive exponents other than 12 are sometimes found in the literature; it is apparent from fundamental arguments that the r-dependence of the repulsive term is too simple.

The Buckingham 6-Exp Potential is given by:

$$\phi(r) = \frac{E_0}{1 - \frac{6}{\alpha}}\left[\frac{6}{\alpha}\exp(\alpha(1-r)) - \frac{1}{r^6}\right] \tag{2}$$

where $\phi(r)$, E_0, and r have the same meaning as above and α is a parameter usually obtained by fitting crossed-beam scattering measurements. The Buckingham potential accounts for the induced-dipole attractive interaction, and the exponential part describes the repulsion due to electron-shell overlap.

The Morse Potential was originally proposed in connection with calculation of the spectra of diatomic molecules, and is given by:

$$\phi(r) = E_0\left[\left(1 - e^{\beta(1-r)}\right)^2 - 1\right] \tag{3}$$

where $\phi(r)$, E_0, and r have the same meaning as before. The parameter β was originally related to the value of the vibrational quantum for the (bound) atomic pair in a diatomic molecule. Now, it is to be interpreted as the lowest level in the well in a solid.

The Rose Potential was originally used to describe the results of atomic scattering from surfaces, and is given by:

$$\varphi(r) = E_0 \cdot E(a)$$
$$E(a) = -e^{-a}(1 + a) \tag{4}$$
$$a = (r_{ws} - r_{wse}) / \ell$$

where r_{ws} is the radius of the Wigner Seitz sphere, r_{wse} is its value at equilibrium, and ℓ is the screening length based on surface interaction studies.

Shock data usually consists of measurements of shock velocity, U, and the particle velocity behind the shock, u, because these are far easier to accurately measure in a dynamic experiment than the alternative pair of variables, pressure and specific volume. Furthermore, once accurate measurements have been made for a standard material, over an appropriate range of shock and particle velocities, shock matching allows determination of U and u for an unknown material simply by measuring the shock velocities in the standard and the unknown.

Shock data have been taken using explosives, explosive-driven flyers, and single- and two-stage light gas guns for a number of years; in the case of metals, the range of particle velocities that is usually accessible lies below the sound speed in the unshocked state. A few measurements have also been made using underground nuclear explosions, and, recently, high-power lasers have also been used, to reach shock states that are inaccessible to gas gun experiments; these measurements have achieved particle velocities, in metals, up to several times the sound speed in

the unshocked state. The situation is somewhat different for non-metals than for metals; here, particle velocities that are several times the sound speed have been attained, in gas-gun experiments.

It was noticed quite early [6] that many shock-data sets, particularly those for metals, were well-represented by a linear relation between shock velocity and particle velocity. Somewhat later, it was observed [7,8] that the data could be better fit by including a term quadratic in particle velocity; in particular, the zero-particle-velocity intercept was a better match to the adiabatic sound speed. An acceptable, microscopic description, based on quantum mechanics has not been forthcoming, and modeling of shock phenomena has emphasised classical models, employing analytic potentials.

THEORY

Although a linear Hugoniot is adequate to describe the majority of existing data for metals, there are some measurements at high particle velocities, made using undergound nuclear explosions or lasers [9-14], that are not well-described by such a relation. In general, the Hugoniot is a functional relation between the shock velocity, U, and the particle velocity, u, behind the shock. As long as the function is analytic, we can write it as a Taylor series:

$$U = \sum_{n=0} s_n u^n.$$

(5)

The coefficients s_n for a given material can be obtained by least-squares fitting the shock data for the material, over regions where phase transitions are absent. For example, data for Iron above the phase transition at 12.5 GPa are shown in Figure 1, together with linear and cubic fits to the data. Including terms up to third order in particle velocity produces a fit that is very close to the data: the calculated points essentially lie under the measured points.

There is a relationship [15] between the s_n and the derivatives of the pressure, with respect to volume, of the shocked material, evaluated at the initial state, $V = V_0$. Expressions for the first few s_n are given in equations 6-9:

$$s_0^2 = -V_0^2 \left(\frac{dP}{dV} \right)_{V=V_0} ;$$

(6)

$$s_1 = \frac{V_0^3}{4s_0^2} \left(\frac{d^2P}{dV^2} \right)_{V=V_0} ;$$

(7)

$$s_2 = \frac{-1}{2s_0} \left[\frac{V_0^4}{6s_0^2} \left(\frac{d^3P}{dV^3} \right)_{V=V_0} + 3s_1^2 \right] ;$$

(8)

$$s_3 = \frac{1}{s_0^2}\left[\frac{V_0^5}{48s_0^2}\left(\frac{d^4P}{dV^4}\right)_{V=V_0} - 4s_2s_1s_0 - 2s_1^3\right].\tag{9}$$

Note that the derivatives appearing above are total derivatiives, because the pressure is a function of only the specific volume, on the Hugoniot. The expression for s_0 agrees with the definition of the adiabatic sound speed, as one would expect. As we shall see, terms up to third order in u are adequate to describe existing data. One should be careful not to extrapolate too far from the region in which data exists, however, as any fit to the data that contains a finite number of terms will eventually diverge from the true functional relation. We now discuss the interaction potential.

Consider a material at temperature T = 0. The pressure is given by

$$P = -\frac{dE}{dV} = -\frac{d\phi(V)}{dV} ,\tag{10}$$

where $\phi(V)$ is the potential energy of interaction of the particles comprising the material, per unit volume. Expanding $\phi(V)$ about the point $V = V_0$, we obtain

$$\phi(V) = \sum_{n=0}\frac{V_0^n}{n!}\left(\frac{d^n\phi}{dV^n}\right)_{V=V_0}\left(\frac{V}{V_0}-1\right)^n = \sum_{n=0}\frac{V_0^n}{n!}\phi_n(V_0)\left(\frac{V}{V_0}-1\right)^n ,\tag{11}$$

where we denote the nth derivative of the potential by ϕ_n in the last expression.

For nonzero temperatures, the thermal (kinetic energy) contribution to the pressure must be added to equation 10; at very high temperatures, terms corresponding to electronic excitation, molecular dissociation and ionization (chemical energy) must be included. It can be shown [16] that the first two derivatives of the pressure with respect to volume on the Hugoniot, evaluated at the initial state, are identical with those on the isentrope passing through the initial state, so that, in terms of $\phi(V)$, we have

$$s_0^2 = V_0^2\left(\frac{d^2\phi}{dV^2}\right)_{V=V_0} = V_0^2\phi_2(V_0) ,\tag{12}$$

and

$$s_1 = -\frac{V_0\phi_3(V_0)}{4\phi_2(V_0)} .\tag{13}$$

The second derivative of the potential must be positive, in order for the material to be stable under small deformations; equation 13 requires that the third derivative of the potential be negative, so that s_1 is positive, for stable shock propagation. Thus, the linear part of the Hugoniot contains information about derivatives of the potential to third order. In particular,

determination of s_1 is equivalent to a measurement of the pressure derivative of the bulk modulus, which is difficult to accurately determine by other means. The nonlinear terms in the Hugoniot, which contain information about derivatives of order higher than three, require knowledge of the pressure derivatives off the isentrope.

The purpose of this note is to extract information about the interaction potential that describes a solid material, from shock data for the material; this can be done using equations 12 and 13, for potentials having two adjustable parameters. For potentials having more than two parameters, one must fix all but two, using other information (such as the sound speed) at one's disposal. We obtain in the next section results for the Lennard-Jones, Morse, Buckingham, and Rose potentials; however it must be borne in mind that a potential that realistically reproduces the behavior of materials at high compression is likely to be more complex than these.

ANALYSIS

We will consider the data for Al, Fe, Cu, and for liquid argon, because existing data for these materials extends to particle velocities much greater than the zero-pressure, adiabatic sound velocity, so that nonlinear effects are expected to be significant. Least-squares fits to the U,u data for these materials are given in Table 1. The data for iron were fit above the α–γ phase transition at 12.5 GPa; data on liquid argon do not determine terms higher than quadratic. In all cases, the standard error in the coefficients is 10% or less of the value given, at 90% confidence.

The fits to the copper and the iron data present some difficulties, because of potential inconsistencies between data sets of different experimenters, and because much of the data at the highest particle velocities was taken using shock matching. In particular, the copper data taken at laser facilities generally employed vapor-deposited target structures, and it is uncertain that these accurately reproduce the bulk material.

The values of s_0 and s_1 given above were used to obtain values for parameters appearing in the potentials by evaluating equations 12 and 13 for each potential, and solving for the parameters. The results of so doing are given in Tables 2,3,4,5. Also shown in the tables are values of the potential parameters calculated from handbook data obtained from other than shock experiments. In some cases, there is insufficient information in the literature to calculate the parameters.

The Lennard-Jones potential yields an analytic expression for s_1 in terms of m and n: $s_1 = (m'+n'+3)/4$, where m' and n' are exponents referred to volume rather than distance, and are three times smaller than the values of m and n appearing in equation 1. If we assume that m = 6, we have a two-parameter potential, while (and this is more reasonable for metals), if we assume that m is a free parameter, we have a three-parameter fit. To obtain the values given in Table 2, we assumed handbook values for the sound speed, and inferred m and n for Cu and Al. For iron, the data we consider is above a phase transition; we just fit plausible m and n. In the case of liquid Argon, we assumed m = 6, and inferred E_0 and n.

It will be seen that the linear and nonlinear fits give rather different values for the parameters. The linear fit would give values nearer those for the nonlinear fit if we restricted it to data at low particle velocities, a percent or less of the sound speed at zero pressure. The Lennard-Jones potential has a peculiarity: it is not possible to obtain a value for s_1 less than 1.75 while retaining the r^{-6} dependence of the attractive term. In their paper [ref 1, op.cit.], Jones and Ingham do not specify a priori a value for the exponent of the attractive term, and one can argue that the dipole-attraction term is not the dominant one for metals; we find above that attractive exponents less

than 5 better fit the data for metals. In general, handbook values of E_0 do not result in good fits to the shock data, when used in the Lennard-Jones potential.

DISCUSSION

We will discuss our results for Copper and liquid Argon, as being representative of metals and nonmetals, respectively. Copper data in the shock-velocity/particle-velocity plane is plotted in Figure 2, and in the pressure/particle-velocity plane in Figure 3. In both planes, the cubic polynomial fit to the data is not obviously better than the linear fit, excluding the single data point at a particle velocity of 12 km/s. Nevertheless, the potential parameters obtained from the two fits are quite different. This is due to the significant difference in s_1 between the two fits.

Boogerd, et al. [17] have calculated s_0 and s_1 for Copper from the Morse potential, using parameters obtained from spectroscopic and crystallographic data, assuming a linear Hugoniot. They obtained s_0 = 3.73 km/s and s_1 = 1.48, whereas we obtain (for data extending to high compressions) s_0 = 3.82 km/s and s_1 = 1.59 from our linear fit. Our full, nonlinear fit to the data gives s_0 = 4.02 km/s and s_1 = 1.26; the sound speed at zero pressure that one obtains from the longitudinal and shear speeds is 3.93 km/s.

In the case of liquid Argon, shown in Figures 4 and 5, the situation is somewhat different. In the U,u plane, the quadratic is obviously a better fit to the data: most of the calculated points fall right on the measured points, whereas the linear fit is close only in the middle of the range of data. In the P,u plane, the differences are less apparent. As was the case for Copper, however, the potential parameter sets obtained from the two fits are quite different. Figure 6 compares the shapes of the Lennard-Jones, Buckingham, and Rose potentials for liquid Argon, with parameters determined from polynomial fits to the shock data; Figure 7 shows the shapes for compression by factors greater than two. Note that only the shape function is plotted in Figures 6 and 7: the well depths of the various potentials in general are all different. For r/r_0 greater than about 0.7 (corresponding to compression by a factor less than three), the Lennard-Jones potential is stiffest. In general, the compressive part of the curves are softer than either a Lennard-Jones 6-12, or curves obtained from handbook values of the parameters for the other potentials.

It is interesting to compare the values of s_0 and s_1 obtained from the liquid Argon data with those calculated from a van der Waals equation of state [18], using handbook (gas phase) values for the van der Waals parameters. One finds s_0 = 0.85 km/s, s_1 = 1.86, and s_2 = .0057, whereas the nonlinear fit to the data, given in Table 1, results in s_0 = .973 km/s, s_1 =1.923, and s_2 = -0.079 s/km. The van der Waals EOS has a term corresponding to a dipole attraction, but the repulsive part is hard-sphere, just as for an ideal gas; this leads to a positive rather than negative s_2. The value of s_2 obtained from the data results in softening of the Hugoniot as one goes to higher compression, whereas a hard-sphere repulsion gets stiffer; thus the van der Waals equation of state does not properly model high shock compressions. This softening of the potential for Argon has been previously noted [19-21].

In the case of iron, we have considered only data above the phase transition at 12.5 GPa, whereas the "handbook" data are for normal iron. Thus, we should not be too surprised to find that the parameters we obtain for the potentials do not agree with those derived from handbook data. It is interesting to note, however, that the well depth above the transition in all cases appears lower than the standard value.

CONCLUSIONS

Realistic potentials for condensed matter are more complicated than those we have considered, particularly those accurate at small average interatomic spacing. Nevertheless, simple analytic potentials are a useful starting point for many calculations, and are all that it is presently feasible to use in others. The potential parameters obtained from nonlinear Hugoniots provide a best fit to behavior from zero compression up to factors of two or more compression; deviations from the values obtained from linear Hugoniots, which represent data at low compressions, provide an indication of the range in which simple potentials are useful.

REFERENCES

1. J.E. Jones and A.E. Ingham, Proc. Roy. Soc. (London) **A107** (1925) 636
2. H.S.W. Massey and R.A. Buckingham, Proc. Roy. Soc. **A168** (1938) 378
3. P.M. Morse, Phys. Rev. **34** (1929) 57
4. J.H. Rose, J.R. Smith, F Guinea, and J Farrnte, Phys.Rev. **B29** (1984) 2963
5. J. H. Rose, J. Ferrate, and J.R. Smith, Phys. Rev. **B28** (1983) 1835
6. Rice, M. H., McQueen, R. G., and Walsh, J. M., in *Solid State Physics*, vol. 6, F. Seitz and D. Turnbull, eds., Academic Press, New York, N.Y., 1958
7. Pastine, D. J., and Piacesi, D., J. Phys. Chem. Solids **27**, 1783-1792 (1966)
8. Ruoff, A. L., J. Appl. Phys. **38**, 4976-4980 (1967)
9. E.N. Avrorin, B.K. Vodolaga, L.P. Volkov, A.S. Vladimirov, V. A. Simonenko, and B.T. Chernovolyuk, JETP Lett. **31** (1980) 685
10. Charles E. Ragan III, Phys. Rev. A **25** (1982) 3360
11. V.A. Simonenko, N.P. Voloshin, A.S. Vladimirov, A.P. Nagibin, V.N. Nogin, V.A. Popov, V.A. Vasilenko, and Yu.A. Shoidin, Sov.Phys. JETP **61** (1985) 869
12. R.F. Trunin, M.A. Podurets, L.V. Popov, B.N. Moiseev, G.V. Simakov, and A.G. Sevast'yanov, JETP **76** (1993) 1095
13. A.C. Mitchell, W.J. Nellis, J.A. Moriarity, R.A. Heinle, N.C. Holmes, R.E. Tipton, and G.W. Repp, J. Appl. Phys. **69** (1991) 2981
14. Yuan Gu, Size Fu, Jiang Wu, Songyu Yu, Yuanlong Ni, and Shiji Wang, Laser and Particle Beams **14** (1996) 157
15. T.R. King and J.H. Shively, *Shock Compression of Condensed Matter - 1995*, 47, AIP Conference Proceedings 370, AIP Press, Woodbury, NY, 1996
16. R.G. McQueen, *High Pressure Equations of State: Theory and Applications*, Proceedings of the International School of Physics "Enrico Fermi", Course CXIII, North-Holland, Amsterdam, 1991, p. 118
17. P. Boogerd, H.J. Verbeek, M. Stuivinga, and A.C. van der Steen, J. Appl. Phys. **78** (1995) 5335
18. T.R. King and J.H. Shively, to be published
19. M. van Thiel and B.J. Alder, J. Chem. Phys. **44** (1965) 1056
20. Marvin Ross, J. Chem. Phys. **73** (1980) 4445
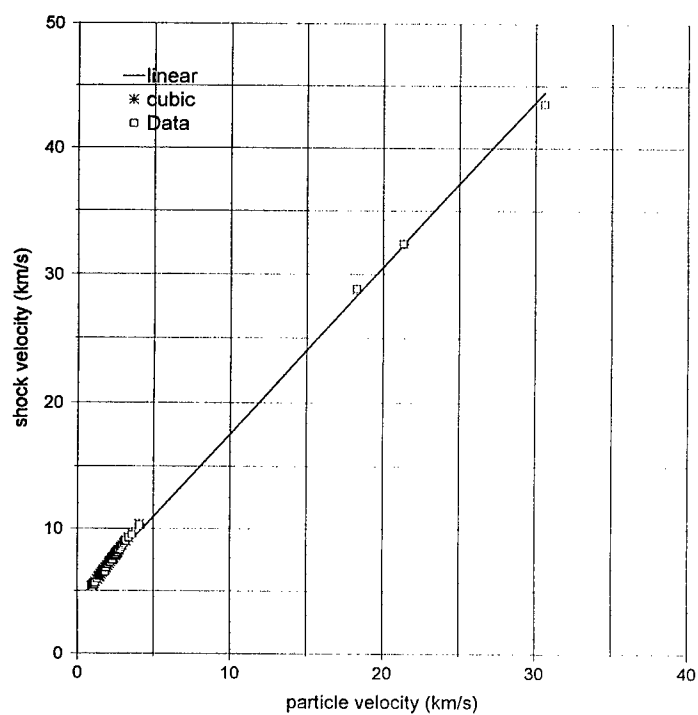21. M. Ross and F.H. Ree, J. Chem. Phys. **73** (1980) 6146

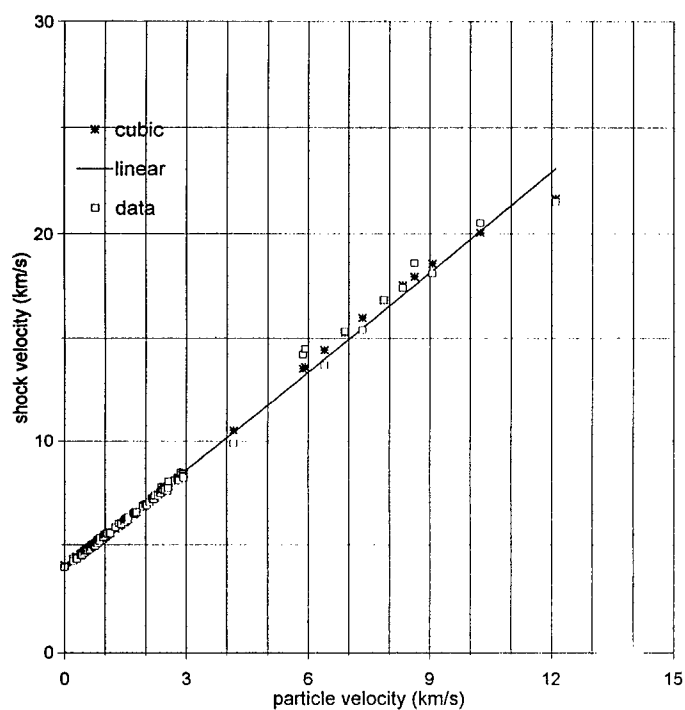Figure 1. Iron Hugoniot with linear and cubic fits to data.

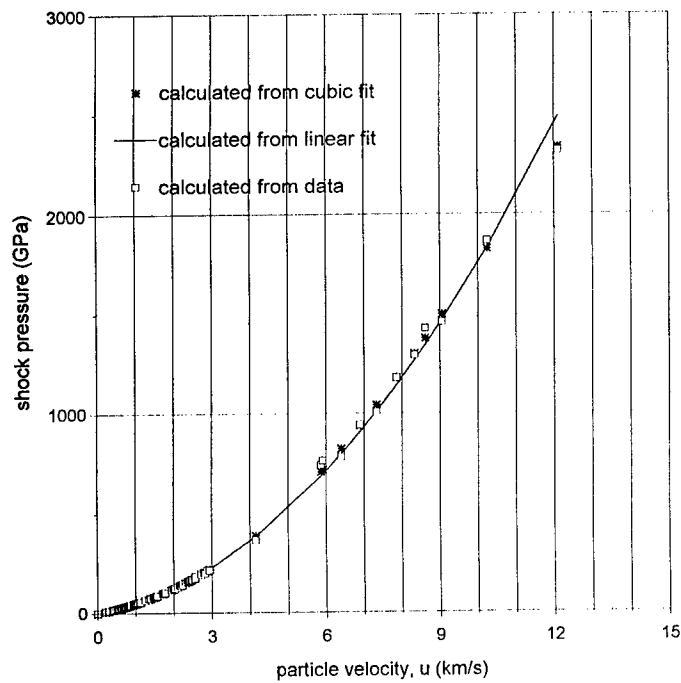Figure 2. Copper Hugoniot with linear and cubic fits to the data.

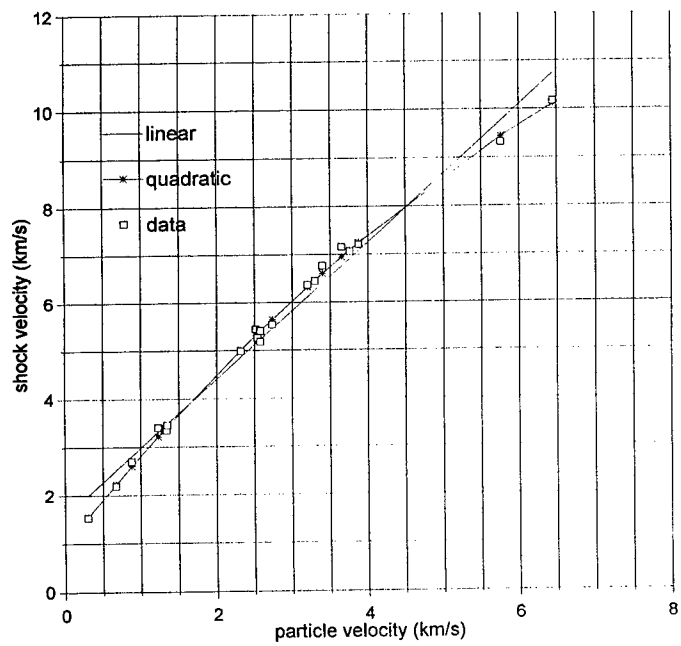Figure 3. Shock pressure in copper.

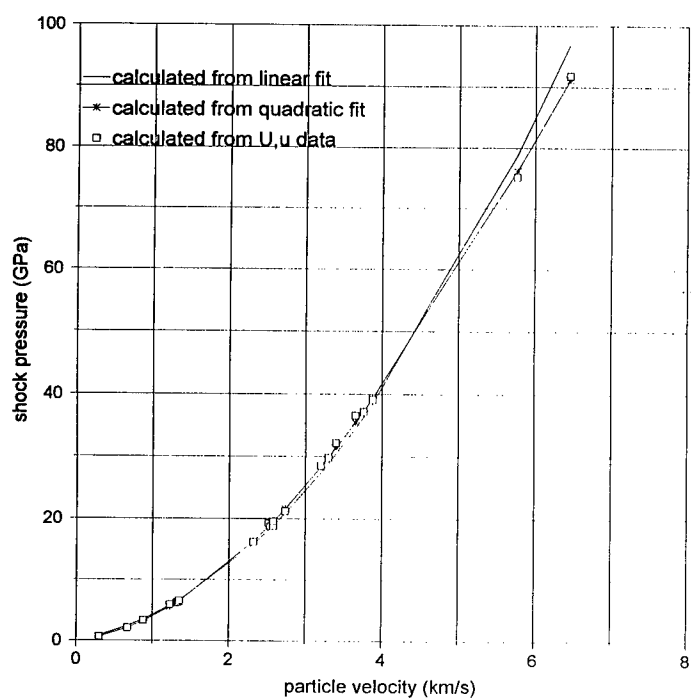Figure 4. Liquid argon data and fits to data.

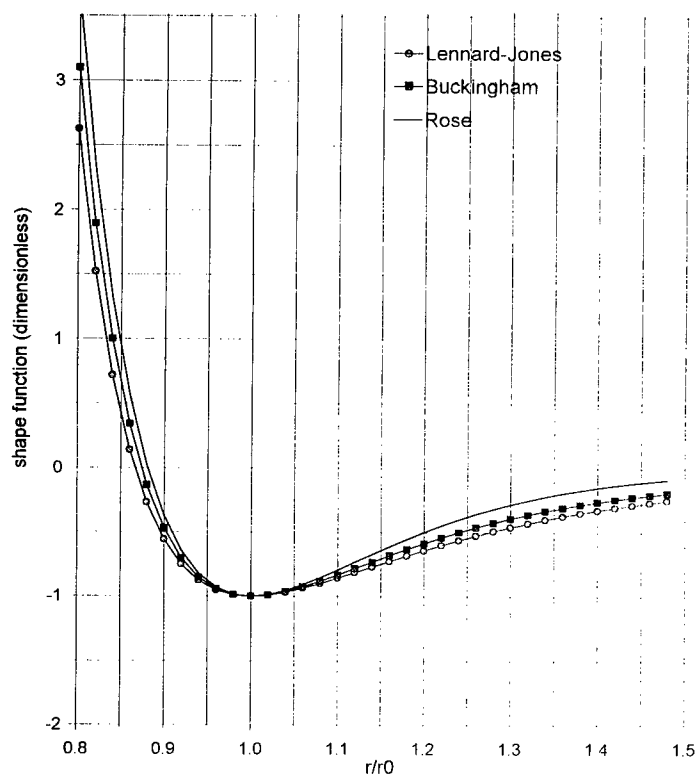Figure 5. Pressure versus particle velocity for liquid argon.

Figure 6. Shapes of Lennard-Jones, Buckingham, and Rose potentials for liquid argon.
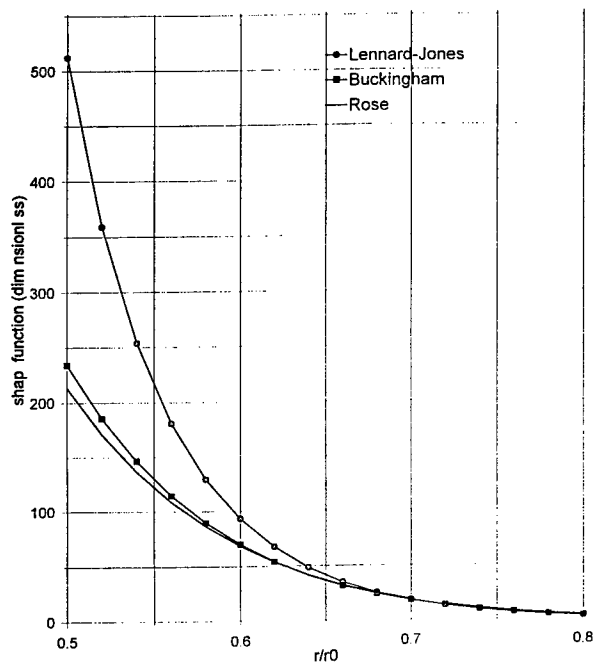
Figure 7. Potential shapes at very high compression.

Table 1. Hugoniot parameters for Aluminum, Iron, Copper, and liquid Argon. The standard error
in the coefficients is in all cases less than 10% at 90% confidence.

Material	s_0 (km/s)	s_1	s_2 (s/km)	s_3 (s^2km^{-2})
Al (linear)	5.603	1.187		
cubic	5.279	1.516	-0.080	0.008
Fe (linear)	4.475	1.306		
cubic	3.70	1.758	-0.0298	0.0005
Cu (linear)	3.816	1.592		
cubic	4.024	1.260	0.103	-0.007
sextic	3.795	1.942	-0.472	0.197
Ar (linear)	1.566	1.422		
quadratic	0.973	1.923	-0.079	NA

Table 2. Potential parameters for the Lennard-Jones potential. The first value in each cell is obtained
from a linear fit to the shock data; the second from a nonlinear fit to the data.

Material/ Parameters	Literature values	Linear fit	Polynomial fit
Copper			
E_0 (eV/atom)	3.5	4.8	2.3
n,m		6.6, 3.6	6, 3.6
Aluminum			
E_0 (eV/atom)	3.3	5.2	3.3
n,m		5.7, 3.3	3.2, 2.5
Iron			
E_0 (eV/atom)	4.3	3.8	3.1
n,m		3.8, 3	7.5, 4.8

Table 3. Parameters for the Morse potential, obtained by fitting shock data, compared with values from the literature.

	Literature	*Linear Fit*	*Polynomial Fit*
Copper			
α (nm)	0.136	0.17	0.12
E_0 (eV/atom)	3.5	1.7	3.6
Aluminum			
α (nm)	0.12	0.14	0.10
E_0 (eV/atom)	3.3	1.7	3.8
Iron			
α (nm)	0.14	0.13	0.2
E_0 (eV/atom)	4.3	1.1	3.4
Argon			
α (nm)		0.14	0.19
E_0 (eV/atom)		0.083	0.013

Table 4. Buckingham exp-6 potential.

	Literature	*Linear Fit*	*Polynomial Fit*
Copper			
α (nm)		9.28	8.16
E_0 (eV/atom)	3.5	1.6 eV	2.6 eV
Aluminum			
α (nm)		8.9	8.05
E_0 (eV/atom)	3.3	1.6 eV	1.9 eV
Iron			
α (nm)		8.26	10.3
E_0 (eV/atom)	4.3	2.42 eV	0.96 eV
Argon			
α (nm)	13.2	8.54	11.7
E_0 (eV/atom)		0.072 eV	0.015 eV

Table 5. Potential parameters for the Rose potential.

	Literature	*Linear Fit*	*Polynomial Fit*
Copper			
r_{wse} (nm)	0.14	0.14	0.14
l (nm)	0.027	0.022	0.031
E_0 (eV/atom)	3.5	2.1	4.5
Aluminum			
r_{wse} (nm)	0.16	0.16	0.16
l (nm)	0.034	0.026	0.038
E_0 (eV/atom)	3.3	2.1	4.1
Iron			
r_{wse} (nm)	0.14	0.141	0.141
l (nm)	0.027	0.026	0.019
E_0 (eV/atom)	4.3	4.5	1.28
Argon			
r_{wse} (nm)	0.21	0.21	0.21
l (nm)	0.032	0.038	0.025
E_0 (eV/atom)		0.239	0.039

POSSIBLE DETECTION OF FAILURE WAVE VELOCITY USING HYPERVELOCITY PENETRATION EXPERIMENTS

A. A. KOZHUSHKO*, D. L. ORPHAL+, A. B. SINANI* and R. R. FRANZEN+

*Ioffe Physico-Technical Institute of the Russian Academy of Sciences, St. Petersburg 194021, Russia
+International Research Associates, Pleasanton, CA 94566, U.S.A.

Summary-- Data for projectile penetration of silicon carbide (SiC) from two types of experiments are combined. For impact velocities, v, in the range 1.5 - 4.6 km/s the data are from reverse ballistic two-stage light-gas gun experiments with long tungsten rods. For impact velocities of about 5 - 7 km/s copper shaped charge jets are the projectile. The data exhibit an apparent inflection in the penetration velocity, u, versus impact velocity curve at $u \approx 3$ km/s, corresponding to $v \approx 4.5$ km/s. The apparent decrease in the slope of u versus v for $u = 3$ km/s, and the consequent rapid increase in the Alekseevskii and Tate target resistance term R_t with v is tentatively interpreted in terms of a failure wave in SiC. With this interpretation the propagation speed of the failure wave in SiC is about 3 km/s or 1/3 of the compressional wave speed. © 1999 Elsevier Science Ltd. All rights reserved.

NOTATION

d	rod diameter
L	rod length
L_c	length of "consumed" rod ($= L - L_r$)
L_r	length of remaining rod
p	penetration depth
r	correlation coefficient for least squares fit
R_t	Target resistance term in Tate-Alekseevskii equation
S_i	shorting gages
u	penetration velocity ($= dp/dt$)
v	impact velocity
v_c	speed of rod "consumption" ($= dL_c/dt$)
Y_p	term in Tate's equation for strength of penetrator
ρ_p	rod density
ρ_t	target density

INTRODUCTION AND BACKGROUND

Kanel, et al. [1] reported detection of a failure wave in K19 glass in plane shock experiments. Brar, et al. [2] report similar experiments and results for soda lime glass. Bless, et al. [3] report direct observation of a failure wave in Pyrex glass rods impacted by steel plates at velocities of about 200 m/s. The detailed characteristics of the observed failure waves are far from understood. The results in the papers cited suggest that the

material behind the failure wave front has zero tensile strength, significantly reduced shear strength and reduced impedance. Bless, et al. [3] suggest that the material behind the failure wave front is comminuted and this appears consistent with the framing camera photographs they report.

In this paper we report the possible detection of a failure wave in silicon carbide (SiC) penetrated by high velocity projectiles. Our suggestion of a failure wave in SiC is based on combining data from two types of experiments. The first type experiment involves penetration of SiC by long tungsten rods at impact velocities from about 1.5 to 4.6 km/s. The second type experiment involves the penetration of SiC with copper shaped charge jets with impact velocities from about 5 to 7 km/s. When these two sets of data are combined there appears to be a change in the slope of the penetration velocity, u, versus impact velocity, v, curve at a penetration velocity of about 3 km/s. We suggest that this inflection in the u-v curve may be the result of a failure wave in SiC.

TWO-STAGE LIGHT-GAS GUN EXPERIMENTS
($1.5 \leq v \leq 4.6$ km/s)

The two-stage light-gas gun experiments are described in detail by Orphal and Franzen [4]. The twenty-seven experiments were performed in the reverse ballistic mode. That is, the confined SiC target was launched from the gun and impacted against a stationary tungsten rod penetrator. The pure (99.95%) tungsten (ρ_p = 19.2 g/cm^3) penetrators were right circular cylinders. The penetrator diameter was 0.762 mm (0.030 inch). For impact velocities $v \leq 4.2$ km/s the ratio of the penetrator length to diameter was L/d = 20. For the tests in which $v > 4.2$ km/s the penetrator was L/d = 15. All impacts were normal and at zero yaw.

Figure 1 shows the confined ceramic targets used in the experiments. The targets were cylindrical. The target with a 38.1 mm (1.5 inch) long ceramic was used for experiments with $v > 4.2$ km/s. The ratio of the diameter of the ceramic (23.6 mm) to the diameter of the penetrator was about 31. The titanium sleeve added additional radial confinement. Finally, the targets were contained in a cylindrical lexan sabot of 38 mm outer diameter, the diameter of the launch tube. Examination of the flash x-rays from these experiments reveals no measurable radial expansion of the targets. Therefore we believe these targets represent a "well-confined" ceramic. In all tests the penetrator was completely eroded and the final hole formed well within the ceramic.

The SiC was hot-pressed ("pressure assisted densified") by CERCOM, Inc. The density (ρ_t) was 3.22 g/cm^3. The hardness (45N) was 92. Typical grain size was about 2 microns.

The primary data from each test are four flash x-rays showing the penetrator in the process of penetrating the target (Fig. 2). Each x-ray shows both the target and a fixed spatial fiducial. The time between each x-ray pulse is known to within less than a microsecond. Thus both the impact velocity and the time of impact can be calculated. The target velocity was also independently measured using two uprange continuous x-rays. The velocities determined by these two methods were always in excellent agreement, typically within 1%.
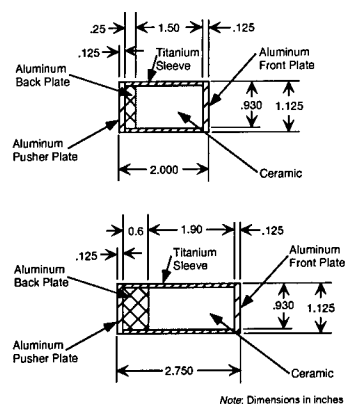
Fig. 1. Confined SiC targets used for reverse ballistic tests
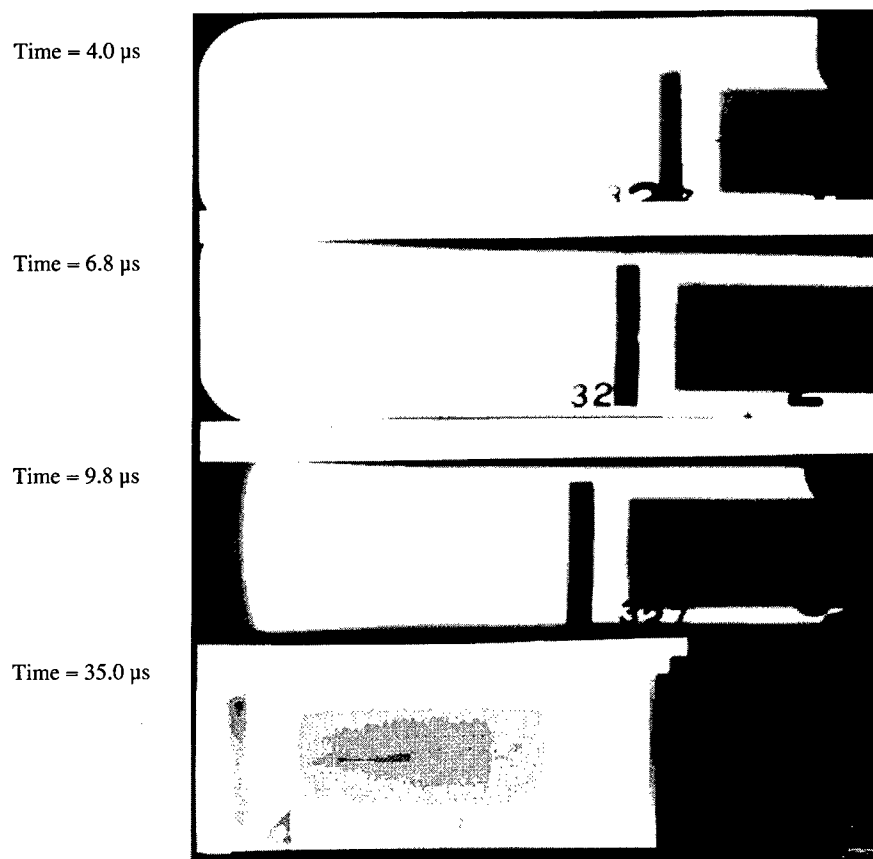

Fig. 2. Flash X-rays from Test 327 showing long tungsten rod penetrating confined SiC at four different times (impact velocity = 3.445 km/s).

The depth of penetration, p, is measured in each x-ray. One X-ray was taken at very late time to determine final penetration. Plots of penetration depth versus time for the other three X-rays and the (0,0) point are well fit by straight lines (Fig. 3). The penetration is steady-state. The penetration velocity, u, is defined as the slope of such a straight line fit, i.e. $u = dp/dt$ = constant. The length of the remaining rod, L_r, is also measured in each x-ray. Plots of the eroded or consumed rod length, $L_c = L - L_r$, versus time are also well fit with straight lines. The "consumption velocity", v_c is defined as $v_c = dL_c/dt$. Measured values for u and v_c along with the corresponding impact velocity, v, are given in Table 1.

Test 327

Diameter = 0.762 mm	Length = 15.210 mm	L/D = 19.96

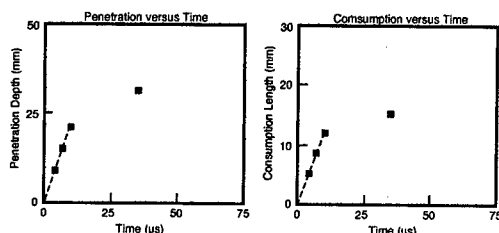| Time (µs)	Penetration (mm)	Cons. Length (mm)	Impact Velocity = 3.445 (km/s)
0.0	0.0	0.0	µ = 2.189 km/s
4.0	9.1	5.1	4 points, Corr. Coeff. = 0.9999
6.8	15.0	8.3	
9.8	21.5	11.9	vc = 1/210 km/s
35.0	31.4	15.2	4 points, Corr. Coeff. = 0.9997

Fig. 3. Summary of typical test data

Table 1. Light-Gas Gun Test Data

Test No.	Impact Velocity v, km/s	Penetration Velocity u, km/s	Consumption Velocity vc, km/s
321	2.532	1.431	1.094
325	2.467	1.325	1.042
326	3.003	1.839	1.067
327	3.445	2.189	1.210
328	1.979	1.094	0.833
329	3.541	2.290	1.170
330	3.943	2.675	1.184
331	4.405	3.020	1.351
333	4.611	3.022	1.503
335	1.521	0.604	0.833
336	1.800	0.885	0.814
337	1.800	0.936	0.752
338	2.780	1.640	1.070
339	3.296	2.016	1.196
340	1.652	0.817	0.730
341	1.659	0.785	0.747
342	1.517	0.753	0.733
343	2.248	1.223	0.995
345	4.243	2.807	1.398
357	2.031	1.082	0.898
358	2.691	1.645	0.939
359	3.168	1.904	1.218
360	3.787	2.391	1.439
361	3.706	2.419	1.294
364	3.180	1.914	1.181

SHAPED CHARGE JET EXPERIMENTS
(5.0 ≤ v ≤ 7.2 km/s)

These experiments were performed by Kozhushko, et al. [5]. The projectile in these six experiments was a copper jet formed by a shaped charge. The targets were SiC tiles of 60 mm X 60 mm plane dimension. The thickness of the tiles varied from 10 to 20 mm. The density, Young's modulus, and microhardness of the SiC were 3.0 g/cm^3, 330 GPa and 25-30 GPa, respectively.

The velocity of a shaped charge jet varies along its length. This somewhat complicates defining the impact velocity, v, and penetration velocity, u. The basic experiment geometry is shown in Figure 4. The copper "cover plate" was used to erode that part of the jet preceding the part with the desired impact velocity on the SiC. Arrival times at the face and rear of the copper cover plate were measured with shorting gages (S$_1$ and S$_2$) and provide an average penetration velocity of the copper jet through the cover plate. This average velocity corresponds to the penetration velocity of the jet at the mid point of the copper plate. This velocity was extrapolated to the Cu/SiC interface, U$_{cu(int)}$, using the dependence of Cu jet penetration velocity versus depth obtained for copper using the same charge and stand-off distance in separate experiments. The impact velocity on the face of the SiC tiles was taken as v$_1$ = 2 u$_{cu(int)}$. Arrival times at the face and rear of the SiC were also measured with shorting gages (S$_2$ and S$_3$) and provided an average penetration velocity, u, of the jet through the SiC tile. Finally the difference in arrival times at shorting gages S$_3$ and S$_4$ provided the velocity of the front of the jet exiting the target, v$_2$. For analysis, the impact velocity, v, associated with the penetration of the SiC is taken as the average v = (v$_1$+v$_2$)/2.
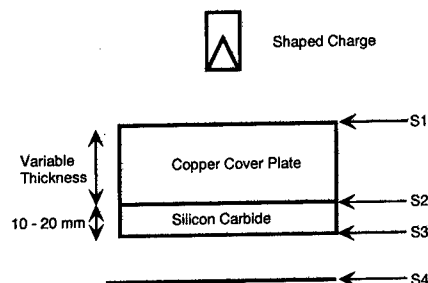

Fig. 4. Schematic of shaped charge experiments

Since the variation of velocity along the length of a jet is not exactly linear and also will vary slightly from test to test, the impact velocity for the shaped charge experiments is not known with the same precision as in the light-gas gun tests. The jet was observed using flash x-rays just before impact with the target and just after exit from the target. In all cases the jet was continuous. The results from the six experiments are:

Table 2. Impact and Penetration Velocity from Shaped Charge Experiments

Test No.	1	2	3	4	5	6
v (km/s)	5.0	5.15	5.2	6.7	7.07	7.17
u (km/s)	2.9	3.1	3.0	3.8	4.05	4.0

ANALYSIS

Figure 5. shows the normalized penetration velocity, $u[1 + (\rho_t/\rho_p)^{1/2}]$ versus impact velocity for both sets of experiments. The penetration velocity was normalized to account for differences in projectile density (tungsten = 19.2 g/cm^3, copper = 8.9 g/cm^3) and SiC density (3.22 g/cm^3 for the light-gas gun tests and 3.0 g/cm^3 for the shaped charge tests). The data appear to exhibit a change in slope at about v = 4.5 km/s and

$u[1 + (\rho_t/\rho_p)^{1/2}]$ = 4.3 km/s. A linear least squares fit to each of sets of data gives:

Light-gas gun data

$$u[1 + (\rho_t/\rho_p)^{1/2}] = -0.719 + 1.101v \quad (km/s)$$ (r = 0.9974)

Shaped charge data

$$u[1 + (\rho_t/\rho_p)^{1/2}] = 0.620 + 0.804v \quad (km/s)$$ (r = 0.9932)

where r is the correlation coefficient. These least squares fits are also shown in Fig. 5. The difference in slopes of these two fits is statistically significant at the 99% confidence level. The intersection of these two curves is v = 4.51 km/s, corresponding to $u[1 + (\rho_t/\rho_p)^{1/2}]$ = 4.24 km/s or u ≈ 3 km/s.
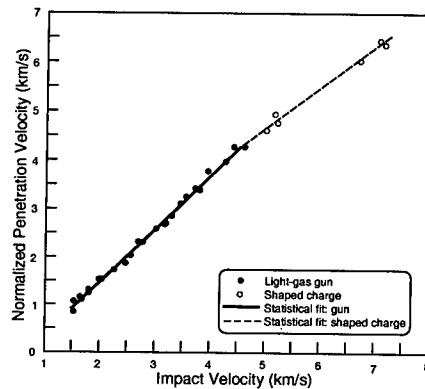
Fig. 5. Normalized penetration velocity versus impact velocity for silicon carbide

It is of interest to examine these data in the context of Alekseevskii's [6] and Tate's [7] models for long rod penetration. These researchers proposed modifying Bernoulli's equation for the steady-state pressure at the projectile target interface by adding the scalar

terms R_t, the target resistance to penetration, and Y_p, the strength of the projectile. Their modified Bernoulli equation is:

$$1/2 \, \rho_p \, (v\text{-}u)^2 + Y_p = 1/2 \, \rho_t \, u^2 + R_t \tag{1}$$

Solving for R_t,

$$R_t = 1/2 \, \rho_p \, (v\text{-}u)^2 - 1/2 \, \rho_t \, u^2 + Y_p \tag{2}$$

The experimental data reported here can be used to calculate R_t with $Y_p = 2$ GPa for the light-gas gun experiments [4] and with $Y_p = 0$ for the shaped charge experiments. Furthermore, for the light-gas gun experiments we use the experimentally measured values for v_c, the projectile consumption velocity, instead of the ideal quantity (v-u) of equations (1) and (2). Using these values, the results for R_t as a function of impact velocity are shown in Figure 6. Figure 7 shows R_t versus the penetration velocity, u. Figure 7 makes evident the dramatic increase of R_t for u > 3 km/s.
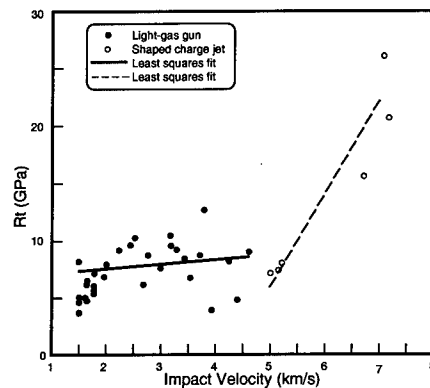
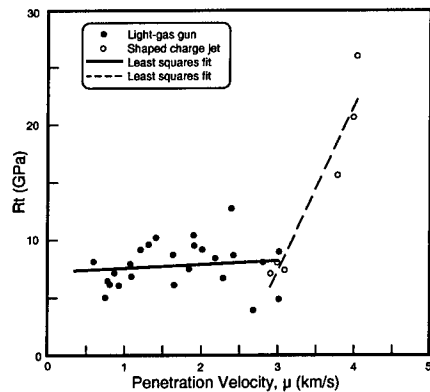Fig. 6. The target resistance, Rt, versus impact velocity for silicon carbide

Fig. 7. The target resistance, Rt, versus penetration velocity for silicon carbide

There is significant scatter in the data for v ≤ 5 km/s. Nevertheless, it is evident that for the light-gas gun data R_t ≈ constant ≈ 5 - 9 GPa. A linear least squares fit to the light-gas gun data gives:

$$R_t \text{ (GPa)} = 6.64 + 0.416 \text{ v (km/s)} \qquad (r = 0.200)$$

$$R_t \text{ (GPa)} = 7.18 + 0.377 \text{ u (km/s)} \qquad (r = 0.142)$$

where r is the correlation coefficient. An r = 0.200 and 0.142 means that there is essentially no dependence of R_t on v or u for the light-gas gun data.

For the shaped charge data at 5.0 ≤ v ≤ 5.2 km/s R_t is 7 - 8 GPa, basically consistent with the light-gas gun data. However, for the shaped charge data R_t appears to increase very rapidly with impact velocity in the range 5.0 ≤ v ≤ 7.2 km/s. At v ≈ 7 km/s R_t ~ 20 GPa or even higher. The estimated error on R_t for the shaped charge experiments is about ± 20% [5]. A linear least squares fit to the shaped charge data gives

$$R_t \text{ (GPa)} = - 30.2 + 7.329 \text{ v (km/s)} \qquad (r = 0.945)$$

$$Rt \text{ (GPa)} = -35.97 + 14.421 \text{ u (km/s)} \qquad (r = 0.955)$$

A correlation coefficient of r = 0.945 and 0.955 means R_t for the shaped charge experiments strongly correlates with the impact velocity and the penetration velocity.

DISCUSSION

Unfortunately the data from the light-gas gun tests and the shaped charge tests do not overlap in impact velocity, although they nearly do with the highest velocity light-gas gun test at 4.6 km/s and the lowest velocity shaped charge test at 5 km/s. The experiments do overlap in penetration velocity as shown in the plot of R_t versus penetration velocity, u, (Fig. 7). It is possible that the apparent change in the slope of penetration velocity versus impact velocity (Fig. 3) is due to differences in the two types of experiments, although we do not believe this to be the case. Such differences include, but are not limited to: 1) target confinement, although the radial or lateral dimension of the targets was very large compared to the diameter of the rod penetrator or the shaped charge jet, 2) differences in SiC material, and 3) the methods used to determine the impact and penetration velocities. Effects of such differences on the relationship of u and v cannot be entirely ruled out. Higher velocity light-gas gun experiments could be performed, using smaller, lighter targets to resolve this question.

At this time we propose an interpretation of the data in terms of a failure wave in the SiC. Specifically we propose that the inflection of the u versus v data at about v = 4.5 km/s, corresponding to a penetration velocity of about u ≈3 km/s, reflects the effect of the projectile penetrating the SiC faster than the failure wave velocity. Thus for v = 4.5 km/s and u = 3 km/s the projectile penetrates undamaged or relatively undamaged SiC. This is why R_t rapidly increases in the range 5 ≤ v ≤ 7 km/s to approach a value

corresponding to the microhardness of the virgin ceramic. If this interpretation of the data is correct the speed of the failure wave in SiC must be approximately 3 km/s. This is about 1/3 of the compressional wave speed. This is consistent with estimates of the speed of failure waves by Kanel, et al. [1], Brar, et al. [2] and Bless, et al. [3], although these authors suggest that the speed of the failure wave may not be constant. Many researchers have proposed that the maximum speed for crack propagation is the Rayleigh wave speed. The Rayleigh wave speed would then be an upper bound for the failure wave speed. The Rayleigh wave speed for SiC is about 6.4 km/s or about twice the penetration velocity observed here for the inflection in the u - v curve.

Careful examination of the X-rays from the light-gas gun experiments does not reveal any obvious visible evidence of a failure wave in SiC. Therefore our interpretation of the inflection in the u-v curve in terms of a failure wave must be considered preliminary.

REFERENCES

1. G. I. Kanel, S. V. Rasorenov and V. E. Fortov, The failure wave and spallations in homogeneous brittle materials, Shock Compression of Condensed Matter (1991) (edited by S. C. Schmidt, et al.), North Holland Press.

2. N. S. Brar, Z. Rosenberg and S. J. Bless, Spall strength and failure waves in glass, Proceedings: Third Congres International sur le Comportement Mechanique et Physique des Materiaux sous Sollicitations Dynamiques, Strasbourg, October 1991.

3. Stephan J. Bless, N. Singh Brar, Gennady Kanel and Zvi Rosenberg, Failure waves in glass, *J. Am. Ceram. Soc.* **75**, 1002-1004 (1992).

4. D. L. Orphal and R. R. Franzen, Penetration of confined silicon carbide targets by tungsten long rods at impact velocities from 1.5 to 4.6 km/s, *Int. J. Impact Engng.* **19**, 1-13 (1997).

5. A. A. Kozhushko, I. I. Rykova and A. B. Sinani, Resistance of ceramics to projectile penetration at high interaction velocities, *Fizika Goreniya I Vzryva* **28**, 89-93 (1992).

6. V. P. Alekseevskii, Penetration of a rod into a target at high velocity, *Fizika Goreniya i Vzryva* **2**, 99-106 (1966).

7. A. Tate, A theory for deceleration of long rods after impact, *J. Mech. Phys. Solids* **15**, 387-399 (1967).

RELATION BETWEEN SPALL STRENGTH
AND MESOPARTICLE VELOCITY DISPERSION

A. M. KRIVTSOV

St.-Petersburg State Technical University, Department of Theoretical Mechanics, Po-
litechnicheskaya Street 29, 195251 St.-Petersburg, Russia. E-Mail: krivtsov@mail.wplus.net

Summary — From the plate impact experiments there were found out that the maximum
spall strength corresponds just to the tests where the mesoparticle velocity dispersion is also
maximum. In the paper computer investigation of this phenomenon is presented. Molecular
dynamics method is used. It is shown that increase of the initial dispersion from zero to
15–25 m/s leads to the essentially increase of the material strength. The further increase of the
initial dispersion leads to the slow decrease of the material strength, so the strength-dispersion
characteristic has maximum. © 1999 Elsevier Science Ltd. All rights reserved.

INTRODUCTION

Impact loading of a plate target by a plate impactor from the same material is considered.
The review articles [1, 2] provide access to most of the literature on this subject. The basic
characteristics that can be measured in real time in spall fracture experiments are average
velocity and dispersion of mesoparticle velocities on the free surface of the target [3, 4]. From
real experiments it is known [4] that mesoparticle velocity dispersion appears to characterise
an ability of the material to relax microstresses during the shock wave passage; and, thereby,
it defines the macroscopic dynamic strength of material. The greater the mesoparticle ve-
locity dispersion — the greater is the spall strength of the material. In the present paper,
computer investigation of this phenomenon is presented. The simple molecular dynamics
method is used [5, 6, 7]. The main distinction of the considered method from classic molecu-
lar dynamics is that the particles are interpreted not as atoms or molecules but as elements
of the mesoscopic scale level. This approach shows a strong influence of mesoparticle velocity
dispersion on the spall strength of material even for the simplest computation scheme.

METHODS

Since the purpose of this study is to understand the strength–dispersion relation generi-
cally, for molecular dynamics simulation a monoatomic two-dimensional lattice with standard
Lennard-Jones 6–12 potential was chosen [6] as shown in (1)

$$U(r_{ij}) = \epsilon \left[\left(\frac{r_0}{r_{ij}} \right)^{12} - 2 \left(\frac{r_0}{r_{ij}} \right)^6 \right] , \qquad (1)$$

where $U(r_{ij})$ is the interaction energy between atoms i and j separated by distance r_{ij}, ϵ is the strength of the interaction, and r_0 is a characteristic length scale. In order to decrease calculation time, the potential is usually truncated at a finite distance, beyond which the interaction is taken to be zero. In the considered numeric experiments the cut-off distance was chosen to be $2.1\,r_0$. In this case, the interaction potential has contributions from the first, second, and third nearest particles in the perfect crystal. However, the contribution of the second and the third neighbours to the total energy are minimal. Hence, r_0 is approximately the equilibrium, nearest-neighbour atomic separation. In order to describe nonelastic losses of energy small dissipative forces proportional to the particles velocities were added [8]. The simulation technique employed in this work is standard molecular dynamics method [5, 6, 9]: the trajectories of each atom are followed through time by integrating Newton's classical equations of motion. The integration is performed using the method of central differences [6]

The computational model is presented in Fig. 1. The particles are arranged in two rectangles lying in the xz plane. The rectangles represent the cross-sections of the impactor (black) and the target (grey). Initially the particles are arranged on a triangular lattice.
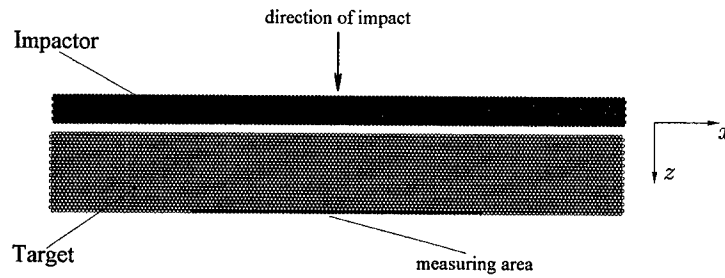

Fig. 1: The initial state of the pattern.

The lattice is orientated in such way that one of the sides of the triangles is extended along the x direction. The impactor is placed at an initial distance from the target greater than the cut-off distance of the interparticle potential. Both impactor and target are made from the same particles arranged on the same crystal lattice. The total number of particles in Fig. 1 is about 5000. Free boundary conditions on all boundaries were used.

Initially the target has zero velocity, the impactor has velocity directed along the z axis towards the target (see "direction of impact" in Fig. 1). In addition to the initial velocity of each particle a random velocity was added which was chosen from a two-dimensional random uniform distribution. Let us consider a set of particles indexed by $k = 1, 2, ..., n$. Denoting V_k as projections of the particle velocities to the direction of impact, the mean velocity $\overline{V}$ of the set in the impact direction is given by

$$\overline{V} = \frac{1}{n} \sum_{k=1}^{n} V_k \,. \tag{2}$$

The dispersion of the velocities is

$$\sigma = \frac{1}{n} \sum_{k=1}^{n} (V_k - \overline{V})^2 \,. \tag{3}$$

Further the square root of the dispersion will be used

$$\Delta V = \sqrt{\sigma} = \sqrt{\frac{1}{n} \sum_{k=1}^{n} (V_k - \overline{V})^2} \,. \tag{4}$$

The quantity ΔV is the mean square deviation of the velocities (further — the deviation) and it has the dimensions of velocity. Given that at the initial moment of time, the impactor and target have the same initial dispersion, σ_0, corresponding to the initial velocity distribution, then the initial deviation is $\Delta V_0 = \sqrt{\sigma_0}$. The aim of the presented computer experiments is to find out the dependence between the initial deviation and the strength characteristics of the material.

Let us note that if the particles are considered as elements of microscopic scale level — atoms or molecules, then the dispersion σ can be interpreted as the absolute temperature of the material. In our consideration, the particles correspond to elements of the meso-scopic scale level, The dispersion σ then corresponds to dispersion that is measured in real experiments [4] which differs from the classic temperature.

One of the main characteristics of the material strength is the spall strength [10] that is proportional to the spall (pull-back) velocity W. The spall velocity can be calculated from the time relation of the average velocity on the free surface [4, 10]. To find out the average velocity and other characteristics on the free surface we shall use the central part of the last particle row of the target (see Fig. 1, "measuring area"). The length of the area is one-half of the total row length to avoid boundary effects.

Another characteristic that will be used to describe the strength of the material is the width h of the spall crack in the impact direction — see Fig. 2. The technique of the crack
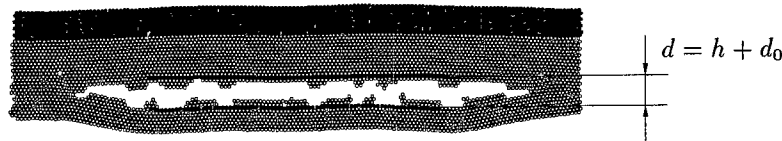

Fig. 2: Measuring of the width of the spall crack.

width measuring in the presented computer experiments as follows. Two rows — above and below the place were the crack appears — are selected in the initial state of the pattern. The averaged distance d_0 between the rows at $t = 0$ is measured. Then, during the experiment $(t > 0)$ the time relation of the averaged distance $d(t)$ is measured (Fig. 2). Then time dependence on the crack width can be obtained as

$$h(t) = d(t) - d_0 \,.$$

To avoid the boundary effects, only the central part of the rows (one-half of the total length) is used for measurement. In Fig. 2 the pattern with crack is shown — rows used for the measurement are coloured black. Note that the presented method can be used in the situation where there are a lot of small microcracks — in this case it gives the integral width of the microcracks.

RESULTS

To clarify our results, the same scales of time, distance and velocity in the computer calculations are used as in the real experiments with ductile steels [4]. We chose the following sizes: impactor thickness (z size) is 2 mm, target thickness is 7 mm, impactor width (x size) is 52 mm, target width is same with the impactor width. In Fig. 3–4 results of the computer experiments are presented. The pattern consists of about 5000 particles. All experiments

were performed with the same impactor velocity — 260 m/s. The initial velocity deviation ΔV_0 was varied from 0, 1, 2 to 100 m/s. Every row in Fig. 3–4 corresponds to some value of deviation. The first column shows the pattern state at $t = 4.1\,\mu s$ ($t = 0$ corresponds to the first contact between impactor and target). Note that the greatest crack size is realised at $\Delta V_0 = 0$. While the deviation increases, the crack width becomes smaller and at $\Delta V_0 = 25$ m/s crack completely disappears. The dispersion increase has absolutely prevented the spall fracture! When deviation ΔV_0 is in range of 25 – 40 m/s there is no spall fracture. For $\Delta V_0 > 40$ m/s the crack appears again and increases while the deviation grows. At deviation value of 100 m/s we can see fracture of the pattern produced with the high level of dispersion (this effect is analogous to temperature fracture).

The second column in Fig. 3–4 shows time dependence of the free surface velocity. The third column in Fig. 3–4 shows time dependence of the crack width h. Note that the deviation increase leads to a lowering of the crack width, especially for the times $t > 3\,\mu s$. For small deviations (0–2 m/s), the $h(t)$ dependence is monotonic. This means that the crack grows during all the time of measurement. For greater values of deviation the $h(t)$ dependence has one or two maximums after which the crack width decreases. Therefore we have the effect of recovering of the material — high level of dispersion stimulates relaxation processes.

Thus from the computer experiments it follows that a material with greater dispersion is stronger. Why is this so? To make it clear let us consider Fig. 5, where patterns are shown for two moments of time. The left column corresponds to $t = 1.4\,\mu s$, it is shortly after the time when the fracture starts. The right column shows the pattern state after the crack formation ($t = 4.1\,\mu s$). The rows, as it was before, correspond to the different values of the initial deviation ΔV_0.

From the first row of Fig. 5, note that when the deviation is absent ($\Delta V_0 = 0$) the crack borders are absolutely straight. When the deviation increases then the crack borders become more and more irregular (the right column). Now look to the left column to see how the fracture appears. For $\Delta V_0 = 0$ there is only one long crack, but for $\Delta V_0 = 4$ m/s we have a lot of short microcracks. Thus, the dispersion leads to smearing of the shock wave, and it is the reason why the strength increases. Note that at $\Delta V_0 = 20$–25 m/s the microcracks that are present at $t = 1.4\,\mu s$ disappear at $t = 4.1\,\mu s$. The small cracks can disappear spontaneously — this is one more reason for the strength increase.

The same experiments for the more complicated model containing about 20000 particles are shown in Fig. 6. The impactor velocity is 297 m/s. The results are similar, but effect of the strength increase is sharper: already at $\Delta V_0 = 9$ m/s no crack appears. The great values of dispersion, as it was for 5000 particles, decrease the material strength — the spall crack appears at $\Delta V_0 = 30$ m/s and became larger while ΔV_0 increases up to 100 m/s.

Experiments with 20000 particles produce better time relations for the free surface velocity — see the second column in Fig. 6. The form of the curves is in good agreement with results of real experiments and theoretical calculations [4, 11]. In the first four graphs ($0 \leq \Delta V_0 \leq 4$ m/s) after the first maximum of the velocity-time relation note the oscillations in the spall plate. Note that dispersion minimises the amplitude of the oscillations. After $\Delta V_0 = 9$ m/s there is no spall — and no oscillations in the spall plate. At these deviations a new maximum appears — the wave of compression that has reflected from the free surface of the impactor, crossed the whole width of the pattern, and appears at the free surface of the target. For the high values of dispersion ($\Delta V_0 \geq 40$ m/s) we have the spall again, and again it is possible to see the oscillations in the spall plate, but with very low amplitude. At $\Delta V_0 > 60$ m/s dispersion almost suppresses the oscillations.
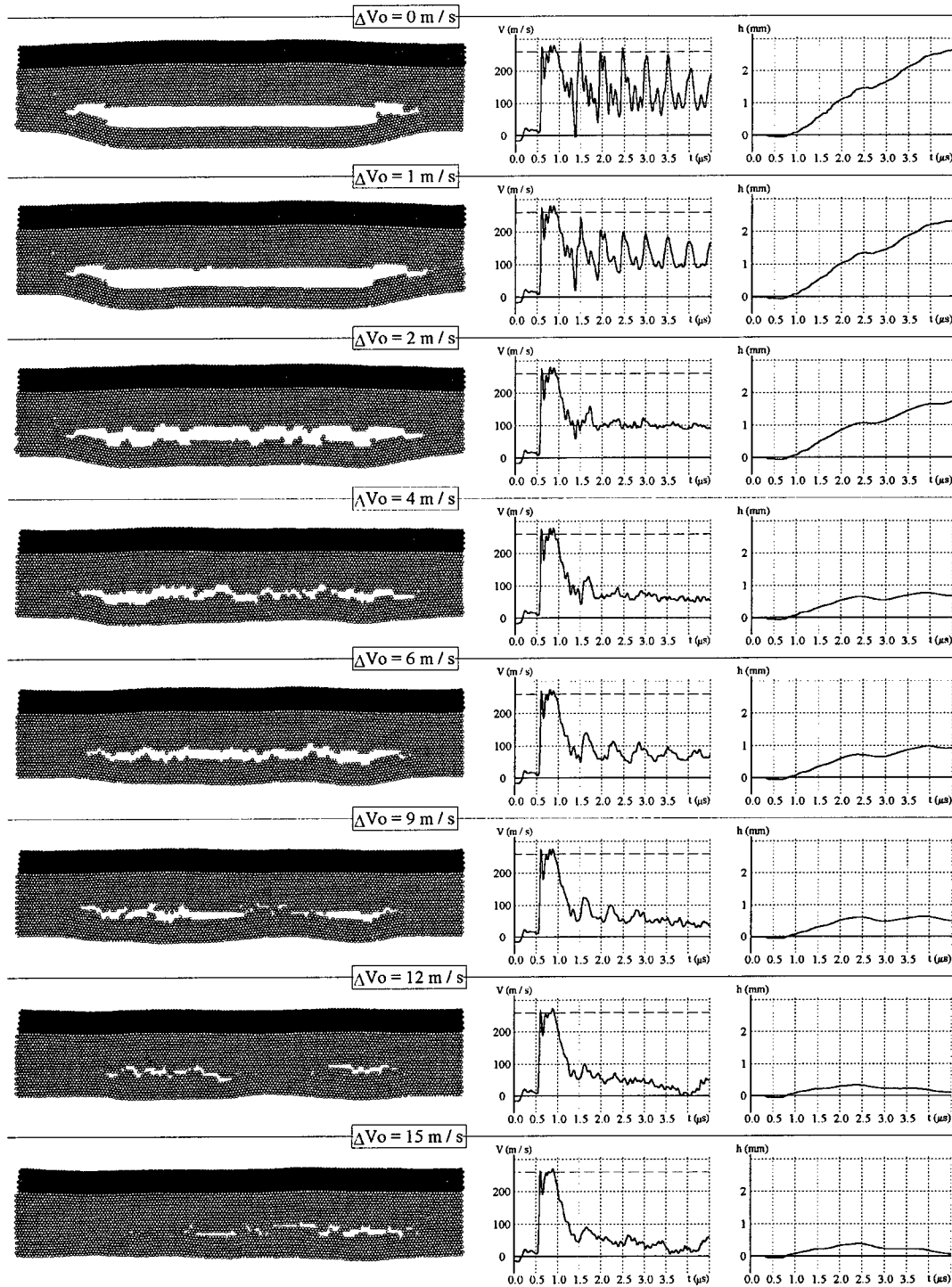
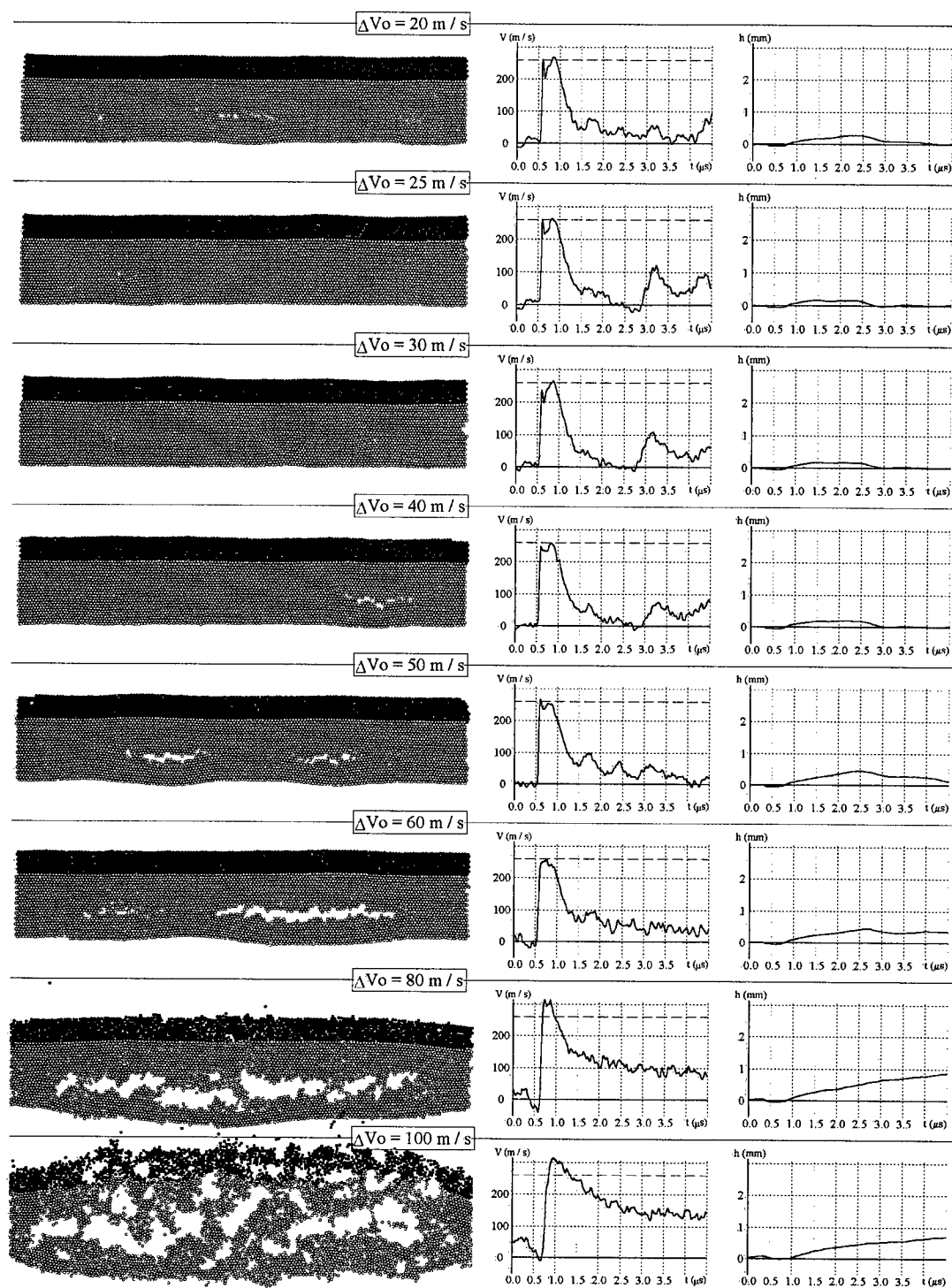Fig. 3: Computer results for $0 \leq \Delta V_0 \leq 15\,\mathrm{m/s}$, 5000 particles.

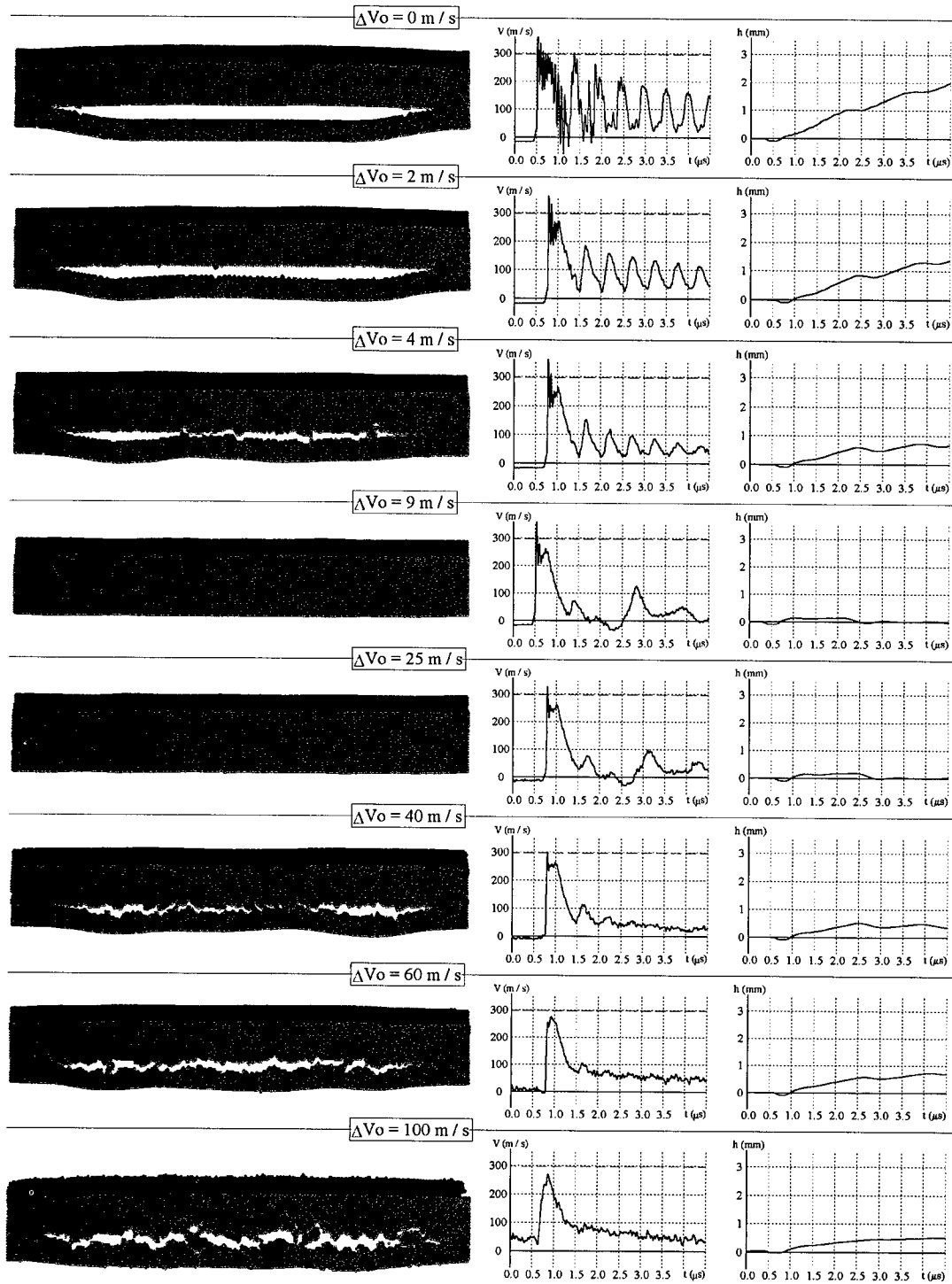Fig. 4: Computer results for $20\,\text{m/s} \leq \Delta V_0 \leq 100\,\text{m/s}$, 5000 particles.

Fig. 5: Comparison of the crack state at $t = 1.4\,\mu s$ (left) and $t = 4.1\,\mu s$ (right column)

Fig. 6: Computer results for $0 \leq \Delta V_0 \leq 100\,\text{m/s}$, 20000 particles.

STRENGTH DEPENDENCE ON THE INITIAL DEVIATION

Results of all the calculations are presented in Fig. 7 where the dependence of crack width, h, and spall velocity, W, on the initial deviation is shown. Fig. 7a corresponds to experiments with 5000 particles; Fig. 7b corresponds to experiments with 20000 particles. The curve marked $h(4.1\,\mu s)$ shows the width of the spall crack at $4.1\,\mu s$ after the first contact between impactor and target. Dots on the curves correspond to results obtained from the computer experiments. Note in Fig. 7a that the width of the spall crack sharply decreases from 2.6 mm (no initial dispersion) to zero at $\Delta V_0 = 20$ m/s. From $\Delta V_0 = 20$ m/s to $\Delta V_0 = 40$ m/s there is no spall. After $\Delta V_0 = 40$ m/s the crack width increases up to 0.8 mm. For the larger system (Fig. 7b) results are the same, but the crack width decreases faster and the area without spall is shifted to the left.

The curve marked $h(1.4\,\mu s)$ (white dots) corresponds to the time of the microcracks appearance (the fracture's beginning). This curve actually gives the integral width of the microcracks. This dependence has the same form of the previous results, but it has far less variation: the crack width $h(1.4\,\mu s)$ vary from the maximum value of 0.5 mm when there is no initial dispersion to the minimum value of 0.2 mm. So, the integral width of the microcracks is more than zero for all values of dispersion, but for big dispersions microcracks disappear after some microseconds — for deviations from 12 m/s to 54 m/s the white curve lies above the black one.

The curve marked W in Fig. 7 shows the spall velocity dependence on the initial deviation. Rememder that the spall (pull-back) velocity, W, is the difference between the first maximum and the first minimum on the time dependence of the free surface velocity [10]. The spall velocity is proportional to the spall strength of the material; it is one of the main strength characteristics that we can get from spall fracture experiments. From Fig. 7 note that W has a maximum at the same place where the width of the spall crack has a minimum. So the both criteria: the spall strength and the width of the spall crack give the same result. Note that to find the proper value of W, the time dependence of the free surface velocity was filtered to remove high-frequency oscillations.
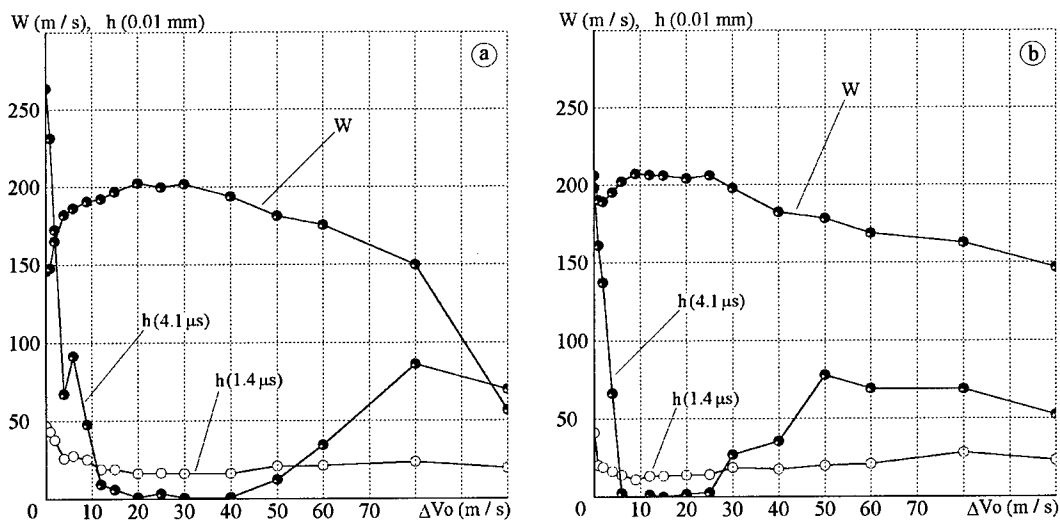

Fig. 7: The spall velocity W and the crack width h dependence on the initial deviation: experiments with a) 5000 particles, b) 20000 particles.

DISCUSSION

The presented computer simulations show that value of the initial velocity dispersion in the impact direction has a strong influence on the spall strength of material. From the analysis of the time relations of the spall crack shape it follows that there are two main reasons why the dispersion increases the material strength. The first is that dispersion reduces localisation of the shock fracture — the thickness of the fracture area is far greater when the dispersion is high. However, since the energy of the shock wave is the same, stresses in the fracture zone became far less. The second reason is that the dispersion stimulates relaxation processes in the material. The microcracks that are present at the beginning of the fracture can disappear after a few microseconds if the dispersion is high enough. These results of the computer calculations coincide with the results obtained from the real experiments with ductile steels and aluminum alloys [4, 12]. In particular in reference [4] it was shown that the mesoparticle velocity dispersion characterises the intensity of relaxation processes at the mesolevel and hence the material strength: if at the onset of spallation, the microstresses at the mesolevel have time to decrease due to relaxation processes, the material reveals the maximum possible dynamic strength.

From the computer calculations it follows that if the initial dispersion is very high, it leads to the opposite result — material strength decreases. In this case we have a situation analogous to the decrease of the material strength at high temperatures. For example, the recent spall fracture experiments with aluminum and magnesium showed precipitous drop in the spall strength of preheated samples as temperatures approached the melting point [13]. From the mesoscale point of view, high dispersion decreases the material density; the material became more porous and less stable.

The computer model used to obtain the considered results was very simple: ideal monoatomic lattice with Lennard-Jones potential. If we consider the particles as elements of microscopic scale level (for example, atoms), then the results can be interpreted in the other way: relation of dynamic strength of the monocrystal on the absolute temperature was obtained. If we consider the particles as elements of mesoscopic scale level, then instead of temperature we should use term "mesoparticle dispersion". Of course the considered model is very crude in its description of dynamic strength properties of real solids, but the obtained results are in good agreement with the real experiment results. Hence the presented model allows describing generically the strength–dispersion relation of the real solids. For exact results more complex models are desirable, but the main tendencies should be similar.

CONCLUSIONS

1. The computer experiments show that the increase of the initial dispersion from zero to 15–25 m/s leads essentially to an increase of the material strength. The further increase of dispersion leads to the slow decreasing of the material strength, so the strength-dispersion characteristic has maximum.

2. If the initial dispersion is close to zero, the fracture is localised in a very thin layer, and borders of the spall crack are absolutely straight. The dispersion increase produced increasing of the thickness of the fracture area, and the spall crack borders became irregular. Thus the dispersion leads to smearing of the shock wave.

3. If the dispersion is great enough, the small cracks can disappear spontaneously, so dispersion stimulates the relaxation processes in the material.

4. The criterion of the spall strength, obtained from the spall (pull-back) velocity gives the same result with the criterion of the spall crack width — maximum of the spall strength corresponds to the minimum (or absence) of the spall crack width. However the criterion of the spall crack width is far more sensitive.

These conclusions are obtained from the molecular dynamics simulation, and they are in a good agreement with the results obtained from the real experiments [4, 12, 13]. In particular, the plate impact experiments [4] with ductile steels show that the maximum spall strength corresponds to the tests with the maximum mesoparticle velocity dispersion; spall fracture experiments with aluminum and magnesium show drop in the spall strength as the temperature (dispersion) approached the melting point [13]; the impact experiments and the microstructure investigation [4, 12] show that the mesoparticle velocity dispersion is strongly connected with the intensity of relaxation processes.

REFERENCES

1. Corbett, G. G., Reid, S. R. and Johnson, W., Impact loading of plates and shells by free-flying projectiles: a review. *International Journal of Impact Engineering*, 1997, **20**, 141–230.
2. Curran, D. R. and Seaman, L., Dynamic failure of solids. *Phys. Reports,* 1987, **147**, 253–388.
3. Asay, J. R. and Barker, L. M., Interatomic measurement of shock-induced internal particle velocity and spatial variation of particle velocity. *J. Appl. Phys.*, 1974, **45**, 2545–2550.
4. Mescheryakov, Y. I. and Divakov, A. K., Multiscale kinetics of microstructure and strain-rate dependence of materials. *DYMAT J.*, 1994, **4**, 271–287.
5. Allen, M. P. and Tildesley, A. K., *Computer Simulation of Liquids.* Clarendon Press, Oxford, 1987.
6. Eckstein, W., *Computer simulation of Ion–Solid Interactions.* Springer-Verlag, Berlin Heidelberg, 1991.
7. Krivtsov, A. M., Zhilin, P. A., Particle Simulation of Large Inelastic Deformations. *Transactions of the 14th Int. Conf. on Structural Mechanics in Reactor technology (SMiRT 14),* 1997, Lyon, France, 121–128.
8. Nagy, I., László, J., and Giber, J., *Z. Phys.*, 1985, **A321**, 221.
9. *Molecular Dynamics Simulation of Statistical-Mechanical systems.* Eds. Ciccotti, G. and Hoover, W. G., North-Holland, Amsterdam, 1986.
10. Cochran, S. and Banner, D. *J. Appl. Phys.*, 1977, **48**, 2729.
11. Chen, D., Al-Hassani, S. T. S., Sarumi, M., and Xiaogang, J., Crack straining-based spall model. *International Journal of Impact Engineering,* 1997, **19**, 107–116.
12. Mescheryakov, Y. I., Mahutov, N. A., and Atroshenko, S. A, Micromechanisms of dynamic fracture of ductile high-strength steels, *J. Mech. Phys. Sol,* 1994, **42**, 1435–1457.
13. Kanel, G. I., Razorenov, S. V., Bogatch, A., Utkin, A. V., and Grady, D. E., Simulation of spall fracture of aluminum and magnesium over a wide range of load duration and temperature. *International Journal of Impact Engineering,* 1997, **20**, 467–478.

TESTING AND SIMULATION OF MICRODEBRIS FROM IMPACTS WITH COMPLEX TARGETS

G.R. KRUSE†, W.R. MENDES†, W.J. SOMMERS†, R.A. WEED†, K.D. NASH‡, and D.V. MAYO*

†Nichols Research Corporation, 4040 S. Memorial Parkway, Huntsville, AL 35802; ‡Program Executive Office, Air and Missile Defense, THAAD Project Office, P.O. Box 1500, Huntsville, AL 35807; *U.S. Army Space and Missile Defense Command, P.O. Box 1500, Huntsville, AL 35807

Summary—Microdebris data from hypervelocity impacts of complex projectiles and ballistic missile targets were collected during three light-gas gun impact test series involving different geometric scales, impact velocities, and vehicle designs. Rotating and stationary witness panels of various materials and at various locations within the test chamber were used to collect microdebris size, mass, material, direction, and velocity data. These data are presented along with preliminary results from associated analyses. Microdebris data provide an important element in understanding and simulating the complete debris environment associated with ballistic missile defense engagements along with the corresponding effects and observables.
© 1999 Elsevier Science Ltd. All rights reserved.

NOTATION

V_{imp} impact velocity, km/s
R   range from target CG to collection device, meters
θ horizontal angle from shotline to collection device, degrees
ϕ vertical angle from shotline to collection device, degrees
t_D deposition thickness, cm

INTRODUCTION

Hypervelocity impacts associated with ballistic missile defense intercepts can produce tens of billions of fragments in excess of several microns in size. While micron-sized (i.e., microdebris) fragments are unlikely to result in structural damage in subsequent encounters with aerospace systems, they are capable of affecting sensitive components associated with these systems. Such components include optical sensors, solar cell arrays, and communication antennae. Microdebris also affect the persistent background signatures associated with impact debris clouds. This paper addresses U.S. Army Space and Missile Defense Command (USASMDC) and THAAD Project Office (TPO) efforts to quantify the microdebris environments associated with hypervelocity impacts and develop simulations which model and propagate these environments.

The Kinetic Impact Debris Distribution (KIDD) simulation [1] is a semi-empirical, Monte Carlo, USASMDC code based on data collected from a wide range of flight tests, light-gas gun tests, and rocket sled tests representing a variety of projectiles, targets, velocities, and geometries. These data have been used to develop debris models for fragment size, shape, area, material, mass, velocity, temperature, ballistic coefficient, and radar cross section [2]

distributions, for ballistic missile defense intercepts, since 1989. A database representing over thirty-eight thousand fragments exceeding one millimeter in size has been used to develop and validate these models. Recent efforts have emphasized obtaining data and refining the models in KIDD for debris sizes extending down to one micron.

Previous versions of KIDD made the simplifying assumption that microdebris material expands isotropically from both the projectile and target debris cloud centers-of-mass after impact. Since the geometry of impact and target/projectile characteristics are expected to result in non-isotropic debris expansion, however, data collected during past tests, and with new techniques, have been analyzed to (a) support better KIDD models for expanding microdebris clouds and (b) better characterize the velocity, size, and mass distributions involved. This paper presents the results of these preliminary efforts.

Microdebris are defined for the purpose of this paper as debris fragments smaller than 100-μm in size. Microdebris data collection efforts discussed in this paper were piggyback experiments conducted on USASMDC impact tests against complex, multi-material, multi-layered targets, on a non-interfering basis. As a result, the number and/or location of microdebris collection devices were not always optimal or even sufficient. Different types of collection media were used to obtain information about what appears to be a complex microdebris cloud resulting from hypervelocity impacts between complex vehicles.

Instrumentation included fragment spin velocimeters [3] which utilize a rotating witness panel positioned behind fixed apertures such that correlated fragment size and velocity data can be determined from the fragment impact craters on the witness panel. These panels also provide data on the population density of debris fragments at various size and velocity thresholds. Makescreens were used to determine the leading edge velocity of the debris cloud, typically microdebris, at various locations in the light-gas gun impact chamber. Static witness panels of various materials and thicknesses were used to record the microdebris deposition at multiple locations in the impact chamber. Measurements of these depositions provide insight into the population density of the microdebris cloud, as well as the material phase and dispersion directions. Additional collections included a proof-of-principle demonstration using small panels of thin, water-soluble foam to soft-catch microdebris fragments.

This paper presents data collection techniques used as well as preliminary qualitative and quantitative results for each of the three test series where microdebris data were collected. For tests where fragment spin velocimeters and makescreens were used, the observed range of microdebris velocities are presented. For tests where passive witness panels were used, the observed microdebris depositions are presented. While the data presented in this paper does not completely define the microdebris cloud, the trends observed provide useful information. They also provide insight as to the types of data that need to be collected in future tests to further understand these phenomena.

TEST CONSIDERATIONS

Microdebris, or microdebris effects, have been observed on flight tests, sled tests, and light-gas gun tests when a target is impacted by a projectile at velocities between 2 and 8 km/s. Two separate, expanding debris clouds are assumed about each newly-formed debris cloud center-of-mass. After impact, the trajectory of each respective debris cloud deviates from the original target and projectile trajectory based on the momentum transferred between each during the impact. For light-gas gun tests with a stationary target, both debris cloud centers of mass will be traveling downrange from the impact point. The projectile debris cloud center-of-mass, however,

will be traveling much faster after impact since the target was initially stationary and relatively little momentum is transferred from the projectile to the target.

In addition to each debris cloud center-of-mass trajectory, it is important to define the target and projectile debris cloud expansion velocities as they relate to the light-gas gun impact chamber geometry. This information is necessary to determine whether the microdebris collection device is only in the target debris cloud or both the target and projectile debris clouds. Since the target is stationary before impact and is significantly heavier than the projectile, the downrange target debris cloud center-of-mass velocity should be much less than the maximum spherical dispersion velocity for microdebris in all of the tests described. This results in simulated target debris that expands almost spherically in all directions, with respect to the impact chamber, with a slight bias in the downrange direction.

The projectile microdebris cloud, on the other hand, has a downrange center-of-mass velocity that is the same order-of-magnitude as the fragment spherical expansion velocity. This results in a projectile debris cloud that is expanding only in the region downrange from the target center-of-gravity (CG) as shown schematically in Figure 1. Shaded arrows in the figure represent the region containing target and projectile debris whereas the entire impact chamber can contain target debris. Solid arrows in Figure 1 represent the direction in which only target debris is expected to travel. Analysis of the collection devices takes into account their location in the impact chamber. The sample microdebris collector in Figure 1 is shown in the combined target and projectile cloud. Collection device locations are defined using spherical coordinates where R is the range from the target CG to the collection device, θ is the horizontal, or azimuth, angle from the shotline to the collection device (positive angles are counterclockwise as viewed from above), and ϕ is the vertical, or elevation, angle from the shotline to the collection device.
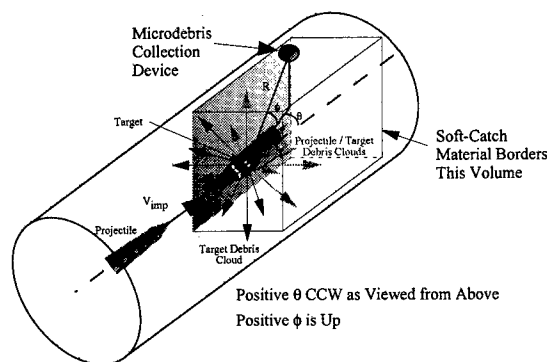

Fig. 1. Impact chamber geometry.

QUARTER-SCALE AEDC LIGHT-GAS GUN TESTS

A series of quarter-scale ballistic missile defense impact tests were performed for the USASMDC in 1993 using the light-gas gun facilities at the Arnold Engineering and Development Center (AEDC). Impact velocities ranged from 5.6 to 6.5 km/s. Four of these tests were conducted with fragment spin velocimeters [3] and makescreens, providing an indication of the range of microdebris velocities. Fragment velocimeters were originally fielded to collect velocity information for millimeter size debris fragments. Such fragments leave craters on the velocimeter disk (i.e., the rotating witness panel) which are measured. Using velocity data, from the crater location, and material data, the correlated particle diameter hitting the disk can be accurately estimated. An unanticipated black material was also deposited on the velocimeter disks, and this was used to identify the leading edge of the debris clouds [4-7]. Closer inspection of these black areas revealed a mixture of small craters, as small as 15-μm, and material that had been deposited. The former are likely due to solid particle impacts while the later are likely due to molten particle

impacts. Figure 2 shows an example of this deposition on a seventeen-inch diameter velocimeter disk, which was rotating clockwise at 4100 RPM.

Table 1 summarizes the impact velocities, data collection geometries, and microdebris velocities measured using the velocimeter disks and makescreens from this test series. All of the debris collectors except for 9304.11 are inside the combined target/projectile debris cloud. Velocities reported from the velocimeters indicate the maximum and minimum computed microdebris arrival velocities. The maximum velocities measured at the leading-edge of the velocimeter depositions are clearly identified by a sharp boundary, as seen in Figures 2 and 3. These maximum values agree well with the makescreen measurements of the microdebris cloud leading-edge velocity where makescreens were co-located with the velocimeters on the first three tests. Microdebris leading edges on the disk in Figure 2 (labeled "A") are at 5.4 km/s.

Table 1. Quarter-scale AEDC microdebris test data

Test.Collection Device Number	Type	V_{imp}	θ	ϕ	R	Microdebris Arrival Velocity[a] (km/s)	
						Maximum	Minimum
9301.01	Velocimeter	6.5	0	22	1.85	5.4	2.0 (some at 1.4)
9301.02	Makescreen	6.5	0	22	1.76	5.6	n/a
9301.03	Velocimeter	6.5	23	0	1.73	6.6	2.0
9301.04	Makescreen	6.5	23	0	1.64	6.67	n/a
9302.05	Velocimeter	5.6	24	8	1.72	5.0	1.3
9302.06	Makescreen	5.6	24	8	1.63	4.87	n/a
9303.07	Velocimeter	5.6	24	8	1.75	5.0	1.0
9303.08	Makescreen	5.6	24	8	1.66	5.16	n/a
9303.09	Makescreen	5.6	0	0	1.9	5.56	n/a
9304.10	Makescreen	6.1	0	90	0.96	6.0	n/a
9304.11	Makescreen	6.1	170	0	1.36	2.6	n/a

a) Calculations are based on the range to the target CG

Minimum velocities measured at the trailing-edges of the velocimeter depositions are also shown in Table 1, but are not as clearly defined as the maximum values. This is observed in Figure 2 as the jagged trailing-edges on the disk (labeled "B"). The minimum values reported are from the disk positions where the last significant black deposition could be found. At these disk locations (i.e., late debris arrival times) it is obvious that the microdebris cloud is less dense. Minimum velocities on the disk in Figure 2 are at 2 km/s. A few sparsely-populated deposition areas were found at a location on the disk corresponding to 1.4 km/s. Figures 2 and 3 show that the microdebris environments are non-isotropic even over the small solid angles subtended by the velocimeter disks.

Velocity measurements from the velocimeter disks provide valuable insight into the velocity and duration of the microdebris cloud. The duration of the microdebris deposition on the disks appears to be directly related to the length of time that the projectile is in contact with interior components in the complex targets. Figure 3 shows a velocimeter disk from a test where, due to the target orientation, the projectile had a pathlength through the target that was eight times longer than the test shown in Figure 2. The minimum microdebris velocity from disk 9303.07 is 1.0 km/s. The longer duration associated with the microdebris cloud is visually illustrated by the width of the black deposition on the disk in Figure 3. Laser photographs from this test show microdebris generation at the rear of the target as well as non-isotropy of the debris cloud. Velocimeter fixed front plate aperture widths used in front of the spinning disks shown in Figures 2 and 3 were 5 degrees and 3.8 degrees, respectively.
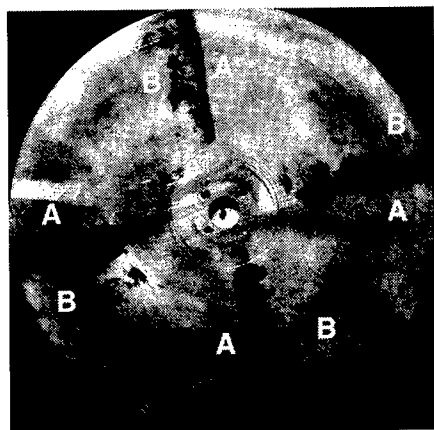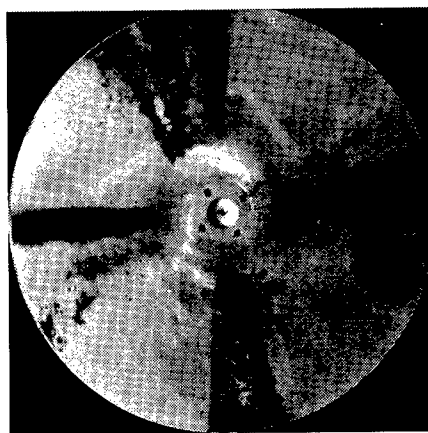
Fig. 2. Disk 9301.01.

Fig. 3. Disk 9303.07.

A small sample of the black deposition from disk 9303.07 was removed using high-tack tape. The velocity of this deposition was 1.5 to 1.8 km/s. The back of this sample was viewed under a microscope to find that the contour of the disk-side of the deposition had taken the form of the virgin velocimeter disk, which was slightly grooved by fine sandpaper before the test. Inspection of the disk surface under the removed material indicates that there was no cratering due to this deposition. This suggests that molten (or soft near-molten) material was deposited. Figure 4 shows a photomicrograph of the disk-side of the removed sample. The cracking was caused by flexing of the tape during removal, and circular areas represent craters from impacts of larger particles.

Velocities in Table 1 have not been adjusted for drag effects from the 1-torr air environment in the impact chamber. Microdebris larger than about 10-μm should not experience much deceleration from such an environment, but microdebris smaller than a few microns will experience significant deceleration. Even microdebris not subjected to significant deceleration, however, could be subjected to aerodynamic heating leading to softening, melting, or erosion in flight. Such factors may affect fragments as large as 100-μm at the higher microdebris speeds presented.
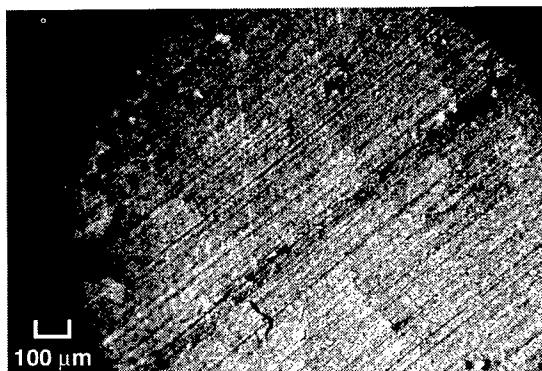

Fig. 4. Disk-side velocimeter disk deposition showing surface characteristics of disk.

SUB-SCALE UAH/ARC LIGHT-GAS GUN TESTS

Instrumentation for USASMDC ballistic missile defense impact tests performed in 1996 at the University of Alabama in Huntsville Aerophysics Research Center (UAH/ARC) included velocimeters and sapphire witness panels. Impact velocities ranged from 2.2 to 4 km/s, allowing the effects of impact velocity and the relationship to microdebris to be addressed. One test during a similar test series conducted in 1995 included water soluble foam witness panels, and is also reported here.

Table 2 summarizes the tests that were instrumented to collect microdebris data. Fragment spin velocimeters were used on tests 9602, 9603, 9604, 9606, and 9607. Velocities for these tests were between 2.2 and 4 km/s and all velocimeters were positioned in the combined target/projectile debris cloud region of the impact chamber. In addition, sapphire witness panels were mounted in holders attached to the velocimeters as well as in other locations in the impact chamber. The maximum and minimum microdebris velocities observed on the disks are shown in Table 2.

Table 2. Sub-scale UAH/ARC microdebris test data

Test.Collection Device Number	Type	V_{imp}	θ	ϕ	R	Microdebris Arrival Velocity[a] / Comments
9602.01	Velocimeter	3.25	31	7	1.57	Max=3.2 / Min=1.3 (shrouding), (solid debris @ 3.5)
9602.02	Sapphire Panel	3.25	38	7	1.54	Mounted on velocimeter 9602.01
9602.03	Sapphire Panel	3.25	-124	0	1.79	-
9603.04	Velocimeter	2.21	33	7	1.4	Max=1.5 / Min=0.7 (shrouding, light deposition)
9603.05	Sapphire Panel	2.21	40	7	1.37	Mounted on velocimeter 9603.04
9603.06	Sapphire Panel	2.21	-124	0	1.79	-
9604.07	Velocimeter	3.82	33	7	1.4	Max=2.5 / Min=0.7 (shrouding)
9604.08	Sapphire Panel	3.82	-124	0	1.79	-
9606.09	Velocimeter	4	33	7	1.42	Max=3.7 / Min=1.3
9606.10	Sapphire Panel	4	-160	0	4.4	-
9607.11	Velocimeter	3.61	33	7	1.4	Max=3.4 / Min=1.0 (shrouding)
9607.12	Sapphire Panel	3.61	40	7	1.37	Mounted on velocimeter 9607.11
9607.13	Sapphire Panel	3.61	-124	0	1.79	45° angle
9608.14	Sapphire Panel	3.58	0	90	1.1	-
9608.15	Sapphire Panel	3.58	-124	0	1.79	Facing wall away from debris
9610.16	Sapphire Panel	2.59	0	90	1.1	-
9610.17	Sapphire Panel	2.59	-124	0	1.79	45° angle
9610.18	Sapphire Panel	2.59	148	0	2.35	-
9501.01	Corn Starch Foam	2.9	150	0	1.9	-

a) Calculations are based on the range to the target CG

Figures 5 and 6 show velocimeter disks from tests that had similar impact conditions and collector locations, but with different impact velocities. Figure 5 shows disk 9603.04 from the third test that had an impact velocity of 2.21 km/s. Disk 9604.07 is shown in Figure 6 from test 9604 that had an impact velocity of 3.82 km/s. Qualitatively, the density and duration of the microdebris cloud, which is indicated by the black deposition on the disks, is much greater for the 3.82-km/s test. This black deposition has the same molten metal characteristics that were observed on the higher velocity tests discussed previously. At 2.21 km/s, however, this deposition appears to be diminishing. It is interesting to note that for all of the tests instrumented with fragment velocimeters on this test series, there were some small craters that had arrival times faster than the microdebris deposition. This was not observed on the higher velocity 1993 series of tests at the AEDC.

Indications of shrouding (i.e., highly non-isotropic depositions due to impacts off the target CG away from the velocimeter) were also observed during this series of tests. The velocimeter disks shown in Figures 5 and 6 show that the apertures closest to the shotline, on the right-hand side of the photographs, were exposed to more microdebris than those farther away. This is consistent with the two similar tests at different velocities. The apertures farthest from the shotline did not have a direct line-of-sight to the impact point.
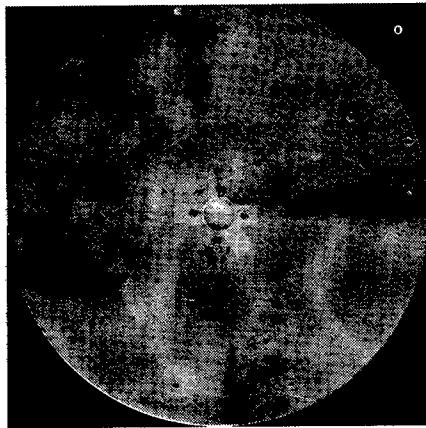
Fig. 5. Disk 9603.04 (V_{imp}=2.21 km/s).
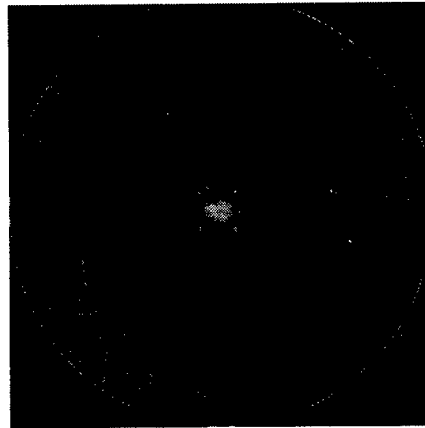
Fig. 6. Disk 9604.07 (V_{imp}=3.82 km/s).

Measurement and analysis of the microdebris deposition on various materials (sapphire, aluminum, steel, and plastic, etc.) from impact tests have been used to improve our understanding of microdebris phenomena and demonstrate effects of interactions with microdebris. Commercial, off-the-shelf sapphire witness panels 25-mm in diameter and 2-mm thick were exposed to debris environments on the tests so listed in Table 2. The thirteen samples included in the table were exposed at various downrange and uprange locations and aspect angles to the target CG.

Figures 7a and 7b show a typical surface deposition at different magnifications from sample 9602.02 located downrange from the target CG in both the projectile and target debris cloud. This sample was broken by a large fragment, but received a significant number of microdebris impacts as well. Dark areas are deposited aluminum (verified by spectrographic analysis) and appear to be impacts by molten, soft material. Analysis shows that aluminum is heated 250-325 K in the initial impact, depending on velocity, and then experiences a further rise in temperature upon impact with the sapphire. This may explain the splattered appearance of the aluminum on the relatively hard sapphire surface. Once again, velocity data in Table 2 are not adjusted for drag effects from the 1-50 torr helium environment in the impact chamber. The smaller microdebris may experience deceleration and/or heating due to interactions with such an environment and these effects may influence the microdebris deposition observed. Similar trends, however, are observed for the 1, 20, and 50-torr tests.

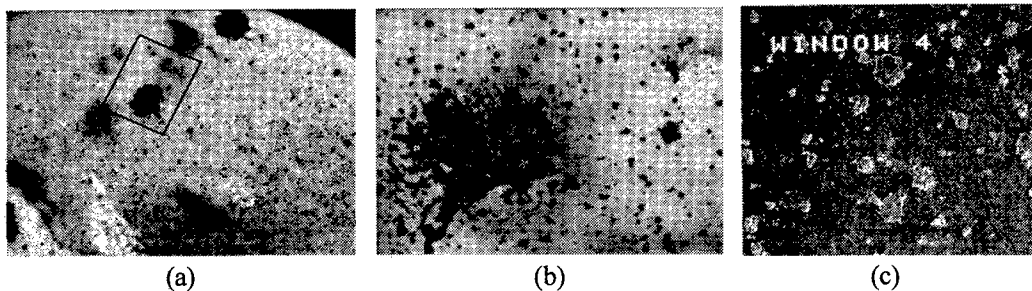(a)   (b)   (c)

Fig. 7. a) Stereomicroscopic image of sample 9602.02 at 10x; b) Stereomicroscopic image of highlighted area in Figure 7a at 40x; c) SEM image of sample 9603.06 at 100x.

Impact sites from Scanning Electron Microscope (SEM) images in Figure 7c and at higher magnifications, not shown here, were analyzed to obtain number densities by size class. Figure 8 plots the image sizes for three magnifications and the isotropic KIDD prediction for this test. The actual particle sizes impacting may be smaller than the image size. Subsequent removal of the aluminum with acid showed little to no damage on the sapphire in the underlying areas of aluminum microdebris impacts. This is consistent with velocimeter disk observations.

On test 9501 a sheet of water-soluble corn-starch foam packing material was attached to the wall approximately 2 meters uprange from the target CG on the side wall. Pieces 1 cm² x 0.35 cm thick were dissolved and the water allowed to evaporate leaving captured microdebris distributed in a thin, transparent sheet of corn-starch. Particles in several size classes were counted at various locations and the resulting size distribution is included in Figure 8. Results compare favorably between the two different collection media shown, however, the isotropic assumption in KIDD underpredicts the microdebris environment in this instance.
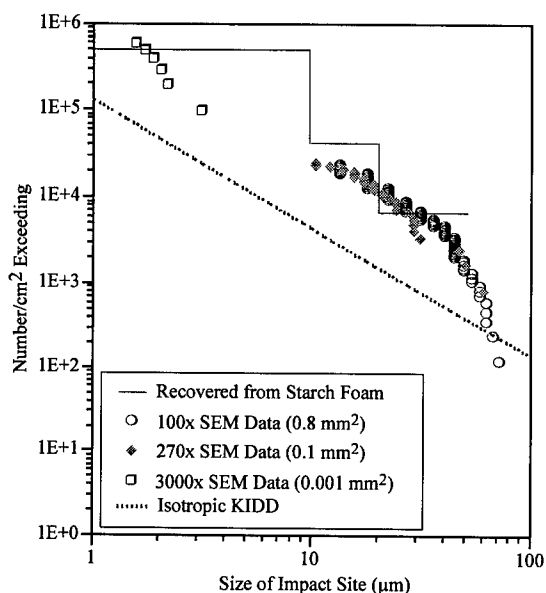
Fig. 8. Microdebris size distribution.

FOUR-TENTHS SCALE AEDC LIGHT-GAS GUN TESTS

Analysis of the microdebris deposited on various witness panel materials continued on four USASMDC impact tests at the AEDC in 1998 using thin stainless-steel witness panels at numerous locations in the impact chamber. This series of tests involved 40-percent scale models of aluminum projectiles impacting aluminum and steel complex targets at closing velocities of 1.75 and 3 km/s with impact chamber environments of 1-5 torr air. Witness panels were 2 x 2 inch squares of stainless steel (SS) and were attached to the soft-catch bundles surrounding the impact chamber in various uprange and downrange locations. Post-test debris were sifted to locate the panels or remnants thereof. Witness panels were color-coded and etched with numbers on the back surface to aid identification. Although reasonable care was exercised, in the search through approximately 200 cubic feet of debris and soft-catch material, some witness panels were not recovered.

Several thicknesses of stainless-steel shim stock were attached to the soft-catch bundles at locations listed in Tables 3 through 6 using the nomenclature given in Figure 1. The seventh column in Tables 3 through 6 provides the deposition thickness measured on each witness panel. The last column in the tables contains the deposition thickness adjusted for the angle with respect to the radius from the target CG to account for the surface area loss resulting from the fact that all of the witness panels were not directly facing the target. The thicknesses were obtained using a ball anvil micrometer, accurate to 0.0001 inches, before and after the tests.

Of the three panel thicknesses attached to the walls on test 9801 (0.002, 0.004, and 0.010 inches thick), very few of the 0.002-inch panels were recovered. The few that were found

showed a high concentration of very small (< 0.2 mm) penetrations. Most of the 0.010-inch panels were recovered intact with the 0.004-inch panels falling in between, although they were quite mangled. The 0.010-inch panels show many incipient penetrations and surface craters. It was therefore concluded that 0.010-inch and 0.025-inch witness panels would be installed on the second test and Table 4 summarizes the results from this test, 9802.

Table 3. Test 9801 witness panel results

Test.Collection Device Number	Type	V_{imp}	θ	ϕ	R	t_D Measured	t_D Adjusted for angle
9801.01	0.0099" SS	3.0	-118.6	0	0.767	0.0005	0.0005
9801.02	0.0101" SS	3.0	-68.5	-12.1	0.739	0.0005	0.0005
9801.03	0.0101" SS	3.0	66	-13.5	0.665	0.0003	0.0004
9801.04	0.0101" SS	3.0	121.8	0	0.701	< 0.0003	< 0.0003
9801.07	0.0041" SS	3.0	-118.6	0	0.767	< 0.0003	< 0.0003
9801.10	0.0040" SS	3.0	121.8	0	0.701	0.0003	0.0004

Table 4. Test 9802 witness panel results

Test.Collection Device Number	Type	V_{imp}	θ^a	ϕ^a	R^a	t_D Measured	t_D Adjusted for angle
9802.00	0.0100" SS	3.0	-130.3	55.9	1.087	< 0.0003	< 0.0003
9802.02	0.0250" SS	3.0	68.5	-14.4	0.739	< 0.0003	< 0.0003
9802.04	0.0100" SS	3.0	122.4	0.3	0.683	< 0.0003	< 0.0003
9802.05	0.0100" SS	3.0	0	118.0	0.775	0.0005	0.0005
9802.06	0.0100" SS	3.0	0	69.0	1.048	0.0003	0.0005
9802.07	0.0100" SS	3.0	0	41.2	0.757	0.0030	0.0033
9802.08	0.0250" SS	3.0	-118.6	0.3	0.767	< 0.0003	< 0.0003
9802.09	0.0250" SS	3.0	68.5	-14.4	0.739	< 0.0003	< 0.0003
9802.10	0.0250" SS	3.0	65.3	-13.7	0.655	0.0003	0.0003
9802.11	0.0250" SS	3.0	122.4	0.3	0.683	< 0.0003	< 0.0003
9802.12	0.0250" SS	3.0	0	118.0	0.775	0.0015	0.0018

a) Witness panels with similar locations were located beside each other

The decision was made to use 0.0250-inch stainless-steel witness panels supplemented by 0.040-inch plastic styrene witness panels co-located with each stainless-steel panel on the third test. The plastic was added to provide data associated with witness panels softer than the microdebris fragments. Table 5 summarizes the results obtained from the witness panels on this test, 9803. With an impact velocity of 1.75 km/s, much less microdebris is anticipated. Plastic witness panel data are not shown because of changes to the surface, apparently due to melting and loss of material. These samples may be analyzed at a future date. Table 6 summarizes the results from test 9804 where only 0.0250-inch stainless-steel witness panels were used.

Table 5. Test 9803 witness panel results

Test.Collection Device Number	Type	V_{imp}	θ	ϕ	R	t_D Measured	t_D Adjusted for angle
9803.02	0.0250" SS	1.75	0	131.9	0.886	0.0003	0.0005
9803.05	0.0250" SS	1.75	0	118.8	0.754	<0.0003	<0.0003
9803.07	0.0250" SS	1.75	-70.4	-14.4	0.752	0.0025	0.0033
9803.09	0.0250" SS	1.75	66.8	-16.9	0.645	0.0010	0.0010
9803.11	0.0250" SS	1.75	0	40	1.029	0.0003	0.0010
9803.12	0.0250" SS	1.75	35.9	-11.1	0.970	0.0003	0.0010

Table 6. Test 9804 witness panel results

Test.Collection Device Number	Type	V_{imp}	θ	ϕ	R	t_D Measured	t_D Adjusted for angle
9804.01	0.0250" SS	3.0	-117	3.6	0.79	<0.0003	<0.0003
9804.02	0.0250" SS	3.0	0	133	0.90	0.0003	0.0005
9804.03	0.0250" SS	3.0	123	4.3	0.67	<0.0003	<0.0003
9804.04	0.0250" SS	3.0	-117	3.6	0.79	<0.0003	<0.0003
9804.06	0.0250" SS	3.0	123	4.3	0.67	<0.0003	<0.0003
9804.07	0.0250" SS	3.0	-68	-15	0.64	0.0074	0.0081
9804.08	0.0250" SS	3.0	0	67	0.72	0.0058	0.0064
9804.09	0.0250" SS	3.0	68	-16	0.67	0.0005	0.0005
9804.10	0.0250" SS	3.0	-39	-11	0.97	0.0109	0.0305
9804.11	0.0250" SS	3.0	0	40	1.03	0.0023	0.0074
9804.12	0.0250" SS	3.0	37	11.5	0.94	0.0066	0.0180

Figure 9 shows a 100-power photomicrograph of a control sample of the stainless-steel shim stock used as witness panels. Although the appearance is cloth-like, in fact the surface is smooth and appears highly polished to the naked eye. All photomicrographs of the stainless-steel witness panels represent 100-power magnification with light from the left side at 20 degrees to the surface of the specimen. Figure 10 shows a crater from panel 9801.04 and Figure 11 shows a complete penetration with a surrounding buildup of deposited material from panel 9801.10. The light central region of the penetration is due to paper behind the sample.
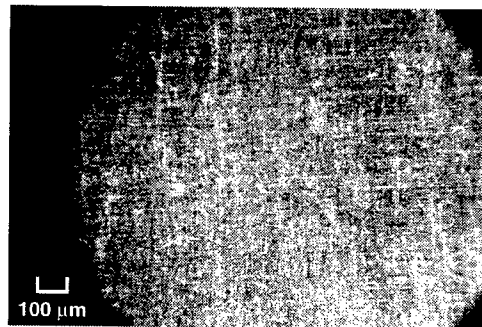
Fig. 9. Stainless steel control sample.

Figure 12 shows a 100-power photomicrograph of deposition on sample 9804.04 located beside the nose tip of the stationary target. This appearance is typical of witness panels located uprange from the target CG, where most of the debris should be from the target. The surface is covered with a very fine buildup in addition to the features seen in the figure. Figure 13 is a 100-power photomicrograph of sample 9804.07 located beside the rear of the target on the same side as sample 9804.04. This witness panel was located in an area impacted by the combined target/projectile debris cloud. The figure shows a typically heavy deposition with surface granularity (i.e., chunky shapes) visible to the micron level.
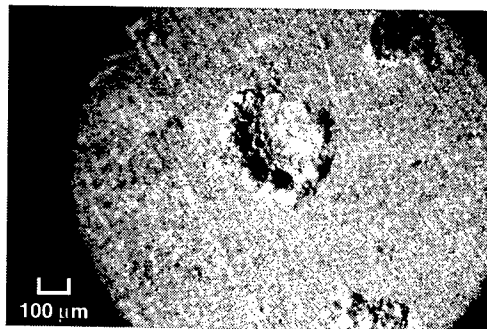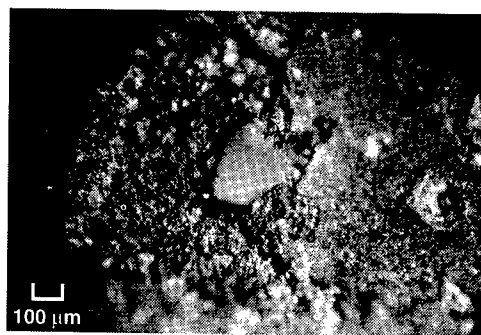

Fig. 10. Sample 9801.04.
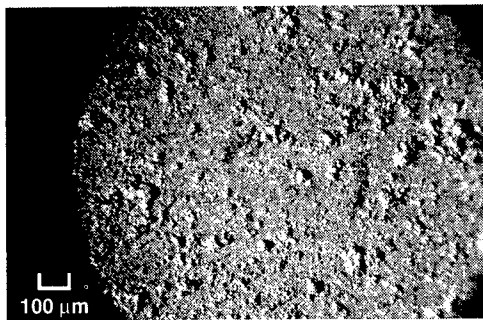

Fig. 11. Sample 9801.10.
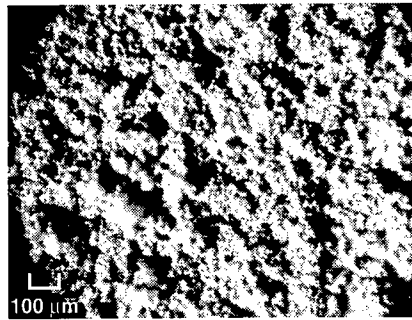
Fig. 12. Sample 9804.04.

Fig. 13. Sample 9804.07.

Material deposited on these panels is relatively easily removed. Figure 14 is a view of panel 9804.08. This panel experienced a penetration with petaling. The out of focus area in the figure is the edge of the penetration. This penetration occurred after some deposition had already occurred and resulted in material being shocked away from the surface leaving a much thinner layer attached to the panel. The shadow shows the edge of the original material. Further deposition occurred as evident from the appearance of the area. Similar flaking occurred on only three witness panels, all downrange from the impact and subjected to impacts by large particles which created large damage zones.
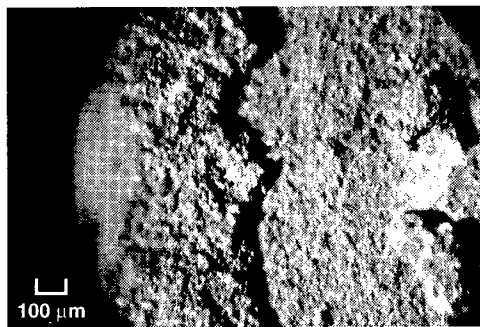
Fig. 14. Sample 9804.08.

CONCLUSIONS

The data and analysis reported represent an improvement in our ability to characterize microdebris environments from complex target impacts. This capability directly supports the development of impact debris environment simulations and will be used to expand future versions of the KIDD simulation. Models for the complete debris environment are desired so that additional factors affecting the mass, momentum, and energy balances of the impact can be addressed and a wider range of debris effects and observables can be assessed.

The data presented confirm a robust population of high-speed microdebris fragments whose number increases rapidly as the size decreases, as currently simulated with KIDD [1], down to at least a few microns. In fact, the power-law fit to the number density data shown in Figure 8 resulted in an exponent of -1.5 which is nearly identical to the value currently used in KIDD. The constants of proportionality, however, are different and suggest that KIDD may currently be underpredicting the microdebris population, particularly at the higher impact velocities. While observed microdebris speeds, and speed variations throughout the microdebris cloud are in general agreement with the current models, the significant non-isotropy indicates the requirement for additional data and model improvements in this area.

Another area of continued interest is the phase of the microdebris and the corresponding affects on microdebris impacts. Microdebris are consistently observed to deposit on the witness

panels without cratering the impacted surface. This effect becomes more pronounced as impact velocities increase, but is observed at all the impact speeds tested. A potential, or partial, explanation is that the microdebris are molten and therefore penetrate less effectively. Aluminum-on-aluminum impacts, however, do not typically result in shock heating to melt until impact velocities exceed 5 km/s [8] and most of the reported tests were below this value. The additional heating could be due to strain heating [9] or other effects associated with the complex interactions between the projectile or target. Or the low-pressure environment within the impact chamber could be affecting fragment velocities and temperatures. The hypersonic, viscous aerodynamics [10] associated with microdebris in these environments, which represent realistic ballistic missile defense engagements, may result in heating, melting, erosion, and vaporization [11] of the microdebris.

Additional analysis of the reported data as well as the collection of additional test data are needed and are planned. The latter are being based on the relative utility of the reported microdebris collection techniques and the areas of high uncertainty with regard to understanding and simulating microdebris phenomena. The complex nature of the projectile and target along with the considerable variability in vehicle designs and impact conditions make this a continuing challenge.

REFERENCES

1. W. J. Sommers, G. R. Kruse, and R. A. Weed, KIDD Kernel version 3.1, task interim report, Nichols Research Corp. report, NRC-TR-96-065 (1996).
2. W. J. Sommers, G. R. Kruse, R. A. Weed, and D. V. Mayo, Radar cross sections and ballistic coefficients of fragments from impacts with complex full-scale targets, *Int. J. Impact Engng*, 20, 753-764, (1997).
3. W. J. Sommers, G. R. Kruse, J. W. Johnston, L. C. Atha, and J. C. Henderson, Spin velocimeters for impact debris fragments, *Int. J. Impact Engng*, 17, 773-784, (1995).
4. J. W. Johnston, Hypervelocity collision debris characterization, spin velocimeter data, Tybrin Corp. report, TYB-93-0105-TR (1993).
5. J. W. Johnston, Hypervelocity collision debris characterization, spin velocimeter data, Tybrin Corp. report, TYB-93-0118-TR (1993).
6. J. W. Johnston, Hypervelocity collision debris characterization, spin velocimeter data, Tybrin Corp. report, TYB-93-0119-TR (1993).
7. J. W. Johnston, Hypervelocity collision debris characterization, spin velocimeter data, Tybrin Corp. report, TYB-94-0022-TR (1994).
8. C. E. Anderson Jr., T. G. Trucano, and S. A. Mullin, Debris cloud dynamics, *Int. J. Impact Engng*, 9, 89-113, (1990).
9. Zukas et al., *High Velocity Impact Dynamics*, John Wiley & Sons, Inc., 76-88, 252-270 (1990).
10. S. F. Hoerner, *Fluid-Dynamic Drag*, Published by author, (1958).
11. E. J. Öpik, *Physics of Meteor Flight in the Atmosphere*, Interscience Publishers, Inc., New York, (1958).

REVIEW OF INVESTIGATIONS UNDER WAY ON THE LARGE-SCALE TSNIIMASH BALLISTIC FACILITY

PAVEL V. KRYUKOV

Ballistic Technologies Scientific Venture, Box 92, Korolev, Moscow Region, 141070, Russia

Summary—The large-scale TsNIIMASH ballistic facility was built in 1992 through modernization of the large shock tunnel. Having 0.5 m caliber, the facility is 200 m long. Each experiment on the facility envisages an explosion of stoichiometric hydrogen-oxygen mixture, up to 300 cub. m by volume. In the air-evacuated ballistic channel 60 m long, the expanding explosion products of the detonating gas mixture boost gyrostabilized steel plates 0.5m in diam which travel along the channel on a magnetic suspension without a mechanical contact with the walls. The case is unique in combining the ballistic facility geometric dimensions with the plate high-precise motion. Results of experiments on graphite crystalline conversion into diamond are given. Investigations to use the shock tunnel for hypervelocity launch of compact projectiles are discussed. © 1999 Elsevier Science Ltd. All rights reserved.

INTRODUCTION

The large-scale TsNIIMASH ballistic facility was developed in 1992 through modernization of the large shock tunnel built back in 1958 (see Fig. 1). The tunnel is 200 m long. The diameter 0.5 m is strictly similar along the whole length. Given the wall thickness of 60 mm, the tunnel made of low-carbon structural steel of ultimate strength of 460 MPa can be safely filled with gas at 150 ata. In pulsed operation in its local segments, the tunnel can withstand surplus pressure of up to 300 ata without failure.

Originally we intended to use the tunnel in designing a mock-up of a launcher to inject in orbit small projectiles. We planned to launch 0.5-1 kg projectiles to 10-11 km/sec in the experiments on the facility. The projectiles were supposed to be preliminarily boosted to 4.5 km/sec in the tunnel with the use of gyrostabilized plate-shaped sabots (see Fig. 3) accelerated
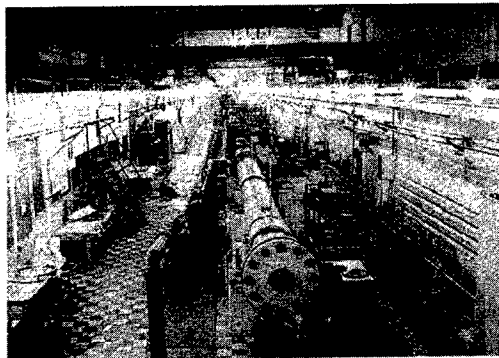

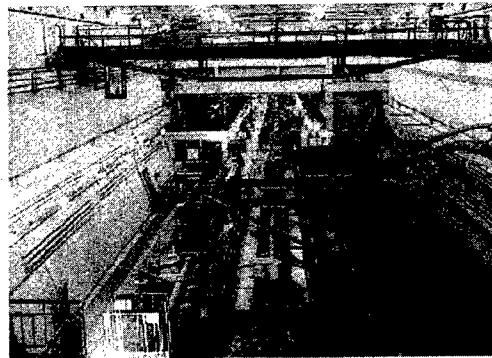Fig. 1. TsNIIMASH large-scale ballistic facility.

Fig. 2. Vacuum chamber of ballistic facility.

through the gasdynamic expansion of the stoichiometric hydrogen/oxygen mixture combustion products. The stoichiometric mixture was to be generated in the tunnel through the injection of oxygen and hydrogen gaseous jets through the tunnel end flange injectors at high pressure, much as in a rocket engine combustion chamber.

To be ultimately accelerated, the projectile must separate from the plate-shaped sabots and be fired into the gascumulative acceleration channel 100 m long (see Fig. 4). On the operation principle, the gascumulative accelerator is similar to RAM-accelerator [1], with the only difference that condensed explosive is used instead of gaseous explosive mixture. The thick-wall tunnel with the inner diam of 100 mm was lined with a thin layer of the explosive, sandwiched with a damping layer. The thick-wall tunnel was fixed along the tunnel axis with plate-shaped supporting elements. The projectile was presumed to be accelerated in the gascumulative accelerator in vacuum through its conic tail symmetric compression (see Fig. 5) with the high-velocity detonation products converging to the tunnel axis, the explosive being initiated simultaneously throughout the entire perimeter of the channel, in synchronism with the projectile motion. The explosive were supposed to be initiated through the high-velocity impact with a liquid ejected through the nozzles (see Fig. 5) on the projectile side surface. The liquid ejection was powered by high-speed rotation of the projectile about its axis of symmetry. That the projectile under symmetric compression with the gas had gyroscopic moment was due to provide its stable motion along the gascumulative accelerator, without mechanical contact with the walls.

The projectiles accelerated in the gascumulative accelerator were planned to be thrown into the vacuum chamber 180 cubic meters (see Fig. 2) butt joined with the facility tunnel. The chamber was fitted with high-speed optical diagnostics instrumentation allowing to investigate projectile hypervelocity motion in the gaseous atmosphere. A projectile catcher weighing 10 tons, 8 m long, was installed on guide rails in the chamber, its retardation on recoil being realized through friction against the rails.

The work on preparation of the projectile gascumulative acceleration was nearly completed, however in early 1992 the financing of the program was stopped. This caused us to change the line of investigation and consider possible civil-purpose applications of the facility, for example, to realize material dynamic synthesis and processing technologies. Even in the early ballistic high-velocity launch experiments performed on the facility the gyrostabilized plates were used as impactors for target dynamic loading, and not as sabots for projectile preliminary acceleration.

UPGRADED LARGE-SCALE BALLISTIC FACILITY

In the experiments having been conducted on the facility by now, we launched steel plates 6 mm and 20 mm thick, weighing 9.1 kg and 30 kg correspondingly (see Fig. 3). The revolving

Fig. 3. Throwing discus.

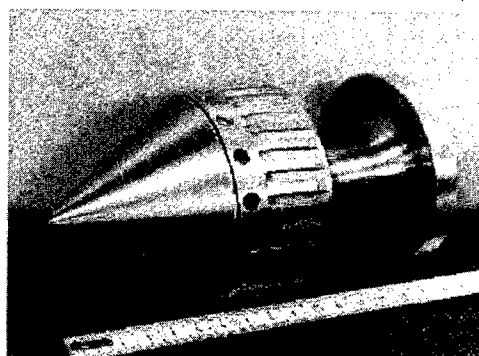Fig. 4. 100-mm ballistic gascumulative facility.

Fig. 5. Projectile for gascumulative accelerator.

magnetic field generated with an electromagnetic stator, mounted in the tunnel body, spins the plate in the tunnel on a string suspension up to the ultimate angular speed (200 rps) limited by their breaking strength. The considerable gyroscopic moment makes it possible to preserve its angular position on acceleration. At synchronous rotation of the magnetic field and plate, specially made of magnetosoft steel, the latter was magnetized. Due to conductivity of the steel, the plate held the magnetic field for some time dependent on the plate thickness. For those thicknesses in use the plate demagnitization time was in excess of the time of plate acceleration in the tunnel. When the magnetized plate moved along the tunnel, electric currents were induced in the electrically-conductive walls. The interaction of these currents with the magnetic field of the plate provided a way for the latter to travel in the tunnel on a magnetic suspension. The adjustment of the plate spin axis, such that its angular deflection from the axis of the tunnel was within 30 angular seconds, effected considerable reduction of lateral component of the resulting force of gas pressure with the result that the plate moved in a magnetic suspension without mechanical contact with the tunnel walls. The plate-to-wall clearance was about 0.5 mm.

To launch gyrostabilized plates we used the tunnel section 60 m long (see Fig. 6), which was adjusted so that the offset of its axis is not greater than 0.5 mm. In the experiments we have performed the boost section of the tunnel was air-evacuated or filled with gaseous hydrogen at low pressure. Of the rest of the tunnel, we used its section of up to 110 m in length, filled with oxygen/hydrogen mixture with an initial pressure, at most, 15 ata. The tunnel section containing oxygen/hydrogen mixture was separated from the boost section by a polyamidic diaphragm, only 0.2 mm thick. The detonation wave initiated in the section containing oxygen/hydrogen mixture propagated along the section from its end towards the projectile to be launched. When impacted by the wave front, the polyamidic diaphragm failed and burned up under the action of the high-temperature detonation products, further impacting the projectile at high velocity, with the result that the projectile was brought to high-rate accelerated motion, the rate of acceleration dying down with increasing velocity. As compared to the high-velocity launching scheme, originally projected for use, the detonation-induced acceleration scheme featured relatively low energy efficiency, but proved to be more simple and safe. The velocity of the projectile, launched in the tunnel, was measured with the use of pulse pressure transducers mounted in the tunnel body lengthwise. The instance the projectile flew past the transducer was registered in response to pressure step change with time.

The projectiles launched in the facility were retarded at the end of the boost section by a heavy anvil with a shock-absorber installed in the tunnel tail section 7 m long. On high-velocity impact of a projectile on the anvil, the end face of the latter suffered severe deformation and called for replacement after each experiment. A ring-shaped recess was designed into the tunnel
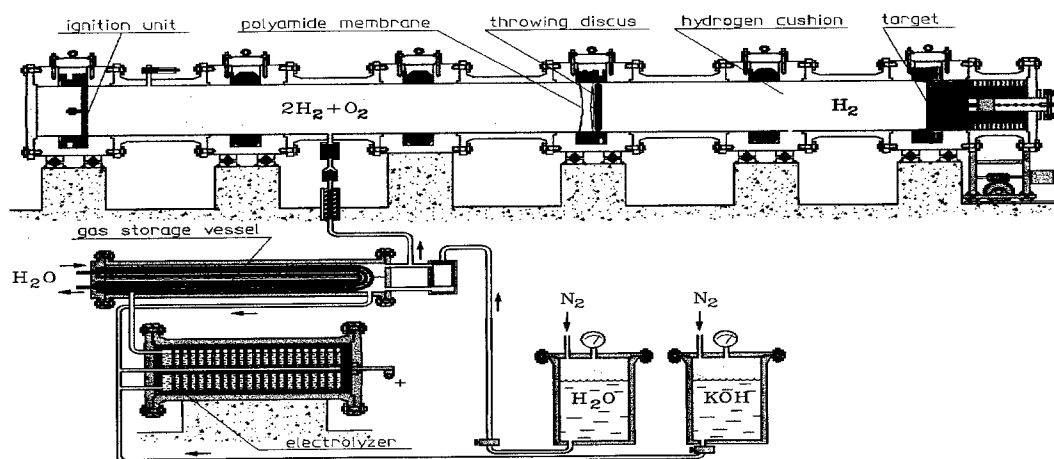

Fig. 6. Upgraded ballistic facility.

body opposite the anvil end face. A thick-walled changeable shell, reinforced by a wire binding, was fitted into the recess with a shell-to-wall clearance. The shell absorbed shock-induced side loads and suffered severe plastic deformations. Owing to the clearance between the shell and the tunnel body, the side loads did not end in failure of the latter. The weight of the anvil was as large as 6.5 tons, resulting in low speed of its recoil on impact and consequent possibility to use for its retardation a rubber shock-absorber, ca. 2 m long, intervening between the anvil and the tunnel end flange. The movable rod of the shock absorber, 140 mm in diameter, was passed through the hole in the tunnel end flange. The recoil of the anvil should not exceed 1 m, lest the force to the end flange of the tunnel be more than tolerable limit of loading equal to 400 tons.

Because of the sizable caliber of the facility and the substantial energy of the launched plates, a rich variety of samples of different composition placed at different depths from the target end face can be exposed to dynamic loading simultaneously in each experiment. The impulse decay at propagation deep into the target allows to realize loading over a wide range of pressures in each experiment. The precision launching of the plates provides possibility to damp the high-velocity impact on the sample-containing target with a layer of gaseous hydrogen, allowing to realize time-resolved loading and off-loading of samples. This prevents the samples not only from shock-wave heating up, but from initiation of rupture stresses, thus precluding their failure. In so doing there is a possibility to control the temperature of the samples, regardless of the pressure being realized. The oriented shearing of the samples with the preset deformation velocity is realized by forcing them during loading against the fast-rotating flywheel surface mounted on the target. Arranging the samples equidistant from the flywheel spin axis, one can achieve shearing over a wide range of velocities in each experiment. The set of parameters realized in each ballistic experiment is unique and unattainable by other known methods. The short-term exposure of the samples to high pressure, together with their high-velocity shear deformation with no shock-wave heating up, makes it possible to synthesize in solids metastable polycrystalline states having amorphous or nanophase structure, possessing high magnetic, mechanical and catalytic parameters, as well as to perform solid powder compaction.

BALLISTIC DIAMOND DYNAMIC SYNTHESIS EXPERIMENTS

Within the period from October 1992 to June 1993 we performed on the facility 10 ballistic experiments on the development of the technology for launching gyrostabilized plates. Each experiment involved launching of plates 9.1 kg weight. In the process the launch velocity increased successively from experiment to experiment. To realize maximum velocity measuring 3.5 km/sec we exploded oxygen/hydrogen mixture of composition $4H_2:O_2$, 330 cub. m by volume, filling in the tunnel section 110 m long under 15 ata. The kinetic energy of the launched plates was in excess of 50 MJ.

The launched plates impacted on cast iron targets 30 kg weight (see Fig. 7,8,9). On ultimate-velocity impact the cast iron's carbon inclusions were partially converted into diamonds as a result of the shock-wave action on the cast iron [2]. Upon chemical treatment of the cast iron target subjected to the shock-wave loading, more than 250 g of diamond dust was extracted, the particle characteristic size being of about 2 μm.

In January and April, 1997, upon upgrading the facility we performed under the ISTC Project#30 two experiments aimed at demonstration of the possibility of graphite crystalline conversion into diamond under dynamic loading with shear. In the experiments we launched plates 30 kg weight to 1.4 km/sec and 1.6 km/sec correspondingly. In the process the high-velocity impact of the plate on the target incorporating graphite samples was damped by gaseous hydrogen, the tunnel boost section was previously filled with. This effected time-resolved loading of the graphite crystals to 26 GPa during 12 μs without shock-wave heating up and failure on relaxation. The shear deformation velocity reached 350 m/sec.
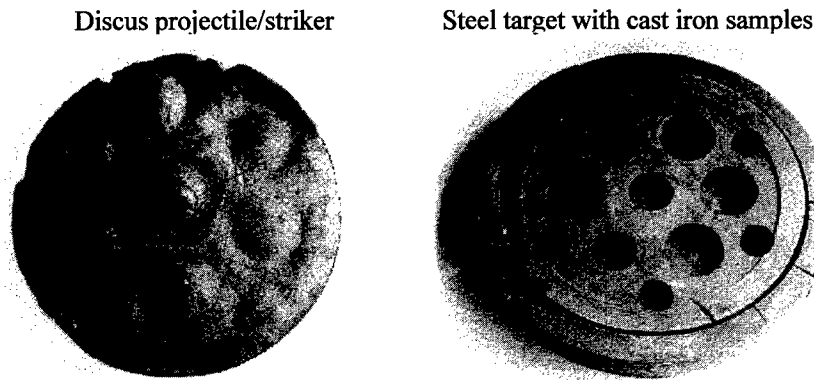
Discus projectile/striker   Steel target with cast iron samples

Fig. 7. High speed throwing: Experimental results (V=1.2 km/s).
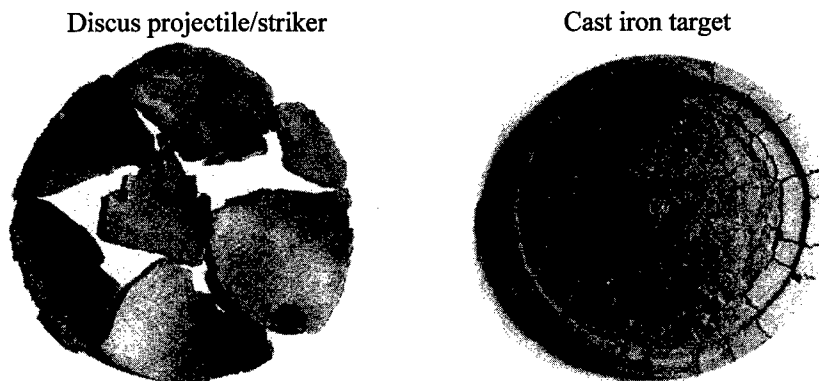
Discus projectile/striker   Cast iron target

Fig. 8. High speed throwing: Experimental results (V=2 km/s).

Fig. 9. High speed throwing:
Experimental results (V=3.5 km/s).

An oriented shear deformation of a compressed graphite sample, strictly along the plane of atomic layers, presents an opportunity for a coherent rearrangement of the graphite crystal lattice into the diamond one [3], whereby a fast relative gliding of atomic layers stimulates a practically simultaneous switch of carbon atoms in a layer into the new electron state with the formation of strong inter-layer covalent bonds, providing graphite crystal structure rearrangement. The chemically bound atomic layers then move as one rigid body, forming a planar nucleus of the diamond phase which goes on "encroaching" into the graphite crystal by additions of subsequent

layers in the same way. This may result in a wave of crystal conversion of graphite into diamond, spreading through a compressed graphite crystal. The shear stress on the wave front (which constitutes the phase boundary) is due to be transmitted from the crystal surface through the newly formed diamond layer, thanks to its extremely high shear strength. In this case, in contrast with shock synthesis, no limits are imposed on the possible size of the synthesized diamond crystal. This provides a possibility to perform synthesis of large diamond crystals under dynamic loading.

The mode of dynamic loading required for the crystal conversion was achieved in the second ballistic experiment only. The results of pre- and after-loading graphite samples investigation by methods of material science verified that due to the high angular disorientation (about 1 degree) of the domains in the initial graphite samples the direct transition into diamond within macro-volume proceeded non-coherently in diffuse mode (and not in wave mode, as expected a priori), with the result that the graphite-to-diamond phase transition penetrated the samples only for a depth of not more than 0.3 mm (graphite samples cross-size was 20×20 mm). The graphite crystalline lattice coherent rearrangement into diamond was evidenced only within individual single-crystal domains sized about 10 μm (see Fig. 10). Relying on the performed investigations we came to the conclusion that for the graphite crystalline lattice coherent rearrangement into a diamond one in wave mode to be realized within the whole volume of a graphite sample up to 5 mm thick with the retention of its initial crystalline quality, it is necessary that only perfect graphite crystals are exposed to the dynamic loading with shear. The diamond dynamic synthesis experiments are planned to be continued on acquisition of large single crystals of graphite, presumed to be synthesized on the facility currently under development.

HYPERVELOCITY LAUNCHER

Based on the TsNIIMASH shock tunnel, the hypervelocity launcher (see Fig.11) was built in 1998 to perform laboratory testing of shield protection for the International Space Station Service Module. To realize hypervelocity launching, the convergent cone 3 m long, going to the acceleration channel 1 cm in diameter, 3 m long, is butt-jointed to the shock tunnel end. The tunnel section 20 m long together with the cone can be filled with stoichiometric mixture to 15 ata, while the acceleration channel is air-evacuated. The launched projectiles are thrown into the vacuum chamber. To measure velocities we use induction coils, which register metallic body passing through.

Leading with the work of Guderley, Landau, Stanyukovich [4] it is well known that detonation wave converging in a long-length cone produces gasdynamic flows at the cone vertex having extremely high density of energy sufficient, as expected before, even to initiate thermonuclear reactions. Casually and quantitatively, the effect of cumulation is conditioned by

Fig. 10. Surface of a graphite sample subjected
to loading.

the diminution of the shock wave front area in its passage through the convergent channel. This phenomenon was theoretically and experimentally studied as applied to the problem of controlled thermonuclear fusion [5]. As to the case of a cone-convergent spherical shock wave, analytical and numerical methods were developed to calculate gasdynamic properties realized under these conditions, as well as factors limiting energy cumulation (radiation, heat conduction, viscosity, hydrodynamic instabilities) were studied. A convergent plane shock wave was also investigated, e.g. as applied to the shock tunnel of TsNIIMASH [6]. Unlike a convergent spherical wave, for which smooth velocity increase in a power fashion is provided along the channel axis, in case of a plane wave Mach reflections from the cone walls are responsible for step increase in velocity, each step followed by smooth decay, so that the power fashion of velocity increase, realized for a spherical wave, is kept on average.

Results of calculation [7] confirm the possibility to realize the high gasdynamic properties on the developed hypervelocity ballistic facility. In the case under consideration the tunnel section, ca. 100 m long, together with the cone, is filled with stoichiometric mixture to the pressure of 10 atm. The detonation wave propagates over the mixture, transforming to a strong shock wave in the cone. Behind the front of the shock wave convergent in the cone the following parameters are realized when the front diameter reduces to ~1 cm: shock wave velocity - 13.6 km/sec, gas velocity - 12.6 km/sec, gas pressure - 9000 atm, gas temperature - 20000 K, gas density - 75 kg/cub.m. Due to the long length of the detonation area and consequent substantial mass of detonation products inflowing into the cone, the high thermodynamic parameters at the cone vertex are maintained for a sufficiently long time ranging up to several hundreds of microseconds. The high density of energy in the working gas is attained mainly through its translational motion, rather than through excitation of its internal degrees of freedom, as for adiabatic compression. At the acceleration channel outlet the calculated velocity of the aluminum projectile 2.7 g by mass exceeds 14 km/sec. When the gas moving behind the shock wave front impacts the projectile resting in the acceleration channel, the projectile experiences severe impact loading, and the reflected shock wave is developed in the working gas. The behind-front pressure reaches 13 GPa, several times greater than the ultimate dynamic strength of the aluminum alloy. Then the pressure declines rapidly (within 20 μs) to the level below the ultimate strength. In this time interval the projectile manages to gain not more than 5% of its kinetic energy. Thus, the launching process is contributed mainly by prolonged nondestructive action on the projectile along the whole length of the acceleration channel, rather than through attainment of extremely high degree of energy cumulation at the cone vertex, accompanied by pulsed acceleration of the projectile, as in explosion launching. In all likelihood, it will be difficult to realize the design behind-front energy density at the acceleration channel inlet due to the occurrence of a variety of gasdynamic instabilities.

In the first experiment, performed in July 1998, we launched the aluminum cylinder 1.3 cm long, 2.85 g by mass. The initial pressure of the hydrogen-oxygen mixture was 15 atm. The
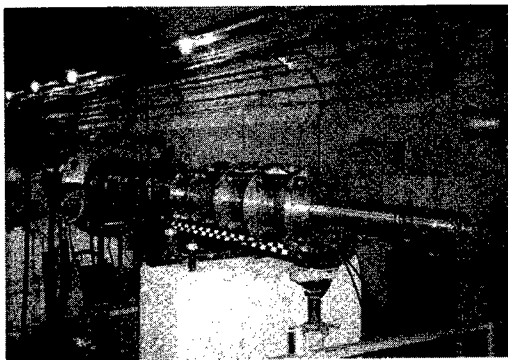

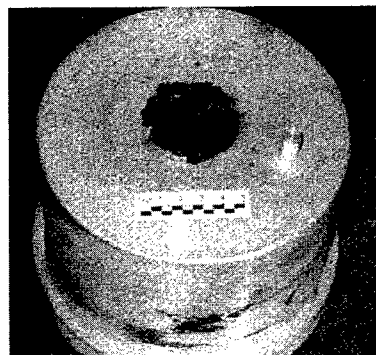Fig. 11. Assembling of the hypervelocity ballistic facility.

Fig. 12. Result of the first hypervelocity experiment.

damping layer of foam plastic was envisaged to prevent projectile failure. Unfortunately, in this experiment we did not manage to realize the design condition of launching. The measured projectile outlet velocity made up only 2.7 km/sec, what is far less than we anticipated. 2.9 μs after the projectile passing through, the coils registered plasma jet coming out from the acceleration channel, with the velocity of more than 30 km/sec. We consider this fact to be evidence that the energy cumulation behind the front of the detonation wave convergent in the cone was realized in this experiment. In the process the projectile was accelerated not through the interaction with the detonation wave, but by the action of prematurely-ignited mixture combustion products. In all likelihood, the premature ignition was conditioned by heating up of the walls nearby the cone vertex, as a result of concentration of light emission from the detonation wave front due to repeated reflection from the cone smooth walls. Figure 12 shows the crater formed on the impact of the projectile on the duralumin target.

To realize the design launch conditions in the next experiment we plan to fill the cone separately from the tunnel, with an inert (e.g. hydrogen/nitrogen) mixture, of the same pressure and density as the hydrogen/oxygen mixture in the tunnel.

REFERENCES

1. A.Hertzberg, A.P.Bruckner, D.W.Bogdanoff, RAM Accelerator: A new chemical method for accelerating projectiles to ultrahigh velocities. *AIAA J.*, **25**(2), 195 - 203 (1988).
2. G.R.Cowan, B.W.Dunnington, A.H.Holtzman, Process for synthesizing diamonds. *U.S. Patent N 3401019* (1968).
3. V.V.Aksenenkov, V.D.Blank, N.F.Borovikov, V.G.Danilov, K.I.Kozorezov, Formation of diamond monocrystals in the plasttically deformed graphite. *Doklady Akademii Nauk*, **338**(4), 472-476 (1994), in russian.
4. L.D.Landau, E.M.Lifshits, Theoretical physics. Hydrodynamics, Nauka, Moscow (1986).
5. I.V.Sokolov, Hydrodynamic cumulative processes in plasma physics. *UFN (Progress in Physics)*, **160**(edition 11), 143-165 (1990).
6. V.A.Belokon, A.I.Petrukhin, V.A.Proskuryanov, Strong shock wave entry in a wedge-shape cavity. *JETF (Experimental and Theoretical Physics Journal)*, **48**(1), 50-60 (1965).
7. N.M.Kuznetsov, Approximate solution of the problem of projectile launching by the ballistic facility. *Report, Institute of Chemical Physics of the Russian Academy of Science* (1997).

COMPARISON OF NITROGEN ALLOYED AUSTENITIC STEELS AND HIGH STRENGTH ARMOR STEELS IMPACTED AT HIGH VELOCITY

E. LACH, G. KOERBER, M. SCHARF and A. BOHMANN

German-French Research Institute Saint-Louis (ISL), Postfach 1260,
D-79574 Weil am Rhein

Summary—The ballistic performance of a work hardened nitrogen alloyed austenitic steel (P900) was studied by a light gas gun at a projectile velocity of 2500 m/s. To compare ballistic efficiency and residual microstructure to classical martensitic armor steels, tests with a high hardness armor steel were performed. The hardness of the work hardened P900 and the armor steel were 380 HV30 and 500 HV30, respectively. Both steels proved to offer an identical ballistic performance. Measurements of hardness around the crater have shown a strong increase of hardness for P900 whereas the hardness of the armor steel did not change. Compression tests on a split-Hopkinson-pressure-bar show that nitrogen alloyed austenitic steel strain harden very strongly and possess very high strain rate sensitivity. Strain hardening and strain rate sensitivity of high hardness armor steels are very small. Grain sizes in the heat-affected zone near the crater of nitrogen alloyed steels give information about temperature and heating time. © 1999 Elsevier Science Ltd. All rights reserved.

INTRODUCTION

Nitrogen alloyed steels, i. e. steels which are intentionally alloyed by a considerable amount of nitrogen, are a comparatively late group of materials, and still in development. They posses an unusual combination of strength, toughness, corrosion resistance, wear resistance und non magnetizability [1]. The nitrogen is in an interstitial solution. Mn, Cr, Mo and V increase its solubility while Ni and Si are decrease the solubility of nitrogen [2, 3]. The main property of nitrogen is to stabilize the austenitic structure, so that no formation of deformation martensite α' will occur. Material deformation up to 95% was achieved without austenit becoming instable. Nitrogen causes a very low stacking fault energy of around 10 mJ/m^2. It causes also a plane arrangement of dislocations in fcc metals. The onset of twinning is shifted to lower deformations. A severe cold deformation leads to a completely twinned microstructure with second order twins in many directions.

Uggowitzer [4] describes how nitrogen alloyed austenitic steel achieved very high tensile strength of 3380 MPa. To develop austenitic structure with high strength, nitrogen must be in solution. Under this condition the microstructure of X5 Cr Mn 18 18 with 0.6% N (P900) was changed by adequate heat as well as mechanical treatment. Tensile yield strength of 1000 MPa can be achieved with a grain size of 10 µm. Then the fine grain steel was subjected to a cold

deformation up to 88% by wire drawing. The measured strength was as high as 3000 MPa. The maximum of 3380 MPa was reached after an additional aging at 500 °C for 10 minutes. It has been shown that these steels can be treated to achieve very high strengths.

The aim of this work is to study the behaviour of nitrogen alloyed austenitic steels during high dynamic loadings. Reference [5] describes tests with an increase of strain rate from 10^{-3} s^{-1} to 10^{-1} s^{-1}. This small step increased the yield point from 680 MPa to 800 MPa. A study of the dynamic behaviour of P900 by split-Hopkinson-pressure-bar (SHPB) is described in [6, 7]. It can be shown that the material behaviour is strongly influenced by strain rate even after high workhardening. Under high dynamic loadings, the compression strength was increased up to 800 MPa compared to quasistatic loadings. P900N (0.85% N) with predeformations up to 540 HV30 was studied in [8]. At a hardness of 540 HV30 the dynamic compression strength amounts 2600 MPa. Nitrogen in solution augments internal friction. The increased internal friction leads to a very high strain rate sensitivity. For that reason these steels can be considered as candidates for hypervelocity impacts.

EXPERIMENTAL SETUP

Ballistic tests were performed in a lightgas gun with a velocity of 2500 m/s. The lancier tube is 6m long and possess a caliber diameter of 30 mm. In the hyperballistic tunnel was a pressure of 420 Torr. Rods (a tungsten sintered alloy) geometry was ϕ 4 mm x 57.5 mm (L/D = 14.375). Its mass 12.7 g. It possess a tensile strength of 1300 MPa and ductility up to 10%. Sabot and projectil mass amounts to 65.5 g in all.

Quasistatic compression tests have been performed on a universal testing machine. Dynamic compression tests were performed using a split-Hopkinson-pressur-bar (SHPB) setup. The bars are of maragin steel with a diameter and length of 20 mm and 1000 mm respectively. Striker bars were flat ended to achieve short rise times of the incident signals. Specimens were lubricated with a lubricant on carbon basis that minimizes the effect of friction during testing.

To determine hardness the Vickers test was used. It can be defined as indentation hardness testing that involves forcing a diamond indenter of square-based pyramidal geometry with face angles of 136° into the surface of the test material. The test consists of applying a constant load, usually 10 kg, 30 kg and 60 kg, for a specified time of 30 s [9]. Parameters used for the hardness test of table 3 and 4 are 30 kg and 30 s.

MATERIALS

A nitrogen alloyed steel named X8 Cr Mn N 18 18 (ASTM A289, W.-Nr. 1.3816)[1] was studied. This steel is also well known as P900. Its chemical composition is shown in table 1.

The nitrogen alloyed steel was workhardened to a hardness of 380 HV30. In the solution (initial) annealed status these steels possess a hardness of 280 HV30. This steel was compared with a classical martensitic armor steel named 30 Cr Ni Mo 5 5 (W.-Nr.: 1.6568). The hardness was in the mean 520 HV30. Its chemical composition is shown in table 2.

---

[1] Producer: VSG, Energie- und Schmiedetechnik GmbH, Westendstr. 15, D-45143 Essen

Table 1: Chemical composition [%] of studied P900

C	Si	Mn	P	S	Cr	N
0.033	0.3	19.02	0.031	0.001	18.43	0.62

Table 2: Chemical composition [%] of the armor steel

C	Si	Mn	Cr	Mo	Ni	P	S
0.295	0.25	0.65	1.35	0.4	1.4	<0.01	<0.004

Macroscopic properties of classical armor steels developed using heat treatment while macroscopic properties of nitrogen alloyed steels depend on workhardening.

EXPERIMENTAL RESULTS

Compression tests

Quasistatic and dynamic true stress-strain curves are determined in the uniaxial compression state at room temperatures.

Figure 1 shows the results obtained for the P900 and the armor steel. The compression yield strength of the nitrogen alloyed austenitic steel is compared to the compression yield
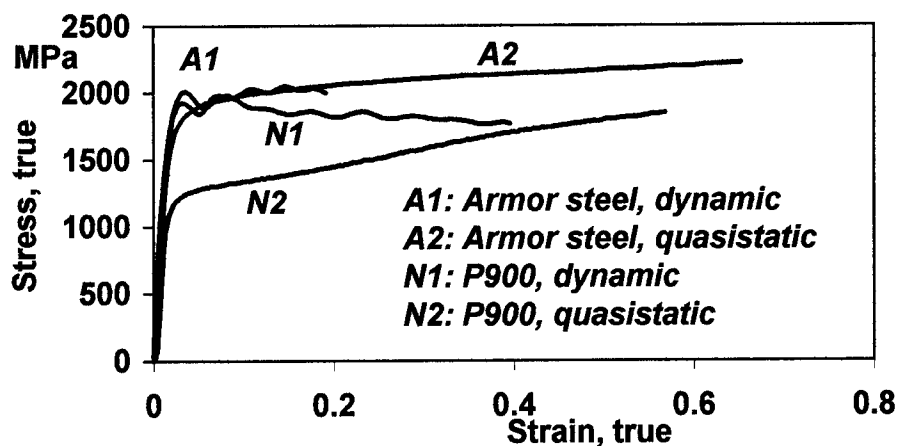
Figure 1: Quasistatic and dynamic true stress-strain compression curves

Figure 1 also shows dynamic compression curves determined by the SHPB. The dynamic compression curves are obtained in an adiabatic condition. Strain rates were 4300 s^{-1} and 3000 s^{-1} for the nitrogen alloyed steel and the armor steel respectively. It is shown that under dynamic conditions, the workhardened nitrogen alloyed steel and the armor steel possess a compression yield strength of the same order. This result demonstrates the high strain rate sensitivity of nitrogen alloyed steels. Strength and hardness are correlated. So a rapid hardening can be also deduced. Another particularity of nitrogen alloyed steels is their high ductility, which is unusual for classical high strength steel. Since these steels are austenitic, they possess a reduced thermal conductivity. Thermal softening occurs and decreases the compression flow curves.

Ballistic results

Figure 2: Semi-infinite target consisting of nitrogen alloyed steel

Figure 3: First plate of the semi-infinite target consisting of classical armor steel

The hypervelocity impact was performed using targets of 100 mm thickness. Since no classical armor plates of 100 mm thickness were available, two plates of 70 mm and 30 mm respectively were combined. For both targets the depth of craters were 73 mm. The ballistic performance of nitrogen alloyed steel predeformed to a hardness of 380 HV30 is equal to a classical armor steel hardened to 520 HV30.

A diametral cross section of the semi-infinite target consisting of nitrogen alloyed steel can be seen in figure 2. The macrostructure shows a conical shaped crater and deflections of the rod near the end of the crater. A high density of microcracks associated partly with fractures is visible along the crater.

Table 3: Vickershardness HV30 around the crater of P900

	2	3	4	5	6	7	8	9	10
Z	384	384	415	442	412	403	385	363	368
Y	387	406	461			439	382	376	363
X	381	394	486			452	427	399	388
W	380	400	472			491	413	408	385
V	380	423				519	423	413	395
U	398	448	509			504	472	390	388
T	398	440	427			505	441	413	379
S	389	439	487			520	447	406	363
R	387	436	487			480	448	396	367
Q	398	436					448	390	362
P	372	402	475			552	475	405	369
O	363	425	491			517	450	400	377
N	376	435	470			470	444	418	377
M	364	413	484			490	440	392	384
L	374	416	451				444	379	363
K	383	450	484				461	399	374
J	366	435	490				474	417	375
I	364	460	499				448	416	382
H	398	465	487				472	439	400
G	392	466	504				467	411	415
F	371	444	492				501	429	390
E	376	433	522				495	439	407
D	389	441	504				484	430	404
C	390	450	515				500	416	389
B	396	470	472				504	456	401
A	408	479					488	450	435

Table 4: Vickershardness HV30 around the crater of armor steel

	1	2	3	4	5	6	7	8	9
O	534	524	546	530			524	522	542
N	539	517	530	523			534	519	539
M	530	537	517	493			528	519	535
L	539	536	542	485			517	539	531
K	545	538	539	542			521	536	537
J	540	530	529	490			501	511	528
I	543	541	509	480			492	510	518
H	544	513	516	502			495	517	505
G	541	523	477	513			480	525	536
F	537	520	481	520			484	523	550
E	518	542	510	539			493	546	544
D	502	516	523	548			510	521	520
C	501	493	533	525			520	509	511
B	497	510	515	520			547	532	518
A	498	504	510	515			546	531	536

A crater shaped like in figure 2 only could be found after hypervelocity impact up to now. Some impacts have been performed at a velocity around 1700 m/s. Under this condition both steels showed, a similarly shaped crater.

Figure 3 shows a diametral cross section of the first plate of the semi-infinite target consisting of classical armor plates. The macrostructure shows a cylindrical shaped crater. To point out changes in the microstructure hardness tests have been performed. On the surface of the target shown in figure 2 squares with a length of 3 mm were drawn. Hardness was measured in the middle of each square. Table 3 shows all measured data.

Lines are marked by letters and columns by numbers. Blanks represent roughly the shape of the crater. Columns which are leaved out are of no importance. The measured data give information about hardness modifications from basic microstructure towards to the border of the crater. It can easily be seen that there is a huge rise in hardness. Dynamic compression tests (figure 1) have shown that a rapid strain hardening occured. The highest hardness value of 552 HV30 was measured near the region where the first deflection happened. This indicates that this region suffered a very high load. As figure 2 shows is this region totally fractured. A zone of 6 mm thickness around the crater is influenced by hypervelocity impact.

Hardness measurements have been performed on the cross section of target consisting of armor steel. The squares drawned on the surface are of 5 mm length, because there were no changes in hardness expected. Table 4 represents the measured data. As it shows there is no significant difference between the basic structure and the region around the crater. No strain hardening happened. This is in good agreement with results obtained by SHPB (figure 1).

The crater volume was estimated for both steels. It amounts to 4.1 cm^3 and 3.3 cm^3 for the armor steel and the nitrogen alloyed steel respectively. This difference could not be found at a lower impact velocity.

MICROSTRUCTURE

Figures 4 and 5 show the microstructure of impacted nitrogen alloyed steel close to the crater. Slip bands in the grains are caused by workhardening. But the density is increased around the crater due to the impact. The microstructure in figure 4 is characterized by an adiabatic shearband which is branched out. It is accompanied by microcracks. All microcracks which can be seen in figure 2 are caused by adiabatic shearbands. Reference 10 shows that workhardened P900 (380 HV30) fractures under dynamic condition around a strain of 40%.

Figure 5 shows the microstructure at the edge of the crater where the heat-affected zone can be seen. The microstructure of the heat-affected zone is only due to recrystallization. Fusing of the steel can be excluded. Grain sizes in this zone are between 2 μm and 4 μm. Paulus [5] describes the condition to get such a fine grained microstructure. At least 1000 °C and a duration not exceeding 0.1 s were necessary.

Figure 6 shows the microstructure around the crater of the armor steel. The white lines are caused by segragation during solidification of the melt and following rolling. They indicate that this region sufferd an enormous shear stress. A lot of adiabatic shear bands partly parallel to the crater can be seen. The heat-affected zone of the armor steel is not suitable to deduce the amount and duration of local heating.
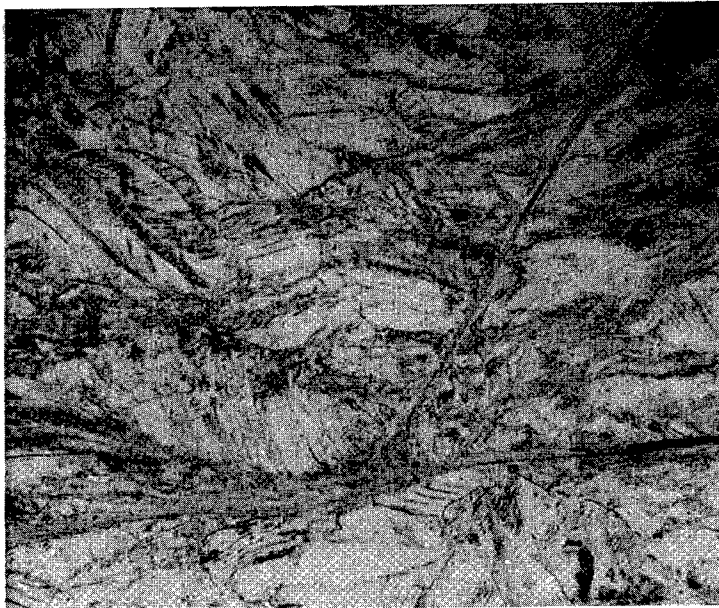
Figure 4: Adiabatic shearbands in nitrogen alloyed steel. x200

Figure 5: Microstructure of nitrogen alloyed steel with heat-affected zone. x200
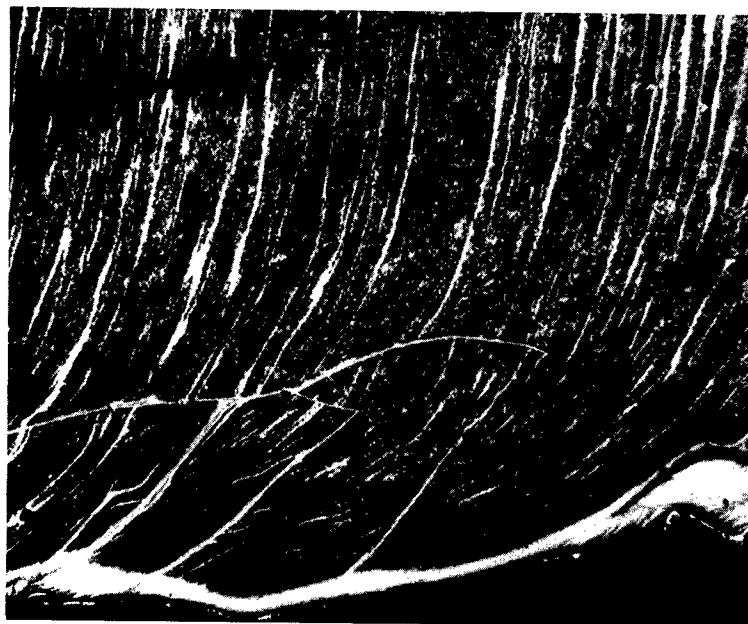
Figure 6: Microstructure of classical armor steel with adiabatic shearbands. x100

SUMMARY

Nitrogen alloyed austenic steel has been well-known because of its work-hardenability to very high strength. Investigations by SHPB showed its very high strain rate sensitivity. This makes this steel a candidate for hypervelocity impact.

The nitrogen alloyed austenitic steel which has been studied was in a workhardened condition. Vickershardness amounts to 380 HV30. Its dynamic behavior was compared to a classical armor steel of Vickershardness 520 HV30.

Dynamic compression tests showed that the strength of both steels are similar though the nitrogen alloyed steel possess lower hardness. A rapid strain hardening of P900 enables this result. The ductility under this condition is considerably high compared to classical armor steel.

Ballistic performance is shown by hypervelocity impacts. The depth of craters were similar for both steels. It was also shown that hardness around the crater of the nitrogen alloyed steel was considerably increased whereas the hardness of the armor steel did not change.

The crater of the nitrogen alloyed steel was slightly conical shaped. Only impacting at 2500 m/s resulted in such a shaped crater.

Further experiments to study hypervelocity behavior of nitrogen alloyed steels also at higher impact velocities are necessary. Tate model analysis will be taken into consideration if more results available.

REFERENCES

1 M. O. Speidel, Uggowitzer P. J., Stickstofflegierte Stähle, Ergebnisse der Werkstoff-Forschung
   Band 4, Thubal-Kain, Zürich, 1991

2 H. K. Feichtinger, Concepts of Nitrogen Solubility, High Nitrogen Steels, HNS 93
   in: Proceedings 3rd Inter. Conference, Kiew, 1993, Ed.: Inst. Met. Physic,
   Academie of Science Ukraine

3 G. Stein, J. Menzel, A. Choudhury, Industrial Manufacture of Massively Nitrogen-Alloyed
   Steels in: Special Melting and Processing Technologies, San Diego, New Jersey: Noyes
   Publications, 1988

4 P. J. Uggowitzer, Festigkeit und Zähigkeit austenitischer Stickstoffstähle, Habilitation,
   ETH Zürich, 1992

5 N. Paulus, Entwicklung von stickstofflegierten austenitischen Stählen höchster Festigkeit,
   Diss. ETH Zürich, Nr.: 10899, Zürich, 1994

6 E. Lach, M. Scharf, Y. Tschamber, Stickstofflegierte austenitische Stähle. 2.Teil:
   Quasistatische und dynamische Eigenschaften von kaltverfestigten stickstofflegierten Stählen am
   Beispiel eines P900, ISL-Report R 129/97, 1997

7 E. Lach, P. Uggowitzer, F. Rondot, Hardening of Nitrogen Alloyed Steels by Shock Waves, in:
   Journal de Physique IV, Eurodymat 97, Les Editions de Physique, Les Ulis, pp 547-552 (1997)

8 A. Lichtenberger, E. Lach, F. Rondot, Dynamical behaviour of very high strength nitrogen alloyed steels
   in: Journal de Physique IV, Eurodymat 97, Les Èditions de Physique, Les Ulis, pp 391-396 (1997)

9 DIN 50133, in: Materialprüfnormen für metallische Werkstoffe, Taschenbuch 19, Beuth Verlag,
   Berlin, 1970

10 A. Lichtenberger, E. Lach, High Plastic Deformation of Nitrogen Alloyed Austenitic Steels under
   Dynamic Compression Loading, Proceedings of Dymat, Technical Meeting Dijon, October, 1998

Short Course Announcement

STRUCTURAL IMPACT

19 - 21 January 2000

Presented by Professor Norman Jones from the University of Liverpool

at

Ashurst Lodge, Southampton, UK

**Organised by
Wessex Institute
of Technology, UK**

**Centre of Excellence
in Engineering
Research and Training**

The objective of this course is to provide participants with an introduction to the response of structures subjected to dynamic loads which produce large inelastic strains. This information is relevant to a broad range of engineering problems for which safety calculations and hazard assessments are required. The topics are relevant to various kinds of dynamic loadings which occur in energy absorbing systems and structural crashworthiness problems as well as the safety and damage of industrial plant under extreme conditions. The topics include a general introduction to the major simplifications and assumptions, dynamic material properties, geometrically similar scaling of experiments and other subjects to provide a sound introduction to the topic.

COURSE OUTLINE

* Dynamic ductile behaviour of beams
* Dynamic ductile behaviour of plates and shells
* Influence of transverse shear and rotary inertia
* Influence of large deflections
* Elementary failure criteria
* Material strain rate sensitivity coefficients.
* Quasi-static behaviour
* Introduction to structural crashworthiness
* Dynamic axial crushing of tubes
* Similitude
* Comments and conclusions

**BOOK NOW
LIMITED PLACES**

For Further Information on this Course

CONTACT

Clare Bridle
Course Secretariat
STRUCTURAL IMPACT (1490)
Wessex Institute of
Technology (WIT),
Ashurst Lodge, Ashurst
Southampton,
SO40 7AA, UK

Tel: 44 (0) 238 029 3223
Fax: 44 (0) 238 029 2853
EMail: cbridle@wessex.ac.uk

VISIT OUR WEBSITE AT: www.wessex.ac.uk

WESSEX INSTITUTE OF TECHNOLOGY
Centre of Excellence in Engineering Research and Training

INTERNATIONAL JOURNAL OF IMPACT ENGINEERING

AIMS AND SCOPE

The *International Journal of Impact Engineering* exists for the publication of original research work concerned with the response of structures and bodies to dynamic loads arising from exposure to blast collision or other impact events. The topics encompassed by the journal include the elastic and plastic response of structures and bodies to impact and blast loading, terminal ballistics, vehicle crashworthiness, containment and other processes and phenomena in which effects due to impact predominate, such as explosive welding. In addition, related matters such as research into fire hazards in association with impact loads will be included. Every paper accepted for publication is strictly refereed and assessed for its contribution to the understanding of impact phenomena or the insight gained for engineering design in areas of high rate loading.

Papers whose concerns are only in the fields of mathematics, materials science or computation are not requested. Similarly, papers whose contents are purely descriptive will not be accepted.

This journal should be of interest to engineers, designers and research workers in the fields of structural crashworthiness, energy-absorbing systems, structural failure, hazard assessments and safety calculations which involve impact loadings. Thus, papers in this journal will be of interest to aeronautical engineers, civil engineers, mechanical engineers, naval architects, nuclear engineers, ocean engineers, offshore engineers, transportation engineers and workers in other branches of engineering and science who are involved in impact loading of various kinds.

INSTRUCTIONS TO AUTHORS

1. The journal is devoted to original papers of high standard which contribute to the understanding of impact in various branches of engineering, and papers offered for publication are refereed and assessed by reference to these aims.

2. The language of the journal is English; however, contributions from all parts of the world are encouraged. Authors are solely responsible for the factual accuracy of their papers.

3. Two copies of the manuscript and figures, etc. of any paper which is offered for publication should be sent to the Editor-in-Chief:

Professor Norman Jones
Department of Engineering
(Mechanical Engineering)
The University of Liverpool
Brownlow Hill
Liverpool L69 3GH, U.K.

4. Only papers not previously published will be accepted and authors must agree not to publish elsewhere a paper submitted to, and accepted by, the journal.

5. Papers of a length exceeding thirty A4 pages (manuscript and figures) will not be acceptable unless a prior arrangement has been made with the Editor.

Authors should examine previous issues of the journal as a general guide to the preparation of papers.